

**A Thesis Submitted for the Degree of PhD at the University of Warwick**

**Permanent WRAP URL:**

<http://wrap.warwick.ac.uk/152946>

**Copyright and reuse:**

This thesis is made available online and is protected by original copyright.

Please scroll down to view the document itself.

Please refer to the repository record for this item for information to help you to cite it.

Our policy information is available from the repository home page.

For more information, please contact the WRAP Team at: [wrap@warwick.ac.uk](mailto:wrap@warwick.ac.uk)

# **Understanding Natural and Synthetic Ice-active Materials to Aid in the Development of New Cryoprotective Formulations**

*by*

**Alice Elizabeth Roisin Fayer**

A thesis submitted to the University of Warwick in partial fulfilment of  
the requirements for the degree of

**Doctor of Philosophy**



University of Warwick, Department of Chemistry

October 2020

# Table of contents

---

<b>Chapters and Sections .....</b>	<b>iii</b>
<b>List of Figures.....</b>	<b>ix</b>
<b>List of Schemes .....</b>	<b>xxx</b>
<b>List of Tables .....</b>	<b>xxx</b>
<b>List of Equations .....</b>	<b>xxxi</b>
<b>Abbreviations .....</b>	<b>xxxii</b>
<b>Acknowledgements.....</b>	<b>xxxvii</b>
<b>Declaration.....</b>	<b>x1</b>
<b>Abstract.....</b>	<b>x1ii</b>

# Chapters and Sections

## Chapter 1

---

<b>Introduction</b> .....	1
1.1 Water and Ice.....	3
1.2 Ice Nucleation.....	10
1.3 Materials which Affect Ice .....	13
1.3.1 Ice Nucleating Particles .....	15
1.3.2 Antifreeze Glycoproteins.....	18
1.3.3 Antifreeze Proteins .....	20
1.4 Mechanisms of Action.....	22
1.4.1 Dynamic Ice Shaping.....	23
1.4.2 Ice Recrystallisation Inhibition.....	25
1.4.3 Thermal Hysteresis .....	26
1.4.4 Ice-binding .....	28
1.4.5 Synthetic AF(G)P Mimics .....	33
1.5 Cold storage of biologics.....	38
1.6 Summary.....	41
1.7 Project Aims and Overview.....	42
1.8 Thesis Summary .....	43
1.9 References .....	45

## Chapter 2

---

<b>Macromolecular Cryoprotectants; Polymer Formulations for Storage of Biological Materials</b> .....	62
2.1 Declarations.....	63
2.2 Chapter Abstract.....	63
2.3 Introduction .....	65
2.3.1 Storage and Transport of Proteins and Cells.....	65
2.3.2 Stability of Biological Materials in Ice .....	65
2.3.3 Freezing Challenges .....	66
2.3.4 Protein Storage .....	67
2.3.4.1 Proteins Studied Here.....	69
2.3.5 Cell Storage.....	71
2.3.5.1 Cells Studied Here.....	71



2.4	Terminology.....	73
2.5	Chapter Aims .....	74
2.6	Results and Discussion.....	75
	2.6.1 Formulation Design.....	75
	2.6.2 Protein Expression and Purification.....	78
	2.6.3 Cryopreservation of Proteins.....	81
	2.6.3.1 Green Fluorescent Protein.....	81
	2.6.3.2 Insulin.....	84
	2.6.3.3 Lactate Dehydrogenase .....	85
	2.6.4 Cryopreservation of Bacteria .....	89
	2.6.4.1 <i>E. coli</i> .....	91
	2.6.4.2 <i>M. smegmatis</i> and <i>B. subtilis</i> .....	96
	2.6.4.3 Formulation Modification: Molecular Weights .....	98
	2.6.4.4 Formulation Modification: Hydrophilic polymer.....	101
2.7	Conclusion .....	105
2.8	Experimental .....	107
	2.8.1 Materials.....	107
	2.8.2 Physical and Analytical Methods.....	107
	2.8.3 Procedures .....	108
	2.8.3.1 Protein Expression and Purification.....	108
	2.8.3.2 Ice Recrystallisation Inhibition ‘Splat’ Assay.....	110
	2.8.3.3 Green Fluorescent Protein Stability Assay .....	110
	2.8.3.4 Insulin Freeze/Thaw Assay .....	111
	2.8.3.5 Lactate Dehydrogenase Activity Assay .....	111
	2.8.3.6 Bacteria Freeze/Thaw Assay.....	112
	2.8.3.7 <i>Lactobacillus delbrueckii subsp. bulgaricus</i> F/T Assay .....	112
	2.8.3.8 Cryoprotectant Toxicity on Bacteria.....	112
	2.8.3.9 OD <sub>600</sub> Turbidity Measurements.....	113
	2.8.3.10 Live/Dead Bacterial Viability Test .....	113
2.9	References .....	114

## Chapter 3

---

<b>Using X-rays to Monitor Ice Growth and a Comparison to Optical Microscopy Methods</b> .....	123
3.1 Declarations.....	124
3.2 Chapter Abstract.....	124
3.3 Introduction .....	125
3.3.1 Ice Crystal Growth Measurements.....	125
3.3.2 Optical Techniques.....	125
3.3.3 X-ray Techniques .....	129
3.3.4 Polycrystalline Material .....	133
3.3.5 XRD of Ice .....	134
3.3.5.1 Hexagonal Ice.....	135
3.3.5.2 Low Temperature XRD.....	136
3.4 Terminology.....	139
3.5 Chapter Aims .....	140
3.6 Results and Discussion.....	141
3.6.1 Compounds Studied .....	141
3.6.2 IRI Activity as Measured by Splat Assays.....	142
3.6.3 Dynamic Ice Shaping as Measured by Sucrose ‘Sandwich’ Assays... 144	
3.6.4 XRD .....	148
3.6.4.1 Methodology .....	150
3.6.4.2 IRI Activity as Measured by XRD.....	153
3.6.4.3 Kinetics of Ice Crystal Growth .....	155
3.6.4.4 Dynamic Ice Shaping as Measured by XRD.....	160
3.7 Conclusion .....	164
3.8 Experimental .....	166
3.8.1 Materials.....	166
3.8.2 Physical and Analytical Methods.....	166
3.8.3 Procedures .....	167
3.8.3.1 Recombinant Expression of His-AFP111.....	167
3.8.3.2 Recombinant Expression of SNAP-AFP111 .....	168
3.8.3.3 XRD Sample Preparation.....	168
3.8.3.4 XRD Data Analysis.....	168
3.8.3.5 XRD Orientation Analysis .....	168
3.8.3.6 Ice Recrystallisation Inhibition ‘Splat’ Assay.....	168
3.8.3.7 Modified Sucrose ‘Sandwich’ Ice Shaping Assay .....	170

3.9	References .....	171
-----	------------------	-----

## **Chapter 4**

---

	<b>Combined Solid State NMR Dynamics and Ice Recrystallisation Inhibition Activity Measurements of Synthetic and Biological Antifreeze (Macro)molecules .....</b>	<b>177</b>
4.1	Declarations.....	178
4.2	Chapter Abstract.....	178
4.3	Introduction .....	180
	4.3.1 SSNMR Study of Motions in Solids .....	186
	4.3.2 Magic Angle Spinning .....	188
4.4	Chapter Aims .....	190
4.5	Results and Discussion.....	191
	4.5.1 PVA; Chain Length and IRI Activity .....	191
	4.5.2 Optimisation of SSNMR Methods.....	194
	4.5.3 $T_1$ and $T_2$ Relaxation .....	195
	4.5.4 $R_1$ and $R_2$ Relaxation Rate Measurements .....	199
	4.5.5 Spinlock $^1\text{H}$ RD Relaxation Dispersion Measurements.....	205
	4.5.6 2D $^1\text{H}$ - $^1\text{H}$ Exchange Spectroscopy.....	208
	4.5.6.1 Antifreeze Macromolecule:ice Interactions .....	212
	4.5.7 SSNMR of $^1\text{H}$ - $^{13}\text{C}$ Labelled Protein .....	213
4.6	Conclusion .....	216
4.7	Experimental .....	218
	4.7.1 Materials.....	218
	4.7.2 Physical and Analytical Methods.....	218
	4.7.3 Procedures .....	218
	4.7.3.1 Ice Recrystallisation Inhibition ‘Splat’ Assay .....	218
	4.7.3.2 SSNMR .....	219
	4.7.3.2.1 Variable Temperature $^1\text{H}$ Relaxation Experiments ( $R_1$ ) .....	219
	4.7.3.2.2 Variable Temperature $^1\text{H}$ Relaxation Experiments ( $R_2$ ) .....	220
	4.7.3.2.3 Variable Temperature $^1\text{H}$ Relaxation Dispersion ( $R_{1\rho}$ ).....	220
	4.7.3.2.4 2D $^1\text{H}$ - $^1\text{H}$ Exchange Spectroscopy .....	220
4.8	References .....	221

## Chapter 5

---

<b>Discovering Non-Proteogenic and Non-Polymeric Nucleating Materials</b> .....	227
5.1 Declarations.....	228
5.2 Chapter Abstract.....	228
5.3 Introduction .....	230
5.3.1 Importance of Ice Nucleation.....	230
5.3.2 Heterogeneous Nucleation .....	230
5.3.3 Good Heterogeneous Ice Nucleators.....	231
5.3.4 How Do Nucleators Work?.....	236
5.3.5 Experimental Methods Used to Study Ice Nucleation .....	239
5.3.6 Finding New Nucleators .....	241
5.4 Chapter Aims .....	245
5.5 Results and Discussion.....	246
5.5.1 Samples Tested.....	246
5.5.2 Comparison of Experimental Methods .....	248
5.5.2.1 Calorimetry-based Methods .....	248
5.5.2.2 Microscopy-based Methods .....	250
5.5.3 Metal Organic Frameworks .....	256
5.5.4 Lignins .....	258
5.5.4.1 Effect of Concentration.....	261
5.5.4.2 Effect of Sample Preparation .....	264
5.5.4.3 Effect of Cooling Rate .....	266
5.6 Conclusion .....	268
5.7 Experimental .....	270
5.7.1 Materials.....	270
5.7.2 Physical and Analytical Methods.....	270
5.7.3 Procedures .....	271
5.7.3.1 Ice Recrystallisation Inhibition ‘Splat’ Assay.....	271
5.7.3.2 Differential Scanning Calorimetry .....	271
5.7.3.3 Cryostage Nucleation Drop Assay .....	271
5.7.3.4 $\mu$ L-NIPI-based Drop Assay .....	272
5.8 References .....	273

## **Chapter 6**

---

<b>Conclusions</b> .....	280
6.1 Overview of Thesis .....	281
6.1 Final Remarks .....	285

## **Appendices**

---

<b>Appendix A - Supplementary Information</b> .....	286
A.1 Cryopreservation of <i>Lactobacillus delbrueckii subsp. bulgaricus</i> .....	287
<b>Appendix B – First Author Publications</b> .....	288
<b>Curriculum Vitae</b> .....	308
<b>Contributions to Published Work</b> .....	312

# List of Figures

## Chapter 1

---

**Figure 1.1.** A) Phase diagram of stable phases of ice and liquid H<sub>2</sub>O from 0 to 400 K over a range of pressures. Including phase boundaries (solid lines), extrapolations of boundaries based on experimental results (dashed lines) and excluding metastable phases. Dotted lines in the negative pressure regime are based on simulations. The different phases of ice are labelled using Roman numerals corresponding to their order of discovery; B) The range of structures of other crystalline ice phases. These are grouped into proton-disordered/ordered pairs (for those that the ordered form has been discovered) as they have the same lattice structure. Adapted from Loerting *et al.* (Comm. Chem., 2020) and Salzmann *et al.* (Phys. Chem. Chem. Phys., 2011).<sup>23,29</sup> .....6

**Figure 1.2.** A) Structure of hexagonal ice, showing one water molecule within each polyhedral joined by covalent bonds (solid) and hydrogen bonds (dashed). B) Possible configurations for locations of hydrogens within a hexagonal ice crystal; C) The tetrahedral structure forms due to the hydrogen bonding between water molecules. These interactions between water molecules in Ih are highlighted here (blue dotted lines), with the O-O-O angle (109.47 °) and average O···O length (2.76 Å) included, as well as the O-H length for free water (0.97 Å) that alters slightly within the Ih tetrahedral structure and the H-O-H angle (104.54 °); D) Hexagonal symmetry in Ih formed by hydrogen bonding in the crystal, which gives rise to the sixfold symmetry observed in snowflakes, with prism plane and basal plane highlighted. Red = oxygen, white = hydrogen. Adapted from Salzmann *et al.* (Phys. Chem. Chem. Phys., 2011)<sup>29</sup> and Brini *et al.* (Chem. Rev., 2017).<sup>23</sup> .....8

**Figure 1.3.** Experimental and calculated X-ray diffraction patterns for hexagonal and cubic ice; A) Experimental result for water droplets frozen (median freezing temperature = -41.3 °C) recorded at -100 °C; B) Simulated Ih pattern; C) Simulated Ic pattern; D) Literature diffraction patterns of amorphous ice; E)

Rietveld refinement of the experimental pattern in A, assuming a mixture of Ic and Ih. Malkin <i>et al.</i> , (Proc. Natl. Acad. Sci., 2012). <sup>54</sup> .....	9
<b>Figure 1.4.</b> Examples of reaction coordinates for the ice nucleation process at A) 0 °C; B) -40 °C; C) 20 °C. ....	11
<b>Figure 1.5.</b> A) Schematic describing the ice nucleation process as explained by classical nucleation theory. According to CNT, a critical nuclei can have a 1 nm radius or longer; B) Critical radius size (nm) required for ice nucleation as a function of temperature. ....	12
<b>Figure 1.6.</b> Schematic of Ostwald ripening in ice .....	12
<b>Figure 1.7.</b> Representation of changes in state for H <sub>2</sub> O and the various materials that are ice-active. *Antifreeze (glyco)proteins (AF(G)Ps) and their synthetic mimics also have other properties (thermal hysteresis (TH)) not shown here. INP = ice nucleating particle. ....	14
<b>Figure 1.8.</b> Examples of the effect of protein length on freezing temperature and freezing efficiency ( $\Delta T_f$ ). A) Ice nucleation temperature ( $T_n$ ) as a function of INP monomer protein length, CNT predicted $T_n$ (blue) consistent with a cooling rate of 1.0 K.min <sup>-1</sup> and experimentally obtained $T_n$ (red) for the INP monomer from <i>P. syringae</i> ; B) Modelled $\Delta T_f$ of $T_m$ INP (red closed) (a modelled protein based on stacking multiple ice-binding loops from the antifreeze protein <i>Tenebrio molitor</i> with fragments of an alcohol INP) compared to $\Delta T_f$ alcohol INP (black circle), $\Delta T_f$ <i>P. syringae</i> INP (blue), $\Delta T_f$ $T_m$ AFP (green triangle) and $\Delta T_f$ $T_m$ INP with the same number of binding sites as $T_m$ AFP (red open square). Inset indicates potential binding of $T_m$ INP (teal) to critical ice nucleus (grey) by an anchored clathrate (orange) (further details in 1.4.4) from three angles. Adapted from Qiu <i>et al.</i> (J. Am. Chem. Soc., 2019). <sup>112</sup> .....	16
<b>Figure 1.9.</b> A) Structure of AFGP repeat unit. AFGPs with four repeat units and molecular weight of 2.6 kDa are AFGP8, and those with molecular weight of 33.7 kDa are AFGP1. Molecular weights of AFGP2-7 are between these two values; <sup>129</sup> B) 25 lowest energy structures calculated for a synthetic AFGP3 using NMR-based constraints. (Peptide backbone = purple, carbohydrate moieties = blue); C) Synthetic AFGP3 structure produced from the closest to average of 25 best calculated models. (methyl carbon = yellow, carbohydrate carbon = white, peptide side chain carbon (bar methyl carbon) = grey, nitrogen	

= blue, oxygen = red). Adapted from Tachibana *et al.*, (Angew. Chemie. Int. Ed, 2004).<sup>130</sup> ..... 19

**Figure 1.10.** Schematic of the dynamic ice shaping process. A) Pure water crystal morphology over time; B) Morphology modification over time, due to binding of AF(G)Ps to the prism plane. Scale bar = 100  $\mu\text{m}$ . ..... 24

**Figure 1.11.** Example of micrographs of nucleated ice crystals obtained from a splat recrystallisation assay before and after 30 minutes annealing, and the difference in crystal size as inhibitor potency increases. Approximate crystal diameter at t=0 minutes: 10-20  $\mu\text{m}$ . Large crystal diameter at t=20 minutes: > 100  $\mu\text{m}$ . Scale bar = 100  $\mu\text{m}$ . ..... 26

**Figure 1.12.** Cartoon depicting thermal hysteresis effect of AF(G)Ps on ice crystal growth. Upon addition of AF(G)Ps, ice crystal growth is suppressed within the TH gap, with growth occurring post the hysteresis freezing point. TH is calculated as the difference between  $T_f$  and  $T_m$ . ..... 27

**Figure 1.13.** Schematic depicting the adsorption-inhibition mechanism (step-pinning model) of ice growth and formation of convex ridges between proteins. As the temperature decreases the curvature of the ice crystals between bound AF(G)Ps grows. The smaller the spacing between the adsorbed proteins, the lower the temperature required for ice propagation due to the increased curvature. This model (and related models including the kinetic pinning model) relate to the size and shapes of proteins involved.<sup>200</sup> ..... 29

**Figure 1.14.** The differing possible mechanisms of action for PVA and AFGP. A) AFGP binding via hydrophobic interactions. Hypothesis supported by work from Mochizuki *et al.* showing the binding is due to hydrophobic interactions between  $\text{CH}_3$  groups (0.93 nm between neighbours) and the primary prismatic face of ice where twice the lattice distance is  $\sim 0.91$  nm; B) PVA interacting with ice via hydrogen bonds. Hypothesis supported by work from Naullage *et al.* where they show the OH-OH distance in PVA highlighted (\*) as 2.92  $\text{\AA}$  (this distance when between 4 groups is 7.46  $\text{\AA}$ ), and the distance between O-O in the primary prismatic plane of ice parallel to the c-axis as 2.70  $\text{\AA}$ .<sup>209</sup> C) Example binding configuration of AFGP8 to the primary prismatic plane. (Orange and green spheres = methyl groups bound); D) Side and front views of PVA bound to ice. Once PVA binds ice, the PVA adopts an isotactic configuration, where all the methylene groups orient in the same direction. The



polymer hydrocarbon backbone lies along the prismatic plane, parallel to the c-axis. Adapted from Mochizuki <i>et al.</i> , (J. Am. Chem. Soc., 2018) and Naullage <i>et al.</i> , (J. Phys. Chem. C, 2017). <sup>164,209</sup> .....	31
<b>Figure 1.15.</b> Chemical structure of PVA.....	34
<b>Figure 1.16.</b> Schematic representations of AFP ice-binding. A) Hypothesis for beneficial interactions of a monomeric AFP compared to that of various multimeric AFP constructs with ice. Adapted from Wilkins (PhD thesis, University of Warwick, 2019); <sup>249</sup> B) Schematic representation of a dendrimer-linked AFPIII (DLTIII) binding ice obtained by Davies <i>et al.</i> <sup>214</sup> First DLTIII binding a single ice crystal via its ice-binding site, IBS (purple binds pyramidal plane, blue binds prism plane). Ice recrystallisation may then occur and DLTIII will simultaneously bind several ice crystals. ....	35
<b>Figure 1.17.</b> Self-assembly of safranin-O. Side and front view of a stack of seven safranin-O molecules. Adapted from Drori <i>et al.</i> , (J. Am. Chem. Soc., 2016). <sup>254</sup> .....	37
<b>Figure 1.18</b> Summary of range of activities observed for different classes of IRI active compounds. It is important to note that the size indication is based on the static 30 minute measurement, and that in all cases the ice crystals keep growing, thus is a snapshot of a rate of growth. Grain size is recorded after 30 minutes annealing at -8 °C. Adapted from Biggs <i>et al.</i> (Macromol. Biosci., 2019) <sup>171</sup>	38
<b>Figure 1.19.</b> Schematic of cryopreservation cold chain workflow and how it is susceptible to variability and thus error. ....	39

## Chapter 2

---

<b>Figure 2.1.</b> Morphology modification over time, due to binding of AF(G)Ps to the prism plane. Scale bar = 100 µm.....	67
<b>Figure 2.2.</b> Effect of freezing and thawing (FT) gold nanoparticle (AuNP) solutions, with a decrease in absorbance at 520 nm represented by a colour change (pink to blue) indicating nanoparticle aggregation. A) AuNP before (black) and post FT (red); B) UV-Vis spectra after FT in the presence of 6.8 kDa PVA (black)	

and 4 kDa PEG (blue). [Polymer] = 10 mg.mL <sup>-1</sup> . Adapted from Mitchell <i>et al.</i> (Sci. Rep., 2015). <sup>59</sup> .....	68
<b>Figure 2.3.</b> Proteins used in this work to study their viability after cold storage in different cryoprotectants. A) Recombinant Green fluorescent protein (53.8 kDa); B) Insulin (5.8 kDa); C) Lactate dehydrogenase (37.7 kDa). Structures not shown at the same scale. (Structures “1GFL”, “3I40” and “5W8L” from the protein data bank). <sup>60–62</sup> .....	69
<b>Figure 2.4.</b> Schematic of how aggregation occurs via interfacial stress between the ice:liquid interface, leading to inactive proteins. ....	70
<b>Figure 2.5.</b> The three bacteria strains used and their corresponding cell wall structure; A) Gram-negative <i>E. coli</i> ; B) Gram-positive <i>B. subtilis</i> ; C) Mycobacterium <i>M. smegmatis</i> . SEM scale bars are 1 μm. Adapted from Deol <i>et al.</i> (J. Bacteriol., 2005), Li <i>et al.</i> (Microbiol. Biotechnol., 2010) and Prince <i>et al.</i> (Sci. Rep., 2016). <sup>101–103</sup> .....	72
<b>Figure 2.6.</b> Structures of compounds used as cryoprotectants or in cryoprotective formulations in this work. ....	75
<b>Figure 2.7.</b> IRI activity of macromolecules used in this work; A) Cryomicrographs of ice wafers grown in the presence of 100 mg.mL <sup>-1</sup> PEG + 1 mg.mL <sup>-1</sup> PVA, 1 mg.mL <sup>-1</sup> PVA, 100 mg.mL <sup>-1</sup> PEG, 1 mg.mL <sup>-1</sup> AFPIII, 50 mg.mL <sup>-1</sup> polyampholyte, and PBS control. Scale bar = 100 μm; B) Example ImageJ analysis of a sample, including i) various tools available to use to enhance visualisation of grain boundaries for crystal counting and ii) example photo taken during a splat assay, explained in 2.8.3.2, which then can be converted to greyscale and the contrast enhanced, as well as magnified to enable ease of measurement; C) mean largest grain size (as % of PBS) over a range of concentrations for protein (black) and synthetic mimic PVA (red) compared to PEG (blue); D) Mean grain size (as % of PBS grain size) of all macromolecules tested in A. *PEG (100 mg.mL <sup>-1</sup> ) appears to show IRI activity here, however this is a colligative effect caused at this high concentration. ....	77
<b>Figure 2.8.</b> Characterisation of AFPIII expression in <i>E. coli</i> . A) SDS-PAGE gel analysis of nickel affinity chromatography purified AFPIII (lane 2) and FLPC purified AFPIII (lane 3) compared to Prism Ultra Protein Ladder (lane 1); B) Full-length Western blot image of AFPIII expression. The numbers on the left represent the molecular mass in kilodaltons. ....	79

- Figure 2.9.** Characterisation of GFP expression in *E. coli*. A) SDS-PAGE gel analysis of nickel affinity chromatography purified GFP compared to Prism Ultra Protein Ladder (lane 1) highlighting GFP and higher oligomer expression; B) Full-length Western blot images of GFP expression. The numbers on the left represent the molecular mass in kilodaltons. ....80
- Figure 2.10.** Schematic of cryopreservation procedures for proteins. Analysis of freeze/thawed samples either *via* dynamic light scattering or fluorescence spectroscopy. Data output represented as example graphs of fluorescence retained after FT cycles and potential hydrodynamic radii sizes. ....81
- Figure 2.11.** Normalised fluorescence recovery of GFP over 4 freeze (-20 °C)/ thaw (25 °C) cycles with either no added CPA (black) or in the presence of 3 polymer formulations; [PVA] = 1 mg.mL<sup>-1</sup>; [PEG] = 100 mg.mL<sup>-1</sup>; [PEG/PVA] = 100 + 1 mg.mL<sup>-1</sup>. First measurement is before freezing, then consecutive freeze/thaw cycles. 100 % fluorescence retained corresponds to the highest fluorescence for individual samples normalised to 100 % for ease of comparison. ....82
- Figure 2.12.** Comparison of cryoprotective activity of PVA at two different molecular weights. Fluorescence recovery of GFP after freeze (-20 °C)/ thaw (25 °C) in A) 10 kDa PVA and B) 23 kDa PVA; All solutions containing 100 mg.mL<sup>-1</sup> PEG + [PVA] indicated in the insert. ....83
- Figure 2.13.** Insulin recovery after 6 and 12 FT cycles. A) DLS curves of insulin before (solid) and after (dashed) 12 freeze/thaw cycles. Black = insulin only, Red = insulin + PVA, Green = + 2 kDa PEG + PVA, Blue = + 4 kDa PEG + PVA. In all cases [PEG] = 100 mg.mL<sup>-1</sup>; [PVA] = 1 mg.mL<sup>-1</sup>. B) Average size of insulin aggregates after 6 or 12 FT cycles stored in PVA alone, PVA + 2 kDa PEG and PVA + 4 kDa PEG compared to that of all before freezing (0 FT cycles). ....84
- Figure 2.14.** Insulin recovery after A) heat stress and B) agitation stress. A) DLS curves of insulin before (solid) and after (dashed) heating to 90 °C for 30 minutes; B) DLS curves of insulin before (solid) and after (dashed) shaking at 300 RPM for 3 hours. Black = insulin only, Red = Insulin + PVA, Green = + 2 kDa PEG + PVA, Blue = + 4 kDa PEG + PVA. In all cases [PEG] = 100 mg.mL<sup>-1</sup>, [PVA] = 1 mg.mL<sup>-1</sup> .....85

- Figure 2.15.** Schematic of cryopreservation protocol for monitoring LDH activity. Analysis of freeze/thawed samples either via absorbance spectroscopy. Complete NADH conversion indicated by a complete loss of absorbance. ..86
- Figure 2.16.** Optimisation of cryopreservation protocol of LDH. A) LDH activity after a range of FT cycles recorded by catalysis of NADH to NAD<sup>+</sup> compared to controls of NADH (orange) and pyruvate (pink) alone; B) LDH activity after storage in in glycerol at a range of concentrations (0.875-50 %) recorded by catalysis of NADH to NAD<sup>+</sup>, observed by a decrease in absorbance, compared to a no CPA control (0 %, grey) and unfrozen LDH (yellow).....87
- Figure 2.17.** LDH activity in the presence of indicated cryoprotectants after FT cycles and storage. A) 7 FT cycles; B) 24 hours storage at -20 °C; C) 1 week storage at -20 °C; D) 1 month storage at -20 °C. Recorded by catalysis of NADH to NAD<sup>+</sup>, observed by a decrease in absorbance, compared to a no CPA control (black) and a no freeze control (grey). All samples were plunge frozen at -196 °C and thawed at 25 °C. In all cases [PEG] = 100 mg.mL<sup>-1</sup>, [PVA] = 1 mg.mL<sup>-1</sup>, [Glycerol] = 25 wt %. .....88
- Figure 2.18.** Waterfall plot of hydrodynamic radius of LDH stored in A) PBS (no cryoprotectant) and B) PEG/PVA, over 7 freeze (-196 °C) thaw (25 °C) cycles. ....89
- Figure 2.19.** Schematic of the concept behind the protocol for the bacteria freeze/thaw assay performed. ....90
- Figure 2.20.** Recovered colonies of *E. coli* after overnight incubation with cryoprotectants. Concentrations of cryoprotectants; [PVA] = 1 mg.mL<sup>-1</sup>; [PEG] = 100 mg.mL<sup>-1</sup>; [PEG/PVA] = 100 + 1 mg.mL<sup>-1</sup>; [polyampholyte] = 50 mg.mL<sup>-1</sup>. Control is LB media alone. ....91
- Figure 2.21.** *E. coli* growth profiles after 7 freeze/thaw cycles then inoculation into LB media compared to a growth profile of unfrozen *E. coli*. A) Freezing at -196 °C; B) Freezing at -20 °C. Concentrations of cryoprotectants; [Glycerol] = 25 wt %; [AFPIII] = 1 mg.mL<sup>-1</sup>; [PEG/PVA] = 100 + 1 mg.mL<sup>-1</sup>; [PEG] = 100 mg.mL<sup>-1</sup>. ....92
- Figure 2.22.** Recovered colonies of *E. coli* after 7 freeze (-196 °C) thaw (20 °C) cycles. Concentrations of cryoprotectants; [Glycerol] = 25 wt %; [AFPIII] = 1 mg.mL<sup>-1</sup>; [PVA] = 1 mg.mL<sup>-1</sup>; [PEG/AFPIII] = 100 + 0.01 mg.mL<sup>-1</sup>; [PEG/PVA] =

100 + 1 mg.mL<sup>-1</sup>; [polyampholyte] = 50 mg.mL<sup>-1</sup>). Control is LB media alone.  
 .....93

**Figure 2.23.** Live/dead viability testing on *E. coli* immediately after freeze/thaw cycles. A) Percentage of green (intact membrane) bacteria determined by confocal microscopy (ratio of live cell membranes to total cell membranes); B-D) Live/dead micrographs; B) PBS control; C) 25 % glycerol; D) PEG/PVA. [PEG/PVA] = 100 + 1 mg.mL<sup>-1</sup> respectively. Error bars represent S.D. from 6 repeats. Scale bar = 10 μm. ....94

**Figure 2.24.** Recovered colonies of *E. coli* after freezing at -196 °C and storage at -20 °C for 1 week (red) or 1 month (green). Concentrations of cryoprotectants; [Glycerol] = 25 wt %; [PEG/PVA] = 100 + 1.0 mg.mL<sup>-1</sup>. Control is LB media alone. ....95

**Figure 2.25.** Cell growth profiles of *M. smegmatis* after 7 freeze (-196 °C) thaw (20 °C) cycles with the indicated cryoprotectants followed by inoculation into LB media. Different starting culture volumes (A - D) are compared. A) Starting culture = 1 μL, B) starting culture = 5 μL, C) starting culture 10 = μL, D) starting culture = 20 μL. ....96

**Figure 2.26.** Cell growth curves of *B. subtilis* (5 μL starting culture) after 7 freeze (-196 °C) thaw (20 °C) cycles with the indicated cryoprotectants then inoculation into LB media. ....97

**Figure 2.27.** Normalised cell recovery for 3 different bacteria upon addition of different cryoprotectants after 7 freeze (-196 °C) thaw (20 °C) cycles, (red = PBS, blue = glycerol, black = PEG/PVA), serial dilution and growth on ampicillin plates at 37 °C overnight. Values obtained are normalised to themselves. [Glycerol] = 25 wt %; [PEG] = 100 mg.mL<sup>-1</sup>; [PEG/PVA] = 100 + 1 mg.mL<sup>-1</sup>. ....97

**Figure 2.28.** Cell growth profiles of *E. coli* with the indicated molecular weight PVAs in combination with different molecular weight PEGs (200 Da – 8 kDa) after 7 freeze (-196 °C) thaw (20 °C) cycles then inoculation into LB media. [PEG] = 100 mg.mL<sup>-1</sup>; [PVA] = 1 mg.mL<sup>-1</sup>. ....99

**Figure 2.29.** Effect of varying PVA concentration on cell recovery. Recovered colonies of *E. coli* after incubation with different concentrations of 4 kDa PEG and 10 kDa PVA after 7 freeze (-196 °C) thaw (20 °C) cycles. [PVA1] = 1 mg.mL<sup>-1</sup>, [PVA10] = 10 mg.mL<sup>-1</sup>, [PEG100] = 100 mg.mL<sup>-1</sup>. .... 100

**Figure 2.30.** A) Effect of varying PEG concentration on number of recovered *E. coli* colonies after 7 freeze (-196 °C) thaw (20 °C) cycles. Control is LB media alone. .... 100

**Figure 2.31.** Structures and IRI activity of hydrophilic polymers used here to compare to that of PEG used in the original polymer formulation; A) Structures; B) MLGS; C) MGS. [Polymer] = 100 mg.mL<sup>-1</sup>. IRI data for HPMC not shown. .... 102

**Figure 2.32.** Recovered colonies of *E. coli* after 7 freeze thaw cycles using formulations consisting of different hydrophilic bulky polymers compared to that of a known cryoprotective formulation (PEG/PVA). A) IRI activity of polymers (red) compared to that of cell recovery (black), HPMC is omitted due to gelation at high concentrations; B) Recovered colonies with (red) and without (black) the addition of IRI active PVA. [Polymer] = 100 mg.mL<sup>-1</sup> except [HPMC] = 10 mg.mL<sup>-1</sup> ..... 103

**Figure 2.33.** Ice crystal morphology upon freezing with different hydrophilic bulky polymers. A-C) 3 different angles for the same samples. [Polymer] = 100 mg.mL<sup>-1</sup> except [HPMC] = 10 mg.mL<sup>-1</sup>. Scale bar = 50 μm. .... 104

## Chapter 3

---

**Figure 3.1.** Optical microscopy analysis of ice recrystallisation. A) Example ice wafer containing 1 mg.mL<sup>-1</sup> 10 kDa PVA in PBS after 30 minutes. An example larger grain (white circle) is shown, which skews results when only ‘largest grain size’ is considered; B) Comparison of MLGS and MGS for some PEG, PVA and AFP III. Concentrations = 1 mg.mL<sup>-1</sup>. Errors are standard deviation. .... 126

**Figure 3.2.** A) Micrographs of ice crystals formed in 45 wt % sucrose over time to enable measurement of ice crystal growth over 120 minutes, a) control solution, b) 60 μg.mL<sup>-1</sup> AFP, c) 140 μg.mL<sup>-1</sup> AFP; B) Example data obtained through calculating mean ice crystal radii,  $r^3$ , in 45 wt % sucrose solutions from the micrographs, a) control solution, b)  $r^3$  in solution containing 60 and 140 μg.mL<sup>-1</sup> AFP, and their associated fits (solid lines), c) temporal development of ice

crystal volume fraction,  $Q$ , of data from a) and b). Adapted from Budke *et al.* (J. Phys. Chem B, 2009).<sup>7</sup> All data obtained at -8 °C. Errors are standard deviation. C) Ice morphology observed in micrographs obtained from sucrose assays; a) pure water, b) in the presence of dilute AFP solution, c) in the presence of high concentration AFP solution. Adapted from Griffith and Yaish (Trends Plant Sci., 2004).<sup>14</sup> ..... 128

**Figure 3.3.** A) Lattice planes and geometry of Bragg reflections in Bragg's Law. (atoms represented in green form the different sets of crystal planes); B) Example idealised diffraction pattern, the Bragg peaks provide the signature of underlying structure Information can be obtained from the peak positions, heights, shapes and areas. Adapted from Sharma *et al.* (Recent Res. Sci. Technol., 2012).<sup>31</sup> ..... 131

**Figure 3.4.** Consumables required and schematic of XRD procedure used here. A) From left to right, 1.0 mm diameter (0.01 mm thick) quartz capillaries, 1 mL syringe, 0.8 x 120 mm needle; B) Samples inserted into capillary, precision required to avoid any air bubbles that could interfere with scattering, then transferred to the cryostage; C) The monochromatic beam hits the crystals in the capillary, those of which that constructively interfere diffract the beam for data collection at the detector. Orientation of ice crystal grains affects the intensity of the diffraction pattern; i) sample with minimum preferred orientation for the (100) plane; ii) sample with increased preferred orientation due to size of grain for the (100) plane. .... 133

**Figure 3.5.** A) Hexagonal unit cell (bold) with 3 axes highlighted ( $a_{\#}$ , blue) from which the Miller indices (shown in brackets) are obtained; B) Calculated X-ray diffraction patterns of hexagonal (black) and cubic (red) ice with associated Miller indices for the crystal planes labelled from 20 – 47 ° (the available range for the setup used here); C) Unit cells for hexagonal ice obtained using various scattering experiments. Adapted from Santra *et al.* (J. Chem. Phys., 2013).<sup>50</sup>C ..... 136

**Figure 3.6.** Structures of compounds studied here with the aim of analysing IRI activity and to gain further understanding of how they affect ice growth. Sizes of materials tested chosen based on previous known IRI activity and length scales are not expected to be of importance. PVA = 10 kDa; AFGP8 = 2.6 kDa; Safranin-O = 350.8 Da; AFPIII = 6.5 kDa; PEG = 4 kDa; Lysozyme = 14.3 kDa; Phenosafranin = 322.8 Da. Average AuNP diameters obtained from TEM

(mean of 100 particles) for SNAP-AFP III@Au <sub>4</sub> = 4.03 ± 1.1 nm and His-AFP III@Au <sub>4</sub> = 4.26 ± 0.9 nm. (Structures AFP III “1KDF” and lysozyme “1GXV” are from the Protein Data Bank).....	141
<b>Figure 3.7.</b> IRI activity of compounds tested here and relative activity of the different types of compounds tested. A) IRI activity as MLGS for proteins tested; B) IRI activity as MLGS for synthetics tested; C) Summary of the range of activities observed here and in the literature for a range of IRI active compounds. Adapted from Biggs <i>et al.</i> , (Macromol. Biosci., 2019). <sup>9</sup> Grain size is recorded after 30 minutes annealing at -8 °C.....	142
<b>Figure 3.8.</b> Optical microscopy ice morphology analysis of IRI active proteins compared to that of Milli-Q H <sub>2</sub> O and a negative control (lysozyme) cooling over time. Scale bars = 100 μm. [AFGP8] = 3 mg.mL <sup>-1</sup> ; [AFP III] = 2.8 mg.mL <sup>-1</sup> ; [Lysozyme] = 3 mg.mL <sup>-1</sup> .....	144
<b>Figure 3.9.</b> Optical microscopy ice morphology analysis of His-AFP III and SNAP-AFP III alone and bound to gold nanoparticles cooling over time. Scale bars = 100 μm. [His-AFP III] = 2.8 mg.mL <sup>-1</sup> ; [His-AFP III@Au <sub>4</sub> ] = 2.3 mg.mL <sup>-1</sup> ; [SNAP-AFP III] = 0.10 mg.mL <sup>-1</sup> ; [SNAP-AFP III@Au <sub>4</sub> ] = 0.13 mg.mL <sup>-1</sup> .....	146
<b>Figure 3.10.</b> Optical microscopy ice morphology analysis of IRI active synthetic compounds tested here compared to that of Milli-Q H <sub>2</sub> O. Scale bars = 100 μm. [Sample] = 1 mg.mL <sup>-1</sup> bar safranin-O; (a) = 0.1 mg.mL <sup>-1</sup> and (b) = 2.5 mg.mL <sup>-1</sup> to visualise how self-assembly of the small molecule affects the DIS. Ice shaping (green tick) or lack of shaping (red cross) indicated.....	147
<b>Figure 3.11.</b> Example waterfall plots of diffraction patterns obtained in this work that are used for kinetic analysis of change in number of crystal orientations over time with expected Ih crystal planes included in black below the plots; A) PVA and B) PEG; Optical micrographs obtained after 30 minutes annealing for C) PVA and D) PEG. All data obtained at -8 °C. [Polymer] = 2.5 mg.mL <sup>-1</sup> .....	150
<b>Figure 3.12.</b> Example 2D detector images for a powder. A) Ag behenate (used to calibrate the sample to detector distance beforehand); B) Example ice measurement; orientations are observed as pixels above the determined background value of 1.5 counts highlighted in semi-transparent band and counted every 0.2 ° over ψ range of 76 – 105 °.....	151



**Figure 3.13.** Example plots used in the quantitative analysis of ice recrystallisation.

A/B) Example XRD plots used to calculate crystallite orientations of; A) IRI active PVA and B) non-IRI active PEG, plotted as a function of  $2\theta$ . Selected  $2\theta$  ranges used to analyse the crystallite orientations scattering are coloured red; C/D) Orientation plots of C) PVA and D) PEG, plotted as a function of  $\psi$  for intensities measured in the selected  $2\theta$  range. All data obtained at  $-8\text{ }^{\circ}\text{C}$ . [Polymer] =  $2.5\text{ mg.mL}^{-1}$ ..... 152

**Figure 3.14.** Comparison of orientation analysis (here shown as inverse number of observed ice crystal orientations after 1800 seconds) and IRI activity (shown as mean length grain size, MLGS, as a percentage of PBS) over a range of concentrations for; A) AFGP8 compared to lysozyme; B) His-AFP III and SNAP-AFP III alone and bound to gold nanoparticles compared to PBS and lysozyme. [His-AFP III] =  $2.8\text{ mg.mL}^{-1}$ ; [His-AFP III@Au] =  $2.3\text{ mg.mL}^{-1}$ ; [SNAP-AFP III] =  $0.10\text{ mg.mL}^{-1}$ ; [SNAP-AFP III@Au] =  $0.13\text{ mg.mL}^{-1}$ . All concentrations are in  $\text{mg.mL}^{-1}$ , errors are standard deviation. All data obtained at  $-8\text{ }^{\circ}\text{C}$ ..... 154

**Figure 3.15.** Comparison of orientation analysis (here shown as inverse number of observed ice crystal orientations after 1800 seconds) and IRI activity (shown as mean length grain size, MLGS, as a percentage of PBS) over a range of concentrations for; A) PVA; B) PEG; C) safranin-O; D) phenosafranin. All concentrations are in  $\text{mg.mL}^{-1}$ , errors are standard deviation. All data obtained at  $-8\text{ }^{\circ}\text{C}$ ..... 155

**Figure 3.16.** Examples of how rates of ice recrystallisation are obtained using XRD. Changes in orientations observed for A) PEG and B) PVA; C) Comparison of rate obtained from the initial gradient of the fit (red line). [Polymer] =  $2.5\text{ mg.mL}^{-1}$ . All data obtained at  $-8\text{ }^{\circ}\text{C}$ ..... 156

**Figure 3.17.** Relative ice growth rates compared to that of ice crystal growth for pure water for a range of concentrations; safranin-O (black) and phenosafranin (red) after 1800 seconds annealing at  $-8\text{ }^{\circ}\text{C}$ ..... 157

**Figure 3.18.** Number of crystal orientations over time for different proteins studied in this work. [Lysozyme] =  $0.7\text{ mg.mL}^{-1}$ , [AFP III-His] =  $0.4\text{ mg.m}^{-1}$ , [AFP III-SNAP] =  $0.1\text{ mg.mL}^{-1}$ , [AFGP8] =  $0.07\text{ mg.mL}^{-1}$ ..... 157

<b>Figure 3.19.</b> Relative ice growth rates compared to that of ice crystal growth for pure water for a range of concentrations of AFGP8 (black) and lysozyme (red) after 1800 seconds annealing at -8 °C.....	158
<b>Figure 3.20.</b> A) Inverse average rate of change in number of observed ice crystal orientations over 1800 seconds for a small molecule (safranin-O), polymer (PVA) and protein (AFGP8) compared to their relative non-IRI active controls (phenosafranin, PEG and Lysozyme); B) Box plot of the mean gradients of change and standard deviation for IRI active (grey) and inactive samples (red). Mean = black square, individual data points = white hexagons. All data obtained at -8 °C.....	159
<b>Figure 3.21.</b> Crystal habit modifications by additives. Left) Ice diffraction patterns after 1800 s annealing for: samples with known ice-binding and shaping abilities, their relative non-binding controls and water/PBS); Right) Optical microscopy ice morphology analysis in 45 wt % sucrose of samples in the corresponding diffractograms. Scale bars = 100 μm. [Safranin-O] = 1.0 mg.mL <sup>-1</sup> ; [AFGP8] = 3.0 mg.mL <sup>-1</sup> ; [Phenosafranin] = 1.0 mg.mL <sup>-1</sup> ; [Lysozyme] = 1.0 mg.mL <sup>-1</sup> . .....	160
<b>Figure 3.22.</b> Ice diffraction patterns after A) 0 s and B) 1800 s annealing for 4 kDa PEG (2.5 mg.mL <sup>-1</sup> ). All data obtained at -8 °C. ....	162
<b>Figure 3.23.</b> Ice diffraction patterns after A) 0 s and B) 1800 s annealing for 4 kDa PEG (0.63 mg.mL <sup>-1</sup> ). All data obtained at -8 °C. ....	162

## Chapter 4

---

<b>Figure 4.1.</b> A) Alignment of spins in a magnetic field; when subject to a magnetic field ( $B_0$ ) spins are no longer isotropically distributed and aligning with or against the field. (A small excess of parallel spins result in a net magnetisation of $M_0$ ); B) Schematic of rotation of bulk magnetisation by RF pulses. When an RF pulse is applied, the bulk magnetisation rotates and is transferred to the x-y plane (signal is detectable). When the pulse is turned off the protons return to $B_0$ and the signal decays; C) NMR signal as an exponentially decaying sine wave (FID). The FID is converted into data used in this work.....	182
---	-----

**Figure 4.2.** NMR data obtained in the literature using a variety of techniques: A) Change in transverse (spin-spin relaxation in the x-y plane) ( $T_2$ ) relaxation times over time for 5 samples. Ice control (black diamonds), ice+BSA ( $10 \mu\text{g.mL}^{-1}$ ) (white circles), ice+[extracellular protein] ( $10 \mu\text{g.mL}^{-1}$ ) (red circles) ice+IBP ( $2 \mu\text{g.mL}^{-1}$ ) (red triangles) and ice+IBP ( $4 \mu\text{g.mL}^{-1}$ ) (red squares). Adapted from Brown *et al.*, (Biotechnol. Reports., 2014);<sup>38</sup> B) Study of type I AFP binding reversibly: NMR spectra of deuterated type I AFP ( $1 \text{ mg.mL}^{-1}$ ) showing molecular exchange between the ice surface and aqueous solution at different exchange times, narrow peaks: aqueous signal (indicating protein in aqueous phase), broad flat peaks: solid/ice signal (indicating protein bound to ice phase). Adapted from Ba *et al.*, (J. Am. Chem. Soc., 2003);<sup>27</sup> Chemical shift difference obtained from  $^{13}\text{C}$ - $^{13}\text{C}$  DARR spectrum for each amino acid in C) AFPIII ( $34 \text{ mg.mL}^{-1}$ ) frozen in water at  $-15 \text{ }^\circ\text{C}$  and D) ubiquitin ( $25 \text{ mg.mL}^{-1}$ ). (Samples in water, spectra recorded on 750 MHz spectrometer with mixing time of 20 ms, 12 kHz MAS at  $-15 \text{ }^\circ\text{C}$ ). Adapted from Siemer and Mcdermott, (J. Am. Chem. Soc., 2008).<sup>25</sup> ..... 184

**Figure 4.3.** SSNMR techniques conducted in this project and their associated timescales at which they are sensitive to motions. Techniques include: Chemical Exchange Saturation Transfer (CEST), which measures exchange between one ‘invisible’ low concentration state and a higher concentration state – if exchange occurs, two peaks will be observed (timescales covered: ms - s); Relaxation Dispersion, which monitors chemical exchange of nuclei between ms – ns timescales; 2D Exchange, which is used to indicate dipolar cross relaxation between two nuclei that are spatially close to one another. 2D experiments are particularly useful for determining which signals arise from protons that are close to each other in space even if they are not bonded. (timescales covered: 1 ms – 100 s);  $R_1$  Relaxation, which measures spin-lattice relaxation (restoration of spin to equilibrium state via z plane), originating from local motions, such as rotation (timescales covered: 10 ps – 10 ns);  $R_2$  Relaxation, which measures transverse relaxation (restoration of spin to equilibrium state via x-y plane) (timescales covered: ns – ms); Adapted from Stevens, R.A., (PhD, University of Warwick, 2018).<sup>46</sup> ..... 187

**Figure 4.4.** An example SSNMR rotor spinning at the "magic angle" ( $54.74 \text{ }^\circ$ ) with respect to the strong magnetic ( $B_0$ ) field at a frequency of  $\nu_{\text{MAS}}$ , which

sufficiently narrows peaks obtained in SSNMR experiments. Most modern rotors are made of zirconia and have decreased in diameter over the years as magic angle spinning (MAS) technology has advanced..... 188

**Figure 4.5.** IRI activity as mean largest grain size (MLGS) for PVAs over a range of chain lengths. A) 0 to 10 mg.mL<sup>-1</sup>; B) Magnification of A, showing activity for 0 to 1 mg.mL<sup>-1</sup>. Grain size is recorded after 30 minutes annealing at -8 °C. Errors are standard deviation of at least 3 measurements..... 192

**Figure 4.6.** A) Ice growth habit analysis for a range of PVA molecular weights used here; (PVA20, PVA64, PVA98, PVA230). [Polymer] = 1 mg.mL<sup>-1</sup>. Scale bar = 50 μm. Samples frozen in sucrose solution. Images recorded after a period of melting to leave a few crystals and then taken whilst cooling at 0.2 °C intervals; B) Schematic of example ice habit growth due to PVA binding the primary prism plane. .... 193

**Figure 4.7.** A) Example assigned 1D <sup>1</sup>H spectra (a spectra obtained from a one-dimensional NMR experiment after Fourier transformation of the FID; the x axis corresponds to the frequency axis and the y axis corresponds to the intensity of the signal) of 10.0 mg.mL<sup>-1</sup> safranin-O in H<sub>2</sub>O at 10 °C (red) and -10 °C (blue). Peak observed at 1.52 ppm corresponds to signal for safranin-O..... 195

**Figure 4.8.** Schematic of the mechanism of A) spin-lattice relaxation: the longitudinal magnetisation, represented by the blue arrow as it returns to its equilibrium value along the z-axis; B) spin-spin relaxation: the transverse magnetisation, represented by the red arrow as it returns to equilibrium..... 196

**Figure 4.9.** A) Preliminary T<sub>1</sub> results for PVA20, safranin-O and phenosafranin for two different temperatures; B) Schematic of relaxation times and associated correlation times (Cτ) for compounds of different size/viscosity. Adapted from Bloembergen *et al.* (Phys. Rev., 1948).<sup>64</sup> [PVA20] = 1.0 mg.mL<sup>-1</sup>; [safranin-O] = 1.0 mg.mL<sup>-1</sup>; [Phenosafranin] = 1.0 mg.mL<sup>-1</sup>..... 196

**Figure 4.10.** T<sub>1</sub> data and IRI activity data for polymer samples; A) T<sub>1</sub> plateaus (black) compared to that of critical inhibition concentration (c<sub>i</sub>) (red); B) T<sub>1</sub> over time; C) Splats over time for PVA230. [Polymer] = 1 mg.mL<sup>-1</sup> unless stated otherwise. .... 198

**Figure 4.11.** VT <sup>1</sup>H R<sub>1</sub> of ice in the presence of different DP PVAs and PEG (4 kDa). ..... 200

<b>Figure 4.12.</b> $C\tau$ for safranin-O (green) and PVA (DP8-230) (orange) compared to their respective negative controls (phenosafranin (teal) and PEG (yellow)) at 5 mg.mL <sup>-1</sup> . Calculated $C\tau$ for the ice protons are recorded at -30 °C.....	201
<b>Figure 4.13.</b> $C\tau$ and IRI activity of PVA samples. A) MLGS % of PVA (DP9-230) and PEG (black) compared to correlation time (red) at 5 mg.mL <sup>-1</sup> ; B) Comparison of $c_i$ (black) and $C\tau$ (red).....	202
<b>Figure 4.14.</b> VT <sup>1</sup> H $R_1$ of ice in the presence of IRI active safranin-O (black) and inactive phenosafranin (red) at 2 concentrations. ....	202
<b>Figure 4.15.</b> VT <sup>1</sup> H $R_2$ of the bulk ice in the presence of IRI active samples and controls. A) PVA (DP5-230) and PEG. [Polymer] = 1 mg.mL <sup>-1</sup> ; B) Safranin-O, 1 mg.mL <sup>-1</sup> and 5 mg.mL <sup>-1</sup> (black), phenosafranin, 1 mg.mL <sup>-1</sup> and 5 mg.mL <sup>-1</sup> (red).....	204
<b>Figure 4.16.</b> VT <sup>1</sup> H $R_{1\rho}$ of ice in the presence of; A) PVA5; B) PVA230; C) PEG. [Polymer] = 1 mg.mL <sup>-1</sup> . ....	206
<b>Figure 4.17.</b> VT <sup>1</sup> H $R_{1\rho}$ of ice in the presence of proteins; A) AFPIII; B) bpAFPI; C) AFGP8; D) Lysozyme. [AFPIII] = 0.659 mg.mL <sup>-1</sup> ; [bpAFPI] = 1.0 mg.mL <sup>-1</sup> ; [AFGP8] = 12.0 mg.mL <sup>-1</sup> ; [Lysozyme] = 12.0 mg.mL <sup>-1</sup> .....	207
<b>Figure 4.18.</b> VT <sup>1</sup> H $R_{1\rho}$ of ice in the presence of; A) safranin-O and B) phenosafranin. [Small molecule] = 1 mg.mL <sup>-1</sup> .....	208
<b>Figure 4.19.</b> 2D EXSY Schematic of crosspeaks (blue filled circles) that would be observed if there is any binding between protons in antifreezes and ice. ....	209
<b>Figure 4.20.</b> 2D <sup>1</sup> H- <sup>1</sup> H EXSY measurements at -10 °C for A) PVA230; B) PEG; C) AFGP8; D) AFPIII; E) Lysozyme. Mixing times were 0 ms (red spectra) and 100 ms (blue spectra). [PVA230] = 5.0 mg.mL <sup>-1</sup> ; [PEG] = 5.0 mg.mL <sup>-1</sup> ; [AFGP8] = 12.0 mg.mL <sup>-1</sup> ; [AFPIII] = 0.659 mg.mL <sup>-1</sup> ; [Lysozyme] = 12.0 mg.mL <sup>-1</sup> .....	210
<b>Figure 4.21.</b> Illustration of how safranin-O and water may interact. Distances measured in Angstroms.....	211
<b>Figure 4.22.</b> A) Western Blot showing no expression/minimal of <sup>13</sup> C, <sup>14</sup> N labelled AFPIII; Attempted optimisation of AFPIII expression to see the issue in protein expression; B) AFPIII whole cell gel; C) AFPIII lysed cell gel. Black triangle represents where AFPIII should appear on the gel. ....	214

## Chapter 5

---

**Figure 5.1.** Selection of materials known to nucleate ice A) *P. syringae*; i) SEM micrograph;<sup>19</sup> ii) Ribbon representation of a  $\beta$ -helical INP from *P. syringae*, depicting the structure of the 144-residue INP model after 300 ps of solvated MD;<sup>20</sup> B) Photographs of birch pollen grains; i) pre-water uptake (25  $\mu\text{m}$  diameter); ii) grains post-water uptake;<sup>12</sup> C) SEM images with a 6000 $\times$  magnification of 3 types of quartz particles; i) Quartz I, average surface diameter 0.5  $\mu\text{m}$ ; ii) Quartz II, average surface diameter 1.2  $\mu\text{m}$ ; iii) Quartz III, average surface diameter 4.8  $\mu\text{m}$ ;<sup>21</sup> D) Chemical structures of the various of carbon nanomaterials tested for their ice nucleation activity; carboxylated graphene nanoflakes (cx-GNF); oxidized-multiwall carbon nanotubes (o-MWCNT); graphene oxide (GO); oxidized-single-wall carbon nanotubes (o-SWCNT). GO sheets have an average lateral diameter of  $\sim 1 \mu\text{m}$ , while the GNFs have an average lateral diameter of  $\sim 30 \text{ nm}$ .<sup>22</sup> .....232

**Figure 5.2.** Ice nucleation activity obtained from a range of nucleation activity studies in the literature. Results for nucleation activity written as ice active site density normalised to surface area ( $n_s$ ). Adapted from Whale, T.F., (PhD, University of Leeds, 2015).<sup>33</sup> .....236

**Figure 5.3.** Representative micrographs of the nucleating spot in ice nucleating feldspar. Sequence of images taken from individual freezing experiments of two separate droplets, on the A) (010) and B) (001) faces. A 1  $\mu\text{L}$  droplet of water is placed on a thin section of feldspar and cooled at  $1^\circ\text{C min}^{-1}$  until nucleation is detected with a high-speed camera operating at 3000 frames per second (fps). Adapted from Holden *et al.*, (Sci. Adv., 2019).<sup>48</sup> .....238

**Figure 5.4.** A) Illustration of the IR-NIPI technique developed by Harrison *et al.*, (Atmos. Meas. Tech. Discuss., 2018).<sup>62</sup> The Infra-red camera is positioned above the multiwell plate and monitors the freezing events as the cold stage cools; B) Example colour map taken during the course of an experiment. The black circle represents a sample nucleating in an individual well (exothermic reaction leads to the higher temperature in this well). Warmer temperatures are represented in red, transitioning to blue for colder temperatures and finally black at  $-30^\circ\text{C}$  and below. Cooling rates used is  $1^\circ\text{C min}^{-1}$  .....241

**Figure 5.5.** Schematic of concept behind the decision to study Zirconium-based MOFs for ice nucleation. A) Concept Underlying the Synthesis of Metal–Organic Frameworks; B) Schematic illustration of the structure features of an example selection of MOFs that could be studied: UiO-66 (–NH<sub>2</sub>, –OH), UiO-67, and MOF-808, showing their large extended surfaces. Adapted from Zhu *et al.*, (J. Am. Chem. Soc., 2019).<sup>71</sup> .....242

**Figure 5.6.** Three important basic building blocks of lignins; A) *p*-coumaryl alcohol; B) coniferyl alcohol; C) sinapyl alcohol, which give rise to *p*-hydroxyphenyl, guaiacyl and syringyl residues in lignin.....243

**Figure 5.7.** A) Chemical structures of ligands used for MOFs tested here. 1,4-benzene dicarboxylic acid (BDC), naphthalenedicarboxylate (NDC), benzene-1,3,5-tricarboxylic acid (BTC); B) Extended structure of the MOFs provided by Ehsan Ghadim. ....246

**Figure 5.8.** Chemical structures of other materials tested here. A) Safranin-O; B) Alkali lignin (471003) 10 kDa (Structure from Sigma-Aldrich). The producer’s elemental analysis data states a carbon content of 47-51 % and that this technical Kraft lignin has a remaining sulfur content of ~4 %. .....247

**Figure 5.9.** DSC traces and how nucleation temperatures are extracted from this data. A) Example DSC traces of liquid water transitioning to I<sub>h</sub> (and melting back to liquid) from the literature. Two scans from the same sample, where the ice was warmed at either 5 °C.min<sup>-1</sup> (solid line) or at 1 °C.min<sup>-1</sup> (dashed line). Both the cooling and heating runs have been included i.e. both endotherms and exotherms are shown and the point at which the nucleation temperature would be recorded highlighted in red. Adapted from Wilson *et al.* (Biophys. J., 1999);<sup>94</sup> B) Raw DSC trace of pure water cooling from 0 °C to -35 °C obtained in this work. Nucleation temperatures are extracted at the point at which the exotherm corresponding to the phase change occurs. It can be seen that the peak slants unlike in the literature example; B) Temperatures obtained from DSC with one 10 μL droplet in direct contact with the aluminium pan; and C) Temperatures obtained from DSC of a few 1 μL droplets dispersed in oil (i.e. not in direct contact with pan) compared to that of the DSC trace for oil (black), water (red), safranin-O (green) and alkali lignin 471003 (blue), their apparent nucleation temperatures (recorded as an exotherm). [Sample] = 1.0 mg.mL<sup>-1</sup>. .....249

<b>Figure 5.10.</b> Diagram illustrating the $\mu\text{L-NIPI}$ -based nucleation drop assay setup used in this work.....	251
<b>Figure 5.11.</b> Example photographs from a multi-point freezing assay. Frame (A) was taken at $-25.0\text{ }^{\circ}\text{C}$ , before the onset of freezing, frame (B) immediately after the first two droplets had frozen ( $-26.2\text{ }^{\circ}\text{C}$ ), frame (C) at $-27.5\text{ }^{\circ}\text{C}$ and frame (D) at $-30.1\text{ }^{\circ}\text{C}$ , after the completion of freezing. Frozen droplets highlighted in red.....	252
<b>Figure 5.12.</b> Example photographs from a nucleation drop freezing assay based on $\mu\text{L-NIPI}$ . Frame (A) was taken at $-10.0\text{ }^{\circ}\text{C}$ , before the onset of freezing, frame (B) immediately after the first two droplets had frozen ( $-18.0\text{ }^{\circ}\text{C}$ ), frame (C) at $-22.5\text{ }^{\circ}\text{C}$ and frame (D) at $-30.7\text{ }^{\circ}\text{C}$ , after the completion of freezing. Frozen droplets highlighted in red. Droplets of this size (1 mm) typically take 2 – 4 seconds to freeze completely. The initial change in the droplet leading to freezing is taken as the occurrence of ice nucleation.....	253
<b>Figure 5.13.</b> Temperatures obtained from nucleation drop assay (45-55 $1\text{ }\mu\text{L}$ droplets per slide, 2-5 repeat experiments per sample). Milli-Q water (red), safranine-O (green) and alkali lignin 471003 (blue). Temperature uncertainty of $\mu\text{L-NIPI}$ -based method is $\pm 0.4\text{ }^{\circ}\text{C}$ . [Sample] = $1.0\text{ mg.mL}^{-1}$ .....	254
<b>Figure 5.14.</b> Temperatures obtained from nucleation drop assay (45-55 $1\text{ }\mu\text{L}$ droplets per slide, 2-5 repeat experiments per sample). Milli-Q water (red) and safranine-O (green). Temperature uncertainty is $\pm 0.4\text{ }^{\circ}\text{C}$ . [Sample] = $2.5\text{ mg.mL}^{-1}$ .....	255
<b>Figure 5.15.</b> IRI activity for a range of MOFs; A) Ce-NDC-UiO-66 synthesised via different synthetic routes as a percent of PBS; B) Ce-MOFs and Zr- MOFs. Black = MGS and red = MLGS. [MOF] = $10\text{ mg.mL}^{-1}$ .....	257
<b>Figure 5.16.</b> IRI activity for Ce-NDC-UiO-66 synthesised via different synthetic routes as a percent of PBS over 3 concentrations. ....	257
<b>Figure 5.17.</b> Frozen fraction of $1\text{ }\mu\text{L}$ droplets containing 3 different MOFs ( $1.0\text{ mg.mL}^{-1}$ ) compared to that of a Milli-Q water control. (45-55 $1\text{ }\mu\text{L}$ droplets per slide, 2-5 repeat experiments per sample).....	258
<b>Figure 5.18.</b> Frozen fraction of droplets containing 3 different lignin samples ( $1.0\text{ mg.mL}^{-1}$ ) compared to that of a Milli-Q water control. (10-20 $1\text{ }\mu\text{L}$ droplets per slide, 2-5 repeat experiments per sample).....	258



- Figure 5.19.** Frozen fraction of droplets containing Alkali lignin 471003 (blue) compared to that of Milli-Q water (black) recorded using two different setups. Nucleation temperatures observed on the cryostage = open square/circle, temperatures obtained using  $\mu\text{L-NIPI}$  = filled square/circle.  $[\text{Lignin}] = 1.0 \text{ mg.mL}^{-1}$  .....259
- Figure 5.20.** Nucleation activity of a range of lignins. A) Frozen fraction of droplets containing 8 different lignin samples ( $5.0 \text{ mg.mL}^{-1}$ , sonicated for 2 minutes); B) Frozen fraction of droplets containing 3 different lignin samples ( $1.0 \text{ mg.mL}^{-1}$ ) compared to that of a Milli-Q water control. ....260
- Figure 5.21.** IRI activity for alkali lignin (471003) over a range of concentrations compared to that of PBS. ....261
- Figure 5.22.** Frozen fraction of droplets containing Alkali lignin (471003) at 3 different concentrations compared to a Milli-Q water control. (45-55  $1 \mu\text{L}$  droplets per slide, 2-5 repeat experiments per sample). ....262
- Figure 5.23.** Frozen fraction of droplets containing Alkali lignin (471003) at 5 different concentrations compared to a Milli-Q water control. (45-55  $1 \mu\text{L}$  droplets per slide, 2-5 repeat experiments per sample). ....262
- Figure 5.24.** Ice nucleation efficiency expressed as sites per mass ( $\text{g}^{-1}$ ) of lignin as a function of temperature ( $n_m(T)$ ) for alkali lignin (471003) tested in this study. Values normalised to mass per droplet. Each line consists of between two and five experiments. Due to the significance of nucleation temperatures differences between lignin and water no background subtraction was conducted. Error bars calculated using the Poisson Monte Carlo procedure. For clarity, as errors were representative, only 1 out of 4 errors bars plotted. Temperature uncertainty is  $\pm 0.4^\circ\text{C}$  .....264
- Figure 5.25.** The effect filtering has on nucleation. A) Frozen fraction of droplets containing alkali lignin (471003) filtered and unfiltered ( $5.0 \text{ mg.mL}^{-1}$ ); B) Frozen fraction of droplets containing alkali lignin (471003) filtered and unfiltered ( $50 \text{ mg.mL}^{-1}$ ) compared to Milli-Q water. Unfiltered = red, filtered = green. (45-55  $1 \mu\text{L}$  droplets per slide, 2-5 repeat experiments per sample). ....265
- Figure 5.26.** Frozen fraction of droplets containing GreenValue lignin filtered and unfiltered solutions compared to Milli-Q water ( $1.0 \text{ mg.mL}^{-1}$ ). Unfiltered =

red, filtered = green. (45-55 1  $\mu\text{L}$  droplets per slide, 2-5 repeat experiments per sample). .....265

**Figure 5.27.** Frozen fraction of droplets containing Alkali lignin 471003 frozen at different cooling rates compared to that of a Milli-Q water control (black, cooled at  $1\text{ }^{\circ}\text{C}\cdot\text{min}^{-1}$ ). A) Four different rates compared; B) comparison of  $1.0\text{ }^{\circ}\text{C}\cdot\text{min}^{-1}$  (red) and  $10\text{ }^{\circ}\text{C}\cdot\text{min}^{-1}$  (orange). (45-55 1  $\mu\text{L}$  droplets per slide, 2-5 repeat experiments per sample). [Lignin] =  $1\text{ mg}\cdot\text{mL}^{-1}$ . .....266

## Appendix A

---

**Figure A2.1.** Comparison of average number of colonies of Lactobacillus strain BAA-365 grown after freezing and storage under 3 different conditions (black = 7 freeze/thaw cycles at liquid nitrogen temperatures, red = 1 week storage at  $-80\text{ }^{\circ}\text{C}$ , green = 1 month storage at  $-80\text{ }^{\circ}\text{C}$ ) with no cryoprotectant, 25% glycerol, or PEG/PVA.....287

# List of Schemes

## Chapter 2

---

<b>Scheme 2.1.</b> Scheme outlining redox reaction of NADH and NAD <sup>+</sup> .....	85
---	----

# List of Tables

## Chapter 1

---

<b>Table 1.1.</b> Magnitudes and lengths of different types of interactions between atoms and molecules .....	4
<b>Table 1.2.</b> Types of antifreeze proteins and respective example masses, structures, binding planes and origin. Adapted from Voets, (Soft Matter, 2017) and Barrett (Int. J. Biochem. Cell Biol., 2001). <sup>145,146</sup> .....	21

## Chapter 2

---

<b>Table 2.1.</b> Mean colonies recovered after 7 freeze/thaw cycles.....	98
---	----

## Chapter 4

---

<b>Table 4.1.</b> Comparison of IRI activity data (compared to that of a PBS control) and SSNMR ice relaxation times (recorded in water) for PVA230 .....	197
---	-----

# List of Equations

## Chapter 1

---

<b>Equation 1.1</b> Mean ice crystal radius as a function of time during the Ostwald ripening process.....	13
--	----

## Chapter 3

---

<b>Equation 3.1</b> Bragg's Law.....	130
<b>Equation 3.2</b> X-ray Scattering Momentum Transfer.....	130

## Chapter 4

---

<b>Equation 4.1</b> Longitudinal Relaxation Rate ( $R_1$ ).....	199
<b>Equation 4.2</b> Transverse Relaxation Rate ( $R_2$ ).....	199
<b>Equation 4.3</b> Contribution of slow chemical exchange to ( $R_2^{obs}$ ).....	204
<b>Equation 4.4</b> Contribution of fast chemical exchange to ( $R_2^{obs}$ ).....	204

## Chapter 5

---

<b>Equation 5.1</b> Calculation of INP ice active site density normalised to surface area as a function of temperature.....	235
<b>Equation 5.2</b> Calculation of INP ice active site density normalised to volume of water droplet as a function of temperature.....	235
<b>Equation 5.3</b> Calculation of INP ice active site density normalised to mass of the ice nucleating particle per droplet as a function of temperature.....	235

# Abbreviations

---

°C	Degrees Centigrade
$\Delta T_f$	Freezing Efficiency
$\lambda$	Wavelength
$\mu$	Micro ( $\times 10^{-6}$ )
$\mu\text{L}$	Microlitre
$\mu\text{L-NIPI}$	$\mu\text{L}$ -Nucleation by Immersed Particle Instrument
<b>1D</b>	1-dimensional
<b>2D</b>	2-dimensional
<b>3D</b>	3-dimensional
<b>AFGL</b>	Antifreeze Glycolipids
<b>AFGP</b>	Antifreeze Glycoprotein
<b>AFP</b>	Antifreeze Protein
<b>AuNP</b>	Gold Nanoparticle
<i>B. subtilis</i>	<i>Bacillus subtilis</i>
<b>BCA</b>	Bicinchoninic Acid Assay
<b>bpAFPI</b>	AFPI from barfin plaice
<b>BSA</b>	Bovine Serum Albumin
<b>CD</b>	Circular Dichroism
<b>CF</b>	Carboxyfluorescein
<b>CFU</b>	Colony Forming Unit
<i>Ci</i>	Critical Concentration for Inhibition Efficiency
<b>CNT</b>	Classical Nucleation Theory
<b>CPA</b>	Cryoprotectant
<b>C<math>\tau</math></b>	Correlation Time
<b>cx-GNF</b>	Small Carboxylated Graphene Nanoflake
<b>cys-AFPI</b>	Cysteine Mutant bpAFPI
<b>DIS</b>	Dynamic Ice Shaping
<b>DLS</b>	Dynamic Light Scattering

<b>DLTIII</b>	Dendrimer-linked type III AFP
<b>DMSO</b>	Dimethyl sulfoxide
<b>DNA</b>	Deoxyribonucleic Acid
<b>DP</b>	Degree of Polymerisation
<b>DSC</b>	Differential Scanning Calorimetry
<b>DTT</b>	Dithiothreitol
<i>E. coli</i>	<i>Escherichia coli</i>
<b>EG</b>	Ethylene Glycol
<b>FDGP</b>	Freeze Depressing (Glyco)protein
<b>FID</b>	Free Induction Decay
<b>FIPA</b>	Fluorescence-Based Ice Plane Affinity
<b>FPLC</b>	Fast Protein Liquid Chromatography
<b>fps</b>	Frames Per Second
<b>FROST</b>	Framework for Reconciling Observable Stochastic Time-Dependence
<b>FT</b>	Freeze Thaw
<b>FT-IR</b>	Fourier-Transform Infrared Spectroscopy
<b>g</b>	Gram
<b>GC-MS</b>	Gas Chromatography-Mass Spectrometry
<b>GFP</b>	Green Fluorescent Protein
<b>GNF</b>	Graphene Nanoflakes
<b>GO</b>	Graphene Oxide
<b>GPC</b>	Gel Permeation Chromatography
<i>H. harveyi</i>	<i>Hypogastrura harveyi</i>
<b>HCl</b>	Hydrochloric Acid
<b>HES</b>	Hydroxyethyl Starch
<b>HPLC</b>	High Performance Liquid Chromatography
<b>HPMC</b>	Hydroxypropyl Methylcellulose
<b>I</b>	Spin Quantum Number
<b>IBP</b>	Ice-Binding Protein

<b>IBS</b>	Ice-Binding Site
<b>Ic</b>	Cubic Ice
<b>Ih</b>	Hexagonal Ice
<b>IMAC</b>	Immobilized Metal Affinity Chromatography
<b>INP</b>	Ice Nucleating Particle
<b>INS</b>	Ice Nucleation Site
<b>IPTG</b>	Isopropyl- $\beta$ -D-thiogalactopyranoside
<b>IR</b>	Ice Recrystallisation
<b>IRI</b>	Ice Recrystallisation Inhibition
<b>IR-NIPI</b>	InfraRed-Nucleation by Immersed Particle Instrument
<b>k</b>	Number of Active Sites Per Droplet
<b>K</b>	Ice Nucleation Active Site Density Normalised to Volume of Water INP Suspended in
<b>KCl</b>	Potassium Chloride
<b>Kd</b>	Equilibrium Constant
<b>kDa</b>	kiloDaltons ( $\times 10^3$ Daltons)
<b>kHz</b>	kilohertz ( $\times 10^3$ Hertz)
<b>L</b>	Litre
<b>LCC</b>	Lignin-Carbohydrate Complex
<b>LDH</b>	Lactate Dehydrogenase
<b>LN2</b>	Liquid Nitrogen
<b>MAS</b>	Magic Angle Spinning
<b><i>M. smegmatis</i></b>	<i>Mycobacterium smegmatis</i>
<b>MD</b>	Molecular Dynamics
<b>mg</b>	Milligram
<b>MGS</b>	Mean Grain Area / Size
<b>min</b>	Minute
<b>mL</b>	Millilitre
<b>MLGS</b>	Mean Largest Grain Size
<b>mm</b>	Millimetre ( $\times 10^{-3}$ metres)

<b>mM</b>	Millimolar
<b>MOF</b>	Metal Organic Framework
<b>ms</b>	Millisecond
<b>MWCNT</b>	Multiwalled Carbon Nanotube
<b>NaCl</b>	Sodium Chloride
<b>NADH</b>	Nicotinamide Adenine Dinucleotide
<b>nm</b>	Nanometre ( $\times 10^{-9}$ metres)
<b>n<sub>m</sub></b>	Ice Nucleation Active Site Density Normalised to Mass
<b>n<sub>s</sub></b>	Ice Active Site Density Normalised to Surface Area
<b>ns</b>	Nanosecond
<b>OH</b>	Hydroxyl
<b>OQCN</b>	Oxidized Quasi-Carbon Nitride Quantum Dots
<b>p(amph)</b>	Poly(ampholyte)
<b><i>P. syringae</i></b>	<i>Pseudomonas syringae</i>
<b>PAAM</b>	Poly(acrylamide)
<b>PBS</b>	Phosphate Buffered Saline (0.01 M)
<b>PEG</b>	Poly(ethylene glycol)
<b>PEO</b>	Polyethylene Oxide
<b>PHPMA</b>	Poly[N-(2-hydroxypropyl) methacrylamide]
<b>POZ</b>	Poly(2-ethyl-2-oxazoline)
<b>PVA</b>	Poly(vinyl alcohol)
<b>PVP</b>	Polyvinylpyrrolidone
<b>Q</b>	Ice Volume Fraction
<b>QLL</b>	Quasi Liquid Layer
<b>QTOF</b>	Quadrupole Time of Flight Mass Spectrometry
<b>r<sup>3</sup></b>	Mean Ice Crystal Radius
<b>RBC</b>	Red Blood Cell
<b>RCF</b>	Relative Centrifugal Force
<b>RF</b>	Radiofrequency
<b>RPM</b>	Revolutions Per Minute



<b>s</b>	Second
<b>SAXS</b>	Small Angle X-ray Scattering
<b>SD</b>	Spin Diffusion
<b>SDS-PAGE</b>	Sodium Dodecyl Sulfate-Polyacrylamide Gel Electrophoresis
<b>SSNMR</b>	Solid State Nuclear Magnetic Resonance
<b>SWCNT</b>	Single Walled Carbon Nanotube
<b>SXRD</b>	Synchrotron X-Ray Diffractometry
<b>T</b>	Temperature
<b>T<sub>50</sub></b>	Temperatures at which 50 % of Droplets have Frozen
<b>TEM</b>	Transmission Electron Microscopy
<b>TEV</b>	Tobacco Etch Virus Protease
<b>T<sub>f</sub></b>	Freezing Temperature
<b>T<sub>g</sub></b>	Glass Transition Temperature
<b>TH</b>	Thermal Hysteresis
<b>THP</b>	Thermal Hysteresis Protein
<b>T<sub>m</sub></b>	Melting Point
<b><i>TmAFP</i></b>	<i>Tenebrio molitor</i> AFP
<b><i>TmINP</i></b>	<i>Tenebrio molitor</i> Ice Nucleating Particle
<b>T<sub>n</sub></b>	Nucleation Temperature
<b>Trx</b>	Thioredoxin
<b>TTMSS</b>	Tris(trimethylsilyl)silane
<b>µm</b>	micrometre (× 10 <sup>-6</sup> metres)
<b>VT</b>	Variable Temperature
<b>WAXS</b>	Wide Angle X-ray Scattering
<b>wt %</b>	Weight Percent
<b>XAS</b>	X-ray Adsorption
<b>XES</b>	X-ray Emission
<b>XRD</b>	X-ray Powder Diffraction
<b>XPS</b>	X-ray Photoelectron Spectroscopy
<b>ZrAc</b>	Zirconium Acetate

# Acknowledgements

---

First and foremost, I would like to thank my supervisor Professor Matthew Gibson. I have been so fortunate to have such an encouraging, motivating and optimistic supervisor throughout this process. He always has a limitless list of ideas of how to work things through and despite being infinitely busy always finds time for a chat. His support has enabled me to grow as a scientist and given me multiple opportunities to travel to a range of conferences and network. I would also like to thank the European Research Council for making my PhD possible.

A special mention goes to Mrs McAllister, who first sparked my interest in chemistry and Dr Chris Mowat for getting me through my Masters, without him I would never have been able to take on a PhD and be who I am today!

I would also like to thank all my collaborators, who without their knowledge and understanding, I would have only been able to perform half of the work in this thesis; Steve Huband for all things X-ray, Rebecca Stevens and Professor Josef Lewandowski for all things SSNMR, Tom Congdon and Chris Stubbs for producing me a range of polymers, and Muhammad Hasan for helping train me on all things biology.

I'm grateful for being a part of the Gibson group, where I have made some lifelong friends who have been there to enjoy lab work day-to-day and some wine of a weekend. In particular, 'Other' Ben, who was my first friend and, quite importantly, introduced me to my husband, and Ben G, who always provided me with laughs, gossip and someone to complain to. Both of which I missed greatly once they left. Marie, Laura, Julia and Ioanna, for chats, walks, socialising and bakes. Alex Baker, for lunch and politics chats. It has always been handy having someone around to talk with during the day. Kat, for having a yoga and spin buddy to get me out of the office away from my thesis. Tom C and Tom W, for all their thesis help, letting me complain when I get bored, and just generally being friendly, approachable chaps.

I'd like to thank the RLT 'cool kids', Ryan, John, Dave, Elle and Rosie, for being the best on-campus colleagues, without you guys I would have probably had no reason to leave the office. Evenings of biscuits, cheese and games were very much appreciated. My fellow-PhD friends, Steph, Tahmina and Jess, you inspired me to keep going and

were always there to understand what life is like when doing a PhD. Steph, you have been an important friend all the way through and I am so glad you're around for tea and cake (when we manage to be in the same city!). Catharina, even though you were far away, our catch-ups and visits were always a highlight, I hope you enjoy reading this thesis.

To my Mum and Dad, who have always believed in me, and have got me through many tough times, as well as great times, with much-needed emotional and financial support. I can never thank you enough! My siblings, who have always been there for me and are so important to me. To my late grandfather, Max, who inspired me in all things science, I wish you could see me now.

Lastly – and by no means least – to Dan. Thank you for all your motivation, encouragement and non-stop pride in my achievements. For listening (and not trying to 'fix' too much) when I complain. I can't think of anyone better to have been by my side during this process. Here's to our next adventures!

*For Grandpa Max*

# Declaration

---

This thesis is hereby submitted to the University of Warwick in partial fulfilment of the requirements for the degree of Doctor of Philosophy. The work reported herein was carried out in the laboratories of the Department of Chemistry, University of Warwick between October 2016 and December 2019.

All reported work was carried out by the author alone except in the case of collaborative research (outlined below), and no part of the reported work has been previously submitted in any shape or form for any other degree at any University.

This project has received funding from the European Research Council (ERC) under the European Union's Horizon 2020 research and innovation programme (grant agreement No. CRYOMAT 638661).

- Throughout all PVA samples were synthesised and provided by Dr Christopher Stubbs or Dr Thomas Congdon.
- All AGFP8 provided by Professor A. L. DeVries

## **Chapter 2:**

- Assistance in AFPI and AFPIII expression by Dr Muhammad Hasan
- Live/Dead microscopy performed by Dr Julia Lipecki

## **Chapter 3:**

- Assistance with wide angle X-ray scattering set-up and writing of the in-house MATLAB code for analysis was kindly given by Dr Steven Huband
- Synthesis and conjugation of gold nanoparticles was performed by Dr Laura Wilkins

## **Chapter 4:**

- All of the work presented in this chapter is in collaboration with Dr Rebecca A. Stevens
- 'Splat' assays for PVAs performed by Dr Thomas Congdon

- Critical inhibitory concentration of polymers calculated by Carsten Budke

Particular sections of this thesis have been published or submitted for publication, as follows:

### Chapter 2:

- **Fayter, A.E.R.**, Hasan, M, Congdon T., Kontopoulou I. & Gibson, M.I., Ice Recrystallisation Inhibiting Polymers Prevent Irreversible Protein Aggregation During Solvent-Free Cryopreservation as Additives and as Covalent Polymer-Protein Conjugates, *European Polymer Journal*, accepted (2020)
- Mitchell, D., **Fayter, A.E.R.**, Deller, R.C., Hasan, M., Gutierrez-Marcos, J. & Gibson, M.I., Ice-Recrystallization Inhibiting Polymers Stabilize Proteins Against Freeze/Thaw Stress Removing Need for Organic Solvents, *Materials Horizons*, 6, 364-368, (2019)
- Hasan, M., **Fayter, A.E.R.** & Gibson, M.I., Ice Recrystallization Inhibiting Polymers Enable Glycerol-Free Cryopreservation of Microorganisms, *Biomacromolecules*, **19**(8), 3371-3376, (2018)

### Chapter 3:

- **Fayter, A. E. R.**, Huband, S. & Gibson, M.I., X-ray Diffraction to Probe the Kinetics of Ice Recrystallization Inhibition, *The Analyst*, 145, 3666-3677, (2020)

### Chapter 4:

- **Fayter, A. E. R.**, Stevens, R.A., Lewandowski, J. & Gibson, M.I., Solid State NMR links quantitative ice growth measurements with molecular-scale ice/polymer interactions of synthetic antifreeze (macro)molecules, *in preparation*

Personal thanks go to all of the above named for their help, assistance, and involvement.

# Abstract

---

Ice formation and growth is of interest to many different fields, including food science, mechanical engineering, agriculture and cryobiology, however little is understood about the underlying mechanisms behind the nucleation and growth processes. The need to increase our understanding of ice and how it is affected by compounds with ‘antifreeze’ properties is fundamental to improving techniques for the storage of biologics. Nature has evolved to contend with a range of harsh climates; in particular, they produce cryoprotectants enabling them to survive sub-zero temperatures. Inspired by Nature’s ingenious response a range of synthetic protein mimics have been developed, which have ice growth inhibition activity. The scientific principles behind ice nucleation and growth, and the materials that affect them, as well as current techniques for analysis are detailed in **Chapter 1**.

This thesis reports on ice-activity for a range of compounds, studying their micro- and macroscopic effects on ice, as well as any potential cryoprotective capabilities, with the view to further fundamental understanding of ice growth inhibition and aid in the development of future potent cryoprotectants. A diverse range of methods including microscopy, X-ray Diffraction (XRD) and solid state nuclear magnetic resonance (SSNMR) were used to aid in characterisation and analysis by monitoring structural changes as well as the antifreeze macromolecule:ice interface.

**Chapter 2** investigates cryostorage of a range of biological materials using an organic solvent-free formulation consisting of an ice growth inhibiting polymer and a secondary bulking agent. **Chapter 3** details X-ray diffraction (XRD) as a new method for studying ice growth continuously as a function of time, confirming its potential as a supplementary tool to study ice growth. **Chapter 4** builds upon results from microscopy and XRD-based methods by using solid state nuclear magnetic resonance (SSNMR) to enable the study of molecular-level details experimentally. SSNMR provides further evidence for the ‘turning on’ of ice recrystallisation activity (IRI) for poly(vinyl alcohol) and ice-binding for a variety of compounds. **Chapter 5** focuses on ice nucleation specifically. A range of previously untested materials that feature design motifs associated with nucleators reported on in the literature were examined

for ice nucleation effectiveness and IRI activity, finding none to inhibit ice growth, and that structure alone is not enough to infer nucleation effectiveness.



# Chapter 1

---

Introduction: From Antifreeze Proteins to  
Antifreeze Materials

## 1.0 Introduction

It is commonly believed that water freezes at 0 °C, however this is not the case, a fact that continues to surprise people to this day. In fact, nanolitre-scale droplets of pure water freeze at closer to -40 °C,<sup>1,2</sup> and ice formation above this is usually seeded by impurities (likelihood of nucleation increases as the size of impurity increases).<sup>3</sup> Life on Earth depends on the presence of considerable amounts of water in all three phases; oceans cover over 70 % of the globe,<sup>4,5</sup> ice (of many kilometres in depth) currently covers 10 % of land mass, up to 60 % of a human adult body consists of water and many gallons of water are required in the production of a great range of foods.<sup>6</sup>

Snow and ice present a range of issues for industrial processes, including unwanted freezing of pipes, freeze/thaw damage to materials such as concrete, disruption of transport and negative impacts on biologic survival throughout the cold chain. However, they also provide much joy (in snow sports and natural wonders), as well as being of great importance in food preservation and essential in the nucleation of clouds and rain.<sup>4,7-9</sup>

A range of industrial processes require the use of antifreeze formulations to either prevent the formation of ice or assist in its removal, *e.g.* in the de-icing of aircraft wings. In most cases, these strategies involve the colligative depression of water's freezing point or the inhibition of ice nucleation. Colligative properties, such as freezing point depression, are solution properties caused by solute particles in proportion to their concentration, *i.e.* the higher the concentration, the greater the effect on the solution. Examples include salts, glycerol and methanol. Freezing leads to irreversible coagulation of paint's constituent parts<sup>10</sup> and reduces the quality of foods stored over long periods. For instance, 'large' ice crystals in ice cream yield a gritty texture.<sup>11</sup> Ice can also be a serious problem for the cold chain; cold storage is important for the successful transport of biological materials,<sup>12</sup> and key challenges for many biotechnology or cell-based processes are transport and storage logistics.<sup>13</sup> An increasing number of biological products require temperature control now including at least 20 % of clinical trial supplies, 14-35 % of vaccine shipments (potentially more),<sup>14</sup> regenerative medicine<sup>12</sup> and organ transplantation, where donor organs can only be stored for a few hours.<sup>15</sup> Cryopreservation techniques have been introduced to enable successful biologic storage, prevention of protein aggregation and the

reversible arrest of cell metabolism by freezing. There are associated problems with freezing (change in osmotic pressure, ice crystal growth) in relation to the materials' intolerance to these temperatures, leading to reduced cell, tissue and organ viability.

Nature has evolved various adaptations to enable life to flourish in sub-zero climates. Organisms (such as extremophiles) tolerate these ice-rich environments by producing cryoprotectants (CPAs) that enable either freeze tolerance (ability to be frozen then thawed) or freeze avoidance (prevention of ice formation).<sup>16-19</sup> These include production of small molecule CPAs such as glycerol<sup>20,21</sup> and trehalose,<sup>22</sup> but also macromolecular CPAs such as antifreeze proteins (AFPs, also known as ice-binding proteins) and antifreeze glycoproteins (AFGPs).

In order to begin to address the problems associated with cryopreservation, an improved understanding of Nature's ingenious response to freezing temperatures would be indispensable. Enabling us to answer such questions as; how can we choose which materials to use for storage of biologics? How do these materials affect ice? By what mechanisms of action to they work? Here, ice nucleation and growth are discussed (and probed), considering a variety of techniques and how they provide insight into micro- and macroscopic effects over differing length scales, so as to assist in answering these questions.

## **1.1 Water and Ice**

Ice, on the atomic scale, consists of water molecules:  $\text{H}_2\text{O}$ . These molecules are of great importance and have been (and continue to be) an interesting subject of study. Water's properties are anomalous and distinctive:<sup>23,24</sup> it has more solid phases and is more cohesive than other materials consisting of similar size and shape molecules, it has a relatively high melting point, boiling point and surface tension due to this high cohesion between the water molecules, its component ions (hydroxide and proton) diffuse at faster rates than other ions, its glassy state is neither fragile nor strong, its supercooled liquid has divergent thermodynamic response functions, has high thermal conductivity and can also be slippery and sticky at the same time, which leads to its distinctive feel. Water also has density anomalies that manifest in many ways: it expands upon freezing (thus the liquid form is denser than would be expected and the solid floats on the liquid), the density maximum (where water has a minimum volume)

is at 4 °C, differing from volumes of simpler liquids that are always increasing, applying pressure will melt the solid phase (applying pressure generally causes a liquid to freeze into a solid), it has a large heat capacity as water stores energy in its van der Waals and hydrogen bonds.<sup>25</sup> Over the years there have been debates over the underlying mechanisms behind these behaviours.<sup>4</sup>

Hydrogen bonding is a weak interaction between molecules (with typical energies <40 kJ.mol<sup>-1</sup>) when compared to the chemical bonding that occurs between two atoms (which can be as high as 569 kJ.mol<sup>-1</sup> for H-F), though it is stronger than hydrophobic interactions such as van der Waals forces. A comparison of these interactions is detailed in **Table 1.1**. Hydrogen bonding in hexagonal ice (Ih) is considered an example of a weak hydrogen bonded system,<sup>26</sup> though it is this flexibility in the hydrogen bonded structure of ice generally that enables the formation of the multiple crystal polymorphs. Generally shorter distances between atoms and smaller hydrogen bond angles lead to increased hydrogen bond strength; the shortest, and therefore strongest, hydrogen bonds to have been recorded in water molecules *via* molecular simulations was 2.43 – 2.61 Å (strength of 82.28 kJ.mol<sup>-1</sup>).<sup>27,28</sup>

**Table 1.1.** Magnitudes and lengths of different types of interactions between atoms and molecules.

Type of Bond	Magnitude	Energy (kJ. mol <sup>-1</sup> )	Length (in water (Å))
<b>Hydrogen bond</b>	Weak	4 – 50* <sup>29</sup>	2.6 – 3.1 <sup>30</sup>
<b>van der Waals forces</b>	Very weak	5** <sup>31</sup>	1 - 4 <sup>32</sup>
<b>Single covalent bond</b>	Strong	~200-500 <sup>31</sup>	0.97

\*Hydrogen bond strength in liquid water is ~23 kJ.mol<sup>-1</sup> and ~28 kJ.mol<sup>-1</sup> in Ih.<sup>28</sup>

\*\*Strength of van der Waals forces is for individual atom pairs.

The general consensus is that some of water's properties may be due to each molecule's ability to form four hydrogen bonds with its four nearest neighbouring water molecules (typical length ranging between 2.6 – 2.9 Å) in an almost tetrahedral arrangement.<sup>33</sup> This highly directional hydrogen bonding is responsible for some

volumetric anomalies, including the hydrophobic effect and ice being of lower density than liquid water, as a water molecule can have only four nearest neighbours.<sup>24</sup> The network is what leads to water's complex phase diagram, which has a number of triple points and possibly two critical points, **Figure 1.1A**.<sup>34</sup> The positions of the hydrogens and oxygens in the lattice in turn leads to differing crystal structures (polymorphs/phases). These ice phases have the same chemical composition but are formed under different conditions; *i.e.* high/low temperatures and pressures. Currently there are 19 known phases of ice, formed under different temperature and pressure conditions, they also vary in that they can be proton-ordered or proton-disordered.<sup>34–37</sup> Roman numerals are used to name the phases in chronological order of their discovery, with Tammann assigning 'I' to his discovery of the first of the high-pressure ice phases in 1900,<sup>38</sup> ice II's structure elucidated in 1964 by Barclay Kamb,<sup>39</sup> ice X successfully made in the laboratory in 1984<sup>40</sup> and recently ice XVIII discovered *via* X-ray experiments on laser-shocked water in 2019.<sup>41</sup> Hexagonal ice (Ih) is the most common form, it is the ice we scrape off our cars in winter, whereas some of the other ice phases are only encountered in the interiors of Neptune and Uranus. High pressure is required to cause the open structure of Ih (density of 0.92 g.cm<sup>-3</sup>), the most common form, to collapse forming dense interconnected lattices, which make up the high density ice phases including, high-density amorphous ice (HDA, density of 1.17 g.cm<sup>-3</sup>),<sup>42</sup> very high-density amorphous ice (VHDA, 1.25 g.cm<sup>-3</sup>)<sup>43</sup> and many crystalline phases *e.g.* ice VII (1.50 g.cm<sup>-3</sup>)<sup>44</sup> and X (2.51 g.cm<sup>-3</sup>)<sup>45</sup> (shown in **Figure 1.1B**). There are also ice phases that occur in the negative pressure regime, these are ultralow-density phases that are significantly less dense than Ih, which have open cage-like structures similar to those of clathrate hydrates.<sup>46,47</sup> There is difficulty in determining the existence and structure of these phases, as without guest molecules, these open cages may form Ih and are thought to only be stable at negative pressures. Thus far ices XVI and XVII are the only known ultralow-density phases (discovered in 2014 and 2016 respectively), though simulations have indicated that there are further stable structures that have not been found experimentally.<sup>48,49</sup> The solid phases surrounding water's liquid phase include ice III and V, which have disordered hydrogen bonding, commonly called proton disorder.<sup>35</sup> Below these initial proton-disordered phases in the diagram is ice II, a proton-ordered phase, which is of particular interest since because it is considered to be proton-ordered at all temperatures and pressures.<sup>39</sup> Proton-ordered ices are blue and proton-disordered ices

are orange/red in **Figure 1.1A**. Water continues to interest researchers; it is complex, many properties are still not well understood and there are still ice phases undiscovered. As experimental techniques improve, and with the aid of computer simulations we have learnt much of this fascinating molecule and its associated structures but there is still much to discover.

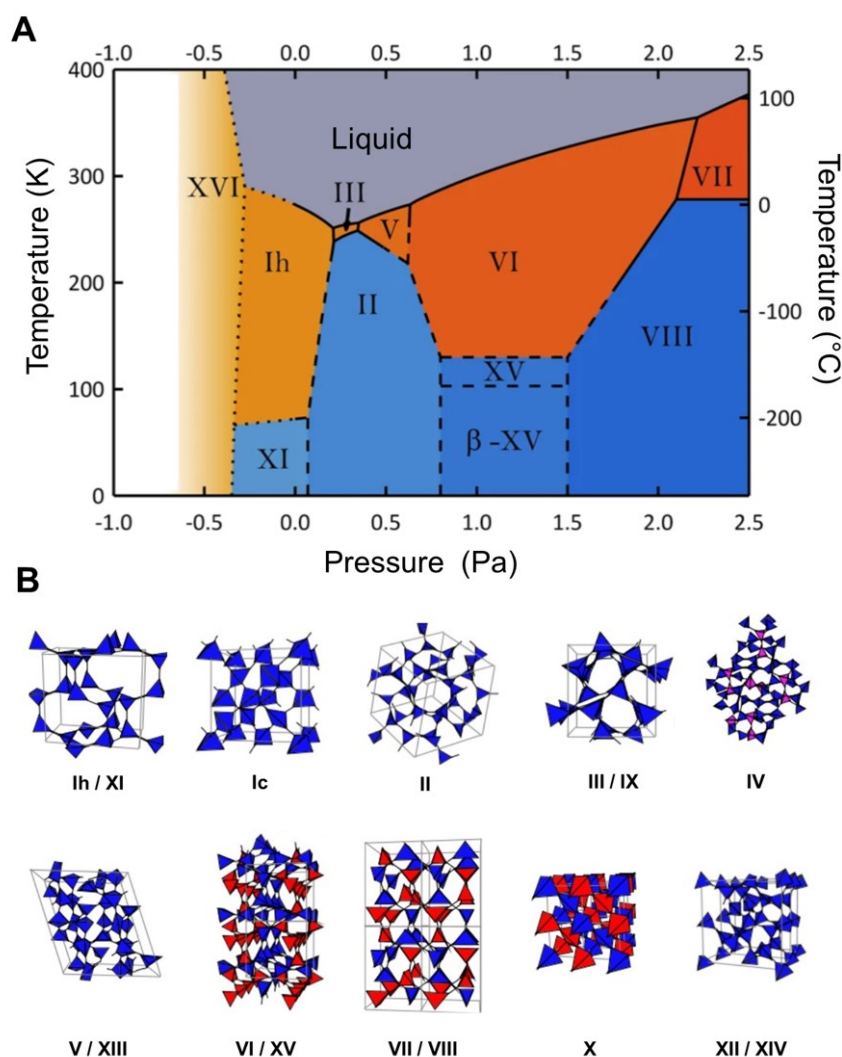


**Figure 1.1.** A) Phase diagram of stable phases of ice and liquid  $\text{H}_2\text{O}$  from 0 to 400 K over a range of pressures. Including phase boundaries (solid lines), extrapolations of boundaries based on experimental results (dashed lines) and excluding metastable phases. Dotted lines in the negative pressure regime are based on simulations. The different phases of ice are labelled using Roman numerals corresponding to their order of discovery; B) The range of structures of other crystalline ice phases. These are grouped into proton-disordered/ordered pairs (for those that the ordered form has been

discovered) as they have the same lattice structure. Adapted from Loerting *et al.* (Comm. Chem., 2020) and Salzmann *et al.* (Phys. Chem. Chem. Phys., 2011).<sup>23,29</sup>

In ice, the stoichiometry of each molecule must be preserved. This is done by observing the Bernal-Fowler rules.<sup>50</sup> These rules state that each oxygen must be covalently bonded to two hydrogens, and that only one hydrogen may be present along each bond. **Figure 1.2A** shows the structure of Ih, indicating the two positions that hydrogen can be positioned along a bond. Because of this, there is a range of possible tetrahedral Ih configurations, **Figure 1.2B**, where the structure has particular angles and lengths, **Figure 1.2C**. The O...O distance between two neighbouring water molecules (including the length of a hydrogen bond) in liquid water is approximately 2.81 Å, shortening to 2.76 Å upon freezing to Ih,<sup>28</sup> with the proton being of ~0.97 Å from one of the oxygen atoms and the associated O-O-O bond angle between three water molecules is 109.47 °.<sup>4</sup> The hydrogen bonding in Ih gives rise to hexagonal symmetry, which is visualised in **Figure 1.2D**, however there is no long-range order in the orientations of the water molecules.<sup>4</sup>

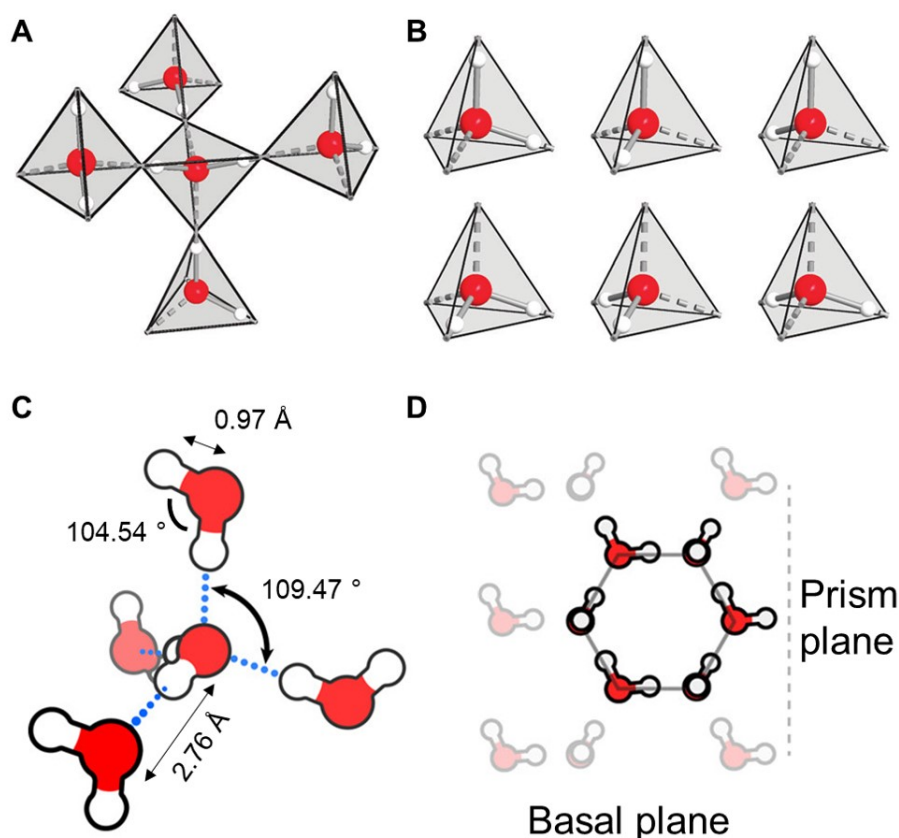


**Figure 1.2.** A) Structure of hexagonal ice, showing one water molecule within each polyhedron joined by covalent bonds (solid) and hydrogen bonds (dashed). B) Possible configurations for locations of hydrogens within a hexagonal ice crystal; C) The tetrahedral structure forms due to the hydrogen bonding between water molecules. These interactions between water molecules in Ih are highlighted here (blue dotted lines), with the O-O-O angle ( $109.47^\circ$ ) and average O $\cdots$ O length ( $2.76 \text{ \AA}$ ) included, as well as the O-H length for free water ( $0.97 \text{ \AA}$ ) that alters slightly within the Ih tetrahedral structure and the H-O-H angle ( $104.54^\circ$ ); D) Hexagonal symmetry in Ih formed by hydrogen bonding in the crystal, which gives rise to the sixfold symmetry observed in snowflakes, with prism plane and basal plane highlighted. Red = oxygen, white = hydrogen. Adapted from Salzmann *et al.* (Phys. Chem. Chem. Phys., 2011)<sup>29</sup> and Brini *et al.* (Chem. Rev., 2017).<sup>23</sup>

X-ray and neutron diffraction are techniques used to determine the crystal structures of ice phases.<sup>29,51,52</sup> Diffraction patterns, like those in **Figure 1.3**, show the ice phase present; indicating any amorphous/vitreous ice (broad peak, **D**), and can be compared to that of simulated patterns, **Figure 1.3B/C**, allowing for identification of phases formed under a range of conditions. The work here focuses on Ih, named as such due



to its hexagonal ‘snowflake’ shaped crystals that form due to its hexagonal close packed unit cell and six-fold symmetry,<sup>53</sup> therefore peaks such as those in **Figure 1.3B** would be expected. It is water’s stable phase that forms at atmospheric pressure below 0 °C. This phase is observed all over the natural world, in lakes, tundra and mountain ranges, as well as being the phase present (along with amorphous/vitreous ice – depending on conditions) in frozen biological material.

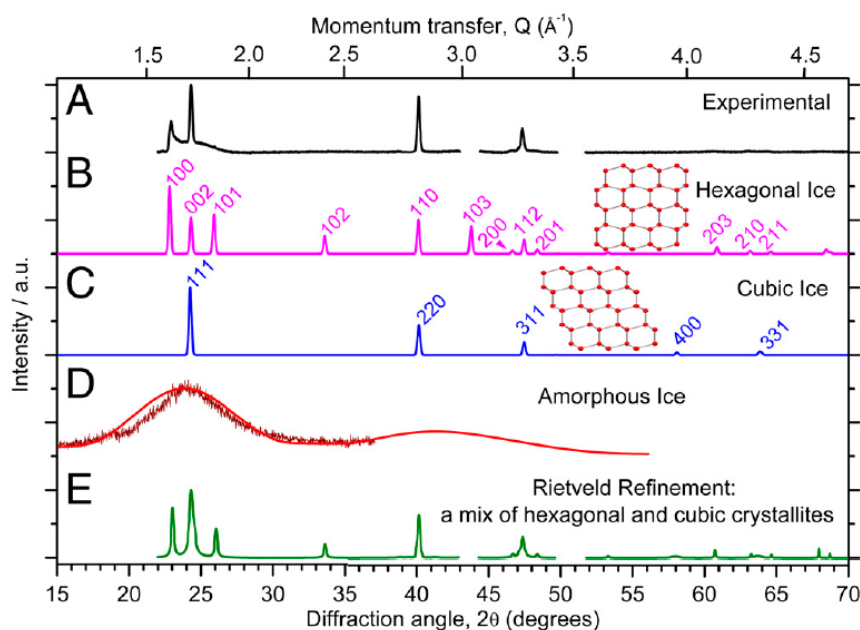


**Figure 1.3.** Experimental and calculated X-ray diffraction patterns for hexagonal and cubic ice; A) Experimental result for water droplets frozen (median freezing temperature = -41.3 °C) recorded at -100 °C; B) Simulated Ih pattern; C) Simulated Ic pattern; D) Literature diffraction patterns of amorphous ice; E) Rietveld refinement of the experimental pattern in A, assuming a mixture of Ic and Ih. Malkin *et al.*, (Proc. Natl. Acad. Sci., 2012).<sup>54</sup>

There can be defects, which lead to the formation of other polymorphs,<sup>29</sup> or can generally affect the crystal’s structure,<sup>55</sup> leading to, for example, crystal strain (as defects increase the strain energy of a crystal), rather than a phase change. Crystal strain is the inhomogeneous local strain on the lattice *i.e.* slight displacements of atoms from their normal lattice positions. Strain can be observed in X-ray diffraction as peak broadening (microstrain) and peak shifts (macrostrain). In a polycrystalline sample the local stress varies for each grain, and peak width analysis can reveal the extent of deviation from the Ih structure.<sup>4,56</sup>

When the Bernal-Fowler rules are violated, water molecules in ice can change their orientations. This occurs generally through the formation of protonic point defects that migrate through a crystal, helping to break the hydrogen bonds.<sup>35</sup> Point defects can be intrinsic (present in pure crystals at thermal equilibrium), extrinsic, (introduced with impurities), or may be frozen in with non-equilibrium concentrations. Their properties are associated with their movement within a crystal through the jumping of atoms or molecules from one site to another.<sup>4</sup> Ionic and Bjerrum defects are point defects specific to ice-like structures.<sup>57</sup> Ionic defects occur when one atom is substituted for another, leading to oxonium or hydroxide ions forming within the lattice. Dopants such as hydroxide (OH<sup>-</sup>), ammonia (NH<sub>3</sub>) and chloride from hydrochloric acid (HCl) are commonly used to introduce these defects as they accelerate the dynamics of phase transitions as they change the thermodynamic state of the ice phase.<sup>58-60</sup> Bjerrum defects can either be D or L. D occurs where two hydrogens are found along a bond between neighbouring oxygens instead of one, and L occurs when no hydrogens are found along that bond.<sup>35</sup>

## 1.2 Ice Nucleation

To form ice, water first needs to nucleate; homogeneously (without the assistance of other surfaces) or heterogeneously (assistance of particles acting as nucleants). This leads to, under ambient pressure at temperatures below 0 °C (or below -38 °C for homogeneous nucleation),<sup>61-64</sup> the formation of Ih crystals (or, stacking disordered ice (Isd) in high clouds). The stable phase needs to nucleate before any crystal growth can occur, thus for homogeneous nucleation the possibility of forming an ice embryo (critical nuclei) of a sufficient size only becomes probable at -38 °C or below.<sup>65</sup> This is due to the energy required to overcome the energy barrier for this phase transition, **Figure 1.4**. Often this barrier preventing ice nucleation is overcome by the introduction of an ice nucleating particle (INP), leading to heterogeneous nucleation.

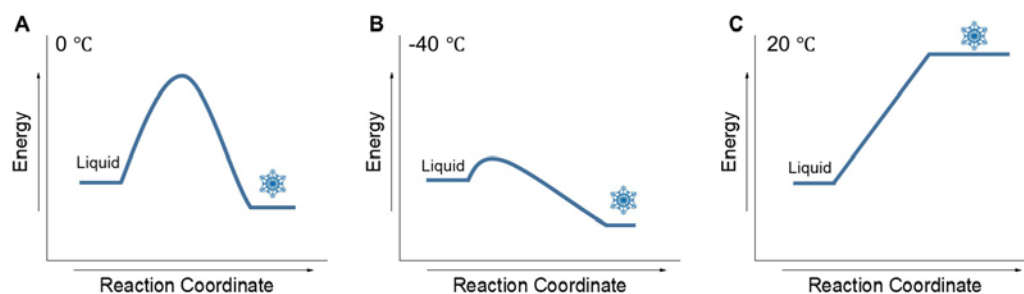


**Figure 1.4.** Examples of reaction coordinates for the ice nucleation process at A) 0 °C; B) -40 °C; C) 20 °C.

Nucleation is a crucial step in ice crystallisation, where in the first instance critical nuclei (crystal embryos) form. Heterogeneous ice nucleation has often been described by Classical Nucleation Theory (CNT);<sup>66–69</sup> where the critical nuclei have to reach a certain size in the nucleating system in order to overcome the free energy barrier and for crystal growth to occur, **Figure 1.5A**. The size of the critical nucleus required for nucleation increases sharply with rising temperature, seen as an exponential curve in **Figure 1.5B**, with a nuclei of a 1 nm radius nucleating at -38 °C, and nuclei with a 10 nm radius nucleating closer to -4 °C. The addition of an INP increases the likelihood of nucleation, though experimental investigation of the critical nuclei/particles which lower the energy barrier for crystallisation is challenging due to the ‘small’ size of the nuclei and the spatial rarity of nucleation events. The molecular diameter of a water molecule is about 2.75 Å (0.275 nm), highlighting that at higher temperatures crystal embryos must consist of many water molecules and that this is not a facile process, despite the size slightly decreasing upon freezing due to a decrease in hydrogen bond length (and increase in strength).<sup>70</sup> The smallest crystals that can form from the nuclei grow from ~75 nm to 130 nm.<sup>71</sup>

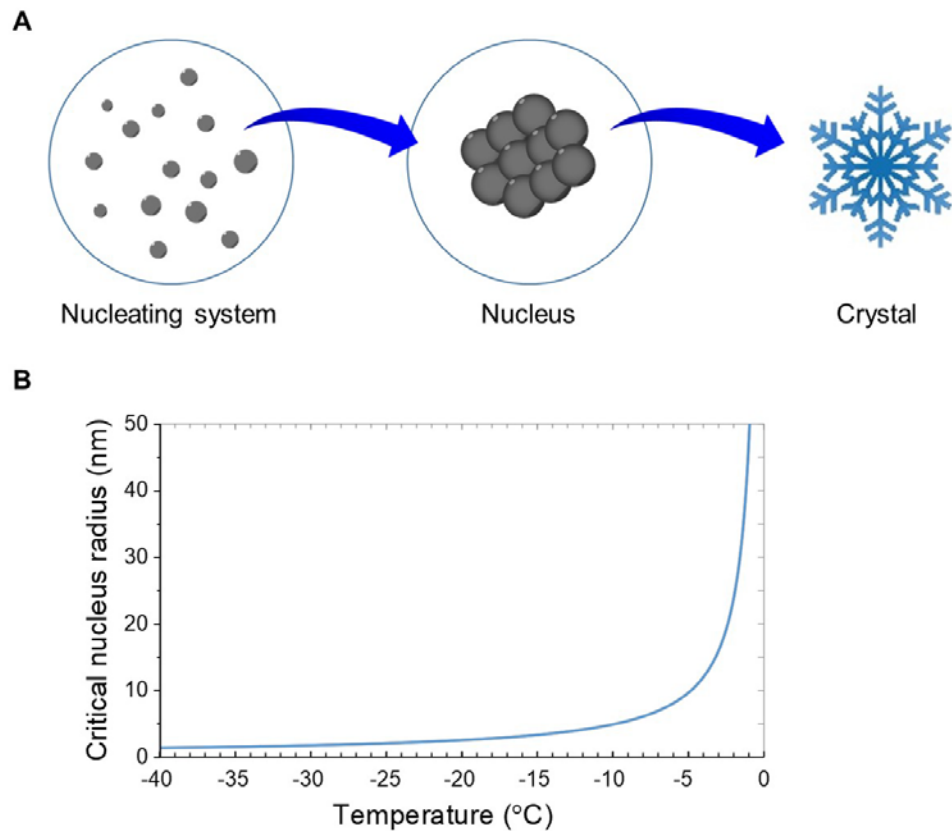


**Figure 1.5.** A) Schematic describing the ice nucleation process as explained by classical nucleation theory. According to CNT, a critical nuclei can have a 1 nm radius or longer; B) Critical radius size (nm) required for ice nucleation as a function of temperature.

The second stage of the freezing process growth, one particular growth process is Ostwald ripening, where ‘large’ ice crystals grow at the expense of smaller ones, **Figure 1.6.**<sup>72,73</sup> This occurs because the ‘small’ ice crystals are more thermodynamically unstable due to their high surface/volume ratio, so possess excess surface energy compared to the larger crystals. To reduce the interfacial energy of the system the water molecules from the smaller crystals diffuse through the solution into the larger, leading to a single ‘large’ crystal remaining.

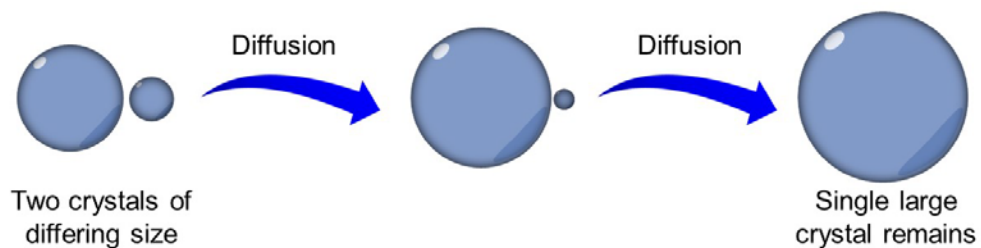


**Figure 1.6.** Schematic of Ostwald ripening in ice

Throughout the process, the total ice phase volume remains constant, but the number of crystals decreases, thus the overall surface area of crystals decreases and the mean crystal size increases (and thus the volume). The increase in mean crystal radius,  $r$ , during Ostwald ripening is described by:

$$r^3(t) = r_0^3 + k_d t \quad (1.1)$$

Where  $t$  is time,  $r_0$  is the initial mean radius at  $t = 0$ , and  $k_d$  the recrystallisation rate constant, which is volume-fraction dependent.

Many applications and processes, including biomineralisation, food production and storage, drug-formulation and anti-icing rely on understanding and controlling nucleation and Ostwald ripening. Control can be attempted by exploiting the different qualities observed in a variety of materials.

### 1.3 Materials which Affect Ice

There are many different materials that are considered ice-active including sugars, proteins, small molecules and polymers. These additives can affect freezing in a variety of ways due to their ice-activity, which is regarded as any effect on ice that is not considered colligative or 'expected' due to a change in the overall system *i.e.* decrease in temperature. This can include promotion of heterogeneous nucleation (INPs), inhibition of nucleation (anti-nucleants), or inhibition of ice growth (antifreeze (glyco)proteins (AF(G)Ps) and their synthetic mimics), this inhibition can be either in size or morphology of the crystals, **Figure 1.7**.

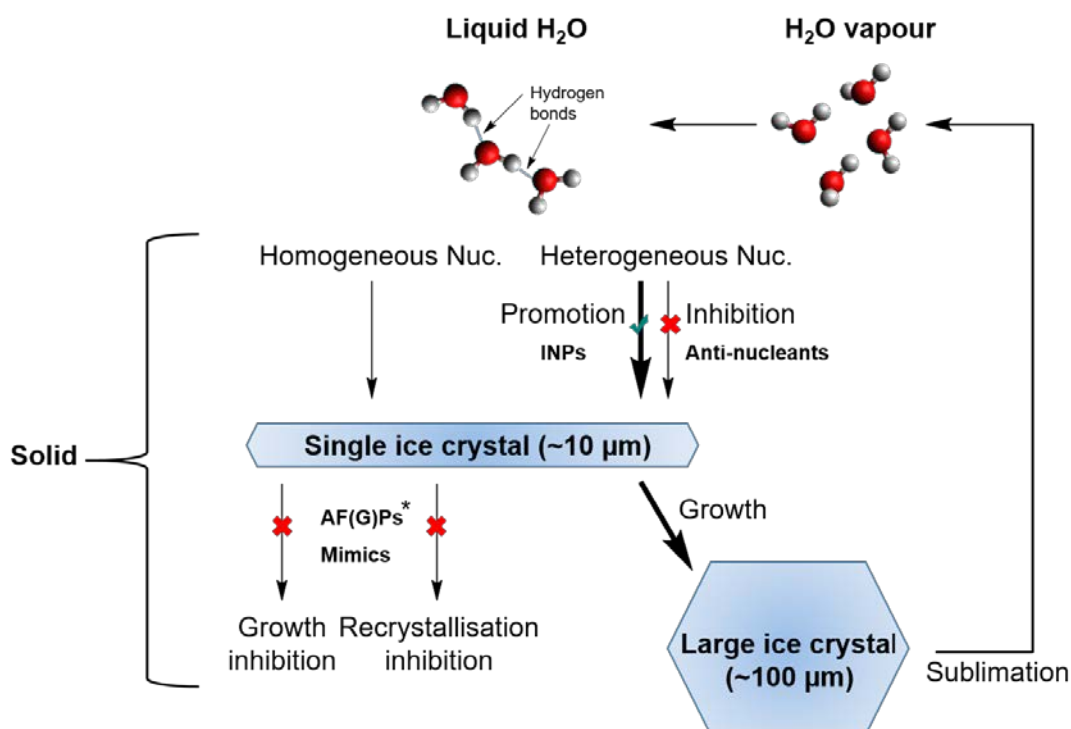


**Figure 1.7.** Representation of changes in state for H<sub>2</sub>O and the various materials that are ice-active. \*Antifreeze (glyco)proteins (AF(G)Ps) and their synthetic mimics also have other properties (thermal hysteresis (TH)) not shown here. INP = ice nucleating particle.

Of these additives, antifreeze proteins (AFPs), antifreeze glycoproteins (AFGPs) and certain polysaccharides have been found in freeze avoidant organisms.<sup>74–77</sup> Examples including the mealworm beetle (*Tenebrio molitor*), which can freeze solid over winter, winter flounder, which survives sub-zero temperatures, and various cold tolerant plants.<sup>78</sup> These antifreezes differ from commonly used colligative antifreezes due to their ability to depress the freezing point of water whilst minimally affecting these organisms' bodily fluids osmolality, whilst only requiring low concentrations for such activity. Carbohydrates are produced in freeze tolerant organisms, such as amphibians and reptiles, allowing them to survive freezing over winter and thawing in spring.<sup>79,80</sup> Other ice-active biomaterials also exist, including antifreeze glycolipids, which also suppress water's freezing point, that have been found in both freeze tolerant and freeze avoidant species.<sup>81</sup> INPs and anti-nucleants are also found in a vast range of organisms; bacteria, fungi, algae, *etc.*<sup>65,82–88</sup>

### 1.3.1 Ice Nucleating Particles

Freeze tolerance is often achieved by utilising INPs extracellularly; an organism can survive ice formation within its bodily fluids by producing INPs, which will promote ice nucleation at higher temperatures, thus preventing supercooling and consequently averting intracellular damage. Biological INPs can be also used for other reasons, particularly by plant pathogens.<sup>89</sup>

Research focussed on ice nucleation often aims to quantify and understand INPs that may nucleate ice in the atmosphere.<sup>90,91</sup> Ice nucleating proteins are particularly 'large' and efficient biological INPs found on the surface of various bacteria including *Pseudomonas syringae*, *Pseudomonas fluorescens* and *Pantoea Agglomerans*.<sup>92</sup> The most commonly studied naturally occurring INP is from *Pseudomonas syringae*, which promotes frost formation on plant leaves, enabling the pathogen to consume nutrients from plants which would otherwise survive cold temperatures by supercooling. *Pseudomonas syringae* can promote ice nucleation at warm temperatures ( $T_n$ ) in the region of  $-2\text{ }^{\circ}\text{C}$  to  $-4\text{ }^{\circ}\text{C}$ .<sup>93</sup> Biological nucleators also include plankton,<sup>94-96</sup> fungi<sup>97-99</sup> (though the INP from these species may be proteins)<sup>65</sup> and pollen,<sup>65,100</sup> which contain ice nucleating and ice-binding polysaccharides.<sup>84</sup>

Mineral dusts emitted into the atmosphere have also been observed nucleating ice in clouds.<sup>101-103</sup> Kaolinite was thought to be responsible for the observed activity in mineral dusts due to its lattice match to Ih. However recent work has shown that feldspars are much more efficient nucleators,<sup>92</sup> causing ice nucleation at temperatures between  $-3\text{ }^{\circ}\text{C}$  and  $-8\text{ }^{\circ}\text{C}$ . Whale *et al.* and Biggs *et al.* have reported a range of synthetic materials that can also promote nucleation; this includes carbon nanotubes, graphene nanoflakes, graphene oxide and associated structures.<sup>104,105</sup> In particular, carbon nanotubes were observed to be more efficient ice nucleators than the flat graphene species, with carboxylated graphene nanoflakes being one of the smallest nucleators observed so far ( $\sim 30\text{ nm}$ ). AgI has also been observed to effectively nucleate ice,<sup>106,107</sup> nucleating at much higher temperatures than any of the other non-biological nucleators tested thus far.

The mechanism by which INPs act is unclear however,<sup>108,109</sup> and the vast range of different INPs (with a range of sizes and structures) adds to the challenge in determining a relationship between physical and chemical properties and nucleation

activity. Lattice matching is considered important for ice nucleation properties,<sup>110</sup> in that substances that have similar crystal structures to ice structurally match with the first layer of ice. Hydrophobicity is thought to be involved,<sup>111</sup> and the concentration of hydroxyl groups is potentially important in lattice matching.

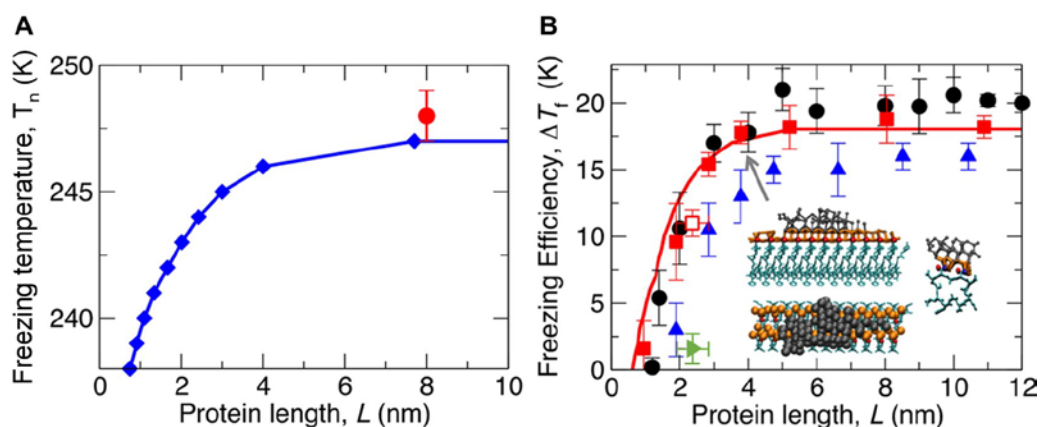


**Figure 1.8.** Examples of the effect of protein length on freezing temperature and freezing efficiency ( $\Delta T_f$ ). A) Ice nucleation temperature ( $T_n$ ) as a function of INP monomer protein length, CNT predicted  $T_n$  (blue) consistent with a cooling rate of  $1.0 \text{ K}\cdot\text{min}^{-1}$  and experimentally obtained  $T_n$  (red) for the INP monomer from *P. syringae*; B) Modelled  $\Delta T_f$  of  $TmINP$  (red closed) (a modelled protein based on stacking multiple ice-binding loops from the antifreeze protein *Tenebrio molitor* with fragments of an alcohol INP) compared to  $\Delta T_f$  alcohol INP (black circle),  $\Delta T_f$  *P. syringae* INP (blue),  $\Delta T_f$   $TmAFP$  (green triangle) and  $\Delta T_f$   $TmINP$  with the same number of binding sites as  $TmAFP$  (red open square). Inset indicates potential binding of  $TmINP$  (teal) to critical ice nucleus (grey) by an anchored clathrate (orange) (further details in 1.4.4). Adapted from Qiu *et al.* (J. Am. Chem. Soc., 2019).<sup>112</sup>

Experiments have shown that the size of the INP is important to ice nucleation efficiency, with the larger ice-binding proteins (IBP) and their aggregates nucleating ice at warmer temperatures.<sup>112</sup> How size affects nucleation is unclear however. Qiu *et al.* utilised molecular simulations and CNT to study the effect of length and aggregation on ice nucleation efficiency (they use the term freezing efficiency ( $\Delta T_f$ )), predicting that proteins with longer ice-binding surfaces will nucleate at warmer temperatures and that  $T_n$  increases with binding site length until the site reaches a certain ‘saturation’ length, causing the  $T_n$  to plateau. They concluded that IBPs are



required to aggregate in order to nucleate ice as efficiently as bacterial and insect INPs, **Figure 1.8.**

As nucleation temperatures relate to particle size and the characteristics of crystals,<sup>113</sup> nucleation assays are used to observe promotion and inhibition of ice nucleation. Both wet dispersion methods (INP dispersed in to water) and dry dispersion methods (particles dispersed in air) have been used to quantitatively study nucleation efficiency.<sup>114</sup> In a wet dispersion method volumes ranging from millilitre to picolitre have been used,<sup>90,115</sup> though generally microlitre size droplets of water are measured (a 1  $\mu\text{L}$  droplet would be  $\sim 1$  mm in diameter, which is observed to freeze completely upon nucleating) and in dry dispersion methods, which include cloud chambers,<sup>116,117</sup> the aerosol size distributions and concentrations can vary and typically lead to crystals above 3 – 5  $\mu\text{m}$ . A range of approaches have been used in attempt to mimic the actions of biological nucleators as well as to determine ice nucleation efficiency,<sup>114</sup> these have studied the effect of a range of variables including, INP concentration, temperature, cooling rate (or isothermal experiments),<sup>118–120</sup> time and droplet size.

The techniques that relate to the work in this thesis are wet dispersion techniques, in particular droplet freezing assays, which involve a sample dispersed in water being divided into sub-samples on a cold stage that is subsequently cooled allowing monitoring of the freezing process. In general, the temperature at which nucleation occurs is recorded alongside video footage, and both linear cooling rates as well as isothermal experiments have been performed.<sup>118–120</sup> Freezing is observed visually, where nucleation is detected by a change in reflection of incident light, using a microscope. Other wet dispersion techniques to obtain nucleation temperatures include using emulsions of water droplets in oil, microfluidics and calorimetry.<sup>1,121,122</sup> Calorimetry has been used as a method for studying AFP activity since 1988, when Hansen and Baust recorded the freezing temperatures of AFP type III from *Tenebrio molitor* suspended in oil.<sup>123</sup> Calorimetry, especially when used in combination with microfluidics (using microemulsions),<sup>124</sup> can provide the option to record nucleation temperatures without the problem of contamination from surfaces (as in microscopy based techniques), though they may lead to a change of location of INPs in droplets.

### 1.3.2 Antifreeze Glycoproteins

In 1957, it was observed that Arctic fish survive well in supercooled waters at temperatures of 0.7 °C below the freezing point of their blood serum (-0.9 °C to -10 °C).<sup>125</sup> The peptides that were found to be the cause of this freezing point depression (a thermal hysteresis effect), initially called freeze depressing (glyco)proteins (FDGPs), were studied in comparison to sodium chloride, and were found to exhibit a greater thermal hysteresis capacity.<sup>126</sup> These FDGPs have been found to also possess two other ice-active properties; ice recrystallisation inhibition, where Ostwald ripening is suppressed, and the ability to shape ice crystals into needles by binding particular ice faces – known as dynamic ice shaping. This led to the re-characterisation of these proteins to antifreeze glycoproteins (AFGPs).<sup>18</sup>

When studying the mechanism of action of these macromolecular antifreezes, their structure must be considered. AFGPs have a highly conserved structure and are produced in a range of chain lengths, with the primary structure (**Figure 1.9A**) consisting of a repeating tripeptide unit (alanyl-alanyl-threonine). *O*-linked disaccharide motifs are attached at the threonine sidechains.<sup>127</sup> AFGPs come in a range of sizes, and are grouped by isoform into groups; AFGP1-5 ('large': with 16 – 52 repeat amino acid chains) and AFGP7-8 ('small': with 4-5 repeat chains),<sup>127</sup> the longer sequences of which exhibit a greater magnitude of antifreeze activity.<sup>128</sup>

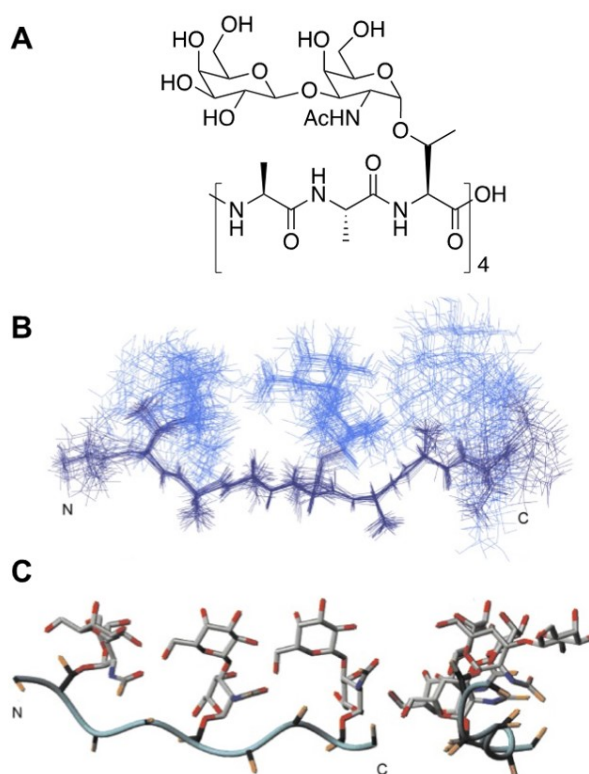


**Figure 1.9.** A) Structure of AFGP repeat unit. AFGPs with four repeat units and molecular weight of 2.6 kDa are AFGP8, and those with molecular weight of 33.7 kDa are AFGP1. Molecular weights of AFGP2-7 are between these two values;<sup>129</sup> B) 25 lowest energy structures calculated for a synthetic AFGP3 using NMR-based constraints. (Peptide backbone = purple, carbohydrate moieties = blue); C) Synthetic AFGP3 structure produced from the closest to average of 25 best calculated models. (methyl carbon = yellow, carbohydrate carbon = white, peptide side chain carbon (bar methyl carbon) = grey, nitrogen = blue, oxygen = red). Adapted from Tachibana *et al.*, (Angew. Chemie. Int. Ed, 2004).<sup>130</sup>

The AFGP structure is considered to be flexible (high number of possible conformers suggests high flexibility),<sup>131,132</sup> and whilst there is general agreement in that they exist as left-handed 3-fold helices (the helix has 3-fold symmetry),<sup>133</sup> their secondary and tertiary structures have not been crystallographically confirmed.<sup>132</sup> Tachibana *et al.* produced a structure for an AFGP3 (essentially identical to naturally occurring AFGPs) by modelling lowest energy structures, **Figure 1.9B**, showing that the peptide backbone folds into a left handed helix, from which the three disaccharide moieties construct a hydrophilic face on one side, concluding that AFGPs activity is derived from its intrinsic conformation.<sup>130</sup> The structure function relationship is not fully

elucidated, however the disaccharide moiety is vital to AFGP efficacy and studies into structural modifications have shown a loss in antifreeze activity upon its removal.<sup>130,134</sup>





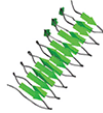
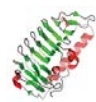
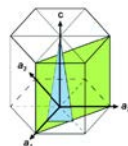
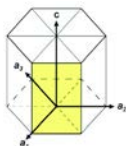
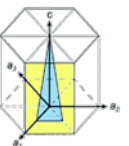
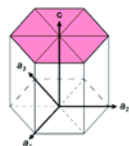
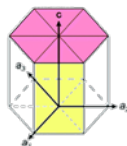
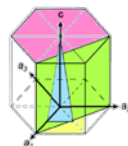
AFGPs have been found to be produced by a range of Antarctic notothenioids and cods, thus protecting them from freezing in the sub-zero environments they live.

### 1.3.3 Antifreeze Proteins

Antifreeze proteins (AFPs) are proteins which, despite lacking the sugar moiety, have similar ice-active properties to AFGPs. A range of isolated species, including insects,<sup>135</sup> fish,<sup>136</sup> bacteria<sup>137</sup> and plants,<sup>138</sup> developed AFPs through convergent evolution.<sup>139</sup> Discovered later and found in a wider range of organisms, they have many more structural variations (and mass ranges), as well as binding capabilities to various ice planes, **Table 1.2**. These proteins are classed as type I, type II, type III, insect AFPs, plant AFPs and 'other' (which includes proteins from algae, diatoms, fungi, bacteria). Structural uniformity within classes of organisms is low (different AFP structures have been observed in the same ocean fish)<sup>140</sup> but generally the AFPI class are alanine rich and alpha helical, AFPII are globular, cysteine rich proteins, type III are smaller globular proteins often with a  $\beta$ -sandwich secondary structure and the AFPs from insects, plants, bacteria, diatoms *etc.* are much more varied, with some composed of  $\beta$ -sheets and others polyproline type II coils<sup>141</sup> or left-handed  $\beta$ -rolls.<sup>142</sup> Some proteins have been found to bind the same ice planes, for example AFPII, AFPIII and plant AFPs have all been observed binding ice's primary prism plane. There is also plane-binding variation within the different AFP types; AFPI from the winter flounder and Alaskan plaice bind pyramidal planes and the shorthorn sculpin AFPI binds secondary prism planes.<sup>143</sup>

These proteins also inhibit ice crystal growth (though to a lesser extent than AFGPs) and depress the freezing point of water non-colligatively. Some AFPs, in particular type I, have displayed even higher thermal hysteresis activity. This hyperactivity can be seen in the example TH activity in **Table 1.2**, where hyperactive AFPs, such as those from *T. molitor* and *M. primoryensis*, have a much higher activity than the moderately active AFPs at concentrations of at least 10x lower.<sup>78,144</sup> Concentrations of AFPs in the table vary due to the concentrations recorded in the literature.

**Table 1.2.** Types of antifreeze proteins and respective example masses, structures, binding planes and origin. Adapted from Voets, (Soft Matter, 2017) and Barrett (Int. J. Biochem. Cell Biol., 2001).<sup>145,146</sup>

	AFPI	AFPII	AFPIII	Insect AFP	Plant AFP	Other
<b>Example Masses (kg.mol<sup>-1</sup>)</b>	3-4.5	11-24	6.5-14	6-9	13	24.5
<b>Example structure</b>						
<b>PDB</b>	1WFA <sup>147</sup>	2PY2 <sup>148</sup>	1KDF <sup>149</sup>	1M8N <sup>150</sup>	3ULT <sup>142</sup>	3VN3 <sup>151</sup>
<b>Binding plane</b>	Pyramidal & 2° prism	1° prism	Pyramidal & 1° prism	Basal plane	Basal & 1° prism	Varied
						
<b>Origin</b>	Right-eyed flounders, sculpins	Herring, sea raven, smelt	Eel pout, ocean pout, wolfish	Beetles, moths, midge, flies	Grasses	Algae, diatoms, fungi, bacteria
<b>Example TH (°C)</b>	Winter flounder: <0.6 °C (1 mM) <sup>78*</sup>	Sea Raven: ~0.4 °C (0.2 mM)	Ocean pout: ~0.8 °C (1 mM) <sup>152</sup>	<i>T. molitor</i> : 3.5 °C (0.1 mM) <sup>153</sup>	<i>Lolium perenne</i> : ~0.2 °C (0.04 mM) <sup>154,155</sup>	<i>M. primoryensis</i> : 0.76-1 °C (0.8 μM)

\*Both moderately active AFPs and hyperactive AFPs have been extracted from Winter Flounder;<sup>156</sup> The hyperactive AFP (dimeric species) has a TH >1 °C at 3 μM, whereas at this concentration the moderate AFP has a TH of <0.1 °C. Planes are colour coded: Basal plane (0001) = pink, primary (1°) prism plane (10 $\bar{1}$ 0) = yellow, secondary (2°) prism plane (11 $\bar{2}$ 0) = green, pyramidal plane (20 $\bar{2}$ 1) = blue.

AFPs are easier to synthesise than AFGPs due to the lack of need for post-translational modification, and can be more easily modified, *e.g.* addition of different protein expression tags and conjugation to other compounds. This has enabled greater bouts

of research into their structures and ice-activity. Their structures include a range of  $\beta$ -barrels and  $\alpha$ -helices,<sup>19</sup> the snow flea (*Hypogastrura harveyi*) AFP for example consists of 6 stacked helices,<sup>141</sup> and the ocean pout (*Zoarces americanus*) is globular and composed of  $\beta$ -sheets.<sup>149</sup> Both AFGPs and AFPs have hydrophobic and hydrophilic domains, with AFPs generally consisting of a large mixed cluster with an ordered ice-binding face. AFPs also consist of a high alanine content (~60 %),<sup>157</sup> whilst remaining water soluble.<sup>158</sup>

AFPs essentially have the same ice-activity despite their structural differences, with hyperactive AFPs such as *H. harveyi* and spruce budworm moth (*Choristoneura fumiferana*) having a greater ability to depress water's freezing point.<sup>159</sup> They are thought to work by binding ice, however it has been difficult to elucidate the exact binding mechanism.<sup>140</sup> Site-directed mutagenesis has been performed on AFPs, enabling modification of the proteins by the substitution of amino acids thought to be involved in ice-binding. This has aided in elucidating the binding site structures, as modification of amino acids involved leads to reduced ice-activity, meaning investigation into their antifreeze properties is possible.<sup>160</sup>

Generally AFPs are thought to bind the prism planes of ice leading to preferential growth at the c-axis (basal plane).<sup>138,161</sup> Theories first suggested that binding occurs due to pattern matching between the growing ice face and the hydroxyl groups of AF(G)Ps due to specific spacing between the groups.<sup>162</sup> Another more recent theory is based on the anchored clathrate mechanism, where the AFP orders nearby water molecules to be more 'ice-like'. This ice-like water can freeze more readily than the bulk water and thus bind the AFP to the ice surface.<sup>163</sup> The ice-binding mechanism is complex and alongside the suggested theories there is also debate as to whether the proteins bind reversibly<sup>164</sup> or irreversibly.<sup>165</sup>

## 1.4 Mechanisms of Action

There currently is a debate over the mechanism of growth of ice and its inhibition, in particular in relation to ice-active materials. Numerous studies have been performed and theories proposed.

Three key macroscopic effects associated with ice-activity for AF(G)Ps have been observed, these are Dynamic Ice Shaping (DIS); morphology of a growing ice crystal is changed; Ice Recrystallisation Inhibition (IRI); crystal growth is inhibited; Thermal Hysteresis (TH); a non-equilibrium depression of the freezing point.<sup>161,166,167</sup>

### 1.4.1 Dynamic Ice Shaping

DIS is where the growth of certain ice crystal faces is inhibited. This happens when an antifreeze binds ice. Different antifreezes have an affinity for different ice planes (as seen with AFPs, **Table 1.2**) leading to variations in crystal shape.

Assays have been important in gaining knowledge of which ice faces are bound.<sup>167,168</sup> Techniques used have included pitting (allows observation of ice-binding as pits observed where binding occurs) and hemispherical etching (pattern of ice layer formed indicates the orientations at which AFPs adsorb onto ice).<sup>169,162</sup> A more recent technique is fluorescence-based ice plane affinity (FIPA), where AFPs are fluorescently labelled before incorporation into an ice crystal prior to imaging under UV light,<sup>170</sup> which provides the option to simultaneously compare different ice-binding patterns of different AFPs with clearer images in a shorter time frame. More commonly microscopy-based assays are used. Concentrated sucrose solutions have been used as a solvent for these assays rather than pure water, as this method allows for liquid to be present between ice crystals, enabling the study of the morphology of the crystals, as well as how they grow without the interference of interactions between grain boundaries.<sup>171,172</sup> During a sucrose ‘sandwich’ assay a sample of interest is pressed and sealed between two glass slides, frozen, warmed briefly and annealed so crystal habits can be observed. Generally sucrose solutions are 30 - 45 wt % sucrose, depending on the procedure followed.<sup>144</sup>

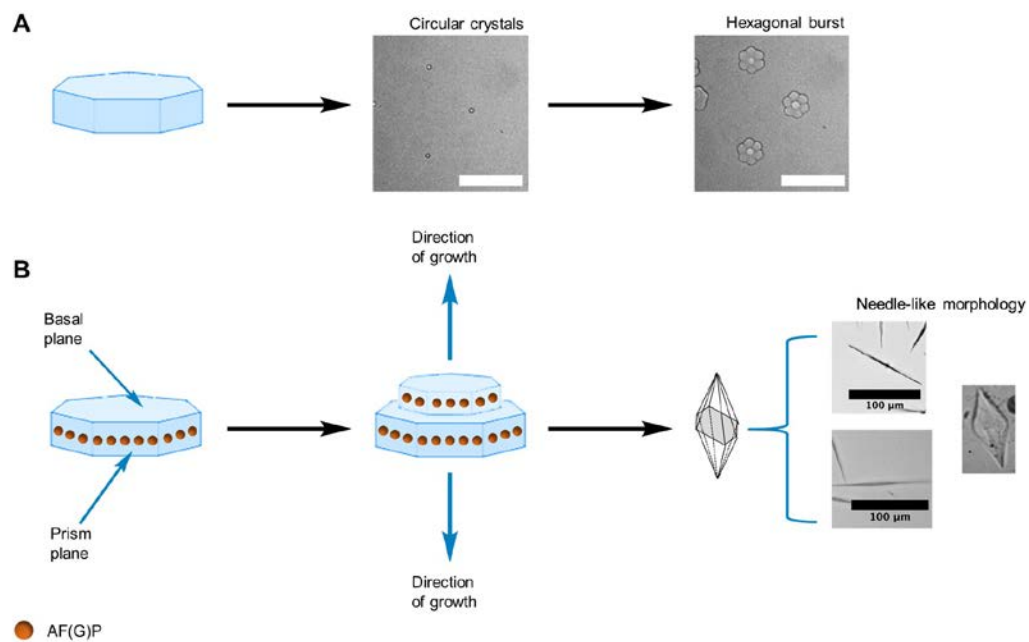


**Figure 1.10.** Schematic of the dynamic ice shaping process. A) Pure water crystal morphology over time; B) Morphology modification over time, due to binding of AF(G)Ps to the prism plane. Scale bar = 100  $\mu\text{m}$ .

Pure Ih ice crystals are round and flat, leading to hexagonal burst patterns upon further cooling, **Figure 1.10A**. Upon addition of ice-binders the surface curvature of the ice increases, depressing the equilibrium freezing temperature.<sup>172,173</sup> An increase of curvature leads to an increase in vapour pressure, a decrease in melting point and the decline in assimilation of further water molecules into the ice at certain points. These limit growth and modification of crystal morphology, an example of which is the addition of AFGPs which bind the prism plane leading to needle-like crystals, **Figure 1.10B**.<sup>174</sup>

DIS is problematic for cryopreservation, as when needle-like crystals form they can puncture cells. DIS is generally observed in TH active materials, such as AF(G)Ps, this makes them less useful for use as CPAs. Thus, colligative antifreezes such as ethylene glycol (EG) or dimethyl sulfoxide (DMSO), which prevent crystallisation without shaping ice, are the most commonly used.



## 1.4.2 Ice Recrystallisation Inhibition

Ice recrystallisation (IR) can be accretive, isomass and migratory, the mechanism of which depends on size of ice crystals;<sup>175</sup> for example accretion dominates when crystals are ‘small’ and close together.<sup>176</sup> IR is the process of change in number, shape and size of ice crystals over time and can be lethal to biological matter as it causes dehydration and cellular damage, particularly to cell membranes.<sup>172,177</sup>

IRI is the observed effect by which this growth of ice crystals is impacted, slowed, or halted when freezing occurs in the presence of an antifreeze, the first measurements of which were demonstrated in 1988 by Knight *et al.*<sup>178 177</sup> IRI can be affected by ions in solution and must be considered when performing assays to test for this activity.<sup>179,180</sup>

The most common technique used to analyse IRI activity currently is the ‘splat’ cooling assay, which follows Ostwald ripening, **Figure 1.11**, which enables the visualisation of ice growth (at a micrometer scale) and thus the inhibitor potency.<sup>181,182,183,184</sup> This method is relevant for monitoring inhibitor potency as it enables the viewer to monitor crystal growth in real time, isolate grain growth (*i.e.* not observe nucleation) and was introduced due to the need to study how ice recrystallisation is affected by the addition of a variety of impurities as there were few techniques that performed this successfully.<sup>178</sup> In a typical splat assay a sample solution is dropped onto an aluminium plate held at -78 °C to form a very thin wafer of polycrystalline ice. The sample is then transferred to a coldstage (-6 °C to -8 °C) for annealing for 30 minutes. The crystal sizes (and how they change over time) are then recorded using a microscope; the length of crystals (mean largest grain size, (MLGS)) can be measured along any axis and the mean ice grain size (MGS) is calculated from the number of crystals observed. Crystals observed through the microscope will be of approximately 10-20 µm in diameter at t=0 minutes. These will grow over the 30 minute anneal and provide a macroscopic visual of inhibitor potency; the smaller the crystals, the more potent the IRI inhibitor. Crystal sizes will be compared to that of a control sample (PBS only), which will have large crystals (>100 µm) with defined grain boundaries. Crystals that are 20 % of the size of control crystals are considered to be highly potent IRI inhibitors.

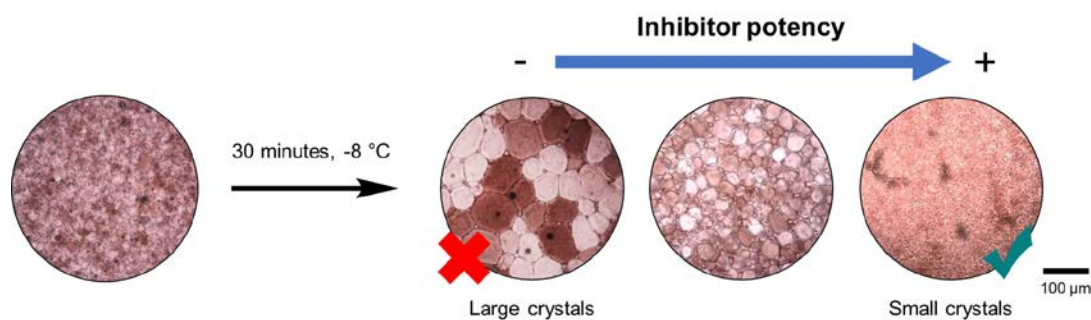


**Figure 1.11.** Example of micrographs of nucleated ice crystals obtained from a splat recrystallisation assay before and after 30 minutes annealing, and the difference in crystal size as inhibitor potency increases. Approximate crystal diameter at  $t=0$  minutes: 10-20  $\mu\text{m}$ . Large crystal diameter at  $t=20$  minutes:  $> 100 \mu\text{m}$ . Scale bar = 100  $\mu\text{m}$ .

Sucrose assays have also been used in a similar manner to follow this ice growth.<sup>144,168,185</sup> The crystals obtained in this assay are more separated due to the high viscosity of the media, and hence image analysis can be used to identify each crystal, as shown by Budke *et al.*<sup>185</sup> It is also important to be able measure growth in the media of interest, and the 20 - 45 wt % sucrose required<sup>168</sup> for this is not relevant for all conditions, and it has emerged recently that salts have a profound effect on growth rates, hence the appeal of measurement in buffers.<sup>186,187</sup>

One considerable downside to these microscopy-based assays is that there is not really an easy to implement high-throughput method. Individual samples take many hours of set-up, annealing and analysis.<sup>185,188</sup> There are also issues with the splat assay in particular, as when ‘large’ anomalous crystals form they can skew results, especially as only ‘small’ sample areas are analysed. Tomczak *et al.* presented another technique for determining IRI activity of an AFP using 10  $\mu\text{L}$  capillaries.<sup>189</sup> These are useful for endpoint measurements, however, do not provide much information on the rate or change in crystal size during experiments. Yet, they do allow for storage of samples, which then can be tested reproducibly in further IRI assays.

### 1.4.3 Thermal Hysteresis

Another property of ice-active materials is TH; this kinetic effect (not highlighted in **Figure 1.7**) is the observed difference between the melting point and non-equilibrium

(hysteresis) freezing point of ice, which is known as the TH gap (within which nucleated ice crystals do not melt or grow), **Figure 1.12**.<sup>146,166,167</sup> This is a non-colligative freezing point depression effect; *i.e.* the freezing point ( $T_f$ ) is lowered whilst the melting point ( $T_m$ ) of the ice remains the same. The effect is much greater than it would be if dependent on the concentration of the solute containing solution, leading to a microcurvature of the rest of the ice surface making binding of other ice molecules thermodynamically unfavourable, thus decreasing the water freezing point.<sup>172</sup>

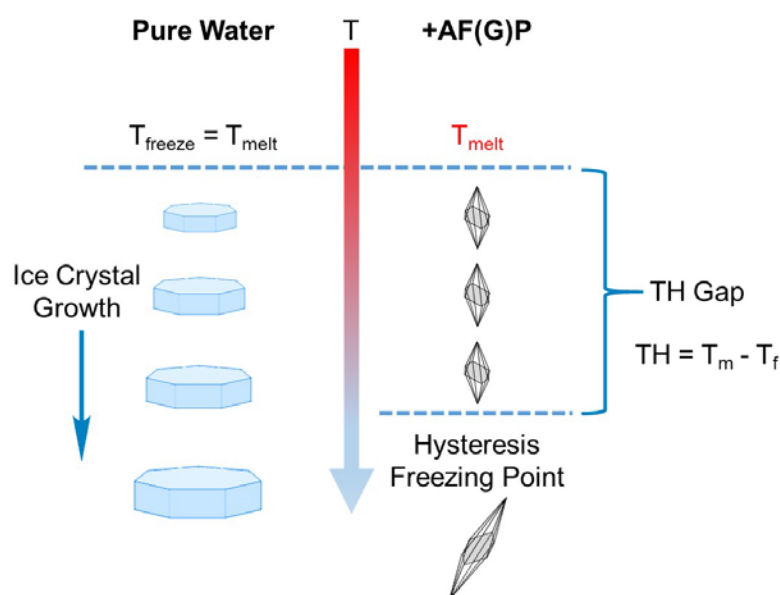


**Figure 1.12.** Cartoon depicting thermal hysteresis effect of AF(G)Ps on ice crystal growth. Upon addition of AF(G)Ps, ice crystal growth is suppressed within the TH gap, with growth occurring post the hysteresis freezing point. TH is calculated as the difference between  $T_f$  and  $T_m$ .

TH has been observed in both freeze tolerant and freeze avoidant organisms, and was thought to be linked to IRI activity, deriving from the AF(G)Ps ice-binding capabilities.<sup>178,190</sup> However, recent studies propose there is no relationship between the two, as IRI and TH activity do not increase at the same rate for different AFPs, implying different proteins may use different mechanisms of action for ice-activity.<sup>155,191</sup> TH and DIS appear to be correlated as all molecules with TH activity cause defined changes in crystal morphologies.<sup>161,192</sup> The precise mechanism is unknown, however it has been suggested that TH occurs due to the AF(G)P binding a single ice crystal in a supercooled solution, which then prevents expansion/melting

within the TH gap. The extent to which proteins are TH active has also been studied, suggesting that size affects activity.<sup>193</sup>

The most common method used to test this mechanism and study TH activity has been nanoliter osmometry, where droplets of aqueous samples are observed under a microscope.<sup>130,167,194,195</sup> Samples are frozen and then melted until a single crystal remains. To determine the TH of a sample the crystal is cooled further until there is a sudden burst in growth. There are limitations in determining TH in this way, as it depends on factors such as cooling and melting rate, the annealing time of the experiment and the initial sizes of sample crystals.<sup>196</sup> Differential scanning calorimetry has more recently also been used to investigate the TH effects of AFP segments.<sup>197</sup> Gaede-Koehler *et al.* developed a sonocrystallisation-based method, in which a sample solution is supercooled slowly to  $\sim -6$  °C, a short ultrasound pulse is then applied, which results in nucleation and freezing.<sup>198</sup> The samples are then slowly melted and the freezing and melting points determined. This method allows for control of the degree of supercooling, the rate, and is independent of initial crystal size and has been observed to provide highly reproducible measurements.<sup>167</sup>

The range of techniques above have enabled researchers to discover and design a range of compounds that can mimic the properties of anti-icing, ice growth inhibition and morphology modification, though how these ice-active materials work has not been wholly confirmed.

#### 1.4.4 Ice-binding

Ice-binding has been considered important;<sup>168,181</sup> research has stated that it was necessary for ice-active materials to bind particular ice faces, especially when explaining their activity using the adsorption-inhibition mechanism, **Figure 1.13**, and this binding may be the cause of freezing point depression and IRI, as macroscopic ice growth is inhibited due to an increased ice crystal curvature between adsorbed proteins and thus increased vapour pressure and increased energetic cost of adding a water molecule to the ice surface.<sup>192</sup> Zepeda *et al.* researched AFGP adsorption, showing that it is not an instant process, but takes seconds to reach maximum coverage, though they noted that ice growth halts upon adsorption of only a small number of protein molecules to the lattice.<sup>199</sup> This led them to conclude that first, protein molecules

strongly bind to the ice surface and halt ice growth, after which proteins will bind weakly. Potentially if weak enough, water molecules could replace the weakly bound proteins enabling ice growth (reversible binding). AF(G)P binding can also be affected by cooling rate and annealing time; Takamichi *et al.* studied TH changes for AFPIII based on the adsorption-inhibition model finding that fast cooling rates ( $0.20\text{ }^{\circ}\text{C}\cdot\text{min}^{-1}$ ) decreased TH and that long anneals (3 hours) enhanced TH up to 2.5-fold,<sup>196</sup> proposing this enhancement to be due to additional ice binding occurring.

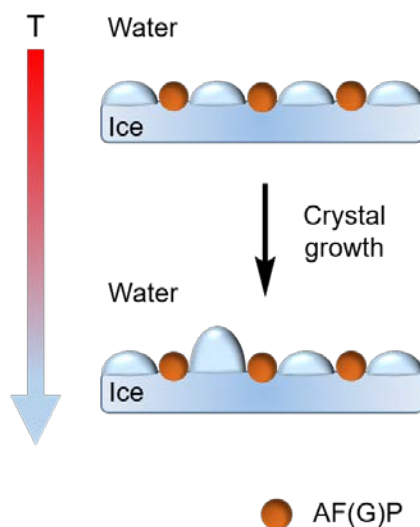


**Figure 1.13.** Schematic depicting the adsorption-inhibition mechanism (step-pinning model) of ice growth and formation of convex ridges between proteins. As the temperature decreases the curvature of the ice crystals between bound AF(G)Ps grows. The smaller the spacing between the adsorbed proteins, the lower the temperature required for ice propagation due to the increased curvature. This model (and related models including the kinetic pinning model) relate to the size and shapes of proteins involved.<sup>200</sup>

However, recent work suggests that inhibitors may function by occupying a liquid-like layer (or thin liquid layer),<sup>17,166</sup> sometimes referred to as a quasi-liquid later (QLL) (which is strictly a definition at surfaces).<sup>201</sup> These interfacial waters have been suggested to be a thin layer (*e.g.*  $10 - 15\text{ \AA}$  wide) on the surface of ice grains, occupying the ‘bulk water’ space where the molecules are neither in a rigid solid structure nor in the liquid state, within which the ice-like structure gradually changes until it is also bulk water.<sup>202,203</sup> These may have a different pH to the bulk of the solution, this could be important as the ice surface may differ to the bulk.<sup>179,180,204</sup>

Data collected through modelling AFPs supports the anchored clathrate mechanism, finding that hyperactive AFPs (such as *mpAFP\_RIV*<sup>163</sup> or *sbwAFP*<sup>205</sup>) bind ice through distinct anchored clathrate motifs rather than by directly binding the ice.<sup>206</sup> As mentioned in **1.3.3**, the mechanism explains that when the temperature of a water:AF(G)P solution becomes low enough, the water molecules in the protein's solvation shell become more structured and less dynamic. This region is more ice-like thus has a lower energy barrier to ice formation. This mechanism considers the QLL/liquid-like layer to be of importance as when the protein approaches ice, it comes into contact with the QLL and the ordered waters at the ice-binding site merge with it.<sup>163</sup> A QLL here is defined as a thin film of liquid water that exists on the surface of ice crystals below melting temperatures.<sup>207,208</sup> Though there are debates as to the definition of a QLL, thus in this thesis we are referring to the behaviour pertaining a liquid-like layer. Garnham and co-workers state that this mechanism is applicable to any AFP, though their studies are primarily molecular dynamics (MD) simulations, meaning studies probing AFPs on the ice surface directly may provide details of the process of AFP adsorption and the role of anchored clathrate waters.

MD has assisted with rationalising and guiding experimentalists, as well as complementing results gathered thus far. Recently computational studies have been performed to help elucidate an AF(G)P synthetic mimic, poly(vinyl alcohol)'s (PVA's) mechanism of action (for further details see **1.4.5**), as well as into how it binds ice, indicating that it binds differently to AFGPs, **Figure 1.14**. Mochizuki *et al.* state that AFGPs are thought to bind through the adsorption of methyl groups of both the peptide backbone and disaccharide moieties to ice, and that segregation of hydrophilic and hydrophobic groups in the protein's helix is integral to the ice-binding mechanism, **Figure 1.14A**.<sup>164</sup> Their theory is based on work utilising simulation cells containing 10,000 water molecules and one AFGP8 molecule to reflect AFGP8's ice-activity at low concentration, showing that the disaccharide moieties in AFGP8 lead to the highly organised and compact 3-fold helical structure and are key to AFGP8 binding ice because of the spatial segregation between the disaccharides and hydrophobic groups on the peptide. They noted that when hydrophobic groups face the growing ice lattice, growth halts but continues if disaccharides face the lattice, and that AFGP8 binds this plane exclusively through the hydrophobic groups because the distance between nearest CH<sub>3</sub> neighbours for each repetition of the 3-fold helix

matches twice the distance in the primary prismatic ice face (0.93 nm and  $\sim 0.91$  nm respectively).

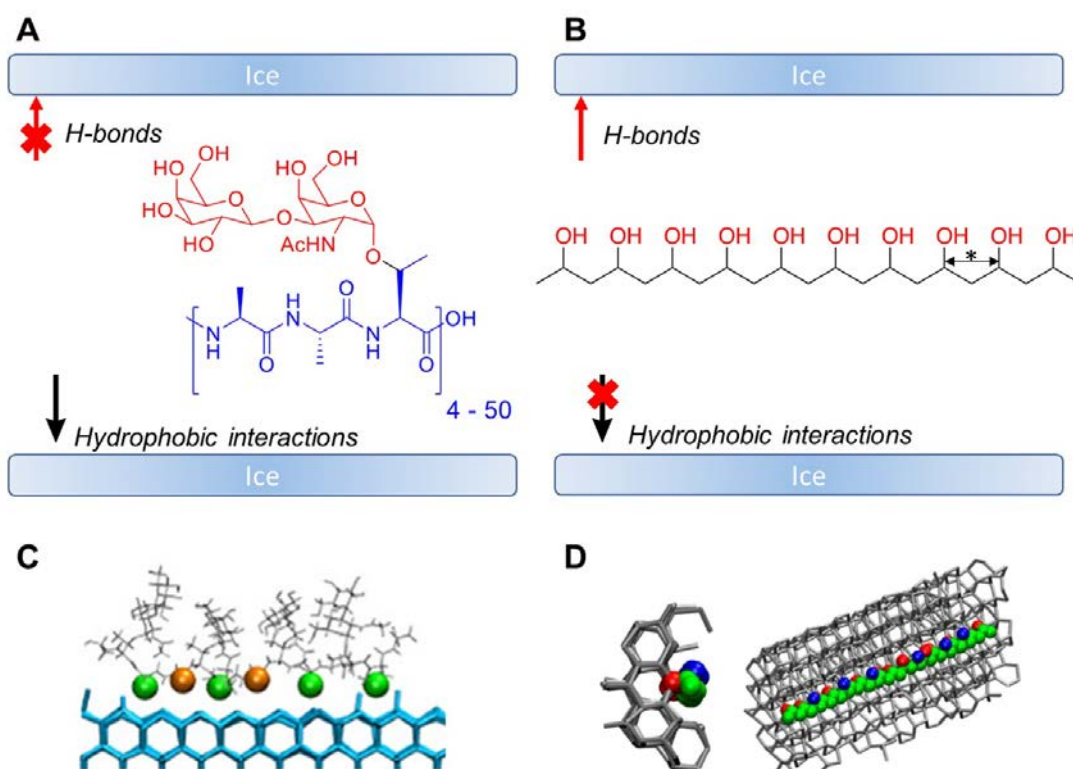


**Figure 1.14.** The differing possible mechanisms of action for PVA and AFGP. A) AFGP binding *via* hydrophobic interactions. Hypothesis supported by work from Mochizuki *et al.* showing the binding is due to hydrophobic interactions between  $\text{CH}_3$  groups (0.93 nm between neighbours) and the primary prismatic face of ice where twice the lattice distance is  $\sim 0.91$  nm; B) PVA interacting with ice *via* hydrogen bonds. Hypothesis supported by work from Naullage *et al.* where they show the OH-OH distance in PVA highlighted (\*) as 2.92 Å (this distance when between 4 groups is 7.46 Å), and the distance between O-O in the primary prismatic plane of ice parallel to the *c*-axis as 2.70 Å.<sup>209</sup> C) Example binding configuration of AFGP8 to the primary prismatic plane. (Orange and green spheres = methyl groups bound); D) Side and front views of PVA bound to ice. Once PVA binds ice, the PVA adopts an isotactic configuration, where all the methylene groups orient in the same direction. The polymer hydrocarbon backbone lies along the prismatic plane, parallel to the *c*-axis. Adapted from Mochizuki *et al.*, (J. Am. Chem. Soc., 2018) and Naullage *et al.*, (J. Phys. Chem. C, 2017).<sup>164,209</sup>

Naullage *et al.* used large-scale MD simulations and computationally efficient coarse-grained models to study PVA. They used the monatomic water model mW, where each molecule is represented as a single particle that interacts only through short-range anisotropic interactions. Their simulation cells used to study the interaction of PVA and ice contained water molecules in both liquid and solid phases (minimum 9216 water molecules in  $9.4 \times 5.4 \times 5.7$  nm cells) and were evolved for up to 600 ns. They noted that PVA remains bound to the secondary prismatic plane for up to 200 ns out of the 600 ns simulation but is remains bound to the primary prismatic plane throughout. Their findings led them to state that PVA recognises ice by a zipper mechanism where PVA selectively binds prismatic ice faces *via* hydrogen bonding and distance matching between the hydroxyl groups of PVA and water molecules at the ice surface, instead of *via* the use of anchored-clathrate motifs or hydrophobic interactions, **Figure 1.14B**.<sup>209</sup> This mechanism involves a random hydroxyl group (OH) of PVA binding to the prismatic plane of ice, the PVA chain then continues to bind parallel to the c-axis *via* a cooperative zipper-like process (named as such due to its sequential nature) with the PVA methylene groups all oriented in the same direction. Naullage *et al.*'s simulations indicate PVA binding *via* direct hydrogen bonding in a regular pattern (two out of every three OH groups hydrogen bond to the ice) due to the distances between the OH groups in PVA. Their simulations show the average distance between two consecutive OH groups of PVA in liquid water to be  $2.92 \pm 0.46$  Å, which is comparable to the nearest oxygen-oxygen distance in the primary prismatic plane parallel to the c-axis (2.70 Å) and that the distance between O-O in the prismatic plane perpendicular to the c-axis is 4.43 Å (4.52 Å in experiments), inhibiting PVA from hydrogen bonding to that plane, thus supporting the theory of PVA lattice matching.

Experimentally, research into understanding the ice-binding of proteins has recently been undertaken using solid state NMR (SSNMR). By measuring the  $^1\text{H}$ - $^1\text{H}$  cross-saturation and cross relaxation of protons in frozen ice:AFP solutions, more detailed structural information has been obtained about the direct contact certain AFPs make with ice as the change in dynamics of the ice protons affects the relaxation rates. These studies into the ice:AFP interface have presented SSNMR as another technique that could be further utilized to study the interactions of more synthetic CPAs and ice.<sup>210</sup>



It is unclear exactly the mechanisms of how these compounds work, the extent of actual ice-binding, and whether they may work *via* different mechanisms,<sup>211</sup> with different compounds targeting different crystallographic faces of ice, either through hydrophobic interactions in AFGPs<sup>164</sup> or by anchored clathrates in some AFPs.<sup>163</sup> Despite the range of techniques available to study ice nucleation, the debate continues.

### 1.4.5 Synthetic AF(G)P Mimics

Existing strategies for protecting biological materials from freeze-induced damage involve the addition of colligative antifreezes. These vitrify the solution, forming a glass where no crystal growth occurs, rather than reducing ice growth *via* IRI activity. However large quantities of these antifreezes need to be added, and these are often cytotoxic (in particular DMSO)<sup>212,213</sup> and require removal post-thaw. AF(G)Ps, due to their macroscopic effects on ice, have been suggested as another option. However, major obstacles stand in the way of using AF(G)Ps for cryopreservation. The most obvious of which is the lack of clarity on their mechanisms of action. The second is that AFP production (*via* recombinant expression/solid phase synthesis) is expensive, time-consuming and produces low yields, meaning there is a lack of large quantities available for research.<sup>19,214</sup> AFGP production is harder again; there are challenges with total synthesis, they cannot generally be produced *via* bacterial protein expression and they require post-translational modifications (addition of disaccharide).<sup>215</sup> Both AFPs and AFGPs also have issues relating to their use in cryopreservation, thus have not been widely used. Despite their use in that they inhibit ice crystal growth, thus theoretically reducing the potential for cellular damage, they affect ice morphology, which in turn damages cells.<sup>216–220</sup> These proteins also have potential immunogenicity/toxicity problems. These strategies however do provide inspiration for new biomimetic-strategies to improve cryopreservation.<sup>16,93,154,221–225</sup>

Though synthetically challenging, analogues of AFGPs have been prepared by Wilkinson *et al.*,<sup>215</sup> enabling insight into the structure-function relationship leading to IRI activity. As a result of this work and the previously addressed issues, research into the production of synthetic mimics has been of great interest.<sup>226</sup> Mimics have emerged that can reproduce their properties as well as benefit from the scalable and tuneable synthesis of synthetic polymers.<sup>166,227,228</sup> These include C-linked glycopeptides,<sup>229–231</sup>

a range of small molecules,<sup>210,232,233</sup> polyampholytes,<sup>234,235</sup> Oxidized Quasi-Carbon Nitride Quantum Dots (OQCNs),<sup>236</sup> safranin-O,<sup>237</sup> graphene oxide (GO),<sup>238</sup> zirconium acetate (ZrAc),<sup>239</sup> nanocelluloses,<sup>240</sup> and poly(vinyl alcohol) (PVA).<sup>241–244</sup> Due to the success of vinyl polymers in a range of biomedical applications and their high biocompatibility, there has been much research into their possible use as CPAs. PVA, structure shown in **Figure 1.15**, has been found to be one of the most active mimics reported to date.<sup>243</sup>

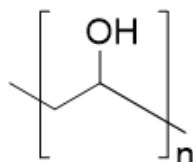


**Figure 1.15.** Chemical structure of PVA

PVA, first reported as an IRI inhibitor in 1995, is a fully flexible compound (in this way it differs from the rigid AFPs) and demonstrates high potency, with significant IRI activity at 1 mg.mL<sup>-1</sup> and the ability to inhibit ice crystal growth to 10 % of a control crystal when <0.1 mg.mL<sup>-1</sup> is dissolved in solution.<sup>241</sup>

PVA is also IRI active over a large range of molecular weights, with an interesting ‘switching on’ of activity at above 14 repeat units (DP14).<sup>242</sup> It does not shape ice crystals into needles and only has weak TH activity at less than 50 mg.mL<sup>-1</sup>,<sup>241,245</sup> making it of interest as a potential CPA; with reports of enhanced cellular recovery when used. However, despite PVA’s high IRI activity, biocompatibility,<sup>246,247</sup> simple synthesis and low cost, it has been observed that its activity cannot be optimised by structural modifications, in fact it is often lost;<sup>241,247</sup> for example multivalency and branched PVAs provide little positive impact.<sup>244,248</sup> Thus PVA may not be of use for all applications, leading to the need for other synthetic mimics or the creation of CPA formulations containing PVA and other compounds that can afford effects that PVA cannot/enhance PVA’s qualities.

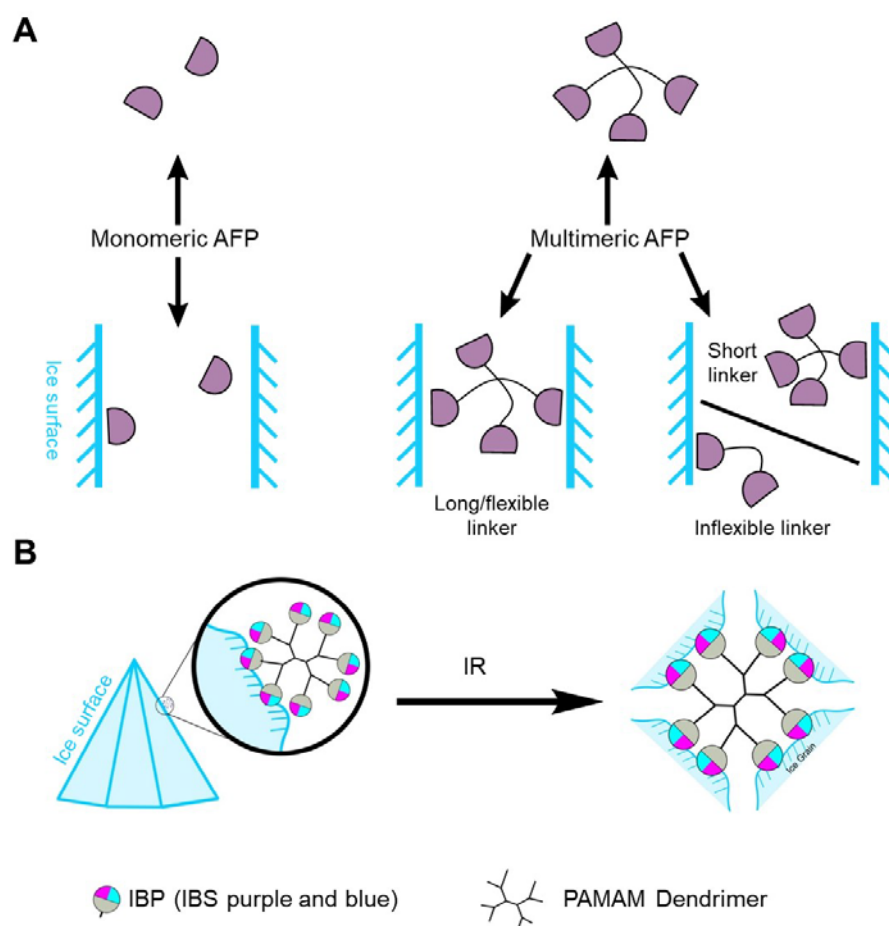


**Figure 1.16.** Schematic representations of AFP ice-binding. A) Hypothesis for beneficial interactions of a monomeric AFP compared to that of various multimeric AFP constructs with ice. Adapted from Wilkins (PhD thesis, University of Warwick, 2019);<sup>249</sup> B) Schematic representation of a dendrimer-linked AFPIII (DLTIII) binding ice obtained by Davies *et al.*<sup>214</sup> First DLTIII binding a single ice crystal *via* its ice-binding site, IBS (purple binds pyramidal plane, blue binds prism plane). Ice recrystallisation may then occur and DLTIII will simultaneously bind several ice crystals.

The impact of architecture has also been considered; especially in relation to AFPs and PVA. This interest is due to the probability that multivalency will lead to increased ice-activity; *i.e.* multiple compounds could bind the same ice face/bridge between other ice faces.<sup>214</sup>

Examples of the possibility of multiple binding using multimeric AFPs can be seen in **Figure 1.16A**, where activity may result from the capacity of the multimeric AFP to span interstitial space to bind several ice crystals simultaneously. Studies suggest a

binding model wherein the size of the scaffold will affect ice-binding; *i.e.* a larger scaffold is key for enabling the whole AFP IBS to be available to bind several ice crystals at once, thus linker size (as well as flexibility of linker) will affect binding activity.<sup>214</sup> Stevens *et al.* found that attaching multiple type III AFPs to the outer termini of a dendrimer to make DLTIII enhanced both TH and IRI activities compared to that of monomeric AFPIII due to the increased ability to cross-link multiple ice faces, **Figure 1.16B**. They think that a single ice crystal will bind only a few of the cross-linked AFPIIIIs, but in three-dimensions there is a higher possibility for interaction with multiple ice grains.

Recent work by Gibson and co-workers reports on the use of polyampholytes as another ice-active polymer option.<sup>250</sup> These polyampholytes display lower IRI activity than PVA, but have been observed to improve red blood cell (RBC) recovery.<sup>251</sup> Matsumura *et al.* has also studied libraries of polyampholytes, again finding cryoprotective capabilities despite their moderate IRI activity.<sup>252</sup> Within these libraries the polymers only have slight structural variations, which can affect overall IRI activity, but the hydrophobic/hydrophilic balance is deemed important.<sup>235,252</sup>

Compounds of interest include metal organic frameworks (MOFs), though only preliminary work has been performed in this area, which have been observed to have limited IRI activity and the potential for ice nucleation as their highly-designable nanostructure may be of use in lattice-matching with ice,<sup>253</sup> GO, which has significant IRI and cryoprotective ability (reducing crystal growth to 20 % MLGS at 5 mg.mL<sup>-1</sup>),<sup>238</sup> and OQCNs, which have been observed to exhibit TH, IRI and DIS, as well as improving sheep RBC recovery compared to the commercially used hydroxyethyl starch (HES) are other options.<sup>236</sup>

Recently, soluble organic dyes have been screened, finding that compounds with flat planar structures can also inhibit IR. Safranin-O specifically, has been identified as highly potent and highlights the fact that hydroxyl groups may not be essential for IRI activity.<sup>254</sup> Drori and co-workers investigated safranin-O suggesting that it self-assembles in solution, forming a supramolecular structure with hydrophobic and hydrophilic regions (similar to the IBS seen in AFGPs), **Figure 1.17**. Analysis of the safranin-O structures show that within the supramolecular stack the gap between each molecule is 3.7 Å, with the distance between two amino groups being 7.4 Å, a good

distance match with every second oxygen in an ice lattice (7.36 Å), implying that this preorganisation of molecules allows for hydrogen bonding to occur along the prism planes of ice.

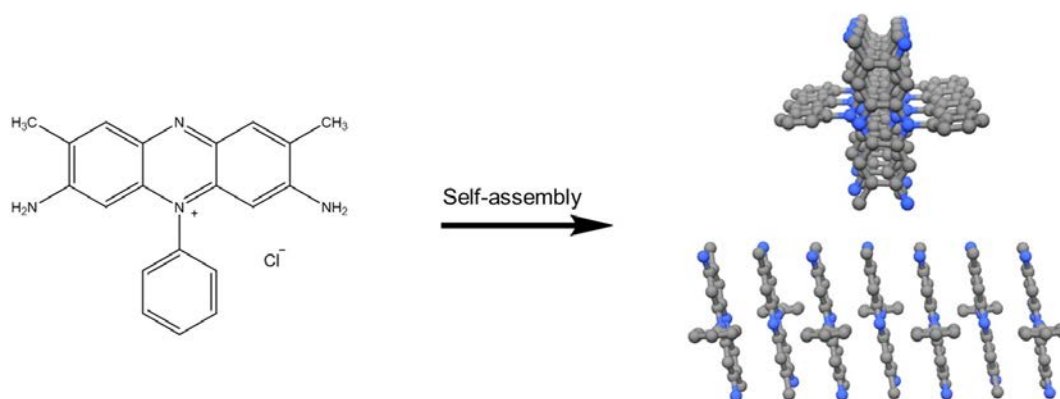


**Figure 1.17.** Self-assembly of safranin-O. Side and front view of a stack of seven safranin-O molecules. Adapted from Drori *et al.*, (J. Am. Chem. Soc., 2016).<sup>254</sup>

Ben *et al.* have reported a range of IRI active AFGP mimetic species (both with and without TH)<sup>229</sup> consisting of a range of C-linked mimetic probes, which are low molecular weight species consisting of a monosaccharide motif attached to peptide repeat units.<sup>229–231</sup> They tested a range of carbohydrates and peptide backbone lengths, finding that IRI activity is highly sensitive to structural modification: the longer the side chain between monosaccharide and peptide backbone<sup>229</sup> the lower IRI activity; choice of sugar residue impacts potency,<sup>255</sup> *e.g.* finding a galactose derivative to be the most active and talose the least. This led Ben *et al.* to put forward an explanation for activity relating to hydration of the sugars;<sup>256</sup> stating that monosaccharides with the highest hydration numbers will bind more water molecules and thus disrupt water's hydrogen bond network. Balczak *et al.* and Graham *et al.* support these findings; stating that hydrophobic moieties are important for IRI<sup>257</sup> and that segregation of hydrophilic and hydrophobic groups (amphipathy) is important.<sup>228</sup>

A graphical representation of synthetic compounds with IRI activity compared to AF(G)Ps can be seen in **Figure 1.18**, showing that no synthetic mimic thus far has activity as high as the natural antifreezes, and that there is a range of structures that are active over a range of concentration. Some materials are not included in the figure as they have been tested in other buffers such as NaCl, though these have low or no activity; for example CNCs and OQCNs.

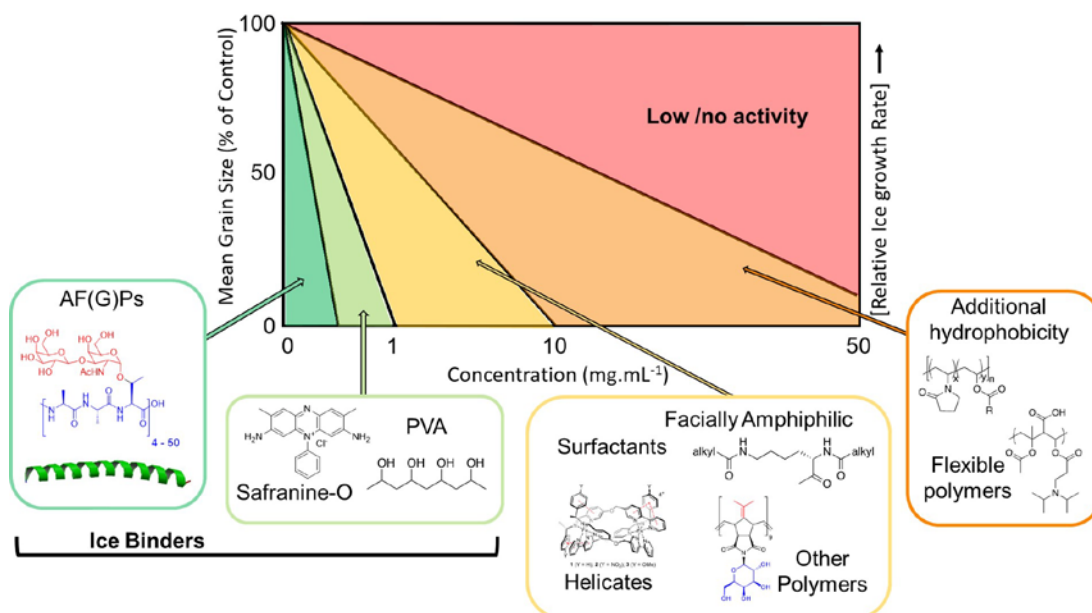


**Figure 1.18** Summary of range of activities observed for different classes of IRI active compounds. It is important to note that the size indication is based on the static 30 minute measurement, and that in all cases the ice crystals keep growing, thus is a snapshot of a rate of growth. Grain size is recorded after 30 minutes annealing at  $-8^{\circ}\text{C}$ . Adapted from Biggs *et al.* (Macromol. Biosci., 2019)<sup>171</sup>

Of many of the above mimics, most are not biocompatible or biodegradable, which reduces their potential as CPAs, however understanding their modes of action may lead to the development of more suitable mimics. The exact link between AF(G)Ps, their mimics and INPs remains unclear, but it has been shown that some synthetic AF(G)P mimics also demonstrate some nucleation inhibition properties.<sup>87</sup>

## 1.5 Cold storage of biologics

The physical state of water is key for successful cryopreservation; it makes up 60 % of the human body, 70 % of cells and 90 % of blood. This highlights how ice formation can be a serious problem for cold storage of these materials as well as a problem in the cold chain in general, (**Figure 1.19**) where there are many stages that require specific temperatures *i.e.* shipment, banking for future use and short-term storage for laboratory experiments. Accurate temperature control and successful transfer between stages is vital.



**Figure 1.19.** Schematic of cryopreservation cold chain workflow and how it is susceptible to variability and thus error.

Current storage techniques include lyophilisation and cryopreservation. Cryopreservation<sup>174,177</sup> is the most commonly used, as no infrastructure (other than a  $-80\text{ }^{\circ}\text{C}$  freezer or liquid nitrogen ( $-196\text{ }^{\circ}\text{C}$ )) is required, ensuring it is easy to use, whereas lyophilisation requires optimisation and more specialised equipment/formulations. Generally freezing is performed with osmolytes *e.g.* glycerol, trehalose and DMSO. These however can be toxic to microorganisms and can cause aggregation of proteins. Glycerol is the current gold-standard CPA for microorganism cryostorage, but it is intrinsically toxic to most microorganisms: only a fraction of cells survive freezing and the presence of glycerol can impact downstream applications and assays. The risk of temperature fluctuations (upon opening and closing freezers) needs to be considered, so potentially adding IRI active CPAs, such as polymer-based formulations, rather than solvents this risk will be reduced. A range of techniques are used in research laboratories to study viability of cells and proteins post-thaw, these include colony counting, activity-based assays, fluorescence and absorbance assays and aggregation studies using dynamic light scattering (DLS). These different techniques enable relatively quick and simple data acquisition, providing insight into freeze-induced damage for a range of biological materials frozen under a range of different conditions.

Can the above described macroscopic effects be applied to the storage of different biological materials? IRI activity is of great use in cryopreservation; it enables storage at higher temperatures than vitrified samples ( $-20\text{ }^{\circ}\text{C}$  to  $-80\text{ }^{\circ}\text{C}$  rather than  $-80\text{ }^{\circ}\text{C}$  or below), less focus on cooling and warming rates (as ice crystals should not grow in the presence of inhibitors thus high rates that would be required to ‘outrun’ the kinetics of ice formation are not needed) as well as a lower antifreeze concentration, as colligative antifreezes require a higher weight percent in solution to act. TH itself may generally not be a useful effect in cryopreservation, however this leads to the selection of materials that have minimal or no TH activity but are still IRI active, though there

are hopes to transport organs within the TH gap ( $\sim -1$  °C). DIS also needs to be monitored, as crystal morphology needs to have no impact on recovery of biological materials. By monitoring these macroscopic effects for a range of potential CPAs we can potentially choose materials for cold storage of biologics.

Nucleation is also of interest regarding cryopreservation; controlled rate freezing procedures are used in laboratories worldwide due to the importance of ‘slow’ cooling (rates of  $\sim 1$  °C.min<sup>-1</sup>), some of these include plateaus in the cooling steps to allow for nucleation before further cooling and then storage at either  $-80$  °C to  $-196$  °C (depending on freezing method). Ideally ice will nucleate at a warm temperature that is as close to the melting point of the CPA formulation/cell media used and externally to the cells,<sup>258</sup> though this often is not the case as controlled rate freezing procedures often do not focus effort onto encouraging external freezing, meaning ice will nucleate on the most efficient nucleant available (primarily inside cells). Under these ideal nucleation conditions cell damage will be avoided during the remainder of the cooling procedure, as the nucleant will maximise the amount of time a particular cell would have to dry whilst allowing solidification at a fast-enough rate. If the nucleation temperature can be controlled (promoted) by the addition of a particular compound these freezing procedures can be improved further. By studying a range of potential INPs, efficient nucleators can be determined, and then tested to see whether they ensure nucleation occurs at warmer temperatures in cell media, and thus assisting in cold storage.



## 1.6 Summary

Nature has evolved expertly to survive freezing temperatures; in particular through the production of AF(G)Ps. These proteins, despite their high IRI activity and ability to lower the freezing point of ice, have issues preventing their use in cold storage of biologics; ice shaping prevents their use in cryopreservation of organs, tissues and cells in general, not to mention their suspected immunogenicity. Synthetic mimics have been developed, of which PVA is the most potent IR inhibitor to date. Research has shown PVA has effectiveness as a CPA, and due to its biocompatibility has potential broad applications. PVA may not be the appropriate CPA in all scenarios, so other synthetic AF(G)P mimics and polymeric formulations are required.

The development of newer, more potent, IR inhibitors is hindered by our lack of understanding of the mechanisms of action by which those that are currently available work. The range of theories and debate surrounding reversible and irreversible ice-binding adds to the confusion, as well as the fact that these ice-active materials potentially work *via* multiple mechanisms. An increased understanding of DIS, TH and IRI on a microscopic level may provide an insight into the mechanisms of action of these ice-active materials. If we can understand the mechanisms of action, it may lead to the production of more effective, less toxic mimics.

The study of ice nucleation has often focused on INPs in the atmosphere; however, it is known that they can be of use in cryopreservation, particularly in increasing the temperature at which ice nucleates during controlled rate freezing, thus reducing cell damage.

Microscopy has been useful for studying macroscopic effects such as IRI and DIS thus far, however it cannot provide detail at an atomic scale or allow us to study the bulk ice as only snapshots of these activities can be obtained from micrographs. More physical techniques including X-ray diffraction (XRD) and nuclear magnetic resonance spectroscopy (NMR) as well as molecular dynamics (MD) have increasingly become of use, as a proper physical understanding on an atomic scale will assist with an understanding of further up the chain, *i.e.* at a cellular level.<sup>3,68,259–262</sup> Herein these experimental techniques have been employed in order to gain insight into micro- and macroscopic effects over differing length scales for the ice-active materials highlighted above with the aim to start connecting these length scales together.

## 1.7 Project Aims and Overview

Various compounds will be investigated for ice-activity; in particular IRI and DIS activity, and then studied for their cryoprotective abilities for a range of microorganisms and proteins. These will include a range of AF(G)Ps, of which some will be recombinantly expressed, and synthetic AF(G)P mimics. The mechanism of action of these same materials will be explored using traditional microscopy techniques (splat and sucrose assays) as well as by XRD and SSNMR, with the aim to further our knowledge of their microscopic effects on ice as well as their macroscopic effects whilst obtaining greater detail on these processes; one such example will be studying in more detail how chain length affects PVA's ice-activity. It is envisioned that a polymeric cryoprotective formulation will be produced, tested, and its mechanism of action understood. A range of previously untested compounds will be studied for their ice nucleation activity with the hope to obtain next-generation promoters of ice nucleation that have the potential to be used in cryopreservation.

## 1.8 Thesis Summary

The following chapters detail potential cryoprotectants for biological materials (natural and synthetic) and investigate their ice-activity (macroscopic and microscopic), and their relative cryoprotecting abilities for a range of proteins and bacteria.

The research described in **Chapter 2** details the need for successful cryostorage of biological materials; specifically, microorganisms and proteins. Macromolecular mimics of AFPs were studied and a new concept for the storage/transport of biological materials using an organic solvent-free formulation is presented. The effect of polymer molecular weight and formulations were studied by comparing IRI activity and cell recovery post-thaw for a range of biological materials and the addition of secondary non-IRI active polymers were tested. A range of Gram negative, Gram positive and Mycobacteria were tested, as well as a range of proteins.

**Chapter 3** reports on the use of X-ray diffraction to further understanding of ice-active materials, in particular those successfully used as cryoprotectants in Chapter 2. The method developed evaluates the total number of ice crystals as a function of time and is confirmed to be a new potential supplementary tool to use in the study of IRI activity. Ice diffraction patterns for samples that both shape and do not shape ice were compared and peak disappearance was confirmed not to relate to specific ice-binding in this work.

**Chapter 4** builds upon the work of Chapter 3, where a combination of microscopy and SSNMR is used to provide experimental molecular-level details of antifreeze macromolecule:ice interactions that cannot be obtained using XRD. The effect of the chain length was studied for PVA and compared to previously published IRI activity data from the Gibson group, finding a change in proton motions for PVA of a chain length  $\geq 20$ , which is the point at which PVA gains IRI activity. Antifreeze protein type I, antifreeze protein type III and AFGP8 are studied alongside PVA and safranine-O to investigate the mobility of solid water and how it is affected by antifreeze macromolecules (some of which with cryoprotective abilities). Results from a range of relaxation rate experiments are presented as well as 2D data investigating ice-binding. Safranine-O was observed to affect ice in a similar manner to PVA, and ice-

binding observed for PVA, which was confirmed to be reversible, as well as for AFPIII and AFGP8.

**Chapter 5** deals with the study of ice nucleants rather than specifically IRI active cryoprotectants. A range of previously untested compounds were tested for ice nucleating activity, using droplet freezing assays, in the hope of providing future solutions for icing problems and to assist in controlling freezing temperatures during cryopreservation. Results from droplet freezing assays were compared to that of calorimetry-based assays and were found to be superior here. Metal organic frameworks were observed to have no IRI activity or nucleating activity, and lignins were observed to be potential nucleants. Concentration, cooling rate and the effect of filtering samples were evaluated as variables with the potential to change nucleation effectiveness.

## 1.9 References

- 1 B. Riechers, F. Wittbracht, A. Hütten and T. Koop, *Phys. Chem. Chem. Phys.*, 2013, **15**, 5873–5887.
- 2 R. J. Herbert, B. J. Murray, S. J. Dobbie and T. Koop, *Geophys. Res. Lett.*, 2015, **42**, 1599–1605.
- 3 M. Fitzner, G. C. Sosso, S. J. Cox and A. Michaelides, *J. Am. Chem. Soc.*, 2015, **137**, 13658–13669.
- 4 V. F. Petrenko and R. W. Whitworth, *Physics of Ice*, Oxford University Press, Oxford, 1999.
- 5 F. Chaitanya, Vimal; Zenhausern, *Technol. Innov.*, 2015, **17**, 1–3.
- 6 T. Bartels-Rausch, V. Bergeron, J. H. E. Cartwright, R. Escibano, J. L. Finney, H. Grothe, P. J. Gutiérrez, J. Haapala, W. F. Kuhs, J. B. C. Pettersson, S. D. Price, C. I. Sainz-Díaz, D. J. Stokes, G. Strazzulla, E. S. Thomson, H. Trinks and N. Uras-Aytemiz, *Rev. Mod. Phys.*, 2012, **84**, 885–944.
- 7 J. Fraxedas, *Water at interfaces : a molecular approach*, CRC Press, Florida, 2014.
- 8 D. S. Eisenberg and W. Kauzmann, *The structure and properties of water*, Clarendon P, Oxford :, 1969.
- 9 P. Ball, *ChemPhysChem*, 2008, **9**, 2677–2685.
- 10 C. Le Zhao, S. Porzio, A. Smith, H. Ge, H. T. Davis and I. E. Scriven, *J. Coatings Technol. Res.*, 2006, **3**, 109–116.
- 11 G. Petzold and J. M. Aguilera, *Food Biophys.*, 2009, **4**, 378–396.
- 12 G. N. Stacey, C. J. Connon, K. Coopman, A. J. Dickson, B. Fuller, C. J. Hunt, P. Kemp, J. Kerby, J. Man, P. Matejtschuk, H. Moore, J. Morris, R. O. Oreffo, N. Slater, S. Ward, C. Wiggins and H. Zimmermann, *Regen. Med.*, 2017, **12**, 553–564.
- 13 C. Sykes, *Pharm. Ther.*, 2018, **43**, 154-157,170.
- 14 O. S. Kumru, S. B. Joshi, D. E. Smith, C. R. Middaugh, T. Prusik and D. B.

- Volkin, *Biologicals*, 2014, **42**, 237–259.
- 15 T. A. Berendsen, B. G. Bruinsma, C. F. Puts, N. Saeidi, O. B. Usta, B. E. Uygun, M. Izamis, M. Toner and M. L. Yarmush, *Nat Med.*, 2014, **20**, 790–793.
- 16 E. V. Pikuta, R. B. Hoover and J. Tang, *Crit. Rev. Microbiol.*, 2007, **33**, 183–209.
- 17 A. K. Balcerzak, C. J. Capicciotti, J. G. Briard and R. N. Ben, *RSC Adv.*, 2014, **4**, 42682–42696.
- 18 M. M. Harding, P. I. Anderberg and A. D. J. Haymet, *Eur. J. Biochem.*, 2003, **270**, 1381–1392.
- 19 P. L. Davies, *Trends Biochem. Sci.*, 2014, **39**, 548–555.
- 20 D. Nichols, J. Bowman, K. Sanderson, C. M. Nichols, T. Lewis, T. McMeekin and P. D. Nichols, *Curr. Opin. Biotechnol.*, 1999, **10**, 240–246.
- 21 J. R. Layne and A. L. Jones, *J. Exp. Zool.*, 2001, **290**, 1–5.
- 22 X. Wen, S. Wang, J. G. Duman, J. F. Arifin, V. Juwita, W. A. Goddard, A. Rios, F. Liu, S.-K. Kim, R. Abrol, A. L. DeVries and L. M. Henling, *Proc. Natl. Acad. Sci.*, 2016, **113**, 6683–6688.
- 23 E. Brini, C. J. Fennell, M. Fernandez-Serra, B. Hribar-Lee, M. Lukšič and K. A. Dill, *Chem. Rev.*, 2017, **117**, 12385–12414.
- 24 I. Brovchenko and A. Oleinikova, *ChemPhysChem*, 2008, **9**, 2660–2675.
- 25 W. Wagner, *J. Phys. Chem. Ref. Data*, 2002, **31**, 387–535.
- 26 C. Schran and D. Marx, *Phys. Chem. Chem. Phys.*, 2019, **21**, 24967–24975.
- 27 J. L. Kuo, C. V. Ciobanu, L. Ojamäe, I. Shavitt and S. J. Singer, *J. Chem. Phys.*, 2003, **118**, 3583–3588.
- 28 A. A. Kananenka and J. L. Skinner, *Phys. Chem. Chem. Phys.*, 2020, **22**, 18124–18131.
- 29 C. G. Salzmann, P. G. Radaelli, B. Slater and J. L. Finney, *Phys. Chem. Chem. Phys.*, 2011, **13**, 18468–18480.

- 
- 30 J. Kyte, *Structure in Protein Chemistry*, Garland Science, New York, NY, 2nd edn., 2006.
- 31 S. Grzesiek and E. D. Becker, in *Encyclopedia of Magnetic Resonance*, John Wiley & Sons, Inc., Chichester, UK, 2011.
- 32 C. P. Gerba, I. L. Pepper and D. T. Newby, *Microbial Transport in the Subsurface*, Elsevier Inc., 2015.
- 33 V. Buch, H. Groenzin, I. Li, M. J. Shultz and E. Tosatti, *Proc. Natl. Acad. Sci. USA*, 2008, **105**, 5969–5974.
- 34 T. Loerting, V. Fuentes-landete, C. M. Tonauer and T. M. Gasser, *Commun. Chem.*, 2020, 1–4.
- 35 W. F. Kuhs, *Physics and chemistry of ice*, RSC Publishing, Cambridge, 1st edn., 2007.
- 36 V. B. Prakapenka, N. Holtgrewe, S. S. Lobanov and A. Goncharov, *arXiv 2007.07715*, 2020, **[Preprint]**, 10–18.
- 37 R. Yamane, K. Komatsu, J. Gouchi, Y. Uwatoko, S. Machida, T. Hattori, H. Ito and H. Kagi, *arXiv 2006.10928v1*, 2019, **[Preprint]**, 2–4.
- 38 G. Tammann, *Ann. Phys.*, 1900, **307**, 1–31.
- 39 B. Kamb, *Acta Crystallogr.*, 1964, **17**, 1437–1449.
- 40 K. R. Hirsch and W. B. Holzapfel, *Phys. Lett. A*, 1984, **101**, 142–144.
- 41 M. Millot, F. Coppari, J. R. Rygg, A. Correa Barrios, S. Hamel, D. C. Swift and J. H. Eggert, *Nature*, 2019, **569**, 251–255.
- 42 T. Loerting, K. Winkel, M. Seidl, M. Bauer, C. Mitterdorfer, P. H. Handle, C. G. Salzmann, E. Mayer, J. L. Finney and D. T. Bowron, *Phys. Chem. Chem. Phys.*, 2011, **13**, 8783–8794.
- 43 T. Loerting, C. Salzmann, I. Kohl, E. Mayer and A. Hallbrucker, *Phys. Chem. Chem. Phys.*, 2001, **3**, 5355–5357.
- 44 B. Y. B. Kamb and B. L. Davis, *Proc. Natl. Acad. Sci.*, 1964, **52**, 1433–1439.
- 45 R. J. Hemley, A. P. Jephcoat, H. K. Mao, C. S. Zha, L. W. Finger and D. E.

- Cox, *Nature*, 1987, **330**, 737–740.
- 46 A. Falenty, T. C. Hansen and W. F. Kuhs, *Nature*, 2014, **516**, 231–233.
- 47 L. Del Rosso, M. Celli and L. Ulivi, *Nat. Commun.*, 2016, **7**, 1–7.
- 48 M. M. Conde, C. Vega, G. A. Tribello and B. Slater, *J. Chem. Phys.*, 2009, **131**, 1–8.
- 49 Y. Liu, Y. Huang, C. Zhu, H. Li, J. Zhao, L. Wang, L. Ojamäe, J. S. Francisco and X. C. Zeng, *Proc. Natl. Acad. Sci. U. S. A.*, 2019, **116**, 12684–12691.
- 50 J. D. Bernal and R. H. Fowler, *J. Chem. Phys.*, 1933, **1**, 515–548.
- 51 S. W. Peterson and H. A. Levy, *Acta Crystallogr.*, 1957, **10**, 70–76.
- 52 C. G. Salzmann, I. Kohl, T. Loerting, E. Mayer and A. Hallbrucker, *Can. J. Phys.*, 2003, **81**, 25–32.
- 53 W. F. Kuhs and M. S. Lehmann, *J. Phys. Chem.*, 1983, **87**, 4312–4313.
- 54 T. L. Malkin, B. J. Murray, V. Andrey, J. Anwar and C. G. Salzmann, *Proc. Natl. Acad. Sci.*, 2012, **109**, 1041–1045.
- 55 I. Baker, *Cryst. Growth Des.*, 2002, **2**, 127–134.
- 56 Y. Zhao and J. Zhang, *J. Appl. Crystallogr.*, 2008, **41**, 1095–1108.
- 57 N. Bjerrum, *Science*, 1952, **115**, 385–390.
- 58 R. W. Whitworth, *J. Phys. Chem. B*, 1999, **103**, 8192–8193.
- 59 J. P. Cowin and M. J. Iedema, *J. Phys. Chem. B*, 1999, **103**, 8194–8194.
- 60 S. Kawada, *J. Phys. Soc. Japan*, 1972, **32**, 1442–1442.
- 61 P. L. Davies and B. D. Sykes, *Curr. Opin. Struct. Biol.*, 1997, **7**, 828–834.
- 62 C. L. Hew and P. L. Davies, *FASEB J.*, 1990, **4**, 2460–2468.
- 63 Z. Jia and P. L. Davies, *Trends Biochem. Sci.*, 2002, **27**, 101–106.
- 64 T. Koop, H. P. Ng, L. T. Molina and M. J. Molina, *J. Phys. Chem. A*, 1998, **102**, 8924–8931.
- 65 B. G. Pummer, C. Budke, S. Augustin-Bauditz, D. Niedermeier, L. Felgitsch,



- C. J. Kampf, R. G. Huber, K. R. Liedl, T. Loerting, T. Moschen, M. Schauperl, M. Tollinger, C. E. Morris, H. Wex, H. Grothe, U. Pöschl, T. Koop and J. Fröhlich-Nowoisky, *Atmos. Chem. Phys.*, 2015, **15**, 4077–4091.
- 66 R. Becker and W. Döring, *Ann. Phys.*, 1935, **416**, 719–752.
- 67 J. Frenkel, *J. Chem. Phys.*, 1939, **7**, 538–547.
- 68 L. Ickes, A. Welti, C. Hoose and U. Lohmann, *Phys. Chem. Chem. Phys.*, 2015, **17**, 5514–5537.
- 69 P. J. M. Smeets, A. R. Finney, W. J. E. M. Habraken, F. Nudelman, H. Friedrich, J. Laven, J. J. De Yoreo, P. M. Rodger and N. A. J. M. Sommerdijk, *Proc. Natl. Acad. Sci.*, 2017, **114**, E7882–E7890.
- 70 C. Knight, *Cryst. Growth Des.*, 2020, **20**, 580–589.
- 71 C. C. Pradzynski, R. M. Forck, T. Zeuch, P. Slavíček and U. Buck, *Science*, 2012, **337**, 1529–1532.
- 72 M. Tokuyama, K. Kawasaki and Y. Enomoto, *Phys. A Stat. Mech. its Appl.*, 1986, **134**, 323–338.
- 73 W. Ostwald, *Zeitschrift für Phys. Chemie*, 1897, **22U**, 1.
- 74 F. T. Dahlke, M. Butzin, J. Nahrgang, V. Puvanendran, A. Mortensen, H. O. Pörtner and D. Storch, *Sci. Adv.*, 2018, **4**, 1–11.
- 75 G. N. Somero and A. L. DeVries, *Science*, 1967, **156**, 257–58.
- 76 S. P. Graethert, M. J. Kulper, S. M. Gagné, V. K. Walker, Z. Jia, B. D. Sykes and P. L. Davies, *Nature*, 2000, **406**, 325–328.
- 77 J. G. Duman, K. R. Walters, T. Sformo, M. A. Carrasco, P. K. Nickell, X. Lin and B. M. Barnes, in *Low Temperature Biology of Insects*, 2010, pp. 59–90.
- 78 A. J. Scotter, C. B. Marshall, L. A. Graham, J. A. Gilbert, C. P. Garnham and P. L. Davies, *Cryobiology*, 2006, **53**, 229–239.
- 79 A. A. Steiner, S. O. Petenusci, L. G. Brentegani and L. G. Branco, *Rev. Bras. Biol.*, 2000, **60**, 321–328.
- 80 K. B. Storey, *Biochem. Cell Biol.*, 1990, **68**, 687–698.

- 81 K. R. Walters, A. S. Serianni, Y. Voituron, T. Sformo, B. M. Barnes and J. G. Duman, *J. Comp. Physiol. B Biochem. Syst. Environ. Physiol.*, 2011, **181**, 631–640.
- 82 P. K. Wolber, *Adv. Microb. Physiol.*, 1993, **34**, 203–237.
- 83 J. Fröhlich-Nowoisky, T. C. J. Hill, B. G. Pummer, P. Yordanova, G. D. Franc and U. Pöschl, *Biogeosciences*, 2015, **12**, 1057–1071.
- 84 K. Dreischmeier, C. Budke, L. Wiehemeier, T. Kottke and T. Koop, *Sci. Rep.*, 2017, **7**, 41890.
- 85 J. Kvíderová, J. Hájek and R. Worland, *CryoLetters*, 2013, **34**, 137–148.
- 86 T. L. Kieft and T. Ruscetti, *J. Bacteriol.*, 1990, **172**, 3519–3523.
- 87 B. Wowk and G. M. Fahy, *Cryobiology*, 2002, **44**, 14–23.
- 88 K. E. Zachariassen and E. Kristiansen, *Cryobiology*, 2000, **41**, 257–279.
- 89 S. E. Lindow, *Ann. Rev. Phytopathol.*, 1983, **21**, 363–384.
- 90 B. J. Murray, D. O’Sullivan, J. D. Atkinson and M. E. Webb, *Chem. Soc. Rev.*, 2012, **41**, 6519–6554.
- 91 C. Hoose and O. Möhler, *Atmos. Chem. Phys.*, 2012, **12**, 9817–9854.
- 92 J. D. Atkinson, B. J. Murray, M. T. Woodhouse, T. F. Whale, K. J. Baustian, K. S. Carslaw, S. Dobbie, D. O’Sullivan and T. L. Malkin, *Nature*, 2013, **498**, 355–358.
- 93 N. Cochet and P. Widehem, *Appl. Microbiol. Biotechnol.*, 2000, **54**, 153–161.
- 94 R. C. Schnell, *Geophys. Res. Lett.*, 1975, **2**, 500–502.
- 95 P. A. Alpert, J. Y. Aller and D. A. Knopf, *Atmos. Chem. Phys.*, 2011, **11**, 5539–5555.
- 96 D. A. Knopf, P. A. Alpert, B. Wang and J. Y. Aller, *Nat. Geosci.*, 2011, **4**, 88–90.
- 97 S. Pouleur, C. Richard, J. Martin and H. Antoun, *Appl. Environ. Microbiol.*, 1992, **58**, 2960–2964.

- 98 J. Fröhlich-Nowoisky, T. C. J. Hill, B. G. Pummer, G. D. Franc and U. Pöschl, *Biogeosciences Discuss.*, 2014, **11**, 12697–12731.
- 99 D. O’Sullivan, B. J. Murray, J. Ross and M. E. Webb, *Atmos. Chem. Phys. Discuss.*, 2016, **2016**, 1–22.
- 100 B. G. Pummer, H. Bauer, J. Bernardi, S. Bleicher and H. Grothe, *Atmos. Chem. Phys.*, 2012, **12**, 2541–2550.
- 101 J. M. Prospero, P. Ginoux, O. Torres, S. E. Nicholson and T. E. Gill, *Rev. Geophys.*, 2002, **40**, 1–31.
- 102 M. Kumai, *J. Meteorol.*, 1961, **18**, 139–150.
- 103 H. R. Pruppacher and J. D. Klett, *Microphysics of Clouds and Precipitation*, Kluwer Academic Publishers, Dordrecht, The Netherlands, 2nd edn., 1997.
- 104 C. I. Biggs, C. Packer, S. Hindmarsh, M. Walker, N. R. Wilson, J. P. Rourke and M. I. Gibson, *Phys. Chem. Chem. Phys.*, 2017, **19**, 21929–21932.
- 105 T. F. Whale, M. Rosillo-Lopez, B. J. Murray and C. G. Salzmann, *J. Phys. Chem. Lett.*, 2015, **6**, 3012–3016.
- 106 W. G. Finnegan and S. K. Chai, *J. Atmos. Sci.*, 2003, **60**, 1723–1731.
- 107 C. Marcolli, B. Nagare, A. Welti and U. Lohmann, *Atmos. Chem. Phys.*, 2016, **16**, 8915–8937.
- 108 R. Pandey, K. Usui, R. A. Livingstone, S. A. Fischer, J. Pfaendtner, E. H. G. Backus, Y. Nagata, J. Fröhlich-Nowoisky, L. Schmu ser, S. Mauri, J. F. Scheel, D. A. Knopf, U. Pöschl, M. Bonn and T. Weidner, *Sci. Adv.*, 2016, **2**, e1501630.
- 109 A. Haji-Akbari and P. G. Debenedetti, *Proc. Natl. Acad. Sci.*, 2015, **112**, 201509267.
- 110 B. Vonnegut, *J. Appl. Phys.*, 1947, **18**, 593–595.
- 111 K. Li, S. Xu, W. Shi, M. He, H. Li, S. Li, X. Zhou, J. Wang and Y. Song, *Langmuir*, 2012, **28**, 10749–10754.
- 112 Y. Qiu, A. Hudait and V. Molinero, *J. Am. Chem. Soc.*, 2019, **141**, 7439–7452.
- 113 G. Vali, *J. Atmos. Sci.*, 1971, **28**, 402–409.

- 114 N. Hiranuma, S. Augustin-Bauditz, H. Bingemer, C. Budke, J. Curtius, A. Danielczok, K. Diehl, K. Dreischmeier, M. Ebert, F. Frank, N. Hoffmann, K. Kandler, A. Kiselev, T. Koop, T. Leisner, O. Möhler, B. Nillius, A. Peckhaus, D. Rose, S. Weinbruch, H. Wex, Y. Boose, P. J. Demott, J. D. Hader, T. C. J. Hill, Z. A. Kanji, G. Kulkarni, E. J. T. Levin, C. S. McCluskey, M. Murakami, B. J. Murray, D. Niedermeier, M. D. Petters, D. O'Sullivan, A. Saito, G. P. Schill, T. Tajiri, M. A. Tolbert, A. Welti, T. F. Whale, T. P. Wright and K. Yamashita, *Atmos. Chem. Phys.*, 2015, **15**, 2489–2518.
- 115 G. Vali, in *Biological Ice Nucleation and Its Applications*, eds. R. Lee Jr, G. J. Warren and L. V. Gusta, American Phytopathological Society, St. Paul, MN, 1995, pp. 1–28.
- 116 M. Niemand, O. Möhler, B. Vogel, H. Vogel, C. Hoose, P. Connolly, H. Klein, H. Bingemer, P. Demott, J. Skrotzki and T. Leisner, *J. Atmos. Sci.*, 2012, **69**, 3077–3092.
- 117 S. Garimella, T. Bjerring Kristensen, K. Ignatius, A. Welti, J. Voigtländer, G. R. Kulkarni, F. Sagan, G. Lee Kok, J. Dorsey, L. Nichman, D. Alexander Rothenberg, M. Rösch, A. C. R. Kirchgäßner, R. Ladkin, H. Wex, T. W. Wilson, L. Antonio Ladino, J. P. D. Abbatt, O. Stetzer, U. Lohmann, F. Stratmann and D. James Cziczo, *Atmos. Meas. Tech.*, 2016, **9**, 2781–2795.
- 118 S. L. Broadley, B. J. Murray, R. J. Herbert, J. D. Atkinson, S. Dobbie, T. L. Malkin, E. Condliffe and L. Neve, *Atmos. Chem. Phys.*, 2012, **12**, 287–307.
- 119 R. J. Herbert, B. J. Murray, T. F. Whale, S. J. Dobbie and J. D. Atkinson, *Atmos. Chem. Phys.*, 2014, **14**, 8501–8520.
- 120 R. P. Sear, *CrystEngComm*, 2014, **16**, 6506–6522.
- 121 T. Zolles, J. Burkart, T. Häusler, B. Pummer, R. Hitzenberger and H. Grothe, *J. Phys. Chem. A*, 2015, **119**, 2692–2700.
- 122 R. W. Michelmore and F. Franks, *Cryobiology*, 1982, **19**, 163–171.
- 123 T. N. Hansen and J. G. Baust, *Biochim. Biophys. Acta (BBA)/Protein Struct. Mol.*, 1988, **957**, 217–221.
- 124 J. Liu, C. E. Nicholson and S. J. Cooper, *Langmuir*, 2007, **23**, 7286–7292.

- 125 P. F. Scholander, L. van Dam, J. W. Kanwisher, H. T. Hammel and M. S. Gordon, *J. Cell. Comp. Physiol.*, 1957, **49**, 5–24.
- 126 A. L. DeVries, S. K. Komatsu and R. E. Feeney, *J. Biol. Chem.*, 1970, **245**, 2901–2908.
- 127 G. Giubertoni, K. Meister, A. L. Devries and H. J. Bakker, *J. Phys. Chem. Lett.*, 2019, **10**, 352–357.
- 128 V. Bouvet and R. N. Ben, *Cell Biochem. Biophys.*, 2003, **39**, 133–144.
- 129 M. Urbańczyk, J. Góra, R. Latajka and N. Sewald, *Amino Acids*, 2017, **49**, 209–222.
- 130 Y. Tachibana, G. L. Fletcher, N. Fujitani, S. Tsuda, K. Monde and S. I. Nishimura, *Angew. Chemie Int. Ed.*, 2004, **43**, 856–862.
- 131 N. M. Tsvetkova, B. L. Phillips, V. V. Krishnan, R. E. Feeney, W. H. Fink, J. H. Crowe, S. H. Risbud, F. Tablin and Y. Yen, *Biophys. J.*, 2002, **82**, 464–473.
- 132 D. H. Nguyen, M. E. Colvin, Y. Yeh, R. E. Feeney and W. H. Fink, *Biophys. J.*, 2002, **82**, 2892–2905.
- 133 A. N. Lane, L. M. Hays, R. E. Feeney, L. M. Crowe and J. H. Crowe, *Protein Sci.*, 1998, **7**, 1555–1563.
- 134 A. I. Ahmed, D. T. Osuga and R. E. Feeney, *J. Biol. Chem.*, 1973, **248**, 8524–8527.
- 135 M. S. Clark and M. R. Worland, *J. Comp. Physiol. B Biochem. Syst. Environ. Physiol.*, 2008, **178**, 917–933.
- 136 Y. Yeh and R. E. Feeney, *Chem. Rev.*, 1996, **96**, 601–618.
- 137 J. G. Duman and T. M. Olsen, *Cryobiology*, 1993, **30**, 322–328.
- 138 M. Griffith and M. W. F. Yaish, *Trends Plant Sci.*, 2004, **9**, 399–405.
- 139 A. Nath, R. Chaube and K. Subbiah, *Comput. Biol. Med.*, 2013, **43**, 817–821.
- 140 K. A. Sharp, *Proc. Natl. Acad. Sci.*, 2011, **108**, 7281–7282.
- 141 B. L. Pentelute, Z. P. Gates, V. Tereshko, J. L. Dashnau, J. M. Vanderkooi, A.

- A. Kossiakoff and S. B. H. Kent, *J. Am. Chem. Soc.*, 2008, **130**, 9695–9701.
- 142 A. J. Middleton, C. B. Marshall, F. Faucher, M. Bar-Dolev, I. Braslavsky, R. L. Campbell, V. K. Walker and P. L. Davies, *J. Mol. Biol.*, 2012, **416**, 713–724.
- 143 C. a Knight, C. C. Cheng and a L. DeVries, *Biophys. J.*, 1991, **59**, 409–418.
- 144 C. Budke, A. Dreyer, J. Jaeger, K. Gimpel, T. Berkemeier, A. S. Bonin, L. Nagel, C. Plattner, A. L. Devries, N. Sewald and T. Koop, *Cryst. Growth Des.*, 2014, **14**, 4285–4294.
- 145 I. K. Voets, *Soft Matter*, 2017, **13**, 4808–4823.
- 146 J. Barrett, *Int. J. Biochem. Cell Biol.*, 2001, **33**, 105–117.
- 147 F. Sicheri and D. S. C. Yang, *Nature*, 1995, **375**, 427–431.
- 148 Y. Liu, Z. Li, Q. Lin, J. Kosinski, J. Seetharaman, J. M. Bujnicki, J. Sivaraman and C. L. Hew, *PLoS One*, 2007, **2**, e548.
- 149 F. D. Sönnichsen, C. I. DeLuca, P. L. Davies and B. D. Sykes, *Structure*, 1996, **4**, 1325–37.
- 150 E. K. Leinala, P. L. Davies, D. Doucet, M. G. Tyshenko, V. K. Walker and Z. Jia, *J. Biol. Chem.*, 2002, **277**, 33349–33352.
- 151 H. Kondo, Y. Hanada, H. Sugimoto, T. Hoshino, C. P. Garnham, P. L. Davies and S. Tsuda, *Proc. Natl. Acad. Sci.*, 2012, **109**, 9360–9365.
- 152 C. I. DeLuca, R. Comley and P. L. Davies, *Biophys. J.*, 1998, **74**, 1502–1508.
- 153 M. Chasnitsky and I. Braslavsky, *Philos. Trans. R. Soc. A Math. Phys. Eng. Sci.*, 2019, **377**, 20180391.
- 154 R. Gupta and R. Deswal, *J. Biosci.*, 2014, **39**, 931–944.
- 155 C. Sidebottom, S. Buckley, P. Pudney, S. Twigg, C. Jarman, C. Holt, J. Telford, A. McArthur, D. Worrall, R. Hubbard and P. Lillford, *Nature*, 2000, **406**, 256.
- 156 C. B. Marshall, G. L. Fletcher and P. L. Davies, *Nature*, 2004, **429**, 153.
- 157 J. G. Duman and A. L. DeVries, *Comp. Biochem. Physiol. Part B Comp. Biochem.*, 1976, **54**, 375–380.

- 158 S. N. Patel and S. P. Graether, *Biochem. Cell Biol.*, 2010, **88**, 223–229.
- 159 L. A. Graham and P. L. Davies, *Science*, 2005, **310**, 461.
- 160 C. P. Garnham, A. Natarajan, A. J. Middleton, M. J. Kuiper, I. Braslavsky and P. L. Davies, *Biochemistry*, 2010, **49**, 9063–9071.
- 161 R. N. Ben, *ChemBioChem*, 2001, **2**, 161–166.
- 162 C. A. Knight, E. Driggers and A. L. DeVries, *Biophys. J.*, 1993, **64**, 252–259.
- 163 C. P. Garnham, R. L. Campbell and P. L. Davies, *Proc. Natl. Acad. Sci.*, 2011, **108**, 7363–7.
- 164 K. Mochizuki and V. Molinero, *J. Am. Chem. Soc.*, 2018, **140**, 4803–4811.
- 165 K. Meister, A. L. DeVries, H. J. Bakker and R. Drori, *J. Am. Chem. Soc.*, 2018, **140**, 9365–9368.
- 166 M. I. Gibson, *Polym. Chem.*, 2010, **1**, 1141–1152.
- 167 L. L. . Olijve, K. Meister, A. L. DeVries, J. G. Duman, S. Guo, H. J. Bakker and I. K. Voets, *Proc. Natl. Acad. Sci.*, 2016, **113**, 3740–3745.
- 168 C. Budke and T. Koop, *ChemPhysChem*, 2006, **7**, 2601–2606.
- 169 J. A. Raymond, P. Wilson and A. L. DeVries, *Proc. Natl. Acad. Sci. U. S. A.*, 1989, **86**, 881–885.
- 170 K. Basu, C. P. Garnham, Y. Nishimiya, S. Tsuda, I. Braslavsky and P. Davies, *J. Vis. Exp.*, 2014, **83**, e51185.
- 171 C. I. Biggs, C. Stubbs, B. Graham, A. E. R. Fayter, M. Hasan and M. I. Gibson, *Macromol. Biosci.*, 2019, **19**, 1–9.
- 172 M. Mangiagalli, M. Bar-Dolev, P. Tedesco, A. Natalello, A. Kaleda, S. Brocca, D. de Pascale, S. Pucciarelli, C. Miceli, I. Bravslavsky and M. Lotti, *FEBS J.*, 2016, **284**, 163–177.
- 173 J. P. Acker, J. A. W. Elliott and L. E. McGann, *Biophys. J.*, 2001, **81**, 1389–1397.
- 174 P. Mazur, *Cryobiology*, 2010, **60**, 4–10.

- 175 R. Cook, K. and Hartel, *Compr. Rev. Food Sci. Food Saf.*, 2010, **9**, 213–222.
- 176 R. L. Sutton, A. Lips, G. Piccirillo and A. Sztchlo, *J. Food. Sci.*, 1996, **61**, 741–745.
- 177 P. Mazur, *Science*, 1970, **168**, 939–949.
- 178 C. A. Knight, J. Hallett and A. L. DeVries, *Cryobiology*, 1988, **25**, 55–60.
- 179 A. A. Burkey, C. L. Riley, L. K. Wang, T. A. Hatridge and N. A. Lynd, *Biomacromolecules*, 2018, **19**, 248–255.
- 180 A. Leiter, S. Rau, S. Winger, C. Muhle-Goll, B. Luy and V. Gaukel, *J. Food Eng.*, 2016, **187**, 53–61.
- 181 C. A. Knight, D. Wen and R. A. Laursen, *Cryobiology*, 1995, **32**, 23–34.
- 182 L. R. Maki, E. L. Galyan, M. M. Chang-Chien and D. R. Caldwell, *Appl. Microbiol.*, 1974, **28**, 456–459.
- 183 T. F. Whale, B. J. Murray, D. O’Sullivan, T. W. Wilson, N. S. Umo, K. J. Baustian, J. D. Atkinson, D. A. Workneh and G. J. Morris, *Atmos. Meas. Tech.*, 2015, **8**, 2437–2447.
- 184 K. Tatsutani and B. Rubinsky, *J. Biomech. Eng. Asme*, 1998, **120**, 27–31.
- 185 C. Budke, C. Heggemann, M. Koch, N. Sewald and T. Koop, *J. Phys. Chem. B*, 2009, **113**, 2865–2873.
- 186 S. Wang, N. Amornwittawat, J. Banatiao, M. Chung, Y. Kao and X. Wen, *J. Phys. Chem. B*, 2009, **113**, 13891–13894.
- 187 R. Surís-Valls and I. K. Voets, *Biomolecules*, 2019, **9**, 347.
- 188 J. P. Pezacki, M. Noestheden, R. N. Ben, J. Jackman, D. Moffat and S. Findlay, *Biochem. Biophys. Res. Commun.*, 2007, **354**, 340–344.
- 189 M. M. Tomczak, C. B. Marshall, J. A. Gilbert and P. L. Davies, *Biochem. Biophys. Res. Commun.*, 2003, **311**, 1041–1046.
- 190 D. G. Hall and A. Lips, *Langmuir*, 1999, **15**, 1905–1912.
- 191 R. Y. Tam, S. S. Ferreira, P. Czechura, J. L. Chaytor, R. N. Ben and J. L.



- Chaytor, *J. Am. Chem. Soc.*, 2008, **130**, 17494–17501.
- 192 J. A. Raymond and A. L. DeVries, *Proc. Natl. Acad. Sci.*, 1977, **74**, 2589–2593.
- 193 Y. Wu, J. Banoub, S. V. Goddard, M. H. Kao and G. L. Fletcher, *Comp. Biochem. Physiol. - B Biochem. Mol. Biol.*, 2001, **128**, 265–273.
- 194 A. Wierzbicki, C. A. Knight, E. A. Salter, C. N. Henderson and J. D. Madura, *Cryst. Growth Des.*, 2008, **8**, 3420–3429.
- 195 A. Chakrabartty, D. S. Yang and C. L. Hew, *J. Biol. Chem.*, 1989, **264**, 11313–11316.
- 196 M. Takamichi, Y. Nishimiya, A. Miura and S. Tsuda, *FEBS J.*, 2007, **274**, 6469–6476.
- 197 H. Kun and Y. Mastai, *Pept. Sci.*, 2007, **88**, 807–814.
- 198 A. Gaede-Koehler, A. Kreider, P. Canfield, M. Kleemeier and I. Grunwald, *Anal. Chem.*, 2012, **84**, 10229–10235.
- 199 S. Zepeda, E. Yokoyama, Y. Uda, C. Katagiri and Y. Furukawa, *Cryst. Growth Des.*, 2008, **8**, 3666–3672.
- 200 L. M. Sander and A. V. Tkachenko, *Phys. Rev. Lett.*, 2004, **93**, 12–15.
- 201 H. Asakawa, G. Sazaki, K. Nagashima, S. Nakatsubo and Y. Furukawa, *Proc. Natl. Acad. Sci.*, 2016, **113**, 1749–1753.
- 202 M. M. Conde, C. Vega and A. Patrykiewicz, *J. Chem. Phys.*, 2008, **129**, 1–11.
- 203 M. Faraday, *Proc. R. Soc. London*, 1860, **10**, 440–450.
- 204 N. Kallay and D. Čakara, *J. Colloid Interface Sci.*, 2000, **232**, 81–85.
- 205 S. Chakraborty and B. Jana, *J. Phys. Chem. B*, 2018, **122**, 3056–3067.
- 206 A. Hudait, N. Odendahl, Y. Qiu, F. Paesani and V. Molinero, *J. Am. Chem. Soc.*, 2018, **140**, 4905–4912.
- 207 M. Elbaum, S. G. Lipson and J. G. Dash, *J. Cryst. Growth*, 1993, **129**, 491–505.
- 208 B. Zakharov, A. Fisyuk, A. Fitch, Y. Watier, A. Kostyuchenko, D. Varshney,

- M. Sztucki, E. Boldyreva and E. Shalaev, *J. Pharm. Sci.*, 2016, **105**, 2129–2138.
- 209 P. M. Naullage, L. Lupi and V. Molinero, *J. Phys. Chem. C*, 2017, **121**, 26949–26957.
- 210 C. J. Capicciotti, M. Leclere, F. A. Perras, D. L. Bryce, H. Paulin, J. Harden, Y. Liu and R. N. Ben, *Chem. Sci.*, 2012, **3**, 1408–1416.
- 211 Y. Celik, R. Drori, N. Pertaya-Braun, A. Altan, T. Barton, M. Bar-Dolev, A. Groisman, P. L. Davies and I. Braslavsky, *Proc. Natl. Acad. Sci.*, 2013, **110**, 1309–1314.
- 212 K. Kawai, Y. S. Li, M. F. Song and H. Kasai, *Bioorganic Med. Chem. Lett.*, 2010, **20**, 260–265.
- 213 B. P. Best, *Rejuvenation Res.*, 2015, **18**, 422–436.
- 214 C. A. Stevens, R. Drori, S. Zalis, I. Braslavsky and P. L. Davies, *Bioconjug. Chem.*, 2015, **26**, 1908–1915.
- 215 B. L. Wilkinson, R. S. Stone, C. J. Capicciotti, M. Thaysen-Andersen, J. M. Matthews, N. H. Packer, R. N. Ben and R. J. Payne, *Angew. Chemie - Int. Ed.*, 2012, **51**, 3606–3610.
- 216 M. Bar-Dolev, Y. Celik, J. S. Wettlaufer, P. L. Davies and I. Braslavsky, *J. R. Soc. Interface*, 2012, **9**, 3249–3259.
- 217 J. F. Carpenter and T. N. Hansen, *Proc. Natl. Acad. Sci. U. S. A.*, 1992, **89**, 8953–8957.
- 218 H. Chao, P. L. Davies and J. F. Carpenter, *J. Exp. Biol.*, 1996, **199**, 2071–2076.
- 219 T. K. Eto and B. Rubinsky, *Biochem. Biophys. Res. Commun.*, 1993, **197**, 927–931.
- 220 T. Wang, Q. Zhu, X. Yang, J. R. Layne and A. L. Devries, *Cryobiology*, 1994, **31**, 185–192.
- 221 M. Hassas-Roudsari and H. D. Goff, *Food Res. Int.*, 2012, **46**, 425–436.
- 222 H. M. Zbikowska, *Transgenic Res.*, 2003, **12**, 379–389.

- 223 H. J. Kim, J. H. Lee, Y. B. Hur, C. W. Lee, S.-H. Park and B.-W. Koo, *Mar. Drugs*, 2017, **15**, 27.
- 224 S. Deville, *J. Mater. Res.*, 2013, **28**, 2202–2219.
- 225 N. Møbjerg, K. A. Halberg, A. Jørgensen, D. Persson, M. Bjørn, H. Ramløv and R. M. Kristensen, *Acta Physiol. (Oxf.)*, 2011, **202**, 409–420.
- 226 S. Sahdev, S. K. Khattar and K. S. Saini, *Mol. Cell. Biochem.*, 2008, **307**, 249–264.
- 227 C. I. Biggs, T. L. Bailey, B. Graham, C. Stubbs, A. E. R. Fayter and M. I. Gibson, *Nat. Commun.*, 2017, **8**, 1546.
- 228 B. Graham, A. E. R. Fayter, J. E. Houston, R. C. Evans and M. I. Gibson, *J. Am. Chem. Soc.*, 2018, **140**, 5682–5685.
- 229 S. Liu and R. N. Ben, *Org. Lett.*, 2005, **7**, 2385–2388.
- 230 R. N. Ben, A. A. Eniade and L. Hauer, *Org. Lett.*, 1999, **1**, 1759–1762.
- 231 M. Leclère, B. K. Kwok, L. K. Wu, D. S. Allan and R. N. Ben, *Bioconjug. Chem.*, 2011, **22**, 1804–1810.
- 232 C. J. Capicciotti, J. D. R. R. Kurach, T. R. Turner, R. S. Mancini, J. P. Acker and R. N. Ben, *Sci. Rep.*, 2015, **5**, 1–10.
- 233 J. G. Briard, S. Jahan, P. Chandran, D. Allan, N. Pineault and R. N. Ben, *ACS Omega*, 2016, **1**, 1010–1018.
- 234 C. Stubbs, J. Lipecki and M. I. Gibson, *Biomacromolecules*, 2017, **18**, 295–302.
- 235 R. Rajan, F. Hayashi, T. Nagashima and K. Matsumura, *Biomacromolecules*, 2016, **17**, 1882–1893.
- 236 G. Bai, Z. Song, H. Geng, D. Gao, K. Liu, S. Wu, W. Rao, L. Guo and J. Wang, *Adv. Mater.*, 2017, **29**, 1–8.
- 237 R. Drori, C. Li, C. Hu, P. Raiteri, A. L. Rohl, M. D. Ward and B. Kahr, *J. Am. Chem. Soc.*, 2016, **138**, 13396–13401.
- 238 H. Geng, X. Liu, G. Shi, G. Bai, J. Ma, J. Chen, Z. Wu, Y. Song, H. Fang and

- J. Wang, *Angew. Chemie - Int. Ed.*, 2017, **56**, 997–1001.
- 239 O. Mizrahy, M. Bar-Dolev, S. Guy and I. Braslavsky, *PLoS One*, 2013, **8**, e59540.
- 240 T. Li, Y. Zhao, Q. Zhong and T. Wu, *Biomacromolecules*, 2019, **20**, 1667–1674.
- 241 T. Congdon, R. Notman and M. I. M. I. Gibson, *Biomacromolecules*, 2013, **14**, 1578–1586.
- 242 N. S. Vail, C. Stubbs, C. I. Biggs and M. I. Gibson, *ACS Macro Lett.*, 2017, **6**, 1001–1004.
- 243 T. Inada and S. Lu, *Cryst. Growth Des.*, 2003, **3**, 747–752.
- 244 T. R. Congdon, R. Notman and M. I. Gibson, *Eur. Polym. J.*, 2017, **88**, 320–327.
- 245 T. Inada and S. S. Lu, *Chem. Phys. Lett.*, 2004, **394**, 361–365.
- 246 C. C. DeMerlis and D. R. Schoneker, *Food Chem. Toxicol.*, 2003, **41**, 319–326.
- 247 G. Paradossi, F. Cavalieri, E. Chiessi, C. Spagnoli and K. Cowman, *Mater. Sci.*, 2003, **14**, 687–691.
- 248 L. L. C. Olijve, M. M. R. M. Hendrix and I. K. Voets, *Macromol. Chem. Phys.*, 2016, **217**, 951–958.
- 249 L. E. Wilkins, University of Warwick, 2018.
- 250 D. E. Mitchell, M. Lilliman, S. G. Spain and M. I. Gibson, *Biomater. Sci.*, 2014, **2**, 1787–1795.
- 251 D. E. Mitchell, N. R. Cameron and M. I. Gibson, *Chem. Commun.*, 2015, **51**, 12977–12980.
- 252 R. Rajan, M. Jain and K. Matsumura, *J. Biomater. Sci. Polym. Ed.*, 2013, **24**, 37–41.
- 253 W. Zhu, J. Guo, J. O. Agola, J. G. Croissant, Z. Wang, J. Shang, E. N. Coker, B. Motevalli, A. Zimpel, S. Wuttke and C. J. Brinker, *J. Am. Chem. Soc.*, 2019, **141**, 7789–7796.

- 
- 254 R. Drori, C. Li, C. Hu, P. Raiteri, A. L. Rohl, M. D. Ward and B. Kahr, *J. Am. Chem. Soc.*, 2016, **138**, s1–s16.
- 255 P. Czechura, R. Y. Tam, E. Dimitrijevic, A. V. Murphy and R. N. Ben, *J. Am. Chem. Soc.*, 2008, **130**, 2928–2929.
- 256 S. A. Galema, J. B. F. N. Engberts, H. Høiland and G. M. Førland, *J. Phys. Chem.*, 1993, **97**, 6885–6889.
- 257 A. K. Balcerzak, M. Febbraro and R. N. Ben, *RSC Adv.*, 2013, **3**, 3232–3236.
- 258 G. John Morris and E. Acton, *Cryobiology*, 2013, **66**, 85–92.
- 259 I. Kratochvílová, M. Golan, K. Pomeisl, J. Richter, S. Sedláková, J. Šebera, J. Mičová, M. Falk, I. Falková, D. Řeha, K. W. Elliott, K. Varga, S. E. Follett and D. Šimek, *RSC Adv.*, 2017, **7**, 352–360.
- 260 D. R. Nutt and J. C. Smith, *J. Am. Chem. Soc.*, 2008, **130**, 13066–13073.
- 261 C. Navarro-Retamal, A. Bremer, J. Alzate-Morales, J. Caballero, D. K. Hinch, W. González and A. Thalhammer, *Phys. Chem. Chem. Phys.*, 2016, **18**, 25806–25816.
- 262 S. J. Cox, S. M. Kathmann, B. Slater and A. Michaelides, *J. Chem. Phys.*, 2015, **142**, 184704.

# Chapter 2

---

Macromolecular Cryoprotectants; Polymer Formulations for Storage of Biological Materials.

## 2.1 Declarations

*The PVA and polyampholyte samples were synthesised by Dr Christopher Stubbs (supervised by Professor Matthew I. Gibson) and assistance with AFP expression by Dr Muhammad Hasan (also supervised by Professor Matthew I. Gibson). AFGP8 was provided by Professor Arthur. L. DeVries (Urbana-Champaign, University of Illinois). Live/Dead microscopy assays performed by Dr Julia Lipecki (supervised by Dr Sascha Ott, University of Warwick).*

*A patent of the application of this work (PCT/GB2019/050732) has been filed.*

## 2.2 Chapter Abstract

Modern molecular biology and microbiology is underpinned not only by the tools to handle and manipulate proteins and microorganisms, but also those to store, bank and transport them. Glycerol is currently the cryoprotectant of choice for freezing microorganisms and proteins, in academic and industrial settings, however it can be toxic to microorganisms, observed by lower cell survival post-thaw, this is partly due to the need for use at high concentrations (10 – 25 wt %) as well as causing oxidative stress, for example. Glycerol can affect down-stream applications and assays. Freeze-avoidant organisms have developed their own mechanisms to survive sub-zero temperatures and repeated freeze/thaw cycles; these include producing antifreeze proteins and antifreeze glycoproteins, which are potent ice recrystallisation inhibitors (>80 % reduction in ice growth compared to a buffer control at <0.1 mg.mL<sup>-1</sup> concentrations), though these have their own inherent issues; they cannot be readily produced on a large scale, are costly to produce, affect ice morphology leading to reduced cell-recovery post-thaw and have limited biomedical applications due to lack of sufficient immunological/toxicological data.

Herein we study synthetic macromolecular (polymer) mimics of antifreeze proteins for the cryopreservation of a range of bacteria and proteins and present a new concept for the storage/transport of biological materials using an all polymer, organic solvent-free, formulation. The mechanism of protection is discussed and demonstrated to link to inhibition of ice recrystallisation. The polymers are also observed to be significantly lower in toxicity than glycerol and prevent irreversible aggregation in proteins.

Optimised formulations are presented and shown to be broadly applicable to the cryopreservation of a panel of Gram negative, Gram positive and Mycobacteria strains as well as for a range of proteins.

This represents a step-change in how biological materials will be stored by the design of new macromolecular ice growth inhibitors; it should enable a transition from traditional solvent-based to macromolecular microbiology and protein storage methods.



## 2.3 Introduction

### 2.3.1 Storage and Transport of Proteins and Cells

As mentioned in Chapter 1, the cold chain process is extremely important for many biotechnology and cell-based processes. In particular, the logistics of this chain requires accurate temperature control, as the recovery of intact and viable cells/proteins is vital. Academic and industrial settings both use cryopreservation and lyophilisation to avoid the need for continuous cell culture and protein expression<sup>1,2</sup> and thus enable these biologics to be available and transportable between laboratories and to potential patients. Cryopreservation is a popular choice in research laboratories, as only a  $-80\text{ }^{\circ}\text{C}$  freezer or liquid nitrogen is required, as well as less need for specialised equipment.<sup>3,4</sup> However, if there is a risk of temperature fluctuation there may be ice recrystallisation. This can irreversibly damage biological materials and work is needed to improve storage and negate this effect.

### 2.3.2 Stability of Biological Materials in Ice

As water cools and solidifies in a solution containing biological materials, the concentration of solutes throughout the medium varies.<sup>5</sup> Freezing can damage proteins due to the resultant stressors; pH shifts due to selective crystallisation of buffer salts,<sup>6–10</sup> cryoconcentration of proteins<sup>11</sup> and increased ice-water interface.<sup>12,13</sup> Cryoconcentration, in particular, can lead to a high increase in protein concentration and ionic strength in the non-ice phase, which can lead to an increase in protein interactions and potential aggregation.<sup>14</sup> Thus the structure of proteins can be greatly affected by ice formation. Gonelli *et al.* observed protein stability and saw that temperature (thermal gradient) and size of water pool affect how much impact ice have on the proteins.<sup>5</sup> The addition of additives has been observed to disrupt ice:protein interactions and lead to proteins retaining their native states. Cells do not survive extreme temperatures easily; biological metabolism reduces at low temperatures to enable preservation, however cryoinjury occurs during cooling, warming and the addition/removal of cryoprotectants (CPAs).<sup>15</sup> Intracellular water loss can lead to rupturing due to volume shrinkage and increased exposure to high concentrations of solutes. There can also be ‘solution effects’ that can cause cell injury.<sup>3</sup>

### 2.3.3 Freezing Challenges

As stated above, cold storage is important, but it is a multifaceted process. Cooling and warming rates need to be optimised,<sup>16</sup> storage temperatures determined and cryopreservation formulations designed and tested for viability and toxicity. To achieve recovery of organisms/proteins from temperatures as low as -196 °C cryoprotectants are required.<sup>17</sup> These range from small molecules to those derived from natural resources such as antifreeze (glyco)proteins (AF(G)Ps). CPAs are used to reduce ice formation during cooling and are often in different concentrations or combinations for different materials. Cryopreservation traditionally requires the addition of organic solvents to mitigate the damage caused by ice formation and growth, as well as membrane rupture and osmotic stress which would otherwise lead to cell death.<sup>18,19</sup> There are obviously benefits for using these CPAs, however they are not without fault.<sup>20</sup> For mammalian cells, dimethyl sulfoxide (DMSO) is the most widely employed cryoprotectant for both 'slow' freezing and vitrification (depending on the DMSO concentration), and for bacteria, glycerol is typically used.<sup>21</sup> Whilst very successful and used globally these require high concentrations (10 – 25 wt %) and the solvents potentially have cytotoxic effects necessitating careful addition and rapid removal (post-thaw) to maintain viability.<sup>22,23</sup> Glycerol toxicity, in particular, has been observed in a range of microorganisms, including *Staphylococcus*, *Micrococcus*, *Lactococcus*, *Streptococcus*, *Pseudomonas*, *Corynebacterium diphtheriae*, and *E. coli*.<sup>24,25</sup> They also do not lead to quantitative recovery of all cells, meaning there is a need to investigate innovative cryopreservation methods.

Cellular damage due to ice growth has been observed to be reduced by the addition of IRI active species such as AF(G)Ps, another potential choice of CPA. However there can be ice-shaping effects: AF(G)Ps can produce crystals of a needle-like shape that in turn damage cells, **Figure 2.1**.<sup>26–30</sup>

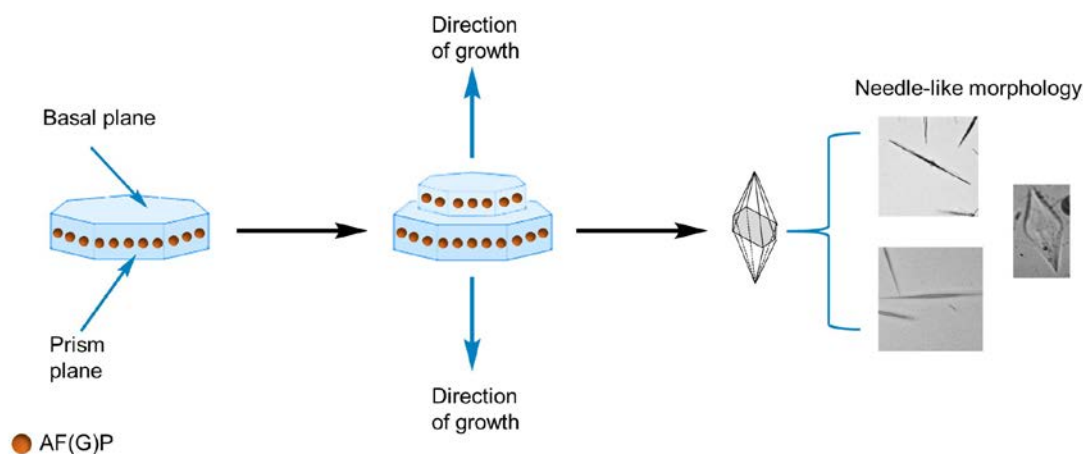


**Figure 2.1.** Morphology modification over time, due to binding of AF(G)Ps to the prism plane. Scale bar = 100  $\mu\text{m}$ .

Synthetic macromolecular mimics of AF(G)Ps have emerged, which can reproduce their properties but benefit from the scalable and tuneable synthesis of synthetic polymers.<sup>31–33</sup> These have been used to enhance the cryopreservation of mammalian cells including blood,<sup>34–36</sup> cell lines<sup>37</sup> and primary cells.<sup>38,39</sup> Their primary function is IRI, where the rate of growth (not formation) of ice is slowed, leading to reduced cell death during thawing. The most active polymer mimics reported to date are based on poly(vinyl alcohol)<sup>40–45</sup> but safranin-O,<sup>46</sup> polyampholytes,<sup>47,48</sup> graphene oxide,<sup>49</sup> zirconium acetate (ZrAc)<sup>50</sup> and glycopeptides have high IRI activity.<sup>51</sup>

### 2.3.4 Protein Storage

Proteins are ubiquitous as laboratory reagents, biocatalysts, medicines, and as food supplements. For example, in the 1980s insulin became the first protein therapeutic, and now >100 are approved in the European Union and the USA.<sup>52</sup> Antibody therapies in particular have grown and are now used for treatment of cancer,<sup>53</sup> inflammatory diseases,<sup>54</sup> and are the fastest growing class of therapeutics.<sup>55</sup> A major challenge, however, is the limited storage lifetime of proteins, with degradation being a significant issue.<sup>56,57</sup> Environmental stressors such as temperature, sunlight and dehydration are all crucial deactivation factors that often lead to irreversible protein aggregation.

Current solutions to this challenge include lyophilisation or direct freezing in solution with the addition of large concentrations of osmolytes that make unfolding

thermodynamically less favourable.<sup>58</sup> Whilst these methods are successful, there are post-thaw issues to do with the compatibility of high concentrations of osmolytes used (*e.g.* 10 – 20 % glycerol) in subsequent applications. Hence direct therapeutic injection or use in biochemical assays may often necessitate an additional purification/dilution step.

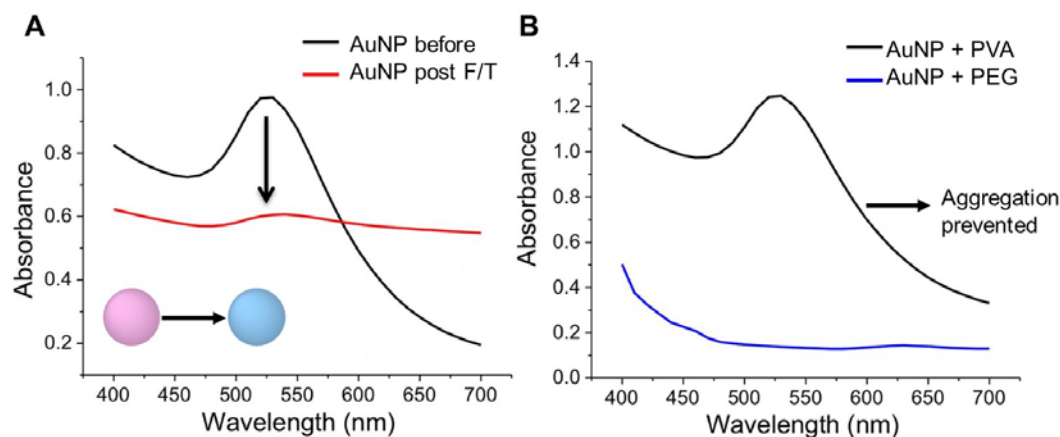


**Figure 2.2.** Effect of freezing and thawing (FT) gold nanoparticle (AuNP) solutions, with a decrease in absorbance at 520 nm represented by a colour change (pink to blue) indicating nanoparticle aggregation. A) AuNP before (black) and post FT (red); B) UV-Vis spectra after FT in the presence of 6.8 kDa PVA (black) and 4 kDa PEG (blue). [Polymer] = 10 mg.mL<sup>-1</sup>. Adapted from Mitchell *et al.* (Sci. Rep., 2015).<sup>59</sup>

Mitchell *et al.* found that the reversible aggregation of gold nanoparticles (visualised by a colorimetric response) during freezing could be modulated by addition of PVA.<sup>59</sup> By slowing the rate of ice growth, the effective surface area of the ice crystals is increased (*i.e.* more ‘small’ crystals) and hence the nanoparticles could not approach each other to aggregate, **Figure 2.2**. We therefore hypothesised that IRI active compounds might prevent protein aggregation during ice-growth induced stress, which normally leads to denaturation/deactivation. This effect could in turn be exploited in the solvent-free storage of proteins.

### 2.3.4.1 Proteins Studied Here

Structures of all proteins studied here are shown in **Figure 2.3**.

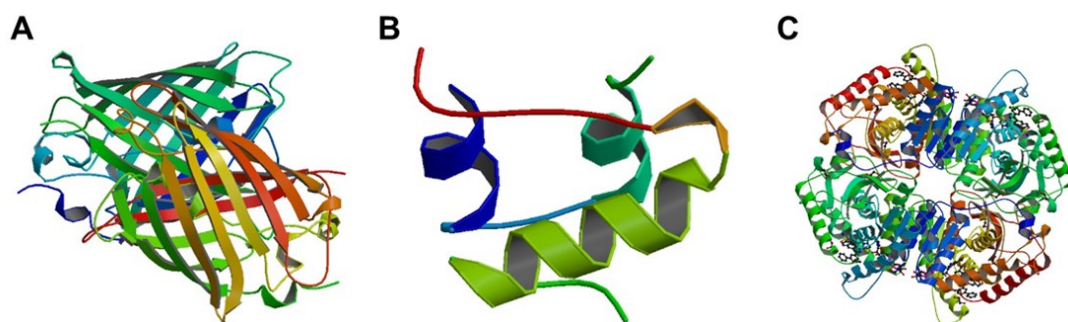


**Figure 2.3.** Proteins used in this work to study their viability after cold storage in different cryoprotectants. A) Recombinant Green fluorescent protein (53.8 kDa); B) Insulin (5.8 kDa); C) Lactate dehydrogenase (37.7 kDa). Structures not shown at the same scale. (Structures “1GFL”, “3I40” and “5W8L” from the protein data bank).<sup>60–62</sup>

To test protein cryopreservation a model protein was used. This was to see if our assay choice worked, as well as to confirm if any particular CPA formulation led to high protein recovery post thaw. Green fluorescent protein (GFP) was chosen as the model protein; it is naturally fluorescent, easy to recombinantly express and loses fluorescence as it denatures.<sup>63,64</sup> GFPs fluorophore is protected: shielded from its environment by  $\beta$ -sheets.<sup>60</sup> This is essential, as otherwise water molecules would interact with the chromophore. Upon aggregation/misfolding the chromophore may not be shielded and thus not release energy as light photons. We chose to take advantage of this process as, upon freezing and thawing, if the protein structure is affected, the fluorescence will decrease, and if GFP is successfully stored in a CPA formulation fluorescence would be retained. This is easy to follow using fluorescence spectroscopy.

Insulin was chosen as a therapeutic protein of interest. It is an extremely important hormone, acting as a molecular messenger assisting in the regulation of blood sugar levels. It is a ‘small’ protein consisting of an A-chain and B-chain stabilised by disulfide bridges,<sup>65–68</sup> which can be present in different oligomerisation states depending on physical conditions. These include a hexamer stabilised by two zinc ions (in its storage form at neutral pH), and as a monomer in its active form, as well as

dimers (when under acidic conditions).<sup>69,70</sup> These structures must be considered for insulin formulations pre- and post-thaw, as the oligomerisation state relates to protein activity. Oligomerisation state has been followed using dynamic light scattering (DLS), and changes in structure visualised by monitoring aggregation using this technique. If insulin function is impaired or a person is deficient in insulin, such as those with diabetes, manual replacement of insulin *e.g. via* injection/patch/pump is required as a treatment.<sup>71-73</sup> The biotech industry produces human insulin for use, and long-term storage of this hormone is of great interest.<sup>74-76</sup> As with GFP, misfolding and aggregation leads to inactivity so successful cryopreservation is vital.

Lactate dehydrogenase (LDH) was also chosen to study. This enzyme comes in two forms; M and H. M converts pyruvate to lactate in skeletal muscles and H, lactate to pyruvate, and is generally the major form in the heart.<sup>77,78</sup> It is used to test for tissue damage, as well as to diagnose particular diseases *via* activity changes and as a marker for germ cell tumours, and successful storage is required for transport from patient to laboratory for analysis.<sup>79-81</sup> Conflicting data on the effect of storage of LDH has been reported<sup>82-84</sup> thus work here aimed to study cold storage of this enzyme and confirm activity retention at these temperatures.

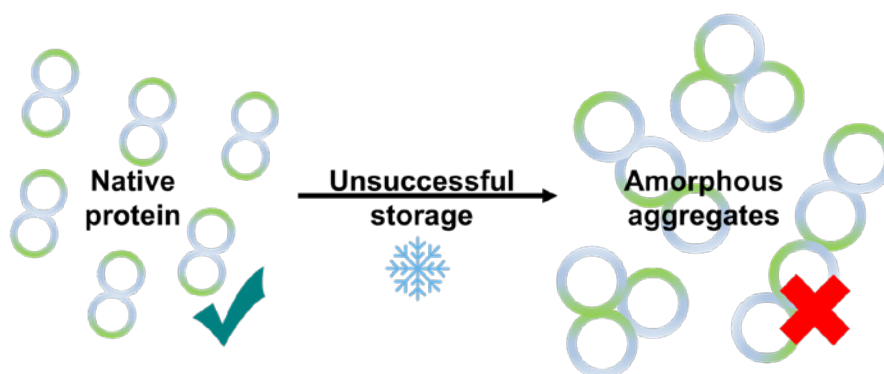


**Figure 2.4.** Schematic of how aggregation occurs *via* interfacial stress between the ice:liquid interface, leading to inactive proteins.

Environmental changes, including pH, temperature and ionic strength, can lead to aggregation and formation of non-native dimers/oligomers, monomer addition and high molecular weight aggregates.<sup>85</sup> A schematic of this process is shown in **Figure 2.4**. Studies here aim to avoid this process.

### 2.3.5 Cell Storage

Cryostorage of both prokaryotic (bacterial) and eukaryotic (of which make up humans and multi-cellular organisms) cells is of great interest in the cryo-field. Eukaryotic cells consist of organelles, with various functions, and can require different, more complex CPA formulations for successful storage.<sup>17,25,86</sup> Some cells (of which range in complexity) studied so far include sperm, oocyte and embryonic,<sup>87,88</sup> muscle<sup>89</sup> and corneal.<sup>90</sup> Prokaryotic cells are generally simpler; they do not consist of organelles, do not have a nucleus and have a cell wall.

Bacteria and their study underpin all research in infectious diseases, microbiology, structural and molecular biology, as well as being crucial in biotechnology and food processes (notably probiotics). The storage of bacteria for supplements such as probiotics, is growing and recent research into the microbiome points towards its involvement in a host of medical disorders including, but not limited to, irritable bowel syndrome, depression, cardiovascular disease and obesity, showing the significant need for strategies to store bacteria,<sup>91-94</sup> especially if microbiome transplants become a reality for the treatment of drug resistant infections, for example,<sup>95</sup> this is because the therapeutic role of probiotics depends on count of viable cells, which can be reduced by inadequate storage.<sup>96</sup>

#### 2.3.5.1 Cells Studied Here

Historically, *Escherichia coli* (*E. coli*) was used as the general model organism for the study of bacterial cells. This was due to the understanding that its membrane lipid biochemistry could be generalised to other cells.<sup>97</sup> However, different bacteria have different cell walls and membrane compositions, of which these can be differently affected by environmental conditions. Here, three bacteria species are studied, each with different cell wall/membrane compositions consisting of peptidoglycan and varying phospholipids, **Figure 2.5**, to ensure a well-rounded analysis of the CPAs cryoprotective abilities on a range of cell types, and that any effects were not unique to *E. coli*. As many factors affect the effectiveness of cryopreservation of bacteria *e.g.* species, strain, cell size, cell water content, composition of cell, it was found to be important to test a range.<sup>25</sup> *Bacillus subtilis* was chosen as a Gram-positive strain and *Mycobacterium smegmatis* as a Mycobacteria. These bacteria have distinct cell wall

structures; therefore, any cryopreservation formulations that may cause toxic effects on types would be observed. Preliminary tests on *Lactobacillus delbrueckii subsp. bulgaricus*, an microorganism of importance in probiotics and research into the microbiome, were also performed (see Appendix).<sup>95,98–100</sup>

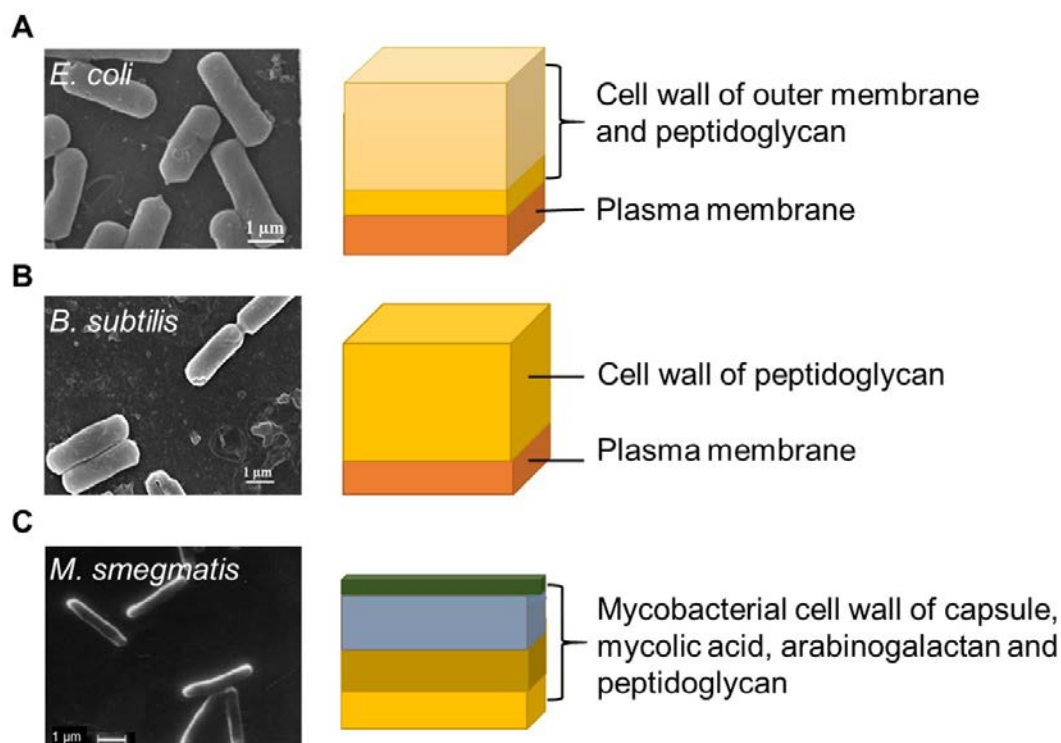


**Figure 2.5.** The three bacteria strains used and their corresponding cell wall structure; A) Gram-negative *E. coli*; B) Gram-positive *B. subtilis*; C) Mycobacterium *M. smegmatis*. SEM scale bars are 1 μm. Adapted from Deol *et al.* (J. Bacteriol., 2005), Li *et al.* (Microbiol. Biotechnol., 2010) and Prince *et al.* (Sci. Rep., 2016).<sup>101–103</sup>

Bacteria have adapted to respond to changes in environment, even minor changes such as those during protein expression in a flask can affect survival. One response is to change their membrane lipid composition. This is a constant process, as nutrient levels will reduce and metabolic products can increase, leading to changes in pH and oxygen levels. These adaptations, however, are not enough to protect bacteria in extreme temperatures, such as those required for cold storage. Research shows that a decrease in temperature causes a decrease in membrane fluidity, and leads to increased production of unsaturated fatty acid/fatty acids of similar structures as well as modification of existing lipids.<sup>97</sup> When cells undergo extreme cooling and transient



warming cycles, such as freeze/thaw (FT) cycles, these changes are not enough, and potentially the change in composition leads to less viable cells post thaw.

## **2.4 Terminology**

**Cryoprotectant (CPA)** – formulation tested here for cryoprotective ability, including either colligative or non-colligative (IRI active) antifreezes. Based on the definition of an additive added to biological materials before freezing that leads to high post-thaw survival compared to no additive. *CPA used from now on to describe any formulation/group of formulations tested.*

## 2.5 Chapter Aims

The primary aim of this study was to evaluate the role of IRI active polymers to enable solvent-free cryopreservation of a range of biological materials, including 4 different bacteria and three different proteins.

- Express and purify an antifreeze protein and study its cryoprotective activity
- Study cryoprotective properties of PEG and PVA in different formulations
- Optimise a protocol for measuring LDH activity and hence study cryostorage of LDH in different CPA formulations

## 2.6 Results and Discussion

### 2.6.1 Formulation Design

Taking inspiration from extremophiles, such as Arctic fish and insects, biologic cryopreservation has been investigated using polymeric, glycerol-free, formulations. The focus is on AF(G)P mimics that do not affect ice crystal morphology. A range of synthetic polymers were selected for this based on their previous use in mammalian cell cryopreservation. These included poly(vinyl alcohol), PVA, which is a potent IRI; poly(ethylene glycol), PEG, which has no IRI but was chosen to provide a hydrophilic ‘bulking’ agent, which has been shown to be important for blood cell cryopreservation;<sup>35,104</sup> and a polyampholyte (p(amph)), which has weaker IRI activity than PVA.<sup>36,105</sup> The polymers were compared to recombinant type III AFP (AFPIII, from Ocean Pout), an antifreeze protein originally isolated from ocean pout, and glycerol, **Figure 2.6**.<sup>106</sup>

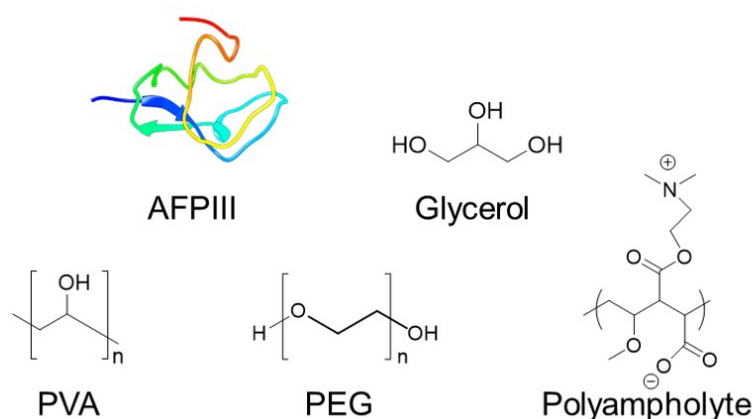


**Figure 2.6.** Structures of compounds used as cryoprotectants or in cryoprotective formulations in this work.

IRI activity of PVA has been observed to improve upon the addition of polymeric depletants, such as PEG,<sup>107</sup> thus if IRI activity is vital to a polymeric formulation’s successful cryoprotection of biologics, then potentially the addition of a secondary polymer will improve post-thaw recovery. It is important to note that PVA and PEG were particularly of interest as they are low-cost (comparable to glycerol), are available in a range of molecular weights and are produced to food/clinical grades making them well-suited for translational applications.<sup>108</sup> The first step in formulation design was to evaluate IRI activity of all candidates by comparing their ice crystal

sizes, **Figure 2.7**. Smaller ice crystals indicate the CPA has more IRI activity and is reported as the mean grain size (MGS) where the average size of all crystals is measured, or mean largest grain size (MLGS), where the largest crystal in view is measured (this is generally recorded as an average of 6). These parameters are the most relevant here, as they enable visualisation of crystal formation and growth over time, giving information on the effect this CPA will have on ice crystal size in a frozen bacteria or protein sample. In this way we could determine the inhibition of ice crystal growth and compare to that of AFPIII (currently known to be the most IRI active additive). Ice growth inhibitors can be potent (leading to >80 % reduction in ice growth compared to a buffer control at <1 mg.mL<sup>-1</sup> concentrations), or weak (>80 % reduction at <10 mg.mL<sup>-1</sup> concentrations). Here, ice wafers were nucleated at -78 °C to give small (< 10 µm) ice crystals, which were allowed to anneal for 30 minutes at - 8 °C, and then measured and ice crystal size recorded. Some more IRI active samples can be harder to count than PBS, particularly those with much smaller crystals or slightly more amorphous-looking grain boundaries. ImageJ provides a variety of tools to assist in analysis of these photographs, **Figure 2.7B**, by enhancing brightness and contrast of the images, as well as magnification. These issues, however, do highlight the need for other complementary techniques to study ice-activity, which are detailed in Chapters 3 and 4.

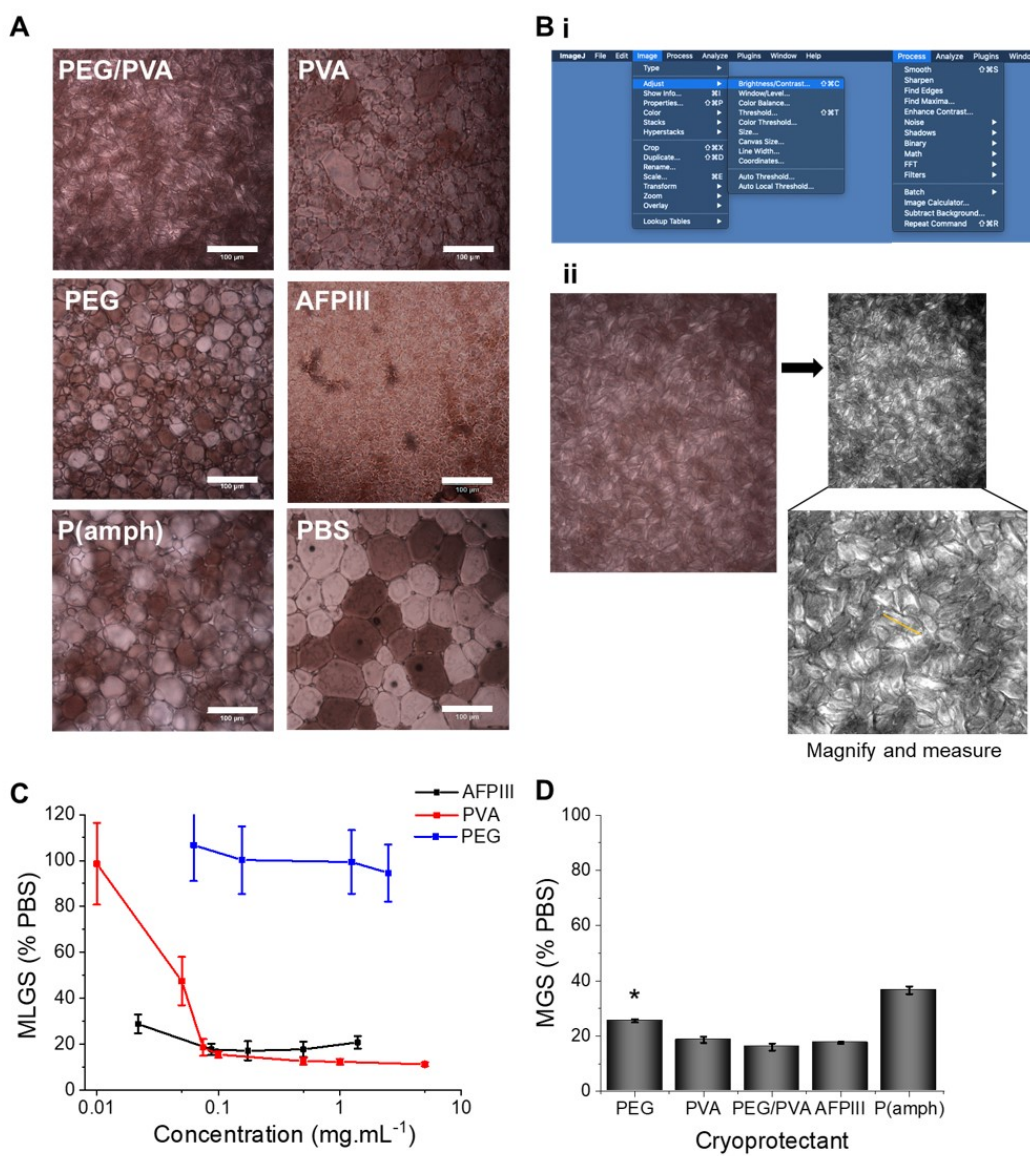


**Figure 2.7.** IRI activity of macromolecules used in this work; A) Cryomicrographs of ice wafers grown in the presence of  $100 \text{ mg.mL}^{-1}$  PEG +  $1 \text{ mg.mL}^{-1}$  PVA,  $1 \text{ mg.mL}^{-1}$  PVA,  $100 \text{ mg.mL}^{-1}$  PEG,  $1 \text{ mg.mL}^{-1}$  AFPIII,  $50 \text{ mg.mL}^{-1}$  polyampholyte, and PBS control. Scale bar =  $100 \mu\text{m}$ ; B) Example ImageJ analysis of a sample, including i) various tools available to use to enhance visualisation of grain boundaries for crystal counting and ii) example photo taken during a splat assay, explained in 2.8.3.2, which then can be converted to greyscale and the contrast enhanced, as well as magnified to enable ease of measurement; C) mean largest grain size (as % of PBS) over a range of concentrations for protein (black) and synthetic mimic PVA (red) compared to PEG (blue); D) Mean grain size (as % of PBS grain size) of all macromolecules tested in A. \*PEG ( $100 \text{ mg.mL}^{-1}$ ) appears to show IRI activity here, however this is a colligative effect caused at this high concentration.

A range of concentrations for PVA, PEG and AFPIII were tested showing that PVA has great IRI activity, supporting work seen in the literature, **Figure 2.7C**.<sup>40,109,110</sup> AFPIII was found to be the most IRI active, even at  $\mu\text{g.mL}^{-1}$  concentrations, as in the literature. PEG has no IRI activity, though has a colligative effect at higher concentrations, **Figure 2.7D**. The concentrations for the p(amph) are chosen to be 50  $\text{mg.mL}^{-1}$ , as concentrations  $\geq 20 \text{ mg.mL}^{-1}$  are IRI active concentrations observed in the literature.<sup>47</sup>

It should be noted that PEG has known cryoprotectant properties at very high concentrations<sup>111</sup> and it has been observed that PEG in a concentration above 50  $\text{mg.mL}^{-1}$  assists with cryoprotection of proteins, therefore 100  $\text{mg.mL}^{-1}$  was the chosen concentration. When the PEG and PVA are combined, the crystal growth continues to be inhibited, and potentially is even more effective, due to the increased IRI activity, and the slightly more amorphous crystals observed in **Figure 2.7A**.

Previous work using red blood cells, which have no nucleus, like bacteria, has shown that IRI active PVA has increased cell survival. Other work has shown that the cryoprotective activity of IRI active polymers increases when used in combination with a hydrating secondary cryoprotectant such as polymer gels or hydroxyl ethyl starch (HES).<sup>35,104</sup> This led us to test the combination of PEG and PVA; with PEG being the bulky hydrating polymer in the formulation. PEG was chosen due to its biocompatibility<sup>112–115</sup> and commercial availability.

Storage at  $-20\text{ }^{\circ}\text{C}$  was of interest here, as it is cheaper and  $-20\text{ }^{\circ}\text{C}$  freezers are ubiquitous in all laboratories, whereas  $-80\text{ }^{\circ}\text{C}$  freezers may not be available to all. Thus, formulations were tested for CPA activity for a range of storage temperatures;  $-20$ ,  $-80$  and  $-196\text{ }^{\circ}\text{C}$ .

## 2.6.2 Protein Expression and Purification

In order to study the cryoprotective properties of AFPs and polymers and their toxicity on bacteria, recombinant protein expression was needed to produce antifreeze proteins, as they are not commercially available. In the first instance *E. coli* competent cells (BL21) were produced, as they are bacterial cells with cell walls that allow foreign DNA (*e.g.* plasmid) to pass through easily.

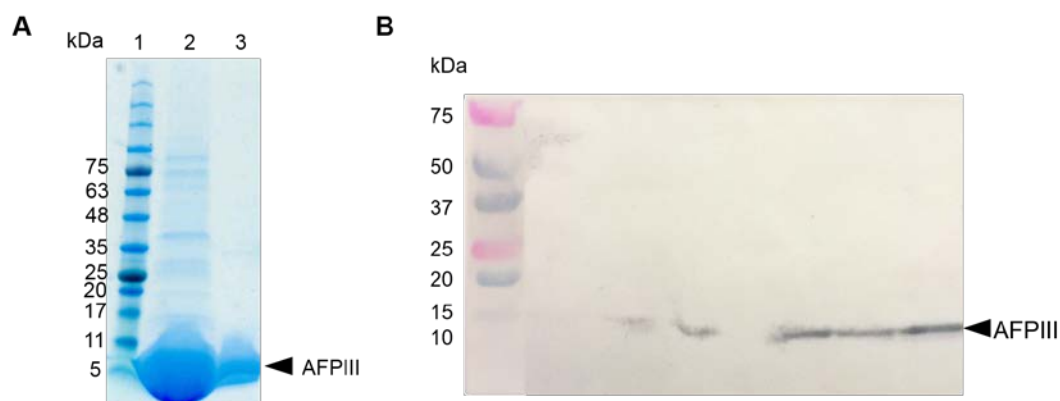


**Figure 2.8.** Characterisation of AFPIII expression in *E. coli*. A) SDS-PAGE gel analysis of nickel affinity chromatography purified AFPIII (lane 2) and FLPC purified AFPIII (lane 3) compared to Prism Ultra Protein Ladder (lane 1); B) Full-length Western blot image of AFPIII expression. The numbers on the left represent the molecular mass in kilodaltons.

AFPIII (T7, pET21b, P19614) was initially expressed *via* auto-induction, though a low yield was obtained (7.18 mg at concentration of  $0.359 \text{ mg}\cdot\text{mL}^{-1}$ ). The AFPIII was purified further using fast protein liquid chromatography (FPLC) to remove the oligomers that remained after the initial filtering and desalting to ensure freeze thaw assays used the purest AFPIII, and sodium dodecyl sulfate-polyacrylamide gel electrophoresis (SDS-PAGE) analysis performed (**Figure 2.8A**). The SDS-PAGE analytical technique is a method for resolving proteins in complex mixtures by separating proteins based on electrophoretic mobility. Sodium dodecyl sulfate (SDS) and a reducing agent (*e.g.* DTT) are used to disrupt the tertiary structure of the proteins in the sample, with SDS binding to the protein, giving the proteins a net negative charge, this charge is proportional to chain length/molecular weight. A voltage is applied across the gel and proteins of different molecular weights, due to their charge, will migrate through at different rates and compared to a marker (**Figure 2.8A, Lane 1**). Oligomers can be observed in faint bands in **Figure 2.8A, Lane 2**, after FPLC, these no longer appear, and only the AFPIII band that is expected at 6.5 kDa appears. An anti-his western blot was also performed to ensure AFPIII was obtained (**Figure 2.8B**); a western blot exploits interactions between antigens and antibodies of proteins, thus is employed here demonstrating that AFPIII has been produced due to its interaction with the antibodies leading to the appearance of bands at 6.5 kDa. The band representing AFPIII appeared for more than one lane, which implies our AFP did not

stick to the nickel-resin and was washed through; this may be a reason for the low yield. AFPIII was then expressed as described in methods (2.8.3.1), leading to a higher yield and the His-tag cleaved. Once expressed AFPIII was used immediately or lyophilised for later use.

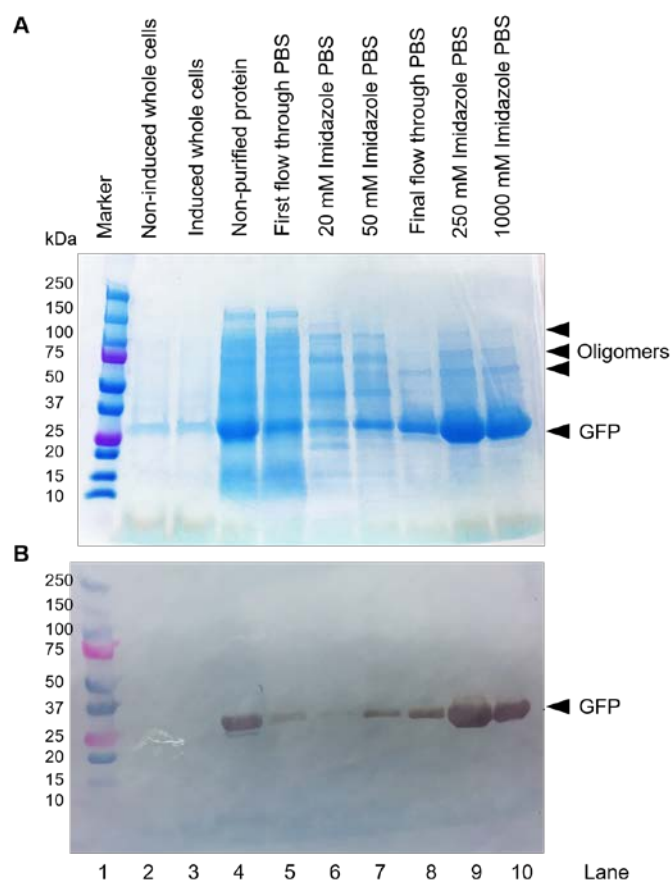


**Figure 2.9.** Characterisation of GFP expression in *E. coli*. A) SDS-PAGE gel analysis of nickel affinity chromatography purified GFP compared to Prism Ultra Protein Ladder (lane 1) highlighting GFP and higher oligomer expression; B) Full-length Western blot images of GFP expression. The numbers on the left represent the molecular mass in kilodaltons.

GFP was expressed using BL21 cells as described in 2.8.3.1 (Figure 2.9, lane 10) for cryopreservation assays. BCA assays were performed indicating the total mass of GFP expressed was 79.3 mg, thus the expression method used was correct for this protein.



### 2.6.3 Cryopreservation of Proteins

The simplicity of our cryopreservation assays for testing ability of CPAs on proteins is highlighted in **Figure 2.10**. The protocols all consist of dissolving and storing proteins in the formulations at three different freezing/storage temperatures and then studying their post thaw activity *via* spectroscopy or DLS.

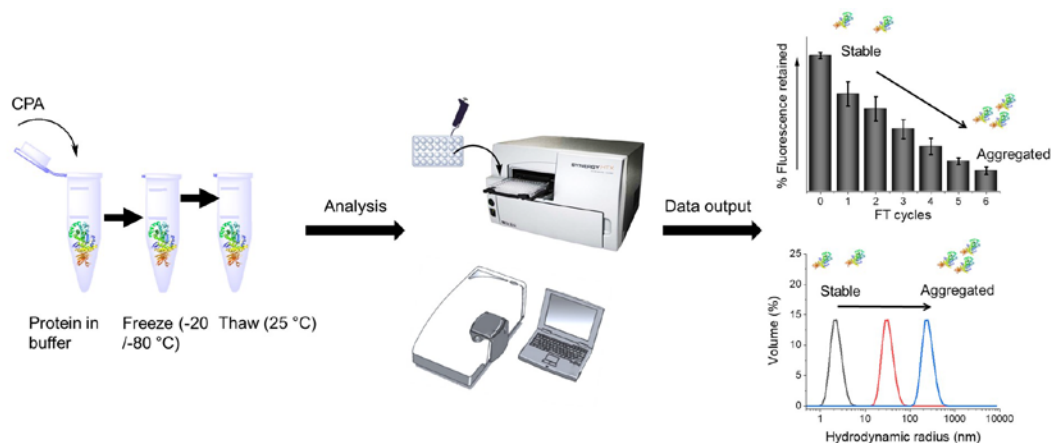


**Figure 2.10.** Schematic of cryopreservation procedures for proteins. Analysis of freeze/thawed samples either *via* dynamic light scattering or fluorescence spectroscopy. Data output represented as example graphs of fluorescence retained after FT cycles and potential hydrodynamic radii sizes.

#### 2.6.3.1 Green Fluorescent Protein

To enable continual monitoring of the same sample through many FT cycles, recombinant green fluorescent protein (GFP) was used. Upon denaturation, the fluorescence decreases providing a convenient readout.

The cryoprotective ability of PVA, PEG and PEG/PVA mixtures on GFP were compared *via* fluorescence spectroscopy. 4 initial FT cycles were run (**Figure 2.11**) to observe the decrease in GFP fluorescence in PBS buffer (black) due to FT stress, showing that the FT process causes aggregation, which in turn decreases the fluorescence relating to protein de-activation. Cryoprotectants were subsequently added to compare their cryoprotective activities. PVA (red) and PEG (blue) both lead to 75 % fluorescence retained after 4 FT cycles, which is much greater than that of GFP alone. The addition of PEG/PVA (green), however, leads to 100 % retention of fluorescence and thus protein activity.

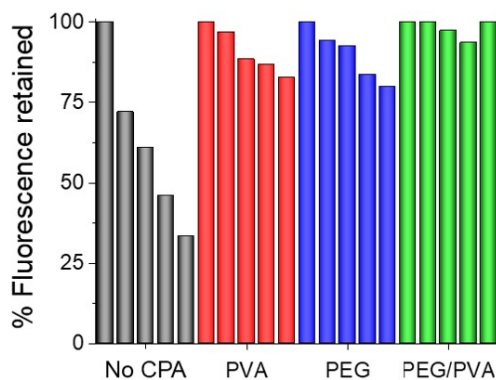


**Figure 2.11.** Normalised fluorescence recovery of GFP over 4 freeze ( $-20\text{ }^{\circ}\text{C}$ )/ thaw ( $25\text{ }^{\circ}\text{C}$ ) cycles with either no added CPA (black) or in the presence of 3 polymer formulations;  $[\text{PVA}] = 1\text{ mg.mL}^{-1}$ ;  $[\text{PEG}] = 100\text{ mg.mL}^{-1}$ ;  $[\text{PEG/PVA}] = 100 + 1\text{ mg.mL}^{-1}$ . First measurement is before freezing, then consecutive freeze/thaw cycles. 100 % fluorescence retained corresponds to the highest fluorescence for individual samples normalised to 100 % for ease of comparison.

To study the effect of concentration and polymer molecular weight further FT assays were performed, **Figure 2.12.** PVA at 10 kDa and 23 kDa were both tested over 8 FT cycles in combination with  $100\text{ mg.mL}^{-1}$  4 kDa PEG. PEG protects GFP the most in combination with  $1\text{ mg.mL}^{-1}$  10 kDa PVA, though fluorescence retention barely differs to that of PEG +  $2.5\text{ mg.mL}^{-1}$  10 kDa PVA. There is no need however to use a higher concentration of cryoprotectant if not needed so  $1\text{ mg.mL}^{-1}$  10 kDa PVA was chosen for later experiments.

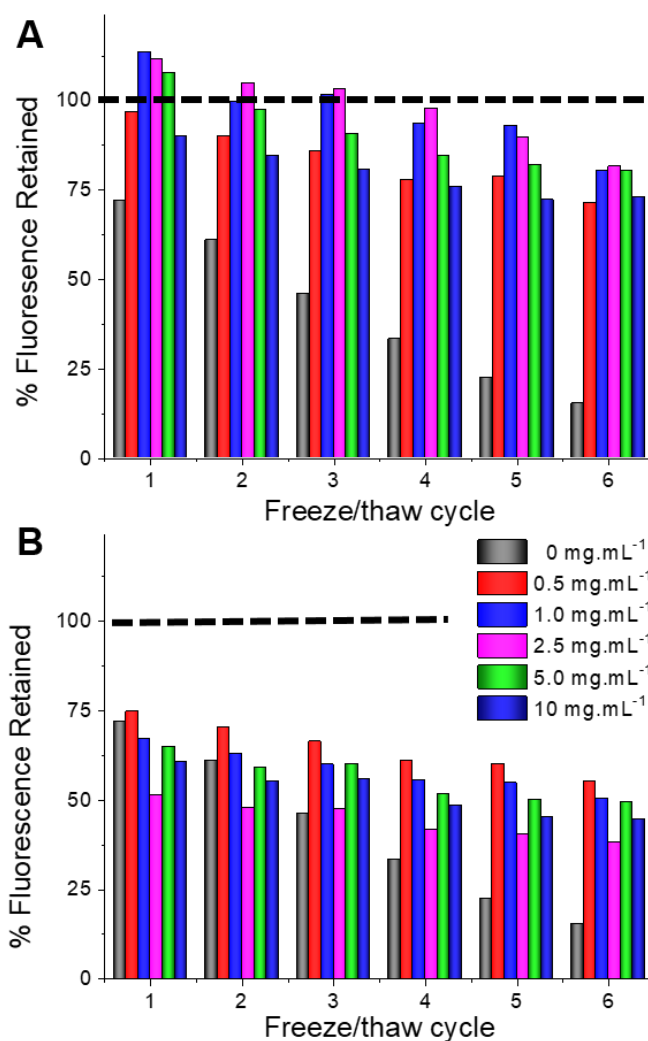


**Figure 2.12.** Comparison of cryoprotective activity of PVA at two different molecular weights. Fluorescence recovery of GFP after freeze ( $-20\text{ }^{\circ}\text{C}$ )/ thaw ( $25\text{ }^{\circ}\text{C}$ ) in A) 10 kDa PVA and B) 23 kDa PVA; All solutions containing  $100\text{ mg.mL}^{-1}$  PEG + [PVA] indicated in the insert.

Higher concentrations of PVA were found to be detrimental as was the use of higher molecular weight PVA (23 kDa), **Figure 2.12B**. We hypothesise this is due to dynamic ice shaping, a common side effect of antifreeze proteins, which is known to compromise cell cryopreservation.<sup>27,34</sup> A more dendritic hexagon crystal shape forms for 23 kDa PVA; this may lead to the aggregation of GFP, or misfolding due to a different ice matrix surrounding the frozen protein. This highlights the delicate balance of IRI activity with ice shaping and that the actual polymer composition is crucial to success.

### 2.6.3.2 Insulin

Further assays were performed using insulin as a more challenging protein; GFP is particularly hardy (and still fluoresced after multiple FT cycles). DLS was used to measure the aggregation of insulin over consecutive FT cycles and whether PVA or PEG prevented it, **Figure 2.13**.

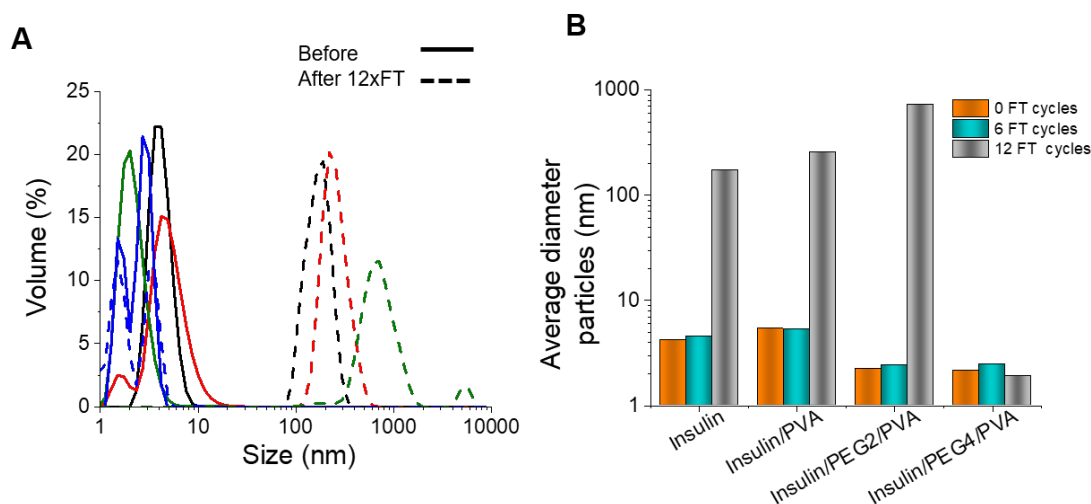


**Figure 2.13.** Insulin recovery after 6 and 12 FT cycles. A) DLS curves of insulin before (solid) and after (dashed) 12 freeze/thaw cycles. Black = insulin only, Red = insulin + PVA, Green = + 2 kDa PEG + PVA, Blue = + 4 kDa PEG + PVA. In all cases [PEG] = 100 mg.mL<sup>-1</sup>; [PVA] = 1 mg.mL<sup>-1</sup>. B) Average size of insulin aggregates after 6 or 12 FT cycles stored in PVA alone, PVA + 2 kDa PEG and PVA + 4 kDa PEG compared to that of all before freezing (0 FT cycles).

PVA, PEG, PEG/PVA (100 + 1 mg.mL<sup>-1</sup>) were tested alongside insulin in buffer alone. The importance of the PEG molecular weight was also tested, **Figure 2.13**. After 6 FT cycles solutions of PVA with PEG 2 kDa and PEG 4 kDa both were equally effective and little aggregation of insulin with no added cryoprotectant had occurred. After 12 FT cycles however, only PVA solutions with PEG 4 kDa have protected insulin from aggregation. It was also observed that PVA alone does not protect insulin from aggregation, observed by the larger particle diameters for insulin alone and insulin/PVA being >100 nm after 12 FT. This supports findings of the GFP assays that PEG and PVA are required for protection, but also displays that PEG 4 kDa is a more optimal molecular weight to use. This is a major advance compared to the current state of the art for protein storage, which requires the addition of ‘large’ quantities of glycerol or other organic solvents.

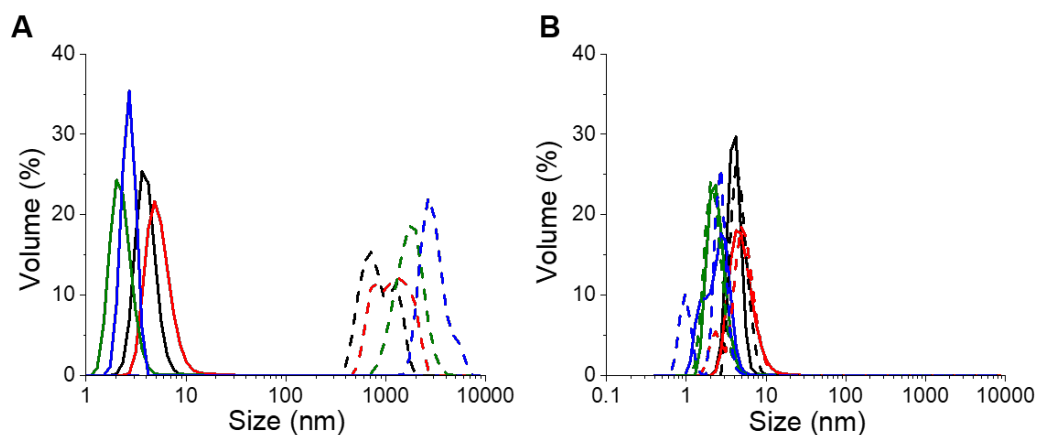
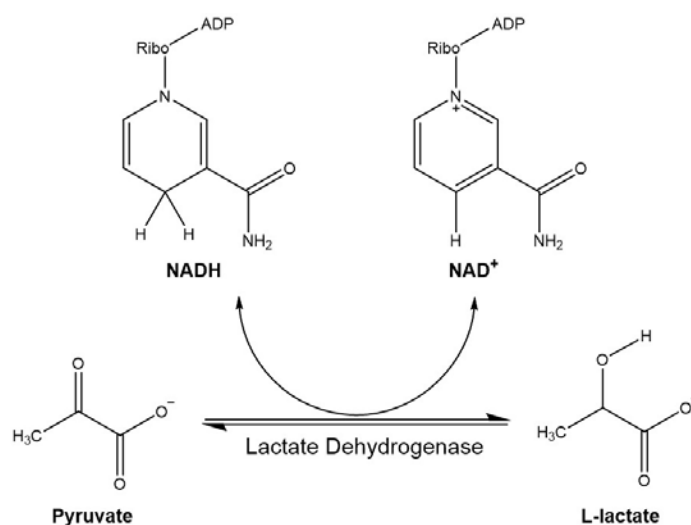


**Figure 2.14.** Insulin recovery after A) heat stress and B) agitation stress. A) DLS curves of insulin before (solid) and after (dashed) heating to 90 °C for 30 minutes; B) DLS curves of insulin before (solid) and after (dashed) shaking at 300 RPM for 3 hours. Black = insulin only, Red = Insulin + PVA, Green = +2 kDa PEG + PVA, Blue = +4 kDa PEG + PVA. In all cases [PEG] = 100 mg.mL<sup>-1</sup>, [PVA] = 1 mg.mL<sup>-1</sup>

Further assays were performed to elucidate whether these polymer formulations have any protective activity when insulin is put under heat stress (**Figure 2.14A**) or agitation stress (**Figure 2.14B**). All formulations were found to not protect insulin from heat stress, and despite agitation at 300 RPM for 3 hours, insulin did not aggregate whether in a polymer formulation or PBS alone.

### 2.6.3.3 Lactate Dehydrogenase



**Scheme 2.1.** Redox reaction of NADH and NAD<sup>+</sup>

LDH activity here is measured following the conversion of pyruvate to lactate, which takes place by oxidising nicotinamide adenine dinucleotide (NADH) to  $\text{NAD}^+$  (**Scheme 2.1**). This reaction is catalysed by the M type LDH enzyme and measured using absorbance spectroscopy at 340 nm. NADH shows more absorbance in comparison to  $\text{NAD}^+$  at 340 nm. The amount of colour product formed as the reaction takes place is directly proportional to the activity of LDH in the sample, **Figure 2.15**. A total loss of colour/absorbance represents efficient conversion to lactate as NADH has been oxidised, catalysed by LDH. Inefficient/incomplete conversion is observed when absorbance is still measured at 340 nm indicating low enzymatic activity.



**Figure 2.15.** Schematic of cryopreservation protocol for monitoring LDH activity. Analysis of freeze/thawed samples either *via* absorbance spectroscopy. Complete NADH conversion indicated by a complete loss of absorbance.

At high concentrations of pyruvate, LDH exhibits feedback inhibition and the rate of conversion of pyruvate to lactate decreases. Thus, the concentrations of pyruvate, NADH and LDH have to be considered for this assay. The protocol followed here was adapted from an enzymatic protocol from Sigma-Aldrich (**2.8.3.5**).<sup>116</sup>

We wanted to compare different cryoprotectants on LDH under different freezing and storage conditions. Firstly, the assay conditions were optimised. The optimal concentration of LDH was determined to enable successful monitoring of the  $\text{NADH} \rightarrow \text{NAD}^+$  reaction. FT cycles were also performed on LDH to confirm at which point enzymatic activity is lost (number of cycles), **Figure 2.16A**.

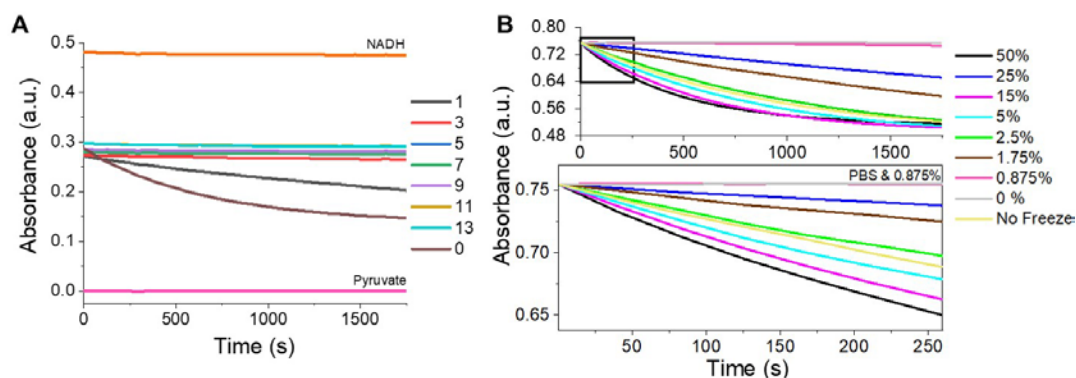


**Figure 2.16.** Optimisation of cryopreservation protocol of LDH. A) LDH activity after a range of FT cycles recorded by catalysis of NADH to NAD<sup>+</sup> compared to controls of NADH (orange) and pyruvate (pink) alone; B) LDH activity after storage in glycerol at a range of concentrations (0.875-50 %) recorded by catalysis of NADH to NAD<sup>+</sup>, observed by a decrease in absorbance, compared to a no CPA control (0 %, grey) and unfrozen LDH (yellow).

After 3 FT there is minimal activity, observed by no change in NADH absorbance. From this result it was decided to perform subsequent assays with a minimum of 3 FT cycles. To ensure the assay worked, LDH underwent FT cycles in the currently used CPA, glycerol. LDH was stored in a range of glycerol concentrations (0.875-50 %), finding a loss in enzymatic activity as the glycerol concentration decreases, observed as a decrease in gradient of NADH absorbance over time. LDH fully denatures when stored in 0.875 % and 0 % glycerol, as the NADH absorbance remains the same throughout. From this data it can also be determined that glycerol at concentrations  $\leq 2.5$  % are insufficient to protect this particular enzyme. 15-50 % glycerol led to highest LDH activity post thaw, indicating these are the optimal concentrations to use for cold storage here. Once the protocol was optimised and confirmed to work our most successful CPA, PEG/PVA, was tested on LDH and compared to the gold-standard glycerol, PEG, PVA and an unfrozen sample. LDH stored in CPAs here appear to be slightly more active compared to the non-frozen LDH in PBS buffer alone, at this time it is not understood why.

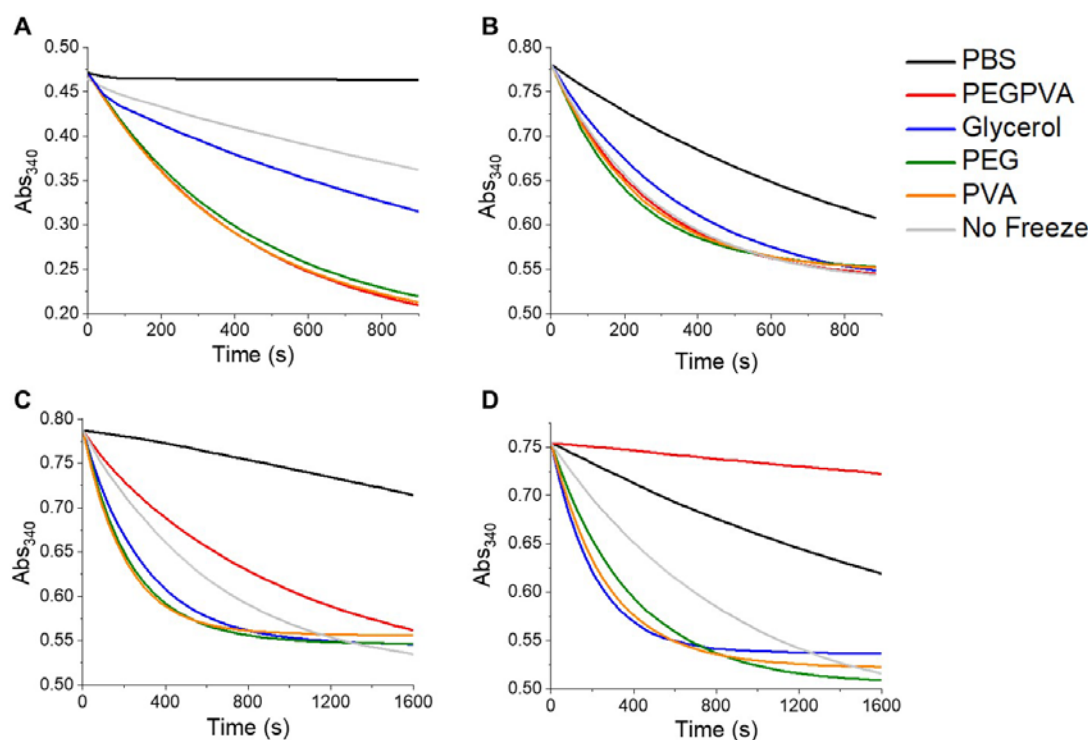


**Figure 2.17.** LDH activity in the presence of indicated cryoprotectants after FT cycles and storage. A) 7 FT cycles; B) 24 hours storage at -20 °C; C) 1 week storage at -20 °C; D) 1 month storage at -20 °C. Recorded by catalysis of NADH to NAD<sup>+</sup>, observed by a decrease in absorbance, compared to a no CPA control (black) and a no freeze control (grey). All samples were plunge frozen at -196 °C and thawed at 25 °C. In all cases [PEG] = 100 mg.mL<sup>-1</sup>, [PVA] = 1 mg.mL<sup>-1</sup>, [Glycerol] = 25 wt %.

Storage of LDH was compared over 4 different time periods, **Figure 2.17**. After 7 FT cycles in liquid nitrogen it can be observed that the polymers protect LDH to a higher degree than glycerol, **Figure 2.17A**. This is also observed for LDH stored at -20 °C for 24 hours, **Figure 2.17B**. There are interesting differences though for the longer-term storage, with all cryoprotectants leading to similar LDH activity post thaw after 1 week and 1 month in storage, bar PEG/PVA, where LDH had reduced activity, **Figure 2.17C/D**. The LDH fully denatured after 7 FT cycles as the PBS control (black) frozen LDH has no activity - thus NADH absorbance remains the same throughout. However, storage at -20 °C does not lead to this inactivity. The CPA results show that, for multiple FT cycles and at lower storage temperatures, all polymer formulations lead to higher enzymatic activity post-thaw, but at higher freezing temperatures the PEG/PVA CPA reduces activity, implying different formulations are required when freezing using different temperatures. Rates observed here might be lower due to



LDH's feedback inhibition, *i.e.* where LDH has lost activity there is a lower concentration of active enzyme, which therefore is converting pyruvate much more slowly.

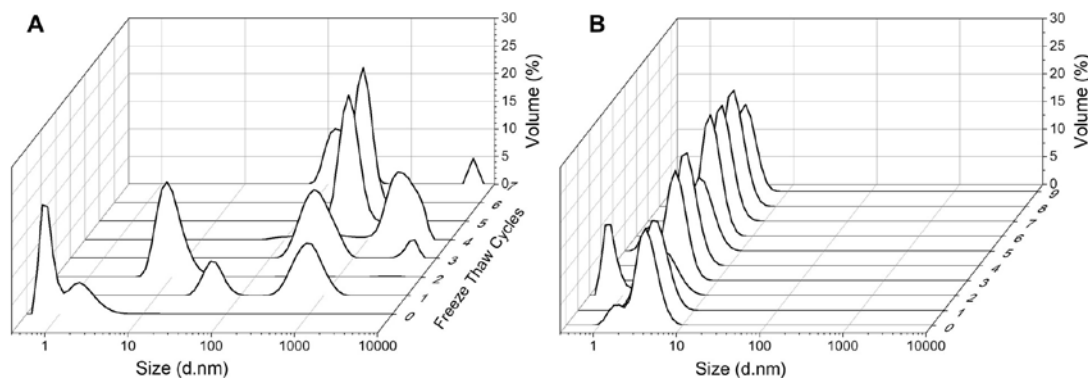


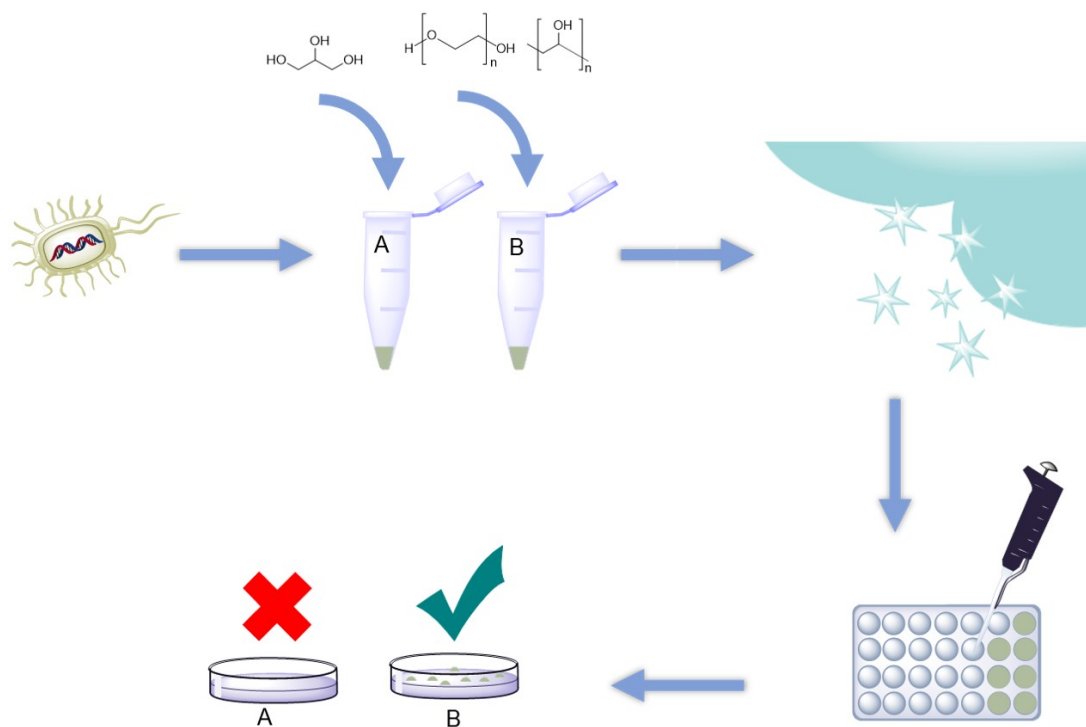
**Figure 2.18.** Waterfall plot of hydrodynamic radius of LDH stored in A) PBS (no cryoprotectant) and B) PEG/PVA, over 7 freeze (-196 °C) thaw (25 °C) cycles.

Dynamic light scattering was used to study the mechanism of action of the polymer formulation on LDH upon freezing, **Figure 2.18**. Over 7 FT cycles the hydrodynamic radius of LDH in buffer alone increases, indicating aggregation of the enzyme. When stored in PEG/PVA, even after 9 FT cycles, the LDH does not aggregate, with the mean hydrodynamic radius being  $3.21 \pm 0.2$  nm leading to successful retention of enzymatic activity. These findings confirm that aggregation of proteins leads to enzymatic inactivity, and that this formulation works *via* a mechanism that prevents aggregation in this protein.

#### 2.6.4 Cryopreservation of Bacteria

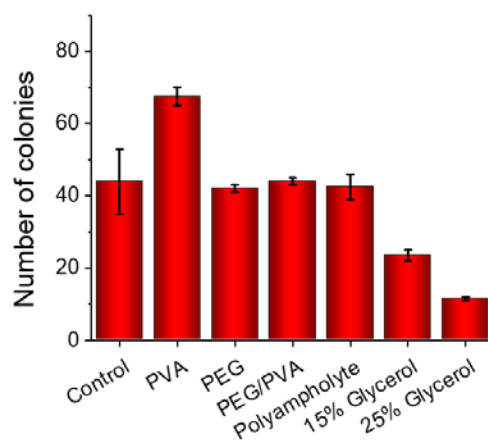
Following inspiration from mammalian studies,<sup>34</sup> and the above success in cryopreservation of proteins, the study of biologics continued, this time focussing on microorganisms. Our work studying proteins highlighted that PEG/PVA performed synergistically to protect proteins from freeze-induced damage and thus retained activity post-thaw,<sup>117</sup> alongside this knowledge and the high IRI activity of PEG/PVA, the combination was chosen for further analysis on its ability to cryoprotect *E. coli*.

To evaluate the performance of the previously selected CPA (PEG/PVA) versus glycerol, a series of cryopreservation experiments were undertaken.



**Figure 2.19.** Schematic of the concept behind the protocol for the bacteria freeze/thaw assay performed.

A FT protocol that allowed the study of bacteria post cryostorage was developed, **Figure 2.19**. In this protocol, cells were added to separate solutions of the different cryoprotectants in a 1:1 ratio, and snap frozen in liquid nitrogen ( $-196\text{ }^{\circ}\text{C}$ ) before thawing at  $37\text{ }^{\circ}\text{C}$  in a water bath for 5 minutes to ensure cells were fully thawed. The samples were exposed to 7 FT cycles and once complete, samples were added to LB in 96 well plates and underwent serial dilutions to prevent overgrowth. Samples were plated onto agar plates and left to grow at  $37\text{ }^{\circ}\text{C}$  overnight for subsequent colony counting. This protocol was chosen to mimic laboratory conditions where stocks are often frozen and thawed during routine use.

2.6.4.1 *E. coli*

**Figure 2.20.** Recovered colonies of *E. coli* after overnight incubation with cryoprotectants. Concentrations of cryoprotectants; [PVA] = 1 mg.mL<sup>-1</sup>; [PEG] = 100 mg.mL<sup>-1</sup>; [PEG/PVA] = 100 + 1 mg.mL<sup>-1</sup>; [polyampholyte] = 50 mg.mL<sup>-1</sup>). Control is LB media alone.

Glycerol is intrinsically toxic at cryopreservation concentrations, so to test our polymeric formulations for intrinsic toxicity they were incubated with *E. coli* and results compared to that of glycerol. Each cryoprotection solution (at the indicated cryopreservation concentration) was incubated with *E. coli* overnight at 4 °C and subsequently the number of colony-forming units determined, **Figure 2.20**. Glycerol, as expected, at 15 or 25 wt % led to a significant reduction in recovered colonies. Conversely, none of the polymers showed toxicity to the *E. coli*. The observed increase in recovered colonies for PVA could be due to some metabolism of the polymer. This supports our hypothesis that biomimetic macromolecular antifreezes may be ‘spectator additives’ which only function when ice is present and are ignored by microorganisms (and indeed other cells), which is crucial for down-stream applications.

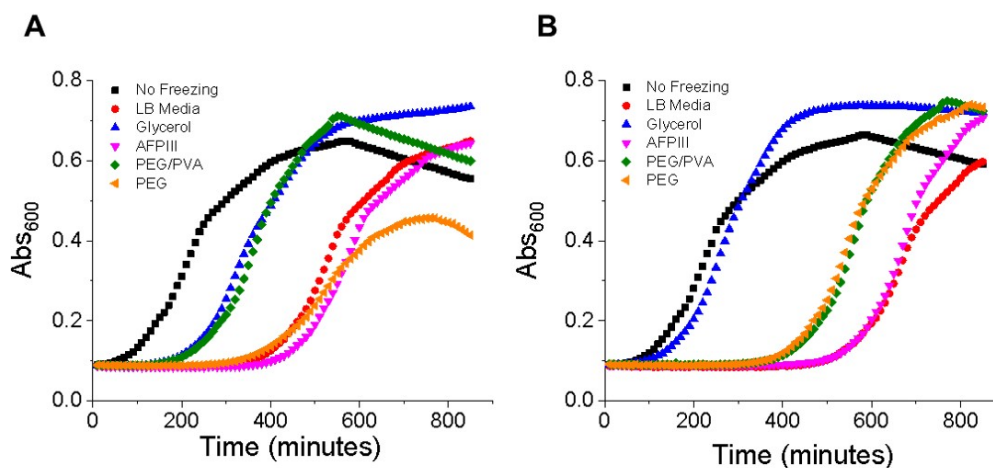


**Figure 2.21.** *E. coli* growth profiles after 7 freeze/thaw cycles then inoculation into LB media compared to a growth profile of unfrozen *E. coli*. A) Freezing at  $-196\text{ }^{\circ}\text{C}$ ; B) Freezing at  $-20\text{ }^{\circ}\text{C}$ . Concentrations of cryoprotectants; [Glycerol] = 25 wt %; [AFPIII] =  $1\text{ mg}\cdot\text{mL}^{-1}$ ; [PEG/PVA] =  $100 + 1\text{ mg}\cdot\text{mL}^{-1}$ ; [PEG] =  $100\text{ mg}\cdot\text{mL}^{-1}$ .

The effect on cell growth after freezing at different temperatures was compared by  $\text{OD}_{600}$  (turbidity) measurements, **Figure 2.21**. Turbidity, the cloudiness/haziness of a sample, is measured by the detection of optical density/absorbance at 600 nm. This represents the growth of bacteria; as the more turbid the sample, *i.e.* higher cell mass, the higher the absorbance value.  $\text{OD}_{600}$  measurements over time produce a standard growth curve, which should have 4 distinct phases; lag, where cellular metabolism is accelerated but no replication occurs (no growth); exponential phase, where microorganisms rapidly grow and divide (exponential growth); stationary phase, shift in environment and reduction in reproduction (rate stabilised); decline/death phase, lack of available nutrients and increased metabolic waste (cell death). The shorter the time period required to move into the exponential phase and the longer this phase, the healthier the bacteria in a given sample. Growth rates of unfrozen *E. coli* (black) are given as a ‘normal’ curve for comparison. Samples frozen in media alone (red) provide a comparison of *E. coli* growth when not stored in a cryoprotectant. PEG/PVA and glycerol lead to almost identical growth profiles when *E. coli* is frozen at  $-196\text{ }^{\circ}\text{C}$ , whereas glycerol alone appears to lead to a more ‘normal’ growth profile when *E. coli* is frozen at  $-20\text{ }^{\circ}\text{C}$ . This may be due to the higher storage temperature, where the glycerol solutions do not completely freeze thus providing an extra nutrient source. AFPIII does not protect *E. coli*, displaying growth curves, at both temperatures, that are of *E. coli* frozen without a CPA, this potentially could be due to the needle-like ice

morphology that AFPIII causes, leading to bursting, thus unviable cells, therefore IRI activity is not sufficient for successful cryopreservation when ice-shaping occurs.

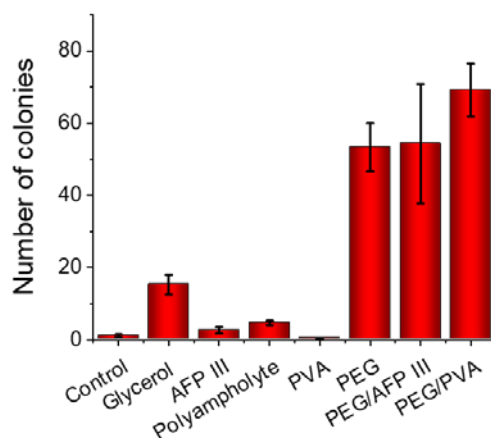


**Figure 2.22.** Recovered colonies of *E. coli* after 7 freeze (-196 °C) thaw (20 °C) cycles. Concentrations of cryoprotectants; [Glycerol] = 25 wt %; [AFPIII] = 1 mg.mL<sup>-1</sup>; [PVA] = 1 mg.mL<sup>-1</sup>; [PEG/AFPIII] = 100 + 0.01 mg.mL<sup>-1</sup>; [PEG/PVA] = 100 + 1 mg.mL<sup>-1</sup>; [polyampholyte] = 50 mg.mL<sup>-1</sup>. Control is LB media alone.

Recovered colonies for *E. coli* (growth curves shown in **Figure 2.21A**) after FT cycles in different formulations are observed in **Figure 2.22**. Concentrations here were chosen based on their relative IRI activity (**Figure 2.7**) to give similar effects on ice growth, and not at equal mass concentration, to enable correlation of physical properties to observed biological responses. Post FT the PEG/PVA CPA (100 mg.mL<sup>-1</sup> + 1 mg.mL<sup>-1</sup>) was found to dramatically increase recovery to 69 colony-forming units, which is a >4-fold increase compared to glycerol alone, **Figure 2.22**. PEG/AFP as a CPA lead to similar results (52 colonies) supporting the hypothesis that controlling IRI is the key mechanism in protecting bacteria during cryopreservation, by reducing ice growth especially during thawing. 25 % glycerol resulted in an average of 15 recovered colonies compared to 1 for no added cryoprotectant. PVA and AFPIII alone gave results almost identical to that of no cryoprotectant. The polyampholyte also showed no cryoprotective effect, despite them previously being used for mammalian cells, where they appear to function *via* cell membrane interactions.<sup>48</sup> Polyampholytes have far weaker IRI than PVA or AFPs thus this supports a mechanism of protection based on limiting ice recrystallisation rather than membrane plasticisation/stabilisation.

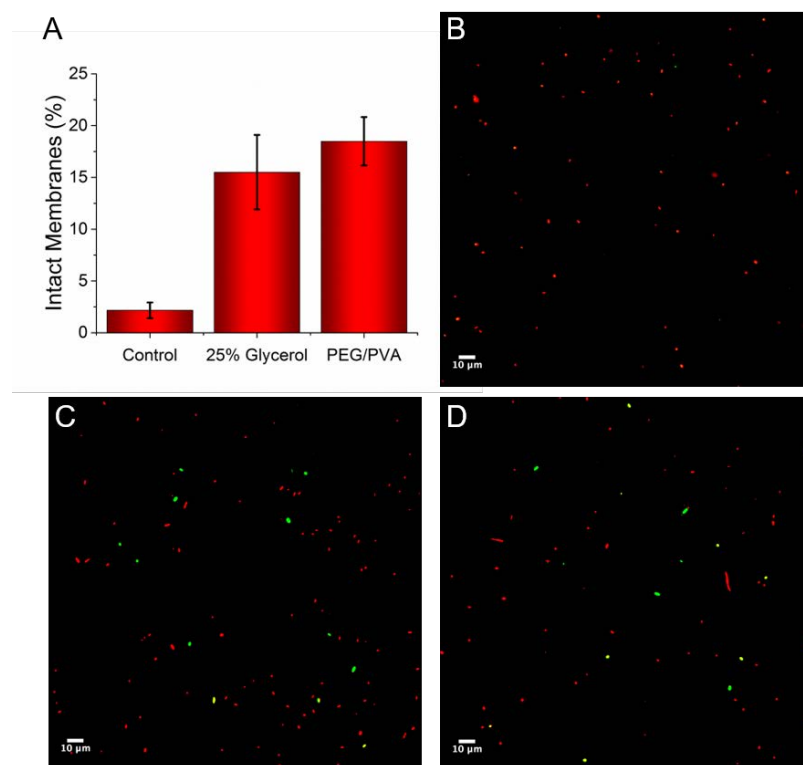


**Figure 2.23.** Live/dead viability testing on *E. coli* immediately after freeze/thaw cycles. A) Percentage of green (intact membrane) bacteria determined by confocal microscopy (ratio of live cell membranes to total cell membranes); B-D) Live/dead micrographs; B) PBS control; C) 25 % glycerol; D) PEG/PVA. [PEG/PVA] = 100 + 1 mg.mL<sup>-1</sup> respectively. Error bars represent S.D. from 6 repeats. Scale bar = 10 μm.

The previous experiments relied on counting colony-forming units, which shows the application of these CPAs, but does not give insight into the mechanisms of cell stress during FT. To assess the bacteria immediately after thawing, confocal microscopy was employed with a live/dead viability assay that measures the integrity of cell membranes, **Figure 2.23**. Percentages are used to allow direct comparison of CPAs; obtained from the number of intact cell membranes divided by the total number of cell membranes, **Figure 2.23A**. Bacterial cells with intact cell membranes exhibit green fluorescence (SYTO-9 dye), while those with compromised cell membranes exhibit red fluorescence (propidium iodide dye). Following FT in PBS alone just 2.2 % of the *E. coli* had intact membranes (green), demonstrating that ice growth causes significant mechanical damage. Post FT in either 25 % glycerol or PEG/PVA resulted in 15 – 18 % of the *E. coli* retaining intact membranes. These observations suggest that the mechanism of cryoinjury limitation of both glycerol and our macromolecular

antifreezes is very similar. However, the colony counting results confirmed the polymer approach to be superior, supporting a hypothesis that the reduced toxicity of the polymers means that more, healthier colonies can grow post-thaw.

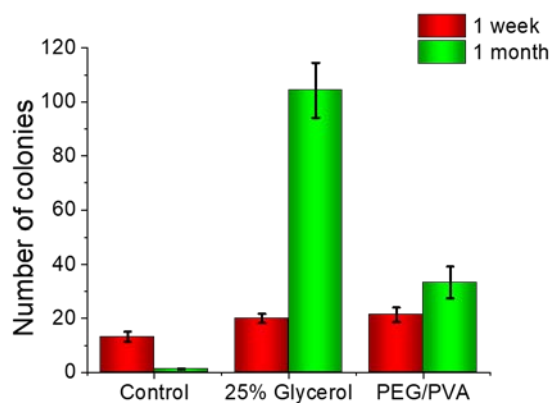


**Figure 2.24.** Recovered colonies of *E. coli* after freezing at  $-196\text{ }^{\circ}\text{C}$  and storage at  $-20\text{ }^{\circ}\text{C}$  for 1 week (red) or 1 month (green). Concentrations of cryoprotectants; [Glycerol] = 25 wt %; [PEG/PVA] = 100 + 1.0 mg.mL<sup>-1</sup>. Control is LB media alone.

The effect of storage at  $-20\text{ }^{\circ}\text{C}$  in a standard laboratory freezer after first snap freezing ( $-196\text{ }^{\circ}\text{C}$ ) was also studied after 1 and 4 weeks of storage, **Figure 2.24**. *E. coli* frozen in buffer alone (control) led to a great reduction in colonies recovered after a week frozen and minimal survival after one month; which is to be expected. Cell recovery appears similar for *E. coli* stored in 25 % glycerol and PEG/PVA after one week storage (red) but after one month (green) 25 % glycerol yielded more colonies, this may relate to the fact that at  $-20\text{ }^{\circ}\text{C}$  the glycerol solutions do not completely freeze, providing a carbon source to the *E. coli* and potentially assisting in exponential (growth). When storing cells, the aim is to have them in a stationary phase rather than growth, even if growth is ‘slow’ (as in the case of 25 % glycerol), as this can lead to phenotypic changes, which would negatively affect experiments post-thaw, providing ‘false’ control cells. PEG/PVA on the other hand actually cryopreserves the cells as they are completely frozen at  $-20\text{ }^{\circ}\text{C}$  and lead to similar levels of cell recovery (within error) after both one week and one month supporting the use of this method for routine laboratory manipulations.

### 2.6.4.2 *M. smegmatis* and *B. subtilis*

Additional bacterial strains for cryopreservation were selected to cover a wide range of genera to ensure these effects are not unique to *E. coli*. Using the same conditions as for *E. coli*, *B. subtilis* and *M. smegmatis* were exposed to 7 FT cycles and growth curves measured as well as recovered colonies counted.

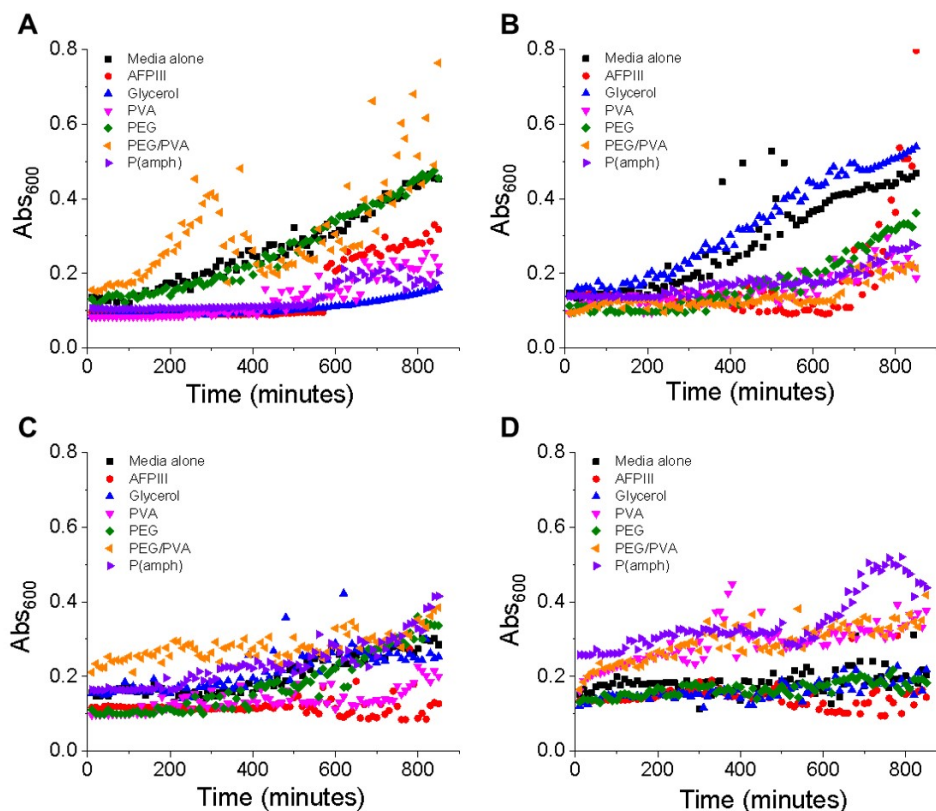


**Figure 2.25.** Cell growth profiles of *M. smegmatis* after 7 freeze (-196 °C) thaw (20 °C) cycles with the indicated cryoprotectants followed by inoculation into LB media. Different starting culture volumes (A - D) are compared. A) Starting culture = 1 µL, B) starting culture = 5 µL, C) starting culture 10 = µL, D) starting culture = 20 µL.

No clear trend can be obtained from the above *M. smegmatis* growth curves, **Figure 2.25**, this is because *M. smegmatis* tends to aggregate resulting in absorbance values that are difficult to interpret.<sup>118</sup> These are included for completeness but should not be considered to be full growth curves.



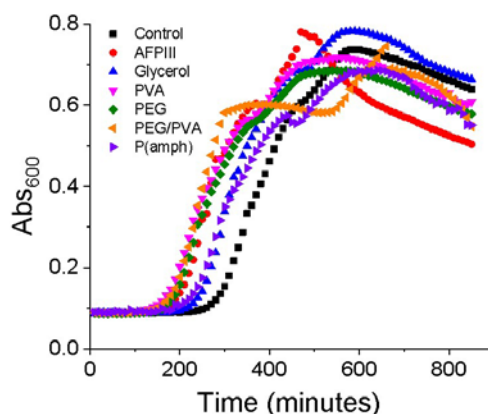


**Figure 2.26.** Cell growth curves of *B. subtilis* (5  $\mu$ L starting culture) after 7 freeze (-196  $^{\circ}$ C) thaw (20  $^{\circ}$ C) cycles with the indicated cryoprotectants then inoculation into LB media.

Growth curves for *B. subtilis* can be seen in **Figure 2.26**, showing similar growth for all, indicating similarity in mechanism for limiting cryoinjury by CPAs in this cell type.

To enable comparison of the data and to account for the different growth rates of each bacterial strain, the recovered colonies were also normalised to the highest recovery, **Figure 2.27**. Total and normalised colonies are listed in **Table 2.1**.

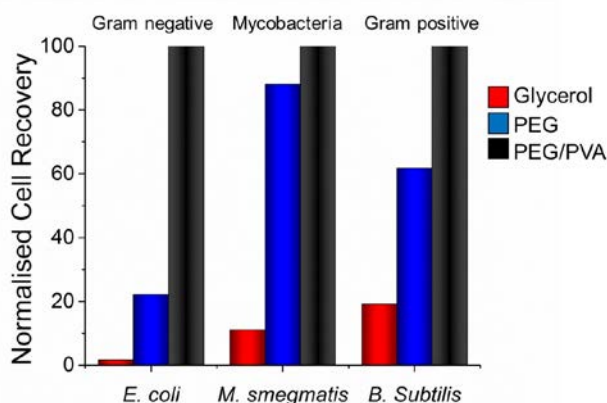


**Figure 2.27.** Normalised cell recovery for 3 different bacteria upon addition of different cryoprotectants after 7 freeze (-196  $^{\circ}$ C) thaw (20  $^{\circ}$ C) cycles, (red = PBS, blue = glycerol, black = PEG/PVA), serial dilution and growth on ampicillin plates at 37  $^{\circ}$ C overnight. Values obtained are normalised to themselves. [Glycerol] = 25 wt %; [PEG] = 100 mg.mL $^{-1}$ ; [PEG/PVA] = 100 + 1 mg.mL $^{-1}$ .

In all cases, the PEG/PVA formulation gave equal or better levels of recovery than glycerol alone. It can be noted that *M. smegmatis* (which is a slow-growing organism compared to other two) gave fewer colonies after a fixed period of growth in all conditions, but the PEG/PVA still matched the performance of glycerol. In some cases, the PEG alone gave favourable recovery levels also (as any uncharged solute will give some protection) but in all cases addition of PVA increased this recovery, showing it is an essential component to ensure recovery of viable cells.

**Table 2.1.** Mean colonies recovered after 7 freeze/thaw cycles.

	<i>E. coli</i>		<i>M. smegmatis</i>		<i>B. subtilis</i>	
	Total (-)	Normalised (%)	Total (-)	Normalised (%)	Total (-)	Normalised (%)
<b>PBS</b>	1 ± 0.4	1	4 ± 0.5	12	29 ± 10.4	11
<b>Glycerol</b>	15 ± 2.8	22	30 ± 6.0	88	93 ± 18.9	35
<b>AFPIII</b>	3 ± 0.9	4	2 ± 0.3	6	26 ± 6.7	10
<b>PVA</b>	0 ± 0.1	0	3 ± 1.5	9	5 ± 0.7	2
<b>PEG</b>	53 ± 6.7	77	28 ± 4.3	82	150 ± 10.7	57
<b>PEG/PVA</b>	69 ± 7.3	100	34 ± 4.2	100	262 ± 39.3	100
<b>P(amph)</b>	5 ± 0.6	7	28 ± 4.5	82	20 ± 5.0	8

[Glycerol] = 25 wt %; [PEG] = 100 mg.mL<sup>-1</sup>; [PEG/PVA] = 100 + 1 mg.mL<sup>-1</sup> respectively; [AFPIII] = 0.1 mg.mL<sup>-1</sup>; Polyampholyte = 50 mg.mL<sup>-1</sup>. Error represents the SD from 6 repeats. *Note that the total colonies recovered for each organism varies based on their own growth rates hence normalised recovery (verses the highest recovery level) is also included.*

These results demonstrate the versatile nature of this approach, and that replacing glycerol in laboratories with this polymer formulation is a reliable way to match or improve current storage methods; it should enable a transition from traditional glycerol-based to macromolecular microbiology storage methods.

#### 2.6.4.3 Formulation Modification: Molecular Weights

This macromolecular cryoprotection solution using ice-inhibiting polymers is clearly suitable for bacteria storage but there are many parameters that can be varied in this system including the molecular weight of the polymers and weight ratios. To enable a large number of conditions to be screened, the post-thaw growth rate of *E. coli* was

also followed by OD<sub>600</sub> (turbidity) measurements, enabling higher-throughput measurements in 96 well plates. *E. coli* were frozen with various formulations of different molecular weight PEGs and PVAs, **Figure 2.28**.

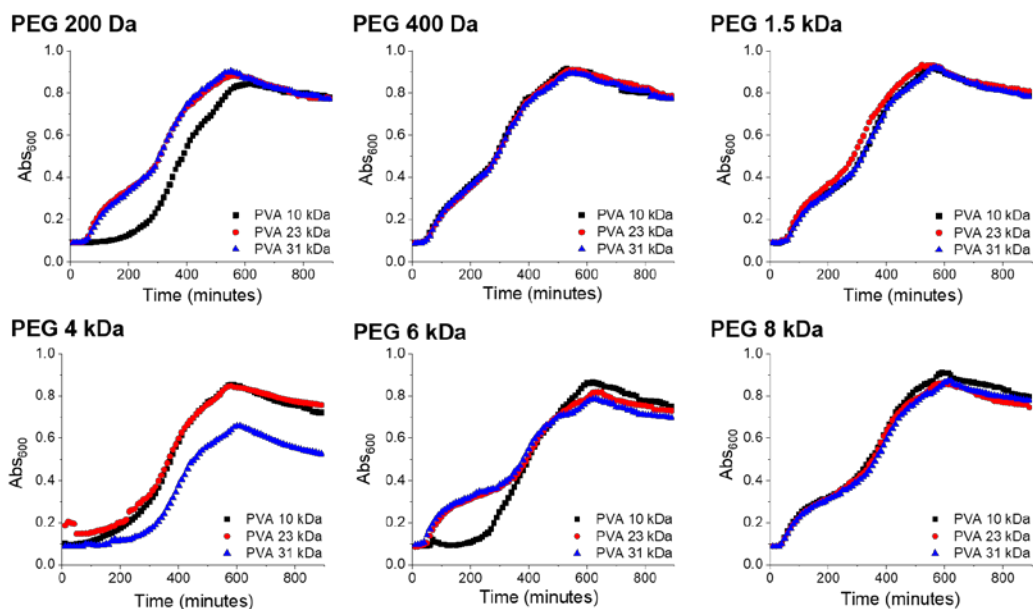


**Figure 2.28.** Cell growth profiles of *E. coli* with the indicated molecular weight PVAs in combination with different molecular weight PEGs (200 Da – 8 kDa) after 7 freeze (-196 °C) thaw (20 °C) cycles then inoculation into LB media. [PEG] = 100 mg.mL<sup>-1</sup>; [PVA] = 1 mg.mL<sup>-1</sup>

For PVA, 10 kDa and 31 kDa gave approximately identical recovery levels. However 10 kDa is easier to dissolve into buffer, making it preferable for real-world applications where concentrated stock solutions are required. Higher molecular weight PVA can also lead to dynamic ice-shaping which is known to reduce recovery of cells post-thaw.<sup>34</sup> Lower molecular weight PEGs (200-1500 Da) alone appeared to have a slightly greater cryoprotective effect than larger PEGs (4 to 8 kDa), as they reach a higher OD<sub>600</sub> and display slower logarithmic decline phases, indicating improved cell health, but these differences were small. Smaller molecular weight polymers in combination with PVA have been observed to improve PVA-PVA interactions and thus improve IRI activity,<sup>107</sup> this ‘depletion-induced enhancement’ may be the reason for the slight improved cryoprotective effect observed here. Considering the cryoprotective effect of each of the mixtures, and the solubility of each of the constituents, it was determined that 10 kDa PVA and 4 kDa PEG were the optimum

molecular masses out of the 18 formulations we tested to use to ensure reliable and easy to use cryopreservation.

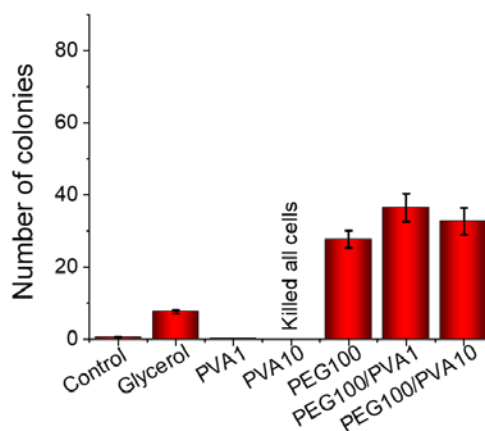


**Figure 2.29.** Effect of varying PVA concentration on cell recovery. Recovered colonies of *E. coli* after incubation with different concentrations of 4 kDa PEG and 10 kDa PVA after 7 freeze (-196 °C) thaw (20 °C) cycles. [PVA1] = 1 mg.mL<sup>-1</sup>, [PVA10] = 10 mg.mL<sup>-1</sup>, [PEG100] = 100 mg.mL<sup>-1</sup>.

Various concentrations of 10 kDa PVA, in combination with 100 mg.mL<sup>-1</sup> 4 kDa PEG, were also screened, **Figure 2.29**. In all cases addition of PVA to PEG increased the cryoprotective effect. The improvement was most significant in the case of 1 mg.mL<sup>-1</sup> PVA.

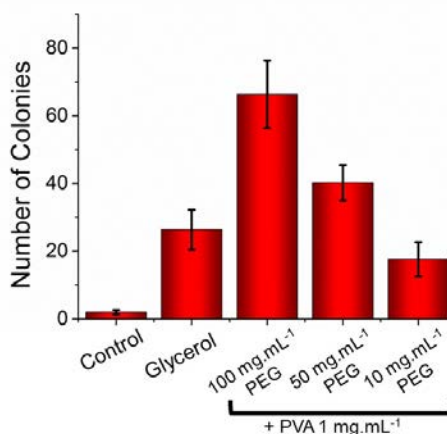


**Figure 2.30.** A) Effect of varying PEG concentration on number of recovered *E. coli* colonies after 7 freeze (-196 °C) thaw (20 °C) cycles. Control is LB media alone.

To further optimise this formulation, the PEG concentration was varied from 100 mg.mL<sup>-1</sup> to 10 mg.mL<sup>-1</sup>, all with addition of 1 mg.mL<sup>-1</sup> PVA, and the number of

recovered colonies after 7 FT cycles counted, **Figure 2.30**. Reducing the concentration of PEG to 50 mg.mL<sup>-1</sup> and 10 mg.mL<sup>-1</sup> led to a significant reduction in the number of colonies recovered, compared to 100 mg.mL<sup>-1</sup>. However, it is important to note that 10 mg.mL<sup>-1</sup> PEG with 1 mg.mL<sup>-1</sup> PVA is just a 1.1 wt % solution but performs equally to 25 wt % glycerol, representing a remarkable cryopreservation outcome with a 25 fold reduction in cryoprotectant. It shows that whilst there is an optimum formulation, there is scope to vary the components and hence supporting ease of use in a realistic laboratory situation. In some down-stream applications (such as food) lowering cryoprotectants concentration, rather than maximising total cell recovery is desirable and this new polymer-only formulation is clearly suitable.

#### **2.6.4.4 Formulation Modification: Hydrophilic Polymer**

As mentioned in **2.6.1**, bulky, hydrophilic polymers have been seen to assist in cryopreservation of cells. PEG is a popular choice in drug delivery systems, manufacturing processes, as a plasticiser and solubility enhancer as well as acting as a nonpermeating CPA.<sup>113,119-123</sup> However, recent developments in the fields of materials science and polymer chemistry has led to an increase in commercial availability of PEG alternatives.<sup>112</sup> PEG can undergo oxidative degradation in solution, as well as under heat, radiation and mechanical stress. Other water soluble hydrophilic polymers have been of interest, particularly as they have a good record of clinical use *e.g.* in modification of proteins, liposomes and biomaterial surfaces, as well as playing carriers for a variety of species such as drugs, genes and oligonucleotides.<sup>124</sup> The target is to produce polymer formulations that are cost effective, biocompatible and less toxic, so that they are successful additives throughout the cold chain and benefit society.<sup>114</sup> Examples of alternative polymers include polyvinylpyrrolidone (PVP), hydroxypropyl methyl cellulose (HPMC), poly(acrylamide) (PAA), poly[N-(2-hydroxypropyl) methacrylamide (PHPMA), poly(oxazoline) (POZ) and hydroxyethyl starch (HES).

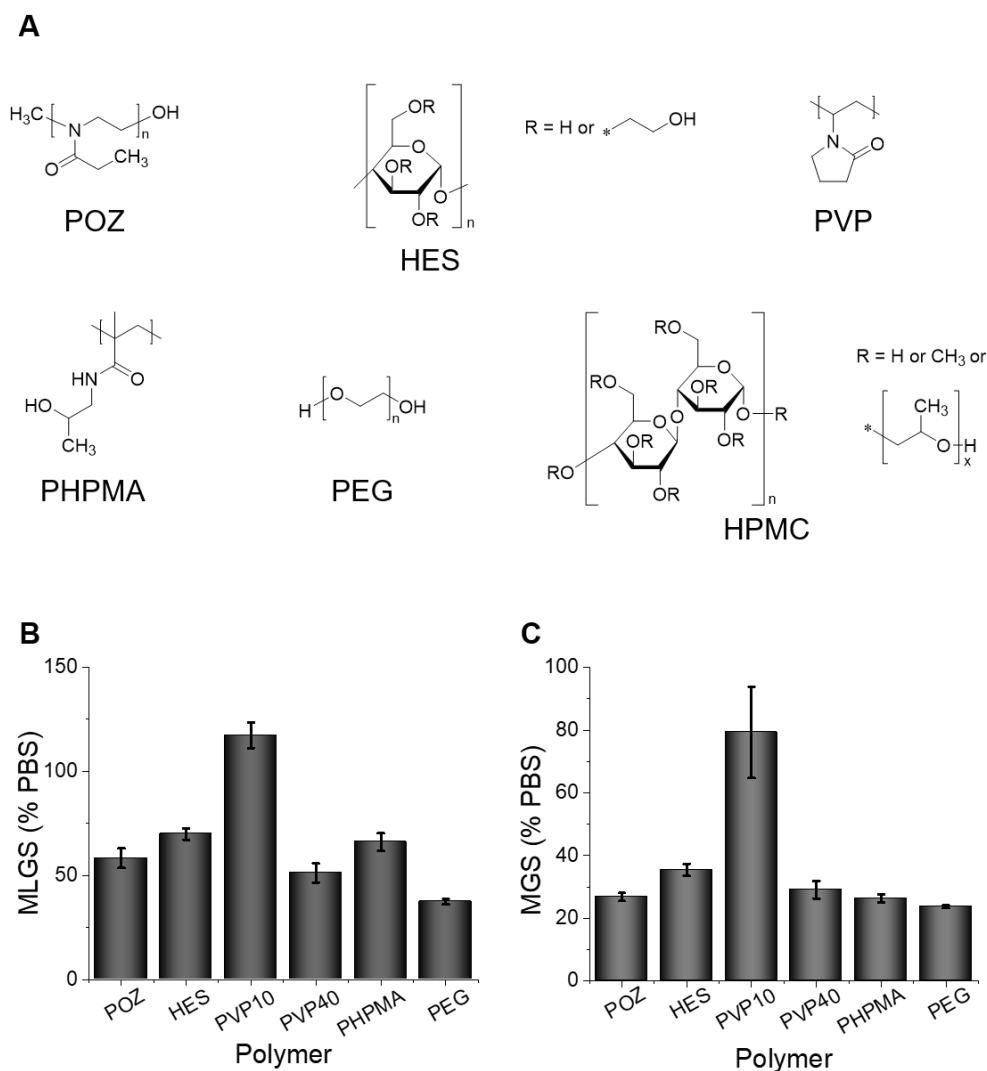


**Figure 2.31.** Structures and IRI activity of hydrophilic polymers used here to compare to that of PEG used in the original polymer formulation; A) Structures; B) MLGS; C) MGS. [Polymer] = 100 mg.mL<sup>-1</sup>. IRI data for HPMC not shown.

Here 6 polymers were tested to compare their cryoprotective ability to that of PEG in formulations with and without 1 mg.mL<sup>-1</sup> PVA, structures shown in **Figure 2.31A**. PVP was chosen (in two molecular weights), partly as it has been used as a nonpermeating CPA before<sup>25</sup> but also due to its low cost, previous FDA approval in certain formulations<sup>125</sup> and known lack of IRI activity, ensuring it would not affect ice in the same way as PVA.<sup>126</sup> HPMC is also low cost, widely available and has generally good bioavailability and biodegradability.<sup>127,128</sup> It is widely used in the food industry due to its tastelessness, lack of odour and FDA approval, thus if successful as a CPA, has potential application for probiotic development.<sup>129–131</sup> POZ was chosen as it also has been in FDA approved formulations<sup>132</sup> and has been of recent interest in the

biology community:<sup>133</sup> it has been investigated (in a similar way to PEG) as a stealth polymer, drug carrier and a hydrogel.<sup>112,134</sup> HES has also been used as a nonpermeating CPA,<sup>25,135</sup> successfully storing RBC with a lower toxicity than DMSO. It has also previously been used in combination with PVA<sup>136</sup> and has been considered a PVP alternative.<sup>137</sup> PHPMA has been considered a viable alternative to PEG in many applications, particularly in nanomedicine,<sup>124</sup> as it is non-immunogenic and nontoxic.<sup>138</sup> PHPMA also, like PVP, has no observed IRI activity.<sup>35</sup>

Initially ‘splat’ assays were performed on these polymers to detect any IRI or colligative activity, **Figure 2.31B/C**. Data for HMPMC is not shown as above 10 mg.mL<sup>-1</sup> gelation occurs, thus ice growth activity cannot be compared to the other polymers. All polymers show similar MLGS and MGS results to that of PEG bar PVP10 (PVP of 10 kDa molecular weight), which has even less activity at 100 mg.mL<sup>-1</sup>. This indicates, except for PVP10, that these polymers have the potential to replace PEG in formulations, as the ice growth should not be affected by their addition.

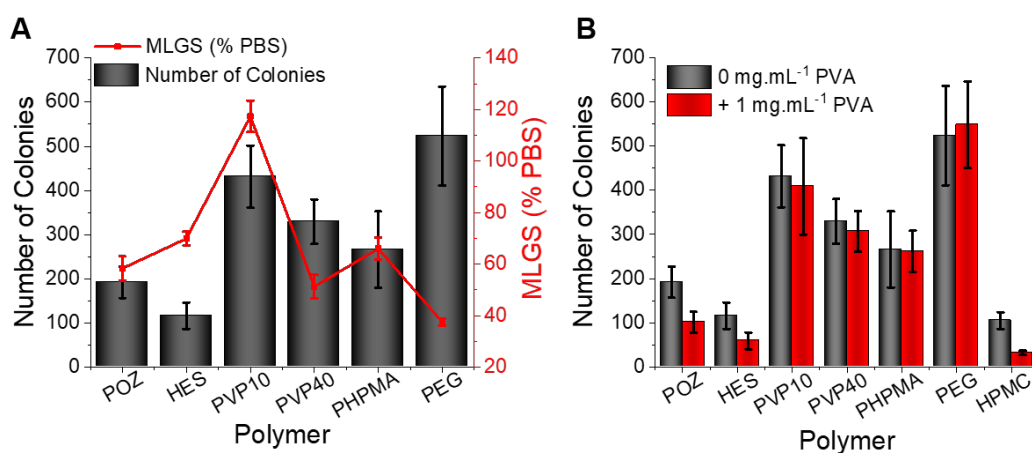


**Figure 2.32.** Recovered colonies of *E. coli* after 7 freeze thaw cycles using formulations consisting of different hydrophilic bulky polymers compared to that of a known cryoprotective formulation (PEG/PVA). A) IRI activity of polymers (red) compared to that of cell recovery (black), HPMC is omitted due to gelation at high concentrations; B) Recovered colonies with (red) and without (black) the addition of IRI active PVA. [Polymer] = 100 mg.mL<sup>-1</sup> except [HPMC] = 10 mg.mL<sup>-1</sup>

The recovered colonies for bulky polymers and bulky polymers+PVA are compared to that of MLGS data in **Figure 2.32**. In general, the lower the IRI activity of the polymer, the worse the cryoprotective ability. However, PVA10 is an anomaly again in that despite no IRI or colligative activity, it leads to the second highest cell recovery

after PEG. There is generally no significant difference in cell recovery for the different bulky polymers, with PEG formulations still leading to the highest cell recovery.

The different polymers may reduce cell recovery for different reasons. To test whether these polymers ice shape thus leading to cell death, sucrose assays were performed. **Figure 2.33** shows crystal morphology of ice when frozen with  $100 \text{ mg.mL}^{-1}$  of each bulky polymer tested at three different angles. Morphology is similar for all, with no particular shaping, except for PHPMA and HPMC, which tend to form more dendritic hexagons. This indicates that low cell recovery is not probably related to ice shaping, though may have an effect in PHPMA and HPMC samples. All experiments performed on HPMC are performed at  $10 \text{ mg.mL}^{-1}$  as at higher concentrations gelation occurs, this may also be happening upon freezing, which in turn may be causing the much lower cell recovery. The high concentrations used or the molecular weights of the chosen polymers may also be reasons for low cell recovery; as observed in **Figure 2.29** varying polymer concentrations can lead to different levels of cell recovery. Studies over a range of concentrations and molecular weights would need to be performed to elucidate further, however, as PEG works well in combination with PVA there is little need to. Some of these polymers may also have bactericidal behaviours

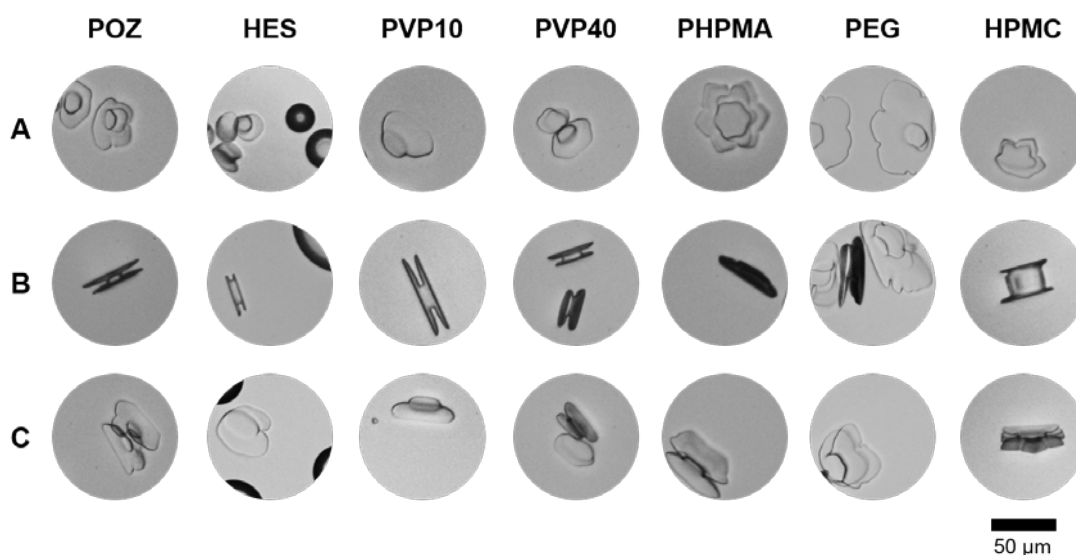


**Figure 2.33.** Ice crystal morphology upon freezing with different hydrophilic bulky polymers. A-C) 3 different angles for the same samples.  $[\text{Polymer}] = 100 \text{ mg.mL}^{-1}$  except  $[\text{HPMC}] = 10 \text{ mg.mL}^{-1}$ . Scale bar =  $50 \mu\text{m}$ .



These results show that PEG is important in this particular CPA formulation for cryostorage of *E. coli*, and that bulky hydrophilic polymers, despite their similar properties, are not interchangeable.

## 2.7 Conclusion

This work highlights a disruptive approach to store bacteria and proteins in the frozen state through modulation of ice recrystallisation with synthetic polymer formulations, which mimic antifreeze proteins used in nature to survive extreme environments. For proteins, the PEG/PVA mechanism of action was proven to be prevention of aggregation, with a secondary hydrophilic (non-IRI active) polymer being essential as a ‘bulking’ agent. Overall, the PEG/PVA cryopreserving formulation was seen to be highly IRI active and the least bactericidal, resulting in a 4-fold increase in *E. coli* yield post-thaw, compared to glycerol, and is equal to or better than glycerol for other cell types, and utilises lower concentrations - with successful cryopreservation at just 1.1 weight percent of additive. The mechanism of protection for cells is demonstrated to be synergistic and linked to inhibiting ice recrystallisation (by comparison to a recombinant antifreeze protein) but also to the significantly lower toxicity of the polymers compared to glycerol. Confocal microscopy showed that similar numbers of bacteria with intact membranes are recovered for both systems, but that the polymer cryoprotectants lead to more viable colonies suggesting their lower toxicity is crucial.

This new cryopreservation approach is shown to be suitable for a range of bacterial genera including Gram negative/positive and Mycobacteria. It was found that the synergistic effect on cell survival was linked to PVAs IRI activity and the PEG bulking agent, as addition of type III antifreeze proteins (at similar total IRI activity) also enabled cryopreservation; although these proteins are significantly more expensive and not practical for routine cryopreservation compared to the polymer formulations. These results highlight the contrast with traditional solvent-based cryoprotectants, which function by distinct mechanisms. Optimal conditions for use of this system in a laboratory or application-focused environment are presented, and as both PEG and PVA are commodity polymers available to food grade standards,<sup>108,139</sup> this system will have wide application across molecular biology, microbiome research and for

translation into the food or biotechnology industry, which are underpinned by the storage and transport of specific bacterial strains.

The polymer additives, PEG and PVA, are both widely used in pharmaceutical products, are available as clinical-grade materials, are biocompatible and non-immunogenic, and are compatible with current biologics, with no additional bio-conjugation being required. These antifreeze protein-inspired polymers will be powerful tools for protein storage in both biotechnology research and healthcare where maximising function and reducing side effects for protein therapeutics is essential.

To further confirm the use of our PEG/PVA formulation in the cryopreservation of biological materials, studies consisting of a larger range of proteins and cells would need to be undertaken. Optimisation of a *L. delbrueckii subsp. bulgaricus* expression protocol is required before further FT studies can be performed to test the cryoprotective ability of polymer formulations on this industrially relevant culture.

## 2.8 Experimental

### 2.8.1 Materials

Poly(ethylene glycol) (200 Da, 400 Da, 1.5 kDa, 2 kDa, 4 kDa, 6 kDa and 8 kDa), poly(vinyl alcohol) (10, 23 and 31 kDa), NaCl, insulin, De Man, Rogosa and Sharpe (MRS) broth and ampicillin were purchased from Sigma-Aldrich and used as supplied unless otherwise stated. Imidazole (Merck), dioxane and glycerol (Fisher Chemical), isopropyl- $\beta$ -D-thiogalactoside (IPTG) (VWR chemical), Novex AP Chromogenic and SYTO-9 (Invitrogen) and Coomassie blue stain (Expedeon) were also used as supplied. The polymer ampholyte was prepared as previously reported.<sup>47</sup>

The *Escherichia coli* (*E. coli*) BL21(DE3) cells were purchased from New England Biolabs, *Bacillus subtilis* (*B. subtilis*) (168 wild type) were donated by Dr Emma Denham, University of Bath, U.K., and *Mycobacterium smegmatis* (*M. smegmatis*) (Mc2155) was kindly donated by Dr. Elizabeth Fullam, University of Warwick, U.K.. Monoclonal Anti-polyHistidine antibody produced in mouse, clone HIS-1, ascites fluid and goat anti-Mouse IgG (H+L) secondary antibody (AP-conjugated) were purchased from Sigma Aldrich and used as received.

### 2.8.2 Physical and Analytical Methods

UV-VIS spectroscopy measurements were performed on a Jenway 6300 Visible Range Spectrophotometer using an absorbance of 600 nm (OD measurements) and 560 nm (BCA assays). Samples for western blot analysis were resolved on a polyacrylamide gel, transferred to a membrane and detected using primary (monoclonal anti-polyhistidine) antibody and a secondary (goat anti-mouse IgG (H+L)) antibody. Fast protein liquid chromatography (FPLC) was performed using AKTA pure (GE Healthcare) with a flow rate of 1 mL.min<sup>-1</sup> using PBS buffer. A Linkam Biological Cryostage BCS196 with T95-Linkpad system controller equipped with a LNP95-Liquid nitrogen cooling pump, using liquid nitrogen as the coolant (Linkam Scientific Instruments U.K., Surrey, U.K.) was used to anneal ice wafers. An Olympus CX41 microscope equipped with a UIS-2 20x/0.45/ $\infty$ /0–2/FN22 lens (Olympus Ltd., Southend on Sea, U.K.) and a Canon EOS 500D SLR digital camera was used to obtain all images. Image processing was performed using ImageJ, which

is freely available from <http://imagej.nih.gov/ij/>. Absorbance spectroscopy was undertaken using a Synergy HT multi-mode microplate reader (BioTek U.K., Bedfordshire, U.K.). Confocal microscopy was performed on a Nikon Eclipse Ti, an inverted widefield fluorescence microscope, equipped with LED illumination, 100x 1.45 NA and 60x 1.4 NA objectives, mCherry and GFP filter sets and a 2k x 2k sCMOS Andor camera system. Dynamic light scattering was undertaken on a Malvern Zetasizer Nano ZS.

## 2.8.3 Procedures

### 2.8.3.1 Protein Expression and Purification

#### 2.8.3.1.1 Standard AFPIII Expression

A plasmid encoding for a hexahistidine-tagged AFP III (T7, pET21b, P19614) was transformed into competent *Escherichia coli* BL21(DE3) cells (New England Biolabs). Single colonies were selected and grown overnight in 10 mL Lysogeny broth (LB)-medium containing 100  $\mu\text{g}\cdot\text{mL}^{-1}$  ampicillin under continuous shaking (37 °C, 180 rpm). Preculture was added (40 mL in 1 L) to LB-medium with ampicillin and grown until  $\text{OD}_{600} = 0.6$ . Isopropyl  $\beta$ -D-1-thiogalactopyranoside (IPTG) was then added to the cells to a final concentration of 0.4 mM to induce protein expression overnight (16 °C, 180 rpm). The cells were harvested by centrifugation (4 °C, 5000 g, 10 minutes), the supernatant decanted and the cells resuspended in prechilled phosphate buffered saline (PBS) (7 mL, ( $>18.2 \Omega$  mean resistivity,  $[\text{NaCl}] = 0.138 \text{ M}$ ,  $[\text{KCl}] = 0.0027 \text{ M}$ , and pH 7.4)). Pierce protease inhibitor mini-tablets were added to the suspension and it was passed through a STANSTED ‘Pressure Cell’ FGP12800 homogeniser to undergo lysis. BugBuster was added (500  $\mu\text{L}$ ) and the sample left spinning for 20 minutes. The cell lysate was centrifuged (4 °C, 40,000 g, 45 minutes) and the supernatant syringe filtered (0.2  $\mu\text{m}$ ) and passed through a pre-equilibrated (20 mL PBS) IMAC Sepharose 6 Fast Flow (GE Healthcare) column charged with Ni(II) ions. The column was washed first with PBS, then with 3 column volumes of 30 mM imidazole in PBS. 300 mM imidazole in PBS was used to elute bound AFP III and the protein purified *via* fast protein liquid chromatography (FPLC). Western blot and SDS-PAGE gel electrophoresis were used to identify AFP III, and the protein

concentration determined using Thermo Scientific Pierce BCA assay kit and verified by measuring absorbance at 280 nm and using Beer-Lambert law.

#### **2.8.3.1.2 Auto-induction AFPIII Expression**

Auto-induction media prepared (55.85 g media, 990 mL H<sub>2</sub>O, 10 mL 50 % glycerol) and autoclaved (15 minutes, 121 °C). 5 separate colonies of *E. coli* overnights grown in 10 mL LB (37 °C, 180 rpm). 20 mL of the preculture was then added to 1 L of LB-medium with added 1 mL ampicillin split into two 500 mL Erlenmeyer flasks and grown for 3 hours under continuous shaking (37 °C, 180 rpm). The OD of the cells was recorded every 2 hours. Once the OD reached 2, the speed and temperature of the samples was reduced (20 °C, 140 rpm) and the cells left overnight. Once the OD no longer increased the cells were harvested and centrifuged (40 °C, 5000 RPM, 30 minutes). The pellet was resuspended in 7 mL prechilled PBS buffer with protease tablet dissolved in it. Samples were passed through a STANSTED 'Pressure Cell' FGP12800 homogeniser twice to undergo lysis, BugBuster (500 µL) was added and the sample left shaking for 20 minutes.

The sample was centrifuged (4 °C, 18000 RPM, 30 minutes) supernatant syringe filtered (0.2 µm) and passed through a pre-equilibrated (20 mL PBS) IMAC Sepharose 6 Fast Flow (GE Healthcare) column charged with Ni(II) ions. The column was washed with 5 mM imidazole and shook for 1 hour, then washed with buffer then washed with 30 mM imidazole three times. The protein was finally eluted using 300 mM imidazole.

#### **2.8.3.1.3 Green Fluorescent Protein Expression**

A pWALDO plasmid encoding for a hexahistidine-tagged GFP (Elizabeth Fullam, University of Warwick, U.K.) was transformed into competent *Escherichia coli* BL21(DE3) cells (New England Biolabs). A single colony was selected and grown overnight in 50 mL of LB-medium containing 100 µg.mL<sup>-1</sup> ampicillin under continuous shaking (37 °C, 180 RPM). 5 mL of the preculture was then added to 500 mL of LB-medium in a 2 L Erlenmeyer flask and grown for 4 hours under continuous shaking (37 °C, 180 RPM). The temperature was reduced to 16 °C and cells were

incubated for an hour further. IPTG was then added to the cells to a final concentration of 1 mM. The protein overexpressed overnight, following which the cells were centrifuged (4 °C, 4000 g, 30 minutes).

Pelleted cells were resuspended in 15 mL PBS ( $>18.2 \Omega$  mean resistivity, [NaCl] = 0.138 M, [KCl] = 0.0027 M, and pH 7.4). Pierce protease inhibitor mini-tablets were added to the suspension and it was passed through a STANSTED 'Pressure Cell' FGP12800 homogeniser to undergo lysis. The cell lysate was centrifuged (4 °C, 14,000 g, 30 minutes) and the supernatant syringe filtered (0.2  $\mu$ m) and passed through a pre-equilibrated (20 mL PBS) IMAC Sepharose 6 Fast Flow (GE Healthcare) column charged with Ni(II) ions. The column was washed first with 10 column volumes of 20 mM imidazole in PBS, then with 5 column volumes of 50 mM imidazole in PBS. 250 mM and 1000 mM imidazole in PBS were used to elute bound GFP and the imidazole removed from the fractions using PD10 desalting columns (GE Healthcare).

### **2.8.3.2 Ice Recrystallisation Inhibition 'Splat' Assay**

Samples were dissolved in PBS buffer (pH 7.4) at concentrations of 10 to 0.05 mg.mL<sup>-1</sup> and 1 drop of the solution was dispensed from a height of 1.4 m onto a glass cover slip on a metal disc cooled with dry ice. An ice wafer instantly formed and was transferred to a cryostage held at -8 °C under liquid nitrogen. Samples were left to anneal for 30 minutes. Images of the wafer were taken before and after the 30 minutes. Image processing was performed using ImageJ software on the 5 largest crystals from at least 3 independent wafers giving the MLGS from 15 measurements.

### **2.8.3.3 Green Fluorescent Protein Stability Assay**

200  $\mu$ L of 6.89 mg.mL<sup>-1</sup> green fluorescent protein (GFP) was diluted in 39.8 mL PBS buffer resulting in a stock solution of 0.034 mg.mL<sup>-1</sup>. PEG and PVA were dissolved in 2 mL of the stock solution to make different samples with final concentrations of 100 mg.mL<sup>-1</sup> PEG and 0.5, 1, 2.5, 5 and 10 mg.mL<sup>-1</sup> PVA. This was repeated for all 3 different molecular weights of PVA tested. Aliquots of 80  $\mu$ L of the GFP/PEG/PVA solution were pipetted into wells of a black 96 well plate and fluorescence recorded at

27 °C. Fluorescence intensity was compared to that of a GFP/PEG solution with a 100 mg.mL<sup>-1</sup> concentration. The plates were placed in a freezer at -20 °C until frozen and then thawed in an Eppendorf SmartBlock™ at 27 °C for 10 minutes. The above freeze-thaw cycle was repeated 6 times with the fluorescence of the samples recorded after each thaw. Fluorescence excitation was measured at 485/20 nm and emission at 528/20 nm.

#### **2.8.3.4 Insulin Freeze/Thaw Assay**

1 mL of 10.5 mg.mL<sup>-1</sup> insulin was diluted in 19 mL PBS buffer resulting in a stock solution of 0.525 mg.mL<sup>-1</sup>. PEG and PVA were dissolved in the stock solution to make different samples with final concentrations of 100 mg.mL<sup>-1</sup> 4 kDa PEG, 50 mg.mL<sup>-1</sup> 2 kDa PEG and 1 mg.mL<sup>-1</sup> PVA. Insulin in PBS buffer was used as a control against solutions of Insulin/PVA, Insulin/PEG2/PVA and Insulin/PEG4/PVA. The samples were placed in a freezer at -20 °C for 1 hour until frozen and then thawed in an Eppendorf SmartBlock™ at 37 °C for 15 minutes. The above freeze-thaw cycle was repeated for 6 and then 12 thaws before hydrodynamic diameter being measured by dynamic light scattering.

#### **2.8.3.5 Lactate Dehydrogenase Activity Assay**

NADH and sodium pyruvate were made up to stock concentrations of 63 mM and 10 mM respectively. NADH (4 µL) and sodium pyruvate (10 µL) were added to 1 mL PBS to make the reaction buffer. All potential cryoprotectants (glycerol, 4 kDa PEG, 10 kDa PVA, PEG/PVA) were added to LDH in a 50:50 volume and frozen in triplicate at the chosen temperature (-196 °C or -20 °C). The samples were thawed at 25 °C after ≥1 cycles.

5 µL of CPA:LDH samples were added to a 96 well plate and diluted by the addition of the reaction buffer (195 µL). Absorbance at 340 nm was recorded over 30 minutes at 25 °C using a BioTek Synergy HTX multimode reader and compared to that of an unfrozen LDH control and unreacted NADH.

In storage experiments the samples were stored at -20 °C for either 24 hours, 1 week or 4 weeks before thawing.

### 2.8.3.6 Bacteria Freeze/Thaw Assay

Different molecular weight PEGs (100 mg.mL<sup>-1</sup>; 200 Da, 400 Da, 1.5 kDa, 4 kDa, 6 kDa and 8 kDa) and PVAs (1 mg.mL<sup>-1</sup>; 10, 23 and 31 kDa) were dissolved in PBS for comparison in cryoprotective activity alongside the polyampholyte, AFPIII and glycerol. Cells (150 µL) were added to separate solutions of the different cryoprotectants (150 µL) and snap frozen in liquid nitrogen before thawing at 37 °C in a water bath. The freeze (-196 °C) thaw (25 °C) cycles were repeated 7 times then the samples were added to LB in 96 well plates (200 µL). Serial dilutions took place and the samples plated on ampicillin plates. These were left to grow at 37 °C for subsequent colony counts. Confocal microscopy was performed to evaluate the number of live/dead cells obtained.

### 2.8.3.7 *Lactobacillus delbrueckii subsp. bulgaricus* Freeze/Thaw Assay

MRS broth was prepared according to manufacturer's instructions and sterilised to make up preculture bottles (30 mL). Cryovials of *L. delbrueckii subsp. bulgaricus* were thawed (5 minutes, 42°C), aseptically transferred to sterilised MRS broth containing and grown over 24 hours at 42 °C. 5 mL of the preculture was then added to 500 mL of culture medium in a 2 L Erlenmeyer flask and grown for at 42 °C until reached the late exponential growth phase. The culture was then transferred to 50 mL centrifuge tubes and pelleted (10,000 g, 10 minutes, 4 °C). The cells were then resuspended in cryoprotective solutions. Samples then either underwent 7 freeze (-196 °C) thaw (25 °C) cycles or varying lengths of long-term storage and then post-thaw were added to saline in 96 well plates (200 µL). Serial dilutions took place and the samples plated on MRS agar plates. These were left to grow under anaerobic conditions at 42 °C for subsequent colony counts.

### 2.8.3.8 Cryoprotectant Toxicity on Bacteria

Equal volumes of bacteria and cryoprotectant solutions were left shaking at 4 °C overnight. The cryoprotectant samples (20 µL) were then added to LB in wells (200 µL) in the first column of 96 well plate and serial dilutions of the samples produced by transferring 20 µL from column 1 to column 2, mixing, then taking 20 µL from column 2 to column 3. This was repeated until column 7 was reached giving dilutions



up to  $10^{-7}$ . Dilutions  $10^{-2}$  to  $10^{-5}$  were plated on ampicillin plates and colonies grown at 37 °C for subsequent counting. Toxicity assays were repeated using 3 PEG concentrations (100, 50 and 10 mg.mL<sup>-1</sup>) combined with a constant PVA concentration of 0, 1 or 10 mg.mL<sup>-1</sup>.

#### **2.8.3.9 OD<sub>600</sub> Turbidity Measurements**

Toxicity and protection of cells in liquid culture was studied using absorbance spectroscopy. Samples were prepared as before and underwent 7 FT cycles. The cells were then grown in LB (200 mL) over 14 hours under continuous shaking at 37 °C and their OD was measured at 600 nm at 10 minute intervals and compared to a control sample that underwent no freeze thaw cycles. This growth assay was performed also on cells combined with different AFP concentrations (0.1, 2.5 and 5 mg.mL<sup>-1</sup>) for comparison, as well as samples frozen at -20 °C as well as -196 °C.

#### **2.8.3.10 Live/Dead Bacterial Viability Test**

Following seven freeze/thaw cycles, samples were spun down at 10,000 x g for 10 minutes and the supernatant was discarded. An aliquot was taken prior to the freeze/thaw cycle as a live cell control and a further aliquot was heat killed (incubated at 80 °C for 30 minutes) for a dead cell control. Cells were re-suspended in 20 µl of 0.85 % NaCl solution. 10 µl of this suspension was diluted in 200 µl of 0.85 % NaCl solution and the samples were incubated at room temperature for 1 h. Samples were pelleted at 10,000 x g for 10 minutes, the supernatant was discarded and the cells were re-suspended in 100 µl of 0.85 % NaCl solution. Next, the LIVE/DEAD bacterial viability staining mixture was prepared by mixing SYTO-9 and propidium iodide to final concentrations of 1.67 mM and 10 mM, respectively. The cells were stained by adding 0.3 µl of the staining solution to 100 µl of cell suspension and incubating in the dark for 15 minutes (at room temperature). Slides for microscopy were prepared by trapping 5 µl of the stained bacterial suspension between a slide and a coverslip. Samples were then analysed by means of fluorescent microscopy (at either 100x or 60x magnification) using GFP (excitation 470/40 nm, emission 525/50 nm) and mCherry (excitation 560/40 nm, emission 630/75 nm) filter sets to visualise the SYTO-9 and propidium iodide staining, respectively.

## 2.9 References

- 1 K. Heylen, S. Hoefman, B. Vekeman, J. Peiren and P. De Vos, *Appl. Microbiol. Biotechnol.*, 2012, **94**, 565–574.
- 2 K. B. P. K. Reddy, S. P. Awasthi, A. N. Madhu and S. G. Prapulla, *Food Biotechnol.*, 2009, **23**, 243–265.
- 3 P. Mazur, *Science*, 1970, **168**, 939–949.
- 4 P. Mazur, *Cryobiology*, 2010, **60**, 4–10.
- 5 G. B. Strambini and M. Gonnelli, *Biophys. J.*, 2007, **92**, 2131–2138.
- 6 J. M. Sarciaux, S. Mansour, M. J. Hageman and S. L. Nail, *J. Pharm. Sci.*, 1999, **88**, 1354–1361.
- 7 T. J. Anchordoquy and J. F. Carpenter, *Arch. Biochem. Biophys.*, 1996, **332**, 231–238.
- 8 K. A. Pikal-Cleland, J. L. Cleland, T. J. Anchordoquy and J. F. Carpenter, *J. Pharm. Sci.*, 2002, **91**, 1969–1979.
- 9 K. A. Pikal-Cleland, N. Rodríguez-Hornedo, G. L. Amidon and J. F. Carpenter, *Arch. Biochem. Biophys.*, 2000, **384**, 398–406.
- 10 E. Y. Shalaev, T. D. Johnson-Elton, L. Chang and M. J. Pikal, *Pharm. Res.*, 2002, **19**, 195–201.
- 11 B. S. Bhatnagar, R. H. Bogner and M. J. Pikal, *Pharm. Dev. Technol.*, 2007, **12**, 505–523.
- 12 C. J. Roberts, *Biotechnol. Bioeng.*, 2007, **98**, 927–938.
- 13 E. Gabellieri and G. B. Strambini, *Biophys. J.*, 1996, **70**, 971–976.
- 14 M. C. Manning, D. K. Chou, B. M. Murphy, R. W. Payne and D. S. Katayama, *Pharm. Res.*, 2010, **27**, 544–575.
- 15 D. Gao and J. K. Critser, *ILAR J.*, 2000, **41**, 187–196.
- 16 U. Roessl, S. Leitgeb and B. Nidetzky, *Biotechnol. Reports*, 2015, **6**, 108–111.
- 17 B. J. Fuller, *Cryo-Letters*, 2004, **25**, 375–388.

- 18 K. E. Zachariassen and E. Kristiansen, *Cryobiology*, 2000, **41**, 257–279.
- 19 R. Tedeschi and P. De Paoli, in *Methods in Biobanking*, ed. J. Dillner, Humana Press, Totowa, NJ, 2011, pp. 313–326.
- 20 B. P. Best, *Rejuvenation Res.*, 2015, **18**, 422–436.
- 21 S. C. Keith, *Science*, 1913, **37**, 877–879.
- 22 Z. Shu, S. Heimfeld and D. Gao, *Bone Marrow Transpl.*, 2014, **49152**, 469–476.
- 23 C. J. Capicciotti, M. Leclere, F. A. Perras, D. L. Bryce, H. Paulin, J. Harden, Y. Liu and R. N. Ben, *Chem. Sci.*, 2012, **3**, 1408–1416.
- 24 R. J. Sharp, *Adv. Biotechnol. ProgR.*, 1984, **3**, 81–109.
- 25 Z. Hubálek, *Cryobiology*, 2003, **46**, 205–229.
- 26 M. Bar-Dolev, Y. Celik, J. S. Wettlaufer, P. L. Davies and I. Braslavsky, *J. R. Soc. Interface*, 2012, **9**, 3249–3259.
- 27 J. F. Carpenter and T. N. Hansen, *Proc. Natl. Acad. Sci. U. S. A.*, 1992, **89**, 8953–8957.
- 28 H. Chao, P. L. Davies and J. F. Carpenter, *J. Exp. Biol.*, 1996, **199**, 2071–2076.
- 29 T. K. Eto and B. Rubinsky, *Biochem. Biophys. Res. Commun.*, 1993, **197**, 927–931.
- 30 T. Wang, Q. Zhu, X. Yang, J. R. Layne and A. L. Devries, *Cryobiology*, 1994, **31**, 185–192.
- 31 M. I. Gibson, *Polym. Chem.*, 2010, **1**, 1141–1152.
- 32 C. I. Biggs, T. L. Bailey, B. Graham, C. Stubbs, A. E. R. Fayter and M. I. Gibson, *Nat. Commun.*, 2017, **8**, 1546.
- 33 B. Graham, A. E. R. Fayter, J. E. Houston, R. C. Evans and M. I. Gibson, *J. Am. Chem. Soc.*, 2018, **140**, 5682–5685.
- 34 R. C. R. C. Deller, M. Vatish, D. A. D. A. Mitchell and M. I. Gibson, *Nat. Commun.*, 2014, **5**, 1–7.

- 35 D. E. Mitchell, J. R. Lovett, S. P. Armes and M. I. Gibson, *Angew. Chemie - Int. Ed.*, 2016, **55**, 2801–2804.
- 36 D. E. Mitchell, N. R. Cameron and M. I. Gibson, *Chem. Commun.*, 2015, **51**, 12977–12980.
- 37 B. Graham, T. L. Bailey, J. R. J. Healey, M. Marcellini, S. Deville and M. I. Gibson, *Angew. Chemie Int. Ed.*, 2017, **56**, 15941–15944.
- 38 R. C. Deller, J. E. Pessin, M. Vatish, D. A. Mitchell and M. I. Gibson, *Biomater. Sci.*, 2016, **47**, 935–945.
- 39 K. Matsumura, J. Y. Bae, H. H. Kim and S. H. Hyon, *Cryobiology*, 2011, **63**, 76–83.
- 40 T. Congdon, R. Notman and M. I. M. I. Gibson, *Biomacromolecules*, 2013, **14**, 1578–1586.
- 41 N. S. Vail, C. Stubbs, C. I. Biggs and M. I. Gibson, *ACS Macro Lett.*, 2017, **6**, 1001–1004.
- 42 T. Inada and S. Lu, *Cryst. Growth Des.*, 2003, **3**, 747–752.
- 43 A. A. Burkey, C. L. Riley, L. K. Wang, T. A. Hatridge and N. A. Lynd, *Biomacromolecules*, 2018, **19**, 248–255.
- 44 T. Inada and P. R. Modak, *Chem. Eng. Sci.*, 2006, **61**, 3149–3158.
- 45 C. Budke and T. Koop, *ChemPhysChem*, 2006, **7**, 2601–2606.
- 46 R. Drori, C. Li, C. Hu, P. Raiteri, A. L. Rohl, M. D. Ward and B. Kahr, *J. Am. Chem. Soc.*, 2016, **138**, 13396–13401.
- 47 C. Stubbs, J. Lipecki and M. I. Gibson, *Biomacromolecules*, 2017, **18**, 295–302.
- 48 R. Rajan, F. Hayashi, T. Nagashima and K. Matsumura, *Biomacromolecules*, 2016, **17**, 1882–1893.
- 49 H. Geng, X. Liu, G. Shi, G. Bai, J. Ma, J. Chen, Z. Wu, Y. Song, H. Fang and J. Wang, *Angew. Chemie - Int. Ed.*, 2017, **56**, 997–1001.
- 50 O. Mizrahy, M. Bar-Dolev, S. Guy and I. Braslavsky, *PLoS One*, 2013, **8**,

- e59540.
- 51 M. Leclère, B. K. Kwok, L. K. Wu, D. S. Allan and R. N. Ben, *Bioconjug. Chem.*, 2011, **22**, 1804–1810.
- 52 D. S. Dimitrov, *Methods Mol. Biol.*, 2012, **899**, 1–26.
- 53 A. M. Scott, J. D. Wolchok and L. J. Old, *Nat. Rev. Cancer*, 2012, **12**, 278–87.
- 54 S. Kotsovilis and E. Andreakos, *Methods Mol. Biol.*, 2014, **1060**, 37–59.
- 55 O. Leavy, *Nat. Rev. Immunol.*, 2010, **10**, 297.
- 56 J. Vlasak and R. Ionescu, *MAbs*, 2011, **3**, 253–63.
- 57 D. Gil and A. G. Schrum, *Adv. Biosci. Biotechnol.*, 2013, **4**, 73–84.
- 58 J. K. Kaushik and R. Bhat, *J. Biol. Chem.*, 2003, **278**, 26458–65.
- 59 D. E. Mitchell, T. Congdon, A. Rodger and M. I. Gibson, *Sci. Rep.*, 2015, **5**, 15716.
- 60 F. Yang, L. G. Moss and G. N. Phillips, *Structure*, 2011, **14**, 1–14.
- 61 V. I. Timofeev, R. N. Chuprov-Netochin, V. R. Samigina, V. V. Bezuglov, K. A. Miroshnikov and I. P. Kuranova, *Acta Crystallogr. Sect. F Struct. Biol. Cryst. Commun.*, 2010, **66**, 259–263.
- 62 G. Rai, K. R. Brimacombe, B. T. Mott, D. J. Urban, X. Hu, S.-M. Yang, T. D. Lee, D. M. Cheff, J. Kouznetsoca, G. A. Benavides, K. Pohida, E. J. Kuenstner, D. K. Luci, C. M. Lukacs, D. R. Davies, D. M. Dranow, H. Zhu, G. Sulikowski, W. J. Moore, G. M. Stott, A. J. Flint, M. D. Hall, V. M. Darley-USmar, L. M. Neckers, C. V. Dang, A. G. Waterson, A. Simeonov, A. Jadhav and D. J. Maloney, *J Med Chem*, 2017, **60**, 9184–9204.
- 63 D. P. Barondeau, C. J. Kassmann, J. A. Tainer and E. D. Getzoff, *J. Am. Chem. Soc.*, 2002, **124**, 3522–3524.
- 64 R. Y. Tsien, *Annu. Rev. Biochem.*, 1998, **67**, 509–544.
- 65 Q. X. Hua, W. Jia, B. H. Frank, N. F. B. Phillips and M. A. Weiss, *Biochemistry*, 2002, **41**, 14700–14715.

- 66 C. W. Ward and M. C. Lawrence, *Front. Endocrinol. (Lausanne)*, 2011, **2**, 1–11.
- 67 E. Ciszak and G. D. Smith, *Biochemistry*, 1994, **33**, 1512–1517.
- 68 T. Blundell, G. Dodson, D. Hodgkin and D. Mercola, *Adv. Protein Chem.*, 1972, **26**, 279–402.
- 69 M. Sklepari, A. Rodger, A. Reason, S. Jamshidi, I. Prokes and C. A. Blindauer, *Anal. Methods*, 2016, **8**, 7460–7471.
- 70 M. L. Dieken, M. Federwisch and P. De Meyts, Eds., *Insulin & Related Proteins - Structure to Function and Pharmacology*, Springer Netherlands, Dordrecht, The Netherlands, 2002.
- 71 Z. Fu, E. R. Gilbert and D. Liu, *Curr Diabetes Rev.*, 2014, **9**, 25–53.
- 72 D. R. Owens, B. Zinman and G. B. Bolli, *Lancet*, 2001, **358**, 739–746.
- 73 J. C. Pickup, *N. Engl. J. Med.*, 2012, **366**, 1616–1624.
- 74 M. Pingel and A. Volund, *Diabetes*, 1972, **21**, 805–813.
- 75 W. E. Scott and G. R. Riser, *J. Am. Oil Chem. Soc.*, 1966, **43**, 55–56.
- 76 G. D. Ogle, M. Abdullah, D. Mason, A. S. Januszewski and S. Besançon, *Diabet. Med.*, 2016, **33**, 1544–1553.
- 77 C. L. Markert, *Cell Biochem. Funct.*, 1984, **2**, 131–134.
- 78 S. Iwata, K. Kamata, S. Yoshida, T. Minowa and T. Ohta, *Nat. Struct. Biol.*, 1994, **1**, 176–185.
- 79 A. K. Jain, D. Singh, K. Dubey, R. Maurya, S. Mittal and A. K. Pandey, in *In Vitro Toxicology*, eds. A. Dhawan and S. Kwon, Elsevier Inc., 2018, pp. 45–65.
- 80 S. M. Smith, M. B. Wunder, D. A. Norris and Y. G. Shellman, *PLoS One*.
- 81 P. Kumar, A. Nagarajan and P. D. Uchil, *Cold Spring Harb. Protoc.*, 2018, **2018**, 465–468.
- 82 E. Jacobs, P. J. Hissin, W. Propper, L. Mayer and L. Sarkozi, *Clin. Biochem.*, 1986, **19**, 183–188.

- 83 J. C. Houle, A. V. Chen, A. C. Brenna, K. L. Mealey and A. M. Kiszonas, *Vet. Clin. Pathol.*, 2015, **44**, 253–261.
- 84 J. W. Starnes, *Int. J. Cardiol.*, 2008, **127**, 114–116.
- 85 S. Amin, G. V. Barnett, J. A. Pathak, C. J. Roberts and P. S. Sarangapani, *Curr. Opin. Colloid Interface Sci.*, 2014, **19**, 438–449.
- 86 J. M. Walker, J. Ewbank, E. Vivier, M. T. Quinn, F. R. DeLeo, P. Molnar, J. J. Hickman, H. P. S Makkar, P. Siddhuraju, K. Becker, J. G. Day and G. Stacey, *Cryopreservation and Freeze-Drying Protocols*, Humana Press, Totowa, NJ, Totowa, 2nd edn., 2008, vol. 368.
- 87 K. Nishijima, M. Tanaka, Y. Sakai, C. Koshimoto, M. Morimoto, T. Watanabe, J. Fan and S. Kitajima, *Cryobiology*, 2014, **69**, 22–25.
- 88 C. Koshimoto and P. Mazur, *Cryobiology*, 2002, **45**, 49–59.
- 89 D. E. Pegg, M. C. Wusteman and S. Boylan, *Cryobiology*, 1997, **34**, 183–192.
- 90 M. C. Wusteman, S. Boylan and D. E. Pegg, *Investig. Ophthalmol. Vis. Sci.*, 1997, **38**, 1934–1943.
- 91 Z. Wang, E. Klipfell, B. J. Bennett, R. Koeth, B. S. Levison, B. DuGar, A. E. Feldstein, E. B. Britt, X. Fu, Y.-M. Chung, Y. Wu, P. Schauer, J. D. Smith, H. Allayee, W. H. W. Tang, J. A. DiDonato, A. J. Lusis and S. L. Hazen, *Nature*, 2011, **472**, 57–63.
- 92 G. Sharon, T. R. Sampson, D. H. Geschwind and S. K. Mazmanian, *Cell*, 2016, **167**, 915–932.
- 93 K. Rea, T. G. Dinan and J. F. Cryan, *Neurobiol. Stress*, 2016, **4**, 23–33.
- 94 N. Navaneetharaja, V. Griffiths, T. Wileman and S. Carding, *J. Clin. Med.*, 2016, **5**, 55.
- 95 C. Manichanh, J. Reeder, P. Gibert, E. Varela, M. Llopis, M. Antolin, R. Guigo, R. Knight and F. Guarner, *Genome Res.*, 2010, **20**, 1411–1419.
- 96 A. Ahmadi, E. Milani, A. Madadlou, S. A. Mortazavi, R. R. Mokarram and D. Salarbashi, *J. Food Sci. Technol.*, 2014, **51**, 1568–1574.

- 97 C. Sohlenkamp and O. Geiger, *FEMS Microbiol. Rev.*, 2015, **40**, 133–159.
- 98 A. M. Valdes, J. Walter, E. Segal and T. D. Spector, *BMJ*, 2018, **361**, 36–44.
- 99 E. Aizawa, H. Tsuji, T. Asahara, T. Takahashi, T. Teraishi, S. Yoshida, N. Koga, K. Hattori, M. Ota and H. Kunugi, *Front. Psychiatry*, 2019, **10**, 1–8.
- 100 M. A. K. Azad, M. Sarker, T. Li and J. Yin, *Biomed Res. Int.*, 2018, **2018**, 1–8.
- 101 P. Deol, R. Vohra, A. K. Saini, A. Singh, H. Chandra, P. Chopra, T. K. Das, A. K. Tyagi and Y. Singh, *J. Bacteriol.*, 2005, **187**, 3415–3420.
- 102 W. R. Li, X. B. Xie, Q. S. Shi, H. Y. Zeng, Y. S. Ou-Yang and Y. Ben Chen, *Appl. Microbiol. Biotechnol.*, 2010, **85**, 1115–1122.
- 103 A. Prince, P. Sandhu, P. Kumar, E. Dash, S. Sharma, M. Arakha, S. Jha, Y. Akhter and M. Saleem, *Sci. Rep.*, 2016, **6**, 37908.
- 104 R. C. Deller, M. Vatish, D. A. Mitchell and M. I. Gibson, *ACS Biomater. Sci. Eng.*, 2015, **1**, 789–794.
- 105 K. Matsumura and S. H. Hyon, *Biomaterials*, 2009, **30**, 4842–4849.
- 106 P. L. Davies and B. D. Sykes, *Curr. Opin. Struct. Biol.*, 1997, **7**, 828–834.
- 107 T. Ishibe, T. Congdon, C. Stubbs, M. Hasan, G. C. Sosso and M. I. Gibson, *ACS Macro Lett.*, 2019, **8**, 1063–1067.
- 108 C. C. DeMerlis and D. R. Schoneker, *Food Chem. Toxicol.*, 2003, **41**, 319–326.
- 109 C. I. Biggs, C. Stubbs, B. Graham, A. E. R. Fayter, M. Hasan and M. I. Gibson, *Macromol. Biosci.*, 2019, **19**, 1–9.
- 110 T. R. Congdon, R. Notman and M. I. Gibson, *Eur. Polym. J.*, 2017, **88**, 320–327.
- 111 J. F. Carpenter, S. J. Prestrelski and T. Arakawa, *Arch. Biochem. Biophys.*, 1993, **303**, 456–64.
- 112 S. Abbina and A. Parambath, in *Engineering of Biomaterials for Drug Delivery Systems: Beyond Polyethylene Glycol*, Elsevier Ltd, 2018, pp. 363–376.
- 113 K. B. Bjugstad, K. Lampe, D. S. Kern and M. Mahoney, *J. Biomed. Mater. Res.*



- Part A, 2010, **95**, 79–91.
- 114 V. G. Kadajji and G. V. Betageri, *Polymers (Basel)*, 2011, **3**, 1972–2009.
- 115 W. F. da Silva Júnior, J. G. de Oliveira Pinheiro, C. D. L. F. A. Moreira, F. J. J. de Souza and Á. A. N. de Lima, in *Multifunctional Systems for Combined Delivery, Biosensing and Diagnostics*, ed. A. M. Grumezescu, Elsevier Inc., 2017, pp. 281–305.
- 116 Sigma-Aldrich, *Lactate Dehydrogenase Activity Assay Kit: Technical Bulletin*, St. Louis, 2018, vol. 1.
- 117 D. E. Mitchell, A. E. R. Fayter, R. C. Deller, M. Hasan, J. Gutierrez-Marcos and M. I. Gibson, *Mater. Horizons*, 2019, **6**, 364–368.
- 118 W. H. Depas, M. Bergkessel and D. K. Newman, *MBio*, 2019, **10**, 1–17.
- 119 G. Pasut, *Polymers (Basel)*, 2014, **6**, 160–178.
- 120 T. Arakawa and S. N. Timasheff, *Biochemistry*, 1985, **24**, 6756–6762.
- 121 J. Brady, T. Drig, P. I. Lee and J. X. Li, in *Developing Solid Oral Dosage Forms: Pharmaceutical Theory and Practice: Second Edition*, 2016, pp. 181–223.
- 122 T. M. Nalawade, K. Bhat and S. H. P. Sogi, *J. Int. Soc. Prev. Community Dent.*, 2015, **5**, 114–9.
- 123 A. Srivastava, T. Yadav, S. Sharma, A. Nayak, A. Akanksha Kumari and N. Mishra, *J. Biosci. Med.*, 2016, **4**, 69–84.
- 124 J. Kopecek and P. Kopeckova, *Adv. Drug Deliv. Rev.*, 2010, **62**, 122–149.
- 125 H. Erothu and A. C. Kumar, in *Biomedical Applications of Polymeric Materials*, eds. R. Francis and D. S. Kumar, Wiley-VCH Verlag GmbH & Co. KGaA, 1993, pp. 163–185.
- 126 C. Stubbs, T. R. Congdon and M. I. Gibson, *Eur. Polym. J.*, 2019, **110**, 330–336.
- 127 K. Nidhi, S. Indrajeet, M. Khushboo, K. Gauri and D. J. Sen, *J. Pharm. Sci.*, 2006, **95**, 2145–2157.

- 128 O. W. Guirguis and M. T. H. Moselhey, *Nat. Sci.*, 2012, **4**, 57–67.
- 129 G. A. Burdock, *Food Chem. Toxicol.*, 2007, **45**, 2341–2351.
- 130 N. Zaritzky, in *Biopolymer Engineering in Food Processing*, 2012, pp. 327–383.
- 131 T. Maity, A. Saxena and P. S. Raju, *Crit. Rev. Food Sci. Nutr.*, 2017, **0**, 1–16.
- 132 R. W. Moreadith, T. X. Viegas, M. D. Bentley, J. M. Harris, Z. Fang, K. Yoon, B. Dizman, R. Weimer, B. P. Rae, X. Li, C. Rader, D. Standaert and W. Olanow, *Eur. Polym. J.*, 2017, **88**, 524–552.
- 133 R. Obeid, in *Polymers for Biomedicine*, ed. C. Scholz, Wiley, Alabama, 1st edn., 2017, pp. 1–609.
- 134 M. Glassner, M. Vergaelen and R. Hoogenboom, *Polym. Int.*, 2018, **67**, 32–45.
- 135 J. S. Poisson, J. G. Briard, T. R. Turner, J. P. Acker and R. N. Ben, *Bioprocess. J.*, 2017, **15**, 15–21.
- 136 C. J. Capicciotti, J. D. R. R. Kurach, T. R. Turner, R. S. Mancini, J. P. Acker and R. N. Ben, *Sci. Rep.*, 2015, **5**, 1–10.
- 137 A. Stolzing, Y. Naaldijk, V. Fedorova and S. Sethe, *Transfus. Apher. Sci.*, 2012, **46**, 137–147.
- 138 J. A. Alfurhood, H. Sun, C. P. Kabb, B. S. Tucker, J. H. Matthews, H. Leusch and B. S. Sumerlin, *Polym. Chem.*, 2017, **8**, 4983–4987.
- 139 A. A. D'souza and R. Shegokar, *Expert Opin. Drug Deliv.*, 2016, **13**, 1257–1275.

# Chapter 3

---

Using X-rays to Monitor Ice Growth and a  
Comparison to Optical Microscopy  
Methods

### 3.1 Declarations

*Assistance with wide angle X-ray scattering setup and writing of in-house MATLAB code for analysis was given by Dr Steven Huband (Department of Physics, University of Warwick). AFGP8 was provided by Professor A. L. DeVries (Urbana-Champaign, University of Illinois). Synthesis and conjugation of gold nanoparticles was performed by Dr Laura Wilkins, and PVA samples were synthesised by Dr Christopher Stubbs or Dr Thomas Congdon (all supervised by Professor Matthew I. Gibson).*

### 3.2 Chapter Abstract

Understanding ice growth is crucial for infrastructure maintenance, the environment and preserving biologics in the cold chain, and is vital in enabling translation into real world applications. Ice-binding and antifreeze proteins are potent ice recrystallisation inhibitors (IRIs), and synthetic materials that mimic this function have emerged, with potential biotechnology applications. To evaluate IRI activity, optical microscopy tools are typically used to monitor ice crystallite (grain) size, either by end-point measurements or as a function of time. However, these methods only provide 2-dimensional (2D) information and image analysis is required to extract the data.

Here wide angle X-ray scattering (WAXS/X-ray powder diffraction (XRD)) is explored and compared to that of microscopy-based techniques as an option for providing 3-dimensional (3D) data on IRI activity. XRD enables the interrogation of 100s of ice crystals in 3D, and due to the random organisation of the ice crystals in the frozen sample, the total number of orientations measured by XRD is proportional to the total number of ice crystals, which can be measured as a function of time. This method was used to evaluate the activity for a panel of known IRI active compounds and shows strong agreement with results obtained from optical microscopy, as well as being advantageous in that time-dependent ice growth is easily extracted. Comparison of obtained diffraction patterns for a range of ice-active materials (ice-binding and non-binding) in relation to crystal face binding and ice morphology is discussed. This method may help in the discovery of new IRI active materials, as well as enabling kinetic analysis of ice growth.

## 3.3 Introduction

### 3.3.1 Ice Crystal Growth Measurements

Microscopy has been employed in the majority of experimental work concerning ice and ice-active compounds thus far. Despite microscopy being a powerful tool; it shows insights at a macroscopic level, it provides little understanding of the bulk ice (only a “snapshot” can be considered from the microscope), especially when studying microscopic changes *e.g.* chemical structure, *i.e.* what is causing the macroscopic change observed. X-ray powder diffraction (XRD), discussed here, can be used to study, *in situ*, the bulk of the sample and allows us here to connect angstroms to micrometre lengths. Particularly as water cools, there are changes on the Å lengthscale (lengths/structures of bonds change), leading to potentially observable changes in the radial distribution function and observed Bragg peaks. [Note, the terms WAXS and X-ray powder diffraction are interchangeable and XRD is used here throughout]. Significant advances in technology, development of full-profile analytical methods and synchrotron radiation have aided progress in the X-ray field; there have been vast improvements in data precision and speed of data collection,<sup>1</sup> in particular the PILATUS 100k detector, used in this work, gives a large (up to  $2^{20}$  photons counted in one pixel per exposure) and fast readout (time of 2.59 ms), as well as having a good signal to noise ratio that allows for the observation of fine details, and improvement of X-ray imaging applications.<sup>2</sup> Ice-active proteins and their mimics can act in different ways; these include as antifreezes, ice-nucleants, ice recrystallisation inhibitors or by changing the morphology of ice crystals.<sup>3</sup> In cryopreservation in particular, the macroscopic effects cryoprotectants (CPAs) have on hexagonal ice (Ih) are of great interest and evaluating their properties is particularly important as changes in the ice crystal morphology leads to damaged/burst cells. The macroscopic effects focused on here are IRI, and dynamic ice shaping (DIS).

### 3.3.2 Optical Techniques

IRI activity is typically measured using either the ‘splat’<sup>4,5</sup> or sucrose ‘sandwich’<sup>6–8</sup> assays, which provide comparisons of ice crystal wafers. Both of these assays involve nucleating ice crystals and observing their growth over time (or more often at a fixed

time point) whilst recrystallisation occurs. [Note, it is crucial to highlight the conditions for these experiments as to avoid false positives.<sup>4,9</sup>] In both assays, smaller ice crystals, after annealing at sub-zero temperatures, indicate more IRI activity and data is reported as an area or relative to a negative control. **Figure 3.1A** shows an example micrograph from the splat assay, whereby large numbers of ‘small’ ice crystals are seeded from a buffer by rapidly freezing a droplet of water. The data is typically analysed after a set period of time and reported as a percentage growth relative to a PBS control. This can be reported as the mean largest grain size (MLGS), where the largest crystal in view is measured or mean grain size (MGS), where the average size of all crystals is measured. MLGS is appealing due to its simplicity for manual measurement but it fails to probe the whole population. **Figure 3.1B** shows a comparison of MLGS versus MGS data, which are generally in agreement, other than MGS being an area (squared) term and thus giving smaller % value for the same amount of inhibition. The ice wafers obtained, like that in **Figure 3.1A**, are challenging to analyse by automated image analysis due to the irregular grain boundaries, although Ben *et al.* have used domain recognition software.<sup>10</sup>

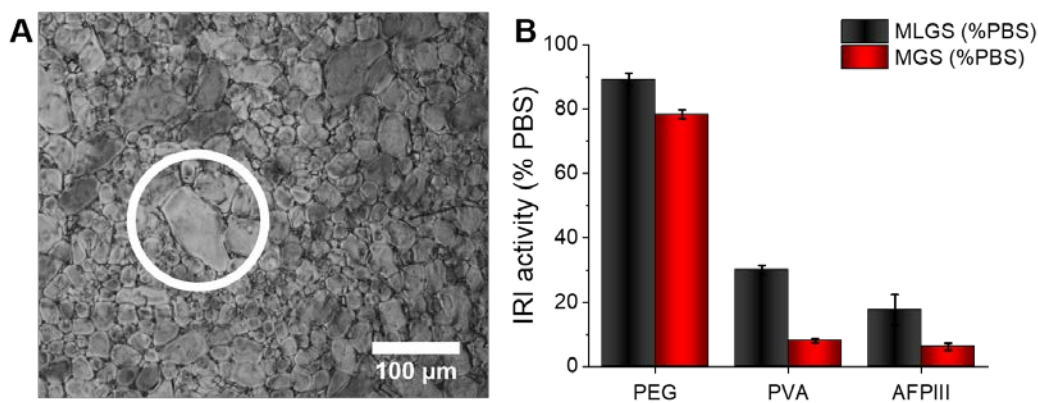


**Figure 3.1.** Optical microscopy analysis of ice recrystallisation. A) Example ice wafer containing  $1 \text{ mg.mL}^{-1}$  10 kDa PVA in PBS after 30 minutes. An example larger grain (white circle) is shown, which skews results when only ‘largest grain size’ is considered; B) Comparison of MLGS and MGS for some PEG, PVA and AFPIII. Concentrations =  $1 \text{ mg.mL}^{-1}$ . Errors are standard deviation.

The splat assay has barely changed since its introduction in 1988,<sup>11</sup> though an alternative method is the sucrose ‘sandwich’ assay, **Figure 3.2.**<sup>6–8</sup> The crystals obtained in this assay are more separated due to the high viscosity of the media, and

hence image analysis can be used to identify each crystal, as shown by Budke *et al.*<sup>7</sup> It is also important to be able measure growth in the media of interest, and the 20 - 45 wt % sucrose required<sup>6</sup> for this is not relevant for all conditions, and it has emerged recently that salts have a profound effect on growth rates, hence the appeal of measurement in buffers.<sup>12,13</sup> The mean crystal radius ( $r^3$ ) can be calculated from micrographs such as those in **Figure 3.2A**, and then plotted with their associated fittings, **Figure 3.2B**. **(a)** shows linear growth for a control solution, indicating that ice recrystallisation kinetics in that sample can be described by the bulk diffusion of water molecules from smaller crystals to the larger ones. This growth is fully inhibited for the higher concentration of AFGP and partially for the lower concentration. [Note, the total ice fraction remains constant; greater number of smaller crystals, fewer larger crystals, visualised as ice volume fraction (Q) in **Figure 3.2B (c)**.]

DIS is traditionally studied using sucrose ‘sandwich’ assays, where a sample of interest is pressed and sealed between two glass slides, frozen, warmed briefly and annealed so crystal habits can be observed, example micrographs shown in **Figure 3.2C**.<sup>6,8,15</sup> Sucrose is used as this allows liquid to be present at the ice crystal grain boundaries, enabling an easier study of the morphology of the ice crystals without interference from neighbouring grains.<sup>9,16</sup> Generally sucrose solutions are 30 - 45 wt % sucrose, depending on procedure followed.<sup>8</sup> The crystal habit of pure water is circular, and develops a hexagonal ‘snowflake’ shape as the crystal grows. This differs to that of samples with added antifreeze (glyco)proteins (AF(G)Ps) where needles can form, as seen in **Figure 3.2C (b,c)**.<sup>3,17</sup>

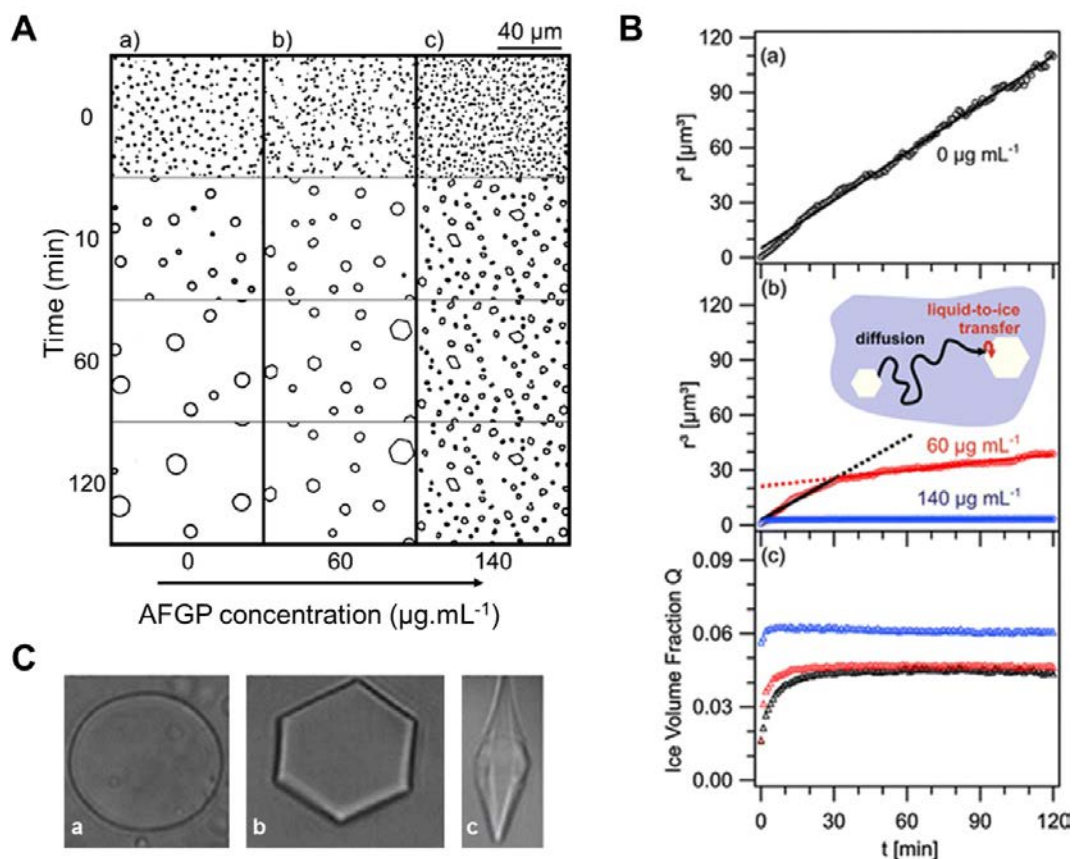


**Figure 3.2.** A) Micrographs of ice crystals formed in 45 wt % sucrose over time to enable measurement of ice crystal growth over 120 minutes, a) control solution, b) 60  $\mu\text{g.mL}^{-1}$  AFGP, c) 140  $\mu\text{g.mL}^{-1}$  AFGP; B) Example data obtained through calculating mean ice crystal radii,  $r^3$ , in 45 wt % sucrose solutions from the micrographs, a) control solution, b)  $r^3$  in solution containing 60 and 140  $\mu\text{g.mL}^{-1}$  AFGP, and their associated fits (solid lines), c) temporal development of ice crystal volume fraction, Q, of data from a) and b). Adapted from Budke *et al.* (J. Phys. Chem B, 2009).<sup>7</sup> All data obtained at  $-8$  °C. Errors are standard deviation. C) Ice morphology observed in micrographs obtained from sucrose assays; a) pure water, b) in the presence of dilute AFP solution, c) in the presence of high concentration AFP solution. Adapted from Griffith and Yaish (Trends Plant Sci., 2004).<sup>14</sup>



### 3.3.3 X-ray Techniques

The microstructure of solids was under debate until the late 19<sup>th</sup> century when Max von Laue suggested the use of X-rays,<sup>18</sup> theorising that 3D crystals could be visualised by X-ray diffraction. Since then, due to its interdisciplinary nature, crystallography has been of vital importance to biologists<sup>19</sup> and chemists,<sup>20</sup> and a range of techniques have been developed, including XRD (which includes powder and single crystal diffraction), small-angle X-ray scattering (SAXS), X-ray absorption (XAS) and emission (XES), for the analysis of solids.<sup>21</sup> XAS (up to sub-nm resolution)<sup>22</sup> and XES (~0.2 – 2 eV energy resolution dependent on setup)<sup>23</sup> provide complementary information on the electronic structure of materials, including speciation and coordination chemistry<sup>24,25</sup> so of less interest here. SAXS measures large features (5 – 500 nm) as the scattering angle is inversely proportional to size, and provides information on the morphology and dynamics of samples. Other parameters such as molecular mass, particle shape, particle size, quaternary structure of proteins and radius of gyration can also be obtained.<sup>26,27</sup> XRD differs in that it makes 0.1-5 nm measurements, and can provide information on secondary structures of biomacromolecules (single crystal XRD), interatomic distances (powder XRD), crystallinity and structural changes (powder XRD). It is sensitive to small changes,<sup>27</sup> grain size and orientation, and is the method focused on here.

A more detailed description of the theory behind diffraction can be found in Giacobazzo's work but a description is provided below.<sup>1</sup> When a crystalline sample is illuminated with X-rays and constructive interference (when waves are in phase) occurs, diffraction patterns are observed. The X-rays are electromagnetic waves that interact with electrons in atoms and will scatter by the process of elastic (wavelength of scattered X-rays remains the same) or inelastic (wavelength of scattered X-rays changes) scattering. The X-rays measured in diffraction experiments are those that undergo elastic scattering. When atoms are positioned periodically in a lattice, diffracted waves will consist of sharp interference maxima (peaks) with the same symmetry as in the distribution of atoms in a unit cell (as the peaks are directly related to atomic distances), enabling structural determination of the sample. **Figure 3.3A** shows an example of atoms, represented as green spheres, which form different sets of planes in a crystal. When the lattice spacing between two planes is  $d$  and the X-ray angle of incidence is  $\theta$ , then the difference in path lengths can be calculated

using  $2d \sin \theta$ .

Diffraction of X-rays is governed by Bragg's Law;

$$2d \sin \theta = n\lambda \quad (3.1)$$

where  $n$  is the order of reflection,  $\lambda$  is the wavelength of the incoming radiation,  $d$  is the lattice spacing and  $\theta$  is the incident angle of radiation between the primary beam and group of lattice planes with Miller indices  $h$ ,  $k$  and  $l$  (**Figure 3.3A**). Dependent on satisfaction of Bragg's law, diffracted X-rays (due to constructive interference) can be detected by scanning the sample through a range of scattering angles ( $2\theta$ ) and the signal converted to a count rate (the higher the number of counts the better the signal to noise ratio). The angle between the incident and diffracted rays is key for identification of a sample as the intensity measured as a function of  $2\theta$  provides information on the sites of atoms within the unit cell, giving diffractograms, which are a 'fingerprint' of a sample's crystal lattice, example shown in **Figure 3.3B**.<sup>28,29</sup> The peaks are related to the planes of atoms through the Miller indices. Crystal faces (planes) and directions (edges) are defined by direction alone, and are described by determining where the three axes of the lattice (*i.e.*  $a_1$ ,  $a_2$  and  $a_3$ ) intersect and then taking the reciprocals (ensuring the final value is a whole number) of these values, giving the Miller indices. Planes are written  $(h k l)$  and edges  $[h k l]$ .<sup>30</sup>

Instead of  $2\theta$ , the amount by which the scattered beam has been deflected by can be described by  $Q$ , the vector that describes the momentum transfer of X-ray scattering, allowing powder diffraction data to be plotted independent of the wavelength ( $\lambda$ ).  $Q$  relates to  $\theta$  by equation 3.2;  $Q$ -range depends on instrument, but a wider  $Q$ -range can provide greater structural information on a sample ( $Q$ -range of the Xenocs Xeuss 2.0 used here is  $\sim 1.3 - 3.3 \text{ \AA}^{-1}$ ).

$$Q = (4\pi/\lambda) \sin \theta \quad (3.2)$$

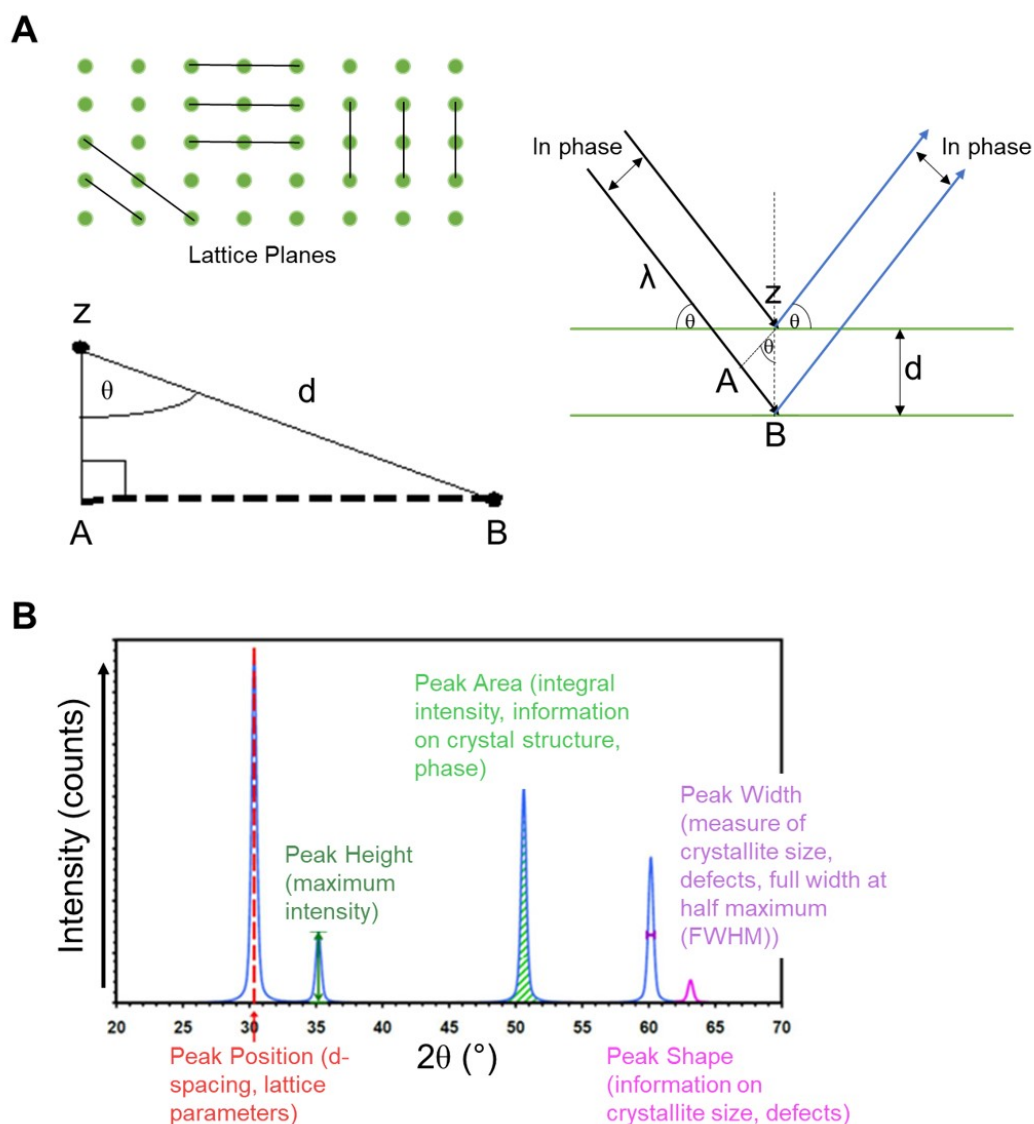


**Figure 3.3.** A) Lattice planes and geometry of Bragg reflections in Bragg's Law. (atoms represented in green form the different sets of crystal planes); B) Example idealised diffraction pattern, the Bragg peaks provide the signature of underlying structure. Information can be obtained from the peak positions, heights, shapes and areas. Adapted from Sharma *et al.* (Recent Res. Sci. Technol., 2012).<sup>31</sup>

Analysis of diffractograms can yield information on the phase present, sample purity, and how crystalline or amorphous a sample is, as well as indicating structural and morphological variations; the formation of flat plate-like and rod-shaped crystallites may introduce significant preferred orientation in specific planes ( $h k l$ ) resulting in peak intensity variations or missing peaks. Intensity of the peaks depends on size and shape of particles (habits), as well as orientation towards the X-ray beam, in particular, preferred orientation can greatly affect peak intensity. Changes in

crystal symmetry causing complete cancellation (systematic absences) can also result in zero intensity from specific ( $h k l$ ) planes, for example plates on a flat surface align and scatter strongly out-of-plane (002) in hexagonal ice plates leading to peak disappearance for (002). Both qualitative (identification of sample pattern) and quantitative (comparison of line intensities) analysis can be accomplished.<sup>29</sup> When physicochemical gradients are applied to a sample the structural changes can be directly probed at these specific conditions, allowing time to be explored as another variable in the experiment.

Here XRD is used to provide a description of the crystal structure of frozen solutions; these samples are not powdered manually, but form samples that are considered 'powdered' upon freezing *in situ* in a static capillary, **Figure 3.4B**. 1.0 mm single use syringes and needles are used to transfer liquid samples to capillaries, **Figure 3.4A**, and then transferred to the cryostage for cooling. Once a solution is frozen, if the crystals in the capillary align with the beam (shown here as blue lines), it is scattered, **Figure 3.4C**. The use of a capillary reduces interference on the sample from the sample holder, whereas if a flat surface is used there will be increased effects due to preferred orientation. However, the ice grains formed here are too large (~20 – 120  $\mu\text{m}$ ) to ensure a random distribution is sampled, because of the capillaries used here, so there is the possibility of some preferred orientation effects; effect of grain orientation is demonstrated in **Figure 3.4Ci/ii**, though there is minimal diffraction interference due to their thickness (0.01 mm). Capillaries of a different diameter could be used, though not possible in our setup as larger capillaries would not fit into our cold stage. The number of orientations being measured could also be increased by using a larger detector or by spinning the capillary.

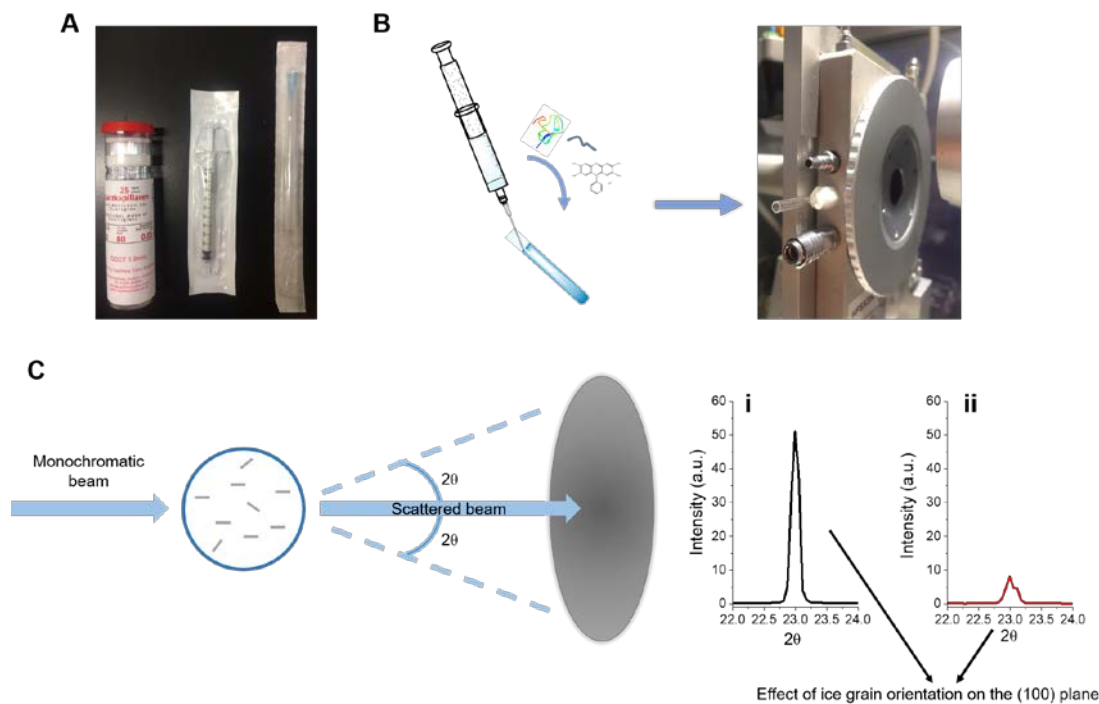


**Figure 3.4.** Consumables required and schematic of XRD procedure used here. A) From left to right, 1.0 mm diameter (0.01 mm thick) quartz capillaries, 1 mL syringe, 0.8 x 120 mm needle; B) Samples inserted into capillary, precision required to avoid any air bubbles that could interfere with scattering, then transferred to the cryostage; C) The monochromatic beam hits the crystals in the capillary, those of which that constructively interfere diffract the beam for data collection at the detector. Orientation of ice crystal grains affects the intensity of the diffraction pattern; i) sample with minimum preferred orientation for the (100) plane; ii) sample with increased preferred orientation due to size of grain for the (100) plane.

### 3.3.4 Polycrystalline Material

Ideal polycrystalline material is an ensemble of a very large number of randomly oriented crystallites (grains). If the material is an aggregate of randomly oriented crystallites, all the possible orientations with respect to the X-ray beam should be observed, offering a route to observing a change in size of a polynucleated sample. This is necessary to understand for ensuring that apparent systematic absences are not a result of preferred orientation or an insufficient number of crystallites within the scattering volume. The crystalline form (crystal habit)<sup>32,33</sup> is the general shape of a crystal,<sup>34</sup> is made up of crystallisation units (ensembles of groups of bonded atoms),

and is affected by the internal structure of the crystal but also any interaction between solute and solvent, thus may differ for the same materials. The faces of the same crystalline form may develop to different extents; these changes in habit are cases of distortion from the 'ideal' crystal shape due to *e.g.* rapid crystallisation. Factors often considered to influence crystal morphology are the growth rate, confinement and any external interactions with atoms or molecules (impurities),<sup>35</sup> *e.g.* strong adsorption of an impurity to a certain face will result in particular growth at this face.

Despite differences in habit, the X-ray peak positions do not change, unlike for polymorphs, as the crystals have identical chemical compositions and chemical and physical properties.<sup>36</sup> The intensities of each diffraction peak may differ however, because the total area of each crystal face is different according to crystal habit. The intensities can only be used for morphological analysis in powder samples, as ideally all orientations should be evenly distributed, and high enough resolution detectors are needed for this type of analysis.

### 3.3.5 XRD of Ice

Ice has been studied using X-ray techniques for over 100 years<sup>37-40</sup> despite the fact limited information can be obtained on the positions of the hydrogen nuclei as X-rays are scattered by electrons, which hydrogen has few of. This has allowed, however, for studies to determine the positions of the oxygen lattice. X-ray techniques provide information on any changes that may be due to changes in coordination of the water molecules, and any differences in hydrogen bonding observed by changes in the lattice. Hydrogen bonds were defined by Pimentel and McCellan as a bond between a functional group, A-H, and an atom (or group of atoms, B) in either the same or different molecule when there is both evidence of bond formation and evidence that this new bond between A-H and B involves the hydrogen already covalently bonded to A.<sup>41-43</sup> These are a weak type of dipole-dipole interaction (typical energies <40 kJ.mol<sup>-1</sup>), resulting from the attractive force between the hydrogen atom bonded to A and B, where both are usually electronegative. The hydrogen bonds affected in the ice are what are studied in this work, as hydrogen bonding in Ih is weak thus has a certain amount of flexibility in the system.<sup>44</sup> The hydrogen bond angle and length varies with temperature and pressure, with an average O...O length of 2.76 Å in Ih

and an angle of  $109.47^\circ$  between three neighbouring oxygens.<sup>28,45</sup> Water molecules in crystalline ice are fully hydrogen bonded<sup>44</sup> and in order to be ideal ice crystals the Bernal-Fowler rules for bonding must be followed.<sup>46</sup> The hydrogen bond network is considered very important for ice structure and therefore an understanding of any changes (as has been seen in doped ice where the density of ice phases has been increased by bending hydrogen bonds and enhancing proton ordering)<sup>44,47-49</sup> that could be observed upon addition of ice-active compounds, *e.g.* stacking faults, would be of great use.

### 3.3.5.1 Hexagonal Ice

This work focuses on Ih, the stable phase that forms at ambient pressure and at temperatures considered in this work *i.e.*  $\geq -80^\circ\text{C}$ . The ice-binding planes (specifically basal and prism) highlighted in Chapter 1 correspond to the Miller indices for the hexagonal unit cell as shown in **Figure 3.5A**. **Figure 3.5C** also displays two Ih unit cells containing water molecules, one modelled using 12 and the other 96, both highlighting the hexagonal form of the crystal. Exemplar X-ray diffraction patterns (as seen in the literature) for metastable cubic ice (Ic) and Ih are provided in **Figure 3.5B** with the associated Miller indices for the unit cells. The indices are written above the peaks corresponding to the related crystal edge. Data obtained here will be analysed and compared to these reference patterns. There are peaks that occur in both Ih and Ic, which can make identification of specific phases difficult, though it is supposed that the metastable Ic forms initially, and then relaxes into Ih, forming a mix of hexagonal and cubic crystallites, which is often referred to as ice I.<sup>51,52</sup> Reports used to study the Ic to Ih transition support this theory (Ic converts quickly to Ih at temperatures above  $-33^\circ\text{C}$ ).<sup>44,53,54</sup> Ic and Ih are similar in that they have equivalent densities and they both form 4 hydrogen bonds with their nearest neighbours, however oxygen atoms in Ic are arranged in a diamond rather than a hexagonal lattice.<sup>55</sup> There also is a peak corresponding to the (400) plane ( $58^\circ$ ) (not shown in **Figure 3.5**) that is only observed in Ic, allowing identification. The cooling rate can also affect if Ic or Ih forms, and if the rate is sufficiently fast, amorphous ice (vitreous ice) forms, observed as a broad band rather than sharp peaks as for Ih and Ic.<sup>56</sup>

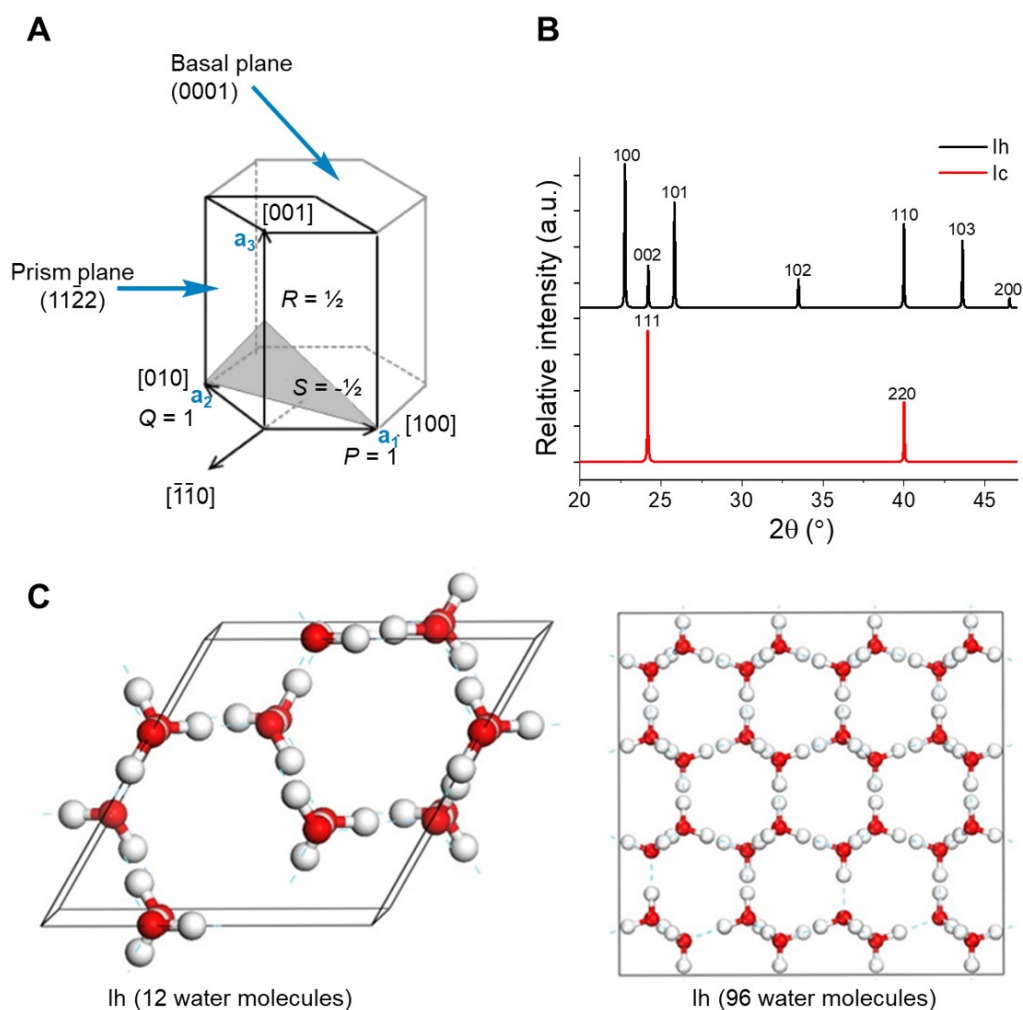


**Figure 3.5.** A) Hexagonal unit cell (bold) with 3 axes highlighted ( $a_{\#}$ , blue) from which the Miller indices (shown in brackets) are obtained; B) Calculated X-ray diffraction patterns of hexagonal (black) and cubic (red) ice with associated Miller indices for the crystal planes labelled from 20 – 47 ° (the available range for the setup used here); C) Unit cells for hexagonal ice obtained using various scattering experiments. Adapted from Santra *et al.* (J. Chem. Phys., 2013).<sup>50</sup>

### 3.3.5.2 Low Temperature XRD

X-ray crystallography has been of the upmost importance in the biology field; X-ray data has led to an increased understanding of mechanisms of action, validation of crystallographic structures and characterisation of protein flexibility and folding.<sup>26,57,58</sup> Scattering, specifically SAXS, has been found useful for probing conformational switching and aiding in assembly of complexes from atomic structures of subunits.<sup>58</sup>



Radiation from the X-ray beam has been an issue when studying proteins as it causes damage. However, recent work using cryo-cooled proteins and nucleic acids shows that cryo-SAXS protects the proteins and nucleic acids from radiation.<sup>59</sup> Knowing that performing experiments at cryo-temperatures protects protein structures is helpful, as we can be sure that the ice-active proteins used in this work (AF(G)Ps) will be folded correctly when studying their interaction with ice and thus give accurate results.

Low temperature XRD and SAXS have been used to determine the structures of certain additives, though limited research has been taken into their effect on ice growth.<sup>60,61</sup> Studies have monitored crystallisation, polymorphism, amorphous ice<sup>62</sup> and disorder in the Ih phase of frozen solutes, including ice-active solutes such as bovine serum albumin (BSA) and sorbitol.<sup>63-67</sup> Brief SAXS studies have been performed to study ice formation and growth. These have provided an initial, yet incomplete picture.<sup>61,68</sup> Cell viability post-thaw has also been examined for a range of cryoprotective media and CPAs, including DMSO and antifreeze proteins, alongside studies of their impact on ice structure.<sup>56,69</sup> As mentioned earlier, two macroscopic effects particularly relevant for X-ray experiments are DIS and IRI.<sup>70</sup> For example, XRD has been used with the aim of clarifying the ice growth inhibition mechanism; *i.e.* do proteins adsorb onto the ice or partition into the quasi-liquid layer (QLL)?<sup>67</sup> Studies include those on AFPs and synthetic mimics and their interaction with specific ice faces.<sup>71</sup> In these studies interaction is observed by monitoring the appearance/intensity of particular Ih diffraction peaks, which correspond to various ice planes and therefore morphology variations due to differing distributions of crystal orientations.<sup>71-73</sup>

Yagci *et al.* suggested that poly(tartar amides) interfere with the ice crystallisation process to cause partially deformed Ih structures.<sup>72</sup> A loss in intensity for diffraction peaks ((100), (002), (101)) has been suggested to be due to a decrease in crystal size, supporting the theory that hyperbranched copolymers containing poly(ethylene oxide)-polyethylenimine blocks have IRI activity as they produce crystals of a smaller size (submicrometer).<sup>73</sup> A complete loss of intensity of the (002) peak has also been suggested to confirm a change in morphology of the ice crystals, potentially due to binding of the plane corresponding to (002) *i.e.* preferential growth along the c-axis.<sup>74</sup> However, the disappearance of peaks does not actually confirm activity, (as we demonstrate later in the chapter).

How PVA exerts its effects on the Ostwald ripening of polycrystalline ice has yet to be studied thoroughly using X-ray techniques, though models have been suggested (based on molecular dynamics (MD) simulations) including the cooperative ‘zipper’ mechanism<sup>75</sup> or by using an anchored clathrate binding motif,<sup>76</sup> and that PVA binds (irreversibly) to the primary (100) prism plane and (reversibly) to the secondary (110) prism plane. This binding could theoretically be monitored by XRD.<sup>75</sup>

Studies here consist of crystal orientation analysis and diffraction pattern evaluation to analyse IRI and DIS. We propose a novel non-invasive method for 3D analysis of ice crystal growth, which provides information on the kinetics of the ice growth process for ice-active molecules.

### 3.4 Terminology

**Hexagonal ice ( $I_h$ )** – The phase of ice formed under atmospheric pressure below 0 °C. This phase is named due to its hexagonal symmetry. *All further mentions of “ice” in this chapter are specifically referring to hexagonal ice unless specifically noted.*

**Cubic ice ( $I_c$ )** - Metastable phase of ice, potentially formed at very low temperatures before converting to hexagonal ice.

**Colligative effects** - Effects that depend not on the identity of the solute, but the concentration of solute molecules dissolved species.

**Non-colligative effects** - Effects that depend on the identity of the dissolved species and the solvent *e.g.* IRI.

### 3.5 Chapter Aims

As written in section 1.3, ice-active additives could work *via* a range of mechanisms; adsorption-inhibition, anchored clathrate, interacting with the liquid-like layer *etc.* Much work has focused on AFPs, are based on molecular dynamics simulations, and there are still debates over the mechanism of ice growth and its inhibition. Due to their use in studying crystal growth mechanisms and crystal structures, X-ray techniques are of particular interest here.<sup>36</sup>

This work aims to:

- Investigate ice-active compounds of different structures and their effect on ice using XRD, these included cryoprotectants (CPAs) as well as those with IRI activity that cannot be used as CPAs due to toxicity<sup>3,70,77</sup>
- Produce a method for kinetic analysis of IRI activity
- Determine whether ice-binding can be determined and hence establish whether different ice-active compounds work *via* the same/different mechanisms

## 3.6 Results and Discussion

### 3.6.1 Compounds Studied

As in section 2.6.1, ice-active additives were chosen for study, this time using microscopy and X-ray diffraction, **Figure 3.6**. These included AFGP8 (antifreeze protein from *Dissostichus mawsoni*, 2.6 kDa), the shortest naturally occurring AFGP fraction, which has great IRI activity as well as ice-shaping abilities,<sup>78</sup> type III AFP (from *Zoarces americanus*, 6.5 kDa) and synthetic IRI's; PVA and safranin-O, as well as their respective inactive controls; lysozyme, PEG, and phenosafranin. The effect of conjugating antifreeze proteins to gold nanoparticles (AuNP) was also tested to study the impact of multivalency on ice- activity. This range of materials was used to test the suitability of X-ray and microscopy methods.

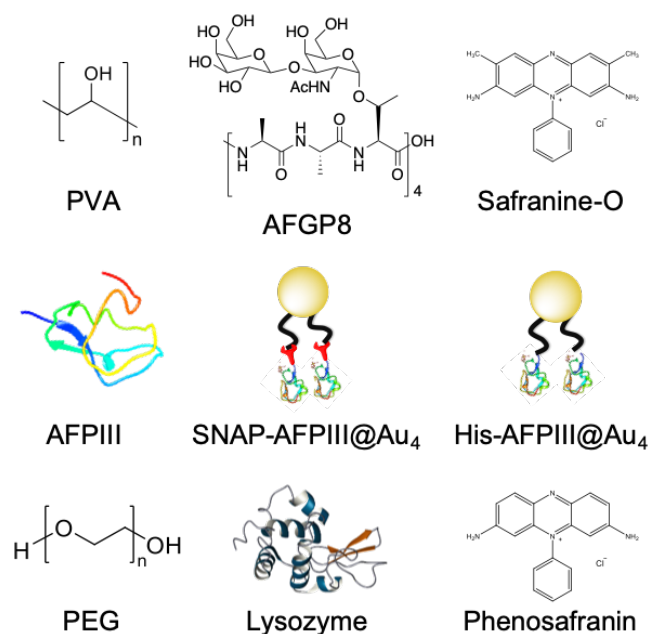


**Figure 3.6.** Structures of compounds studied here with the aim of analysing IRI activity and to gain further understanding of how they affect ice growth. Sizes of materials tested chosen based on previous known IRI activity and length scales are not expected to be of importance. PVA = 10 kDa; AFGP8 = 2.6 kDa; Safranin-O = 350.8 Da; AFPIII = 6.5 kDa; PEG = 4 kDa; Lysozyme = 14.3 kDa; Phenosafranin = 322.8 Da. Average AuNP diameters obtained from TEM (mean of 100 particles) for SNAP-AFPIII@Au<sub>4</sub> = 4.03 ± 1.1 nm and His-AFPIII@Au<sub>4</sub> = 4.26 ± 0.9 nm. (Structures AFPIII “1KDF” and lysozyme “1GXV” are from the Protein Data Bank).

### 3.6.2 IRI Activity as Measured by Splat Assays

The splat assay, as mentioned in 3.3.2, is the most commonly used method of determining IRI activity, thus has been selected here as the microscopy-based method of choice.

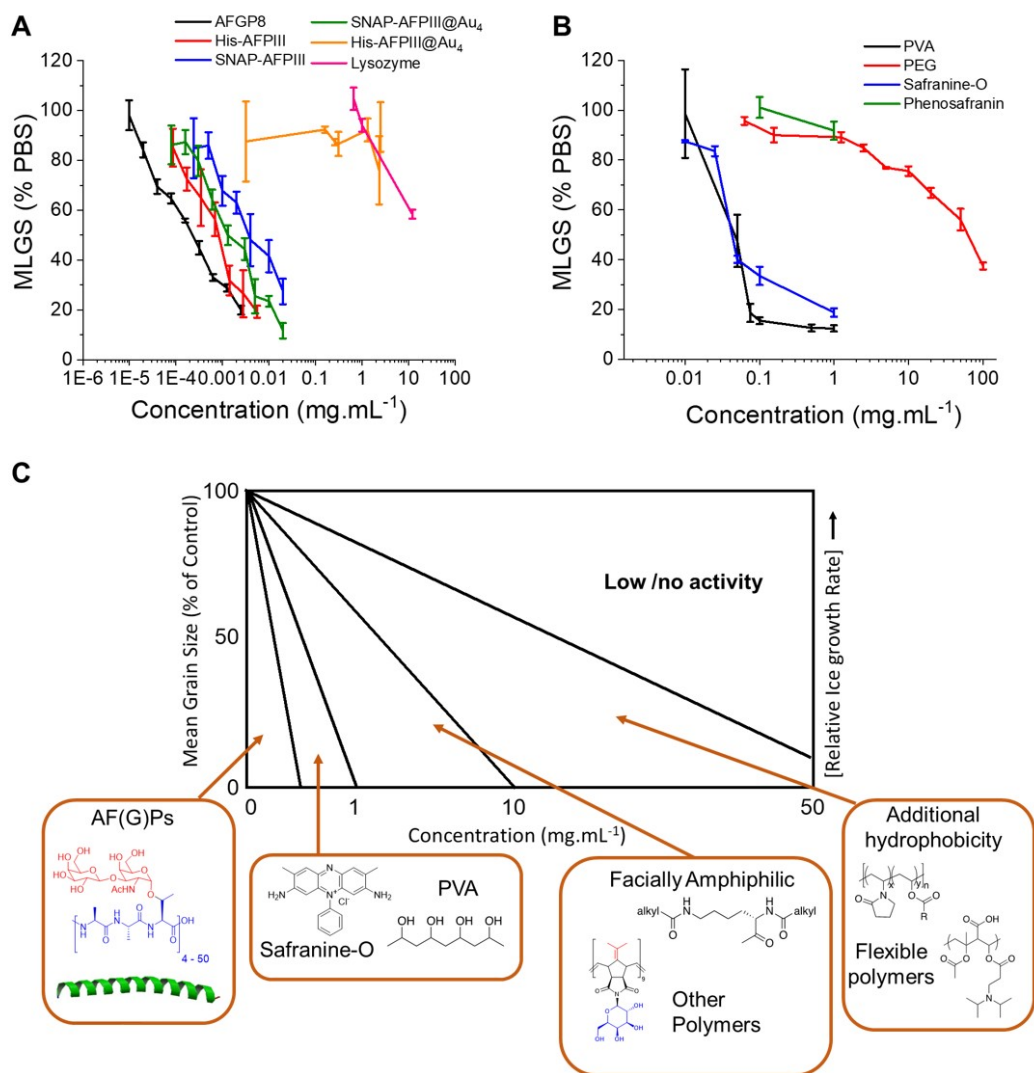


**Figure 3.7.** IRI activity of compounds tested here and relative activity of the different types of compounds tested. A) IRI activity as MLGS for proteins tested; B) IRI activity as MLGS for synthetics tested; C) Summary of the range of activities observed here and in the literature for a range of IRI active compounds. Adapted from Biggs *et al.*, (Macromol. Biosci., 2019).<sup>9</sup> Grain size is recorded after 30 minutes annealing at  $-8^{\circ}\text{C}$ .

Though the appropriate method of reporting IRI data is under debate; both MGS and MLGS have been used, and are compared here to identify IRI activity in the compounds chosen, **Figure 3.7A/B**. AFGP8 (black) is confirmed to have the highest

IRI activity, with 50 % activity at concentrations as low as  $0.15 \mu\text{g}\cdot\text{mL}^{-1}$ , followed by AFPIII (bound to both His- and SNAP-tags), then PVA and safranin-O. The inactivity of lysozyme, PEG and phenosafranin are also confirmed. As concentrations increase for compounds that exert colligative effects on ice *e.g.* PEG, the crystal size does reduce but in a manner that is expected due to the high concentrations in solution, **Figure 3.7B**.

Taking inspiration from Baardsnes *et al.*, who showed a gain in antifreeze activity upon formation of an AFP dimer,<sup>79</sup> and work by Stevens *et al.* on a dendrimer-linked AFPIII that had enhanced TH,<sup>80</sup> ice-activity was studied for AFPIII upon conjugation to a AuNP scaffold. The AuNP scaffolds were produced by Dr Laura Wilkins, University of Warwick. AFPIII was recombinantly expressed with both His- and SNAP-tags, and IRI activity tested; both of which lead to high IRI activity (red and blue lines respectively), **Figure 3.7A**. In multimeric ice-active protein samples, it has been suggested that the entire AFP ice-binding site is required to be sterically available for enhanced activity, indicating that a large scaffold/long linker between AuNP and the AFPIII would enable this availability. However, a smaller scaffold/shorter linker would enable the AFPIII molecules to be closer in space, potentially leading to multiple AFPIIIIs binding to the same surface and improving activity. Thus, two tags were chosen for the direct comparison of the length of linker; His being the shorter and SNAP being the longer. Successful conjugation was confirmed using X-ray photoelectron spectroscopy (XPS) and zeta potential measurements, and the AFP@Au<sub>4</sub> nanoparticles were characterised by DLS and transmission electron microscopy (TEM) by Dr Laura Wilkins, University of Warwick. Upon conjugation of the recombinant AFPs, the organic character of the samples was observed to have changed (N 1s proportion from XPS spectra increased from 0 % to ~12 % upon binding AFPIII for both samples and the O 1s peak decreased) and the zeta potential of the AuNPs decreased by over 5 mV upon AFPIII binding (because of the change in surface composition).<sup>81,82</sup> Upon conjugation IRI activity was retained, and slightly enhanced for SNAP-AFPIII (green), however activity was greatly reduced for His- AFPIII (orange), implying that a larger linker is preferable for an increase in activity when using multimeric proteins.

Other polymers of varying structures, with lower IRI activity, that have been tested using splat assays were not studied here, though the mean grain size and relative

growth rates compared to AF(G)Ps, PVA and safranin-O are visualised in **Figure 3.8C**.

### 3.6.3 Dynamic Ice Shaping as Measured by Sucrose ‘Sandwich’ Assays

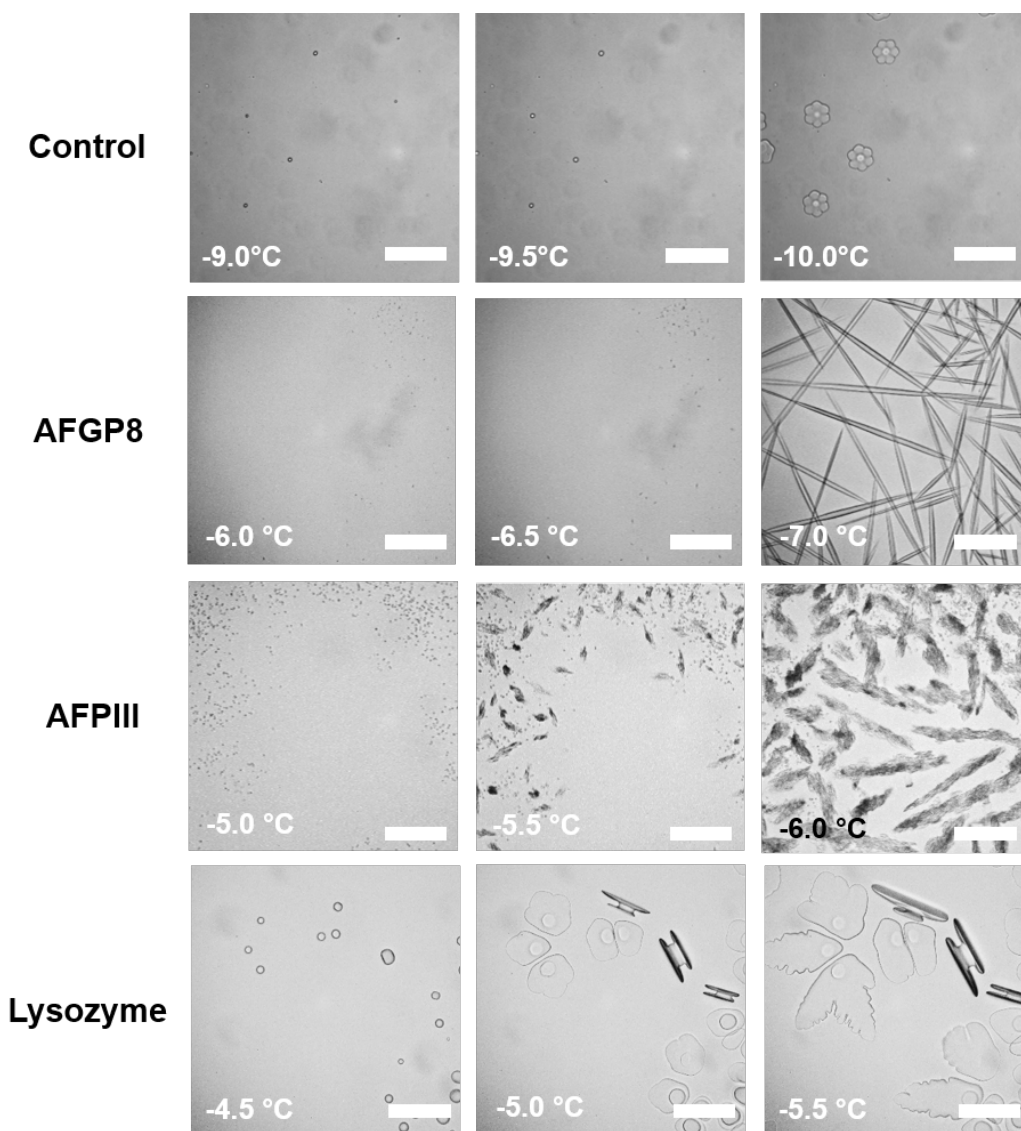


**Figure 3.8.** Optical microscopy ice morphology analysis of IRI active proteins compared to that of Milli-Q H<sub>2</sub>O and a negative control (lysozyme) cooling over time. Scale bars = 100  $\mu\text{m}$ . [AFGP8] = 3  $\text{mg}\cdot\text{mL}^{-1}$ ; [AFPIII] = 2.8  $\text{mg}\cdot\text{mL}^{-1}$ ; [Lysozyme] = 3  $\text{mg}\cdot\text{mL}^{-1}$ .

IRI is not the only macroscopic property of ice-binding/antifreeze proteins; ice shaping, due to binding to specific crystal faces also occurs<sup>70,77</sup> although it has



emerged that binding might not be essential for IRI and hence these macroscopic properties are not always present.<sup>77,83</sup> DIS is traditionally studied using sucrose ‘sandwich’ assays, and 45 wt % sucrose solutions were chosen here for the study of the samples in **Figure 3.6**.

Growth and morphology of ice crystals was monitored using an optical microscope. As well as proteins (**Figure 3.8**), ice shaping properties of polymers and small molecules have been tested (**Figure 3.10**). Typically water and dilute aqueous solutions (such as PBS, see control) display a crystal circular in shape, this is because this habit reduces interfacial energy between the ice crystal and solvent, which has a hexagonal burst pattern upon continued cooling.<sup>8</sup> The majority of samples tested show some ice shaping, albeit at varying strength and many form dendritic crystal shapes.

The differential affinities of AFGP8 and AFPIII to ice crystal planes compared to that of lysozyme are shown in **Figure 3.8**. Lysozyme is known to have no effect on ice formation and growth, and this is confirmed in the micrographs above; the crystals observed are similar to that of the control, leading to a hexagonal burst pattern, though at a faster rate. Both AFGP8 and AFPIII produce distinctive specular (needle-like) crystals due to ice-binding at the primary prism plane. The high IRI activity of these samples can also be observed, as the ice crystals at the starting point of the experiment are smaller ( $\sim 3 \mu\text{m}$  for AFGP8 and AFPIII) than that of the non-IRI active lysozyme ( $\sim 9 \mu\text{m}$ ).

The dynamic ice shaping abilities of metal-core nanoparticles bearing multiple copies of AFPIII bound to their surface compared to that of pure AFPIII were then studied, **Figure 3.9**. Faceting and dendritic morphologies was observed for all samples; consistent with ice-binding and shaping, as seen for dendronised AFP.<sup>80</sup> Binding of His-AFPIII to AuNP negatively affected IRI activity (larger crystals observed), supporting the observed results in the splat assays previously, they also affected ice morphology; crystals were no longer needle-like. SNAP-AFPIII@Au<sub>4</sub> also affected the morphology of the ice crystals compared to that of SNAP-AFPIII alone, leading to much more dendritic shapes than prisms/columns. The IRI activity is only affected slightly (as seen in the splat assays); grains are similar in size.

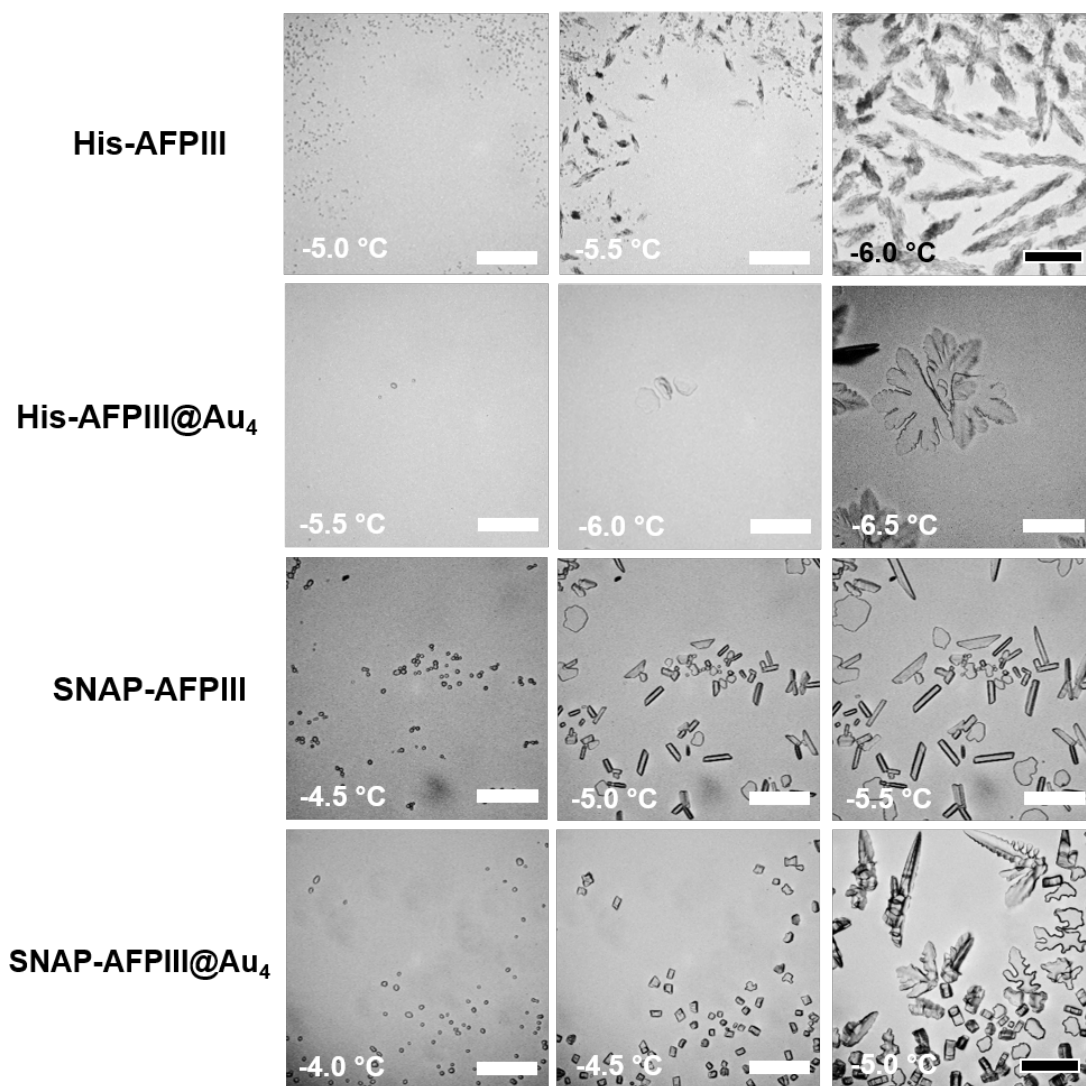


**Figure 3.9.** Optical microscopy ice morphology analysis of His-AFP1III and SNAP-AFP1III alone and bound to gold nanoparticles cooling over time. Scale bars = 100  $\mu\text{m}$ . [His-AFP1III] = 2.8  $\text{mg}\cdot\text{mL}^{-1}$ ; [His-AFP1III@Au<sub>4</sub>] = 2.3  $\text{mg}\cdot\text{mL}^{-1}$ ; [SNAP-AFP1III] = 0.10  $\text{mg}\cdot\text{mL}^{-1}$ ; [SNAP-AFP1III@Au<sub>4</sub>] = 0.13  $\text{mg}\cdot\text{mL}^{-1}$ .

Synthetic polymers have been designed to reproduce AF(G)P properties even without any structural similarities to native antifreeze proteins.<sup>3,70,77</sup> In particular, it has been shown that IRI activity can be selectively retained, over TH/DIS, implying there are multiple mechanisms of action for the different ice-active molecules.<sup>84</sup> Sucrose ‘sandwich’ assays performed on synthetic mimics here (**Figure 3.10**) show that DIS does not occur for some samples, even IRI active ones, supporting the theory that there are multiple mechanisms of action and that DIS does not infer IRI activity or vice versa.<sup>77,83</sup>

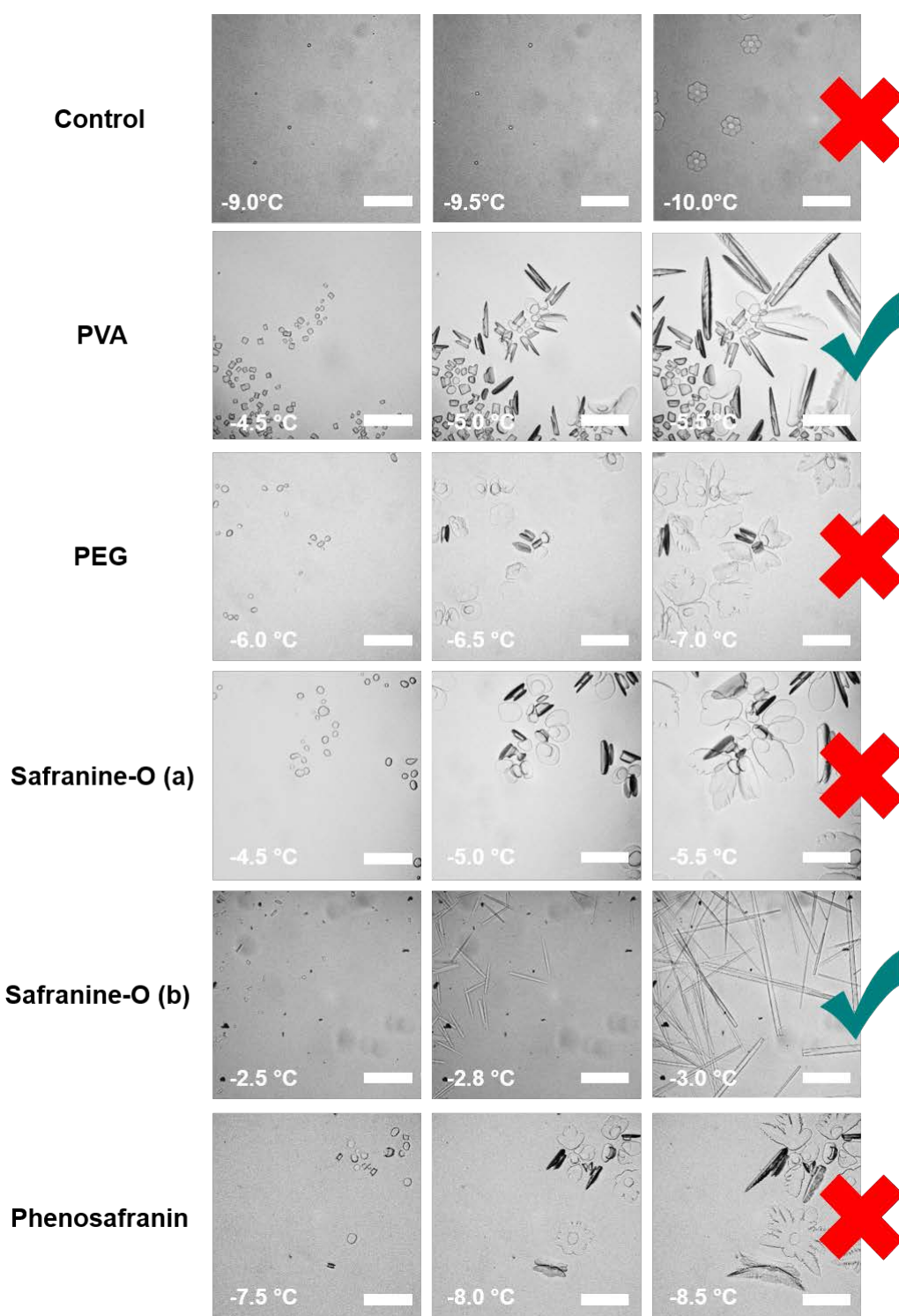


**Figure 3.10.** Optical microscopy ice morphology analysis of IRI active synthetic compounds tested here compared to that of Milli-Q H<sub>2</sub>O. Scale bars = 100 μm. [Sample] = 1 mg.mL<sup>-1</sup> bar safranin-O; (a) = 0.1 mg.mL<sup>-1</sup> and (b) = 2.5 mg.mL<sup>-1</sup> to visualise how self-assembly of the small molecule affects the DIS. Ice shaping (green tick) or lack of shaping (red cross) indicated.

It can be observed that PVA shapes ice by binding the prismatic plane leading to the

growth of the crystal grains observed in **Figure 3.10**, whereas PEG alone appears to affect the ice grains minimally – producing crystals of a similar shape to that of pure water, ruling out strong and specific ice face recognition. Safranin-O, above  $1 \text{ mg.mL}^{-1}$ , is known to self-assemble in solution,<sup>85</sup> and the effect of self-assembly is observed here; ice-shaping is not observed at low concentration (a), however ice-shaping is observed for (b), where the concentration is high enough for self-assembly, leading to the formation of needle-like crystals. All DIS-inactive samples show a slight difference in morphology to the water control (though are similar), this is due to the crystal bursting (into the hexagonal burst pattern) at a faster rate as well as the ice crystals that remain in these samples (as the sample is warmed) being closer in proximity to each other, causing growth of certain planes to be obstructed.

### 3.6.4 XRD

Both SAXS and XRD were used initially, however the resolution of SAXS results were not high enough to obtain any reliable data so only XRD was continued with.

Using XRD, the concerning I<sub>h</sub> crystals formed under standard conditions were examined and from the resulting diffractograms ice-activity was followed for the same samples tested in **3.6.2** and **3.6.3**. No broad, low intensity peaks were observed, indicating no amorphous phases are formed in these samples upon freezing. Thus all ice observed in this work is polycrystalline, containing hundreds of crystallites, leading to diffraction patterns consisting of all expected diffraction peaks for hexagonal ice.<sup>52</sup> As mentioned in **3.3.3**, a percentage of these crystallites will orient to diffract the X-ray beam, meaning it is possible that the peak intensity will differ for identical samples, depending on how the crystallites are oriented. Generally, the peak intensities (height) are related to the composition and structure of the crystal and are what would normally be used for analysing XRD data. Peak width (area) is dependent on instrumental function and any size related effects; the smaller the grain size, the wider the peak. In this work the ice grains are too large to have much of an effect on peak widths, therefore work here considers the number of crystal orientations obtained from the integration of the peak areas.

The XRD Xenocs Xeuss 2.0 used here was particularly useful due to its ability to see scattering from individual grains because of the 2D detector. This was only possible

because of the large size of the ice grains, which reduces the number of possible orientations that can exist in a set sample volume. This means there are not grains diffracting at every  $\psi$  (psi) angle and allows information proportional to number of grains to be calculated.

Splat assays have been used to follow ice recrystallisation (or lack of), and XRD is tested here, as another technique that, due to its use in observation of crystal formation in other fields;<sup>27,86</sup> including observing nucleation/growth of gold nanoparticles<sup>86,87</sup> and titanium oxide particles over time,<sup>88</sup> as well as evaluating phase structure, precipitate growth and coarsening of alloys using combined ultra-small, small and wide angle X- ray scattering,<sup>89</sup> and observing ice polymorphs,<sup>44</sup> can observe ice growth easily *via* 3D analysis of an entire sample over time. Here, the diffracted X-rays hit the Pilatus detector sensor and repeat measurements were taken over 10 s for a total of 1800 s. The photons are absorbed and generate a charge cloud, which is carried through the sensor by an electric field. These charge-induced photons are detected by a readout chip and amplified and digitally stored as data. The data obtained for each 10 s measurement is converted into a plot consisting of the intensity per pixel as a function of  $2\theta$ , with each individual measurement plotted together over time, **Figure 3.11A**. Each peak represents the different lattice planes for the ice crystals in the samples [Note, further details on XRD fundamentals provided in **3.3.3**]. Example diffractograms as a function of time for ice crystals annealed at -8 °C in the presence of a potent IRI (PVA) and a negative control (PEG) are seen in **Figure 3.11A/B**. The characteristic peaks of ice at 22.7, 24.2 and 25.8 ° (corresponding to the (100), (002) and (101) planes respectively) are clearly visible as would be expected for Ih and is in agreement with **Figure 3.5**. Of note, is that in the presence of PVA, the diffractograms are essentially constant over the whole time period, indicative of there being no ice recrystallisation (growth). In contrast, the PEG sample shows significant decreases in the scattering intensity for most peaks, which is consistent with ice recrystallisation (large ice crystals growing). This confirms that in principle, XRD should allow for both endpoint and kinetic analysis of IRI activity. Example ice wafers from the splat assay under the same conditions are shown in **Figure 3.11C/D**; this technique does not allow continuous data acquisition in the same way and measurements are only of the section of sample observed under the microscope.

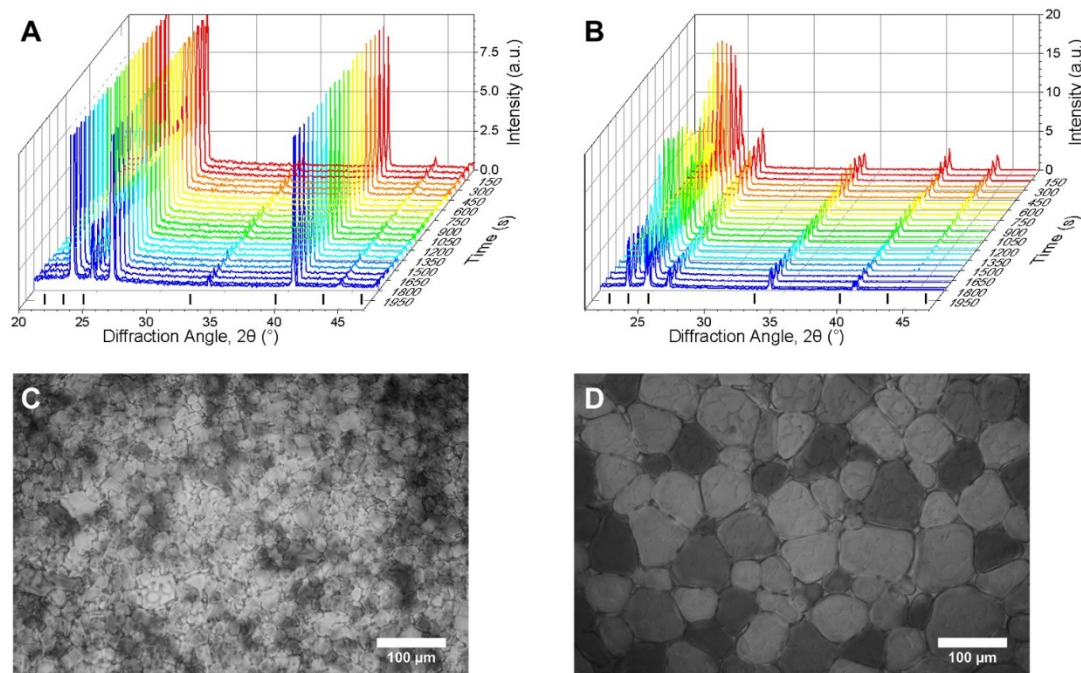


**Figure 3.11.** Example waterfall plots of diffraction patterns obtained in this work that are used for kinetic analysis of change in number of crystal orientations over time with expected Ih crystal planes included in black below the plots; A) PVA and B) PEG; Optical micrographs obtained after 30 minutes annealing for C) PVA and D) PEG. All data obtained at  $-8\text{ }^{\circ}\text{C}$ .  $[\text{Polymer}] = 2.5\text{ mg.mL}^{-1}$ .

#### 3.6.4.1 Methodology

XRD provides details on crystallite orientations and intensity; the number of crystallite orientations for each sample, and how this number changes over continuous measurements. The sum of the intensity of the whole X-ray detector can be calculated, as well as the intensity for individual  $2\theta$  values.

To enable quantitative analyses of the ice recrystallisation, the total number of ice crystal orientations observed for a sample was calculated, which in a powder sample is proportional to the number of crystals, and hence inversely proportional to the size of the ice crystals. When ice crystals in a sample increase in size (recrystallisation), the number of grains detected by XRD decreases, which may lead to a decrease in scattering intensity.



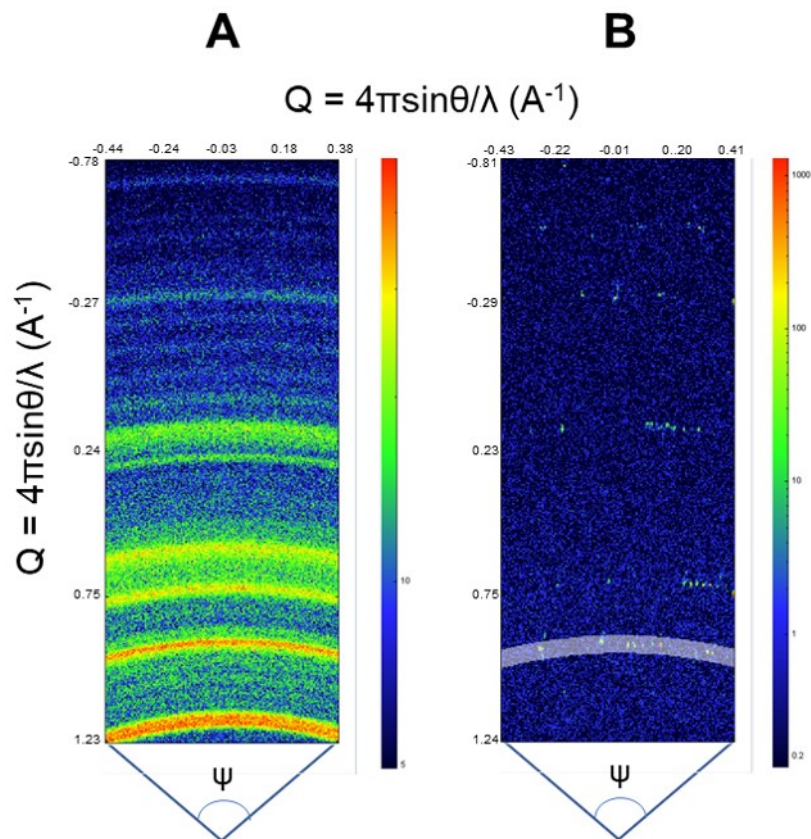


**Figure 3.12.** Example 2D detector images for a powder. A) Ag behenate (used to calibrate the sample to detector distance beforehand); B) Example ice measurement; orientations are observed as pixels above the determined background value of 1.5 counts highlighted in semi-transparent band and counted every  $0.2^\circ$  over  $\psi$  range of  $76 - 105^\circ$ .

To obtain the number of ice crystal orientations (# orientations) over time from 2D detector images (examples in **Figure 3.12**), a series of steps are followed:

First, the  $2\theta$  ranges that cover each of the seven peaks (for the Miller indices that correspond to the different planes in Ih) that are measured in the diffraction patterns (like those seen in **Figure 3.11A**) are selected for each time point. An example  $2\theta$  range for the first peak is shown in **Figure 3.13A/B**. The 2D detector image is then integrated azimuthally [along the powder diffraction rings/bands] as a function of  $\psi$  seven times with  $2\theta$  ranges determined from the diffraction peaks to obtain the intensity at each  $\psi$  angle. (The step size in  $\psi$  for this was  $0.2^\circ$ . For this work, the size of the detector limits the available orientation range in  $\psi$  to between  $76$  and  $105^\circ$ ). The intensity versus  $\psi$  data for the selected  $2\theta$  range is then plotted and the number

of data points above a determined background value (1.5 counts used) are then counted. These data points are relative to the number of orientations in that particular plane, examples of IRI active and inactive samples are shown filled in red in **Figure 3.13C/D**. The total counts for each plane are summed to give the total number of orientations for a sample. With this methodology orientations are obtained as not every individual pixel is counted (unlike in a normal powder pattern).

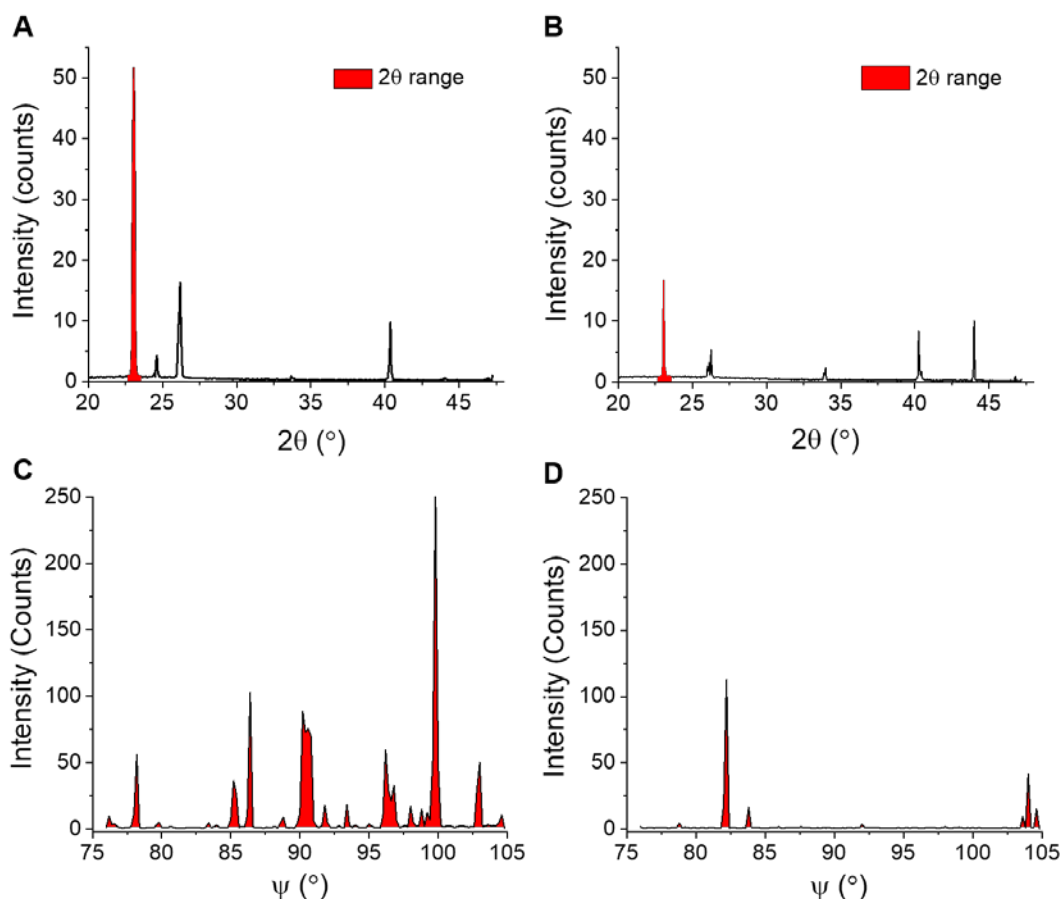


**Figure 3.13.** Example plots used in the quantitative analysis of ice recrystallisation. A/B) Example XRD plots used to calculate crystallite orientations of; A) IRI active PVA and B) non-IRI active PEG, plotted as a function of  $2\theta$ . Selected  $2\theta$  ranges used to analyse the crystallite orientations scattering are coloured red; C/D) Orientation plots of C) PVA and D) PEG, plotted as a function of  $\psi$  for intensities measured in the selected  $2\theta$  range. All data obtained at  $-8^\circ\text{C}$ .  $[\text{Polymer}] = 2.5 \text{ mg.mL}^{-1}$ .

As the concentration of an IRI active substance increases, the relative ice growth rate is expected to decrease due to the inhibition of ice crystal growth. This is because there are many orientations, which correspond to many small crystals. If there is an observed



decrease in the number of orientations, this is due to Ostwald ripening; where the larger crystals increase in size at the expense of the small crystals.

One limit in using this technique is reached when the number of grains is large enough that diffraction occurs at all  $\psi$  angles. Under-determination of number of crystals could be an issue if the crystallites are sufficiently small and the number of orientations very large (when the number of grains is large enough that diffraction occurs at all  $\psi$  angles), resulting in the measured intensity being above the threshold value at every data point. This would put a limit on the maximum number of orientations that can be determined as the total number of data points in the azimuthal integrations. This is not an issue in the samples tested here but it is important to highlight that evaluation with an optical method in parallel is still required. This limit is equipment dependent and could be improved by increasing the sample to detector distance or by using a detector with a reduced pixel size. In the lab-based system used here the physical size of the detector reduces the total number of peaks that can be measured. Larger detectors are available for some lab-based systems and are readily available at synchrotrons.

#### 3.6.4.2 IRI Activity as Measured by XRD

To assess the use of the above method, the compounds chosen in **3.6.1** were tested and compared against the standard splot assay. In each case, XRD experiments were performed over 1800 seconds (30 minutes) and then the number of orientations is calculated as described above and plotted as inverse number of orientations to enable easier comparison to microscopy data.

A comparison of XRD and microscopy results for AFGP8 and lysozyme are seen in **Figure 3.14A**. The MLGS and XRD methods show broad agreement. There are more ice crystal orientations at IRI active concentrations (MLGS <20 %), indicating more, smaller crystals. This trend is also observed in **Figure 3.14B**, where the IRI active samples have similar inverse number of crystal orientations, and the inactive samples, His-AFP<sub>III</sub>@Au, lysozyme and PBS, also have similar inverse number of orientations.

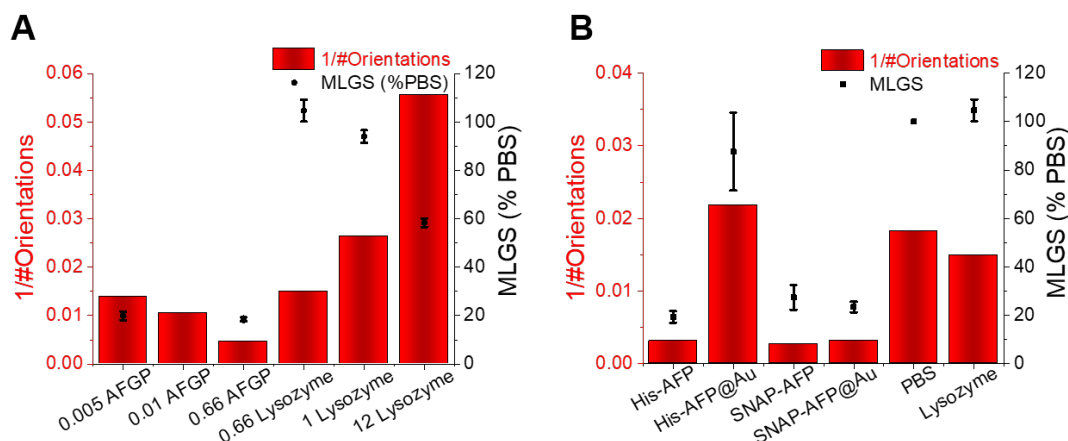


**Figure 3.14.** Comparison of orientation analysis (here shown as inverse number of observed ice crystal orientations after 1800 seconds) and IRI activity (shown as mean length grain size, MLGS, as a percentage of PBS) over a range of concentrations for; A) AFGP8 compared to lysozyme; B) His-AFP and SNAP-AFP alone and bound to gold nanoparticles compared to PBS and lysozyme. [His-AFP] = 2.8 mg.mL<sup>-1</sup>; [His-AFP@Au] = 2.3 mg.mL<sup>-1</sup>; [SNAP-AFP] = 0.10 mg.mL<sup>-1</sup>; [SNAP-AFP@Au] = 0.13 mg.mL<sup>-1</sup>. All concentrations are in mg.mL<sup>-1</sup>, errors are standard deviation. All data obtained at -8 °C.

For PVA, the MLGS values also trend with the inverse number of orientations; with MLGS increasing and number of orientations decreasing (due to Ostwald ripening) as the concentration decreases, **Figure 3.15A**. **Figure 3.15B** shows PEG, indicating essentially no activity even at very high concentrations (up to 50 mg.mL<sup>-1</sup>), where non-specific effects dominate. Encouraged by these results, the self-assembling IRI active safranine-O was tested, versus phenosafranin, which cannot self-assemble and has no IRI. By both MLGS and XRD analysis, it can be seen that only safranine-O inhibits ice growth, with the same trend being observed for inverse number of orientations and MLGS values as for proteins and PVA, **Figure 3.15C/D**. These results demonstrate that this is a valid analysis method for IRI activity for a range of compounds, including more complex structures, and is complementary to the traditional optical-based methods.

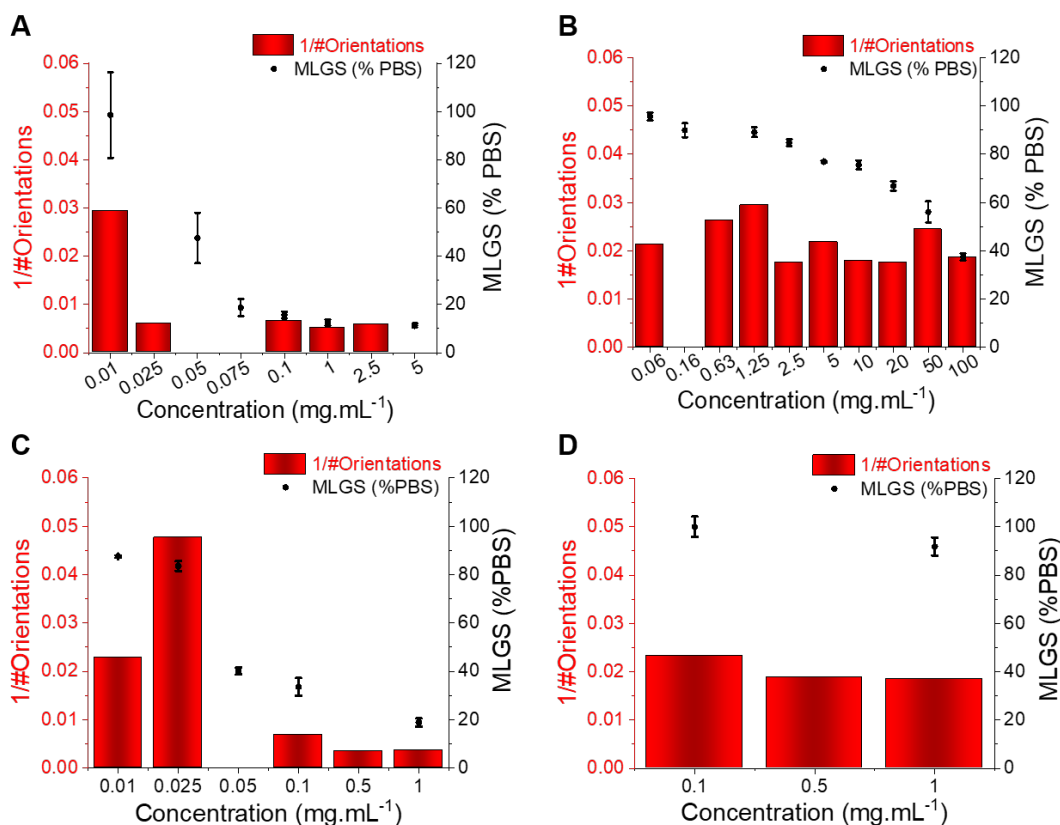


**Figure 3.15.** Comparison of orientation analysis (here shown as inverse number of observed ice crystal orientations after 1800 seconds) and IRI activity (shown as mean length grain size, MLGS, as a percentage of PBS) over a range of concentrations for; A) PVA; B) PEG; C) safranin-O; D) phenosafranin. All concentrations are in mg.mL<sup>-1</sup>, errors are standard deviation. All data obtained at -8 °C.

### 3.6.4.3 Kinetics of Ice Crystal Growth

A common challenge in the microscopy-based methods is extracting kinetic information. For XRD this is far simpler; the Xenocs Xeuss 2.0 used here has a PILATUS 100k detector that can collect 3D data every 14 seconds (10 s acquisition with a 4 s delay between measurements). This diffraction data includes, for example, information on the number of crystal orientations in each 14 s collection. When there is Ostwald ripening there is a decrease in the number of crystal orientations. The kinetics of this process can be followed by obtaining the rate of change in number of orientations over time.

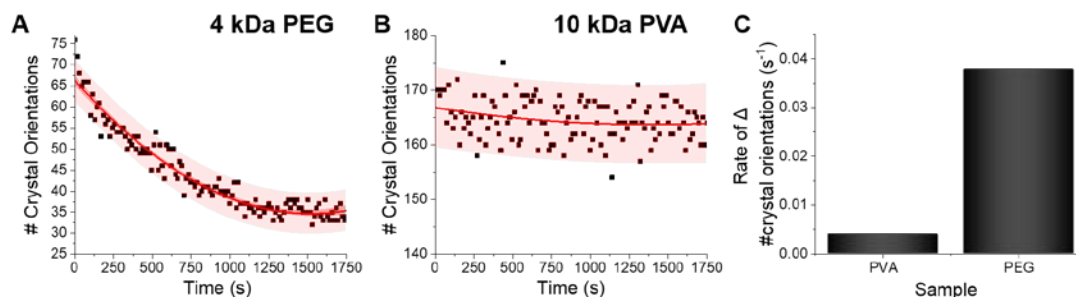


**Figure 3.16.** Examples of how rates of ice recrystallisation are obtained using XRD. Changes in orientations observed for A) PEG and B) PVA; C) Comparison of rate obtained from the initial gradient of the fit (red line). [Polymer] = 2.5 mg.mL<sup>-1</sup>. All data obtained at -8 °C.

The change in the number of orientations (*i.e.* number of crystals) for ice in the presence of non-IRI active PEG can be seen in **Figure 3.16A**. There is a clear decrease in number of crystals due to ice growth over the time course of the experiment. The same analysis for PVA (**Figure 3.16B**) shows a constant number of orientations, indicating a static process, and hence recrystallisation inhibition. It is important to note at this point that the actual magnitude of the number of crystals will vary in each sample due to the different nucleation rates (which is also hard to control), however the change is the part which is of interest here, and data can be normalised to the  $t=0$  points.

Ice crystal growth rates were obtained for PVA and PEG from the gradient of change in number of crystal orientations, **Figure 3.16C**, showing that a parameter for ice growth can be extracted if required; the steeper the slope, the faster the ice crystal growth. The rate of change in number of crystal orientations is much greater for PEG than for PVA.

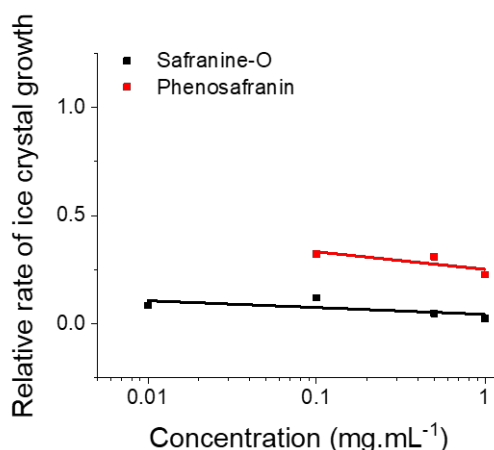


**Figure 3.17.** Relative ice growth rates compared to that of ice crystal growth for pure water for a range of concentrations; safranine-O (black) and phenosafranin (red) after 1800 seconds annealing at  $-8\text{ }^{\circ}\text{C}$ .

Relative growth rates were also obtained for samples over a certain concentration range. Relative rates were calculated by comparing the rate of change in number of orientations for a sample to that of a water control. As the concentration of IRI active safranine-O increases, the calculated gradient of initial change in number of crystal orientations gradually tends towards zero, from an increase in  $0.007\text{ crystals.s}^{-1}$  to  $0.002\text{ crystals.s}^{-1}$ , though the growth is minimal in any case, **Figure 3.17**. The rate for inactive phenosafranin also decreases but is up to 10x faster than that of safranine-O, with an average increase of  $0.026\text{ crystals.s}^{-1}$ .

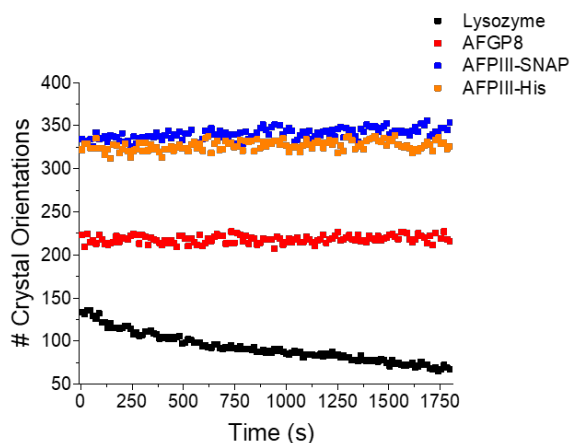


**Figure 3.18.** Number of crystal orientations over time for different proteins studied in this work.  $[\text{Lysozyme}] = 0.7\text{ mg.mL}^{-1}$ ,  $[\text{AFPIII-His}] = 0.4\text{ mg.mL}^{-1}$ ,  $[\text{AFPIII-SNAP}] = 0.1\text{ mg.mL}^{-1}$ ,  $[\text{AFGP8}] = 0.07\text{ mg.mL}^{-1}$

Analysis of number of crystal orientations over time for several protein samples was

then obtained, showing similar trends to that of PVA and PEG, with the AF(G)Ps showing no change in number of orientations (and number decreasing for lysozyme) over 1800 s, **Figure 3.18**. The concentrations chosen were concentrations at which comparable IRI activity has been observed (AFGP8 is known to be highly active down to concentrations of  $0.15 \mu\text{g}\cdot\text{mL}^{-1}$ ), bar lysozyme, as this is a non-IRI active material.

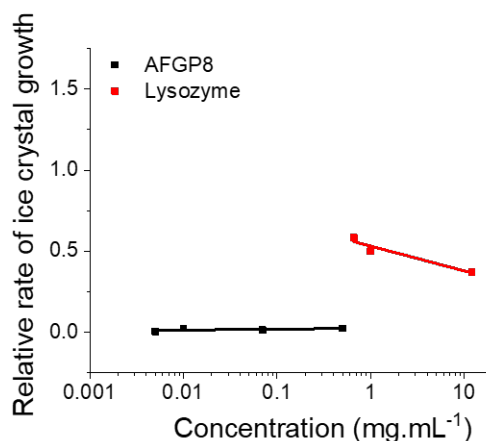


**Figure 3.19.** Relative ice growth rates compared to that of ice crystal growth for pure water for a range of concentrations of AFGP8 (black) and lysozyme (red) after 1800 seconds annealing at  $-8 \text{ }^{\circ}\text{C}$ .

Further concentrations of AFGP8 were tested by XRD and the relative rate of ice crystal growth plotted. For the concentrations of AFGP8 here, **Figure 3.19**, the mean rate of change in ice crystal orientations does not change – this is because AFGP8 is extremely active, even at low concentrations (lowest concentration tested here was  $0.005 \text{ mg}\cdot\text{mL}^{-1}$ ). The average rate for all concentrations is  $0.00125 \text{ crystals}\cdot\text{s}^{-1}$ , which is much lower than that of the lysozyme control, which is  $0.041 \text{ crystals}\cdot\text{s}^{-1}$ . 3 concentrations of lysozyme, a non-IRI active protein were tested and the initial rate of change in number of crystal orientations barely differed; even between concentrations of 1 and 12  $\text{mg}\cdot\text{mL}^{-1}$ , with rates of  $0.042$  and  $0.031 \text{ crystals}\cdot\text{s}^{-1}$  respectively, thus lysozyme decreases in number of orientations therefore has fewer, but larger ice crystals after the 1800 s anneal. The mean rate for the samples was found to be  $0.041$  and was compared to all AF(G)P samples tested.

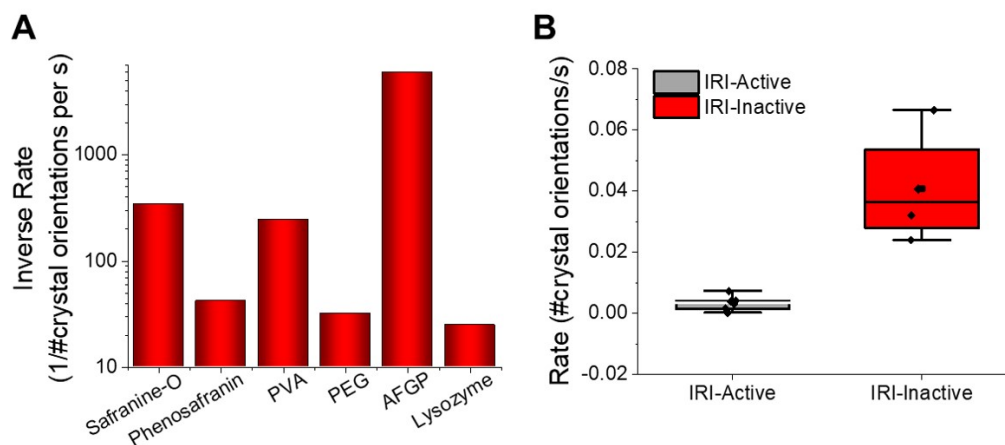


**Figure 3.20.** A) Inverse average rate of change in number of observed ice crystal orientations over 1800 seconds for a small molecule (safranin-O), polymer (PVA) and protein (AFGP8) compared to their relative non-IRI active controls (phenosafranin, PEG and Lysozyme); B) Box plot of the mean gradients of change and standard deviation for IRI active (grey) and inactive samples (red). Mean = black square, individual data points = white hexagons. All data obtained at  $-8^{\circ}\text{C}$ .

The rates obtained from the change in number of crystal orientations are compared for safranin-O and PVA compared to AFGP8 in **Figure 3.20**. The rates of crystal growth for all IRI active compounds can be seen to be close to zero, whereas that of the inactive controls it is higher, **Figure 3.20B**. A more thorough investigation of the  $I_h$  diffraction patterns using a different setup (other diffractometers can more precisely record peak widths) would need to be undertaken to obtain the exact number of ice crystals and possibly acquire rate constants and allow for a more in-depth discussion of the meaning of peak width in relation to strain and crystal size. This could include using larger detectors, readily available at synchrotrons, to increase the number of crystal orientations measured and improve the counting statistics when measuring large grain sizes or a detector that could be moved in  $2\theta$  to allow for an increased number of points across a peak to be measured than can be achieved when relying on the pixel size of a static detector like the one used here. This could be combined with a monochromated X-ray source giving pure  $\text{Cu K}\alpha_1$  radiation to allow accurate comparisons of peak widths. Light scattering is another potential technique that could be used to investigate light scattering properties of ice crystals as the scattering pattern would be determined by the ice crystal's size and shape. Though, this technique would be of more use in cloud chambers. The X-ray scattering technique

works for bulk ice samples because the diffraction pattern is formed by X-rays that have only interacted with one crystal grain. The light scattering method would struggle when interacting with multiple crystallites.

### 3.6.4.4 Dynamic Ice Shaping as Measured by XRD

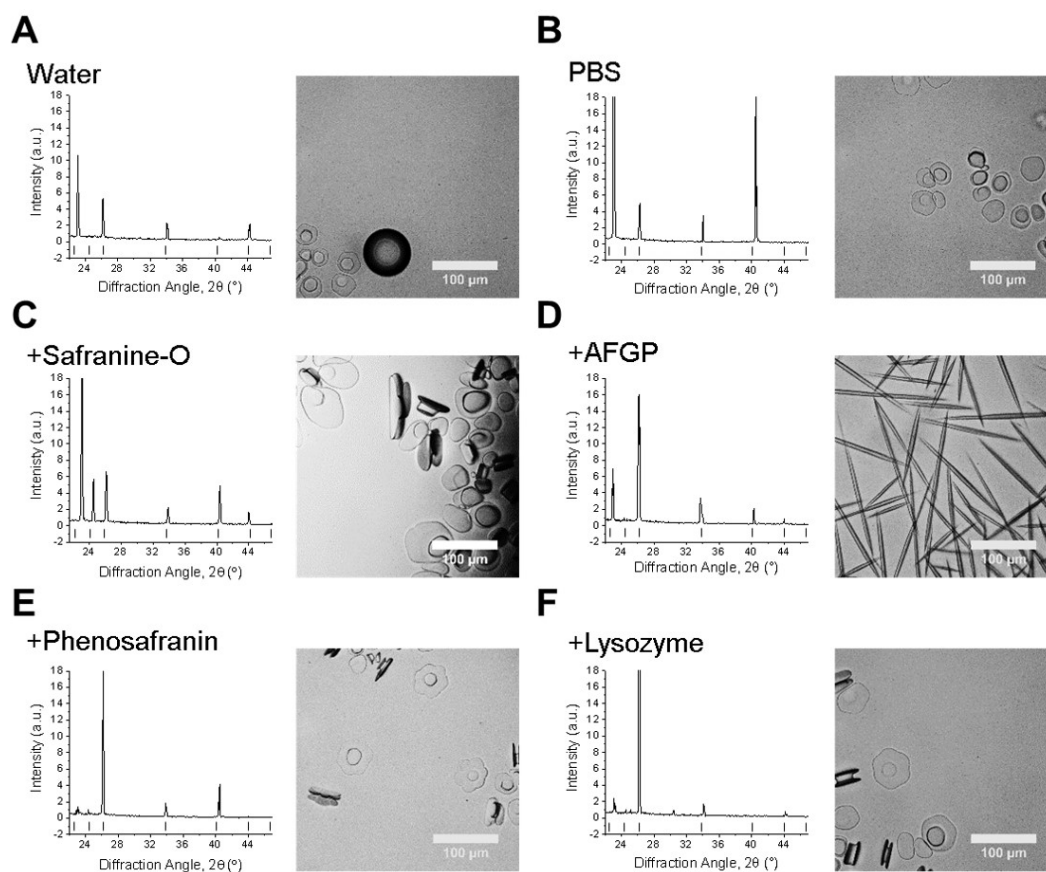


**Figure 3.21.** Crystal habit modifications by additives. Left) Ice diffraction patterns after 1800 s annealing for: samples with known ice-binding and shaping abilities, their relative non-binding controls and water/PBS); Right) Optical microscopy ice morphology analysis in 45 wt % sucrose of samples in the corresponding diffractograms. A) Water control; B) PBS control; C) Safranin-O; D) AFGP; E) Phenosafranin; F) Lysozyme. Scale bars = 100  $\mu\text{m}$ . [Safranin-O] = 1.0  $\text{mg}\cdot\text{mL}^{-1}$ ; [AFGP8] = 3.0  $\text{mg}\cdot\text{mL}^{-1}$ ; [Phenosafranin] = 1.0  $\text{mg}\cdot\text{mL}^{-1}$ ; [Lysozyme] = 1.0  $\text{mg}\cdot\text{mL}^{-1}$ .

Ice diffraction patterns and ice shaping for all three groups of compounds tested here are seen in **Figure 3.21**. The difference in the diffraction patterns between water and



PBS was first analysed to confirm similarities and differences – this was due to the salts' potential colligative effects on ice growth and Ih structure, **Figure 3.21A/B**. The results from PBS samples are more relatable to biological samples and those in water would be more relatable to samples used in other fields, for example engineering and atmospheric chemistry. The structure for both is deemed to be Ih, though there are slight intensity variations for the Ih pattern between the two, but intensity variations are also seen in other samples, and are due to which crystallites orient towards the beam and not related to any 'ice-activity' of PBS.

The (002) plane ( $2\theta = 24.2^\circ$ ) has been said to be missing in ice samples with additives,<sup>72,73</sup> and is often explained as the additive showing ice-binding/DIS activity. Here measurements are taken using a static capillary, where the crystallites formed are too large to ensure a random distribution is sampled, thus structure analysis cannot be completely determined. A potential method to solve this problem would be to perform XRD whilst spinning the capillary, however there could still be preferred orientation effects. However, the static nature of this setup means that the range of orientation angles we are sensitive to does not change over time, meaning that for randomly distributed ice crystallites the number of orientations measured are proportional to the total in the sample. Due to differences in experimental setup and lack of detail in the literature, it is difficult to determine whether studies had randomly oriented crystallites/sampled a large enough range of crystallites to confirm ice-binding/DIS.<sup>73,90,91</sup> Measurements made when freezing on a surface, will be affected by preferred orientation, thus may not give clear evidence of binding. Hence, the disappearance of a peak cannot solely be used to describe ice crystal morphology/binding accurately. For example, AFGP8 affects ice morphology by binding the primary prism plane, so would have a peak missing corresponding to this plane, but pure water (or PBS) would show all Ih peaks, however the  $24.2^\circ$  peak is missing in all samples, **Figure 3.21A/B/D**. The same peak should also be missing for safranin-O, however, is observed here, **Figure 3.21C**. Similarly, phenosafranin and lysozyme have no known ice-binding so the lack of  $24.2^\circ$  peak seen in **Figure 3.21E/F** cannot represent this. This shaping or lack of ice shaping is observed in the provided micrographs.

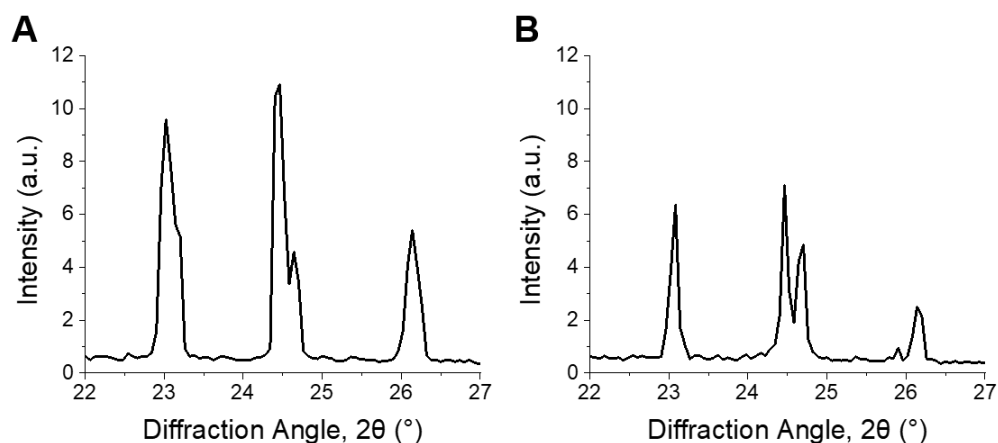


**Figure 3.22.** Ice diffraction patterns after A) 0 s and B) 1800 s annealing for 4 kDa PEG ( $2.5 \text{ mg.mL}^{-1}$ ). All data obtained at  $-8^\circ\text{C}$ .

Peak disappearance, if relating to binding, would occur repeatedly, yet PEG at  $2.5 \text{ mg.mL}^{-1}$  shows peak splitting at (002), which becomes more pronounced over the 1800 s anneal. This peak remains throughout, further refuting the claim that this indicates binding to an ice plane, **Figure 3.22**.

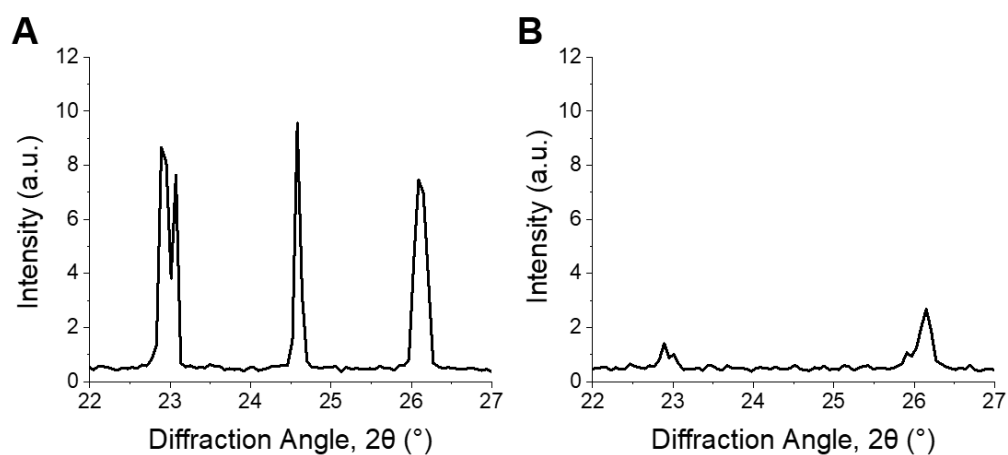


**Figure 3.23.** Ice diffraction patterns after A) 0 s and B) 1800 s annealing for 4 kDa PEG ( $0.63 \text{ mg.mL}^{-1}$ ). All data obtained at  $-8^\circ\text{C}$ .

Another example contradicting the theory peak disappearance relates to binding is for PEG at  $0.63 \text{ mg.mL}^{-1}$ , **Figure 3.23**. PEG is known not to bind ice or affect morphology, and at  $t=0$  minutes the (002) peak is observed, however as the ice annealed, the intensity of the peak decreased gradually, until at 30 minutes it was no longer observed. This supports the theory that peak intensity relates to the size of the crystallites rather than ice-binding. This may be because as the grain size increases,

the scattering signal from that grain will also increase, but as the grains in the system grow in size, the total number of grains decreases, which can also result in a decrease in signal.

When there is a change in ice grain size, particularly growth due to Ostwald ripening, fewer crystal orientations are observed and peak intensity changes. This can cause particular orientations to not scatter the X-ray beam leading to peak disappearance, thus the diffraction pattern peaks cannot be used to describe ice crystal morphology accurately in these disordered samples. This is crucial to show the limitations and applications of this method to explore the kinetics of ice recrystallisation as a complementary tool to optical microscopy.

### 3.7 Conclusion

XRD was used as a non-invasive method for 3D analysis of ice crystal growth (recrystallisation) and compared to the more commonly used optical techniques. This method gives the number of orientations in polynucleated samples (which is proportional to the number of crystals), rather than the actual number of ice crystals that may be counted from a micrograph. This method is complementary, as measurements are performed in a capillary (3D conditions), which facilitates the measurement of a larger number of crystals in the system, as well as being preferable to 2D systems, where the sample holder will have a greater effect on the growth mechanisms. This technique provides more information at another lengthscale not only micrometres. Furthermore, data can be obtained every 14 seconds (for this particular instrument, with the rate depending on individual facilities), enabling real-time kinetic analysis without analysing each frame from videos/micrographs.

Using this method, the IRI activity of a range of synthetic and biological ice-active compounds was compared and found that it was in good agreement optical methods. This was performed by following ice growth by calculating the relative number of ice crystal orientations from  $2\theta$  ranges that cover each of the seven  $I_h$  peaks from each diffraction pattern at every time point. A fitting method was then developed to obtain simple kinetic data, which provides an advantage over that of optical methods. This consisted of plotting the number of crystal orientations as a function of time and obtaining the gradient of change in number of orientations, which was then extracted as a rate and compared to that of pure water and PBS controls.

Peak widths (*e.g.* to determine crystallinity using full width at half maximum (FWHM)) have not been analysed in this work, as the data required could not be collected, however with newer machines it is possible. Changes in peak width however will not affect the number of orientations, as the resolution in counting orientations is from the  $\psi$  angle and not  $2\theta$ . For a more in-depth discussion of peak width in relation to strain and crystal grain size, analysis would have to be performed on patterns obtained from a higher resolution (not in-lab) setup with a detector that could be moved in  $2\theta$ , thus allowing for an increased number of points across a peak to be obtained. This combined with a monochromated X-ray source giving pure Cu  $K_{\alpha 1}$  radiation to allow accurate comparisons of peak widths.

We also evaluated the ice diffraction patterns obtained in the presence of ice-active materials, confirming the phase present was I<sub>h</sub>, noting the loss of intensity of the (002) peak, in cases where there was, and was not ice-binding, and that any potential changes in hydrogen bonding cannot be visualised here, in that they do not affect the oxygen lattice. Peak disappearance could be interpreted as indicating specific ice-binding, but we show with controls that this cannot be inferred due to preferred orientations and insufficient crystallites within the scattering volume. This confirms that the method is a useful addition to the suite of tools for discovering and investigating new ice recrystallisation inhibitors but that, in the setup used here, care must be taken not to overfit the data and extrapolate information about specific crystal face binding.

Overall, XRD can be successfully used as a supplementary tool to study IRI, however thus far provides little extra on the mechanism of action of AF(G)Ps and their mimics on ice.

## 3.8 Experimental

### 3.8.1 Materials

Poly(ethylene glycol) (PEG) (4kDa) and poly(vinyl alcohol) (PVA) (10 kDa), phosphate-buffered saline (PBS) preformulated tablets, lysozyme and ampicillin were purchased from Sigma-Aldrich and used as supplied unless otherwise stated. Imidazole (Merck), isopropyl- $\beta$ -D-thiogalactoside (IPTG) (VWR chemical), safranin-O and phenosafranin (ACROS organics), Novex AP Chromogenic and Coomassie blue stain (Expedeon) were also used as supplied. IMAC Sepharose 6 Fast Flow columns, HiLoad 16/600 Superdex 75 pg gel filtration columns and PD10 desalting columns were purchased from GE Healthcare and used according to manufacturer's instructions. AFGP8 CC-86-XVII was kindly provided by A. L. DeVries (University of Illinois at Urbana-Champaign, USA) and used as received. Gold nanoparticles were synthesised as reported previously.<sup>82</sup> For washing of AuNPs, Amicon Ultra-0.5 centrifugal filter units with Ultracel-30 membrane were used. 40 nm citrate-stabilised gold colloid solution was purchased from BBI solutions. The pET20b-AFP<sub>III</sub> plasmid encoding for a hexahistidine-tagged AFP<sub>III</sub> from ocean pout (*rQAE isoform*, M1.1HISPET20b) was kindly provided by Peter Davies (Queens University, Kingston, Canada). Competent *Escherichia coli* BL21(DE3) cells were sourced from New England Biolabs.

### 3.8.2 Physical and Analytical Methods

A Linkam Biological Cryostage BCS196 with T95-Linkpad system controller equipped with a LNP95-Liquid nitrogen cooling pump, using liquid nitrogen as the coolant (Linkam Scientific Instruments UK, Surrey, U.K.) was used to anneal ice wafers. An Olympus CX41 microscope equipped with a UIS-2 20x/0.45/ $\infty$ /0-2/FN22 lens (Olympus Ltd., Southend on sea, U.K.) and a Canon EOS 500D SLR digital camera was used to obtain all images. Image processing was performed using ImageJ, which is freely available from <http://imagej.nih.gov/ij/>.

X-ray diffraction measurements were made using a Xenocs Xeuss 2.0 equipped with a micro-focus Cu  $K_{\alpha}$  source collimated with Scatterless slits. The scattering was measured using a Pilatus 100k detector with a pixel size of 0.172 mm x 0.172 mm.

The distance between the detector and the sample was calibrated using silver behenate ( $\text{AgC}_{22}\text{H}_{43}\text{O}_2$ ), giving a value of 0.161(3) m. The detector was fixed at an angle of  $36^\circ$  giving a  $2\theta$  range of  $18.5$  to  $47.5^\circ$ .

Samples were inserted into 1 mm diameter, 0.01 thick, 70 mm long quartz capillaries (Capillary Tube Supplies Ltd) and mounted in a Linkam THMS350 furnace. Measurements were made with a counting time of 10 seconds and a delay of 4 seconds between each measurement.

### 3.8.3 Procedures

#### 3.8.3.1 Recombinant Expression of His-AFP<sub>III</sub>

A pET20b-AFP<sub>III</sub> plasmid encoding for a hexahistidine-tagged AFP<sub>III</sub> from ocean pout (*rQAE isoform*, M1.1HISPET20b) was kindly provided by Peter Davies (Queens University, Kingston, Canada). The plasmid was transformed into competent *Escherichia coli* BL21(DE3) cells (New England Biolabs). A colony was selected to inoculate 50 mL of LB-medium containing  $100 \mu\text{g}\cdot\text{mL}^{-1}$  ampicillin and was grown overnight at  $37^\circ\text{C}$  under continuous shaking of 180 rpm. The following day, 5 mL of the preculture was added to 500 mL of LB-medium in a 2 L Erlenmeyer flask and grown at  $37^\circ\text{C}$  with a shaking speed of 180 rpm till an  $\text{OD}_{600}$  of 0.6 was reached. The temperature was then reduced to  $16^\circ\text{C}$  and IPTG was added to a final concentration of 0.4 mM. The overexpression of the protein was allowed to take place overnight following which the cells were centrifuged at 4000 g for 30 minutes at  $4^\circ\text{C}$ .

Pelleted cells were resuspended in PBS supplemented with Pierce™ Protease Inhibitor Mini Tablets. The suspension was passed through a STANSTED ‘Pressure Cell’ FPG12800 homogeniser in order to lyse the cells. The cell lysate was centrifuged at 14,000 g and the supernatant was passed through a 0.45  $\mu\text{m}$  filter and applied to an IMAC Sepharose 6 Fast Flow (GE Healthcare) column charged with Ni(II) ions and pre-equilibrated with PBS. The column was washed with 20 column volumes of 20 mM imidazole in PBS. Bound AFP<sub>III</sub> was eluted using 300 mM Imidazole in PBS. The AFP<sub>III</sub> was further purified using a HiLoad 16/600 Superdex 75 pg gel filtration column (GE Healthcare) with PBS as the running buffer. Fractions exclusively containing the AFP<sub>III</sub> were pooled and concentrated to  $5 \text{ mg}\cdot\text{mL}^{-1}$ . Purity was

estimated using SDS-PAGE and protein concentration determined using Thermo Scientific Pierce BCA assay kit. This was verified by measuring absorbance at 280 nm and obtaining protein's extinction coefficient [as predicted by ProtParam (<http://web.expasy.org/protparam/>)] for use in Beer-Lambert law.

### 3.8.3.2 Recombinant Expression of SNAP-AFPIII

A genetic fragment encoding for AFPIII fused to a hexahistidine tag was amplified using PCR from the pET20b-AFPIII plasmid using 5'-GTACGGATCCAACCAGGCTAGCGTTGTG-3' (BamHI site underlined) as the forward primer and 5'-ATTAGCGGCCGCAGCCGGATCTCAGTG-3' (NotI site underlined) as the reverse primer. The BamHI/NotI digested products were ligated into a pSNAP-tag® (T7)-2 vector (New England Biolabs). The plasmid was then transformed into competent *Escherichia coli* BL21(DE3) cells (New England Biolabs). The subsequent expression and purification was performed as detailed for AFPIII.

AFPIII conjugation to AuNP was performed by Dr Wilkins as described in Wilkins *et al.*, (Polym. Chem., 2019) for use in the following ice-activity experiments.<sup>82</sup>

### 3.8.3.3 XRD Sample Preparation

Samples were prepared, in either PBS solution or using Milli-Q ultrapure water with resistance < 18  $\Omega$  obtained from a Milli-Q® Integral Water Purification System, over a range of concentrations and 10  $\mu$ L was inserted into 1 mm thick quartz capillaries using a hypodermic needle (Sterican) and 1 mL syringe, and mounted in a Linkam HFSX350 stage and cooled to -35 °C at 30 K.min<sup>-1</sup>. The samples were then heated to -8 °C where X-ray scattering was performed.

### 3.8.3.4 XRD Data Analysis

Diffraction pattern plotting, orientation analysis and any statistical tests were performed using OriginPro software, version 2018b. Three major diffraction peaks: (100), (002) and (101) were focused on. Positions (2 $\theta$ ) of these peaks are 22.7 °, 24.5 ° and 25.8 ° respectively.



### 3.8.3.5 XRD Orientation Analysis

Measurements as a function of temperature were made with a counting time of 10 seconds repeatedly, with a 4 second delay between each acquisition, over 1800 seconds annealing, enabling analysis of the number of crystal orientations observed over time and comparison to splat assay data. A radial integration of the 2D scattering profile was performed using FOXTROT 3.3.4 software resulting in 1D intensity versus  $2\theta$  plots. In addition, azimuthal integrations for each Bragg peak were performed producing 1D intensity versus  $\psi$  plots. Data was then ran through an in-house MATLAB (The MathWorks, Natick, MA) code to obtain the number of ice crystal orientations. Each data point with an intensity greater than a threshold value (1.5 counts) was counted as a crystal orientation. The total number of data points (#orientations) was calculated for a 1D intensity versus  $\psi$  file using the following line of code:

```
NumberOfOrientations{i}=sum(Intensities{i}>IntensityThreshold);
```

This was run in a script to calculate the number of orientations for each Bragg peak, and to handle the large number of datasets produced in the annealing studies. To compare the rate of crystal growth, the gradient of change in orientations over time was obtained.

### 3.8.3.6 Ice Recrystallisation Inhibition ‘Splat’ Assay

A 10  $\mu\text{L}$  droplet of additive in PBS solution is dropped from 1.4 m onto a glass microscope coverslip on top of an aluminium plate cooled to  $-78\text{ }^{\circ}\text{C}$  using dry ice. Upon impact with the plate the droplet instantly freezes, spreading out and forming a thin wafer of ice. This wafer is then placed on a liquid nitrogen cooled cryostage cooled to  $-8\text{ }^{\circ}\text{C}$ . The wafer is then left to anneal for 30 min at  $-8\text{ }^{\circ}\text{C}$ . Three photographs are then taken of the wafer in different locations at  $20\times$  zoom under cross polarizers. Using ImageJ, the numbers of crystals in the images were counted and the average crystal size per wafer was calculated as mean grain area (MGS) as well as the mean grain length size (MLGS) and reported as a % of area compared to PBS control.

### 3.8.3.7 Modified Sucrose ‘Sandwich’ Ice Shaping Assay

Samples dissolved in PBS buffer containing 45 % sucrose were sandwiched between two glass coverslips and sealed with immersion oil. Samples were cooled to  $-50\text{ }^{\circ}\text{C}$  on a Linkam Biological Cryostage BCS196 with T95-Linkpad system controller equipped with a LNP95-Liquid nitrogen cooling pump, using liquid nitrogen as the coolant (Linkam Scientific Instruments UK, Surrey, U.K.). The temperature was then increased to  $-8\text{ }^{\circ}\text{C}$  and held for 1 hour to anneal. The samples were then heated at  $0.5\text{ }^{\circ}\text{C}\cdot\text{min}^{-1}$  until few ice crystals remained and then cooled at  $0.05\text{ }^{\circ}\text{C}\cdot\text{min}^{-1}$  and the shape of ice crystals observed. Micrographs were obtained every  $0.1\text{ }^{\circ}\text{C}$  using an Olympus CX41 microscope equipped with a UIS-2 20x/0.45/ $\infty$ /0-2/FN22 lens (Olympus Ltd., Southend on sea, U.K.) and a Canon EOS 500D SLR digital. Image processing was conducted using ImageJ.

### 3.9 References

- 1 C. Giacovazzo, *Fundamentals of crystallography*, International Union of Crystallography, Oxford, 1992.
- 2 M. Bech, O. Bunk, C. David, P. Kraft, C. Brönnimann, E. F. Eikenberry and F. Pfeiffer, *Appl. Radiat. Isot.*, 2008, **66**, 474–478.
- 3 I. K. Voets, *Soft Matter*, 2017, **13**, 4808–4823.
- 4 C. A. Knight, D. Wen and R. A. Laursen, *Cryobiology*, 1995, **32**, 23–34.
- 5 T. Congdon, R. Notman and M. I. Gibson, *Biomacromolecules*, 2013, **14**, 1578–1586.
- 6 C. Budke and T. Koop, *ChemPhysChem*, 2006, **7**, 2601–2606.
- 7 C. Budke, C. Heggemann, M. Koch, N. Sewald and T. Koop, *J. Phys. Chem. B*, 2009, **113**, 2865–2873.
- 8 C. Budke, A. Dreyer, J. Jaeger, K. Gimpel, T. Berkemeier, A. S. Bonin, L. Nagel, C. Plattner, A. L. Devries, N. Sewald and T. Koop, *Cryst. Growth Des.*, 2014, **14**, 4285–4294.
- 9 C. I. Biggs, C. Stubbs, B. Graham, A. E. R. Fayter, M. Hasan and M. I. Gibson, *Macromol. Biosci.*, 2019, **19**, 1–9.
- 10 J. P. Pezacki, M. Noestheden, R. N. Ben, J. Jackman, D. Moffat and S. Findlay, *Biochem. Biophys. Res. Commun.*, 2007, **354**, 340–344.
- 11 C. A. Knight, J. Hallett and A. L. DeVries, *Cryobiology*, 1988, **25**, 55–60.
- 12 S. Wang, N. Amornwittawat, J. Banatiao, M. Chung, Y. Kao and X. Wen, *J. Phys. Chem. B*, 2009, **113**, 13891–13894.
- 13 R. Surís-Valls and I. K. Voets, *Biomolecules*, 2019, **9**, 347.
- 14 M. Griffith and M. W. F. Yaish, *Trends Plant Sci.*, 2004, **9**, 399–405.
- 15 L. L. C. Olijve, A. S. Oude Vrielink and I. K. Voets, *Cryst. Growth Des.*, 2016, **16**, 4190–4195.
- 16 M. Mangiagalli, M. Bar-Dolev, P. Tedesco, A. Natalello, A. Kaleda, S. Brocca, D. de Pascale, S. Pucciarelli, C. Miceli, I. Bravslavsky and M. Lotti, *FEBS J.*, 2016, **284**, 163–177.
- 17 A. Chakrabartty, D. S. Yang and C. L. Hew, *J. Biol. Chem.*, 1989, **264**,

- 11313–11316.
- 18 M. Eckert, *Ann. Phys.*, 2012, **524**, 83–85.
- 19 P. Putzeys and J. Brosteaux, *Trans. Faraday Soc.*, 1935, **13**, 1314–1325.
- 20 P. P. Ewald, *Nature*, 1962, **195**, 320-.
- 21 J. J. Rehr, *Radiat. Phys. Chem.*, 2006, **75**, 1547–1558.
- 22 M. Sakamaki and K. Amemiya, *Rev. Sci. Instrum.*, 2017, **88**, 1–5.
- 23 P. Zimmermann, S. Peredkov, P. M. Abdala, S. DeBeer, M. Tromp, C. Müller and J. A. van Bokhoven, *Coord. Chem. Rev.*, 2020, **423**, 213466.
- 24 O. Hirsch, K. O. Kvashnina, L. Luo, M. J. Süess, P. Glatzel and D. Koziej, *Proc. Natl. Acad. Sci. U. S. A.*, 2015, **112**, 15803–15808.
- 25 J. Uhlig, W. B. Doriese, J. W. Fowler, D. S. Swetz, C. Jaye, D. A. Fischer, C. D. Reintsema, D. A. Bennett, L. R. Vale, U. Mandal, G. C. O’Neil, L. Miaja-Avila, Y. I. Joe, A. El Nahhas, W. Fullagar, F. Parnefjord Gustafsson, V. Sundström, D. Kurunthu, G. C. Hilton, D. R. Schmidt and J. N. Ullom, *J. Synchrotron Radiat.*, 2015, **22**, 766–775.
- 26 M. H. Koch, P. Vachette and D. I. Svergun, *Q. Rev. Biophys.*, 2003, **36**, 147–227.
- 27 M. A. Graewert and D. I. Svergun, *Curr. Opin. Struct. Biol.*, 2013, **23**, 748–754.
- 28 V. F. Petrenko and R. W. Whitworth, *Physics of Ice*, Oxford University Press, Oxford, 1999.
- 29 B. D. Cullity and S. R. Stock, *Elements of x-ray diffraction*, Pearson Education, Harlow, 3rd edn., 2014.
- 30 M. Truffer, University of Alaska Fairbanks, 2013.
- 31 R. Sharma, D. P. Bisen, U. Shukla and B. G. Sharma, *Recent Res. Sci. Technol.*, 2012, **4**, 77–79.
- 32 G. Petzold and J. M. Aguilera, *Food Biophys.*, 2009, **4**, 378–396.
- 33 K. G. Libbrecht, *Rep. Prog. Phys.*, 2005, **68**, 855–895.
- 34 A. F. Wells, *London, Edinburgh, Dublin Philos. Mag. J. Sci.*, 1946, **37**, 184–199.

- 35 K. Domin, K. Y. Chan, H. Yung, K. E. Gubbins, M. Jarek, A. Sterczynska and M. Sliwinska-Bartkowiak, *J. Chem. Eng. Data*, 2016, **61**, 4252–4260.
- 36 M. Inoue and I. Hirasawa, *J. Cryst. Growth*, 2013, **380**, 169–175.
- 37 D. M. Dennison, *Proc. Phys. Soc. London*, 1921, **3**, 3–5.
- 38 W. H. Bragg, *Proc. Phys. Soc.*, 1922, **34**, 98–103.
- 39 W. H. Barnes, *Proc. R. Soc. London*, 1929, **A125**, 670–693.
- 40 A. B. Dobrowolski, *Historia naturalna lodu (The natural history of ice)*, Kasa im. Józefa Mianowskiego, Warsaw, 1923.
- 41 E. D. Becker, in *Encyclopedia of Magnetic Resonance*, John Wiley & Sons, Inc., Chichester, UK, 2007.
- 42 S. Grzesiek and E. D. Becker, in *Encyclopedia of Magnetic Resonance*, John Wiley & Sons, Inc., Chichester, UK, 2011.
- 43 G. C. Pimental and A. L. McClellan, *The Hydrogen bond*, W.H. Freeman and Company, San Francisco, 1960.
- 44 C. G. Salzmann, P. G. Radaelli, B. Slater and J. L. Finney, *Phys. Chem. Chem. Phys.*, 2011, **13**, 18468–18480.
- 45 C. Schran and D. Marx, *Phys. Chem. Chem. Phys.*, 2019, **21**, 24967–24975.
- 46 J. D. Bernal and R. H. Fowler, *J. Chem. Phys.*, 1933, **1**, 515–548.
- 47 S. Kawada, *J. Phys. Soc. Japan*, 1972, **32**, 1442–1442.
- 48 A. Nagoe, H. Kusukawa and M. Oguni, *J. Phys. Chem. C*, 2015, **119**, 23910–23916.
- 49 J. J. Shephard, B. Slater, P. Harvey, M. Hart, C. L. Bull, S. T. Bramwell and C. G. Salzmann, *Nat. Phys.*, 2018, **14**, 569–572.
- 50 B. Santra, J. Klimeš, A. Tkatchenko, D. Alfè, B. Slater, A. Michaelides, R. Car and M. Scheffler, *J. Chem. Phys.*, 2013, **139**, 154702.
- 51 E. B. Moore and V. Molinero, *Phys. Chem. Chem. Phys.*, 2011, **13**, 20008–16.
- 52 T. L. Malkin, B. J. Murray, V. Andrey, J. Anwar and C. G. Salzmann, *Proc. Natl. Acad. Sci.*, 2012, **109**, 1041–1045.
- 53 Y. P. Handa, D. D. Klug and E. Whalley, *Can. J. Chem.*, 1988, **66**, 919–924.
- 54 K. Thürmer and S. Nie, *Proc. Natl. Acad. Sci.*, 2013, **110**, 11757–11762.

- 55 H. Koenig, *Zeitschrift fur Krist.*, 1943, **105**, 279–86.
- 56 J. Huebinger, H. M. Han, O. Hofnagel, I. R. Vetter, P. I. H. Bastiaens and M. Grabenbauer, *Biophys. J.*, 2016, **110**, 840–849.
- 57 R. P. Rambo and J. A. Tainer, *Curr. Opin. Struct. Biol.*, 2010, **20**, 128–137.
- 58 D. I. Svergun and M. H. J. Koch, *Rep. Prog. Phys.*, 2003, **66**, 1735–1782.
- 59 S. P. Meisburger, M. Warkentin, H. Chen, J. B. Hopkins, R. E. Gillilan, L. Pollack and R. E. Thorne, *Biophys. J.*, 2013, **104**, 227–236.
- 60 L. L. C. Olijve, T. J. Sun, T. Narayanan, C. Jud, P. L. Davies and I. K. Voets, *RSC Adv.*, 2013, **3**, 5903–5908.
- 61 J. Michielsen, J. Dings and J. van der Elsken, *Phys. Rev. A*, 1991, **44**, 4068–4071.
- 62 C. U. Kim, M. W. Tate and S. M. Gruner, *Proc. Natl. Acad. Sci.*, 2015, **112**, 11765–11770.
- 63 E. J. Shalaev, D. V. Malakhov, A. N. Kanev, V. I. Kosyakov, F. V. Tuzikov, N. A. Varaksin and V. I. Vavilin, *Thermochim. Acta*, 1992, **196**, 213–220.
- 64 D. B. Varshney, S. Kumar, E. Y. Shalaev, S.-W. Kang, L. A. Gatlin and R. Suryanarayanan, *Pharm. Res.*, 2006, **23**, 2368–2374.
- 65 N. V. Surovtsev, S. V. Adichtchev, V. K. Malinovsky, A. G. Ogienko, V. A. Drebuschak, A. Y. Manakov, A. I. Ancharov, A. S. Yunoshev and E. V. Boldyreva, *J. Chem. Phys.*, 2012, **137**, 065103.
- 66 B. J. Murray, A. K. Bertram, S. L. Clegg, P. Brimblecombe, K. S. Knight, R. I. Smith, A. A. Zardini, U. K. Krieger, T. Corti, D. J. Cziczko, S. Fueglistaler, P. K. Hudson, D. S. Thomson and T. Peter, *Phys. Chem. Chem. Phys.*, 2008, **10**, 3287.
- 67 B. Zakharov, A. Fisyuk, A. Fitch, Y. Watier, A. Kostyuchenko, D. Varshney, M. Sztucki, E. Boldyreva and E. Shalaev, *J. Pharm. Sci.*, 2016, **105**, 2129–2138.
- 68 J. van der Elsken, W. Bras, J. Dings and J. Michielsen, *Phys. Rev. B*, 1996, **54**, 3110–3114.
- 69 I. Kratochvílová, M. Golan, K. Pomeisl, J. Richter, S. Sedláková, J. Šebera, J. Mičová, M. Falk, I. Falková, D. Řeha, K. W. Elliott, K. Varga, S. E. Follett

- and D. Šimek, *RSC Adv.*, 2017, **7**, 352–360.
- 70 M. I. Gibson, *Polym. Chem.*, 2010, **1**, 1141–1152.
- 71 M. L. Huang, D. Ehre, Q. Jiang, C. Hu, K. Kirshenbaum and M. D. Ward, *Proc. Natl. Acad. Sci.*, 2012, **109**, 19922–19927.
- 72 Y. E. Yagci, M. Antonietti and H. G. Börner, *Macromol. Rapid Commun.*, 2006, **27**, 1660–1664.
- 73 E. Baruch and Y. Mastai, *Macromol. Rapid Commun.*, 2007, **28**, 2256–2261.
- 74 Y. Mastai, J. Rudloff, H. Cölfen and M. Antonietti, *ChemPhysChem*, 2002, **3**, 119–123.
- 75 P. M. Naullage, L. Lupi and V. Molinero, *J. Phys. Chem. C*, 2017, **121**, 26949–26957.
- 76 L. L. C. Olijve, M. M. R. M. Hendrix and I. K. Voets, *Macromol. Chem. Phys.*, 2016, **217**, 951–958.
- 77 C. I. Biggs, T. L. Bailey, B. Graham, C. Stubbs, A. E. R. Fayter and M. I. Gibson, *Nat. Commun.*, 2017, **8**, 1546.
- 78 M. M. Harding, P. I. Anderberg and A. D. J. Haymet, *Eur. J. Biochem.*, 2003, **270**, 1381–1392.
- 79 J. Baardsnes, M. J. Kuiper and P. L. Davies, *J. Biol. Chem.*, 2003, **278**, 38942–38947.
- 80 C. A. Stevens, R. Drori, S. Zalis, I. Braslavsky and P. L. Davies, *Bioconjug. Chem.*, 2015, **26**, 1908–1915.
- 81 L. E. Wilkins, University of Warwick, 2018.
- 82 L. E. Wilkins, M. Hasan, A. E. R. Fayter, C. Biggs, M. Walker and M. I. Gibson, *Polym. Chem.*, 2019, **10**, 2986–2990.
- 83 C. J. Capicciotti, M. Leclere, F. A. Perras, D. L. Bryce, H. Paulin, J. Harden, Y. Liu and R. N. Ben, *Chem. Sci.*, 2012, **3**, 1408–1416.
- 84 A. Eniade, M. Purushotham, R. N. Ben, J. B. Wang and K. Horwath, *Cell Biochem. Biophys.*, 2003, **38**, 115–124.
- 85 R. Drori, C. Li, C. Hu, P. Raiteri, A. L. Rohl, M. D. Ward and B. Kahr, *J. Am. Chem. Soc.*, 2016, **138**, 13396–13401.

- 
- 86 X. Chen, J. Schröder, S. Hauschild, S. Rosenfeldt, M. Dulle and S. Förster, *Langmuir*, 2015, **31**, 11678–11691.
- 87 E. D. Bojesen and B. B. Iversen, *CrystEngComm*, 2016, **18**, 8332–8353.
- 88 D. R. Hummer, P. J. Heaney and J. E. Post, *J. Cryst. Growth*, 2012, **344**, 51–58.
- 89 R. N. Andrews, J. Serio, G. Muralidharan and J. Ilavsky, *J. Appl. Crystallogr.*, 2017, **50**, 734–740.
- 90 S. Deville, C. Viazzi, J. Leloup, A. Lasalle, C. Guizard, E. Maire, J. Adrien and L. Gremillard, *PLoS One*, 2011, **6**, e26474.
- 91 D. B. Varshney, J. A. Elliott, L. A. Gatlin, S. Kumar, R. Suryanarayanan and E. Y. Shalaev, *J. Phys. Chem. B*, 2009, **113**, 6177–6182.



# Chapter 4

---

Combined solid state NMR dynamics and ice recrystallisation inhibition activity measurements of synthetic and biological antifreeze (macro)molecules.

## 4.1 Declarations

*All the work presented in this chapter is in collaboration with Dr Rebecca A. Stevens, supervised by Józef Lewandowski (Department of Chemistry, University of Warwick). The PVA samples were synthesised by Dr Christopher Stubbs or Dr Thomas Congdon (supervised by Professor Matthew I. Gibson), 'splat' assays for PVAs performed by Dr Thomas Congdon, critical inhibitory concentration of polymers calculated by Carsten Budke (Faculty of Chemistry, Bielefeld University), and assistance with AFP expression by Dr Muhammad Hasan (also supervised by Professor Matthew I. Gibson). AFGP8 was provided by Professor A. L. DeVries (Urbana-Champaign, University of Illinois).*

## 4.2 Chapter Abstract

Antifreeze and ice-binding proteins have evolved to recognise and inhibit the growth of ice, and function *via* defined ice-binding faces. Synthetic mimics, including PVA, are also potent ice growth inhibitors, but are fully flexible molecules without a defined ice-binding face. Current understanding is limited to indirect measurements of macroscopic outcome or modelling studies. Low temperature solid state NMR (SSNMR) measurements of proteins are becoming more commonly used to investigate dynamic processes such as ligand binding and folding, as well as characterising the timescales of these motions. However, research thus far has focussed on two of the components that make up frozen protein samples: the proteins and the liquid water phase. The third component, ice, has been rarely studied until recently due to the ice protons' long relaxation times.

Here a combination of microscopy and SSNMR is used to provide the experimental molecular-level details of antifreeze (macro)molecule:ice interactions. We show that the critical ice growth inhibition constant for PVA as a function of chain length scales with the correlation times ( $C\tau$ ) of the ice, with longer chains ( $DP \geq 20$ ) being IRI active and affecting ns - ps dynamics in the ice ( $C\tau$  of  $< 200$  ps for IRI active PVAs,  $> 350$  ps for non-IRI active PVAs). This supports a model of extended hydrogen bonding (the longer chain PVAs contain more hydroxyl groups available for hydrogen bonding), and enthalpy-entropy compensation driving affinity for ice for longer polymer chains.

Clear reductions in correlation time are also observed for safranine-O solutions (<100 ps), indicating more rapid motions for IRI active materials tested here

2D Exchange Spectroscopy (EXSY) is used to show direct antifreeze (macro)molecule:ice interactions absent in controls by detecting chemical or conformational exchange. These findings provide clear evidence for how polymeric ice growth inhibitors recognise ice surfaces and help our understanding of this complex recognition process, as well as the development of new cryoprotectants.

These studies into the antifreeze (macro)molecule:ice interface present SSNMR as another technique that could be further utilised to study the interactions of more synthetic cryoprotectants and ice.

### 4.3 Introduction

Antifreeze and ice-binding proteins (IBPs) have evolved to bind to specific crystallographic planes of ice leading to the macroscopic properties of non-colligative freezing point depression, crystal shaping and IRI.<sup>1-4</sup> Many applications have been suggested for these proteins and their ice-interacting mimics, ranging from cryopreservation to aerospace/engineering.<sup>5-10</sup> The question of how a protein can recognise a dynamic interface such as ice in a large excess of water, which also undergoes the same range of hydrogen bonding interactions, is a complex one. Crystal structures of AFPs reveal large, rigid ice-binding sites, which can potentially pre-organise clathrate water molecules that then engage with ice.<sup>11</sup> In contrast, AFGPs are more flexible; though there is no published crystal structure, it is not clear if their glycans or the protein backbone engage the ice. Conflicting research states that AFGPs may bind either reversibly or irreversibly.<sup>12,13</sup> PVA has emerged as a potent AFGP mimic, despite it being fully flexible and not possessing an ice-binding surface,<sup>14</sup> and a variety of mechanisms have been proposed as to how these antifreezes act. In particular, AFGPs are suspected to bind ice *via* hydrophobic interactions, whereas PVA recognizes ice by a zipper mechanism and interacts using hydrogen bonding.<sup>12,15</sup>

Koop proposed that the spacing between hydroxyls of PVA matches that of the prismatic planes of ice, which agrees with macroscopic observations of changes in crystal growth habits.<sup>16</sup> Gibson *et al.* have shown that PVA has a strong molecular weight/chain length dependence on its activity, demonstrating a multivalent enhancement in its binding affinity, though this is not fully understood.<sup>17,18</sup>

Experimental studies, such as XRD and microscopy (explored in Chapter 3), rely on macroscopic observations on length, and timescales far greater than that of the likely interactions between the PVA and ice. There is no direct experimental observation of binding, due to the challenge of using techniques such as, but not limited to, electron microscopy on ice, and much research into the role of structure, orientation of functional groups and hydrophobicity/hydrophilicity of antifreezes has been performed using MD simulations. For example, Naullage *et al.* have predicted using MD, that PVA binds *via* an extended array of hydrogen bonds, which they describe as where the PVA binding follows a regular pattern controlled by distance matching, with two out of every three hydroxyl groups hydrogen bonding to the ice. They also discuss

entropy-enthalpy compensation as part of the binding mechanism, observing that as water molecules are lost from the polymer's hydration shell (into the ice lattice), the enthalpic contribution of the hydrogen bonding is enhanced, potentially through their entropy of desolvation. Their findings indicate that longer chain PVAs show increased affinity (and thus a 'switch on' of ice-activity) due to this entropy-enthalpy compensation; as they interpret PVA binding (arising from a different scaling of the enthalpy and entropy of binding) to be a function of hydroxyl groups bound.<sup>15</sup>

Microscopy has been useful for studying macroscopic effects thus far. However, it cannot provide detail at an atomic scale or allow us to study the bulk ice, as only snapshots of these activities can be obtained from micrographs. However, these snapshots have been important in gaining knowledge of which ice faces are bound by different cryoprotectants.<sup>19,16</sup>

If we can understand the mechanisms of action of these ice-interacting compounds, this could lead to the discovery of more effective, less toxic mimics (AFPs are cytotoxic so cannot be used in cryopreservation). More physical techniques including XRD and NMR, as well as molecular dynamics (MD) have increasingly become of use, as a comprehensive physical understanding on an atomic scale will assist with an understanding of how ice-active compounds work further up the chain, *i.e.* at a cellular level.<sup>20-23</sup>

All atomic nuclei possess electric charge, mass and spin (also known as angular momentum). The latter is critical for NMR, as NMR-active nuclei have non-zero spin quantum numbers ( $I$ ) and are inherently magnetic, which produce a magnetic dipole moment ( $\mu$ ). The nuclei transition between different spin states is related to the energy difference between the states. When the nuclear spins are placed in an external magnetic field ( $B_0$ ), they reorient themselves with or against the magnetic field. In this work hydrogen is used as a probe to investigate (macro)molecule:ice interactions since this is the most abundant element of interest in these systems.  $^1\text{H}$  has a spin quantum number of  $\frac{1}{2}$  and splits into two energy levels when placed in a magnetic field. When a sample is being analysed, there is an extremely large number of nuclear spins, and net bulk magnetisation ( $M_0$ ) arises parallel to the magnetic field, **Figure 4.1A**.

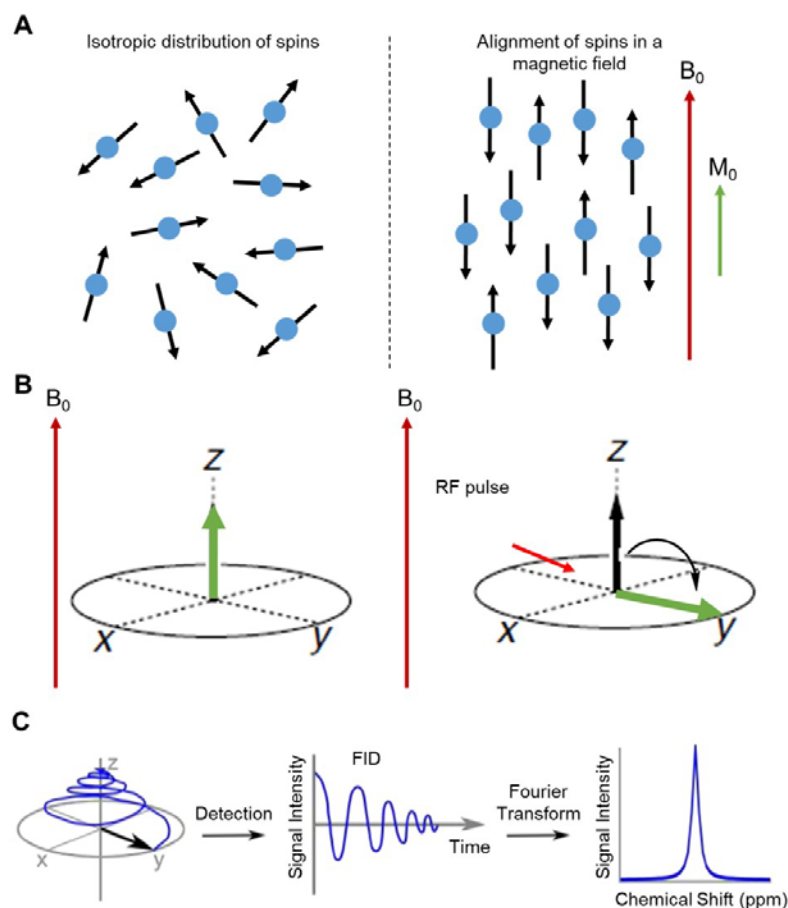


**Figure 4.1.** A) Alignment of spins in a magnetic field; when subject to a magnetic field ( $B_0$ ) spins are no longer isotropically distributed and aligning with or against the field. (A small excess of parallel spins result in a net magnetisation of  $M_0$ ); B) Schematic of rotation of bulk magnetisation by RF pulses. When an RF pulse is applied, the bulk magnetisation rotates and is transferred to the x-y plane (signal is detectable). When the pulse is turned off the protons return to  $B_0$  and the signal decays; C) NMR signal as an exponentially decaying sine wave (FID). The FID is converted into data used in this work.

To detect NMR in a spectrometer, the magnetic moment is perturbed from the z-axis by the application of a radiofrequency (RF) pulse. This rotates the magnetisation from the z-axis to the x-y plane (**Figure 4.1B**), producing a signal that can be detected. When the pulse is turned off, bulk magnetisation returns to equilibrium (parallel to z-axis). The rate at which this occurs depends on longitudinal relaxation ( $T_1$ ) and transverse relaxation ( $T_2$ ).  $T_1$  describes the return to equilibrium as a result of spins interacting with the surrounding lattice and  $T_2$  describes the return as a result of spin-spin interactions. Both  $T_1$  and  $T_2$  relaxation are caused by transient magnetic fields due

to molecular motion/reorientation, however  $T_2$  is also caused by the swapping of chemical shifts (or coupling constants) due to conformational change or chemical exchange. The signal that is detectable decays over time, and is known as free induction decay (FID) and is Fourier transformed to obtain an NMR spectrum, **Figure 4.1C**. The chemical shift, intensity and linewidth ( $\lambda$ , full peak width at half maximum height) can be quantified from the spectra. The linewidth of an NMR signal is determined by  $T_2$ ; increased linewidths can be due to short  $T_2$  relaxation. When relaxation is very fast, broadening may lead to difficulties in detecting the signal.

NMR has been used to provide information about the actual structure of ice but is also informative for determining the time scale for diffusive motion of the protons.<sup>24</sup> It is particularly relevant for studying ice as it is a non-destructive technique, and SSNMR can give atomic resolution information over a range of timescales (picoseconds to seconds) over a range of temperatures and can investigate samples that are neither in solution nor crystalline as well as interfaces. SSNMR has recently been added to the arsenal of techniques used to study AF(G)Ps as crystalline protein is not required and has been previously used to study the structure and dynamics of both crystalline and non-crystalline molecular assemblies at solid/liquid interfaces.<sup>25–28</sup>

Recent research involving MD and NMR includes that of gas-to-ice chemical shifts, studies into the local structure of AFGPs, SSNMR and MD of AFPIII concerning the ice-binding site (IBS), and ice microstructure.<sup>26,29–35</sup> SSNMR investigations has also concerned synthetic AF(G)P mimics and ice-binding, for example Ben *et al*'s work on IRI active carbohydrates found ice-binding to not be a requirement for IRI activity. This further led them to postulate that IRI activity must relate to a compounds ability to alter the bulk water structure rather than interaction with the ice lattice.<sup>36</sup> The effect ice-active materials have on the bulk water structure is what is of interest here. These studies have been useful for discussing the motions in these samples. Agreement between experimentally measured relaxation times and predicted ones is important and could lead to further understanding of the ice formation and growth process. So far, in the ice field little work has been undertaken into NMR (due to the broad peaks), with the focus on proteins and the liquid water phase,<sup>37</sup> and most simulations consider different timescales.

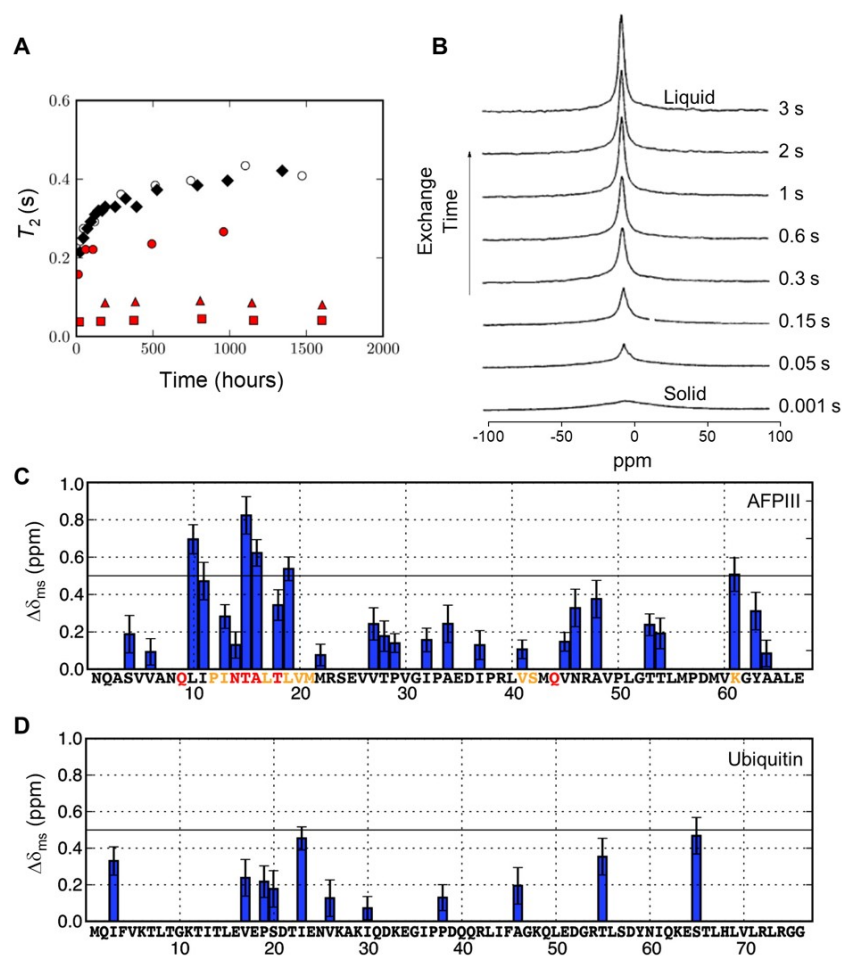


**Figure 4.2.** NMR data obtained in the literature using a variety of techniques: A) Change in transverse (spin-spin relaxation in the x-y plane) ( $T_2$ ) relaxation times over time for 5 samples. Ice control (black diamonds), ice+BSA ( $10 \mu\text{g.mL}^{-1}$ ) (white circles), ice+[extracellular protein] ( $10 \mu\text{g.mL}^{-1}$ ) (red circles) ice+IBP ( $2 \mu\text{g.mL}^{-1}$ ) (red triangles) and ice+IBP ( $4 \mu\text{g.mL}^{-1}$ ) (red squares). Adapted from Brown *et al.*, (Biotechnol. Reports., 2014);<sup>38</sup> B) Study of type I AFP binding reversibly: NMR spectra of deuterated type I AFP ( $1 \text{ mg.mL}^{-1}$ ) showing molecular exchange between the ice surface and aqueous solution at different exchange times, narrow peaks: aqueous signal (indicating protein in aqueous phase), broad flat peaks: solid/ice signal (indicating protein bound to ice phase). Adapted from Ba *et al.*, (J. Am. Chem. Soc., 2003);<sup>27</sup> Chemical shift difference obtained from  $^{13}\text{C}$ - $^{13}\text{C}$  DARR spectrum for each amino acid in C) AFPIII ( $34 \text{ mg.mL}^{-1}$ ) frozen in water at  $-15 \text{ }^\circ\text{C}$  and D) ubiquitin ( $25 \text{ mg.mL}^{-1}$ ). (Samples in water, spectra recorded on 750 MHz spectrometer with mixing time of 20 ms, 12 kHz MAS at  $-15 \text{ }^\circ\text{C}$ ). Adapted from Siemer and Mcdermott, (J. Am. Chem. Soc., 2008).<sup>25</sup>



As ice-binding materials affect the ice interface,<sup>14,39–41</sup> there will also be a change in the dynamics of the ice and water. SSNMR is an ideal method for studying frozen solutions for three reasons: firstly, many biomolecules have hydration shells that do not freeze with the bulk solvent; secondly, the existence of a disordered layer, which behaves differently to the bulk water space; finally, unlike other techniques, it allows the study of AFPs and other antifreezes *in situ*. A variety of different solution state and SSNMR approaches have been used to identify the ice-binding surface of AFPs/evidence for a molecular contact surface between ice and AFPIII; including <sup>13</sup>C spin-lattice relaxation, <sup>1</sup>H-<sup>1</sup>H cross-saturation,  $T_2$  relaxation and <sup>13</sup>C-<sup>13</sup>C dipolar assisted rotational resonance (DARR) experiments on labelled samples, **Figure 4.2**.

Work has been performed on IBPs using solution state NMR, showing that microbial extracellular IBPs inhibit recrystallisation activity (short  $T_2$  relaxation times for IBPs indicate ice growth inhibition) and modify the 3D ice structure. This results in persistent small size ice crystals, demonstrating a potential mechanism for microbial survival in sub-zero temperatures, **Figure 4.2A**.<sup>38</sup> By measuring the <sup>1</sup>H-<sup>1</sup>H cross-saturation and cross relaxation of protons in frozen AFP:ice solutions, more detailed structural information has been obtained about the direct contact certain AFPs make with ice. Cross-saturation and cross relaxation experiments involve mapping protein–molecule interfaces and are based on <sup>1</sup>H resonance signals of a non-deuterated sample (*e.g.* protein), which are saturated, leading to magnetisation of a second lower concentration deuterated sample (*e.g.* ice) by cross relaxation through their interface. If there is an interface saturation will be transferred, indicating binding. Ba *et al.* studied AFPI in a similar way, specifically investigating dynamics and reversibility of AFPI binding. They observed increased liquid-phase signals for AFPI as molecular exchange times were increased from 0.001 to 3 s, indicating desorption of peptide from ice surfaces into the aqueous solution at higher exchange times and thus reversible binding, **Figure 4.2B**.<sup>27,28</sup> Siemer and McDermott compared frozen SSNMR spectra of AFPIII and ubiquitin (as it has no non-colligative antifreeze activity) to solution state spectra to examine chemical shift perturbation for the different amino acid residues in solid-state experiments compared to that of solution-state, observing more pronounced chemical shift changes (up to 1.5 ppm) for AFPIII, with the largest shifts detected for amino acid residues previously shown to be involved in ice-binding, such as Thr18, **Figure 4.2C/D**.<sup>25,42,43</sup>

The range of techniques applicable to the investigation of ice make SSNMR a valuable tool for understanding how ice-interacting proteins impact the 3D vein network and recrystallisation processes, which is critical for exploiting the full potential of these proteins in biotechnology applications.<sup>38</sup>

Considering the above, here the combined use of optical microscopy alongside variable temperature SSNMR is reported, and the first experimental evidence that PVA can form an extended hydrogen bonded array at the ice surface, which is chain-length dependent is provided supporting that enthalpy-entropy compensation helps drive activity. Additionally, 2D NMR evidence for a direct antifreeze:ice interaction is presented.

### 4.3.1 SSNMR Study of Motions in Solids

A range of SSNMR techniques can be used to extract dynamic information from a solid sample.<sup>44</sup> Each technique is sensitive to a certain range of motions; for example  $R_1$  relaxation measurements can be used to probe motions on the ps – ns timescale, which can be due to side chain rotations or molecular tumbling. As well as exploring a range of motions, NMR can measure their amplitude and frequency,<sup>45</sup> enabling an understanding of how these motions arise and their relation to the structure of a sample, its properties and any phase transitions. A combination of different SSNMR techniques is used here to provide an overall picture of the dynamics in these samples, **Figure 4.3**. [Note, when processes are described as fast or slow, these are on the NMR timescale, which is relative to the difference in resonance frequencies between exchanging nuclei.]

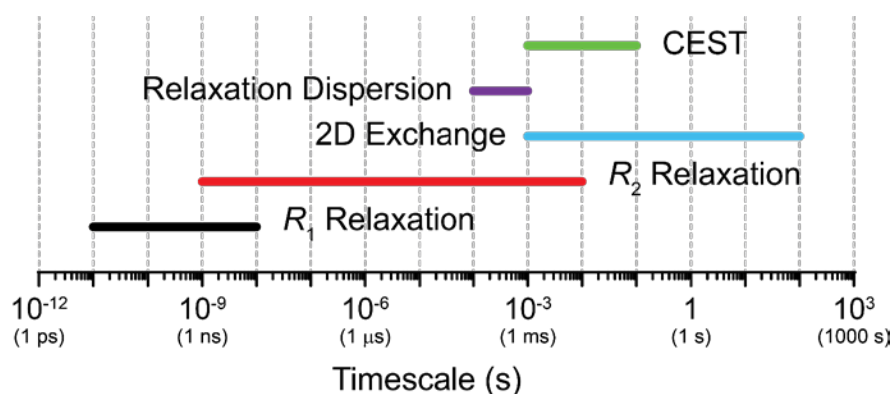


**Figure 4.3.** SSNMR techniques conducted in this project and their associated timescales at which they are sensitive to motions. Techniques include: Chemical Exchange Saturation Transfer (CEST), which measures exchange between one ‘invisible’ low concentration state and a higher concentration state – if exchange occurs, two peaks will be observed (timescales covered: ms - s); Relaxation Dispersion, which monitors chemical exchange of nuclei between ms – ns timescales; 2D Exchange, which is used to indicate dipolar cross relaxation between two nuclei that are spatially close to one another. 2D experiments are particularly useful for determining which signals arise from protons that are close to each other in space even if they are not bonded. (timescales covered: 1 ms – 100 s);  $R_1$  Relaxation, which measures spin-lattice relaxation (restoration of spin to equilibrium state *via* z plane), originating from local motions, such as rotation (timescales covered: 10 ps – 10 ns);  $R_2$  Relaxation, which measures transverse relaxation (restoration of spin to equilibrium state *via* x-y plane) (timescales covered: ns – ms); Adapted from Stevens, R.A., (PhD, University of Warwick, 2018).<sup>46</sup>

As mentioned previously, when performing NMR experiments, a RF pulse affects the magnetisation of a sample. Relaxation is the change in time as the system moves back towards equilibrium from some non-equilibrium state imposed by these pulses.<sup>47</sup> The relaxation rate of a sample changes depending on motion in the sample; it is sensitive to the nucleus’ environment and its dynamics. Relaxation measurements have successfully been used to extract information on solids,<sup>45</sup> membrane protein structures<sup>48,49</sup> and dynamics in *e.g.* lipid bilayers<sup>50</sup> and ion channels,<sup>51,52</sup> as they provide information on the motion’s timescales, amplitudes and, in some cases, directionality. Relaxation measurements are used here to characterise molecular motions in the solid water.

Proton dynamics in polycrystalline hexagonal ice can include proton translation, diffusion and Bjerrum defect dynamics.<sup>53,54</sup> The dynamics of the protons determine the ice phase, and any defects in the hexagonal structure, which may originate from distortions in the hydrogen bond network (*e.g.* due to OH-rotation), should be considered when analysing (macro)molecule:ice interactions. It has been observed that antifreezes affect the dynamics in ice, and this potentially relates to defects in the structure of the water. Generally, the Bernal Fowler (BF) rules are violated leading to defects in ice crystals, such as Bjerrum (D- or L-defects) and ionic defects.<sup>55</sup> Point defects such as interstitials or Schottky (vacancies), where one or more water molecules are missing from the regular ice lattice, can also form. In samples of Ih, both, Bjerrum defect dynamics and translational diffusion of protons have been identified by  $^2\text{H}$  NMR stimulated echo experiments,<sup>53</sup> and it has been theorised that the most reasonable mechanism of fast reorientation dynamics in Ih, such as those seen in  $R_1$  experiments, is due to a Bjerrum defect at the central oxygen atom.<sup>53</sup>

### 4.3.2 Magic Angle Spinning

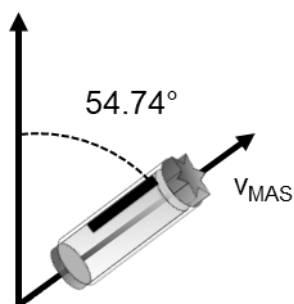


**Figure 4.4.** An example SSNMR rotor spinning at the "magic angle" ( $54.74^\circ$ ) with respect to the strong magnetic ( $B_0$ ) field at a frequency of  $\nu_{\text{MAS}}$ , which sufficiently narrows peaks obtained in SSNMR experiments. Most modern rotors are made of zirconia and have decreased in diameter over the years as magic angle spinning (MAS) technology has advanced.

A major difference between NMR in the solid state and in the solution state is the lack of rapid overall motion in solids. Molecules tumble quickly and undergo random motions in solution, thus NMR parameters that are orientation dependent (anisotropic) will be averaged out to their orientation independent (isotropic) values, but this is not

the case in the solid state. “Magic angle” spinning (MAS) is routinely applied in SSNMR experiments as it improves the averaging out of the anisotropic interactions and so narrows the linewidths *i.e.* removes line-broadening effects due to various interactions by introducing artificial motion, thus simplifying NMR spectra, **Figure 4.4**.

The frequency at which this is applied has to be significantly larger than the size of the interaction. Due to recent advances MAS of up to 150 kHz is possible, with 60 kHz typically being chosen for protein SSNMR experiments. Here a frequency of 10 kHz has been chosen, as the larger the spinning frequency the smaller the rotor chosen to spin the sample. 4 mm rotors were chosen here.

## 4.4 Chapter Aims

This work focuses on observing solid water in the presence of various ice-interacting materials that act as non-colligative antifreezes (proteins, polymers and a small molecule) to further understand ice-activity of synthetic antifreezes. [From this point onwards all ice-active “non-colligative antifreezes”, including IRI active and those that shape ice are termed “antifreezes”.]

- Investigate the mobility of nuclei in frozen water and how it is affected by antifreezes using SSNMR
- Compare the IRI activity of antifreezes and ice proton mobility using relaxation by measuring  $R_1$ ,  $R_2$  and  $R_{1\rho}$  of antifreeze:ice samples; observe where activity ‘turns on’ for different length PVAs
- Monitor any changes in relaxation over time as ice crystals grow
- Investigate exchange between ice and antifreezes *via* 2D EXSY

## 4.5 Results and Discussion

Three types of ice-interacting materials were investigated for further analysis in this work (**Figure 4.5**):

- PVA - polymer known to have non-colligative antifreeze properties
- Safranin-O - small molecule recently found to be an antifreeze<sup>56</sup>
- AFP type III (AFPIII), AFP type I from *Liposetta pinnifasciata* (barfin plaice) (bpAFPI) and AFGP8 – antifreezes found in nature

Additional samples were used as negative controls for the three types of antifreezes: PEG, phenosafranin and lysozyme, respectively; these were selected as they have no non-colligative antifreeze properties.

It is likely that there are regions of water/ice present, *e.g.* a disordered layer such as the quasi-liquid layer (QLL), rather than a specific antifreeze:ice interface, and that water molecules will exchange between these regions. These regions may have different structures, dynamics and capabilities of binding to antifreezes. SSNMR provides measurements averaging dynamics of the water protons from all the regions involved, and a combination of different SSNMR techniques (**Figure 4.3**) are used to obtain information on motions and exchange in these samples.

### 4.5.1 PVA; Chain Length and IRI Activity

As mentioned in Chapter 3, the IRI and shaping effects of AF(G)Ps have been well studied using optical techniques, but this is less so for synthetic mimics. Ice-activity of these proteins and synthetic mimics has been studied in this thesis so far using both microscopy and XRD, providing results supporting that of the literature, as well as an alternative technique for gauging activity. This chapter delves further into the mechanism by which IRI activity is ‘turned on’ in PVA as the polymer chain length increases. [Note, the degree of polymerization (DP) is written after the polymer, *i.e.* PVA20 corresponds to chain length of 20. Both molecular weight and DP are used to describe PVA throughout]. Results for IRI activity (‘splats performed by Dr Thomas Congdon, University of Warwick) are shown in **Figure 4.6**.

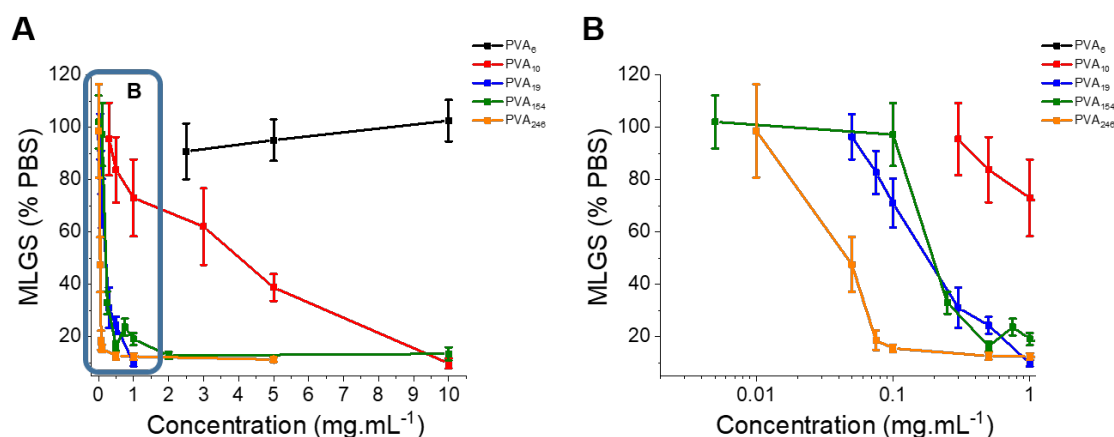


**Figure 4.5.** IRI activity as mean largest grain size (MLGS) for PVAs over a range of chain lengths. A) 0 to 10 mg.mL<sup>-1</sup>; B) Magnification of A, showing activity for 0 to 1 mg.mL<sup>-1</sup>. Grain size is recorded after 30 minutes annealing at -8 °C. Errors are standard deviation of at least 3 measurements.

As the polymer chain length increases, IRI activity also increases; activity is non-existent for chain lengths shorter than 10 units (black), with MLGS being almost the same as that of the PBS control at all concentrations tested. Activity for the longest chain tested (DP = 246), which is the chain length of the 10 kDa PVA tested in Chapters 2 and 3, is highest with IRI activity at 0.05 mg.mL<sup>-1</sup> (MLGS = 47.5 %). This analysis also highlights the dramatic increase in IRI activity of PVA as the chain length increases; from 10 units (MLGS = 95.4 %) to 19 units (MLGS = 31.1 %).

Analysis of individual ice crystal morphology also confirmed that PVA tested here has a preference for the prism plane of ice (when tested at 1.0 mg.mL<sup>-1</sup>). This binding is observed as capped column crystals, **Figure 4.7A**. This morphology can be explained using the schematic in **Figure 4.7B**, where PVA binds to the prism plane of the ice crystal preventing growth at this face upon addition of water molecules. When water adds onto the crystal it binds the basal plane causing growth along the c-axis, and thus the formation of a new prism plane. No further PVA binds, therefore, as water molecules add to the crystal, they preferentially bind this new face leading to faster growth there, leading to a capped morphology.



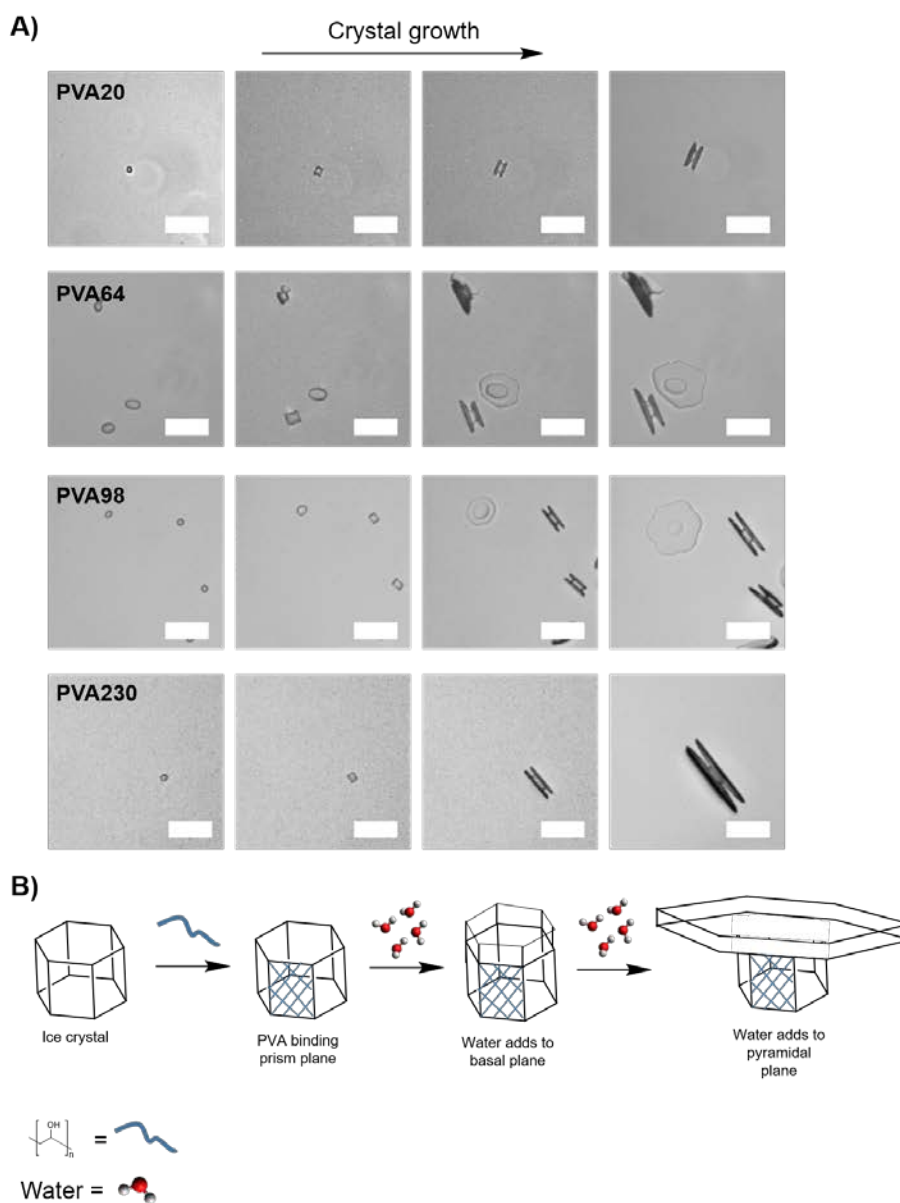


**Figure 4.6.** A) Ice growth habit analysis for a range of PVA molecular weights used here; (PVA20, PVA64, PVA98, PVA230). [Polymer] = 1 mg.mL<sup>-1</sup>. Scale bar = 50  $\mu\text{m}$ . Samples frozen in sucrose solution. Images recorded after a period of melting to leave a few crystals and then taken whilst cooling at 0.2 °C intervals; B) Schematic of example ice habit growth due to PVA binding the primary prism plane.

The observations in **Figure 4.6** and **Figure 4.7** provide insight into the potency of PVA, but are only macroscopic. That is, they provide indirect evidence of a molecular level interaction and do not show the mechanism for the change in activity between DPs of 10 and 20, where IRI is ‘turned on’. The results also do not prove that the PVA

is hydrogen bonding to the ice, as opposed to a hydrophobic interaction which is proposed to occur for AF(G)Ps and some synthetic inhibitors.<sup>57</sup>

## 4.5.2 Optimisation of SSNMR Methods

The relaxation properties of protons in hexagonal ice are generally challenging to observe using NMR due to very long longitudinal (spin-lattice) relaxation times and very short transverse (spin-spin) relaxation times.<sup>58,59</sup> These lead to line-broadening (and potentially a loss of signal) and can make analysis of direct (macro)molecule:ice interactions difficult.<sup>26,60,61</sup> Due to recent improvements in noise reduction and optimisation of SSNMR methods, line-broadening can be minimised and as different protons in frozen solutions exchange, informing us of the crystalline and ‘bulk’ water, SSNMR is being used more readily to study ice.

Under the conditions employed here (all the experiments samples were frozen *in situ* at -36 °C and data obtained at temperatures between -36 and -5 °C), the spectra are dominated by the more mobile interfacial water (similar to ‘crystal’ water described in previous studies on protein-water interactions)<sup>62</sup> with shorter longitudinal relaxation rates (allowing for faster repetition of experiments) and longer transverse relaxation times (resulting in narrower lines). While this is a disadvantage for studies of the bulk crystalline ice, it is beneficial here, as we focus on the interactions between antifreezes and ice. It is important to keep in mind that even though the interfacial water dominates the relaxation measurements, that relaxation data obtained is an average, which does not distinguish between different types of water molecules within the sample.

The dynamics of water molecules in frozen solutions of antifreezes were determined by studying relaxation rates ( $R_1$  and  $R_2$ ) as well as by performing relaxation dispersion ( $R_{1\rho}$ ) experiments. All measurements focus on the ice peak in the 1D  $^1\text{H}$  spectra collected, so results provide information on the dynamics of the ice (rather than the antifreezes). An example 1D  $^1\text{H}$  spectrum for the liquid and solid water peaks obtained in these SSNMR experiments can be seen in **Figure 4.8**. The  $^1\text{H}$  NMR spectrum for  $\text{H}_2\text{O}$  and antifreeze: $\text{H}_2\text{O}$  comprises a single line, which broadens and changes shape on decreasing temperature. This occurs for all samples, enabling us to know that the sample has frozen. These spectra match those of Lee *et al.* and Wittebort *et al.*, supporting our confirmation of ice formation.<sup>50,63</sup> Any isotropic peaks observed in the

middle of sample spectra indicate molecules experiencing rapid reorientational motions. As these peaks disappear by  $-35\text{ }^{\circ}\text{C}$ , all experiments were performed at this temperature or below, unless stated otherwise.

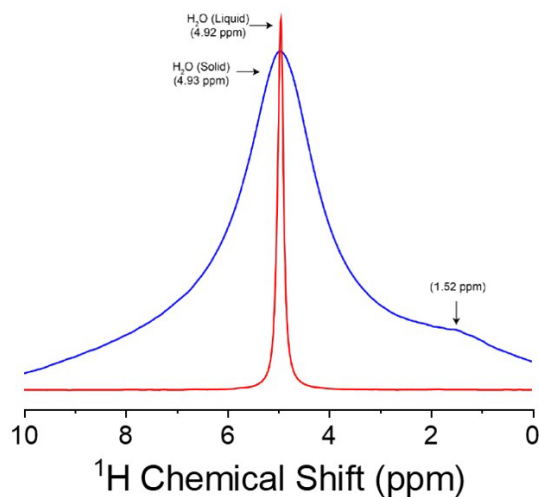


**Figure 4.7.** A) Example assigned 1D  $^1\text{H}$  spectra (a spectra obtained from a one-dimensional NMR experiment after Fourier transformation of the FID; the x axis corresponds to the frequency axis and the y axis corresponds to the intensity of the signal) of  $10.0\text{ mg}\cdot\text{mL}^{-1}$  safranine-O in  $\text{H}_2\text{O}$  at  $10\text{ }^{\circ}\text{C}$  (red) and  $-10\text{ }^{\circ}\text{C}$  (blue). Peak observed at  $1.52\text{ ppm}$  corresponds to signal for safranine-O.

### 4.5.3 $T_1$ and $T_2$ Relaxation

Two types of relaxation are focused on here: longitudinal (spin-lattice) relaxation (**Figure 4.8A**), which is relaxation in the z-axis; and transverse (spin-spin) relaxation (**Figure 4.8B**), which occurs in the x-y plane. The time taken for the return of the longitudinal magnetisation is called spin-lattice relaxation time ( $T_1$ ) and the time taken to decay magnetisation in the x-y plane is spin-spin relaxation time ( $T_2$ ). Relaxation times are measured from saturation recovery spectra.

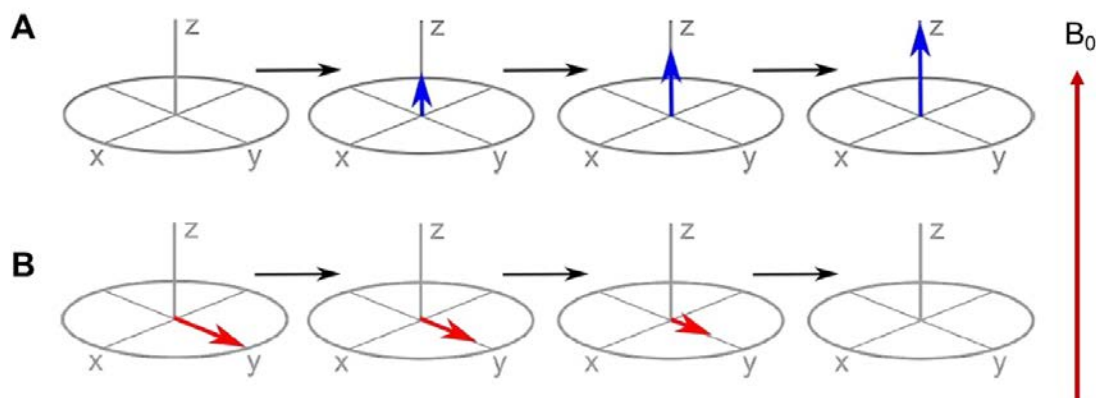


**Figure 4.8.** Schematic of the mechanism of A) spin-lattice relaxation: the longitudinal magnetisation, represented by the blue arrow as it returns to its equilibrium value along the z-axis; B) spin-spin relaxation: the transverse magnetisation, represented by the red arrow as it returns to equilibrium.

$T_2$  are measured from signal arising from the entire volume of the ice sample and therefore represent an average over the three-dimensional space.

Initial studies consisted of  $T_1$  measurements at two different temperatures comparing synthetic antifreezes over time, **Figure 4.9**. In most cases during the first 2.5 hours after freezing the  $T_1$  value rapidly increased before reaching a plateau, suggesting that there could be a decrease in motion during the ice annealing process. This can be explained by the relationship between  $T_1$  and motion not being linear, **Figure 4.9B**.

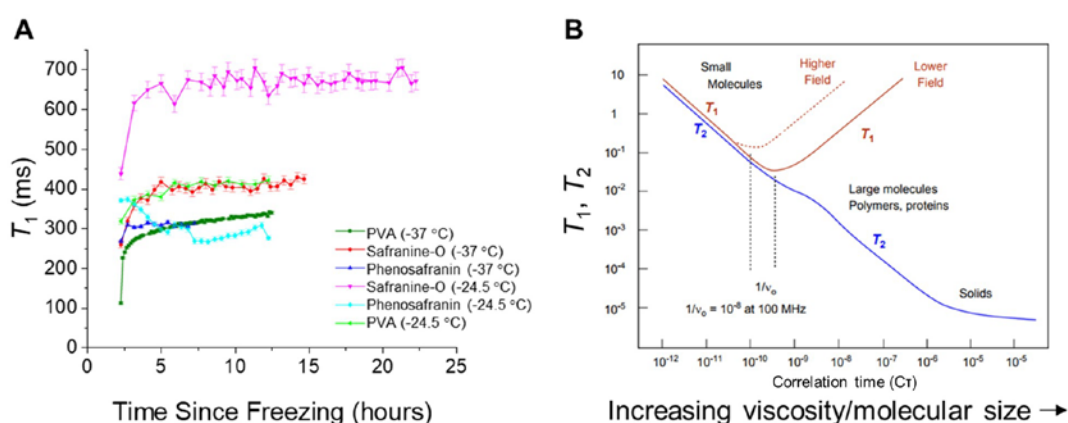


**Figure 4.9.** A) Preliminary  $T_1$  results for PVA20, safranin-O and phenosafranin for two different temperatures; B) Schematic of relaxation times and associated correlation times ( $C\tau$ ) for compounds of different size/viscosity. Adapted from

Bloembergen *et al.* (Phys. Rev., 1948).<sup>64</sup> [PVA20] = 1.0 mg.mL<sup>-1</sup>; [safranin-O] = 1.0 mg.mL<sup>-1</sup>; [Phenosafranin] = 1.0 mg.mL<sup>-1</sup>.

There is also an obvious temperature dependence for safranin-O, **Figure 4.9**;  $T_1$  values recorded at -24.5 °C are much higher than those recorded at -37 °C. This is not observed as clearly for PVA, and phenosafranin does not show this result. This may be explained using the schematic in **Figure 4.9B**. If the initial  $T_1$  is in the lower field for a sample at -37 °C, the  $T_1$  value will increase whilst annealing (or if the concentration increases - due to an increase in viscosity). If the sample is annealed at -24.5 °C instead, the  $T_1$  value may decrease due to increased motion at this higher temperature. However, at some point the average molecular motions become slower than  $v_0$ , and  $T_1$  becomes longer again, thus there is a possibility for the  $T_1$  to cross the minimum and increase: this is seen by the changes in  $T_1$  for phenosafranin at -24.5 °C. Phenosafranin has been frozen at a higher temperature (-24.5 °C rather than -37 °C) so the  $T_1$  value is to the left of the minimum, as it anneals the motion may decrease due to increasing viscosity, then the  $T_1$  will shorten and subsequently cross the minimum leading  $T_1$  to increase again.

$T_1$  experiments for different polymer samples were repeated until the  $T_1$  values were no longer changing significantly, and relaxation times compared to that of IRI activity results from splat assays, **Table 4.1** and **Figure 4.10**.

**Table 4.1.** Comparison of IRI activity data (compared to that of a PBS control) and SSNMR ice relaxation times (recorded in water) for PVA230.

Time (minutes)	$T_1$ (ms)	$T_2$ (ms)	MGS (%PBS)	MLGS (%PBS)
30	212.6	0.260	8.1±0.7	30.0±1.4
60	211.3	0.261	9.1±1.2	30.9±2.0
90	139.6	0.259	9.8±0.6	28.8±0.5
120	137.5	0.255	9.1±0.3	33.1±2.8
150	136.8	0.261	8.7±0.7	37.8±1.7
180	137.4	0.251	15.1±1.0	36.3±0.7

The length of crystals (mean largest grain size, (MLGS)) can be measured along any axis and the mean ice grain area (MGS) is calculated from the number of crystals observed. The smaller the crystals, the more potent the IRI inhibitor.

The average  $T_1$  value (after plateauing) of each PVA and PEG was compared to IRI activity shown as  $c_i$  (a term used to describe the concentration at which the ice recrystallisation rate is reduced by 50 %); this method monitors the average crystal radii over time, ( $c_i$  values obtained by Carsten Budke), **Figure 4.10A**. There is an obvious trend in  $T_1$  plateau values, which decrease as the size of PVA increases and IRI activity increases; the more IRI active the polymer (smaller  $c_i$ ) the faster the relaxation time. **Figure 4.10B** follows the  $T_1$  up to 250 minutes, showing a drop in  $T_1$  for all samples, bar PVA20, during the initial 30 minutes annealing. Once plateaued, the average  $T_1$  value is  $137.85 \pm 1.23$  ms. **Figure 4.10C** shows micrographs of the PVA230 crystals over the same time period recorded for the  $T_1$  experiments. These show minimal change in the crystal size observed for PVA230 over the 180 minutes, with MGS and MLGS increasing by 5 %, which is in agreement with the lack of change in  $T_1$ . No change in  $T_2$  is observed either, with all values being  $0.25 \pm 0.002$  ms, **Table 4.1**.

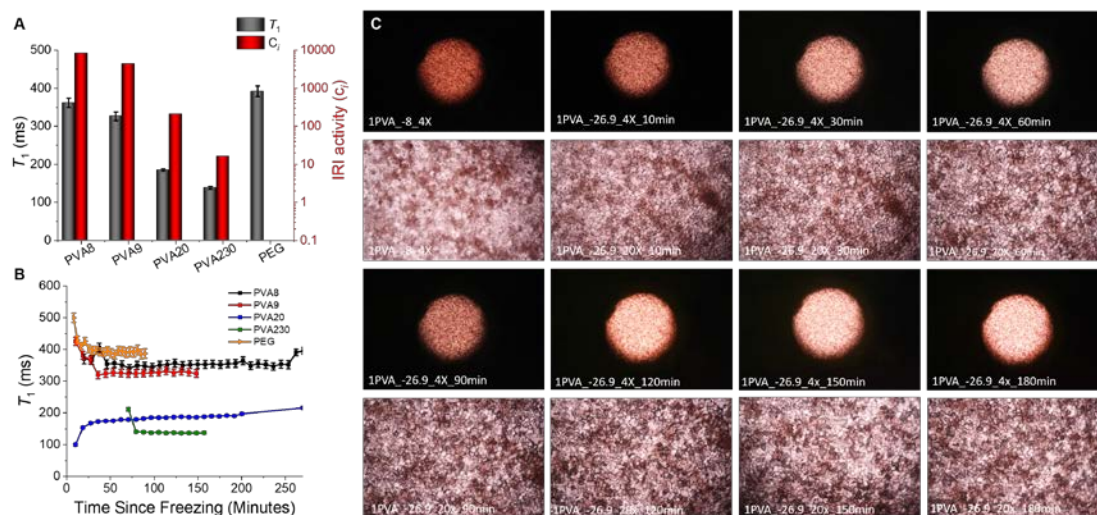


**Figure 4.10.**  $T_1$  data and IRI activity data for polymer samples; A)  $T_1$  plateaus (black) compared to that of critical inhibition concentration ( $c_i$ ) (red); B)  $T_1$  over time; C) Splats over time for PVA230. [Polymer] =  $1 \text{ mg}\cdot\text{mL}^{-1}$  unless stated otherwise.

Gaining specific conclusions with regards to the antifreeze activity of these samples is challenging as so many factors affect the  $T_1$  value. However direct comparisons between, for example, safranin-O and phenosafranin in identical conditions may lead to some conclusions: on average the  $T_1$  values of safranin-O are slower than phenosafranin, suggesting more motion in the safranin-O sample. Nevertheless, factors such as viscosity need to be taken into account (safranin-O forms a

supramolecular structure in solution, phenosafranin does not) as this is also likely to influence the  $T_1$  values. Due to difficulties optimising these  $T_1$  and  $T_2$  experiments,  $R_1$  and  $R_2$  relaxation rate experiments were then focused on to provide more informative results.

#### 4.5.4 $R_1$ and $R_2$ Relaxation Rate Measurements

An alternative way of describing the relaxation process can be by a rate.<sup>65</sup> Rates can be calculated over a range of temperatures (variable temperature  $^1\text{H}$  longitudinal relaxation rates (VT  $R_1$  or  $R_2$ )) and from the rate correlation times ( $C\tau$ ) can be calculated.

The  $R_1$  relaxation rate is calculated as:

$$R_1 = \frac{1}{T_1} \quad (4.1)$$

To calculate the  $R_2$  relaxation rate equation 4.2 is used:

$$R_2 = \frac{1}{T_2} \quad (4.2)$$

##### 4.5.4.1 Longitudinal Relaxation ( $R_1$ ) and Calculated Correlation Times ( $C\tau$ )

First, we measured VT  $R_1$  for frozen water in the presence of different additives.  $^1\text{H}$  chemical shifts of ice versus water could be clearly distinguished (as described in 4.5.2), and due to the concentrations of the additives to be probed (typically  $< 1 \text{ mg.mL}^{-1}$ ), the ice peaks dominated.  $R_1$  rates report on fast motions, *i.e.* motions occurring on a nanosecond - picosecond timescale. By using a series of  $90^\circ$  pulses separated by variable delays (0.01 - 5.0 s), relaxations on the nanosecond – picosecond timescale, which include bond rotations and vibrations (could include that of hydrogen bonds), could be observed as the temperature was increased between  $-36$  and  $-10^\circ\text{C}$ . Under the employed experimental conditions detailed in 4.7.3.2.1, a process called proton spin diffusion (SD) leads to a very fast polarisation transfer between protons, resulting in averaging of the relaxation rates between water molecules characterised

by different dynamic behaviours. However, the fastest relaxing molecules, which here correspond to the interfacial waters, typically dominate the observed average.

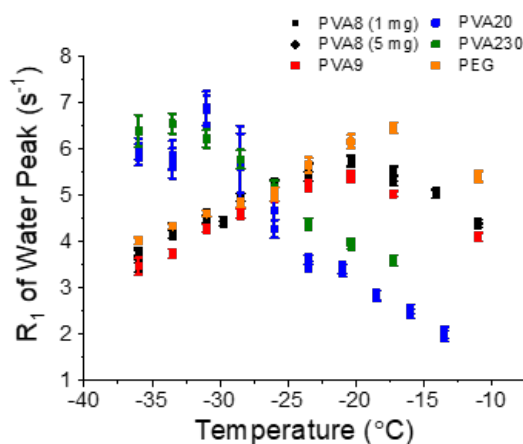


**Figure 4.11.** VT  $^1\text{H}$   $R_1$  of ice in the presence of different DP PVAs and PEG (4 kDa).

Variable Temperature  $^1\text{H}$  relaxation experiments were performed on frozen polymer solutions to obtain the ice proton relaxation rates, **Figure 4.11**. At  $-36\text{ }^\circ\text{C}$ , the ice  $^1\text{H}$   $R_1$  values in the presence of longer PVAs with  $\text{DP} \geq 20$  are much higher than that of shorter DP PVAs with  $\text{DP} < 20$ , **Figure 4.11**. The  $R_1$  rates equalise at around  $-26\text{ }^\circ\text{C}$ ; rates for longer PVAs drop and those of shorter chain lengths increase, with rate maxima around  $-33\text{ }^\circ\text{C}$  for the longer chains and  $-20\text{ }^\circ\text{C}$  for the shorter chains. As a negative control,  $^1\text{H}$   $R_1$  values for ice in the presence of PEG were compared to that of PVA samples.<sup>66</sup> The observed  $R_1$  trends were very similar to the shorter PVA, supporting macroscopic observations that above DP10, PVA gains the ability to modulate the behaviour of water molecules at the ice-additive interface at the molecular level.

The predominant relaxation mechanism often depends on magnetic dipole-dipole interactions, which are mediated by random molecular motions described by correlation times.<sup>67</sup> [ $C\tau$  here is defined as the amount of time for the frozen water  $^1\text{H}$ s to move 1 radian from a starting position, thus the larger  $C\tau$  the slower motion and vice versa.] The correlation times for the fast motions of the interfacial water molecules that dominate the relaxation measurements can be estimated by fitting the  $^1\text{H}$   $R_1$  trends (fitting script written and performed by Dr Stevens and not included as beyond the scope of this work but can be found in Stevens R.A., PhD. Thesis, University of Warwick, 2018).<sup>46</sup> These can include bond rotations accompanied by a



transient breakage of a hydrogen bond. Hydrogen bonding between two species leads to slower bond rotation and translation due to the formation of a ‘complex’ larger than nonbonded species, leading to a change in  $C\tau$ . Because of this, it is of interest to study  $R_I$  as a function of temperature or concentration to potentially provide information on hydrogen bonding.

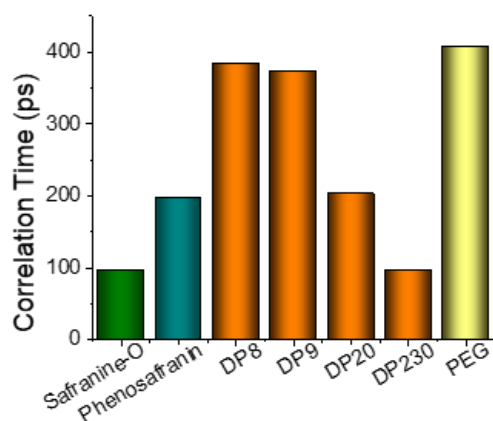


**Figure 4.12.**  $C\tau$  for safranin-O (green) and PVA (DP8-230) (orange) compared to their respective negative controls (phenosafranin (teal) and PEG (yellow)) at  $5 \text{ mg.mL}^{-1}$ . Calculated  $C\tau$  for the ice protons are recorded at  $-30 \text{ }^\circ\text{C}$ .

The shifting of the  $R_I$  maxima for PVA20 and PVA230 to lower temperatures compared to lower DP PVAs and PEG indicates an increase in frequency of the fast motions at the same temperatures. For example, as shown in **Figure 4.12**, significantly shorter effective correlation times were observed for PVA20 and PVA230, compared to that of lower DP PVAs and PEG.

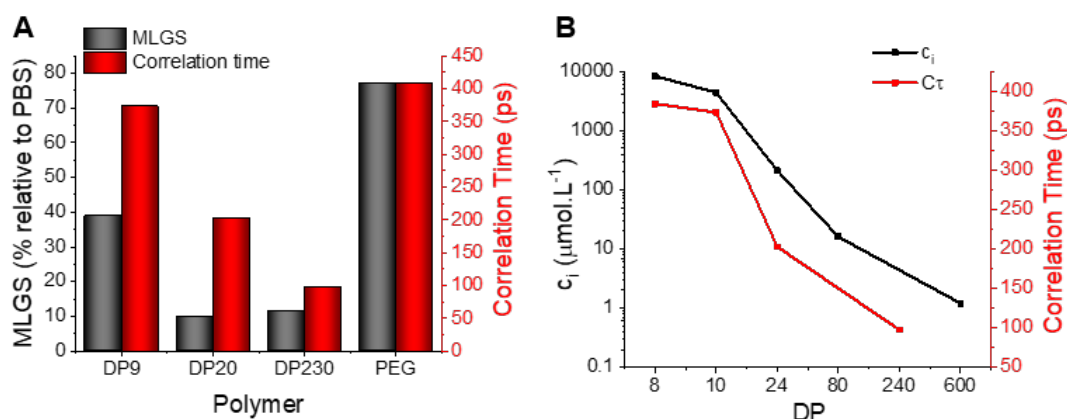


**Figure 4.13.**  $C\tau$  and IRI activity of PVA samples. A) MLGS % of PVA (DP9-230) and PEG (black) compared to correlation time (red) at  $5 \text{ mg.mL}^{-1}$ ; B) Comparison of  $c_i$  (black) and  $C\tau$  (red).

To compare the value of correlation times, they were compared to both MLGS and  $c_i$  for 3 different DP PVAs at  $5 \text{ mg.mL}^{-1}$ , showing that as the PVA chain length increases there are faster  $C\tau$ , **Figure 4.13**. Even at this high polymer concentration, PVA9 which is known to be non-IRI active (crystals are 70 % of the size of PBS and  $>1000 \mu\text{mol.L}^{-1}$  required for 50 % activity), has a correlation time similar to that of PEG, indicating no concentration dependence in this sample.

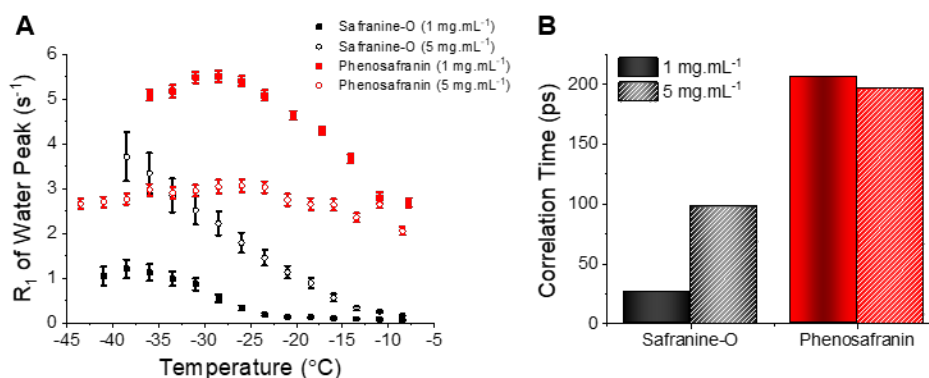


**Figure 4.14.** VT  $^1\text{H}$   $R_1$  of ice in the presence of IRI active safranin-O (black) and inactive phenosafranin (red) at 2 concentrations.

Safranin-O (active) and phenosafranin (inactive) were also tested, **Figure 4.12** and **Figure 4.14**, with correlation times showing similar trends to PVA; the estimated  $C\tau$  for water molecules in ice in the presence of safranin-O and PVA230 are significantly shorter than that of the controls, and are similar at the same concentration ( $\sim 97 \text{ ps}$ ).

There is likely a disruption of the ice network in the presence of these antifreezes, which relates to the grain boundaries between crystals; when ice crystals are smaller there are larger boundaries, and therefore a greater liquid-like disordered layer will be present. At these boundaries H<sub>2</sub>O molecules are less immobilised than those within the ice, and (on average) can move faster than H<sub>2</sub>O molecules within ice crystals. These ‘boundary’ molecules will thus have faster average observed relaxation rates and will potentially dominate any rates and  $C\tau$  obtained. As IRI activity increases, the fraction of ‘boundary’ molecules increases, leading to, on average, faster relaxation rates (which we observe here) thus confirming a disruption of sorts in the ice network.

These relaxation experiments were performed on a range of AF(G)Ps, however the results were inconclusive for a variety of reasons, including large errors in obtained rates and difficulty in sample preparation; proteins denature more quickly in water (the samples could not be prepared in PBS, as the salt interfered with the NMR spectra), thus are not included here.

#### 4.5.4.2 Transverse Relaxation ( $R_2$ )

$R_2$  relaxation is another key relaxation process commonly studied. As  $R_2$  relaxation is dominated by relatively slow dynamics (millisecond – nanosecond), compared to  $R_1$ , VT <sup>1</sup>H  $R_2$  were performed to ensure observation of slower motions at timescales not covered by  $R_1$  experiments. These experiments allow analysis of a sample to see whether reorientational motion dominates.

In general, as the temperature of a sample increases,  $R_2$  will decrease due to local motions such as reorientational motions. This would be observed by a simple decay in rates over an increase in temperature.<sup>68</sup> Besides local motions, exchange and coherent contributions can contribute to the  $R_2$  value. Determination of the extent that coherent contributions affect  $R_2$  was not possible, however these contributions are not affected by a temperature change. Thus, variations observed in the following variable temperature measurements are only due to local motions or exchange. Exchange processes could be slow ( $k \ll |\Delta\nu|$ ) or fast ( $k \gg |\Delta\nu|$ ) relative to the difference in chemical shift ( $\Delta\nu$ ) between the two states ( $a$  and  $b$ ) exchanging;<sup>68</sup> if there is contribution from slow exchange,  $R_2$  should increase with temperature, as chemical exchange will add to the relaxation rate:

$$R_2^{obs} = R_2^0 + k \quad (4.3)$$

Where  $R_2^{obs}$  is the observed relaxation rate,  $R_2^0$  is relaxation in absence of exchange and  $k$  is the rate of exchange.

Over the same temperature change, if there are contributions from fast exchange processes, these will decrease as  $R_2$  increases:

$$R_2^{obs} = R_2^0 + \frac{p_a p_b \Delta\omega^2}{k} \quad (4.4)$$

Where  $p_a$  and  $p_b$  are the populations of states  $a$  and  $b$ , and  $\Delta\omega^2$  is the difference in chemical shift between the two states.

There are different trends for the  $^1\text{H}$   $R_2$  for the samples tested here, indicating that contributions are not only from reorientational motions. However, reorientation of water molecules generally dominates  $R_2$  relaxation rates rather than slow exchange.

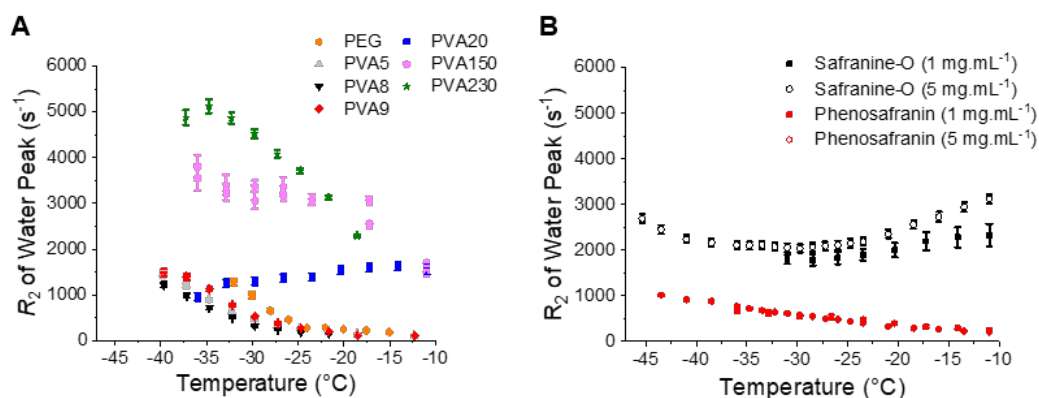


**Figure 4.15.** VT  $^1\text{H}$   $R_2$  of the bulk ice in the presence of IRI active samples and controls. A) PVA (DP5-230) and PEG. [Polymer] = 1  $\text{mg.mL}^{-1}$ ; B) Safranin-O, 1  $\text{mg.mL}^{-1}$  and 5  $\text{mg.mL}^{-1}$  (black), phenosafranin, 1  $\text{mg.mL}^{-1}$  and 5  $\text{mg.mL}^{-1}$  (red).

$R_2$  values over a range of temperatures for all negative controls are low (initial rate  $\sim 1000 \text{ s}^{-1}$ ) and decrease upon heating, indicating that the rates in these samples are in line with the relationship mentioned above, and that the reorientation of water molecules rather than slow exchange dominates the  $R_2$  rates.

Three trends are observed for the different length PVA samples, **Figure 4.15A**.  $R_2$  rates of frozen solutions of shorter chain PVAs (DP < 20) are similar to that of control samples, once again indicating that reorientation dominates in these samples. This is to

be expected as these PVAs have been shown to have no antifreeze activity and thus should lead to no difference in dynamics. DP20  $R_2$  values (blue) appear to be dominated by reorientational motions at temperatures below 30 °C. Then, as the temperature increases these values also increase, indicating a contribution from slow exchange. For PVA150 and PVA230, simple decays are also observed, though these polymers produced higher  $R_2$  values ( $>3500\text{ s}^{-1}$ ) than the low DP PVAs. However, having a higher DP (or concentration) needs to be considered, as both cause an increase in the viscosity of the sample,<sup>69,70</sup> which will slow motions and lead to an increase in reorientational contribution to  $R_2$ . PEG used here has an average DP of 90, though has low  $R_2$  values (orange), thus appears to not cause a significant increase in viscosity.

Trends in  $R_2$  of safranin-O are similar to that of PVA20, **Figure 4.15B**; where, as temperature increases,  $R_2$  also increases. These trends are confirmed by concentration range experiments, which show that  $R_2$  values of safranin-O are not affected by concentration, potentially due to the ‘small’ size of the compound.

Initial VT  $^1\text{H}$   $R_2$  experiments were performed on AF(G)Ps, but results were unsatisfactory and inconclusive.

#### 4.5.5 Spinlock $^1\text{H}$ RD Relaxation Dispersion Measurements

The third type of relaxation studied was spin-lattice relaxation in the rotating frame ( $R_{1\rho}$ ). This is a  $R_1$  measurement undergoing a spin-lock pulse of varying lengths (0.001 – 1.5 ms). This relaxation also is sensitive to motion on the millisecond – nanosecond timescale. Nevertheless, it is considered more suitable for measuring slow dynamics than  $R_2$ , as  $R_2$  is to a greater extent affected by other processes and interactions.  $^1\text{H}$   $R_{1\rho}$  relaxation dispersion signifies presence of a chemical exchange, which is a reversible process whereby water molecules in ice exchange on a microsecond time scale between two (or more) states. As the main difference between the studied samples is the presence of the additives, one of the most plausible interpretations would be that the observed process corresponds to a reversible binding of ice to the additives.

Spinlock  $R_{1\rho}$  relaxation dispersion measurements were performed on samples to investigate exchange; if there are motions in a sample at the microsecond timescale an exponential decay should be observed (measured by monitoring the change in  $R_{1\rho}$  as a function of the spin-lock frequency). Exchange can be probed by applying different spinlock powers to samples; at lower powers exchange dominates  $R_{1\rho}$  measurements.

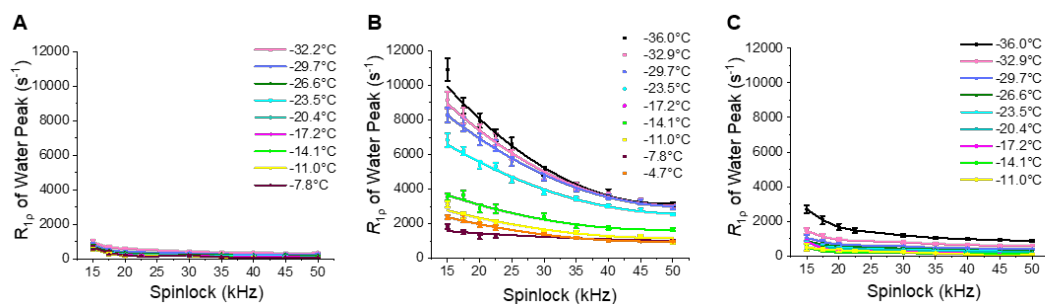


**Figure 4.16.** VT  $^1\text{H}$   $R_{1\rho}$  of ice in the presence of; A) PVA5; B) PVA230; C) PEG.  $[\text{Polymer}] = 1 \text{ mg.mL}^{-1}$ .

For ice in the presence of PVA230 a pronounced exponential decay is observed, indicating motion and a large contribution from a millisecond chemical exchange process, **Figure 4.16B**. This is in support of the formation of an extended hydrogen bond network between the PVA and the ice, as well as the model of entropy-enthalpy compensation; when the polymer is sufficiently long, the enthalpic gains of hydrogen bonding overcome the entropic penalty of binding. The shorter chain PVA and PEG (not antifreezes) have a more gradual decline indicating no exchange at these timescales, **Figure 4.16A/C**. Some PVAs were repeated at lower concentrations such as  $0.1 \text{ mg.mL}^{-1}$  (not shown), and the  $R_{1\rho}$  values were observed to be slightly lower than those observed at  $1 \text{ mg.mL}^{-1}$  but not significantly different. Therefore, there does not appear to be concentration dependence for  $R_{1\rho}$  of polymer:ice systems.

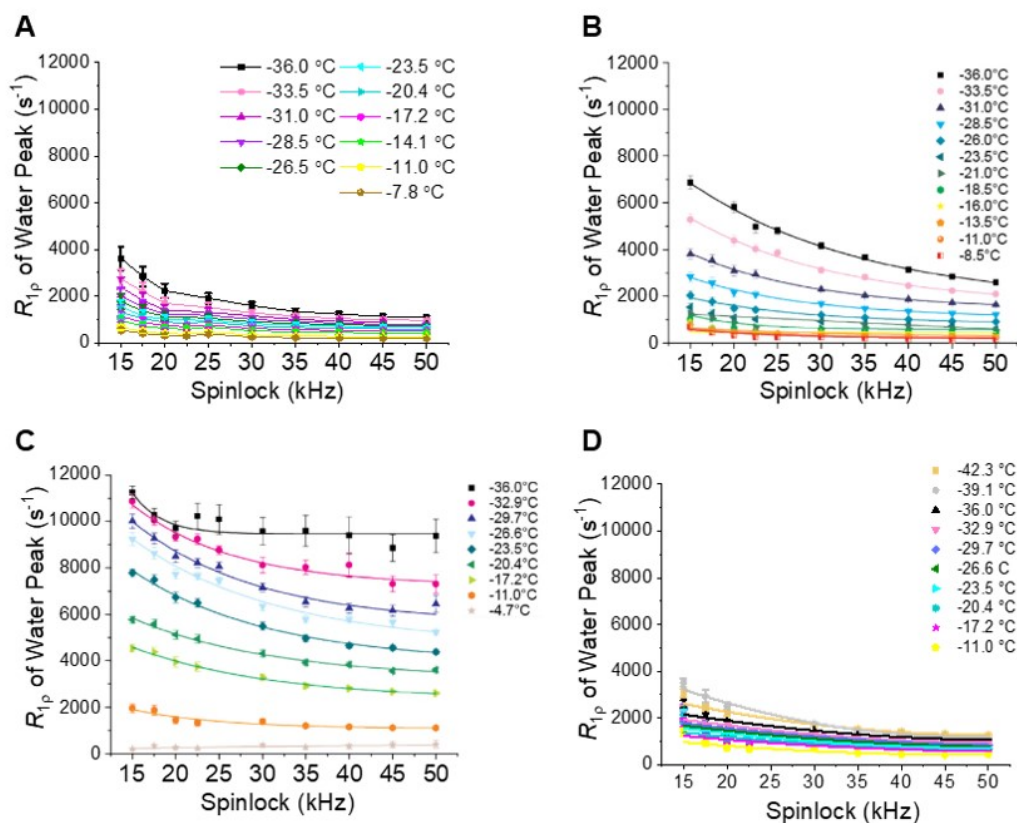


**Figure 4.17.** VT  $^1\text{H}$   $R_{1\rho}$  of ice in the presence of proteins; A) AFPIII; B) bpAFPI; C) AFGP8; D) Lysozyme.  $[\text{AFPIII}] = 0.659 \text{ mg}\cdot\text{mL}^{-1}$ ;  $[\text{bpAFPI}] = 1.0 \text{ mg}\cdot\text{mL}^{-1}$ ;  $[\text{AFGP8}] = 12.0 \text{ mg}\cdot\text{mL}^{-1}$ ;  $[\text{Lysozyme}] = 12.0 \text{ mg}\cdot\text{mL}^{-1}$ .

Evidence that AFGP8 affects ice differently to AFPI and AFPIII is seen in the  $R_{1\rho}$  plots, **Figure 4.17**. There is a large change in base  $R_{1\rho}$  for AFGP over the recorded temperature range and little change in dispersion, indicating that exchange may be in slower microsecond regime, whereas bpAFPI shows greater dispersion suggesting potential contributions from exchange in the faster microsecond regime. AFPIII differs again, with values similar to that of lysozyme, meaning microsecond motions are not affected by any significant contribution from exchange.

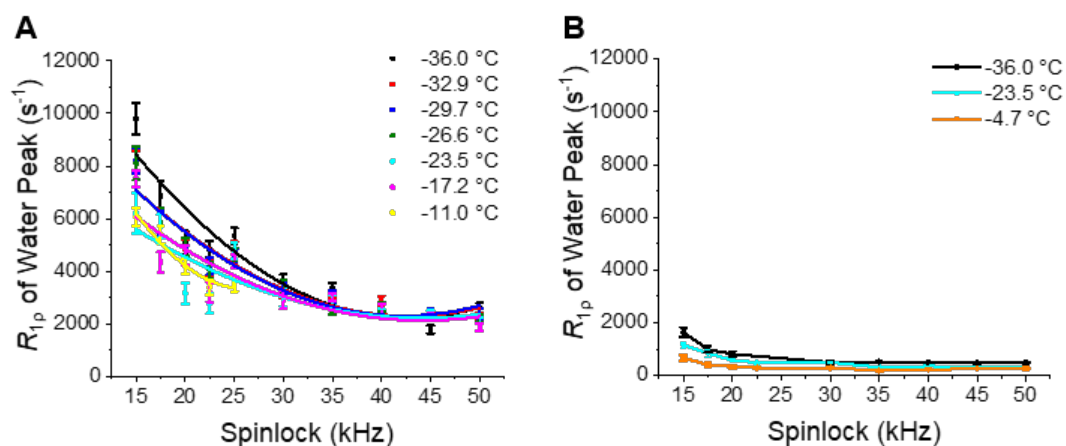


**Figure 4.18.** VT  $^1\text{H}$   $R_{1p}$  of ice in the presence of; A) safranin-O and B) phenosafranin. [Small molecule] = 1 mg.mL $^{-1}$ .

Safranin-O also is seen to have significant contributions from microsecond exchange, **Figure 4.18**, signaling that the synthetic samples here work in the same way as bpAFPI, and showing that both directly interface with an ice surface. PEG, lysozyme and phenosafranin do not show this decay suggesting that only the antifreezes have this particular 100 ps – 2ms motion or exchange.

#### 4.5.6 2D $^1\text{H}$ - $^1\text{H}$ Exchange Spectroscopy

The debate as to whether ice-binding for different antifreezes is reversible continues. The most commonly used model, the adsorption-inhibition model, assumes that AF(G)Ps bind irreversibly to ice,<sup>13,71</sup> though evidence now support both reversible and irreversible binding for a range of AF(G)Ps.<sup>14,27,30,72–76</sup>

Preliminary studies of 2D  $^1\text{H}$ - $^1\text{H}$  exchange spectroscopy (EXSY) measurements were performed on PVA230, AFPIII and AFGP8 alongside their relative negative controls to determine whether any samples bind to water molecules, and potentially elucidate whether they reversibly or irreversibly bind. In 2D EXSY chemical or conformational exchange between nuclei is measured, here this can indicate potential binding as there will be cross relaxation between two nuclei that are spatially close.

These measurements involve a mixing period after the initial  $90^\circ$  pulse, during which magnetisation can exchange, due to the nuclear Overhauser effect (NOE) or slow chemical exchange. After mixing, acquisition of nuclei at their new frequency is recorded and spectra obtained. These spectra will have off-diagonal crosspeaks



between nuclei that are exchanging or are close in space. An example spectrum with off-diagonal crosspeaks between nuclei showing interactions and off-diagonal crosspeaks can be seen in **Figure 4.19**.

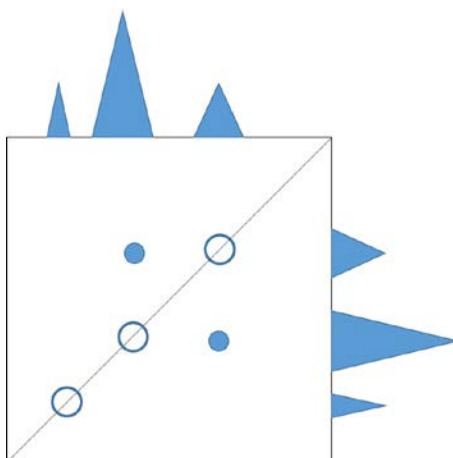


**Figure 4.19.** 2D EXSY Schematic of crosspeaks (blue filled circles) that would be observed if there is any binding between protons in antifreezes and ice.

The aim of these experiments was to look for exchange (crosspeaks) between the ice peak (~4.7 ppm) and any of the antifreeze peaks. The longer the exchange period, the greater the time for exchange: both a 100 ms delay and no delay were chosen for comparison. In all of the 2D spectra here, the red peaks represent no delay and the blue peaks represent the signal after a 100 ms exchange period, **Figure 4.20**.

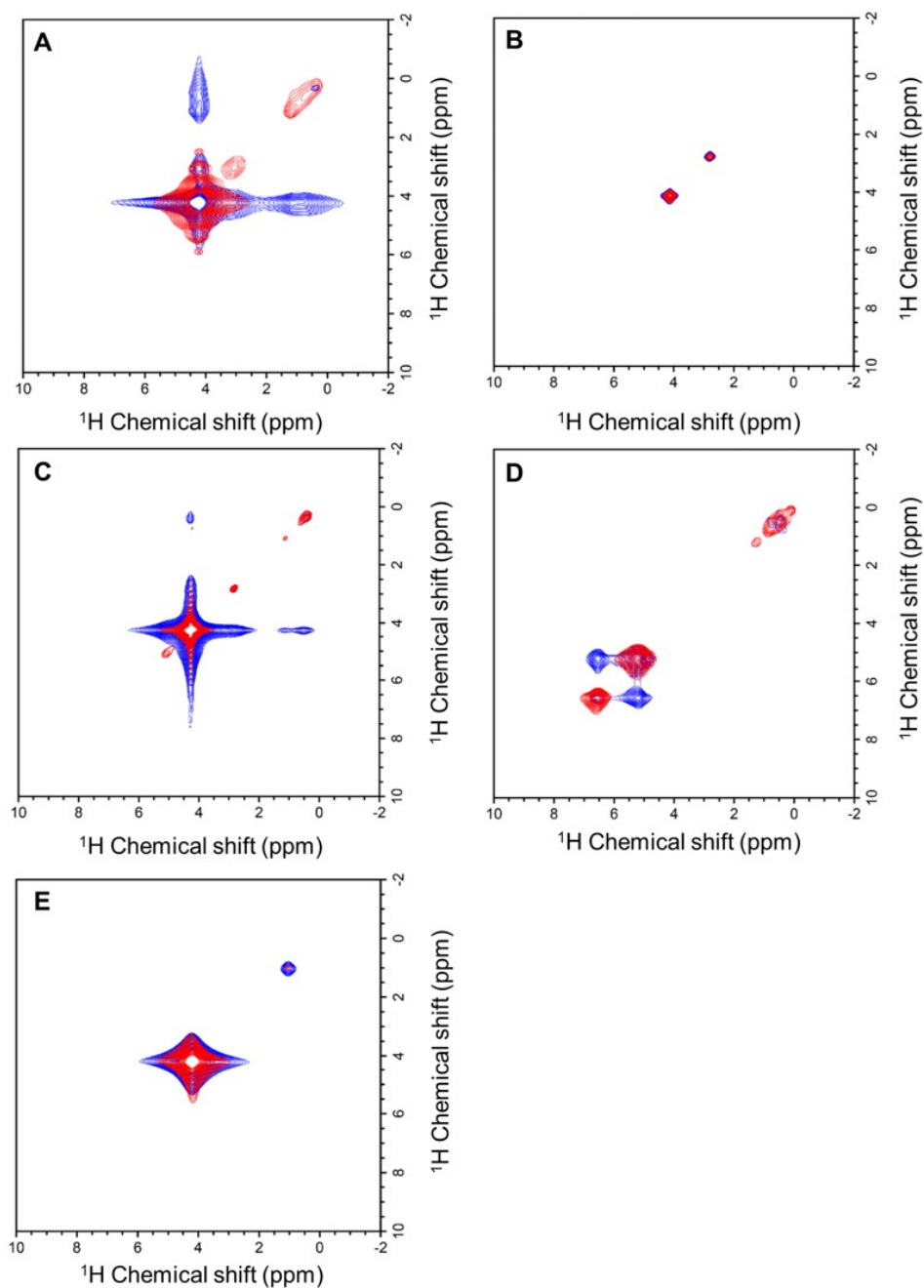


**Figure 4.20.** 2D  $^1\text{H}$ - $^1\text{H}$  EXSY measurements at  $-10\text{ }^\circ\text{C}$  for A) PVA230; B) PEG; C) AFGP8; D) AFPIII; E) Lysozyme. Mixing times were 0 ms (red spectra) and 100 ms (blue spectra).  $[\text{PVA230}] = 5.0\text{ mg}\cdot\text{mL}^{-1}$ ;  $[\text{PEG}] = 5.0\text{ mg}\cdot\text{mL}^{-1}$ ;  $[\text{AFGP8}] = 12.0\text{ mg}\cdot\text{mL}^{-1}$ ;  $[\text{AFPIII}] = 0.659\text{ mg}\cdot\text{mL}^{-1}$ ;  $[\text{Lysozyme}] = 12.0\text{ mg}\cdot\text{mL}^{-1}$ .

$R_{1\rho}$  data for AFGP, bpAFPI and synthetic polymer mimics showed an exchange process at the microsecond timescale is taking place. This was not observed for AFPIII. The crosspeaks observed in the EXSY spectra show that PVA230, AFGP8 and AFPIII bind to water molecules, **Figure 4.20A/C/D**; crosspeaks for AFGP are

observed between the bulk water and aliphatic protons, supporting the theory that AFGP8 directly binds to the primary prismatic plane of ice *via* methyl groups, for AFPIII they are seen between bulk water and amide protons. Importantly, crosspeaks for PVA230 are observed to be between bulk water, aliphatic protons and potentially hydroxyls, providing the first direct evidence for PVA binding to ice on a molecular level, suggesting that PVA hydroxyls could be reversibly binding the ice.

Hydration around the methyl side chains of threonine residues has been observed in the literature and becomes significant at low temperatures as it is said to stabilise the anchored clathrate water array leading to dual H-bonding.<sup>77</sup> The importance of these methyl side chains may link to the proteins studied here where crosspeaks are observed between aliphatic protons and water, indicating that these proteins may bind *via* an anchored clathrate mechanism where the AFP adsorbs to the ‘cage’ around the threonine CH<sub>3</sub> groups.

PEG and lysozyme do not show any interaction between bulk water and the sample; further supporting the theory if there is no interaction with bulk ice molecules will not be IRI active. Low DP PVAs were not studied, however, as all other results indicate similar effects on dynamics as PEG, it can be inferred that they will not produce off-diagonal crosspeaks. This agrees with the crystal faceting data, which showed that IRI inactive PVAs cause no faceting (no binding), whereas IRI active PVAs efficiently bind and thus giving rise to the observed macroscopic properties (faceting and IRI).

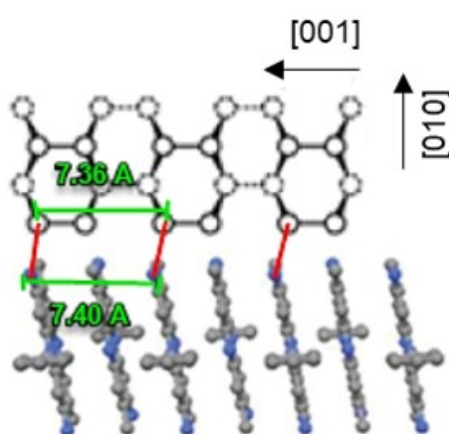


**Figure 4.21.** Illustration of how safranin-O and water may interact. Distances measured in Angstroms.

Crystal structures of safranin-O show that the molecules form alternating stacks with the distance between two NH<sub>2</sub> groups in the stack being 7.40 Å,<sup>56</sup> **Figure 4.21**. This is a smaller distance than that of the gap between every third hydroxyl in PVA (7.56 Å);<sup>15</sup> therefore even though safranin-O has not been studied thus far using EXSY, it may interact with ice in a similar way. The phenosafranin crystal structure is much less ordered and does not form these same stacks and therefore cannot have the same interaction with the ice, thereby not having IRI or TH activity, and a good choice for a negative control.

bpAFPI also was not studied by 2D EXSY, however considering the results already obtained, bpAFPI would bind bulk water in a similar way to the IRI active samples. These results along with relaxation data infer that PVA bind ice reversibly. 2D <sup>1</sup>H-<sup>1</sup>H measurements were recorded on liquid samples to determine whether samples were binding the liquid or solid water. These did not display the expected crosspeaks seen in the frozen solutions; therefore, the IRI active compounds are binding to ice.

#### 4.5.6.1 Antifreeze Macromolecule:ice Interactions

Theories on how antifreezes bind ice are based on molecular dynamics simulations but SSNMR has allowed the investigation of these theories physically by probing motions and facilitated the answering of questions such as: Do PVA, AF(G)Ps and safranin-O affect the ice structure in the same way? Or, can ice-binding be observed? If the different types of ice-binding materials have the same macroscopic effects, potentially they would have the same molecular mechanism.

The exact mechanism of action of different ice-active compounds, and the extent of actual ice-binding is not clear;<sup>78</sup> with different proteins targeting different crystallographic faces of ice, either through hydrophobic interactions in AFGPs<sup>12</sup> or by anchored clathrates in some AFPs.<sup>79</sup> Data obtained through modelling AFPs supports the anchored clathrate mechanism, which is where water molecules in the protein's solvation shell at the IBS become more structured and less dynamic as the temperature decreases leaving the ice-like water at the IBS with a lower energy barrier to ice formation, finding that hyperactive AFPs bind ice through distinct anchored clathrate motifs.<sup>80</sup> Data obtained in the 2D EXSY experiments conducted here differs to that of the literature; some work states the methyl side-chains of threonine residues

in AFPs lead to water ordering and stabilise the anchored clathrate array,<sup>77</sup> however crosspeaks with aliphatic protons are only observed for AFGPs with amines observed for AFPs.

The common structure between all of the antifreezes used here is that the hydrophilic group (either  $-\text{OH}$  or  $-\text{NH}_2$ ) is next to a hydrophobic group ( $-\text{CH}_3$  or  $-\text{CH}_2-$ ). There will be hydrogen bonding between the hydrophilic group and the ice, but clearly the hydrophobic group has an important role too. Perhaps the ice forms a hydrogen bond with the hydrophilic group but then the nearby hydrophobic group causes this bond to be unfavourable, leading to the water breaking this hydrogen bond, rotating  $180^\circ$  and forming the opposite hydrogen bond. This could repeat causing the water molecule to constantly rotate and make and break hydrogen bonds with the antifreezes. In the AFPs, where the threonine group can freely rotate any way this effect could be enhanced even more.

There is also the potential for the creation of ionic defects in the ice networks upon addition of antifreezes, leading to changes in relaxation and thus the observed macroscopic effects. It is possible that there is a substitution ( $-\text{OH}$  or  $-\text{NH}_2$ ) for a water molecule leaving a bond that lacks a proton, leading to the rotation of the water molecule below in order to provide a proton to that bond, resulting in a defect and consequently a change in relaxation values. From the work here however, it cannot be determined whether specific defects are formed, but rather that the dynamics in antifreeze macromolecule:ice samples as well as binding mechanisms do in fact differ. Future work using, such as molecular dynamics simulations, could elucidate this further.

#### 4.5.7 SSNMR of $^1\text{H}$ - $^{13}\text{C}$ Labelled Protein

The major purposes for protein labelling are monitoring of biological processes, reliable quantification of compounds and specific detection of protein modifications and isoforms in multiplexed samples, enhancement of detection sensitivity, and simplification of detection workflows. Proteins can be labelled during cell growth by incorporation of amino acids containing different isotopes, or in biological fluids, cells or tissue samples by attaching specific groups to the  $\epsilon$ -amino group of lysine,

the N-terminus, or the cysteine residues.<sup>81</sup> 1D  $^1\text{H}$ - $^{13}\text{C}$  experiments were performed to further investigate binding of antifreezes to ice.

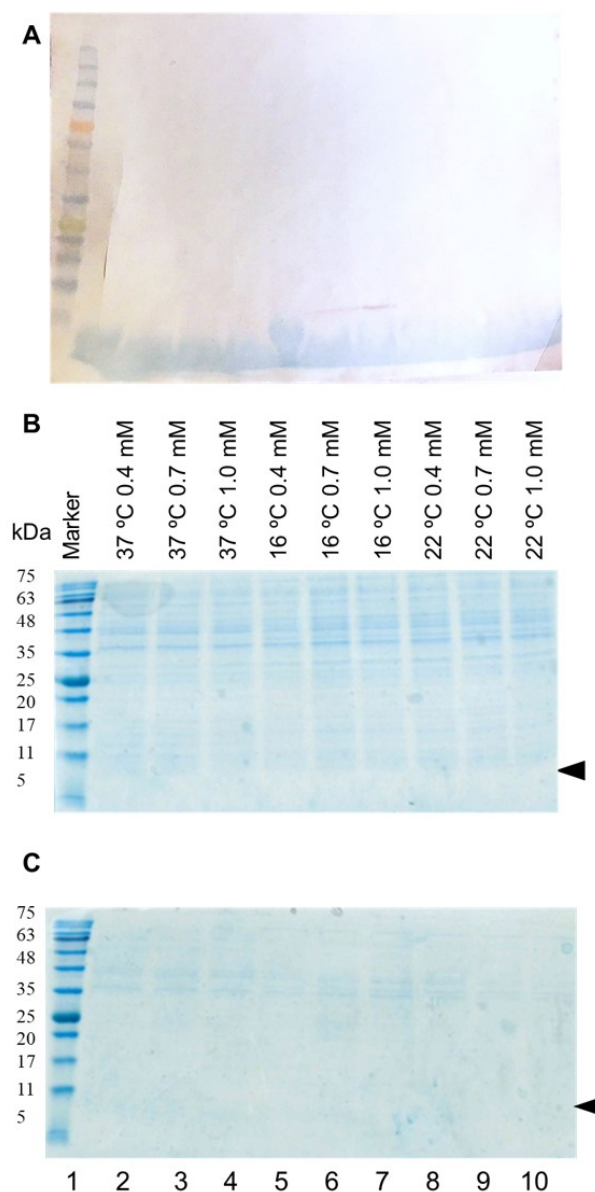


**Figure 4.22.** A) Western Blot showing no expression/minimal of  $^{13}\text{C}$ ,  $^{14}\text{N}$  labelled AFPIII; Attempted optimisation of AFPIII expression to see the issue in protein expression; B) AFPIII whole cell gel; C) AFPIII lysed cell gel. Black triangle represents where AFPIII should appear on the gel.

$^1\text{H}$ - $^{13}\text{C}$  labelled AFPIII was expressed using the same protocol as for unlabelled AFPIII, though a very low mass of protein was obtained. This issue during expression was tested by performing cell growth at 37, 22 and 16 °C, as well as by using three different concentrations of IPTG to determine which stage of expression errors

occurred, **Figure 4.22**. Whole cell and lysed cell gels were taken to see whether the protein had expressed but had been lost in the lysis process.

Initial 1D  $^1\text{H}$ - $^{13}\text{C}$  experiments were run using  $^1\text{H}$ - $^{13}\text{C}$  labelled AFPIII, however no  $^{13}\text{C}$  signal was obtained (as such no plots displayed here). In future, a higher protein concentration, once expression is optimised, should be used.

## 4.6 Conclusion

For the first time, direct evidence for the interaction of PVA to ice crystals is presented, as well as support for the ice-binding of AF(G)Ps to ice. The relaxation measurements confirm the addition of IRI active compounds greatly affect the bulk ice  $^1\text{H}$  dynamics compared to that of negative controls (ensuring any colligative contributions are negated), even at low concentrations. SSNMR studies indicated to that relaxation rates ( $R_1$  and  $R_2$ ) as well as relaxation times ( $T_1$  and  $T_2$ ) differ for ice-active and ice-inactive materials. The relaxation time measurements were complex, and values obtained were dependant on temperature, time frozen, concentration and viscosity, hence proved challenging to make clear comparions between samples. Relaxation measurements were chosen to focus on and provided many interesting trends. Variable temperature  $R_2$  measurements showed a clear difference between antifreezes (large  $R_2$ , exponential decay) and negative controls (small  $R_2$ , little variation, not exponential). This difference is thought to be due to exchange dominating the measurements rather than the ms – ns motions.

Quantitative ice growth measurements confirm that above a critical chain length of 10 units PVA's unique IRI activity is activated. Using SSNMR, the  $R_1$  relaxation of bulk ice in the presence of PVA was measured and was found to scale with the macroscopic critical inhibitory concentrations and MLGS values, with longer polymers being more active inhibitors and having faster correlation times. This supports a mechanism of the PVA forming an extended hydrogen bonded network to the prism planes of ice but only above the critical chain length, and hence enthalpy-entropy compensation is a driving force. Spin-lattice relaxation measurements showed significant exchange process in IRI active polymers compared to negative controls supporting a reversible binding process, again consistent with the need for multivalent presentation of the hydroxyls to provide sufficient affinity.

Safranin-O is seen to work similarly to PVA, further supporting that ice dynamics are affected by frozen solutions of IRI active compounds and not their respective controls or in a colligative manner, and that ice proton motions are of importance for IRI activity.

Finally, 2D EXSY experiments showed through-space correlation between PVA of DP>20 and ice, demonstrating binding is occurring. Taken together, these results



prove how a flexible macromolecule such as PVA can reversibly bind and inhibit ice, through an extended hydrogen bonded 'zipper', and that multivalency is essential. These results are significant as it is the first example of molecular, rather than indirect macroscopic, measurements of a synthetic IRI demonstrating ice-binding. Safranine-O also shows a decrease in  $C\tau$  as well as exchange, indicating reversible binding in this case also. Ice-binding was additionally observed for AFPIII and AFGP8, though the data obtained from relaxation experiments was insufficient to allow confirmation of whether these proteins bind reversibly or irreversibly.

These results are significant in both basic cryo-science and in the development of new materials for low temperature applications. The next steps in this area would be to continue relaxation experiments with labelled antifreeze samples, as attempted briefly in 4.5.7, as well as by performing 2D EXSY using  $D_2O$ , where this would elucidate further the exchange occurring and allow site-specific interrogation of intermolecular contacts and structures.

Potentially, this work will lead to the use of SSNMR as an assay to see if samples could have antifreeze activity.

## 4.7 Experimental

### 4.7.1 Materials

Poly(ethylene glycol) (PEG, 4 kDa), polyvinyl alcohol (PVA230 10 kDa), safranine-O, and phenosafranin were purchased from Sigma Aldrich and used as supplied unless otherwise stated. Phosphate-buffered saline solution was prepared using in Milli-Q water ( $>18.2 \Omega$  mean resistivity) to give  $[\text{NaCl}] = 0.138 \text{ M}$ ,  $[\text{KCl}] = 0.0027 \text{ M}$ , and pH 7.4) Tetrakis(trimethylsilyl)silane was purchased from Fisher Scientific. PVA  $\text{DP} \leq 20$  were produced as previously described.<sup>82</sup> AFPIII and AFPI and AFGP8 were used as provided. Expression and purification of the antifreeze proteins detailed in Chapter 1.

### 4.7.2 Physical and Analytical Methods

All samples were studied using  $^1\text{H}$  saturation recovery MAS NMR and spin echo MAS NMR spectra which were acquired on a Bruker Avance III spectrometer operating at 11.75 T ( $^1\text{H}$  resonance frequency of 500 MHz) using a 4.0 mm Bruker triple resonance probe, using temperatures between  $-30$  and  $10 \text{ }^\circ\text{C}$ . (0.20 ppm reference) soaked in methanol was put into the rotor and used as an internal thermometer.

### 4.7.3 Procedures

#### 4.7.3.1 Ice Recrystallisation Inhibition ‘Splat’ Assay

Samples were dissolved in PBS buffer (pH 7.4) at concentrations of 10 to  $0.05 \text{ mg.mL}^{-1}$  and dropped onto a glass cover slip on a metal disc cooled with dry ice ( $-78 \text{ }^\circ\text{C}$ ). An ice wafer instantly formed and was transferred to a cryostage held at  $-8 \text{ }^\circ\text{C}$  under liquid nitrogen. Samples were left to anneal for 30 minutes. Images of the wafer were taken before and after the 30 minutes. Image processing was performed using ImageJ software on the 5 largest crystals from at least 3 independent wafers giving the MLGS from 15 measurements.

### 4.7.3.2 SSNMR

Saturation recovery spectra were acquired to measure the  $T_1$  and  $T_2$  of hydrogen in  $H_2O$  in the different samples and the obtained data was analysed by calculating correlation functions for the nuclear spin interactions acting on the observed spin, from these calculations the relaxation time is obtained. The experiments were repeated multiple times to improve the signal to noise ratio and yield more accurate relaxation rates.

Samples for all experiments were dissolved to appropriate concentrations using Milli-Q ultrapure water and transferred to rotors (50  $\mu$ L), which were then sealed with top caps. The rotors were inserted into 4.0 mm triple-resonance MAS probes and placed in the SSNMR. MAS was confirmed to be at 10 kHz spinning frequency then samples were cooled to  $-36$  °C. The temperature was recorded using a variable temperature unit (VTU) and calibrated by calculating the difference between methyl and hydroxyl  $^1H$  chemical shifts in methanol using TTMSS as a reference. The sample temperature was regulated using Bruker BCU-Xtreme cooling unit. Experiments were performed as a function of sample temperature between  $-36$  and  $10$  °C (0.20 ppm reference); the upper limit of which was restricted only by the sample melting point. All the measurements were performed after equilibration time to allow for freezing of the sample as indicated by the broadening of the water  $^1H$  resonance. The chemical shifts for liquid and solid water overlap, however the intensity of these peaks differ greatly; the ice peak is broad with low intensity and the water peak narrow with intensity orders of magnitude higher. Therefore, frozen samples were determined by the highly observable change in intensity.

#### 4.7.3.2.1 Variable Temperature $^1H$ Relaxation Experiments ( $R_1$ )

The samples were set up as described above and the spins saturated with a series of  $90^\circ$  pulses separated by variable delays (0.01 – 5 s). The data obtained from these experiments refers to motions in the sample on the nanosecond – picosecond timescale.

#### 4.7.3.2.2 Variable Temperature $^1\text{H}$ Relaxation Experiments ( $R_2$ )

Samples were prepared as described above and  $R_2$  recorded using a CPMG pulse sequence. Measurements were initialised by a 100 kHz  $\pi/2$   $^1\text{H}$  pulse, followed by  $n$  spin-echoes. The pulse sequence was repeated  $n$  times in line with the number of spin-echoes. The data obtained from these experiments refers to motions in the sample on the millisecond – nanosecond timescale.

#### 4.7.3.2.3 Variable Temperature $^1\text{H}$ Relaxation Dispersion ( $R_{1\rho}$ )

These samples were initialised with a 100 kHz  $\pi/2$   $^1\text{H}$  pulse followed by a spin-lock pulse of varying length and power. These experiments access only motions at the microsecond timescale in the ice and are recorded as  $R_{1\rho}$ . These experiments were performed over a range of temperatures to investigate the relationship between motion and temperature.

#### 4.7.3.2.4 2D $^1\text{H}$ - $^1\text{H}$ Exchange Spectroscopy

Samples were initialised with a 100 kHz  $\pi/2$   $^1\text{H}$  pulse followed by indirect evolution time ( $t_1$ ). This is followed by another a 100 kHz  $\pi/2$   $^1\text{H}$  pulse, a mixing time of 0 or 100 ms, a final a 100 kHz  $\pi/2$   $^1\text{H}$  pulse and then a direct acquisition period.

## 4.8 References

- 1 E. V. Pikuta, R. B. Hoover and J. Tang, *Crit. Rev. Microbiol.*, 2007, **33**, 183–209.
- 2 N. Møbjerg, K. A. Halberg, A. Jørgensen, D. Persson, M. Bjørn, H. Ramløv and R. M. Kristensen, *Acta Physiol.*, 2011, 202, 409–420.
- 3 P. L. Davies, *Trends Biochem. Sci.*, 2014, **39**, 548–555.
- 4 J. G. Duman, *J. Exp. Biol.*, 2015, **218**, 1846–1855.
- 5 M. Hassas-Roudsari and H. D. Goff, *Food Res. Int.*, 2012, **46**, 425–436.
- 6 N. Cochet and P. Widehem, *Appl. Microbiol. Biotechnol.*, 2000, 54, 153–161.
- 7 R. Gupta and R. Deswal, *J. Biosci.*, 2014, **39**, 931–944.
- 8 H. M. Zbikowska, *Transgenic Res.*, 2003, **12**, 379–389.
- 9 H. J. Kim, J. H. Lee, Y. B. Hur, C. W. Lee, S.-H. Park and B.-W. Koo, *Mar. Drugs*, 2017, **15**, 27.
- 10 S. Deville, *J. Mater. Res.*, 2013, **28**, 2202–2219.
- 11 H. Kondo, Y. Hanada, H. Sugimoto, T. Hoshino, C. P. Garnham, P. L. Davies and S. Tsuda, *Proc. Natl. Acad. Sci.*, 2012, **109**, 9360–9365.
- 12 K. Mochizuki and V. Molinero, *J. Am. Chem. Soc.*, 2018, **140**, 4803–4811.
- 13 K. Meister, A. L. Devries, H. J. Bakker and R. Drori, *J. Am. Chem. Soc.*, 2018, **140**, 9365–9368.
- 14 M. I. Gibson, *Polym. Chem.*, 2010, **1**, 1141–1152.
- 15 P. M. Naullage, L. Lupi and V. Molinero, *J. Phys. Chem. C*, 2017, **121**, 26949–26957.
- 16 C. Budke and T. Koop, *ChemPhysChem*, 2006, **7**, 2601–2606.
- 17 C. Stubbs, L. E. Wilkins, A. E. R. Fayter, M. Walker and M. I. Gibson, *Langmuir*, 2019, **35**, 7347–7353.
- 18 T. R. Congdon, R. Notman and M. I. Gibson, *Eur. Polym. J.*, 2017, **88**, 320–327.

- 19 L. L. . Olijve, K. Meister, A. L. DeVries, J. G. Duman, S. Guo, H. J. Bakker and I. K. Voets, *Proc. Natl. Acad. Sci.*, 2016, **113**, 3740–3745.
- 20 I. Kratochvílová, M. Golan, K. Pomeisl, J. Richter, S. Sedláková, J. Šebera, J. Mičová, M. Falk, I. Falková, D. Řeha, K. W. Elliott, K. Varga, S. E. Follett and D. Šimek, *RSC Adv.*, 2017, **7**, 352–360.
- 21 L. Ickes, A. Welti, C. Hoose and U. Lohmann, *Phys. Chem. Chem. Phys.*, 2015, **17**, 5514–5537.
- 22 D. R. Nutt and J. C. Smith, *J. Am. Chem. Soc.*, 2008, **130**, 13066–13073.
- 23 C. Navarro-Retamal, A. Bremer, J. Alzate-Morales, J. Caballero, D. K. Hinch, W. González and A. Thalhammer, *Phys. Chem. Chem. Phys.*, 2016, **18**, 25806–25816.
- 24 V. F. Petrenko and R. W. Whitworth, *Physics of Ice*, Oxford University Press, Oxford, 1999.
- 25 A. B. Siemer and A. E. Mcdermott, *J. Am. Chem. Soc.*, 2008, **130**, 17394–17399.
- 26 A. B. Siemer, K.-Y. Huang and A. E. Mcdermott, *Proc. Natl. Acad. Sci. USA*, 2010, **107**, 17580–17585.
- 27 Y. Ba, J. Wongsakhaluang and J. Li, *J. Am. Chem. Soc.*, 2003, **125**, 330–331.
- 28 Y. Mao and Y. Ba, *Biophys. J.*, 2006, **91**, 1059–1068.
- 29 B. G. Pfrommer, F. Mauri and S. G. Louie, *J. Am. Chem. Soc.*, 2000, **122**, 123–129.
- 30 R. E. Feeny and T. S. Burcham, *Annu. Rev. Biophys. Biophys. Chem.*, 1986, **15**, 59–78.
- 31 C. C. M. Groot, K. Meister, A. L. DeVries and H. J. Bakker, *J. Phys. Chem. Lett.*, 2016, **7**, 4836–4840.
- 32 T. Ko, H. Robinson, Y. Gao, C. C. Cheng, A. L. Devries and A. H. Wang, *Biophys. J.*, 2003, **84**, 1228–1237.
- 33 T. I. Brox, M. L. Skidmore and J. R. Brown, *J. Glaciol.*, 2015, **61**, 55–64.
- 34 M. Matsumoto, S. Saito and I. Ohmine, *Nature*, 2002, **416**, 409–413.

- 35 P. M. Singer, D. Asthagiri, W. G. Chapman and G. J. Hirasaki, *J. Magn. Reson.*, 2017, **277**, 15–24.
- 36 C. J. Capicciotti, M. Leclere, F. A. Perras, D. L. Bryce, H. Paulin, J. Harden, Y. Liu and R. N. Ben, *Chem. Sci.*, 2012, **3**, 1408–1416.
- 37 T. Bauer, J. Gath, A. Hunkeler, M. Ernst, A. Böckmann and B. H. Meier, *J. Biomol. NMR*, 2017, **67**, 15–22.
- 38 J. R. Brown, J. D. Seymour, T. I. Brox, M. L. Skidmore, C. Wang, B. C. Christner, B. H. Luo and S. L. Codd, *Biotechnol. Reports*, 2014, **3**, 60–64.
- 39 D. E. Mitchell, A. E. R. Fayter, R. C. Deller, M. Hasan, J. Gutierrez-Marcos and M. I. Gibson, *Mater. Horizons*, 2019, **6**, 364–368.
- 40 R. C. R. C. Deller, M. Vatish, D. A. D. A. Mitchell and M. I. Gibson, *Nat. Commun.*, 2014, **5**, 1–7.
- 41 C. I. Biggs, T. L. Bailey, B. Graham, C. Stubbs, A. E. R. Fayter and M. I. Gibson, *Nat. Commun.*, 2017, **8**, 1546.
- 42 A. A. Antson, D. J. Smith, D. I. Roper, S. Lewis, L. S. D. Caves, C. S. Verma, S. L. Buckley, P. J. Lillford and R. E. Hubbard, *J. Mol. Biol.*, 2001, **305**, 875–889.
- 43 J. Baardsnes and P. L. Davies, *Biochim. Biophys. Acta - Proteins Proteomics*, 2002, **1601**, 49–54.
- 44 M. J. Duer, in *Solid-State NMR Spectroscopy Principles and Applications*, ed. M. J. Duer, Blackwell Science Ltd, 2002, pp. 237–279.
- 45 J. R. Lewandowski, *Acc. Chem. Res.*, 2013, **46**, 2018–2027.
- 46 R. A. Stevens, University of Warwick, 2018.
- 47 M. J. Duer, in *Solid-State NMR Spectroscopy Principles and Applications*, ed. M. J. Duer, Blackwell Science Ltd, 2002, pp. 2–72.
- 48 F. Cruzet, A. E. Mcdermott, R. Gebhard, K. van der Hoef, M. B. Spijker-Assink, J. Herzfeld and J. Lugten, *Science*, 1991, **251**, 783–786.
- 49 S. J. Opella and F. M. Marassi, *Annu. Rev. Anal. Chem.*, 2004, **104**, 3587–3606.

- 50 D. K. Lee, B. S. Kwon and A. Ramamoorthy, *Langmuir*, 2008, **24**, 13598–13604.
- 51 S. D. Cady, K. Schmidt-rohr, J. Wang, C. S. Soto, W. F. Degrado and M. Hong, *Nature*, 2010, **463**, 689–692.
- 52 A. Lange, K. Giller, S. Hornig, M. F. Martin-Eauclaire, O. Pongs, S. Becker and M. Baldus, *Nature*, 2006, **440**, 959–962.
- 53 B. Geil, T. M. Kirschgen and F. Fujara, *Phys. Rev. B - Condens. Matter Mater. Phys.*, 2005, **72**, 1–10.
- 54 J. A. Hernandez and R. Caracas, *J. Chem. Phys.*, , DOI:10.1063/1.5028389.
- 55 P. K. Wang, in *Physics and Dynamics of Clouds and Precipitation*, Cambridge University Press, Cambridge, 2013, pp. 68–85.
- 56 R. Drori, C. Li, C. Hu, P. Raiteri, A. L. Rohl, M. D. Ward and B. Kahr, *J. Am. Chem. Soc.*, 2016, **138**, 13396–13401.
- 57 O. Mizrahy, M. Bar-Dolev, S. Guy and I. Braslavsky, *PLoS One*, 2013, **8**, e59540.
- 58 G. Siegle and M. Weithase, *Zeitschrift fur Phys.*, 1969, **219**, 364–380.
- 59 T. G. Nunes, E. W. Randall and G. Guillot, *Solid State Nucl. Magn. Reson.*, 2007, **32**, 59–65.
- 60 T. Bauer, J. Gath, A. Hunkeler, M. Ernst, A. Böckmann and B. H. Meier, *J. Biomol. NMR*, 2017, **67**, 15–22.
- 61 D. E. Barnaal and I. J. Lowe, *J. Chem. Phys.*, 1968, **48**, 4614–4618.
- 62 A. Böckmann, C. Gardiennet, R. Verel, A. Hunkeler, A. Loquet, G. Pintacuda, L. Emsley, B. H. Meier and A. Lesage, *J. Biomol. NMR*, 2009, **45**, 319–327.
- 63 R. J. Wittebort, M. G. Usha, D. J. Ruben, D. E. Wemmer and A. Pines, *J. Am. Chem. Soc.*, 1988, **110**, 5668–5671.
- 64 N. Bloembergen, E. M. Purcell and R. V. Pound, *Phys. Rev.*, 1948, **73**, 679–712.
- 65 J. Keeler, in *Understanding NMR Spectroscopy*, Wiley, 2nd edn., 2010, pp.



- 292–380.
- 66 M. Hasan, A. E. R. Fayter and M. I. Gibson, *Biomacromolecules*, 2018, **19**, 3371–3376.
- 67 E. D. Becker, *eMagRes.*, 2007, DOI:10.1002/9780470034590.emrstm0216.
- 68 I. R. Kleckner and M. P. Foster, *Biochim Biophys Acta*, 2011, **1814**, 942–968.
- 69 M. V. S. Rao, *Polymer*, 1993, **34**, 592–596.
- 70 R. F. Fedors, *Polymer*, 1979, **20**, 225–228.
- 71 J. A. Raymond and A. L. DeVries, *Proc. Natl. Acad. Sci.*, 1977, **74**, 2589–2593.
- 72 C. A. Bush, R. E. Feeney, D. T. Osuga, S. Ralapati and Y. Yeh, *Int. J. Pept. Protein Res.*, 1981, **17**, 125–129.
- 73 M. M. Harding, P. I. Anderberg and A. D. J. Haymet, *Eur. J. Biochem.*, 2003, **270**, 1381–1392.
- 74 Y. Tachibana, G. L. Fletcher, N. Fujitani, S. Tsuda, K. Monde and S. I. Nishimura, *Angew. Chemie Int. Ed.*, 2004, **43**, 856–862.
- 75 S. Zepeda, E. Yokoyama, Y. Uda, C. Katagiri and Y. Furukawa, *Cryst. Growth Des.*, 2008, **8**, 3666–3672.
- 76 C. P. Garnham, A. Natarajan, A. J. Middleton, M. J. Kuiper, I. Braslavsky and P. L. Davies, *Biochemistry*, 2010, **49**, 9063–9071.
- 77 S. Chakraborty and B. Jana, *J. Phys. Chem. B*, 2018, **122**, 3056–3067.
- 78 Y. Celik, R. Drori, N. Pertaya-Braun, A. Altan, T. Barton, M. Bar-Dolev, A. Groisman, P. L. Davies and I. Braslavsky, *Proc. Natl. Acad. Sci.*, 2013, **110**, 1309–1314.
- 79 C. P. Garnham, R. L. Campbell and P. L. Davies, *Proc. Natl. Acad. Sci.*, 2011, **108**, 7363–7367.
- 80 A. Hudait, N. Odendahl, Y. Qiu, F. Paesani and V. Molinero, *J. Am. Chem. Soc.*, 2018, **140**, 4905–4912.
- 81 C. Obermaier, A. Griebel and R. Westermeier, in *Proteomic Profiling*, ed. A.

Posch, Humana Press, New York, NY, 2015, pp. 153–165.

- 82 T. Congdon, B. T. Dean, J. Kasperczak-Wright, C. I. Biggs, R. Notman and M. I. Gibson, *Biomacromolecules*, 2015, **16**, 2820–2826.

# Chapter 5

---

## Discovering Non-Proteogenic and Non-Polymeric Nucleating Materials

## 5.1 Declarations

*Setup of the  $\mu\text{L-NIPI}$  nucleation drop assay and LabView program optimised by Dr Thomas Whale (University of Warwick). Lignins provided by Dr Goran Rashid (supervised by Professor Tim Bugg, University of Warwick). Metal organic frameworks provided by Ehsan Ghadim (supervised by Professor Richard Walton, University of Warwick).*

## 5.2 Chapter Abstract

The phenomenon of ice nucleation has both intrigued and demanded the attention of scientists from a wide range of disciplines. Control of ice formation has broad applications in the food, pharmaceutical, and chemical industries, *e.g.* anti-icing coatings for aircrafts; reducing frost and ice accumulation in refrigerators and heat exchangers to improve heat transfer efficiency; controlling nucleation temperatures for cell cryopreservation. Much work has focused on synthesis of materials for inhibiting the growth of ice crystals, but control of ice nucleation is less studied.

Here a range of previously untested compounds, including metal organic frameworks and lignins, have been tested for their ice nucleating efficiency using droplet freezing assays (a type of immersion technique where a sample of interest is dissolved/immersed in water), in the hope of providing potential future solutions for a range of icing problems. One particular lignin, alkali lignin, was found to nucleate ice well in the immersion mode but not to inhibit ice recrystallisation, whereas the other tested compounds had neither IRI nor nucleating activity. Nucleant concentration and experimental cooling rate were varied to test their effect on lignin ice nucleation efficiency, finding, strikingly, that there was no concentration or cooling rate dependence on the efficiency for alkali lignin. Two lignin samples were also filtered to establish the size of particles responsible for ice nucleation, finding that ice nucleating particles (INP)s for alkali lignin are  $<0.2\ \mu\text{m}$ , which are much smaller than atmospheric INP, and those of GreenValue are  $>0.2\ \mu\text{m}$ .

Different wet-dispersion measurement techniques were studied for their use in observing nucleation activity, with the  $\mu\text{L-NIPI}$ -based ( $\mu\text{L-Nucleation}$  by Immersed

Particle Instrument) nucleation drop assay providing the most useful, high-throughput results.

A discussion of further experiments that could be performed to further understand the origin of lignin's ice nucleation efficiency is included *e.g.* characterisation and aggregation studies.

## 5.3 Introduction

### 5.3.1 Importance of Ice Nucleation

Sub-microlitre volumes of liquid water can supercool to temperatures below  $-35\text{ }^{\circ}\text{C}$ , therefore, despite ice Ih being the thermodynamically stable form of water below  $0\text{ }^{\circ}\text{C}$ , ice nucleation needs to occur before ice crystal growth can take place.<sup>1</sup> Ice nucleation is the process which initiates freezing of supercooled liquid water. There is an energy barrier to the formation of ice clusters large enough to grow, so called critical nuclei, resulting from the interfacial tension between supercooled liquid water and ice. Once an ice cluster larger than the critical size is present crystal growth can proceed. In general, ice nucleation is achieved through the addition of a heterogeneous ice nucleating particle (INP), which lowers the energy barrier to nucleation thus promoting nucleation above the homogeneous freezing temperature.<sup>2</sup>

As mentioned in **1.3.1**, ice nucleation is of great importance for freeze-tolerant organisms, the survival of certain pathogens and for cloud formation. An understanding of this process, and of INPs themselves will have substantial implications for biological ice nucleation promotion and anti-icing/de-icing strategies.<sup>3</sup> A brief description of modes of heterogeneous ice nucleation and a discussion of currently known INPs and experimental methods for studying ice nucleation are provided, with the aim of detailing the motivation for the work performed here.

### 5.3.2 Heterogeneous Nucleation

Nucleation is divided into homogeneous (without the addition of an INP) and heterogeneous (promoted by presence of INPs). Homogeneous nucleation is well described by classical nucleation theory (CNT). Heterogeneous ice nucleation, which is less well understood, and the only relevant type of nucleation occurring in the real world,<sup>4,5</sup> is focused on here. Heterogeneous ice nucleation is caused by foreign particles/surfaces, usually solids. A more comprehensive description of currently researched nucleators is provided in **5.3.3**,<sup>6</sup> and ice nucleation happens *via* two modes; deposition and freezing. Deposition is described as a gas to solid phase transition where ice nucleates on an INP from supersaturated vapour. Freezing nucleation is a

liquid to solid phase transition where nucleation occurs within a body of supercooled liquid due to the presence of an INP. Freezing nucleation is then further subdivided into immersion freezing (INP is immersed in water), contact freezing (INP comes into contact with supercooled water at the air-water interface) and condensation freezing (freezing occurs simultaneously with liquid water formation). This project centres on immersion mode ice nucleation due to its relevance to cryobiology, where biological materials are frozen in liquid solutions.

Heterogeneous ice nucleation has been extensively studied since the 1940's,<sup>7</sup> yet understanding of the process remains incomplete, with the mechanism by which INPs work generally unknown.

### 5.3.3 Good Heterogeneous Ice Nucleators

Research into heterogeneous ice nucleation has focused on determining the ice nucleation effectiveness of potentially atmospherically relevant nucleants.<sup>8,9</sup> There is a vast range of different nucleators; including biological aerosol particles, mineral dusts, soots, sea sprays particles and volcanic ash. Non-atmospheric substances including anti-icing surfaces and superhydrophobic coatings have also been studied extensively.<sup>10,11</sup>

A common component of atmospheric aerosol is biological aerosol particles. These consist of viruses, algae, spores, pollen, bacteria, protozoa and small plant fragments, ranging in sizes from 5 – 50 nm, though some bacteria of diameters including up to 0.2 – 1 mm have been observed nucleating ice.<sup>12</sup> These particles have been observed to initiate freezing at very warm temperatures up to -2 °C.<sup>13–15</sup> One bacteria observed nucleating ice in the range of -2 °C to -4 °C is *Pseudomonas syringae*, **Figure 5.1Ai**.<sup>16</sup> *P. syringae*, along with *Pseudomonas fluorescens* and *Pantoea agglomerans* (previously named *Erwinia herbicola*), is a bacteria found to promote ice nucleation and thus frost formation on plant leaves, enabling the pathogen to survive by digesting nutrients from the plants more readily.<sup>17</sup> It has been confirmed that an ice nucleating protein found on the surface of the bacteria causes this nucleation, a ribbon representation of the protein is given in **Figure 5.1Aii**. These proteins are large and efficient INPs,<sup>16,18</sup> and are thought to order water molecules into an ice-like lattice by an anchored clathrate water mechanism similar to AFPs. The INP from *P. syringae*

has a unique hydrophobic-hydrophilic pattern, which is thought to enhance ice nucleation.

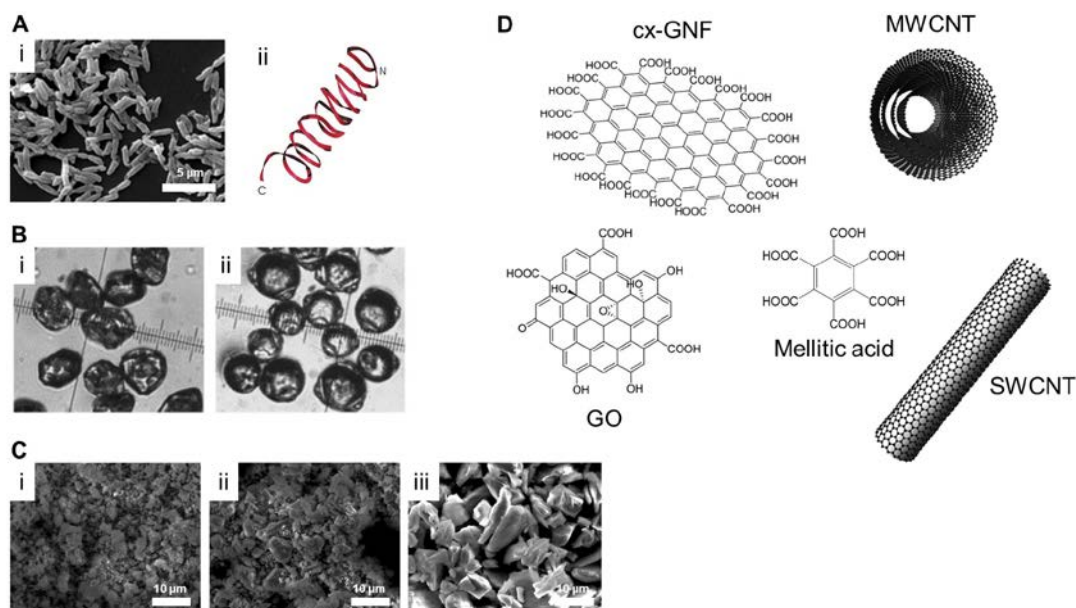


**Figure 5.1.** Selection of materials known to nucleate ice A) *P. syringae*; i) SEM micrograph;<sup>19</sup> ii) Ribbon representation of a  $\beta$ -helical INP from *P. syringae*, depicting the structure of the 144-residue INP model after 300 ps of solvated MD;<sup>20</sup> B) Photographs of birch pollen grains; i) pre-water uptake (25  $\mu\text{m}$  diameter); ii) grains post-water uptake;<sup>12</sup> C) SEM images with a 6000 $\times$  magnification of 3 types of quartz particles; i) Quartz I, average surface diameter 0.5  $\mu\text{m}$ ; ii) Quartz II, average surface diameter 1.2  $\mu\text{m}$ ; iii) Quartz III, average surface diameter 4.8  $\mu\text{m}$ ;<sup>21</sup> D) Chemical structures of the various of carbon nanomaterials tested for their ice nucleation activity; carboxylated graphene nanoflakes (cx-GNF); oxidized-multiwall carbon nanotubes (o-MWCNT); graphene oxide (GO); oxidized-single-wall carbon nanotubes (o-SWCNT). GO sheets have an average lateral diameter of  $\sim 1$   $\mu\text{m}$ , while the GNFs have an average lateral diameter of  $\sim 30$  nm.<sup>22</sup>

Some studies also claim AFPs may nucleate ice.<sup>23</sup> Du *et al.* suggested that specific interactions between AFPIII proteins are required for binding to ice, and that the self-assembly of AFPIII on the surface of ice may be expected.<sup>24,25</sup> AFPIII presents hydrophilic and hydrophobic regions (akin to INPs), and from results based on ice nucleation, surface tension, and dynamic light scattering studies, Du *et al.* proposed that above a critical protein concentration value (2.5  $\text{mg}\cdot\text{mL}^{-1}$ ), the amphipathic AFPIII self-assembles into micelle-like structures. It has been suggested that these



aggregation properties could play a key role in antifreeze efficiency; at critical aggregation concentrations AFPIII has been observed to inhibit nucleation by adsorbing onto both the ice surface and foreign particles thus improving growth inhibition (antifreeze activity is related to surface activity of AFPs), however at higher aggregation concentrations they appear to promote nucleation, which could hinder their ice growth inhibition. However, there is debate as to whether this work was correctly interpreted as later studies showed that AFPIII does not form aggregates at higher concentrations thus the surface activity of AFPIII may not correlate with aggregation of the protein.

Other ice nucleating compounds from bacteria (and insects, plants, lichen, fungi *etc.*) include polysaccharides and lipoproteins, some of which have been found to not be bound to the ‘particles’ and have been found to nucleate ice when separated from them.<sup>26–29</sup> For example, certain types of pollen release INPs when immersed in water.<sup>30</sup> One pollen known to nucleate ice efficiently is birch pollen.<sup>30</sup> Pollen is a large biological aerosol particle with diameters between 10 – 100  $\mu\text{m}$ ,<sup>12</sup> with birch pollen grains being approximately 25  $\mu\text{m}$  in diameter, photographs of which are provided in **Figure 5.1B**. The pollen appears to take up water as well as release ice nucleating macromolecules. These macromolecules are thought to be polysaccharides that bear carboxylate functional groups, they have been observed to have ice-binding capabilities and IRI activity,<sup>31</sup> and it has been proposed that they gain ice nucleation activity by forming clusters/aggregates.

Mineral dusts are another type of aerosol particle that has been observed to nucleate ice effectively, though it is unclear what the exact nature of nucleation sites on these INPs is. These dusts’ compositions mirror soil cover and the continental crust in that they are mainly composed of clay minerals, quartz and feldspars (group of aluminium silicates) and are thought to be important for nucleation in clouds due to their abundance in the atmosphere.<sup>32</sup> Feldspar and quartz are two of which that have been thoroughly studied, and although they nucleate, they are not as effective as many biological INPs.<sup>33</sup> K-feldspar in particular has been recorded to have the highest ice nucleating ability out of Na-, Ca- and K-feldspar (up to  $-2\text{ }^{\circ}\text{C}$ ),<sup>17,34</sup> with nucleation occurring over a range of temperatures for the different feldspars. SEM images of three types of quartz can be seen in **Figure 5.1C**, of which quartz I (the sample containing the largest fraction of particles of diameters  $<1\text{ }\mu\text{m}$ ) showed the most ice nucleating

activity, again only  $-21\text{ }^{\circ}\text{C}$  (which is much lower than the  $-2\text{ }^{\circ}\text{C}$  caused by biological INPs). Work by Zolles *et al.* shows that it is not a perfect surface, but rather local defects that nucleate ice, though further work needs to be undertaken into understanding the mechanism by which these defects nucleate ice (*e.g.* by lattice matching).<sup>21</sup>

A range of carbon-based synthetic materials have been studied in relation to ice nucleation, **Figure 5.1D**. These include carbon nanotubes, graphene nanoflakes (GNF), graphene oxide (GO) and associated structures.<sup>22,35</sup> GO, large sheets of carbon with alcohol, epoxide and carboxylic acid groups present with an average diameter of  $1\text{ }\mu\text{m}$ , has significant IRI activity and cryoprotective ability (reducing crystal growth to 20 % MLGS at  $5\text{ mg}\cdot\text{mL}^{-1}$ ) thus appeared of great interest.<sup>36</sup> cx-GNFs are small graphene sheets ( $\sim 0.03\text{ }\mu\text{m}$ ), the edges of which consist of only carboxylic acid groups. o-MWCNTs are needle-like tubes consisting of multiple single layers of carbon and o-SWCNTs are tubes but consist of one layer of carbon. These are oxidised species and chosen due to the fact that their oxidised nature enables them to disperse in water. Whale *et al.* found that water droplets containing cx-GNFs, GO, MWCNTs and SWCNTs all nucleated ice at temperatures higher than pure water; with the median ice nucleation temperature ( $T_n$ ) of cx-GNFs being  $-21.3\text{ }^{\circ}\text{C}$  and  $-12.2\text{ }^{\circ}\text{C}$  for MWCNTs (median  $T_n$  water:  $\sim -26.5\text{ }^{\circ}\text{C}$ ). Shape and degree of oxidation appears to be important for these materials, as the carbon nanotubes were observed to be more effective ice nucleators than the flat graphene species, and the less oxidised materials (carbon nanotubes) nucleated ice more effectively than more oxidised species (GO and cx-GNFs).

One way to compare the activity of different heterogeneous ice nucleators is to compare their ice active site densities. This is a measurement of activity that allows for comparison between nucleants and can be normalised to surface area of nucleator ( $n_s$ ) (calculating  $n_s$  from droplet data is performed using **equation 5.1**), volume of water in which the INP is suspended ( $K$ ) (**equation 5.2**) or mass of INP ( $n_m$ ) (**equation 5.3**). Normalisation can be performed by applying the relevant multiplier to the temperature and number of drops frozen/unfrozen data. These calculations are based on the differential nucleus spectrum (graphical representation of the concentration of active nuclei in a volume derived from drop-freezing experiments), which directly

connects with the frozen fraction curves obtained by recording nucleation temperatures.<sup>37</sup>

Calculating normalisation are performed using:

$$n_s(T) = -\frac{1}{A} \ln\left(1 - \frac{N_F(T)}{N_0}\right) \quad (5.1)$$

Where  $n_s(T)$  is the measure of the number of sites per unit surface area,  $A$  is the surface area of the nucleator per droplet,  $N_F(T)$  is the number of droplets frozen at temperature  $T$  and  $N_0$  is the total number of droplets.

For normalisation to droplet volume used in the experiment,  $A$  is changed to  $V$ , the droplet volume:

$$K(T) = -\frac{1}{V} \ln\left(1 - \frac{N_F(T)}{N_0}\right) \quad (5.2)$$

For normalisation to mass,  $A$  is changed to  $m$ , mass of the ice nucleating particle per droplet:

$$n_m(T) = -\frac{1}{m} \ln\left(1 - \frac{N_F(T)}{N_0}\right) \quad (5.3)$$

A comparison of different INPs from the literature is plotted as  $n_s$  as a function of temperature in **Figure 5.2**, highlighting the many studies into mineral dusts, pollen and bacterial nucleators, showing that biological nucleators are generally more effective than inorganic nucleators, with *P. syringae* nucleating much more effectively than any other nucleant reported. Silver iodide (AgI) is also reported, and is more effective than the other non-biological nucleators tested but is still not as effective as *P. syringae*.<sup>38</sup>

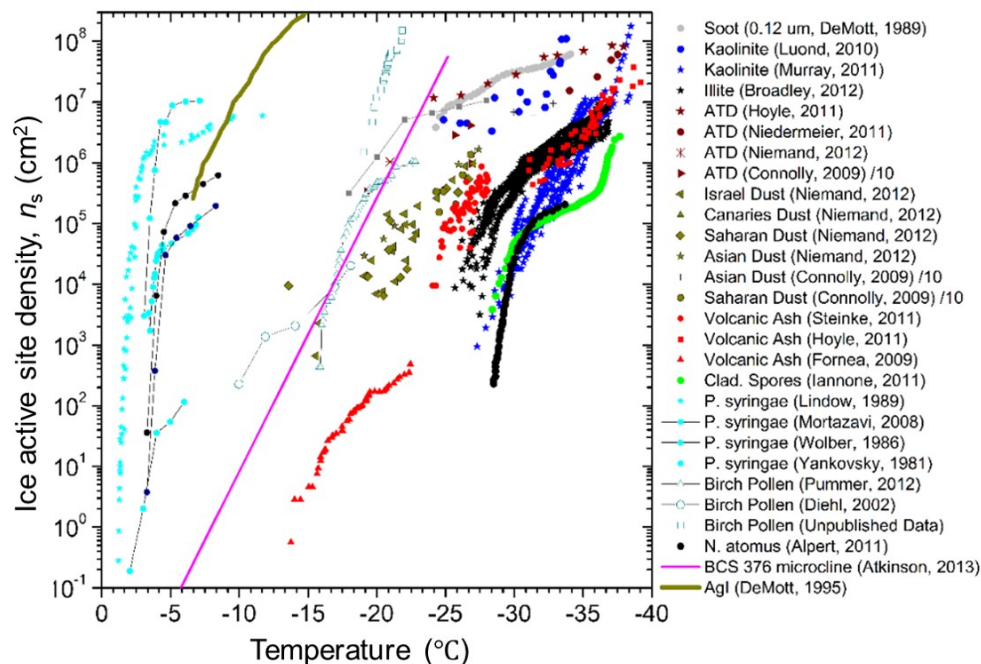


**Figure 5.2.** Ice nucleation activity obtained from a range of nucleation activity studies in the literature. Results for nucleation activity written as ice active site density normalised to surface area ( $n_s$ ). Adapted from Whale, T.F., (PhD, University of Leeds, 2015).<sup>33</sup>

### 5.3.4 How Do Nucleators Work?

Despite the quantification of various ice nucleators and their comparative efficiencies, there is little insight into why certain species are more effective than others. It is challenging to determine the physical properties required for a substance to be an efficient ice nucleator as the nucleation event is rare (typically nm across in  $\mu\text{m}$  to mm scale droplets) and happens on very short timescale. However, there are some properties that are thought to make a ‘good’ heterogeneous ice nucleant.

INPs are often assumed to be ‘large’ in size,<sup>39–41</sup> and  $T_n$  do relate to particle size and characteristics of crystals.<sup>37</sup> Reports from Georgii and Kleinjung relating to biological INPs implies larger biological particles should show efficient ice nucleating ability.<sup>12</sup>

Lattice matching is considered important for ice nucleation properties;<sup>7</sup> this is the idea that substances that have similar crystal structures to ice, have similar lattice constants thus there is a structural match with the first layer of ice. Hydrophobicity is thought to be involved,<sup>42</sup> and the concentration of hydroxyl groups important in lattice matching.

AgI was thought to have the potential to be a ‘good’ nucleator due to its similar crystal structure to ice,<sup>43</sup> and this was found experimentally correct. However, the role of lattice matching has been debated; Zettlemoyer *et al.* argued that topography/oxidized sites on the AgI surface may be involved in ice-binding and thus nucleation rather than the lattice matching of the crystal itself.<sup>44</sup> Finnegan and Chai have also suggested that nucleation promoted by AgI may work *via* a mechanism where surface charge clusters control it, and that lattice matching may be coincidental.<sup>45</sup>

Specific locations have been determined to affect ice nucleation; for example molecular roughness of carbon surfaces impacts ice nucleation efficiency.<sup>22</sup> These nucleation ‘active sites’ are considered to be where the critical ice embryo forms and can vary with between different nucleants;<sup>21,46,47</sup> for biological INPs such as for *P. syringae*, the active site is thought to be where the ice nucleating proteins cluster/aggregate on the cell membrane,<sup>29</sup> whereas this is considered to be a defect or nanoscale crack in feldspar materials.<sup>48</sup> Active sites have been followed by high speed cameras; Gurganus *et al.* performed droplet freezing experiments seeing no propensity for nucleation at the same sites, indicating that no specific sites on their material nucleated ice more efficiently than others.<sup>49</sup> Later work of theirs considered different textured surfaces, indicating that topography is important for ice nucleation behavior, and that nucleation processes are at least partly ‘site specific’.<sup>50</sup>

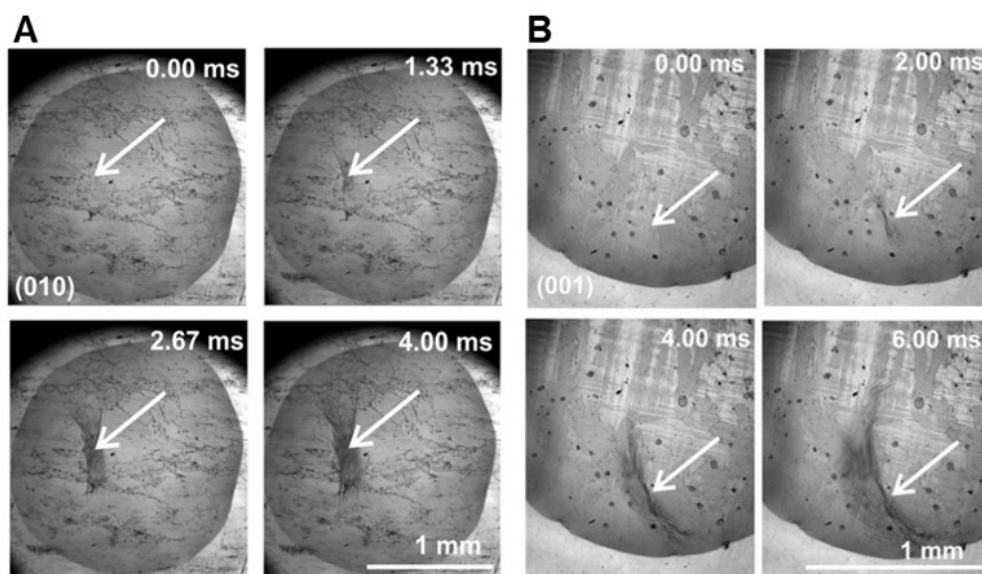


**Figure 5.3.** Representative micrographs of the nucleating spot in ice nucleating feldspar. Sequence of images taken from individual freezing experiments of two separate droplets, on the A) (010) and B) (001) faces. A 1  $\mu\text{L}$  droplet of water is placed on a thin section of feldspar and cooled at  $1^\circ\text{C min}^{-1}$  until nucleation is detected with a high-speed camera operating at 3000 frames per second (fps). Adapted from Holden *et al.*, (Sci. Adv., 2019).<sup>48</sup>

Zolles *et al.* suggested that defects in the surface of a material are important for ice nucleation,<sup>21</sup> and Whale *et al.* determined that topography acts to promote ice nucleation,<sup>51</sup> inspiring Holden *et al.* to identify ice nucleation sites (INS) on macroscopic feldspar, finding that substrate heterogeneities are important in promoting nucleation.<sup>48</sup> **Figure 5.3** shows an example sequence of images recorded during a high-speed observation of droplet freezing, recorded at 10,000 fps; **Figure 5.3A** follows cooling of water droplets on the (010) plane and **Figure 5.3B** follows droplets on the (001). The nucleation site is identified by the white arrows, from which dendritic ice grows. These INS were found to be contained within a micron-scale pore/crack. To ensure the identified active sites were the INS, repeat freeze/thaw cycles were performed, finding that a small number of INS existed for each sample, which nucleated at similar temperatures in multiple repeat measurements.

No universal mechanism of action for nucleators has been agreed upon, and it remains unclear as to the extent of importance of lattice matching, topography and chemical composition.

### 5.3.5 Experimental Methods Used to Study Ice Nucleation

In general, techniques used to analyse ice-activity involve direct observation of a sample. Recorded activity, whether TH, IRI or ice nucleation, can vary depending on technique performed (within or between laboratories), with potential results affected by human error, contamination (due to condensation or extraneous samples) or setup. Experimental investigation of the critical nuclei is near impossible due to the size and rarity of the nuclei and rate at which crystal growth occurs post-nucleation thus the majority of techniques focus on quantifying ice nucleation effectiveness of materials, which is much more straightforward.

A range of approaches have been used in attempt to mimic the actions of biological nucleators as well as to determine ice nucleation efficiency,<sup>52</sup> these study the effect of a range of variables including, INP concentration, temperature, cooling rate (or isothermal experiments),<sup>53–55</sup> time and droplet size.

The two broad families of techniques used to determine ice nucleation effectiveness are wet dispersion and dry dispersion methods.<sup>52</sup> Wet dispersion methods involve dispersing INPs in water, unlike in dry methods, where particles are dispersed in air then exposed to wet air to generate water droplets containing the particles. Wet dispersion techniques are focused on in this work, with droplet assays and differential scanning calorimetry, both being performed to provide  $T_n$ . Droplet assays, are the most commonly utilised wet dispersion methods, and include approaches where droplets are supported on surfaces and where droplets are suspended in oils or gases.<sup>9</sup> Samples are dispersed in water, which is then cooled and freezing monitored. Nucleation data from these assays is obtained in the form of fraction of droplets frozen as a function of time and temperature. Droplet volumes have varied widely, with studies conducted using everything from millilitre to picolitre volumes.<sup>56</sup> The size of droplet is important, as larger droplets of a particular sample may run into ‘background problems’ where the native nucleation temperature of the system is warmer than that of the nucleants under investigation. Smaller (pL or nL) droplets enable measurements much closer to the homogenous freezing temperature as there is a lower probability for contaminants but do not allow investigation of rarer, more active INPs/INS.<sup>52,57</sup>

The droplet freezing method used here is based on  $\mu$ L-Nucleation by Immersed Particle Instrument ( $\mu$ L-NIPI) from Whale *et al.* where a camera is used to monitor

droplet freezing, observed as an abrupt flash due to light scattering from numerous rapidly formed ice crystals.<sup>58</sup> The  $\mu\text{L}$ -NIPI was designed to measure the effectiveness of atmospherically relevant INPs in  $\mu\text{L}$  water droplets. It uses an electronic micropipette to produce an array of droplets, the freezing temperatures of which are then measured. The technique is advantageous as it allows experiments to be performed relatively quickly, relatively high numbers of droplets (50+) can be measured simultaneously, no cooling fluids (such as liquid nitrogen) are required and the instrument is highly portable.<sup>33</sup> However, many repeat measurements have to be taken (as with all droplet assays), but this is less of a problem due to the ease and speed of each measurement.

Other wet dispersion techniques include using emulsions of water droplets in oil, microfluidics and calorimetry.<sup>1,21,59,60</sup> DSC has been used as a method for studying AFP activity since 1988, when Hansen and Baust recorded the freezing temperatures of *Tm*AFP suspended in oil.<sup>60</sup> Calorimetry, especially when used in combination with microfluidics (using microemulsions),<sup>61</sup> can provide the option to record nucleation temperatures without the problem of contamination from surfaces (as in microscopy based techniques), though may lead to a change of location of INPs in droplets. Other techniques that have been developed, one of which by Harrison *et al.*, involves the use of an infra-red camera (InfraRed-Nucleation by Immersed Particle Instrument (IR-NIPI)) to monitor 50  $\mu\text{L}$  scale droplets, **Figure 5.4**.<sup>62</sup> IR-NIPI involves using an infrared camera to follow the temperature of individual wells of sample to be monitored. Samples are divided into 50  $\mu\text{L}$  droplets per well, and freezing temperatures of these drops are determined by detecting the change in temperature for each well (an increase caused by a release of heat).



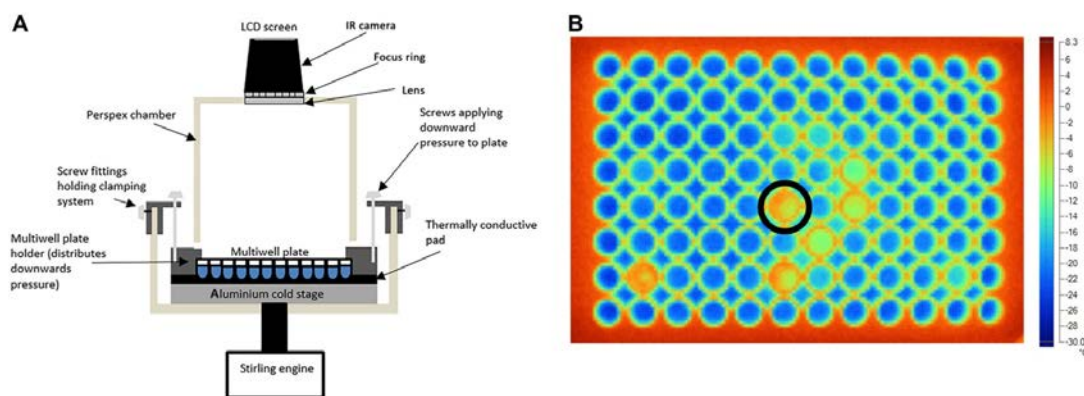


**Figure 5.4.** A) Illustration of the IR-NIPI technique developed by Harrison *et al.*, (Atmos. Meas. Tech. Discuss., 2018).<sup>62</sup> The Infra-red camera is positioned above the multiwell plate and monitors the freezing events as the cold stage cools; B) Example colour map taken during the course of an experiment. The black circle represents a sample nucleating in an individual well (exothermic reaction leads to the higher temperature in this well). Warmer temperatures are represented in red, transitioning to blue for colder temperatures and finally black at  $-30\text{ }^{\circ}\text{C}$  and below. Cooling rates used is  $1\text{ }^{\circ}\text{C min}^{-1}$ .

Molecular dynamics (MD) is often used to study the physical nature of nucleation processes, due to the difficulty of experimental observation of critical nuclei,<sup>5,47,63–65</sup> in particular assisting in understanding the nucleation event and critical nucleus itself, though these can suffer from miscalculations, in particular for heterogeneous nucleation, due to incorrect estimations of properties of samples and nuclei *e.g.* radius of curvature.<sup>66</sup>

It has been shown that there are many effective approaches for controlling ice crystal growth (see Chapter 1), however, as yet it has proven challenging to control ice nucleation. There is great difficulty in predicting what foreign particles or surfaces may promote nucleation, and due to experimental challenges the mechanism of action by which currently known effective INPs work is unclear.<sup>67</sup>

### 5.3.6 Finding new nucleators

As it is unclear as to how nucleators work, there is no preferred structure focused on for identifying new nucleators. No current technique can locate or measure the physical properties of the critical nuclei that form in ice. Due to this, ice nucleators

and their effectiveness are currently inferred from experimental results. IRI activity is generally not been observed for nucleators (except for AFPIII potentially at high concentrations), thus polymers such as PVA and AF(G)Ps used in previous chapters were not selected for study in this work. Instead, using a blue-sky approach (as many different materials are nucleators), a selection of materials with large structures or that form extended arrays were selected, because if structure/size is important to nucleation there may be a correlation with efficiency.

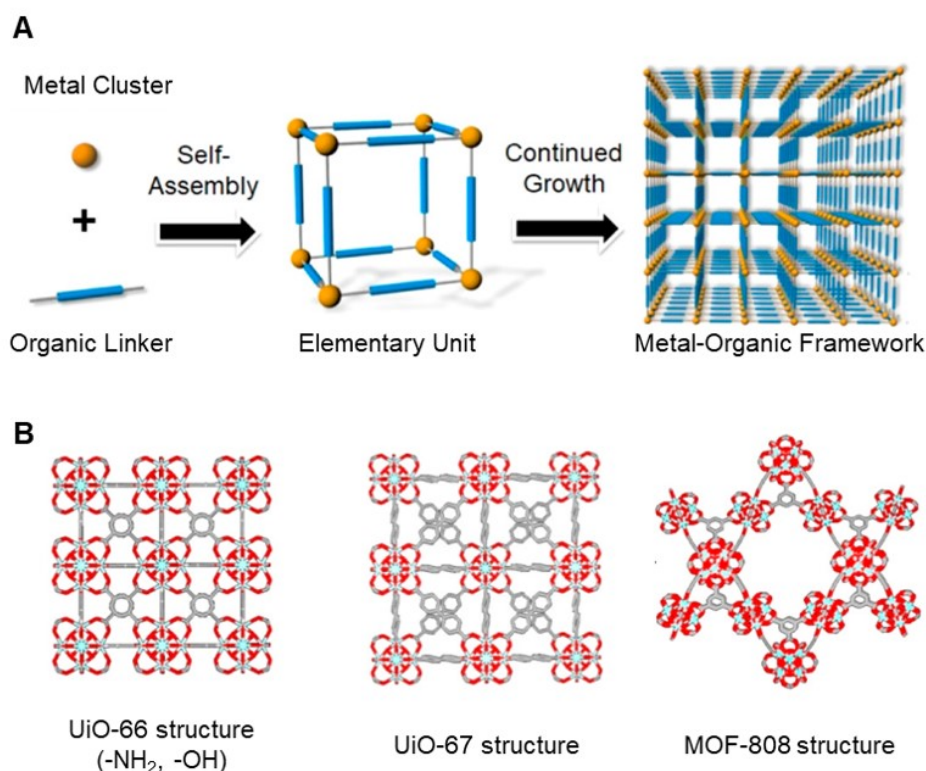


**Figure 5.5.** Schematic of concept behind the decision to study Zirconium-based MOFs for ice nucleation. A) Concept Underlying the Synthesis of Metal–Organic Frameworks; B) Schematic illustration of the structure features of an example selection of MOFs that could be studied: UiO-66 (–NH<sub>2</sub>, –OH), UiO-67, and MOF-808, showing their large extended surfaces. Adapted from Zhu *et al.*, (J. Am. Chem. Soc., 2019).<sup>71</sup>

Metal organic frameworks (MOFs) are materials consisting of coordination bonds between multidentate organic linkers (ligands) and transition-metal cations. They are made *via* reticular synthesis, where the inorganic and organic linkers are assembled together, the assembly of the elementary unit and final MOF is depicted in **Figure 5.5A**. They have many uses including gas storage, catalysis, biomedical imaging and

drug delivery.<sup>68–70</sup> They are characterised by their open frameworks and can highly porous. MOF structures can be modified, thus their adsorption properties can be tuned, leading to the possibility for structures that may bind ice because of particular spacing of functional groups/ligands on the surface.<sup>71</sup>

If MOFs nucleate ice well, they could be used for cloud seeding, providing a possible application in arid regions to increase rainfall. MOFs have been also observed to absorb water from air, so act as desiccants.<sup>72</sup> Zhu *et al.* found a zirconium based MOF had IRI activity, cryopreserved red blood cells and had potential nucleation properties. A range of MOF structures tested by Zhu *et al.* for activity are shown in **Figure 5.5B**.

A separate, biological material of interest is lignin. Lignin is a major component of plant biomass, which consists of two carbohydrate polymers (cellulose and hemicellulose) as well as lignin, which is an aromatic polymer.<sup>73,74</sup> Lignocellulosic biomass is the major component in all types of plants and is the most abundant carbon source on Earth. Lignin itself is found in a range of woody plants and non-woody plants, including grasses.<sup>75</sup> This polymer provides structure to the plant, assists in modifying cell permeability and temperature stability, supports tissues and gives a certain stiffness and woodiness.<sup>76</sup> Some industrial uses of lignin include feedstock and biofuels,<sup>73,75,77</sup> leading to them being readily available for research.

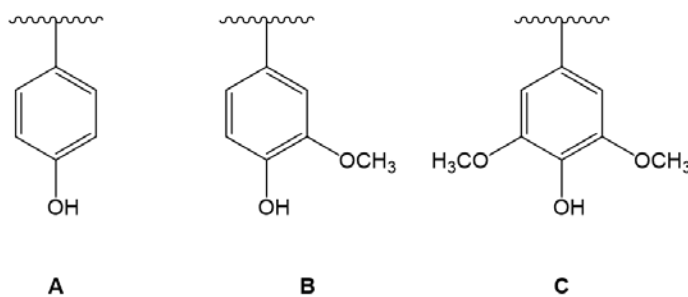


**Figure 5.6.** Three important basic building blocks of lignins; A) *p*-coumaryl alcohol; B) coniferyl alcohol; C) sinapyl alcohol, which give rise to *p*-hydroxyphenyl, guaiacyl and syringyl residues in lignin.

Lignin is biosynthesised from three monolignols (coumaryl alcohol, coniferyl alcohol and sinapyl alcohol), **Figure 5.6**,<sup>78</sup> percentages of which vary in different types of wood/crops. For example, hardwoods consist of more coniferyl alcohol and sinapyl alcohol units, whereas softwoods (and plants) consist of more coumaryl alcohol.<sup>74</sup> These monolignols conjugate in a variety of ways during biosynthesis to form 3D

polymers that do not consist of regular, ordered macromolecular structures, leading to the great diversity in lignin structures due to the numerous different combinations of *p*-hydroxyphenyl, guaiacyl and syringyl available.<sup>79</sup>

Lignins are generally insoluble and hydrophobic in nature, thus enabling woody materials to resist chemical and biological degradation.<sup>80</sup> This property may be useful for ice nucleation, as efficient ice nucleants such as mineral dusts are also insoluble. They also have a large number of polar hydrophilic groups (hydroxyls), therefore some may have similar functional group patterns allowing them to crystallographically match that of ice, leading to nucleation. However, there is debate as to the importance of hydrophilicity.<sup>46</sup> Lignocellulosic materials may act as heterogeneous ice nucleating agents; they have been observed assisting in nucleation of other materials, for example polypropylene,<sup>81</sup> and cellulose particles themselves have been observed to be potential sources of atmospheric INPs, though further investigation is required.<sup>82</sup> Isolation of pure lignins is futile, due to its covalent bonding to carbohydrates forming lignin-carbohydrate complexes (LCCs).<sup>78</sup> Thus if these materials nucleate ice, deciphering the active site/characteristics involved in nucleation will be a challenging task.

If any materials show promise, further study can take place on a more specific range of MOF or lignin structures.

## 5.4 Chapter Aims

- Test a range of previously untested compounds for their ice nucleation activity with the aim of obtaining next-generation promoters of ice nucleation, thus providing potential new ice nucleating compounds based on polymers and composites to control freezing temperatures during cryopreservation.
- Compare different wet-dispersion techniques for observing nucleation activity in these samples.
- Compare concentration ranges and cooling rates for their effect on nucleation activity, *i.e.* assist in determining what causes nucleation in these samples.

## 5.5 Results and Discussion

### 5.5.1 Samples Tested

The materials chosen for study here include larger, extended structures, none of which have been tested in any meaningful way for ice nucleation activity bar safranin-O.

Metal organic frameworks (MOFs) were chosen as they have many, varied, highly-designable, easily-modified structures (over 20,000 different MOFs have been reported),<sup>74</sup> meaning there is a possibility for tuneable ice-activity due to the possibility for lattice-matching with ice.<sup>71</sup> A variety of ligands were chosen with phenolic acid/carboxylic acid groups arrayed around a cerium ion giving an extended structure such as that in **Figure 5.8**.

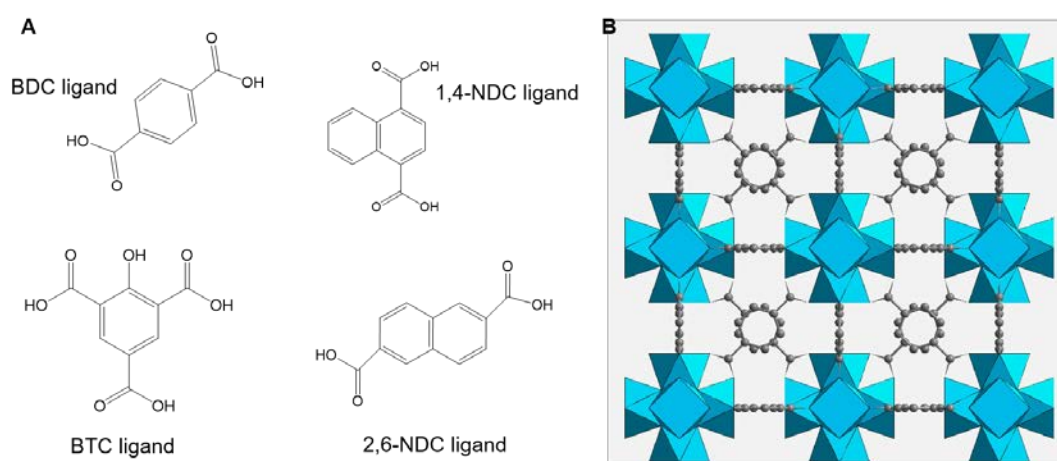


**Figure 5.7.** A) Chemical structures of ligands used for MOFs tested here. 1,4-benzenedicarboxylic acid (BDC), naphthalenedicarboxylate (NDC), benzene-1,3,5-tricarboxylic acid (BTC); B) Extended structure of the MOFs provided by Ehsan Ghadim.

The common ice growth inhibitor safranin-O was also tested, structure shown in **Figure 5.8A**. Safranin-O, with its flat planar structure, and propensity to self-assemble into supramolecular aggregates at concentrations above  $1.0 \text{ mg.mL}^{-1}$ , has been observed interacting with specific ice faces, leading to ice shaping as well as growth inhibition. In the literature there is no mention of ice nucleation activity. Safranin-O's structure differs from the other materials tested here; it has amine groups rather than hydroxyls/carboxylic acids. The hydroxyls are not required for IRI activity, and may not be essential for nucleation either, though the supramolecular structure may be involved.<sup>83</sup>

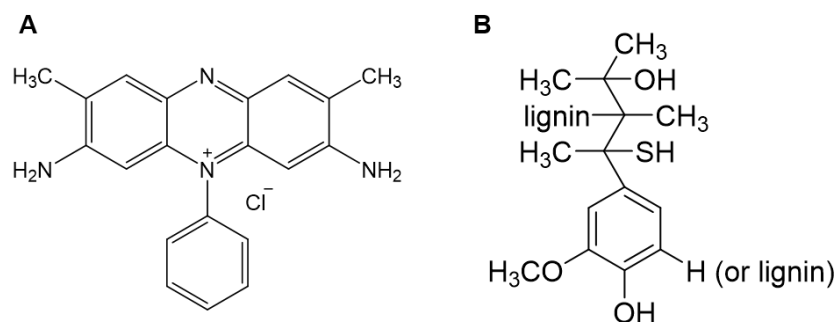


**Figure 5.8.** Chemical structures of other materials tested here. A) Safranin-O; B) Alkali lignin (471003) 10 kDa (Structure from Sigma-Aldrich). The producer's elemental analysis data states a carbon content of 47-51 % and that this technical Kraft lignin has a remaining sulfur content of ~4 %.

A range of lignins were also tested, one of which is commercially available from Sigma Aldrich; Alkali lignin (471003) (average molecular weight: ~10 kDa), structure shown in **Figure 5.8B**. The structure of lignin is defined as an amorphous polyphenolic polymer material and is not regarded to be an inherently defined compound but as a composite.<sup>84</sup> Structural analysis has been studied using elemental analysis, <sup>1</sup>H-NMR, <sup>13</sup>C-NMR, FTIR and gel permeation chromatography (GPC). These enable quantification of the lignin substructures (within the lignin) shown in **Figure 5.6**, for example this alkali lignin has been determined to contain a guaiacyl unit. The other lignins chosen for testing can be extracted from a range of plant genera, these include *Triticum* commonly known as wheat (MK lignin), *Populus* (ammonia lignin), *Miscanthus* (miscanthus lignin), *Eucalyptus globulus* (OrganoSolv) and a range of hard woods (OrganoAlkali). The two final lignins tested were Zambezi and GreenValue, which can be extracted from multiple different botanical origins comprising of wood, corn, sugar beet and sugarcane.

Lignins were chosen because they are highly abundant natural resources that, if ice-active, have the potential to be technologically useful; *e.g.* they are stable enough to be mixed with acrylic resins so could be used in 96-well plates during cryopreservation experiments (they are thermally stable and have been used in the production of plastics and integrated with acrylic monomers previously).<sup>73,85</sup> The lignins are named after the process by which they are isolated; they are often fractionated by processes such as delignification by alkali [labelled as alkali lignin here], organosolv pre-treatment

[labelled as OrganoSolv here],<sup>86,87</sup> Kraft process, hydrolysis *etc.* or by the plant they are extracted from.

If nucleation is a structure related event, and other materials with large flat structures (GO) have been observed to nucleate ice effectively, lignins, which also have this structure, may also nucleate. The phenolic hydroxyl group may be of interest, as many currently researched INPs have these same functional groups, or phenolic acid/carboxylic acid groups.

## 5.5.2 Comparison of Experimental Methods

As mentioned in 5.3.5, there is a range of different methods that can be utilised for the study of ice nucleation. A description of the two methods used in this work are provided here.

### 5.5.2.1 Calorimetry-based Methods

Calorimetry techniques measure the thermal properties of materials, and how these physical properties link to changes in temperature.<sup>74</sup> These techniques have been used in chemistry, cell biology, biotechnology, physics and nanoscience, measuring the thermodynamic properties of a range of materials, biomolecules and ice phases.<sup>88–91</sup> DSC is a technique that monitors the heat flow of a sample whilst the temperature of a sample is changed, thus monitoring changes in phase/state in a sample due to a change in temperature with time.<sup>92</sup> The amount of heat absorbed or released by the sample is recorded and to account for any background, the change in heat flow for a sample is compared to that of an empty crucible. Samples for nucleation can be directly pipetted into the crucible, or can be dispersed in oil/emulsions, and the nucleation event followed by the production of an exotherm upon freezing. These are known as closed droplet systems where monitoring of freezing can be difficult as the droplets are not visible.<sup>93</sup> Example DSCs traces from work by Wilson *et al.* detail the endo- and exotherms obtained from the heating and cooling runs in a typical experiment and the point at which the  $T_n$  would be obtained off the graph for Ih, **Figure 5.9A**.<sup>94</sup> Initial obtained data for our pure water sample can be seen in **Figure 5.9B**, the axes have not been reversed to highlight how the data looks on the Perkin Elmer DSC6000 used here. Again the point at which the  $T_n$  is recorded is noted in red.



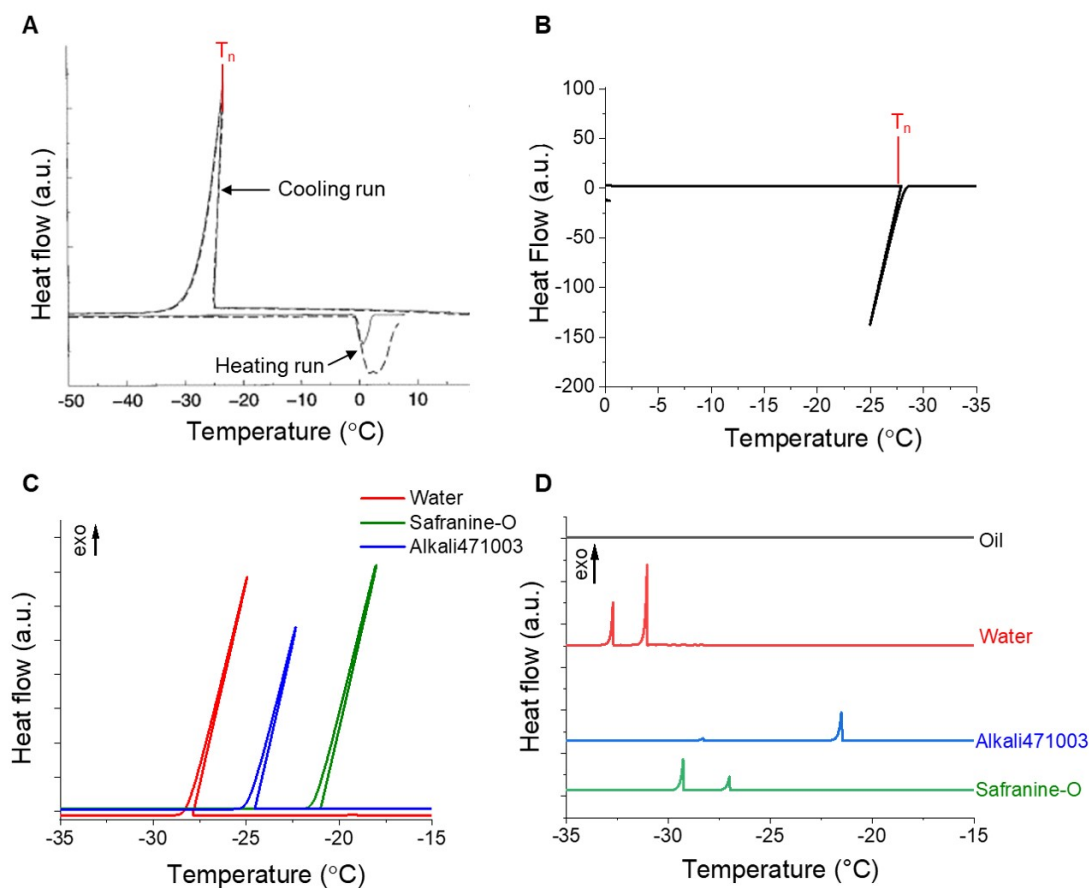


**Figure 5.9.** DSC traces and how nucleation temperatures are extracted from this data. A) Example DSC traces of liquid water transitioning to Ih (and melting back to liquid) from the literature. Two scans from the same sample, where the ice was warmed at either  $5\text{ °C}\cdot\text{min}^{-1}$  (solid line) or at  $1\text{ °C}\cdot\text{min}^{-1}$  (dashed line). Both the cooling and heating runs have been included *i.e.* both endotherms and exotherms are shown and the point at which the nucleation temperature would be recorded highlighted in red. Adapted from Wilson *et al.* (Biophys. J., 1999);<sup>94</sup> B) Raw DSC trace of pure water cooling from 0 °C to -35 °C obtained in this work. Nucleation temperatures are extracted at the point at which the exotherm corresponding to the phase change occurs. It can be seen that the peak slants unlike in the literature example; B) Temperatures obtained from DSC with one 10  $\mu\text{L}$  droplet in direct contact with the aluminium pan; and C) Temperatures obtained from DSC of a few 1  $\mu\text{L}$  droplets dispersed in oil (*i.e.* not in direct contact with pan) compared to that of the DSC trace for oil (black), water (red), safranin-O (green) and alkali lignin 471003 (blue), their apparent nucleation temperatures (recorded as an exotherm). [Sample] =  $1.0\text{ mg}\cdot\text{mL}^{-1}$ .

Initial tests on safranin-O and alkali lignin (471003) were performed using differential scanning calorimetry (DSC) and compared to that of pure water, **Figure 5.9C/D**. The first experiment involved 10  $\mu\text{L}$  droplets being directly pipetted into the aluminium pan and then transferred into the DSC. Using this method, it appears that safranin-O nucleates ice at  $\sim -21$   $^{\circ}\text{C}$ , alkali lignin at  $\sim -25$   $^{\circ}\text{C}$ , and water at  $\sim -28$   $^{\circ}\text{C}$ . It is difficult to follow homogeneous nucleation, and there will generally be an impurity leading to heterogeneous nucleation (nucleation seen occurring at between  $-24$   $^{\circ}\text{C}$  and  $-31$   $^{\circ}\text{C}$  rather than between  $-35$  and  $-40$   $^{\circ}\text{C}$ ).<sup>4</sup> There was a large change in heat flow for the samples, which was affected by the high sample volume in the crucible (10  $\mu\text{L}$ ), leading to oddly oriented DSC traces, **Figure 5.9C**, thus the values obtained cannot be considered accurate.

To improve the first method by reducing sample volume, and reduce any potential error due to contamination of sample (the crucible itself may consist of INS), the samples were then dispersed in immersion oil filled crucibles, **Figure 5.9D**. The DSC traces obtained here were more typical, with freezing temperatures observed  $< -30$   $^{\circ}\text{C}$  for water, between  $-25$  and  $-30$   $^{\circ}\text{C}$  for safranin-O and  $\sim -22$   $^{\circ}\text{C}$  for the lignin, these were also compared to the DSC trace of oil to ensure there was no effect on nucleation temperature due to addition of oil. However, as only a few droplets can be recorded at once there is a high possibility for error/low statistical significance as well as potential contamination from sample preparation; many chances for contamination as sample transferred to crucible and then into DSC.

The increase in nucleation temperature for safranin-O in **Figure 5.9C** is probably due to contamination. Potentially the  $T_n$  of safranin-O solutions in **Figure 5.9D** may be attributable to homogeneous ice nucleation itself, as they are observed much closer to this temperature range, or more likely, heterogeneous nucleation.

These calorimetry-based techniques require more optimisation and many more runs to obtain enough data to ensure nucleation temperatures are accurate, thus are not focused on in the remainder of this work.

### 5.5.2.2 Microscopy-based Methods

Microscopy-based multi-point freezing assays (droplet freezing assays) using cameras were used to visually observe ice nucleation; once ice nucleation occurs droplets

freeze on a short time scale, over the course of a fraction of a second. As such, any observation of freezing can be tied directly to a nucleation event. The probability of two nucleation events occurring in a single droplet is vanishingly small. In a droplet freezing assay, an aqueous suspension is taken and subdivided into ideally identical volume aliquots, which are cooled identically. A diagram of a typical setup for this microscopy-based immersion technique is shown in **Figure 5.10**. The setup consists of a cold stage, chamber to ensure humidity of an experiment is controlled and a digital camera to follow the nucleation process. Hydrophobic glass slides (22 mm diameter, 0.22 mm thick, Hampton Scientific) were used to reduce heterogeneous nucleation caused by the surface to a minimum. Prior to running any experiments these slides were cleaned using methanol and water. A gentle flow of dry gas is used to stop freezing droplet influencing their neighbours.

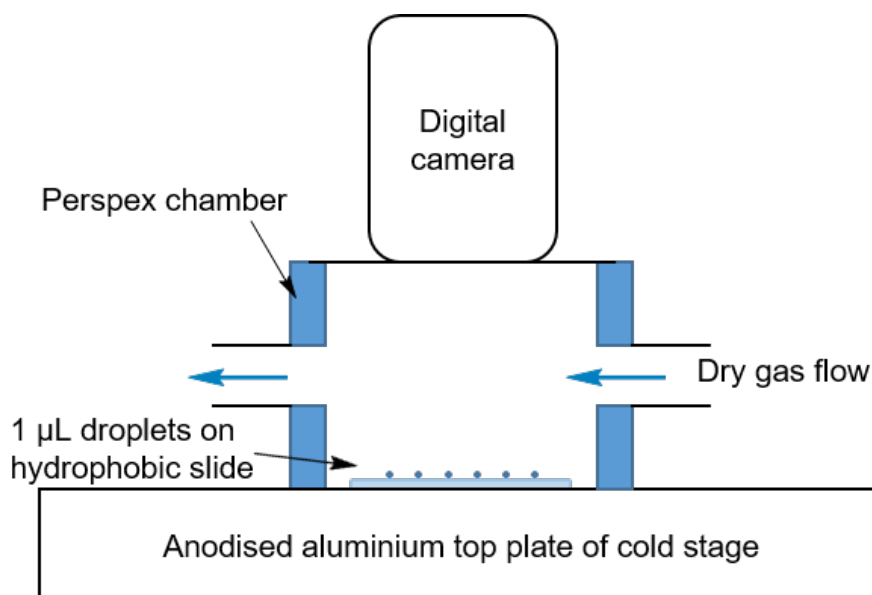


**Figure 5.10.** Diagram illustrating the  $\mu\text{L}$ -NIPI-based nucleation drop assay setup used in this work.

The first multi-point freezing assays used a crude setup consisting of a basic camera, a cryostage cooled using a T95-Linkpad system controller with liquid nitrogen pump, and no dry gas flow. These were performed to provide a proof of concept for later nucleation experiments. Example photographs obtained for freezing droplets in this way are seen in **Figure 5.11**. Between 10 and 20 drops can be observed using this setup, due to the size of the cryostage focal window. As expected, nucleation is observed by the change in light scattering (frozen drops circled in red). The assays

here were not filmed but photographs taken every  $0.1\text{ }^{\circ}\text{C}\cdot\text{min}^{-1}$ . The size of the droplets in immersion assays is important, so that the  $T_n$  recorded is not affected by, for example, a range in droplet volumes (smaller droplets nucleate at lower temperatures)<sup>9,33,56</sup> and here this is controlled as much as possible by using a Picus Biohit electronic pipette. The dispersity of nucleants in a sample may vary, particularly at low concentrations, this is accounted for by the high number of droplets counted, as well as by performing up to 5 repeat experiments (*i.e.* 20 – 100 droplets are monitored for their  $T_n$ ). If a sample has nucleating efficiency, then the dispersity should not affect the freezing temperature, as the water droplet will freeze at the same temperature

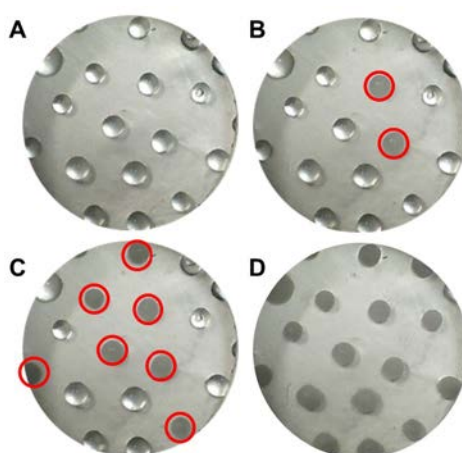


**Figure 5.11.** Example photographs from a multi-point freezing assay. Frame (A) was taken at  $-25.0\text{ }^{\circ}\text{C}$ , before the onset of freezing, frame (B) immediately after the first two droplets had frozen ( $-26.2\text{ }^{\circ}\text{C}$ ), frame (C) at  $-27.5\text{ }^{\circ}\text{C}$  and frame (D) at  $-30.1\text{ }^{\circ}\text{C}$ , after the completion of freezing. Frozen droplets highlighted in red.

After performing these initial studies, further experiments were performed with more precise temperature control and measurement as well as a dry nitrogen gas flow ( $0.2\text{ L}\cdot\text{min}^{-1}$ ) and a video camera, allowing for videos of the nucleation assay continuously monitored. This provided a higher-throughput technique (experiments can be performed relatively quickly), with more accurate temperature reading and simpler data analysis. Individual frames where freezing occurs are selected from videos, and the associated freezing temperature of each droplet recorded. Example photographs obtained for freezing droplets in this way are seen in **Figure 5.12**.

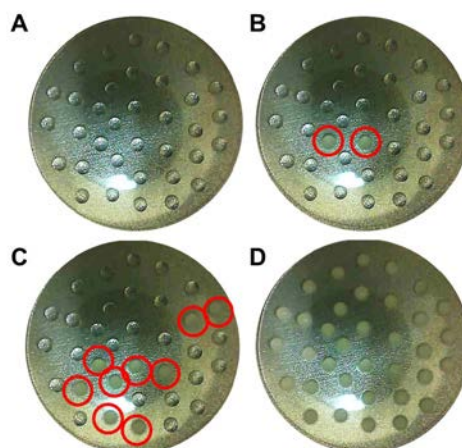


**Figure 5.12.** Example photographs from a nucleation drop freezing assay based on  $\mu\text{L-NIPI}$ . Frame (A) was taken at  $-10.0\text{ }^{\circ}\text{C}$ , before the onset of freezing, frame (B) immediately after the first two droplets had frozen ( $-18.0\text{ }^{\circ}\text{C}$ ), frame (C) at  $-22.5\text{ }^{\circ}\text{C}$  and frame (D) at  $-30.7\text{ }^{\circ}\text{C}$ , after the completion of freezing. Frozen droplets highlighted in red. Droplets of this size (1 mm) typically take 2 – 4 seconds to freeze completely. The initial change in the droplet leading to freezing is taken as the occurrence of ice nucleation.

With this setup between 30 and 50 drops can be observed, a much greater number than with the previous assay. Having the dry gas flow ensured prevention of condensation of water and ice on the slide, and thus leading to less error in the nucleation temperatures recorded, as droplets would not be contaminated and would remain the same size throughout the experiment. The peltier chiller requires no cooling fluids unlike in the first assay. Drops were pipetted onto the slides using a Picus Biohit electronic pipette to ensure that each individual droplet contained the same volume of material.

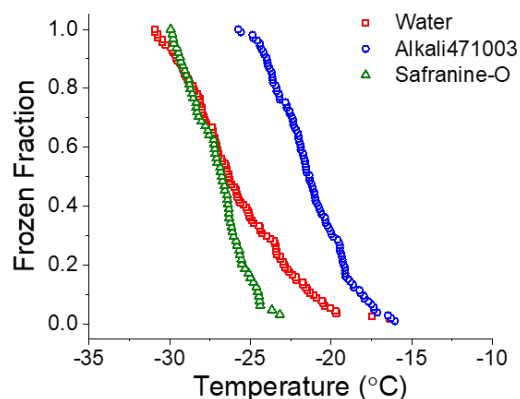


**Figure 5.13.** Temperatures obtained from nucleation drop assay (45-55 1  $\mu\text{L}$  droplets per slide, 2-5 repeat experiments per sample). Milli-Q water (red), safranine-O (green) and alkali lignin 471003 (blue). Temperature uncertainty of  $\mu\text{L}$ -NIPI-based method is  $\pm 0.4$   $^{\circ}\text{C}$ .  $[\text{Sample}] = 1.0$   $\text{mg}\cdot\text{mL}^{-1}$ .

The frozen fraction of droplets as a function of temperature can be obtained from photographs recorded in  $\mu\text{L}$ -NIPI-based assays, **Figure 5.13**. All droplet nucleation temperatures from repeat experiments are plotted for each sample (*i.e.* the total number of data points for one sample consists of 100 – 250 individual temperature measurements) and droplets that nucleate at the same temperature are included in the same data point. As with DSC experiments, safranine-O and alkali lignin were tested using the  $\mu\text{L}$ -NIPI-based method and compared to that of pure water. A difference in nucleation temperature for safranine-O was not observed unlike in the DSC, further supporting that safranine-O is not an INP, suggesting that in the previous DSC experiments only one end of the distribution of nucleation temperatures was observed (only 1-3 droplets recorded). However, nucleation of the alkali lignin does seem to occur at a higher temperature than water (-15 to -25  $^{\circ}\text{C}$ ), with 50 % of the droplets freezing ( $T_{50}$ ) at  $\sim -21$   $^{\circ}\text{C}$ , which is similar to the freezing temperature observed in **Figure 5.9B**.

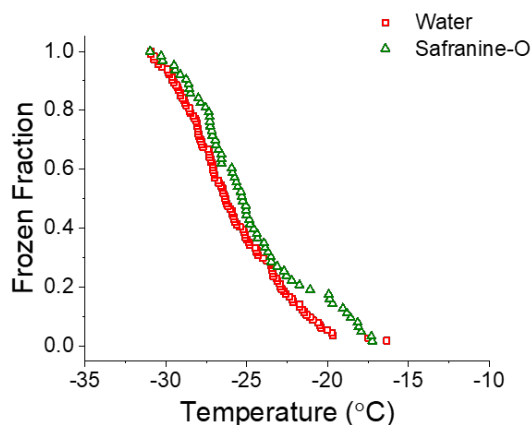


**Figure 5.14.** Temperatures obtained from nucleation drop assay (45-55 1  $\mu\text{L}$  droplets per slide, 2-5 repeat experiments per sample). Milli-Q water (red) and safranin-O (green). Temperature uncertainty is  $\pm 0.4$   $^{\circ}\text{C}$ . [Sample] =  $2.5$   $\text{mg}\cdot\text{mL}^{-1}$ .

Safranin-O at a concentration above  $1$   $\text{mg}\cdot\text{mL}^{-1}$  self-assembles,<sup>83</sup> and was tested in Chapter 3 for ice shaping using a concentration of  $2.5$   $\text{mg}\cdot\text{mL}^{-1}$ , here this concentration has also been used to study ice nucleation to check whether there is an increase in activity for this concentration, **Figure 5.14**. However, even at this higher concentration safranin-O does not promote ice nucleation, with the  $T_{50}$  of water being  $-26.3$   $^{\circ}\text{C}$  and safranin-O  $-25.3$   $^{\circ}\text{C}$ .

The above results obtained from the  $\mu\text{L}$ -NIPI-based drop assay are encouraging; using  $1$   $\mu\text{L}$  droplets allows for the monitoring of a range of nucleation temperatures and the ease at which it is performed means a large number of repeat measurements can be performed. The addition of materials to water, may affect the surface tension of the droplets, which in turn could also affect the  $T_n$ . This is because surface tension decreases with increasing curvature, in turn reducing the equilibrium radius of an ice embryo, thus increasing the probability of a nucleation event.<sup>95</sup> This was not tested here, but the contact angle of the water droplets could be measured in future experiments. A change in viscosity may also affect nucleation temperatures (potentially leading to a reduction in ice nucleation efficiency, as observed in Fayer *et al*'s research on hydrogel nucleation),<sup>96</sup> this is because as viscosity increases, the diffusion constant for the water molecules reduces, leading to a lengthening of diffusional mixing time and a larger barrier to molecular rearrangements within the sample, which hinders the formation of a critical nucleus causing the  $T_n$  to decrease. This could be monitored by performing rheometry or viscometry experiments.

### 5.5.3 Metal Organic Frameworks

Splat assays testing IRI activity for Ce-NDC-UiO-66 synthesised *via* a range of processes were performed. These include synthesis using acetic acid, acetic acid:water solutions and ethanol:water solutions, **Figure 5.15A**. UiO-66 was originally chosen as a ligand for MOFs tested here as Zhu *et al.* found that UiO-66 structures (concentrations included 0.1 to 2 mg.mL<sup>-1</sup>) had IRI activity and potential nucleating activity.<sup>71</sup> The different synthetic routes were chosen to study whether the synthesis had an effect on ice-activity, as the samples may incorporate acetic acid or ethanol as impurities, which may lead to promotion of ice nucleation.

Ce-NDC-UiO-66 [from here called Ce-NDC] synthesised using 50:50 ethanol:water has slightly higher IRI activity than the other samples (MGS of 71.9 %), though this is not a beneficial level of IRI activity for cryopreservation. This synthesis was repeated and purified further and the IRI activity dropped, implying the impurities in that sample were what led to activity. Experiments using zirconium-based MOFs were then performed to see if there was any change in IRI activity due to the Zr. This is because ZrAc has been found to be IRI active<sup>97</sup> and potentially, if due to the Zr, the MOFs will also be IRI active. Zr-MOFs were in fact slightly less active than the Ce-MOFs, **Figure 5.15B**, with both MLGS and MGS being ~100 % of PBS. Another Ce-MOF (Ce(BTC)<sub>3</sub>.6H<sub>2</sub>O) was compared to Ce-NDC and no IRI activity was observed here either.



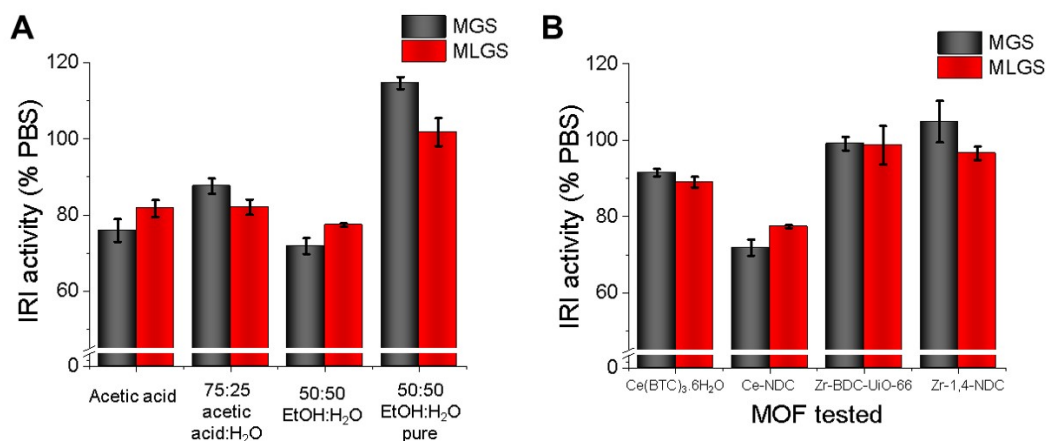


**Figure 5.15.** IRI activity for a range of MOFs; A) Ce-NDC-UiO-66 synthesised *via* different synthetic routes as a percent of PBS; B) Ce-MOFs and Zr-MOFs. Black = MGS and red = MLGS. [MOF] = 10 mg.mL<sup>-1</sup>.

IRI activity for Ce-NDC-UiO-66 was also tested over a range of concentrations (1.0 mg.mL<sup>-1</sup> to 10 mg.mL<sup>-1</sup>), with no activity observed at any concentration; a slight increase ‘activity’ from 1 to 10 mg.mL<sup>-1</sup> was observed for all synthetic routes; however the crystals are still  $\geq 71.9\%$  of the size of PBS crystals.

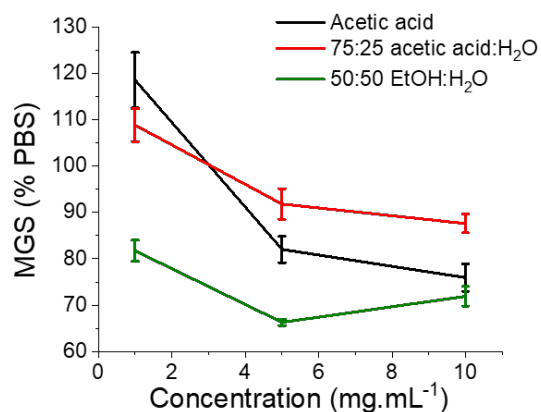


**Figure 5.16.** IRI activity for Ce-NDC-UiO-66 synthesised *via* different synthetic routes as a percent of PBS over 3 concentrations.

Nucleation was then performed on these samples, as nucleation and IRI are not expected to be linked. Neither Ce-NDC (blue) nor the two Zr-MOFs (red/green) have nucleation activity, with all three  $T_n$  being that of water, **Figure 5.17**. From the work performed so far, results indicate that the previously recorded IRI activity of ZrAc

does not solely relate to the Zr metal or acetic acid, and that its antifreeze activity is complex.

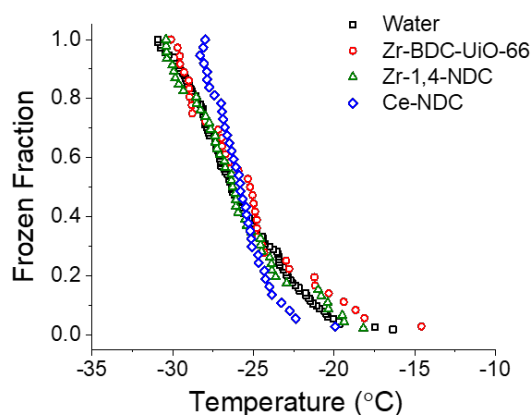


**Figure 5.17.** Frozen fraction of 1  $\mu\text{L}$  droplets containing 3 different MOFs ( $1.0 \text{ mg.mL}^{-1}$ ) compared to that of a Milli-Q water control. (45-55 1  $\mu\text{L}$  droplets per slide, 2-5 repeat experiments per sample).

Despite the extended structures the MOFs tested here and the possibility for lattice matching with the ice surface there may be more to being an INP.

### 5.5.4 Lignins

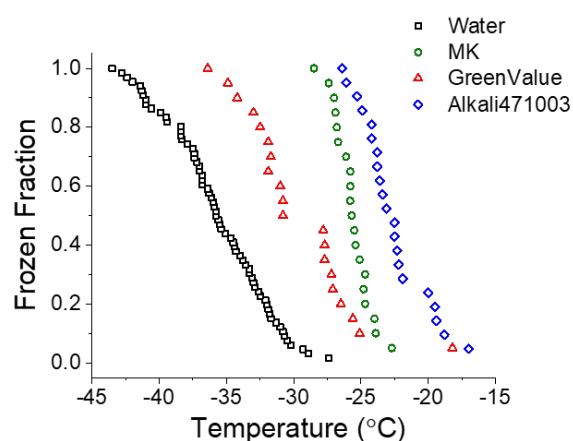


**Figure 5.18.** Frozen fraction of droplets containing 3 different lignin samples ( $1.0 \text{ mg.mL}^{-1}$ ) compared to that of a Milli-Q water control. (10-20 1  $\mu\text{L}$  droplets per slide, 2-5 repeat experiments per sample).

The first nucleation assays on lignins were performed using a cryostage setup and compared to that of water, indicating promise (though the values obtained for water

are too cold for this type of setup), **Figure 5.18**. The slopes for the three lignin samples are similar, with the  $T_n$  shifting along the  $x$ -axes to higher temperatures. Alkali lignin appeared to nucleate ice at the highest temperatures ( $T_{50}$ :  $-23.1$  °C) followed by MK lignin ( $T_{50}$ :  $-25.7$  °C) and then GreenValue ( $T_{50}$ :  $-30.8$  °C). From this data, a mechanism of action cannot be inferred, though the mechanism by which the lignins nucleate could be the same, with the alkali lignin nucleating more efficiently. This may be due to surface tension or viscosity changes in the droplets, which would need to be studied in more depth using viscometry or rheometry. Despite these  $T_n$  being much lower than that of any biological nucleants, there is a definite temperature shift between lignins and pure water, leading us to believe lignins are another potential INP. Our next steps to ensure these findings were correct involved using the  $\mu\text{L-NIPI}$ -based method, as the method, described above, has less error in recording nucleation temperatures.

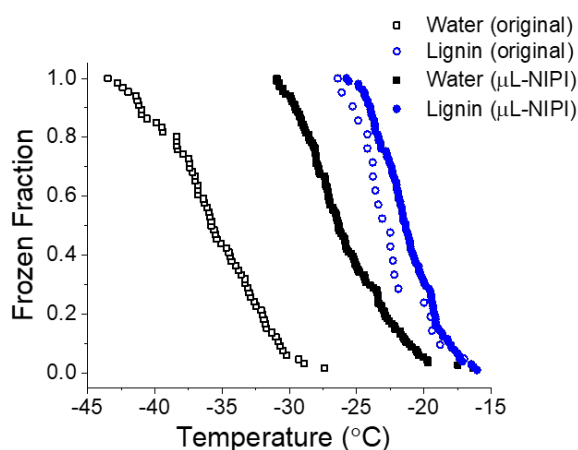


**Figure 5.19.** Frozen fraction of droplets containing Alkali lignin 471003 (blue) compared to that of Milli-Q water (black) recorded using two different setups. Nucleation temperatures observed on the cryostage = open square/circle, temperatures obtained using  $\mu\text{L-NIPI}$  = filled square/circle.  $[\text{Lignin}] = 1.0 \text{ mg}\cdot\text{mL}^{-1}$

Using the  $\mu\text{L-NIPI}$ -based method, alkali lignin was tested again; the results comparing  $T_n$  of water and lignin are shown in **Figure 5.19**. Minimal variation in  $T_n$  is observed between the lignin samples, however there is a difference in the water samples. Implying, even though the water nucleation temperatures may be inaccurate for the cryostage setup (due to the large error in taking measurements at below  $-30$  °C) under those conditions, that the alkali lignin does in fact nucleate ice between  $-16$  and  $-20$  °C, which is higher than that of the water control, and a similar nucleation temperature

to other non-biological nucleants. After this, all experiments were carried out using the  $\mu\text{L-NIPI}$ -based method only.

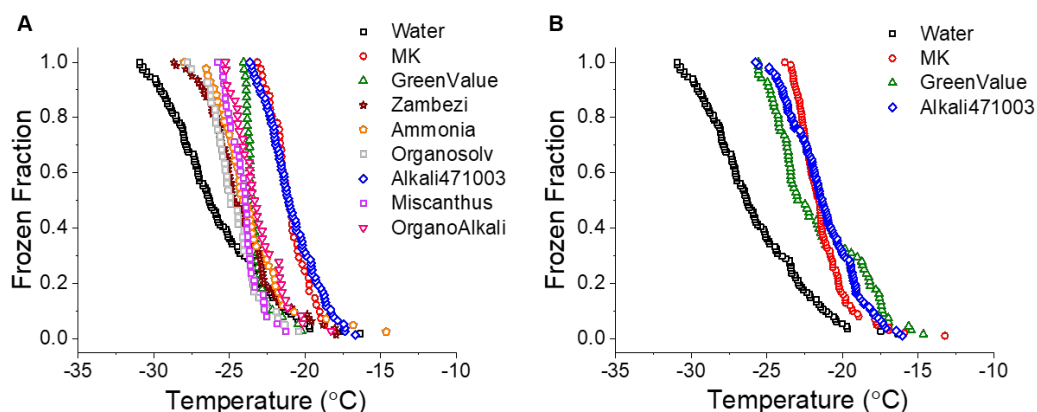


**Figure 5.20.** Nucleation activity of a range of lignins. A) Frozen fraction of droplets containing 8 different lignin samples ( $5.0 \text{ mg.mL}^{-1}$ , sonicated for 2 minutes); B) Frozen fraction of droplets containing 3 different lignin samples ( $1.0 \text{ mg.mL}^{-1}$ ) compared to that of a Milli-Q water control.

Nucleation for a range of lignins was tested, showing as with the cryostage setup, a larger increase in  $T_n$  for alkali lignin (471003) and MK lignin, and a smaller one for the others, indicating that there may be specific features required for nucleation activity, **Figure 5.20A**. This potentially could relate to the fact that all lignins have linkages to different carbohydrates, thus have different concentrations of contaminants/fragments of contaminants, which are assisting in nucleation.<sup>98</sup> Further characterisation of the lignins tested would need to be performed to understand their structures and degradation assays performed (biological, chemical or enzymatic) on MK and alkali lignin to study what causes a loss in activity. Lignin degradation has been studied for a range of species; some fungi are known to decay wood and lignin;<sup>74</sup> bacteria has been observed to be directly involved in lignin mineralisation and more recently has involvement in degradation; yeasts have been reported to depolymerise short lignins ( $200 - 600 \text{ Da}$ )<sup>99</sup> as well as modify the structures in general.<sup>100</sup> Lignin-degrading enzymes are well known and much research has been performed into those from fungi in particular.

These two active lignins and GreenValue (chosen as a less nucleating comparison) were tested at  $1 \text{ mg.mL}^{-1}$ , **Figure 5.20B**. Interestingly, nucleation appeared to be enhanced for all 3 lignins at this lower concentration, not just alkali and MK. As the

alkali lignin is commercially available and a structure is available for it, further tests into its ice-activity, and the effect of different variables on its ice nucleation efficiency were performed.

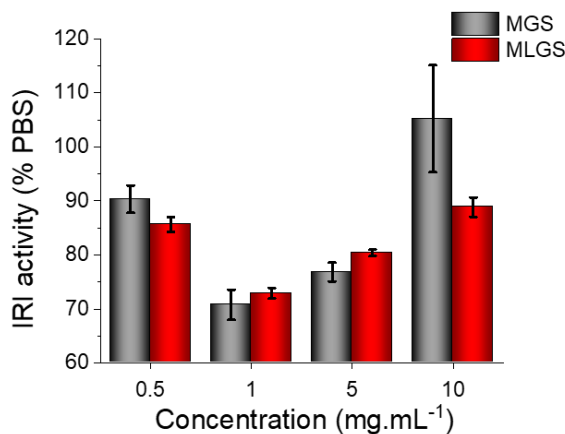


**Figure 5.21.** IRI activity for alkali lignin (471003) over a range of concentrations compared to that of PBS.

Alkali lignin was tested for IRI activity, **Figure 5.21**, showing crystals at ~70 % of the size of a PBS control at 1 mg.mL<sup>-1</sup>, but generally no ice growth inhibition. Interestingly the increase in activity from 0.5 to 1 mg.mL<sup>-1</sup> decreases again upon increase in concentration, with larger ice crystals formed for both 5 and 10 mg.mL<sup>-1</sup> concentrations. Indicating that there is an upper and lower limit to activity for this sample.

Active sites on INPs are hard to find, so a range of variables were tested to see if the nucleating activity of alkali lignin could be understood further.

#### 5.5.4.1 Effect of Concentration

Firstly, three different concentrations of alkali lignin were tested to monitor the change in ice nucleating efficiency, **Figure 5.22**. Over the three concentrations tested, the nucleation activity of the lignin appears to remain the same (within error), suggesting that nucleation is not concentration dependent, and that even if the number of potential INS is increasing, there is a limit to the number of sites available for binding on the growing ice face.

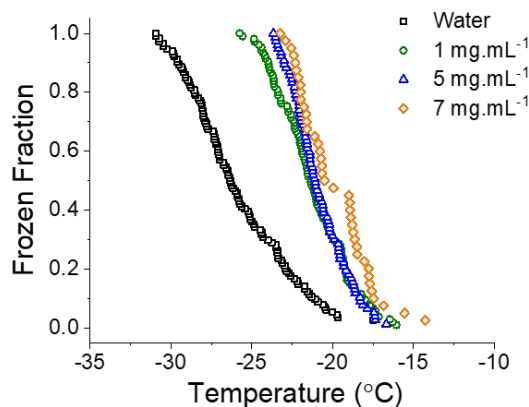


**Figure 5.22.** Frozen fraction of droplets containing Alkali lignin (471003) at 3 different concentrations compared to a Milli-Q water control. (45-55  $\mu\text{L}$  droplets per slide, 2-5 repeat experiments per sample).

Two further concentrations were tested;  $0.1 \text{ mg.mL}^{-1}$  (to test where activity was lost) and  $50 \text{ mg.mL}^{-1}$  (to test if there was an upper limit to activity). Frozen fractions for all 5 concentrations are compared to water in **Figure 5.23**.

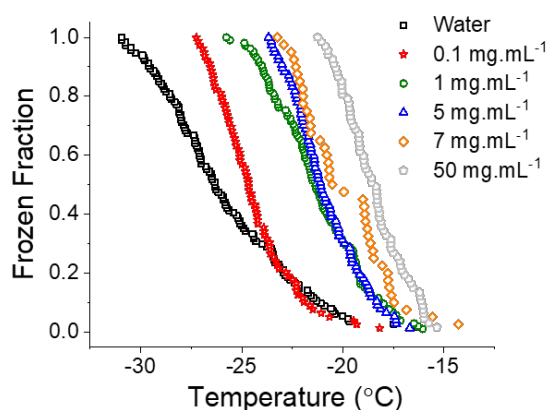


**Figure 5.23.** Frozen fraction of droplets containing Alkali lignin (471003) at 5 different concentrations compared to a Milli-Q water control. (45-55  $\mu\text{L}$  droplets per slide, 2-5 repeat experiments per sample).

It can be observed that alkali lignin no longer appears to nucleate ice at  $0.1 \text{ mg.mL}^{-1}$ , with all  $T_n$  occurring within temperature ranges that pure water nucleation also occurs. According to Beydoun *et al.*  $n_m$  curves for a system should remain the same as the concentration is varied, and only if there is a decrease in particle concentration, a shift in frozen fraction curves would occur.<sup>101</sup> This is observed between  $50 \text{ mg.mL}^{-1}$  (grey) and  $7 \text{ mg.mL}^{-1}$  (orange), thus  $50 \text{ mg.mL}^{-1}$ , though appearing to be a more efficient

concentration for ice nucleation, may not be and this may be in fact due to the increase in particles available.

Beydoun *et al.* proposed that there is a critical area threshold, that below which the distribution of any nucleating sites will have changed and that, rather than a shift, a broadening of the curve will occur.<sup>101</sup> This however, does not appear to be the case between 0.1 mg.mL<sup>-1</sup> (red) and 1.0 mg.mL<sup>-1</sup> (green), implying there is no threshold between these two concentrations, though there is a decrease in particle concentration (curve shifts).

To test for any effect on concentration/mass variation, normalisation of the data from **Figure 5.23** was performed, and represented as cumulative total number of nucleation sites per gram as a function of temperature, **Figure 5.24**. Uncertainty in this work is estimated using a Monte Carlo procedure described by Vali,<sup>74</sup> (program written by Dr Thomas Whale, University of Warwick) where 100 modelled ‘runs’ of  $\mu$ L-NIPI assays are simulated using Poisson distributed random numbers. These are generated lists of possible values for number of active sites per droplet ( $k$ ) which are related to the fraction of droplets frozen. This is performed because there is a certain randomness to the distribution of active sites in each drop in droplet freezing experiments and, theoretically, if 100 – 1000 experiments were performed then the results obtained would mirror that of the calculated results.

The results for normalisation are written here as ice nucleation active site density ( $n_m$ ) normalised to mass. In general  $n_m$  does not change with decreasing concentration, though a slight step in  $n_m$  between 1.0 and 5.0 mg.mL<sup>-1</sup> can be observed, with  $n_m$  increasing as the concentration decreases, implying there is potentially a critical area threshold here. There is, however, agreement (within error) between 0.1 and 1.0 mg.mL<sup>-1</sup> and the 3 samples  $\geq 5.0$  mg.mL<sup>-1</sup> indicating that the ice nucleation efficiency of lignin between these groups is similar.

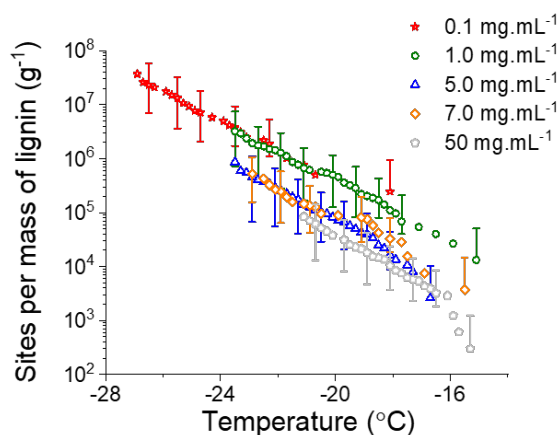


**Figure 5.24.** Ice nucleation efficiency expressed as sites per mass ( $\text{g}^{-1}$ ) of lignin as a function of temperature ( $n_m(T)$ ) for alkali lignin (471003) tested in this study. Values normalised to mass per droplet. Each line consists of between two and five experiments. Due to the significance of nucleation temperatures differences between lignin and water no background subtraction was conducted. Error bars calculated using the Poisson Monte Carlo procedure. For clarity, as errors were representative, only 1 out of 4 errors bars plotted. Temperature uncertainty is  $\pm 0.4^\circ\text{C}$

#### 5.5.4.2 Effect of Sample Preparation

Generally INPs are considered to be large particles (atmospheric INP efficiency correlates with particles being larger than  $0.5 \mu\text{m}$  in diameter),<sup>38</sup> so to test the size of the lignin INP, both alkali lignin and GreenValue were filtered through filters ( $0.2 \mu\text{m}$  diameter pores) and the filtrate tested for nucleation activity and the frozen fractions compared.



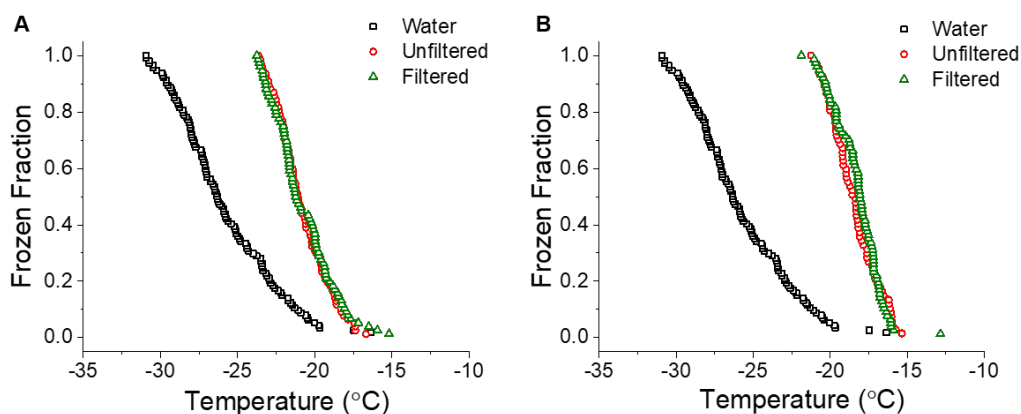


**Figure 5.25.** The effect filtering has on nucleation. A) Frozen fraction of droplets containing alkali lignin (471003) filtered and unfiltered ( $5.0 \text{ mg.mL}^{-1}$ ); B) Frozen fraction of droplets containing alkali lignin (471003) filtered and unfiltered ( $50 \text{ mg.mL}^{-1}$ ) compared to Milli-Q water. Unfiltered = red, filtered = green. (45-55  $1 \mu\text{L}$  droplets per slide, 2-5 repeat experiments per sample).

The alkali lignin's  $T_n$  were not affected by filtering, **Figure 5.25**, indicating that the size of the INPs are  $<0.2 \mu\text{m}$ , which is much smaller than suggested for the atmospheric INPs.  $50 \text{ mg.mL}^{-1}$  was tested to see if filtering had any difference at this higher concentration, as potentially there would be a loss in efficiency if any particles had aggregated (and because there is a difference in  $n_m$  for these two samples).

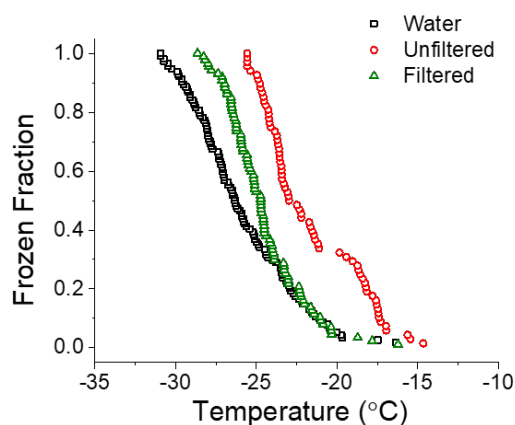


**Figure 5.26.** Frozen fraction of droplets containing GreenValue lignin filtered and unfiltered solutions compared to Milli-Q water ( $1.0 \text{ mg.mL}^{-1}$ ). Unfiltered = red, filtered = green. (45-55  $1 \mu\text{L}$  droplets per slide, 2-5 repeat experiments per sample).

Green value lignin was then tested again filtered; as the sample does not fully dissolve in pure water,  $1 \text{ mg.mL}^{-1}$  was filtered and then tested for nucleation activity in the

filtrate, **Figure 5.26**, where a drop in activity was observed, indicating the size of the nucleants are  $>0.2 \mu\text{L}$ .

### 5.5.4.3 Effect of Cooling Rate

Cooling rates have been studied for a range of materials, with some showing nucleation has either weak or no cooling rate dependence compared to that of temperature dependence,<sup>9,102,103</sup> and others exhibit a certain dependence at high concentrations.<sup>53</sup> If there is a particular INS,  $T_n$  should not be affected by cooling rate, as this site would promote nucleation at the same temperature (temperature required for a particular size critical nucleus) each time.

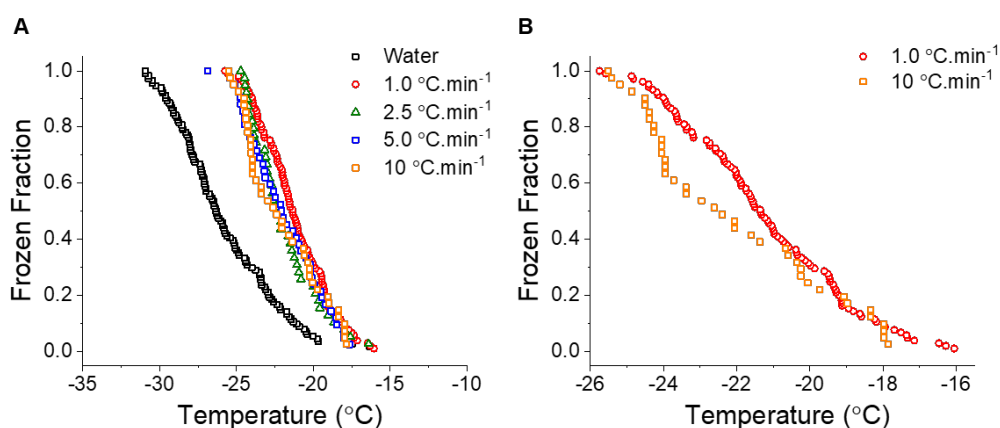


**Figure 5.27.** Frozen fraction of droplets containing Alkali lignin 471003 frozen at different cooling rates compared to that of a Milli-Q water control (black, cooled at  $1 \text{ }^\circ\text{C}\cdot\text{min}^{-1}$ ). A) Four different rates compared; B) comparison of  $1.0 \text{ }^\circ\text{C}\cdot\text{min}^{-1}$  (red) and  $10 \text{ }^\circ\text{C}\cdot\text{min}^{-1}$  (orange). (45-55  $1 \mu\text{L}$  droplets per slide, 2-5 repeat experiments per sample).  $[\text{Lignin}] = 1 \text{ mg}\cdot\text{mL}^{-1}$ .

To check for any effect of cooling rate on  $T_n$  for alkali lignin, assays were performed using four different cooling ramp rates, **Figure 5.27A**. It can be seen that modifying the cooling rate of this system (between  $1$  and  $10 \text{ }^\circ\text{C}\cdot\text{min}^{-1}$ ) does not greatly affect the temperatures at which alkali lignin nucleates ice. The fastest ( $10 \text{ }^\circ\text{C}\cdot\text{min}^{-1}$ , orange) and slowest ( $1.0 \text{ }^\circ\text{C}\cdot\text{min}^{-1}$ , red) cooling rates are magnified in **Figure 5.27B**, showing that there is little effect on  $T_n$  overall. 20 % of droplets have frozen for both rates at  $-19.2 \text{ }^\circ\text{C}$ , and though the percent of frozen droplets differs as the sample cools, with 55 % of those cooled using the  $1.0 \text{ }^\circ\text{C}\cdot\text{min}^{-1}$  rate frozen by  $-21.6 \text{ }^\circ\text{C}$  but only 40 % for those

---

cooled with the  $10\text{ }^{\circ}\text{C}\cdot\text{min}^{-1}$  rate, 100 % of the droplets are frozen by  $-25.5\text{ }^{\circ}\text{C}$  ( $10\text{ }^{\circ}\text{C}\cdot\text{min}^{-1}$ ) and  $-25.7\text{ }^{\circ}\text{C}$  ( $1.0\text{ }^{\circ}\text{C}\cdot\text{min}^{-1}$ ).

In general, if two sets of droplets that contain the same mass/surface area of INP are cooled at different rates, a greater percentage of droplets will be frozen, at a given temperature (*e.g.*  $-20\text{ }^{\circ}\text{C}$ ), for the droplets cooled at the slower rate. This is because the longer the time interval, the greater probability for freezing. This can be a problem when analysing potential INPs, as the rate may interfere with results *i.e.* giving false positives. In this work there appears to be little correlation between rate and  $T_n$  thus the nucleating efficiency of alkali lignin can be confirmed to be correct. Herbert *et al.* derived the Framework for Reconciling Observable Stochastic Time-dependence (FROST) to assist in reconciling data obtained from experiments *via* different cooling rates.<sup>54</sup> Full details of this work are beyond the scope of this work, but it is important to note, for future work, that any effect of rate due to different experimental setups, experiment timescales and different materials can be compared using this framework.

## 5.6 Conclusion

Using a blue-sky approach in combination with  $\mu$ L-NIPI was successful, in that the high-throughput nature of the technique allowed a variety of different materials to be tested quickly and easily.

Metal organic frameworks were demonstrated to have no ice nucleation, or IRI activity, despite their potential to lattice match with the ice surface. Findings of Zhu *et al.* are challenged in this work, as MOF concentrations used in this work are both the same and higher, and yet no ice-activity can be observed. Further investigation into structural motifs required for activity need to be performed in order to potentially use MOF-like structures. Though, despite their inactivity, the MOFs could be used as another option for protein scaffolds, enabling multivalency in a similar way to the AuNP in Chapter 3.

Safranine-O was also confirmed to not perform as a nucleator at concentrations where self-assembly is known to occur, indicating that despite having a structure conducive for ice growth inhibition and shaping, self-assembling in general does not lead to nucleating efficiency. However, large disordered structures were found to have some nucleation activity; alkali lignin and MK lignin were observed to have the highest nucleating efficiency out of the 8 different lignins tested, with the focus of later experiments on alkali lignin, due to its commercial availability.

In an attempt to understand the nucleation effectiveness of alkali lignin, different variables were tested. Firstly concentration; where nucleation effectiveness was found to remain constant over a range of concentrations, indicating that despite any change in quantity of potential INS, only a low number is required for activity. Secondly, in order to determine whether the INS were on particles in a particular size range, alkali lignin was filtered, the filtrate analysed (and compared to that of GreenValue filtrate) and was observed to have no influence on effectiveness for alkali lignin, indicating a smaller particle size.

To further confirm alkali lignin's efficiency droplet assays were performed using different cooling ramp rates, and again nucleation efficiency remained equal over different rates, thus not necessitating specific further analysis using frameworks such as FROST.

This work highlights the differences in results obtained from different wet-dispersion techniques, with the nucleation temperatures for pure water, as well as samples, changing depending on type of DSC protocol followed. The droplet assays were shown to provide a faster, more thorough method of data acquisition, with the capability to monitor nucleation for up to 50 droplets at once, compared to between one and three for DSC, thus ensuring a lower level of error in the obtained results. Further optimisation of calorimetry-based techniques is required for their use.

More indepth investigations are required to understand the importance of the particles themselves and what causes nucleation. In particular, characterisation of both alkali and MK lignins would enable understanding of any similarities in their structures that may be leading to their higher nucleation efficiency. Gel permeation chromatography (GPC) could be performed to obtain molecular weight fractions, which could then be tested for nucleation efficiency. Potentially, chemical/enzymatic degradation could be performed to assist with determining the structural subunits that lead to this increase in activity.

Overall, if nucleation could be related to particular structures/subunits, then more control could be achieved. If nucleation temperatures could be increased to  $>-10\text{ }^{\circ}\text{C}$ , there would be potential cryopreservation applications.

## 5.7 Experimental

### 5.7.1 Materials

Safranin-O and alkali lignin (471003) were purchased from Sigma-Aldrich and used as supplied unless otherwise stated. Phosphate-buffered saline solution was prepared using in Milli-Q water ( $>18.2 \Omega$  mean resistivity) to give  $[\text{NaCl}] = 0.138 \text{ M}$ ,  $[\text{KCl}] = 0.0027 \text{ M}$ , and pH 7.4). GreenValue, MK, zambezi, ammonia, organosolv, miscanthus and OrganoAlkali lignins were kindly provided by Dr Goran Rashid, University of Warwick and Ce(BTC)<sub>3</sub>·H<sub>2</sub>O, Ce-NDC, Zr-BDC-UiO<sub>66</sub> and Zr-1,4-NDC MOFs were kindly provided by Ehsan Ghadim, University of Warwick.

### 5.7.2 Physical and Analytical Methods

A Linkam Biological Cryostage BCS196 with T95-Linkpad system controller equipped with a LNP95-Liquid nitrogen cooling pump, using liquid nitrogen as the coolant (Linkam Scientific Instruments U.K., Surrey, U.K.) was used to anneal ice wafers. An Olympus CX41 microscope equipped with a UIS-2 20x/0.45/ $\infty$ /0-2/FN22 lens (Olympus Ltd., Southend on Sea, U.K.) and a Canon EOS 500D SLR digital camera was used to obtain all images. Image processing was performed using ImageJ, which is freely available from <http://imagej.nih.gov/ij/>. Absorbance spectroscopy was undertaken using a Synergy HT multi-mode microplate reader (BioTek U.K., Bedfordshire, U.K.). Differential scanning calorimetry was performed using a Perkin Elmer DSC6000 with intracooler and autosampler using 40  $\mu\text{L}$  aluminium crucibles (Perkin Elmer, USA). The Peltier cold stage used for NIPI-style experiments consisted of a Meerstetter TEC-1091 driving a TEC-12704 Peltier. An aluminium plate was bonded to the Peltier using thermal paste. The temperature of the plate (and the droplet mounted on it) was monitored using two Netshushin wound PT100 thermometers monitored by PT-104 temperature loggers. A 0.22 mm thick, 22mm diameter hydrophobic glass slide (Hampton research) was placed on the aluminium plate and covered by a droplet shield. Droplets were pipetted into the slide using a Picus Biohit electronic pipette and were monitored through a glass window using a digital camera. A Teca Ameritemp<sup>TM</sup> recirculating chiller attached was used to cool the hot side of the Peltier.

### 5.7.3 Procedures

#### 5.7.3.1 Ice Recrystallisation Inhibition ‘Splat’ Assay

Samples were dissolved in PBS buffer (pH 7.4) at concentrations of 10 to 0.05 mg.mL<sup>-1</sup> and 1 drop of the solution was dispensed from a height of 1.4 m onto a glass cover slip on a metal disc cooled with dry ice. An ice wafer instantly formed and was transferred to a cryostage held at -8 °C under liquid nitrogen. Samples were left to anneal for 30 minutes. Images of the wafer were taken before and after the 30 minutes. Image processing was performed using ImageJ software on the 5 largest crystals from at least 3 independent wafers giving the MLGS from 15 measurements.

#### 5.7.3.2 Differential Scanning Calorimetry

Aluminium crucibles (40 µL) were weighed, then either single drops of sample (10 µL) were pipetted directly into the crucibles, or multiple drops of sample (1.0 µL) were pipetted into crucibles containing immersion oil type B, which were then sealed and reweighed.

Crucibles were then inserted into the Perkin Elmer DSC600 *via* an autosampler. Samples were then cooled to -40 °C at a cooling rate of 1.0 °C.min<sup>-1</sup> and nucleation temperatures recorded as the temperature at which a phase change is observed on the DSC trace. Data was analysed using Perkin Elmer Pyris thermal analysis software version 13.1.1.0160.

#### 5.7.3.3 Cryostage Nucleation Drop Assay

Samples were dissolved in Milli-Q water. Drops of sample (1.0 µL) were pipetted onto clean coverslips with a hydrophobic organosilane coating (Fluka, 5 % dimethyldichlorosilane in heptane) ensuring the glass cover slip did not interfere with ice nucleation. The coverslip was placed in a Linkam Cryostage, which was rapidly cooled to 0 °C at a rate of 50 °C.min<sup>-1</sup>, then held at this temperature for 3 minutes to allow the temperature of the glass slide and droplets to equilibrate. The samples were then cooled from 0 °C to -49 °C at 1.0 °C.min<sup>-1</sup>. Nucleation was recorded using a USB microscope and Veho Microcapture software version 1.3.

#### 5.7.3.4 $\mu\text{L}$ -NIPI-based Drop Assay

Samples were dissolved in Milli-Q water. 45-55  $1\ \mu\text{l}$  droplets were placed on a 0.22 mm thick silanised slide (Hampton Research HR3-231) supported by a Teca Ameritemp<sup>TM</sup> solid-state peltier chiller using a Picus Biohit electronic micropipette. Suspensions were made up using 18.2 M $\Omega$  Milli-Q water and carefully weighed quantities of the nucleant under test. Temperatures were measured using a PT-104 temperature logger reading two Netshushin wound PT100 thermometers. A custom LabView software combines the temperature and video footage into easily analysed data using VirtualDub 1.10.4.

The peltier is used to cool down the droplets in the custom-made apparatus at a controlled rate and a Meerstetter TEC-1091 thermoelectric controller is used to control and monitor temperature. In this study a cooling rate of  $1.0\ \text{°C}\cdot\text{min}^{-1}$  has been used unless otherwise stated. The slide and droplets were covered by a Perspex chamber with a port for a camera and a gas inlet and outlet. Dry nitrogen (gas flow  $0.2\ \text{L}\cdot\text{min}^{-1}$ ) was gently flown over the droplets to prevent condensation of water and ice. A camera was used to monitor droplet freezing. **Figure 5.10** shows the layout of the apparatus. This assay is used to determine the fraction of droplets frozen at a given temperature. All datasets reported here consist of multiple (2-5) individual experiments.



## 5.8 References

- 1 B. Riechers, F. Wittbracht, A. Hütten and T. Koop, *Phys. Chem. Chem. Phys.*, 2013, **15**, 5873–5887.
- 2 J. Lv, Y. Song, L. Jiang and J. Wang, *ACS Nano*, 2014, **8**, 3152–3169.
- 3 A. Chakrabartty, D. S. Yang and C. L. Hew, *J. Biol. Chem.*, 1989, **264**, 11313–11316.
- 4 T. Koop and B. J. Murray, *J. Chem. Phys.*, 2016, **145**, 211915.
- 5 E. Sanz, C. Vega, J. R. Espinosa, R. Caballero-Bernal, J. L. F. Abascal and C. Valeriani, *J. Am. Chem. Soc.*, 2013, **135**, 15008–15017.
- 6 Z. Zhang and X. Y. Liu, *Chem. Soc. Rev.*, 2018, **47**, 7116–7139.
- 7 B. Vonnegut, *J. Appl. Phys.*, 1947, **18**, 593–595.
- 8 C. Hoose and O. Möhler, *Atmos. Chem. Phys.*, 2012, **12**, 9817–9854.
- 9 B. J. Murray, D. O’Sullivan, J. D. Atkinson and M. E. Webb, *Chem. Soc. Rev.*, 2012, **41**, 6519–6554.
- 10 G. Heydari, E. Thormann, M. Järn, E. Tyrode and P. M. Claesson, *J. Phys. Chem. C*, 2013, **117**, 21752–21762.
- 11 Q. Li and Z. Guo, *J. Mater. Chem. A*, 2018, **6**, 13549–13581.
- 12 K. Diehl, C. Quick, S. Matthias-Maser, S. K. Mitra and R. Jaenicke, *Atmos. Res.*, 2001, **58**, 75–87.
- 13 G. Vali, M. Christensen, R. W. Fresh, E. L. Galyan, L. R. Maki and R. C. Schnell, *J. Atmos. Sci.*, 1976, **33**, 1565–1570.
- 14 L. R. Maki and K. J. Willoughby, *J. Appl. Meteorol.*, 1978, **17**, 1049–1053.
- 15 Z. Levin and S. A. Yankofsky, *J. Clim. Appl. Meteorol.*, 1983, **22**, 1964–1966.
- 16 N. Cochet and P. Widehem, *Appl. Microbiol. Biotechnol.*, 2000, **54**, 153–161.
- 17 J. D. Atkinson, B. J. Murray, M. T. Woodhouse, T. F. Whale, K. J. Baustian, K. S. Carslaw, S. Dobbie, D. O’Sullivan and T. L. Malkin, *Nature*, 2013, **498**, 355–358.

- 18 C. E. Morris, D. G. Georgakopoulos and D. C. Sands, *J. Phys. IV*, 2004, **121**, 87–103.
- 19 J. Verdon, P. Coutos-Thevenot, M. H. Rodier, C. Landon, S. Depayras, C. Noel, S. La Camera, B. Moumen, P. Greve, D. Bouchon, J. M. Berjeaud and C. Braquart-Varnier, *Front. Microbiol.*, 2016, **7**, 1484.
- 20 S. P. Graether and Z. Jia, *Biophys. J.*, 2001, **80**, 1169–1173.
- 21 T. Zolles, J. Burkart, T. Häusler, B. Pummer, R. Hitzenberger and H. Grothe, *J. Phys. Chem. A*, 2015, **119**, 2692–2700.
- 22 T. F. Whale, M. Rosillo-Lopez, B. J. Murray and C. G. Salzmann, *J. Phys. Chem. Lett.*, 2015, **6**, 3012–3016.
- 23 L. Eickhoff, K. Dreischmeier, A. Zipori, V. Sirotinskaya, C. Adar, N. Reicher, I. Braslavsky, Y. Rudich and T. Koop, *J. Phys. Chem. Lett.*, 2019, **10**, 966–972.
- 24 N. Du, X. Y. Liu and C. L. Hew, *J. Biol. Chem.*, 2003, **278**, 36000–36004.
- 25 N. Du, X. Y. Liu and C. L. Hew, *J. Phys. Chem. B*, 2006, **110**, 20562–20567.
- 26 P. K. Wolber, *Adv. Microb. Physiol.*, 1993, **34**, 203–237.
- 27 T. L. Kieft and T. Ruscetti, *J. Bacteriol.*, 1990, **172**, 3519–3523.
- 28 R. Lundheim, J. Laybourn-Parry, D. Hall and C. Gerday, *Philos. Trans. R. Soc. B Biol. Sci.*, 2002, **357**, 937–943.
- 29 K. E. Zachariassen and E. Kristiansen, *Cryobiology*, 2000, **41**, 257–279.
- 30 B. G. Pummer, H. Bauer, J. Bernardi, S. Bleicher and H. Grothe, *Atmos. Chem. Phys.*, 2012, **12**, 2541–2550.
- 31 K. Dreischmeier, C. Budke, L. Wiehemeier, T. Kottke and T. Koop, *Sci. Rep.*, 2017, **7**, 41890.
- 32 P. Ginoux, J. M. Prospero, T. E. Gill, N. C. Hsu and M. Zhao, *Rev. Geophys.*, 2012, **50**, 1–36.
- 33 T. F. Whale, University of Leeds, 2016.
- 34 A. D. Harrison, T. F. Whale, M. A. Carpenter, M. A. Holden, L. Neve, D.

- O'Sullivan, J. Vergara Temprado and B. J. Murray, *Atmos. Chem. Phys.*, 2016, **16**, 10927–10940.
- 35 C. I. Biggs, C. Packer, S. Hindmarsh, M. Walker, N. R. Wilson, J. P. Rourke and M. I. Gibson, *Phys. Chem. Chem. Phys.*, 2017, **19**, 21929–21932.
- 36 H. Geng, X. Liu, G. Shi, G. Bai, J. Ma, J. Chen, Z. Wu, Y. Song, H. Fang and J. Wang, *Angew. Chemie - Int. Ed.*, 2017, **56**, 997–1001.
- 37 G. Vali, *J. Atmos. Sci.*, 1971, **28**, 402–409.
- 38 P. J. DeMott, *Atmos. Res.*, 1995, **38**, 63–99.
- 39 H. R. Pruppacher and J. D. Klett, *Microphysics of Clouds and Precipitation*, Kluwer Academic Publishers, Dordrecht, The Netherlands, 2nd edn., 1997.
- 40 A. Hudait, N. Odendahl, Y. Qiu, F. Paesani and V. Molinero, *J. Am. Chem. Soc.*, 2018, **140**, 4905–4912.
- 41 H. W. Georgii and E. Kleinjung, *J. Rech. Atmos.*, 1967, **3**, 145–146.
- 42 K. Li, S. Xu, W. Shi, M. He, H. Li, S. Li, X. Zhou, J. Wang and Y. Song, *Langmuir*, 2012, **28**, 10749–10754.
- 43 M. Truffer, University of Alaska Fairbanks, 2013.
- 44 A. C. Zettlemoyer, N. Tcheurekdjian and J. J. Chessick, *Nature*, 1961, **192**, 653.
- 45 W. G. Finnegan and S. K. Chai, *J. Atmos. Sci.*, 2003, **60**, 1723–1731.
- 46 S. J. Cox, S. M. Kathmann, B. Slater and A. Michaelides, *J. Chem. Phys.*, 2015, **142**, 184704.
- 47 L. Lupi, A. Hudait and V. Molinero, *J. Am. Chem. Soc.*, 2014, **136**, 3156–3164.
- 48 M. A. Holden, T. F. Whale, M. D. Tarn, D. O'Sullivan, R. D. Walshaw, B. J. Murray, F. C. Meldrum and H. K. Christenson, *Sci. Adv.*, 2019, **5**, eaav4316.
- 49 C. Gurganus, A. B. Kostinski and R. A. Shaw, *J. Phys. Chem. C*, 2013, **117**, 6195–6200.
- 50 C. W. Gurganus, J. C. Charnawskas, A. B. Kostinski and R. A. Shaw, *Phys. Rev. Lett.*, 2014, **113**, 235701.

- 51 T. F. Whale, M. A. Holden, A. N. Kulak, Y. Y. Kim, F. C. Meldrum, H. K. Christenson and B. J. Murray, *Phys. Chem. Chem. Phys.*, 2017, **19**, 31186–31193.
- 52 N. Hiranuma, S. Augustin-Bauditz, H. Bingemer, C. Budke, J. Curtius, A. Danielczok, K. Diehl, K. Dreischmeier, M. Ebert, F. Frank, N. Hoffmann, K. Kandler, A. Kiselev, T. Koop, T. Leisner, O. Möhler, B. Nillius, A. Peckhaus, D. Rose, S. Weinbruch, H. Wex, Y. Boose, P. J. Demott, J. D. Hader, T. C. J. Hill, Z. A. Kanji, G. Kulkarni, E. J. T. Levin, C. S. McCluskey, M. Murakami, B. J. Murray, D. Niedermeier, M. D. Petters, D. O’Sullivan, A. Saito, G. P. Schill, T. Tajiri, M. A. Tolbert, A. Welti, T. F. Whale, T. P. Wright and K. Yamashita, *Atmos. Chem. Phys.*, 2015, **15**, 2489–2518.
- 53 S. L. Broadley, B. J. Murray, R. J. Herbert, J. D. Atkinson, S. Dobbie, T. L. Malkin, E. Condliffe and L. Neve, *Atmos. Chem. Phys.*, 2012, **12**, 287–307.
- 54 R. J. Herbert, B. J. Murray, T. F. Whale, S. J. Dobbie and J. D. Atkinson, *Atmos. Chem. Phys.*, 2014, **14**, 8501–8520.
- 55 R. P. Sear, *CrystEngComm*, 2014, **16**, 6506–6522.
- 56 G. Vali, in *Biological Ice Nucleation and Its Applications*, eds. R. Lee Jr, G. J. Warren and L. V. Gusta, American Phytopathological Society, St. Paul, MN, 1995, pp. 1–28.
- 57 C. Budke and T. Koop, *Atmos. Meas. Tech.*, 2015, **8**, 689–703.
- 58 A. Bogdan, M. J. Molina, H. Tenhu, E. Bertel, N. Bogdan and T. Loerting, *Sci. Rep.*, 2014, **4**, 33–37.
- 59 R. W. Michelmore and F. Franks, *Cryobiology*, 1982, **19**, 163–171.
- 60 T. N. Hansen and J. G. Baust, *Biochim. Biophys. Acta (BBA)/Protein Struct. Mol.*, 1988, **957**, 217–221.
- 61 J. Liu, C. E. Nicholson and S. J. Cooper, *Langmuir*, 2007, **23**, 7286–7292.
- 62 A. D. Harrison, T. F. Whale, R. Rutledge, S. Lamb, M. D. Tarn, G. C. E. Porter, M. Adams, J. B. McQuaid, G. J. Morris and B. J. Murray, *Atmos. Meas. Tech. Discuss.*, 2018, 1–22.

- 63 A. Reinhardt and J. P. K. Doye, *J. Chem. Phys.*, 2014, **141**, 084501–10.
- 64 E. B. Moore and V. Molinero, *Nature*, 2011, **479**, 506–508.
- 65 D. Pan, L. M. Liu, B. Slater, A. Michaelides and E. Wang, *ACS Nano*, 2011, **5**, 4562–4569.
- 66 X. Y. Liu and N. Du, *J. Biol. Chem.*, 2004, **279**, 6124–6131.
- 67 M. Bayer-Giraldi, G. Sazaki, K. Nagashima, S. Kipfstuhl, D. A. Vorontsov and Y. Furukawa, *Proc. Natl. Acad. Sci.*, 2018, **115**, 7479–7484.
- 68 H. Furukawa, K. E. Cordova, M. O’Keeffe and O. M. Yaghi, *Science*, 2013, **341**, 1230444–12.
- 69 B. Liu, Y. He, L. Han, V. Singh, X. Xu, T. Guo, F. Meng, X. Xu, P. York, Z. Liu and J. Zhang, *Cryst. Growth Des.*, 2017, **17**, 1654–1660.
- 70 K. Lu, C. He, N. Guo, C. Chan, K. Ni, G. Lan, H. Tang, C. Pelizzari, Y. X. Fu, M. T. Spiotto, R. R. Weichselbaum and W. Lin, *Nat. Biomed. Eng.*, 2018, **2**, 600–610.
- 71 W. Zhu, J. Guo, J. O. Agola, J. G. Croissant, Z. Wang, J. Shang, E. N. Coker, B. Motevalli, A. Zimpel, S. Wuttke and C. J. Brinker, *J. Am. Chem. Soc.*, 2019, **141**, 7789–7796.
- 72 H. Furukawa, F. Gándara, Y.-B. Zhang, J. Jiang, W. L. Queen, M. R. Hudson and O. M. Yaghi, *J. Am. Chem. Soc.*, 2014, **136**, 4369–4381.
- 73 H. Hatakeyama and T. Hatakeyama, in *Biopolymers*, eds. A. Abe, K. Dusek and S. Kobayashi, Springer, Berlin, Heidelberg, 2010, vol. 5, pp. 1–63.
- 74 G. M. M. Rashid, University of Warwick, 2015.
- 75 N. P. Kutscha and J. R. Gray, *Tech. Bull.*, 1970, **40**, 1–3.
- 76 D. J. Phillips and M. I. Gibson, *Biomacromolecules*, 2012, **13**, 3200–3208.
- 77 M. Drahanaky, M. . Paridah, A. Moradbak, A. . Mohamed, F. Abdulwahab taiwo Owolabi, M. Asniza and S. H. . Abdul Khalid, in *Lignin - Trends and Applications*, ed. M. Poletto, InTechOpen, 2018, pp. 181–205.
- 78 T. K. Kirk, O. Gifford, P. Drive and R. L. Farrell, *Ann. Rev. Microbiol.*, 1987,

- 41**, 465–505.
- 79 R. Vanholme, B. Demedts, K. Morreel, J. Ralph and W. Boerjan, *Plant Physiol.*, 2010, **153**, 895–905.
- 80 J. Banoub, G. H. Delmas, N. Joly, G. Mackenzie, N. Cachet, B. Benjelloun-Mlayah and M. Delmas, *J. Mass Spectrom.*, 2015, **50**, 1–284.
- 81 S. Borysiak, *J. Therm. Anal. Calorim.*, 2013, **113**, 281–289.
- 82 N. Hiranuma, O. Möhler, K. Yamashita, T. Tajiri, A. Saito, A. Kiselev, N. Hoffmann, C. Hoose, E. Jantsch, T. Koop and M. Murakami, *Nat. Geosci.*, 2015, **8**, 273–277.
- 83 R. Drori, C. Li, C. Hu, P. Raiteri, A. L. Rohl, M. D. Ward and B. Kahr, *J. Am. Chem. Soc.*, 2016, **138**, 13396–13401.
- 84 S. Y. Lin and C. W. Dence, Eds., *Methods in Lignin Chemistry. Springer Series in Wood Science.*, Springer-Verlag Berlin Heidelberg, Berlin, Heidelberg, 1992.
- 85 X. Liu, Y. Xu, J. Yu, S. Li, J. Wang, C. Wang and F. Chu, *Int. J. Biol. Macromol.*, 2014, **67**, 483–489.
- 86 F. Xu, J. X. Sun, R. Sun, P. Fowler and M. S. Baird, *Ind. Crops Prod.*, 2006, **23**, 180–193.
- 87 X. Zhao, K. Cheng and D. Liu, *Appl. Microbiol. Biotechnol.*, 2009, **82**, 815–827.
- 88 L. N. Lin, A. B. Mason, R. C. Woodworth and J. F. Brandts, *Biochem. J.*, 1993, **293**, 517–522.
- 89 I. Protasevich, B. Ranjbar, V. Lobachov, A. Makarov, R. Gilli, C. Briand, D. Lafitte and J. Haiech, *Biochemistry*, 1997, **36**, 2017–2024.
- 90 U. von Stockar and I. W. Marison, *Adv. Biochem. Engineering/Biotechnology*, 1989, **40**, 93–136.
- 91 C. G. Salzmann, P. G. Radaelli, B. Slater and J. L. Finney, *Phys. Chem. Chem. Phys.*, 2011, **13**, 18468–18480.

- 
- 92 D. T. Haynie, *Biological Thermodynamics*, Cambridge University Press, Cambridge, Second., 2008.
- 93 E. Stopelli, F. Conen, L. Zimmermann, C. Alewell and C. E. Morris, *Atmos. Meas. Tech.*, 2014, **7**, 129–134.
- 94 P. W. Wilson, J. W. Arthur and A. D. J. Haymet, *Biophys. J.*, 1999, **77**, 2850–2855.
- 95 A. Bogdan, *J. Chem. Phys.*, 1997, **106**, 1921–1929.
- 96 A. E. R. Fayter, M. I. Gibson and E. R. Draper, *J. Mater. Chem. B*, 2018, **6**, 7274–7279.
- 97 O. Mizrahy, M. Bar-Dolev, S. Guy and I. Braslavsky, *PLoS One*, 2013, **8**, e59540.
- 98 T. Koshijima, T. Watanabe and F. Yaku, in *Lignin properties and materials*, eds. W. G. Glasser and S. Sarkanen, American Chemical Society, Washington, DC, 1998, pp. 11–28.
- 99 S. A. Chambers, University of Warwick, 1989.
- 100 A. R. Hainal, A. M. Capraru, V. Irina and V. I. Popa, *Cellul. Chem. Technol.*, 2012, **46**, 87–96.
- 101 H. Beydoun, M. Polen and R. C. Sullivan, *Atmos. Chem. Phys.*, 2016, **16**, 13359–13378.
- 102 T. P. Wright, M. D. Petters, J. D. Hader, T. Morton and A. L. Holder, *J. Geophys. Res. Atmos.*, 2013, **118**, 10535–10543.
- 103 D. Niedermeier, S. Hartmann, T. Clauss, H. Wex, A. Kiselev, R. C. Sullivan, P. J. Demott, M. D. Petters, P. Reitz, J. Schneider, E. Mikhailov, B. Sierau, O. Stetzer, B. Reimann, U. Bundke, R. A. Shaw, A. Buchholz, T. F. Mentel and F. Stratmann, *Atmos. Chem. Phys.*, 2011, **11**, 11131–11144.

# Chapter 6

---

## Conclusions



## 6.1. Overview of Thesis

The development of synthetic ice recrystallisation inhibition (IRI) active materials with activity rivalling that of AF(G)Ps remains a challenge, with current methods often limited to analysis of macroscopic effects using microscopy, in particular the use of older techniques that have not been updated since their introduction that have issues of only providing data on a ‘snapshot’ of a whole sample. Modelling has provided a useful insight into the molecular-level activities and mechanisms of action of both natural and synthetic ice-active compounds, however experimental work has yet to provide a final verification for these theories.

AF(G)Ps are extremely effective non-colligative antifreezes, though are less suitable for other applications, particularly in cryopreservation due to toxicity, expense and challenges in production at large scale. Hence discovery, development and understanding of synthetic mimics is of particular interest. This thesis has shown that IRI active PVA in combination with non-IRI active PEG, as a formulation, has the capability to work as a potent cryoprotectant for both bacteria and proteins, enabling storage without the need for organic solvents, using much lower concentrations. **Chapter 2** highlights this disruptive approach to store bacteria and proteins in the frozen state through modulation of ice recrystallisation with synthetic polymer formulations that mimic the antifreeze proteins used in nature to survive extreme environments. AFPIII was expressed and purified for use as a comparison for both IRI activity and cryoprotective ability, showing that PVA works as a more competent cryoprotectant despite its lower IRI activity, potentially due to its lack of ice shaping activity. The PEG/PVA cryopreserving formulation was seen to be highly IRI active and the least bactericidal, resulting in a 4-fold increase in *E. coli* yield post-thaw, compared to glycerol, and was found to be equal to or better than glycerol for other cell types. The use of a secondary hydrophilic polymer is essential as a bulking agent in these systems and the formulation was found to work by preventing aggregation of proteins, and by inhibiting ice recrystallisation (whilst being less toxic than glycerol) in cells, unlike in traditional solvent-based cryoprotectants, which function by distinct mechanisms.

To further test these results and their potential wide-reaching application across biology and the biotechnology industry, cryopreservation studies of a wider range of

proteins and cell-lines should be undertaken, in particular by testing more industrially relevant cells, including *L. delbrueckii subsp. bulgaricus*. Preliminary work was performed on this species in this project but optimisation of expression and growth of this strain needs to be completed to confirm cryopreservative ability of our polymer formulation for this culture. Further work could also include repetition of freeze/thaw assays in other laboratories, to ensure the protocols, and subsequent results, can be transferred successfully to other research groups, as well as performing further experiments to confirm cell viability post-thaw. This work centred around colony counting and live/dead assays, however studies could be performed, on *E. coli* for example, post-thaw to ensure these cells are viable *i.e.* can still be used for protein expression *etc.*

The microscopy-based techniques allow for observation of size and morphology of ice grains, however, do not help elucidate the mechanisms of action behind ice-active materials. In **Chapter 3**, XRD was investigated as another method for analysis of ice recrystallisation. A method was developed, and was found to be a successful, complementary, non-invasive method for 3D analysis of crystal growth. Real-time kinetic analysis is possible with this method without the need for time-consuming analysis of individual video-frames obtained during optical techniques. IRI activity results obtained *via* XRD for a range of compounds was compared to that of optical methods and was found to be in good agreement. Diffraction patterns were analysed and no specific indications for ice-binding were observed. In this work peak widths were not analysed and would be interesting to study. Full width at half maximum (FWHM) could be used to characterize crystal properties, analyse stress/strain and determine crystallinity of a sample. Changes in peak width does not affect the number of orientations in this work as resolution here is obtained from the  $\psi$  angle and not  $2\theta$ , however, analysing results using a detector that could be moved in  $2\theta$  combined with a monochromated X-ray source giving pure Cu  $K_{\alpha 1}$  radiation would enable a more in-depth discussion of peak width in relation to strain and crystal grain size. As the hydrogens in the ice lattice cannot be easily studied *via* XRD, neutron studies could be performed to provide further information on the positioning of the protons, hydrogen bonding in the system and any deformation of the hexagonal ice structure upon addition of ice-active materials.

As XRD provides little extra on the mechanism of action of AF(G)Ps and their mimics

on ice, **Chapter 4** focused on providing a more fundamental understanding using SSNMR. SSNMR techniques are extremely versatile and have been used on a range of materials, with relaxation measurements applied to antifreeze-ice systems in this thesis, which have provided detailed information on these dynamic systems. Evidence for the interaction of PVA with ice crystals was obtained for the first time using 2D EXSY, and support for AF(G)P ice-binding obtained. Relaxation measurements, for the first time, confirm that the addition of IRI active compounds greatly affects the bulk ice  $^1\text{H}$  dynamics unlike negative controls (ensuring any colligative contributions are negated), even at the low concentrations used in this work. Relaxation measurements provided interesting trends, with variable temperature  $R_2$  measurements showing a clear difference between antifreezes and negative controls, with the difference thought to be due to exchange dominating rather than ms – ns motions. It was confirmed that above a chain length of 10 units PVA's unique ice-activity is 'switched on', and the  $R_1$  relaxation of bulk ice in the presence of PVA scaled with the macroscopic critical inhibitory concentrations and MLGS values, with longer polymers being more active inhibitors and having faster correlation times. The results from the range of relaxation measurements support a mechanism of PVA forming an extended hydrogen bonded network to the prism planes of ice where PVA binds reversibly, and that enthalpy-entropy compensation is a driving force. Safranine-O was seen to work *via* a mechanism like that of PVA, supporting the idea that ice dynamics are affected by frozen solutions of IRI active compounds and not their respective controls or in a colligative manner, and that ice proton motions are of importance for IRI activity.

Further information could be obtained by performing these SSNMR measurements on a wider range of proteins; initial studies have been included on bpAFPI, AFPIII and AFGP8, nonetheless these results cannot yet be generalised across all antifreeze proteins and antifreeze glycoproteins as there is such a great range that may work *via* different mechanisms, as visualised in Chapter 1. Further SSNMR measurements could be performed, including  $^2\text{H}$  and  $^{13}\text{C}$ -labelled measurements, as well as additional 2D exchange measurements on unlabelled and  $^{13}\text{C}$ -labelled antifreezes to elucidate the exchange occurring and allow site-specific interrogation of intermolecular contacts and structures. SSNMR measurements, in combination with findings from other techniques, will hopefully lead to the determination of the

mechanisms of action of ice-active materials and thus enable production of well understood, improved cryopreservation formulations and hence improve the viability of cryopreserved biological materials.

In **Chapter 5**  $\mu\text{L-NIPI}$  was successfully utilised as a technique to study nucleation efficiency for a range of previously untested materials. Calorimetry was used to compare to  $\mu\text{L-NIPI}$ , finding it to be a slower and less thorough technique for following ice nucleation here. MOFs were found to not have IRI activity or promote ice nucleation, though further investigation could be undertaken into potential structural motifs required for nucleation activity, though this may be of difficulty due to the wide-ranging structures that make up metal organic frameworks. Safranin-O was used as a comparison, as it has thus far no known nucleating efficiency, finding no activity, even at self-assembling concentrations, indicating that self-assembly does not directly infer nucleating effectiveness. 8 different lignins were tested, with all showing at least minimal nucleation activity. Alkali lignin, which nucleated ice at high temperatures, and is commercially available, was focused on. Multiple variables were modified to test this lignin's nucleation efficiency, finding that effectiveness does not change over a range of concentrations, cooling rates or upon filtration, thus the INP/INS involved is small. This initial work implies more control of  $T_n$  could be achieved with further investigation into the lignin particles and their topography, and that if nucleation temperatures could be increased to  $>-10\text{ }^\circ\text{C}$ , there would be potential cryopreservation applications.

Further investigation is required to understand what is causing nucleation in the lignins, *i.e.* defects on the particles/relevant surface features, size of particles or functional groups involved. Microscopy could also be used to identify individual features that nucleate ice and characterisation could be undertaken using gel permeation chromatography as well as by using chemical or enzymatic degradation to identify structural subunits involved in nucleation efficiency for these materials. In regards to the  $\mu\text{L-NIPI}$  technique, automation of freezing detection would be greatly beneficial and allow for much quicker data generation. Other research groups have attempted this by using video analysis software and infra-red cameras and could be something used in the future here also.

## 6.2. Final Remarks

This project confirms that the relationship between physical and chemical properties of different materials and ice-activity is complex, and that despite shedding light on techniques that assist in analysis of these activities and their underlying mechanisms of action, a great deal remains to be understood. Results have shown that a vast range of materials have ice-activity, and that mimics can be obtained for AF(G)Ps that have much potential as cryoprotectants. Clearly, these materials tested here may not perform as well in cryoprotecting other biologics, we have however laid the groundwork for future experimental work in this area. We wanted to link the macroscopic findings from traditional optical-based methods to the atomic scale and study the bulk ice and have successfully utilised XRD to obtain further detail on ice growth. Significant advances in SSNMR technology and methodology have enabled us to use this tool for the study of these complicated samples, and there is great potential for this rapid development to continue. This project represents progress in the understanding of how ice-active materials behave and these results overall are significant in both basic cryo-science and in the development of new materials for low temperature applications.

# Appendices

---

## Appendix A - Supplementary Information

## Appendix A – Chapter 2

### A.1 Cryopreservation of *Lactobacillus delbrueckii subsp. bulgaricus*

*L. delbrueckii*, a gram-positive anaerobic organism, is an important lactic acid bacteria used in the dairy industry to manufacture fermented products.<sup>116</sup> In particular, it is used as a starter culture as well as providing flavour, texture and nutritional value to products. Accordingly storage of this important bacteria is of great interest. The FT protocol used previously was also used here to obtain preliminary results. CPAs were added to cells of *L. delbrueckii* (BBA-365 strain) in a 1:1 weight ratio using PBS for dilutions. The cells were snap frozen in liquid nitrogen and stored at -80 °C over two storage periods and cell recovery compared to cells that underwent 7 FT cycles, **Figure A2.1**. Upon thawing there is little observed difference in cell recovery between the control (no CPA), glycerol and PEG/PVA. The most colonies were recovered after 1 week storage. 7 FT and 1 month storage lead to a much lower colony count. Further work needs to be performed in this area to perfect the *lactobacillus* cell growth and assay protocol, to ensure valid results are obtained.

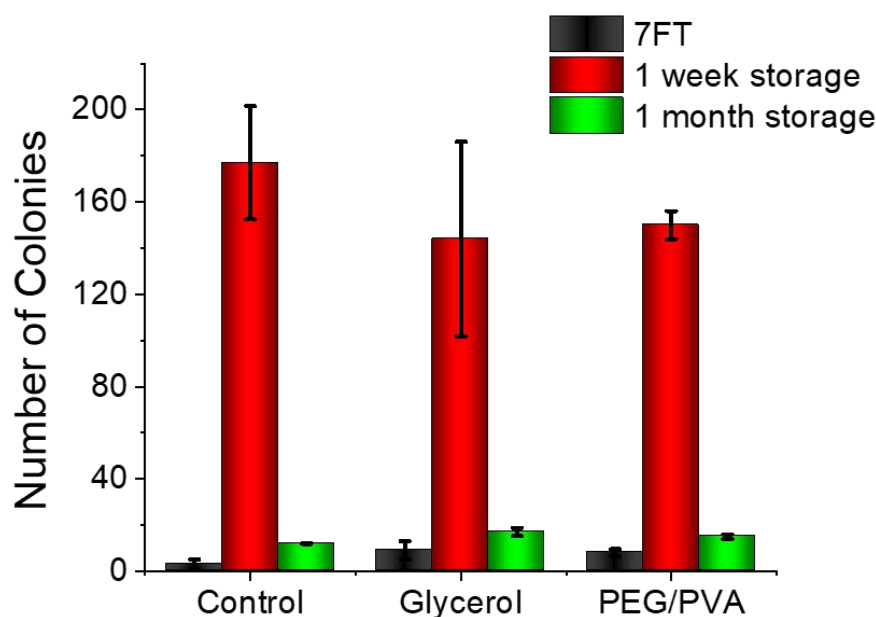


**Figure A2.1.** Comparison of average number of colonies of *Lactobacillus* strain BAA-365 grown after freezing and storage under 3 different conditions (black = 7 freeze/thaw cycles at liquid nitrogen temperatures, red = 1 week storage at -80 °C, green = 1 month storage at -80 °C) with no cryoprotectant, 25% glycerol, or PEG/PVA.

# Appendices

---

## Appendix B – Publications



**Appendix B – Publications**



Cite this: *Analyst*, 2020, **145**, 3666

## X-ray diffraction to probe the kinetics of ice recrystallization inhibition†

Alice Fayer, <sup>a</sup> Steven Huband<sup>b</sup> and Matthew I. Gibson \*<sup>a,c</sup>

Understanding the nucleation and growth of ice is crucial in fields ranging from infrastructure maintenance, to the environment, and to preserving biologics in the cold chain. Ice binding and antifreeze proteins are potent ice recrystallization inhibitors (IRI), and synthetic materials that mimic this function have emerged, which may find use in biotechnology. To evaluate IRI activity, optical microscopy tools are typically used to monitor ice grain size either by end-point measurements or as a function of time. However, these methods provide 2-dimensional information and image analysis is required to extract the data. Here we explore using wide angle X-ray scattering (WAXS/X-ray powder diffraction (XRD)) to interrogate 100's of ice crystals in 3-dimensions as a function of time. Due to the random organization of the ice crystals in the frozen sample, the number of orientations measured by XRD is proportional to the number of ice crystals, which can be measured as a function of time. This method was used to evaluate the activity for a panel of known IRI active compounds, and shows strong agreement with results obtained from cryo-microscopy, as well as being advantageous in that time-dependent ice growth is easily extracted. Diffraction analysis also confirmed, by comparing the obtained diffraction patterns of both ice binding and non-binding additives, that the observed hexagonal ice diffraction patterns obtained cannot be used to determine which crystal faces are being bound. This method may help in the discovery of new IRI active materials as well as enabling kinetic analysis of ice growth.

Received 25th October 2019,  
Accepted 16th February 2020

DOI: 10.1039/c9an02141h

rsc.li/analyst

## Introduction

Despite water's heterogeneous freezing point of 0 °C, many organisms have evolved to survive in sub-zero climates; these include the wood frog (*Lithobates sylvaticus*), Antarctic fish such as *Zoarces americanus* and *Macrozoarces americanus*, and various cold tolerant plants.<sup>1–4</sup> These extremophiles produce increased levels of small molecule cryoprotectants such as glycerol<sup>5,6</sup> and trehalose,<sup>7</sup> but also macromolecular cryoprotectants such as antifreeze proteins (AFPs, also known as ice binding proteins) and antifreeze glycoproteins (AFGPs) providing freeze-tolerance or freeze avoidance.<sup>4,8–10</sup> These proteins are potent ice recrystallization (growth) inhibitors (IRIs). Ice recrystallization is the process whereby larger crystals grow at the expense of smaller ones, reducing the surface area to volume ratio over time due to Ostwald ripening. This can be particularly lethal to biological matter, as ice recrystallization leads to dehydration and cellular damage, therefore is of inter-

est, particularly in the cryopreservation of cells and tissue, as well as proteins.<sup>2,11</sup>

Synthetic mimics of AF(G)Ps have emerged that can reproduce their properties and benefit from the scalable and tuneable synthesis of synthetic polymers.<sup>12–14</sup> However, questions remain if these function by the same mechanisms.<sup>12,15</sup> These include C-linked glycopeptides,<sup>16–18</sup> a range of small molecules,<sup>3,19,20</sup> polyampholytes,<sup>21,22</sup> oxidized quasi-carbon nitride quantum dots (OQCNs),<sup>23</sup> safranine-O,<sup>24</sup> graphene oxide,<sup>25</sup> zirconium acetate (ZrAc),<sup>26</sup> nanocelluloses,<sup>27</sup> and poly(vinyl alcohol) (PVA); which is one of the most active mimics reported to date.<sup>28–31</sup> The development and use of appropriate assays of activity is crucial to develop this field and understand the mode of action.

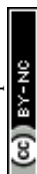
Optical microscopy has been employed in the majority of experimental work concerning ice and ice-active compounds thus far. IRI activity is typically measured using either the 'splat'<sup>28,31,32</sup> or sucrose 'sandwich'<sup>4,33</sup> assays, providing visual comparisons of ice crystal wafers. Both of these assays involve nucleating small ice crystals and observing their growth over time (or more often at a fixed time point) whilst recrystallization occurs. Challenges with these microscopy techniques include time-consuming data analysis, small sampling size (micrographs of isolated regions analysed rather than whole sample) and that only 2D information is obtained.

<sup>a</sup>Department of Chemistry, University of Warwick, Gibbet Hill Road, CV4 7AL, UK.  
E-mail: [redacted]

<sup>b</sup>Department of Physics, University of Warwick, Gibbet Hill Road, CV4 7AL, UK

<sup>c</sup>Warwick Medical School, University of Warwick, Gibbet Hill Road, CV4 7AL, UK

† Electronic supplementary information (ESI) available. See DOI: 10.1039/c9an02141h



X-ray powder diffraction is used to study, *in situ*, the bulk of the sample.<sup>34,35</sup> [Note, the terms WAXS and X-ray powder diffraction are often interchangeable and XRD is used here throughout]. Significant advances in technology, development of full-profile analytical methods and synchrotron radiation have aided progress in the X-ray field, as there have been vast improvements in data precision and speed of data collection.<sup>36</sup> XRD is highly sensitive to small changes and aids identification of structural similarities and changes, especially phase or particle size changes,<sup>34,37</sup> and has been used in many areas to monitor these changes; including observing nucleation/growth of gold nanoparticles<sup>38</sup> and titanium oxide particles over time,<sup>39</sup> as well as evaluating phase structure, precipitate growth and coarsening of alloys using combined ultra-small-, small- and wide-angle X-ray scattering,<sup>40</sup> for example. Using X-ray techniques it is possible to report crystallographic form, polymorphism, peak intensity changes, peak splitting and peak disappearance.<sup>41,42</sup> Scattering has been used to obtain crystal structures of cryoprotectants such as AFPs,<sup>43</sup> though little research has been taken into their effect on ice growth.<sup>44</sup> Studies have also monitored crystallization, polymorphism and disorder of ice upon addition of solutes such as bovine serum albumin (BSA) and sorbitol<sup>45,46</sup> as well as investigating potential ice growth inhibition mechanisms.<sup>47</sup> However XRD has not been used thus far to study the kinetics of ice growth, which is crucial in the design of new IRIs.

Here we report the use of XRD to probe the kinetics of ice recrystallization (and inhibition) using a range of IRI active macromolecules. The relative change in ice crystal size is determined by calculating the change in number of crystal orientations over a set time. The number of orientations is inversely proportional to the size of the ice crystals, and is obtained by integrating each individual diffraction peak as a function of  $\psi$  (psi), and then plotting intensity *versus*  $\psi$  to obtain time-dependant data points proportional to the number of crystals. This is significant as it enables automated analysis of ice recrystallization (or inhibition of) with high temporal resolution, and interrogates 100's of crystals, unlike traditional optical methods. This method may help provide understanding and discovery of new IRI active materials, alongside established optical microscopy methods.

## Experimental section

### Materials

Poly(ethylene glycol) (PEG) (4 kDa) and poly(vinyl alcohol) (PVA) (10 kDa), phosphate-buffered saline (PBS) preformulated tablets, lysozyme and ampicillin were purchased from Sigma-Aldrich and used as supplied unless otherwise stated. Imidazole (Merck) and glycerol (Fisher), isopropyl- $\beta$ -D-thiogalactoside (IPTG) (VWR chemical), safranin-O and phenosafranin (ACROS organics), Novex AP Chromogenic and coomassie blue stain (Expedeon) were also used as supplied. IMAC Sepharise 6 Fast Flow columns, HiLoad 16/600 Superdex 75 pg gel filtration columns and PD10 desalting columns were pur-

chased from GE Healthcare and used according to manufacturer's instructions. AFGP8 CC-86-XVII was kindly provided by A. L. DeVries (University of Illinois at Urbana-Champaign, USA) and used as received. The pET20b-AFP III plasmid encoding for a hexahistidine-tagged AFP III from ocean pout (*rQAE isoform*, M1.1HISPET20b) was kindly provided by Peter Davies (Queens University, Kingston, Canada). Competent *Escherichia coli* BL21(DE3) cells were sourced from New England Biolabs. Gold nanoparticles were synthesised as reported previously.<sup>48</sup> For washing of AuNPs, Amicon Ultra-0.5 centrifugal filter units with Ultracel-30 membrane were used. 40 nm citrate-stabilised gold colloid solution was purchased from BBI solutions.

### X-ray sample preparation

Samples were prepared, in either PBS solution or using Milli-Q ultrapure water with resistance <18  $\Omega$  obtained from a Milli-Q<sup>®</sup> Integral Water Purification System, over a range of concentrations and 10  $\mu$ L was inserted into 1 mm thick quartz capillaries and mounted in a Linkam THMS350. Samples were cooled to  $-35$   $^{\circ}$ C at 30 C min<sup>-1</sup>, then heated to  $-8$   $^{\circ}$ C where X-ray scattering was performed.

### XRD data analysis

A Xenocs Xeuss 2.0 equipped with a micro-focus Cu K $_{\alpha}$  source and a Pilatus 300k detector was used for XRD measurements. Diffraction pattern plotting, orientation analysis and any statistical tests were performed using OriginPro 2019 software. Three major diffraction peaks: (100), (002) and (101) were focused on. Positions ( $2\theta$ ) of these peaks are 22.7 $^{\circ}$ , 24.5 $^{\circ}$  and 25.8 $^{\circ}$  respectively.

### XRD orientation analysis

Measurements were made repeatedly, with a counting time of 10 seconds and a 4 seconds delay between each acquisition, over 1800 seconds annealing, enabling analysis of the number of crystal orientations observed over time and comparison to 'splat' assay data. A radial integration of the 2D scattering profile was performed using FOXTROT 3.3.4 software resulting in 1D intensity *versus*  $2\theta$  plots. In addition, azimuthal integrations for each Bragg peak were performed producing 1D intensity *versus*  $\psi$  plots. Data was then run through an in-house MATLAB (The MathWorks, Natick, MA) programme to obtain the number of ice crystal orientations.

### Ice recrystallization inhibition 'splat' assay

The sample was prepared in PBS solution, and 10  $\mu$ L was dropped onto a glass microscope coverslip atop an aluminum plate cooled to  $-78$   $^{\circ}$ C with dry ice. The thin wafer of ice that forms upon contact with the coverslip was transferred to a cryostage held at  $-8$   $^{\circ}$ C using liquid nitrogen, and left to anneal for 1800 seconds at this temperature. Three images were taken at different locations on this wafer at 20 $\times$  zoom under cross polarizers. Using ImageJ, the numbers of crystals in the images were counted and the average crystal size per wafer was calculated as mean grain area (MGS) as well as the mean grain length size (MLGS).



### Sucrose 'sandwich' ice shaping assay

Samples dissolved in PBS buffer containing 45 wt% sucrose were sandwiched and sealed between two glass coverslips. Samples were cooled to  $-50\text{ }^{\circ}\text{C}$  and then heated to  $-8\text{ }^{\circ}\text{C}$  to anneal. The samples were then heated at  $0.5\text{ }^{\circ}\text{C min}^{-1}$  until few ice crystals remained and then cooled at  $0.05\text{ }^{\circ}\text{C min}^{-1}$  and the shape of ice crystals observed. Micrographs were obtained every  $0.1\text{ }^{\circ}\text{C}$ .

## Results and discussion

In microscopy-based assays, smaller ice crystals (less growth) after annealing at sub-zero temperatures indicate more IRI activity, and data is reported as an area/length relative to a negative control. [Note, it is crucial to highlight the conditions for these experiments to avoid false positives.<sup>15,49</sup>] Fig. 1A is an example micrograph from a 'splat' assay. The data is typically analysed after a set period of time, and reported as a percentage growth relative to a PBS control. This can be reported as the mean largest grain size (MLGS), where the largest crystal in view is measured from multiple samples or mean grain size (MGS), where the average size of all crystals is measured. MLGS is appealing due to its simplicity for manual measurement, but it fails to probe the whole population and a single large crystal can dominate the measurement (example shown in Fig. 1A). Fig. 1B shows a comparison of MLGS versus MGS data, which are generally in agreement, other than MGS being an area (squared) term and thus giving smaller % value for the same amount of inhibition. The ice wafers obtained, such as in Fig. 1A, can be challenging to analyse by automated image analysis due to the irregular grain boundaries, although Ben *et al.* have used domain recognition software.<sup>50</sup> Alternatively, the sucrose 'sandwich' assay, which is also used to study dynamic ice shaping (DIS); indicating ice-binding properties of a sample, Fig. 1C, is used. In this assay the crystals are more separated due to the high viscosity of the media, and image analysis can be used to identify each crystal, as shown by Budke *et al.*<sup>51</sup> It is also important to be able measure growth in the media of interest, and 20–45 wt% sucrose required for this is not relevant for all conditions, and it has emerged recently that salts have a profound effect on growth rates hence the appeal of measurement in buffers.<sup>52,53</sup>

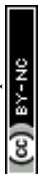
Fig. 2A/B shows example powder diffractograms as a function of time for ice crystals annealed at  $-8\text{ }^{\circ}\text{C}$  in the presence of the potent IRI (poly(vinyl alcohol)), PVA, and a negative control (poly(ethylene glycol)), PEG. The characteristic peaks of ice at  $22.7$ ,  $24.2$  and  $25.8^{\circ}$  (corresponding to the (100), (002) and (101) planes respectively) are clearly visible, as would be expected for hexagonal ice.<sup>54</sup> Of note, is that in the presence of PVA, the diffractograms are constant over the whole time period, indicative of no ice recrystallization (growth). In contrast, PEG shows significant decreases in the scattering intensity for most peaks, which is consistent with ice recrystallization (larger ice crystals). This confirms that in principle, powder diffraction should allow for both end-point and kinetic

analysis of IRI activity. Example ice wafers from the 'splat' assay under the same conditions are shown (Fig. 2C/D).

In this XRD analysis, no broad, low intensity peaks were observed, indicating no amorphous phases are formed in these samples upon freezing. Thus all ice observed here is polycrystalline; containing hundreds of crystallites. A percentage of these crystallites will orient to diffract the X-ray beam, thus there is a possibility the peak intensity will differ for identical samples, depending on how the crystallites are oriented. Therefore an understanding of the number of crystallites is required for evaluating the diffraction pattern. From here we will consider the number of crystal orientations as well as the observed diffraction patterns.

XRD provides details on crystallite orientations and intensity; the number of crystallite orientations for each sample, and how this number changes over continuous measurements. The sum of the intensity of the whole X-ray detector can be calculated, as well as the intensity for individual  $2\theta$  values. To enable quantitative analyses of ice recrystallization the total number of ice crystal orientations observed for a sample was calculated, which in a powder sample is proportional to the number of crystals, and hence inversely proportional to the size of the ice crystals. When ice crystals in a sample increase in size (recrystallisation), the number of grains detected by XRD decreases, which may lead to a decrease in total scattering intensity. To obtain the number of ice crystal orientations over time, the  $2\theta$  ranges that cover each of the seven peaks that are measured in the diffraction patterns are selected for each time point. An example  $2\theta$  range for the first peak is shown in Fig. 3A/B. The 2D detector image is then integrated azimuthally as a function of  $\psi$  (psi) seven times with  $2\theta$  ranges determined from the diffraction peaks. The step size in  $\psi$  for this was  $0.2^{\circ}$ . The size of the detector limits the available orientation range in  $\psi$  to between  $76$  and  $105^{\circ}$ . The intensity *versus*  $\psi$  data for the selected  $2\theta$  range is plotted and the number of data points above a determined background value (1.5 counts used) are then counted, these data points refer to the number of orientations and are filled in red to show an example of IRI active and inactive samples in Fig. 3C/D. As the concentration of an IRI active substance increases, the relative ice growth rate is expected to decrease due to the inhibition of ice crystal growth. This is because there are many orientations, which correspond to many small crystals. If there is an observed decrease in the number of orientations, this is due to Ostwald ripening; where the larger crystals increase in size at the expense of the small crystals.

To evaluate the use of this method, a range of known IRI active compounds (biological and synthetic) were tested and compared against the standard 'splat' assay, Fig. 4. In each case, XRD experiments were performed over 1800 seconds (30 min). Fig. 4A shows PVA, with the MLGS values trending with the inverse number of orientations. Fig. 4B shows PEG (a negative control), indicating essentially no activity even at very high concentrations (up to  $50\text{ mg mL}^{-1}$ ), where non-specific effects dominate. Encouraged by these results, the self-assembling IRI active safranin-O was tested, versus phenosafranin,





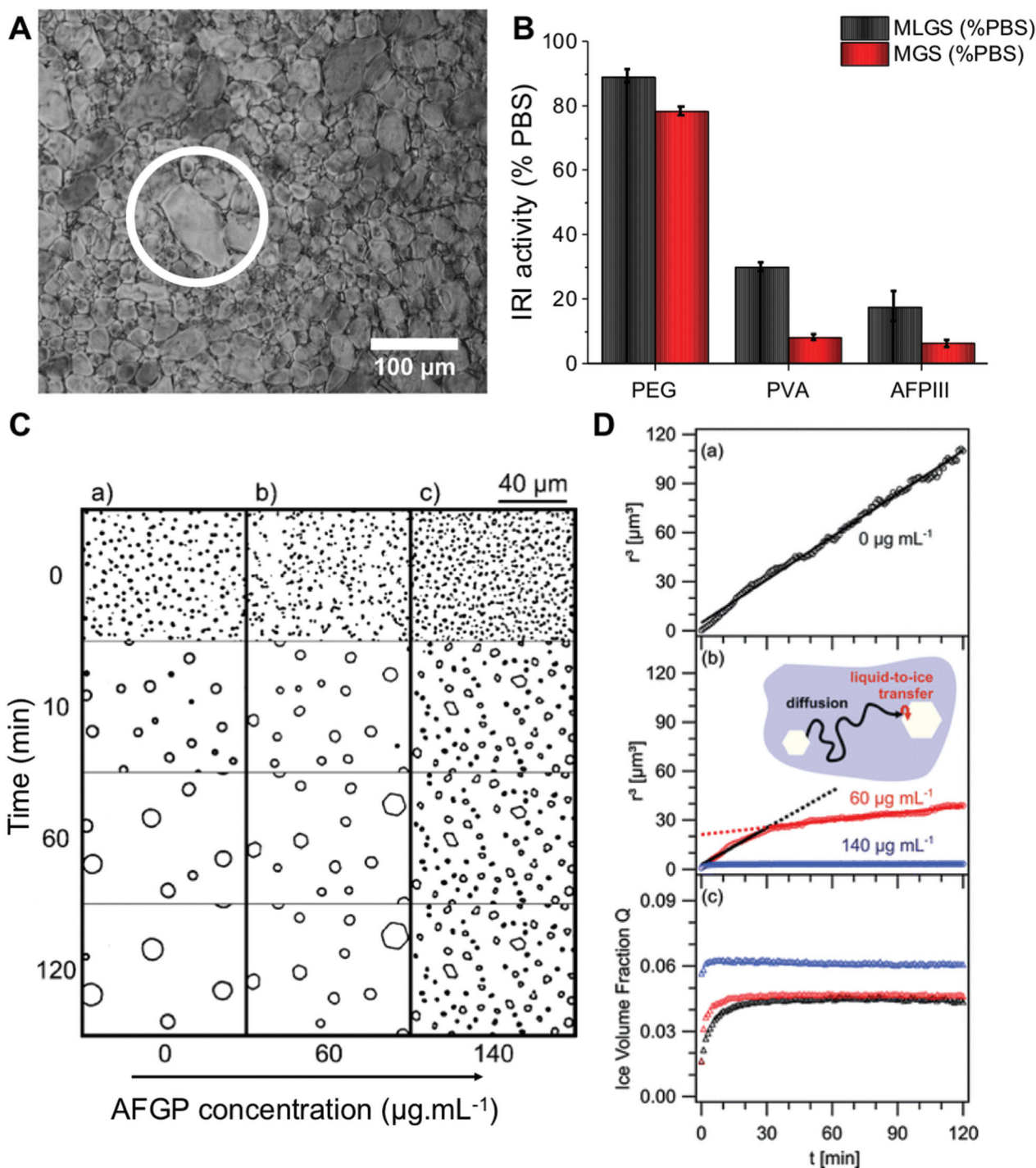


**Fig. 1** Optical microscopy analysis of ice recrystallization. (A) Example ice wafer containing  $1\text{ mg mL}^{-1}$  10 kDa PVA in PBS after 30 minutes. An example larger grain (white circle) is shown, which skews results when only 'largest grain size' is considered; (B) comparison of MLGS and MGS for some IRI active compounds. Concentrations =  $1\text{ mg mL}^{-1}$ . Errors are standard deviation; (C) micrographs of ice crystals grown in 45 wt% sucrose: (a) control solution, (b)  $60\text{ }\mu\text{g mL}^{-1}$  AFGP, (c)  $140\text{ }\mu\text{g mL}^{-1}$  AFGP; (D) data obtained through calculating mean ice crystal radii,  $r^3$ , in 45 wt% sucrose solutions from the micrographs, (a) control solution, (b)  $r^3$  in solution containing 60 and  $140\text{ }\mu\text{g mL}^{-1}$  AFGP, and their associated fits (solid lines), (c) temporal development of ice crystal volume fraction,  $Q$ , of data from (a) and (b). Reprinted (adapted) from with permission from Koop *et al.*,<sup>51</sup> *J. Phys. Chem. B*, 2009, **113**(9), 2865–2873. Copyright (2009) American Chemical Society. All data obtained at  $-8\text{ }^\circ\text{C}$ .



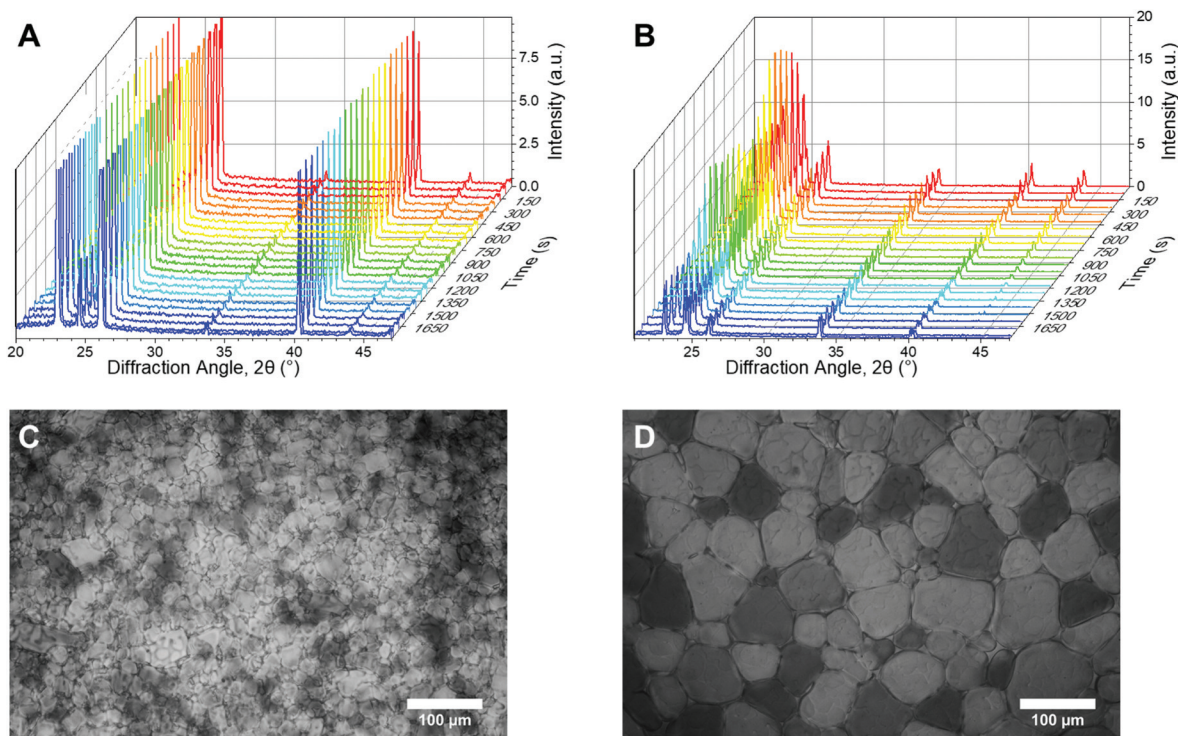


**Fig. 2** Example XRD and microscopy data. (A and B) Waterfall plots of diffraction patterns used for kinetic analysis of change in number of crystal orientations, obtained using powder diffraction, over time for (A) PVA and (B) PEG; (C and D) Example micrographs for (C) PVA and (D) PEG. All data obtained at  $-8\text{ }^{\circ}\text{C}$ .  $[\text{Polymer}] = 3\text{ mg mL}^{-1}$ .

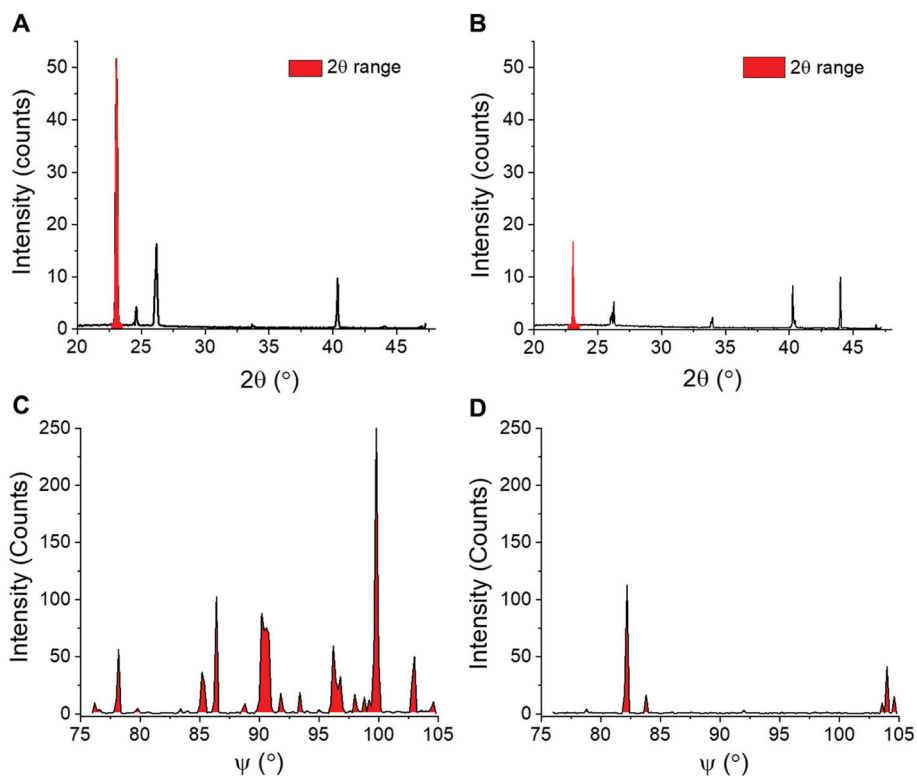


**Fig. 3** Extraction of ice recrystallization data. (A and B) Example XRD plots used to calculate crystallite orientations of (A) IRI active PVA and (B) non-IRI active PEG, plotted as a function of  $2\theta$ . Selected  $2\theta$  ranges used to analyse the crystallite orientations scattering are coloured red; (C and D) Orientation plots of (C) PVA and (D) PEG, plotted with as a function of  $\psi$  for intensities measured in the selected  $2\theta$  range.







tion every 14 seconds. This diffraction data includes, for example, information on number of crystal orientations for all measurements, which can be analysed to give kinetic information. Fig. 5A shows the change in the number of orientations (*i.e.* total number of crystals) for ice in the presence of

non-IRI active PEG. There is a clear decrease in number of crystals due to ice growth over the time course of the experiment. The same analysis for PVA shows a constant number of orientations, indicating a static process, and hence recrystallization is fully inhibited. It is important to note at this point that the

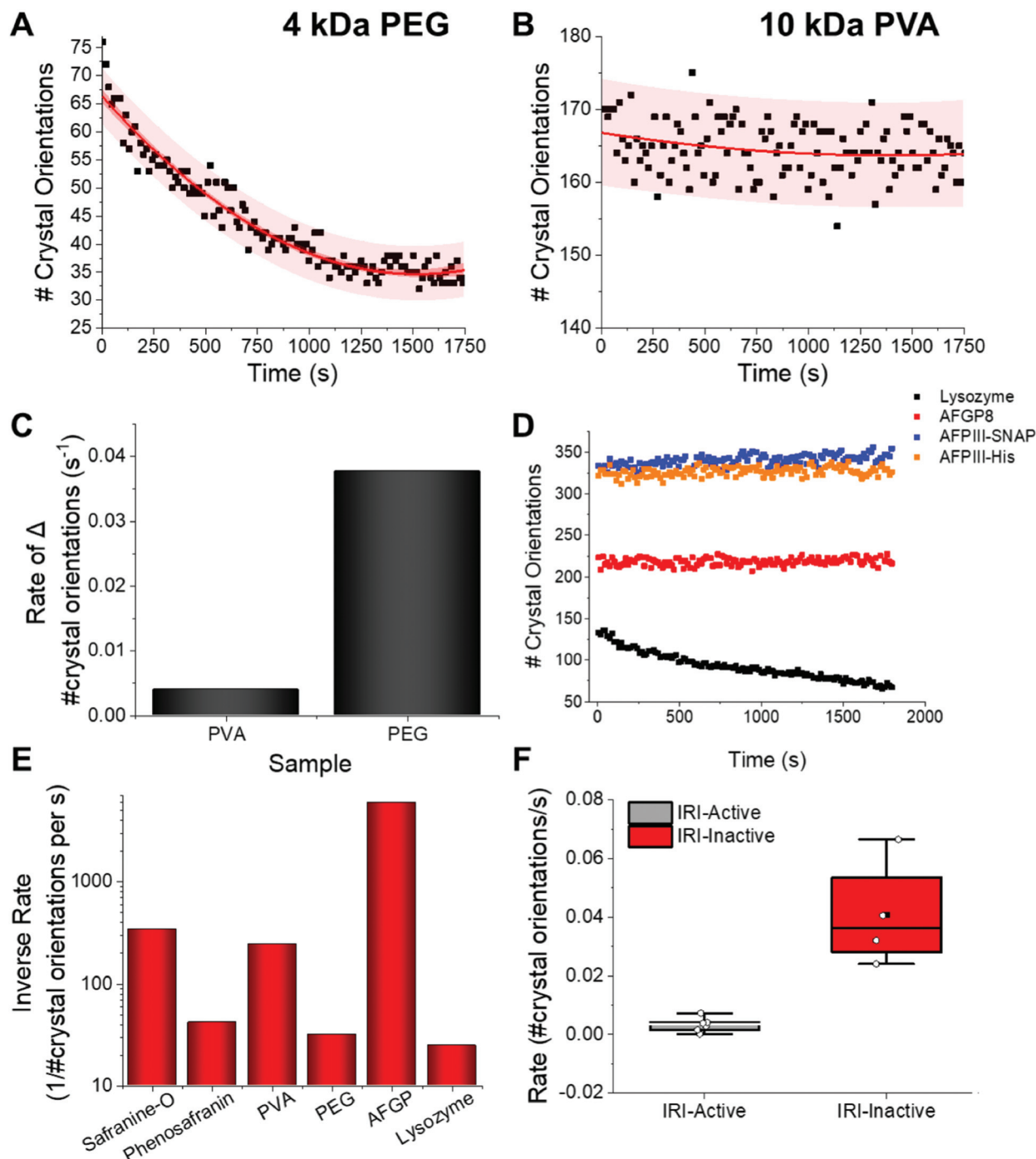


**Fig. 5** IRI analysis by XRD. Kinetic profiles for (A) PEG ( $3 \text{ mg mL}^{-1}$ ) and (B) PVA ( $3 \text{ mg mL}^{-1}$ ) at  $-8^\circ \text{C}$ ; (C) comparison of PVA/PEG rates of ice growth from A/B. [Polymer] =  $3 \text{ mg mL}^{-1}$ ; (D) number of crystal orientations as a function of time for a range of proteins. [Lysozyme] =  $0.7 \text{ mg mL}^{-1}$ , [AFPIII-His] =  $0.4 \text{ mg mL}^{-1}$ , [AFPIII-SNAP] =  $0.1 \text{ mg mL}^{-1}$ , [AFGP8] =  $0.07 \text{ mg mL}^{-1}$ ; (E) inverse average rate of change in number of observed ice crystal orientations over 1800 seconds for a small molecule (safranin-O), polymer (PVA) and protein (AFGP) compared to their relative IRI inactive controls (phenosafranin, PEG and lysozyme); (F) box plot of the mean gradients of change and standard deviation for IRI active (grey) and inactive samples (red). Mean = black square, individual data points = white hexagons. All data obtained at  $-8^\circ \text{C}$ .





actual magnitude of the number of crystals will vary in each sample due to the different nucleation rates (which is also hard to control), however the change is the part which is of interest here, and data can be normalised to the  $t = 0$  points.

Relative ice crystal growth rates were obtained from the gradient of change in number of crystal orientations, examples shown in Fig. 5, showing that a parameter for ice growth can be extracted if required. The steeper the slope, the faster the ice crystal growth. The rate of change in number of crystal orientations is much greater for PEG than for PVA. Fig. 5D shows this analysis for several other compounds also, confirming the trends. For example, the rate of change in ice crystal orientations for AFPs are slightly faster than that of AFGP8, this may be due to their slightly lower IRI activity, (see ESI†). Further measurements on more complex structures have been performed, which exhibit the same trends, showing that this

XRD method works for a range of structures, Fig. S1.† However they are still much lower rates than that of lysozyme. The rates of crystal growth for IRI active molecules tested can be seen to be close to zero, whereas that of the inactive controls it is higher, Fig. 5E/F.

IRI is not the only macroscopic property of ice binding/anti-freeze proteins. Ice shaping, due to binding to specific crystal faces also occurs<sup>12,13</sup> although it has emerged that binding might not be essential for IRI and hence the two properties are not always present.<sup>3,12</sup> Fig. 6 shows ice diffraction patterns and ice shaping for all three groups of compounds tested here. The difference in the diffraction patterns between water and PBS was first analysed to confirm similarities and differences – this was due to the salts' potential colligative effects on ice growth and hexagonal ice (Ih) structure, Fig. 6A/B. The results from PBS samples are more relevant to biological samples and

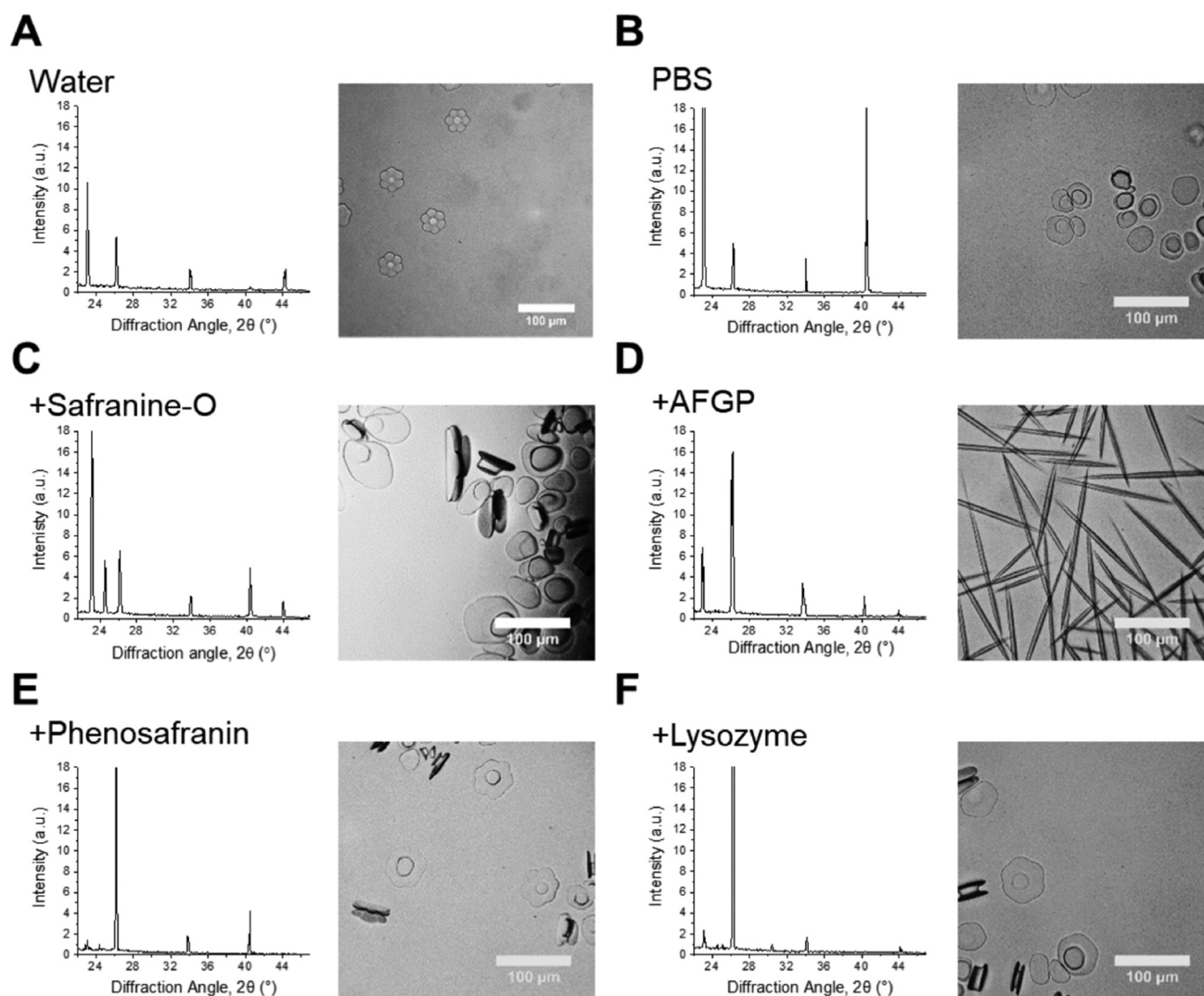


**Fig. 6** Crystal habit modifications by additives. Left: Ice diffraction patterns after 1800 s annealing for: samples with known ice binding and shaping abilities, their relative non-binding controls and water/PBS. Right: Optical microscopy ice morphology analysis in 45 wt% sucrose of samples in the corresponding diffractograms. Scale bars = 100  $\mu\text{m}$ . [Safranin-O] = 1.0  $\text{mg mL}^{-1}$ ; [AFGP8] = 3.0  $\text{mg mL}^{-1}$ ; [phenosafranin] = 1.0  $\text{mg mL}^{-1}$ ; [lysozyme] = 1.0  $\text{mg mL}^{-1}$ .



those in water would be more relatable to samples used in other fields, for example engineering and atmospheric chemistry. The structure for both is deemed to be Ih, though there are slight intensity variations for the Ih pattern between the two, but intensity variations are also seen in other samples, and are due to which grains orient towards the beam and not related to any 'ice-activity' of PBS.

Sometimes the (002) plane ( $2\theta = 24.2^\circ$ ) is said to be missing in ice samples with additives<sup>55,56</sup> and is often explained as the additive showing ice binding/DIS activity. Here measurements are taken using a static capillary, where the ice grains formed are too large to ensure a fully random distribution is sampled, thus structure analysis cannot be completely determined. A potential method to solve this problem would be to perform XRD whilst spinning the capillary, however there could still be preferred orientation effects. Due to differences in experimental set-up it is difficult to determine whether previous studies had randomly oriented grains/sampled a large enough range of grains to confirm ice binding/DIS.<sup>47,56,57</sup> Measurements made by freezing on a surface (*i.e.* flat), in particular, will be strongly affected by preferred orientation and thus may not give clear evidence of binding. Hence, the disappearance of a peak cannot solely be used to describe ice crystal morphology/binding accurately. For example, AFGP affects ice morphology by binding the primary prism plane, so would have a peak missing corresponding to this plane, but pure water (or PBS) would show all Ih peaks, however the  $24.2^\circ$  peak is missing in these samples, Fig. 6A/B/D. The same peak should also be missing for safranin-O, however is observed here, Fig. 6C. Similarly, phenosafranin and lysozyme have no known ice-binding so the lack of  $24.2^\circ$  peak seen in Fig. 6E/F cannot represent this. This shaping or lack of ice shaping is observed in the provided micrographs. When there is a change in ice grain size, particularly growth due to Ostwald ripening, fewer crystal orientations are observed and peak intensity changes. This can cause particular orientations to not scatter the X-ray beam leading to peak disappearance, thus the diffraction pattern peaks cannot be used to describe ice crystal morphology accurately in these disordered samples. This is crucial to show the limitations and applications of this method to explore the kinetics of ice recrystallization as a complementary tool to optical microscopy.

## Conclusions

Here, X-ray powder diffraction is used as a non-invasive method for 3D kinetic analysis of ice crystal growth (recrystallization) and compared to the more commonly used optical techniques. This method is complementary as measurements are performed in a capillary (3D conditions), which facilitates the measurement of a larger number of crystals in the system, as well as being preferable to 2D systems, where the sample holder will have a greater effect on the growth mechanisms. Furthermore, data can be obtained every 14 seconds (in this particular instrument, with the rate depending on individual

facilities), enabling real-time kinetic analysis without analysing each frame from videos. Ice growth was followed by calculating the relative number of ice crystal orientations from  $2\theta$  ranges that cover each of the seven Ih peaks from each diffraction pattern at every time point. We developed a fitting method to obtain kinetic data, which consisted of plotting the number of crystal orientations as a function of time and obtaining the gradient of change in number of orientations. This was then extracted as a rate and compared to that of pure water and PBS controls. Using this method we compared the IRI activity of a range of synthetic and biological IRI's and found that it was in good agreement optical methods with the advantage that for each sample kinetic data was obtained.

We also evaluated the diffraction patterns obtained in the presence of the antifreeze-active compounds noting the loss of intensity of the (002) peak. This could be interpreted as indicating specific ice binding, but we show with controls that this cannot be inferred due to preferred orientations and insufficient crystallites within the scattering volume. This confirms that the method is a useful addition to the suite of tools for discovering and investigating new ice recrystallization inhibitors but that, in the set up used here, care must be taken not to overfit the data and extrapolate information about specific crystal face binding.

## Conflicts of interest

There are no conflicts to declare.

## Acknowledgements

M.I.G. holds an ERC starting grant (CRYOMAT 638661), and is a Royal Society Industry Fellow (R1\191037). The Royal Society are also thanked for funding the cryo-microscopes used in this study. We would also like to thank Peter Davies (Queen's University, Kingston, Canada) for providing the genetic construct encoding for AFPIII from ocean pout (rQAE isoform, M1.1HISPET20b), and A. L. DeVries (University of Illinois at Urbana-Champaign, USA) for kindly providing the AFGP8 used in this work. We thank the University of Warwick X-ray Diffraction Research Technology Platform for the XRD measurements.

## References

- 1 A. J. Scotter, C. B. Marshall, L. A. Graham, J. A. Gilbert, C. P. Garnham and P. L. Davies, The Basis for Hyperactivity of Antifreeze Proteins, *Cryobiology*, 2006, **53**(2), 229–239.
- 2 M. Mangiagalli, M. Bar-Dolev, P. Tedesco, A. Natalello, A. Kaleda, S. Brocca, D. de Pascale, S. Pucciarelli, C. Miceli, I. Bravslavsky, *et al.* Cryo-Protective Effect of an Ice-Binding Protein Derived from Antarctic Bacteria, *FEBS J.*, 2016, **284**, 163–177.



- 3 C. J. Capicciotti, M. Leclere, F. A. Perras, D. L. Bryce, H. Paulin, J. Harden, Y. Liu and R. N. Ben, Potent Inhibition of Ice Recrystallization by Low Molecular Weight Carbohydrate-Based Surfactants and Hydrogelators, *Chem. Sci.*, 2012, **3**(5), 1408–1416.
- 4 M. Smallwood, D. Worrall, L. Byass, L. Elias, D. Ashford, C. J. Doucet, C. Holt, J. Telford, P. Lillford and D. J. Bowles, Isolation and Characterization of a Novel Antifreeze Protein from Carrot (*Daucus Carota*), *Biochem. J.*, 1999, **340**, 385–391.
- 5 D. Nichols, J. Bowman, K. Sanderson, C. M. Nichols, T. Lewis, T. McMeekin and P. D. Nichols, Developments with Antarctic Microorganisms: Culture Collections, Bioactivity Screening, Taxonomy, PUFA Production and Cold-Adapted Enzymes, *Curr. Opin. Biotechnol.*, 1999, **10**(3), 240–246.
- 6 J. R. Layne and A. L. Jones, Freeze Tolerance in the Gray Treefrog: Cryoprotectant Mobilization and Organ Dehydration, *J. Exp. Zool.*, 2001, **290**(1), 1–5.
- 7 X. Wen, S. Wang, J. G. Duman, J. F. Arifin, V. Juwita, W. A. Goddard, A. Rios, F. Liu, S.-K. Kim, R. Abrol, *et al.* Antifreeze Proteins Govern the Precipitation of Trehalose in a Freezing-Avoiding Insect at Low Temperature, *Proc. Natl. Acad. Sci. U. S. A.*, 2016, **113**(24), 6683–6688.
- 8 A. K. Balcerzak, C. J. Capicciotti, J. G. Briard and R. N. Ben, Designing Ice Recrystallization Inhibitors : From Antifreeze (Glyco) Proteins to Small Molecules, *RSC Adv.*, 2014, **4**, 42682–42696, DOI: 10.1039/c4ra06893a.
- 9 M. M. Harding, P. I. Anderberg and A. D. J. Haymet, “Antifreeze” Glycoproteins from Polar Fish, *Eur. J. Biochem.*, 2003, **270**(7), 1381–1392.
- 10 P. L. Davies, Ice-Binding Proteins: A Remarkable Diversity of Structures for Stopping and Starting Ice Growth, *Trends Biochem. Sci.*, 2014, **39**(11), 548–555.
- 11 P. Mazur, Cryobiology: The Freezing of Biological Systems, *Science*, 1970, **168**(3934), 939–949.
- 12 C. I. Biggs, T. L. Bailey, B. Graham, C. Stubbs, A. E. R. Fayter and M. I. Gibson, Polymer Mimics of Biomacromolecular Antifreezes, *Nat. Commun.*, 2017, **8**(1), 1546, DOI: 10.1038/s41467-017-01421-7.
- 13 M. I. Gibson, Slowing the Growth of Ice with Synthetic Macromolecules: Beyond Antifreeze (Glyco)Proteins, *Polym. Chem.*, 2010, **1**(8), 1141–1152.
- 14 B. Graham, A. E. R. Fayter, J. E. Houston, R. C. Evans and M. I. Gibson, Facially Amphipathic Glycopolymers Inhibit Ice Recrystallization, *J. Am. Chem. Soc.*, 2018, **140**(17), 5682–5685.
- 15 C. I. Biggs, C. Stubbs, B. Graham, A. E. R. Fayter, M. Hasan and M. I. Gibson, Mimicking the Ice Recrystallization Activity of Biological Antifreezes. When Is a New Polymer “Active”?, *Macromol. Biosci.*, 2019, **19**(7), 1–9.
- 16 S. Liu and R. N. Ben, C-Linked, Galactosyl Serine AFGP Analogues as Potent Recrystallization Inhibitors, *Org. Lett.*, 2005, **7**(12), 2385–2388.
- 17 R. N. Ben, A. A. Eniade and L. Hauer, Synthesis of a C-Linked Antifreeze Glycoprotein (AFGP) Mimic: Probes for Investigating the Mechanism of Action, *Org. Lett.*, 1999, **1**(11), 1759–1762.
- 18 M. Leclère, B. K. Kwok, L. K. Wu, D. S. Allan and R. N. Ben, C-Linked Antifreeze Glycoprotein (C -AFGP) Analogues as Novel Cryoprotectants, *Bioconjugate Chem.*, 2011, **22**(9), 1804–1810.
- 19 C. J. Capicciotti, J. D. R. R. Kurach, T. R. Turner, R. S. Mancini, J. P. Acker and R. N. Ben, Small Molecule Ice Recrystallization Inhibitors Enable Freezing of Human Red Blood Cells with Reduced Glycerol Concentrations, *Sci. Rep.*, 2015, **5**(9692), 1–10, DOI: 10.1038/srep09692.
- 20 J. G. Briard, S. Jahan, P. Chandran, D. Allan, N. Pineault and R. N. Ben, Small-Molecule Ice Recrystallization Inhibitors Improve the Post-Thaw Function of Hematopoietic Stem and Progenitor Cells, *ACS Omega*, 2016, **1**(5), 1010–1018, DOI: 10.1021/acsomega.6b00178.
- 21 C. Stubbs, J. Lipecki and M. I. Gibson, Regioregular Alternating Polyampholytes Have Enhanced Biomimetic Ice Recrystallization Activity Compared to Random Copolymers and the Role of Side Chain versus Main Chain Hydrophobicity, *Biomacromolecules*, 2017, **18**(1), 295–302, DOI: 10.1021/acs.biomac.6b01691.
- 22 R. Rajan, F. Hayashi, T. Nagashima and K. Matsumura, Toward a Molecular Understanding of the Mechanism of Cryopreservation by Polyampholytes: Cell Membrane Interactions and Hydrophobicity, *Biomacromolecules*, 2016, **17**(5), 1882–1893, DOI: 10.1021/acs.biomac.6b00343.
- 23 G. Bai, Z. Song, H. Geng, D. Gao, K. Liu, S. Wu, W. Rao, L. Guo and J. Wang, Oxidized Quasi-Carbon Nitride Quantum Dots Inhibit Ice Growth, *Adv. Mater.*, 2017, **29**(28), 1–8, DOI: 10.1002/adma.201606843.
- 24 R. Drori, C. Li, C. Hu, P. Raiteri, A. L. Rohl, M. D. Ward and B. Kahr, A Supramolecular Ice Growth Inhibitor, *J. Am. Chem. Soc.*, 2016, **138**(40), 13396–13401, DOI: 10.1021/jacs.6b08267.
- 25 H. Geng, X. Liu, G. Shi, G. Bai, J. Ma, J. Chen, Z. Wu, Y. Song, H. Fang and J. Wang, Graphene Oxide Restricts Growth and Recrystallization of Ice Crystals, *Angew. Chem., Int. Ed.*, 2017, **56**(4), 997–1001, DOI: 10.1002/anie.201609230.
- 26 O. Mizrahy, M. Bar-Dolev, S. Guy and I. Braslavsky, Inhibition of Ice Growth and Recrystallization by Zirconium Acetate and Zirconium Acetate Hydroxide, *PLoS One*, 2013, **8**(3), e59540, DOI: 10.1371/journal.pone.0059540.
- 27 T. Li, Y. Zhao, Q. Zhong and T. Wu, Inhibiting Ice Recrystallization by Nanocelluloses, *Biomacromolecules*, 2019, **20**(4), 1667–1674, DOI: 10.1021/acs.biomac.9b00027.
- 28 T. Congdon, R. Notman and M. I. Gibson, Antifreeze (Glyco)Protein Mimetic Behavior of Poly(Vinyl Alcohol): Detailed Structure Ice Recrystallization Inhibition Activity Study, *Biomacromolecules*, 2013, **14**(5), 1578–1586, DOI: 10.1021/bm400217j.
- 29 N. S. Vail, C. Stubbs, C. I. Biggs and M. I. Gibson, Ultralow Dispersity Poly(Vinyl Alcohol) Reveals Significant Dispersity Effects on Ice Recrystallization Inhibition





- Activity, *ACS Macro Lett.*, 2017, **6**(9), 1001–1004, DOI: 10.1021/acsmacrolett.7b00595.
- 30 T. Inada and S. Lu, Inhibition of Recrystallization of Ice Grains by Adsorption of Poly(Vinyl Alcohol) onto Ice Surfaces, *Cryst. Growth Des.*, 2003, **3**(5), 747–752, DOI: 10.1021/cg0340300.
- 31 T. R. Congdon, R. Notman and M. I. Gibson, Synthesis of Star-Branched Poly(Vinyl Alcohol) and Ice Recrystallization Inhibition Activity, *Eur. Polym. J.*, 2017, **88**, 320–327, DOI: 10.1016/j.eurpolymj.2017.01.039.
- 32 C. A. Knight, J. Hallett and A. L. DeVries, Solute Effects on Ice Recrystallization: An Assessment Technique, *Cryobiology*, 1988, **25**, 55–60, DOI: 10.1016/0011-2240(88)90020-X.
- 33 C. Budke and T. Koop, Ice Recrystallization Inhibition and Molecular Recognition of Ice Faces by Poly(Vinyl Alcohol), *ChemPhysChem*, 2006, **7**(12), 2601–2606, DOI: 10.1002/cphc.200600533.
- 34 M. A. Graewert and D. I. Svergun, Impact and Progress in Small and Wide Angle X-Ray Scattering (SAXS and WAXS), *Curr. Opin. Struct. Biol.*, 2013, **23**(5), 748–754, DOI: 10.1016/j.sbi.2013.06.007.
- 35 K. D. M. Harris, M. Tremayne and B. M. Kariuki, Contemporary Advances in the Use of Powder X-Ray Diffraction for Structure Determination, *Angew. Chem., Int. Ed.*, 2001, **40**, 1626–1651, DOI: 10.1002/chin.200132293.
- 36 C. Giacovazzo, *Fundamentals of Crystallography*, International Union of Crystallography, Oxford, 1992.
- 37 X. Chen, J. Schröder, S. Hauschild, S. Rosenfeldt, M. Dulle and S. Förster, Simultaneous SAXS/WAXS/UV-Vis Study of the Nucleation and Growth of Nanoparticles: A Test of Classical Nucleation Theory, *Langmuir*, 2015, **31**(42), 11678–11691, DOI: 10.1021/acs.langmuir.5b02759.
- 38 J. C. Houle, A. V. Chen, A. C. Brenna, K. L. Mealey and A. M. Kiszonas, Determination of Optimal Storage Temperature and Duration for Analysis of Total and Isoenzyme Lactate Dehydrogenase Activities in Canine Serum and Cerebrospinal Fluid, *Vet. Clin. Pathol.*, 2015, **44**(2), 253–261, DOI: 10.1111/vcp.12263.
- 39 D. R. Hummer, P. J. Heaney and J. E. Post, In Situ Observations of Particle Size Evolution during the Hydrothermal Crystallization of TiO<sub>2</sub>: A Time-Resolved Synchrotron SAXS and WAXS Study, *J. Cryst. Growth*, 2012, **344**(1), 51–58, DOI: 10.1016/j.jcrysgro.2012.01.044.
- 40 R. N. Andrews, J. Serio, G. Muralidharan and J. Ilavsky, An in Situ USAXS-SAXS-WAXS Study of Precipitate Size Distribution Evolution in a Model Ni-Based Alloy, *J. Appl. Crystallogr.*, 2017, **50**(3), 734–740, DOI: 10.1107/S1600576717006446.
- 41 W. H. Bragg, The Crystal Structure of Ice, *Proc. Phys. Soc.*, 1922, **34**, 98–103.
- 42 C. G. Salzmann, P. G. Radaelli, B. Slater, J. L. Finney and J. L. Finney, The Polymorphism of Ice: Five Unresolved Questions, *Phys. Chem. Chem. Phys.*, 2011, **13**(41), 18468–18480, DOI: 10.1039/c1cp21712g.
- 43 L. L. C. Olijve, T. J. Sun, T. Narayanan, C. Jud, P. L. Davies and I. K. Voets, Solution Structure of Hyperactive Type I Antifreeze Protein, *RSC Adv.*, 2013, **3**(17), 5903–5908, DOI: 10.1039/c3ra22729d.
- 44 J. Michielsen, J. Dings and J. van der Elsken, Small-Angle x-Ray Scattering in the Early Stages of Ice Formation, *Phys. Rev. A*, 1991, **44**(6), 4068–4071.
- 45 E. J. Shalaev, D. V. Malakhov, A. N. Kanev, V. I. Kosyakov, F. V. Tuzikov, N. A. Varaksin and V. I. Vavilin, Study of the Phase Diagram Water Fraction of the System Water-Glycine-Sucrose by DTA and X-Ray Diffraction Methods, *Thermochim. Acta*, 1992, **196**(1), 213–220, DOI: 10.1016/0040-6031(92)85021-M.
- 46 B. Zakharov, A. Fisyuk, A. Fitch, Y. Watier, A. Kostyuchenko, D. Varshney, M. Sztucki, E. Boldyreva and E. Shalaev, Ice Recrystallization in a Solution of a Cryoprotector and Its Inhibition by a Protein: Synchrotron X-Ray Diffraction Study, *J. Pharm. Sci.*, 2016, **105**(7), 2129–2138, DOI: 10.1016/j.xphs.2016.04.020.
- 47 D. B. Varshney, J. A. Elliott, L. A. Gatlin, S. Kumar, R. Suryanarayanan and E. Y. Shalaev, Synchrotron X-Ray Diffraction Investigation of the Anomalous Behavior of Ice During Freezing of Aqueous Systems, *J. Phys. Chem. B*, 2009, **113**(18), 6177–6182, DOI: 10.1021/jp900404m.
- 48 L. E. Wilkins, M. Hasan, A. E. R. Fayter, C. Biggs, M. Walker and M. I. Gibson, Site-Specific Conjugation of Antifreeze Proteins onto Polymer-Stabilized Nanoparticles, *Polym. Chem.*, 2019, **10**, 2986–2990, DOI: 10.1039/c8py01719k.
- 49 C. A. Knight, D. Wen and R. A. Laursen, Nonequilibrium Antifreeze Peptides and the Recrystallization of Ice, *Cryobiology*, 1995, **32**(1), 23–34, DOI: 10.1006/cryo.1995.1002.
- 50 J. P. Pezacki, M. Noestheden, R. N. Ben, J. Jackman, D. Moffat and S. Findlay, Assessing Antifreeze Activity of AFGP 8 Using Domain Recognition Software, *Biochem. Biophys. Res. Commun.*, 2007, **354**(2), 340–344, DOI: 10.1016/j.bbrc.2006.12.225.
- 51 C. Budke, C. Heggemann, M. Koch, N. Sewald and T. Koop, Ice Recrystallization Kinetics in the Presence of Synthetic Antifreeze Glycoprotein Analogues Using the Framework of LSW Theory, *J. Phys. Chem. B*, 2009, **113**(9), 2865–2873, DOI: 10.1021/jp805726e.
- 52 S. Wang, N. Amornwittawat, J. Banatiao, M. Chung, Y. Kao and X. Wen, Hofmeister Effects of Common Monovalent Salts on the Beetle Antifreeze Protein Activity, *J. Phys. Chem. B*, 2009, **113**(42), 13891–13894, DOI: 10.1021/jp907762u.
- 53 R. Suris-Valls and I. K. Voets, The Impact of Salts on the Ice Recrystallization Inhibition Activity of Antifreeze (Glyco) Proteins, *Biomolecules*, 2019, **9**(8), 347.
- 54 T. L. Malkin, B. J. Murray, V. Andrey, J. Anwar, C. G. Salzmann, T. L. Malkin, B. J. Murray, A. V. Brukhno, J. Anwar and C. G. Salzmann, Structure of Ice Crystallized from Supercooled Water, *Proc. Natl. Acad. Sci. U. S. A.*, 2012, **109**(4), 1041–1045, DOI: 10.1073/pnas.1201020109.
- 55 Y. E. Yagci, M. Antonietti and H. G. Börner, Synthesis of Poly(Tartar Amides) as Bio-Inspired Antifreeze Additives,



- Macromol. Rapid Commun.*, 2006, **27**(19), 1660–1664, DOI: 10.1002/marc.200600451.
- 56 E. Baruch and Y. Mastai, Antifreeze Properties of Polyglycidol Block Copolymers, *Macromol. Rapid Commun.*, 2007, **28**(23), 2256–2261, DOI: 10.1002/marc.200700501.
- 57 S. Deville, C. Viazzi, J. Leloup, A. Lasalle, C. Guizard, E. Maire, J. Adrien and L. Gremillard, Ice Shaping Properties, Similar to That of Antifreeze Proteins, of a Zirconium Acetate Complex, *PLoS One*, 2011, **6**(10), e26474.



Cite this: *J. Mater. Chem. B*, 2018,  
6, 7274Received 25th June 2018,  
Accepted 2nd August 2018

DOI: 10.1039/c8tb01668b

rsc.li/materials-b

## Sub-zero temperature mechanically stable low molecular weight hydrogels†

Alice E. R. Fayer, <sup>a</sup> Matthew I. Gibson <sup>ab</sup> and Emily R. Draper <sup>\*c</sup>

We show here a low molecular weight hydrogelator based on a functionalised-dipeptide which is stable down to temperatures of  $-12\text{ }^{\circ}\text{C}$  despite being made from  $>99\%$  water. This stability at low temperature can be extended to  $\sim -40\text{ }^{\circ}\text{C}$  by gelling water: glycerol mixtures. The temperature range is wider than that of the glycerol: water mixtures alone. The rheological properties of the gels do not change at this low temperature compared to that of gels at  $25\text{ }^{\circ}\text{C}$ . This freezing point depression offers a potentially new method of transporting gels and offers the prospect of hydrogels being used at much lower working temperatures whilst retaining the desired rheological properties, this is useful for cryopreservation.

## Introduction

Freezing-point depression of water is useful when low working temperatures are needed, for example in cryopreservation of bacteria, mammalian cells and enzymes.<sup>1–3</sup> All of these can be damaged by high temperatures, so storage at low temperatures is desirable. However, they can also be damaged by the formation of ice crystals, so the inhibition of these ice crystals is needed.<sup>2,4</sup> Other situations where low temperature stability is also essential include when using smart materials in an uncontrolled temperature setting, such as windows on the outside of buildings, which go through various temperature changes throughout the day and year.<sup>5</sup> Some analytical methods, such as Dynamic Nuclear Polarisation (DNP) NMR work at very low temperatures, so if one wanted to analyse something in solution such as a hydrogel, this would be almost impossible without a freezing point suppressant. Decreasing the freezing point can be achieved by using freezing depressant additives such as salts, glycerol, sorbitol, glycoproteins, or organic solvents with low freezing points.<sup>6</sup> However, the addition of some additives is detrimental to biological samples or can completely change the properties of the water they are in, and so completely change the sample.<sup>7–9</sup>

Low molecular weight gels (LMWGs) are a class of material with interesting and diverse range of properties and have been used with biological samples such as in cell culture and drug delivery.<sup>10–13</sup> In the case of hydrogels, they can be made from  $>99\%$  water, with less than 1% of material self-assembling

into long fibrous structures that entangle and trap the water. It is these long gel fibres which can be used as artificial extracellular matrices but also as conductive fibres, depending on what they are made from.<sup>14,15</sup> They are now finding uses in water purification,<sup>16</sup> solar fuel cells, electronic devices, actuators *etc.* all of which will be subject to a range of working temperatures.

There are many examples of the effect of heat on these gels to either form the gels *via* a heat-cool trigger, to control the supramolecular structures formed from the LMWGs and so control morphology of the gel fibres or behaviour of the gel properties.<sup>17–20</sup> Melting of the gels can also be used to determine gel fibre composition in multicomponent gel systems.<sup>21,22</sup> There are however very few examples of these gels at low temperatures, apart from to the control the kinetics of gelation.<sup>23</sup> Berillo *et al.* looked at gelling a Fmoc-Phe-Phe gelator in water at  $-12\text{ }^{\circ}\text{C}$  with and without salt present.<sup>24</sup> They found gels formed in the cold temperatures were less mechanically strong than ones formed at room temperature. In polymer systems, the upper/lower critical solution temperatures (U/LCST) are often considered as their phase behaviour (solubility) is modulated by the external temperature but this is rarely discussed for LMWGs.<sup>25</sup> Polymer gels can be used as actuators and can swell, move and even change shape in response to an increase in temperature.<sup>26</sup> There are many examples of temperature stable polymer gels using PVA with or without glycerol present in the systems.<sup>27–30</sup> In anti-freezing polymer gel systems, the water is often replaced entirely with a solvent with a lower freezing point or an additive added into the water. For example, recently Zhou and co-workers showed an organohydrogel based on a Ca-alginate/polyacrylamide blend where they replaced water with either glycol, sorbitol or glycerol and showed stability of the gel down to  $-70\text{ }^{\circ}\text{C}$ .<sup>31</sup> However, the shape and the mechanical properties were dramatically altered by this process and so the original properties of the gel were not

<sup>a</sup> Department of Chemistry, University of Warwick, CV4 7AL, UK<sup>b</sup> Warwick Medical School, University of Warwick, CV4 7AL, UK<sup>c</sup> School of Chemistry, University of Glasgow, Glasgow, G12 8QQ, UK.E-mail: 

† Electronic supplementary information (ESI) available: Full experimental procedures, rheology and supplementary images. See DOI: 10.1039/c8tb01668b



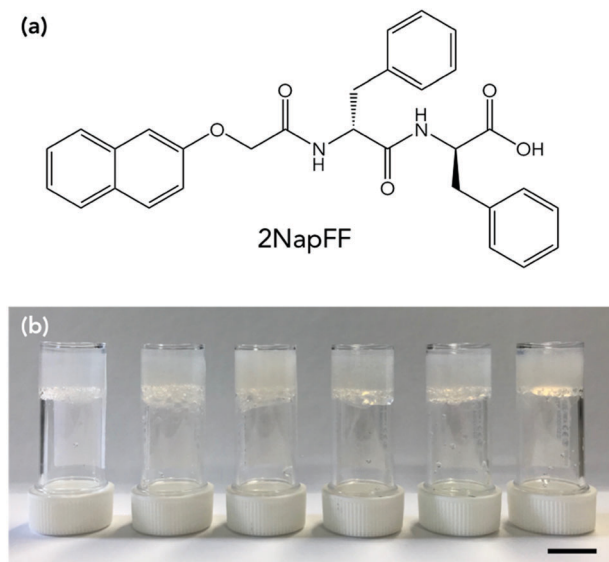


**Fig. 1** (a) Chemical structure of gelator 2NapFF. (b) Photographs of 2NapFF at (left to right) 10 mg mL<sup>-1</sup>, 5 mg mL<sup>-1</sup>, 2.5 mg mL<sup>-1</sup>, 20 : 80 glycerol : water (5 mg mL<sup>-1</sup>), 40 : 60 glycerol : water (5 mg mL<sup>-1</sup>) and 60 : 40 glycerol : water (5 mg mL<sup>-1</sup>). Scale bar is 1 cm.

retained. Since a significant amount of the water was replaced with the additive, the biocompatibility would also be different to the original gel. LMWGs would be expected to be less tolerant to these cold temperatures as they are held together by weak non-covalent bonding compared to polymer gel systems, and they generally contain less structuring materials. The formation of ice would logically be expected to destroy the LMWG network, as opposed to making the polymers gels more mechanically ridged or sometimes more fragile.<sup>32</sup>

Here, we use a LMWG based on a dipeptide, which we refer to as 2NapFF throughout (Fig. 1a). We gel 2NapFF in water at different concentrations and assess the stability at low temperatures by monitoring the rheological properties and by microlitre nucleation measurements to separate heterogeneous nucleation events. We then use glycerol as an additive to improve the properties of the gels at low temperatures.

## Results and discussion

2NapFF solutions were prepared at 2.5, 5 and 10 mg mL<sup>-1</sup>. The gelator was dissolved in water by the addition of one molar equivalent of NaOH and made up to the correct volume with distilled water. The samples were stirred overnight until all the gelator had dissolved. This resulted in a viscous transparent solution at pH 9.<sup>33,34</sup> In the case of the glycerol:water solutions, these were all prepared at a concentration of 5 mg mL<sup>-1</sup> of 2NapFF. The solutions were prepared as described above but the water replaced with 20:80, 40:60 and 60:40 glycerol:water by volume (higher volumes of glycerol did not result in a gel).

A slow acidification method was used to gel the solution. This was achieved by adding 8 mg mL<sup>-1</sup> of glucono- $\delta$ -lactone (GdL) per 5 mg of gelator in solution.<sup>35</sup> The GdL was gently

mixed in the solutions by hand to ensure dissolution, and then the samples left untouched overnight to result in self-supporting gels with a pH of around 3.3 (Fig. 1b). Gels were prepared in aluminium cups for rheological measurements to ensure efficient heat transfer from the rheometer to the gels. The effect of gelator concentration on freezing point was investigated. Each of the gels was first characterised by rheological strain and frequency sweeps at 25 °C (Fig. S1, ESI<sup>†</sup>). The gels were reproducible and each yielded at low strains (between 5–10%), flowed at higher strain (>100%) and varied in storage modulus ( $G'$ ) and loss modulus ( $G''$ ) depending on gelator concentration, with 10 mg mL<sup>-1</sup> being the stiffest and 2.5 mg mL<sup>-1</sup> the softest. The concentration affected the strain behaviour as well as  $G'$  and  $G''$ . The gel at 2.5 mg mL<sup>-1</sup> was found to have essentially a single fracture break (Fig. S1a, ESI<sup>†</sup>), whereas 5 and 10 mg mL<sup>-1</sup> showed multiple yield points before flowing (Fig. S1c and e, ESI<sup>†</sup>). 2NapFF structures in the gel phase have been shown to be dependent on concentration previously, explaining the different strain behaviours.<sup>33,34</sup> All the gels showed behaviour that was independent of frequency. Adams and co-workers have previously studied the effect of concentration on 2NapFF GdL gels. They found that at all concentrations the morphology and gel fibres were very similar, and the differences in  $G'$  and  $G''$  were a result in density of the fibres present, rather than a different gel network or fibre morphology.<sup>34</sup>

The temperature stability of the gels was then determined. This was done by lowering the temperature of the gel at a rate of 0.5 °C min<sup>-1</sup> at 10 rad s<sup>-1</sup> and 0.5% strain (within the linear viscoelastic region (LVR) of the gel as determined from the previous measurements). The freezing point was determined by the point at which  $G'$  and  $G''$  dramatically increased in value due to ice crystals being formed and the sample becoming a solid (Fig. 2a and Fig. S2, ESI<sup>†</sup>). All of the gels measured showed very little change in mechanical properties until the gel froze. This is seen by there being no change in  $\tan \delta$  when the temperature is lowered until the gel freezes and  $\tan \delta$  changes dramatically. The freezing point of the gels were depressed in line with the concentration of gelator in the gel, with 10 mg mL<sup>-1</sup> having a freezing point of -12 °C, 5 mg mL<sup>-1</sup> a freezing point of -9 °C and 2.5 mg mL<sup>-1</sup> a freezing point of -8 °C. What is most

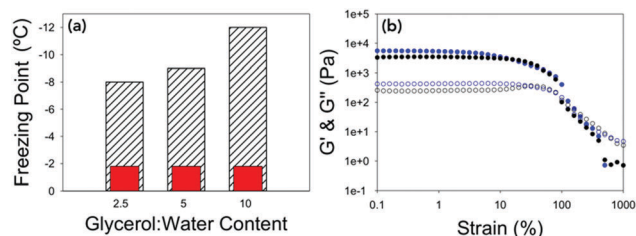


**Fig. 2** (a) Bar chart showing the expected freezing point of the water vs. the freezing point of the gels at different concentrations of 2NapFF. Hatched bars are the measured freezing point and red bars are the freezing point of distilled water on the rheometer (Fig. S2d, ESI<sup>†</sup>). (b) Strain sweeps performed at 10 rad s<sup>-1</sup> for 2.5 mg mL<sup>-1</sup> 2NapFF at 25 °C (black data) and at -7 °C (blue data). In both graphs,  $G'$  is the closed shapes and  $G''$  is the open shapes. No error bars included for clarity.





remarkable is that the rheological properties of the gels just before the freezing point were the same as if they were at room temperature (Fig. 2b and Fig. S3, ESI<sup>†</sup>) showing despite changing the temperature dramatically, the mechanical properties of the gels remain the same. The difference in the freezing points could be due to there being more organic material in the gel, which suppresses the freezing point by colligative effects. Alternatively, the increased amount of organic material may result in a denser network leading to segregation of any ice crystals which do nucleate, preventing them spreading. The gel fibres could also be acting as a freezing point suppressant in a similar way to glycerol by having an extended hydrogen bonded network which changes the hydrogen bonding between the water molecules.<sup>36</sup>

The differences in the frozen gels and unfrozen gels could be clearly seen by eye. The frozen gels would stick to the geometry of the rheometer and were opaque whereas the unfrozen gels (still at a cold temperature) remained transparent and soft (Fig. S4, ESI<sup>†</sup>). To investigate if the gels were inhibiting the heterogeneous nucleation of ice (the most common form of ice nucleation due to impurities) a microlitre ice nucleation assay was employed. As nucleation is a stochastic process, small droplets are essential to reduce the number of unwanted nucleators, and a large number of repeats are necessary as the individual nucleator temperatures will always vary.<sup>37</sup> Fig. 3 shows example freezing of microlitre drops of set gels as a function of temperature in a cryo-microscope, with freezing identified by the droplets becoming cloudy. In this system pure water showed a homogeneous freezing point of  $\sim -35$  °C, as expected taking into account some thermal gradients in the system. 2NapFF gels showed heterogeneous nucleation temperature of  $-20$  to  $-28$  °C as the concentration increased (Fig. 3b). These values are lower than the bulk, as the mechanical action of the rheometer will promote ice nucleation in super-cooled water.

Another method of suppressing the freezing point is to add a cosolvent into the water. The additive would need to be miscible with water and not affect the gelation ability of 2NapFF. A gelator concentration of  $5 \text{ mg mL}^{-1}$  was used to examine the addition of glycerol into the water. Glycerol is known to lower the freezing point of water<sup>38</sup> and is widely used a cryoprotective agent in microbiology.<sup>39</sup> Different ratios of glycerol to water can be used to tune the freezing point of the water, and therefore the gel. Ratios of 20:80, 40:60, 60:40 and 80:20 glycerol:water were compared to the data for 0:100 described above. The 80:20 mixture did not result in gelation, but gelation occurred in the other mixtures. Gelation of the glycerol:water mixtures using the 2NapFF were reproducible, with gels at 20:80 and 40:60 having comparable rheological properties to that of water-only gels at the same concentration (Fig. S5a–d, ESI<sup>†</sup>).

This suggests that the glycerol is not having a significant effect on the gelation process. The gels at 60:40 had a slightly lower  $G'$  and  $G''$  value than the other gels but have a similar strain behaviour (Fig. S5e and f, ESI<sup>†</sup>).

Again, the temperature dependence and freezing points of the glycerol:water gels were determined by keeping a constant strain and frequency and lowering the temperature until the gels froze (Fig. 4a and Fig. S6, ESI<sup>†</sup>). For the gel prepared at

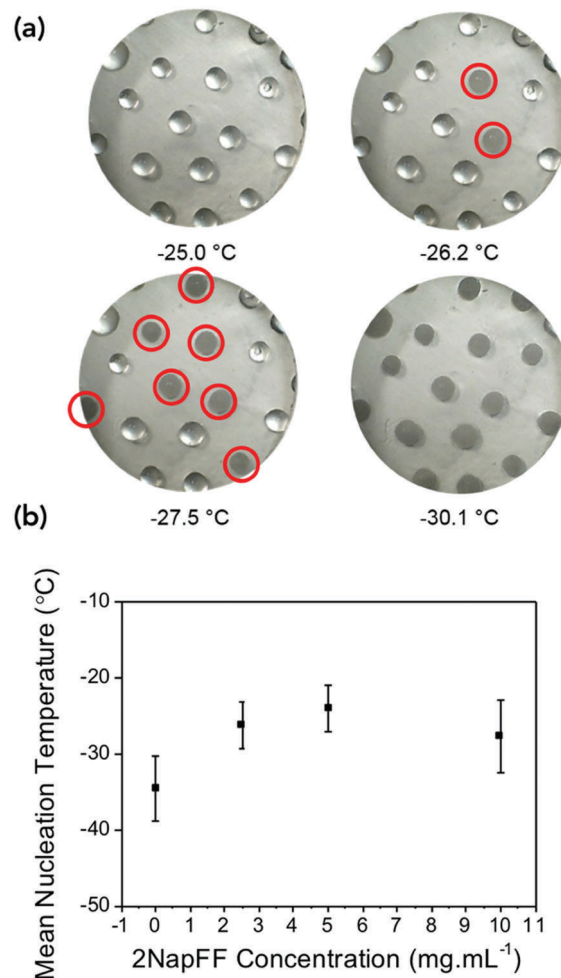


Fig. 3 Ice nucleation assay. (a) Example multi-point freezing assay used to assess the nucleation temperature as the temperature is reduced. Nucleating droplets are circled in red. (b) Mean nucleation temperature as a function of gelator concentration.

20:80, the freezing point was  $-22$  °C, the gel at 40:60  $-27$  °C and the gel at 60:40 did not freeze at  $-40$  °C, which is the lowest temperature to which the rheometer is able to achieve. Interestingly the freezing points are lower than the expected colligative freezing point values of water and glycerol mixtures.<sup>40</sup> For glycerol:water mixtures, a mixture of 20:80 should freeze at  $-5$  °C, 40:60 at  $-15$  °C and 60:40 at  $-34$  °C.<sup>38</sup> This suggests that the 2NapFF and the glycerol are acting synergistically to reduce the freezing point of the gels. Compared to the freezing point of the 100% water gel of  $-9$  °C, this a dramatic increase in the freezing point with little to no change to the rheological properties. The strain sweeps were then conducted a few degrees above the freezing point (Fig. 4b and Fig. S7, ESI<sup>†</sup>). The gels prepared at 20:80 and 40:60 have almost identical rheological properties to the gels prepared at  $25$  °C, showing that the cold temperature has no effect on the mechanical properties of the gels.

The gels could be chilled at a temperature above the freezing point and held at that temperature before being returned to room temperature and again the mechanical properties are





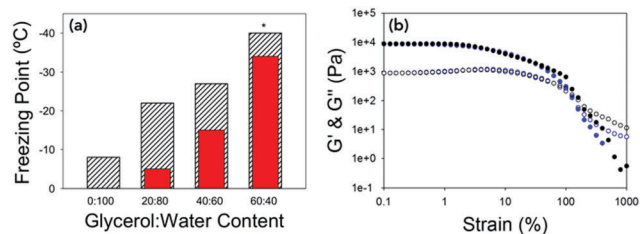


Fig. 4 (a) Bar chart showing the expected colligative freezing point of the water vs. the freezing point of the gels at different ratios of glycerol: water. Hatched bars are the measured freezing point and red bars are the expected freezing points.<sup>38</sup> \*For 60:40 the freezing point was not reached, but is beyond  $-40$  °C. (b) Strain sweeps performed at  $10 \text{ rad s}^{-1}$  for 40:60 at  $25$  °C (black data) and at  $-25$  °C (blue data). In both graphs  $G'$  is the closed shapes and  $G''$  is the open shapes. No error bars included for clarity.

unaffected (Fig. S8, ESI<sup>†</sup>). However, if the gel was allowed to freeze and then warmed back up the gel had been damaged and was now significantly changed mechanical properties due to the network being damaged due to ice-crystal formation (Fig. S9, ESI<sup>†</sup>). Microlitre nucleation assays were again used to probe the nucleation temperature of glycerol-containing gels, (Fig. 5 and Fig. S9, ESI<sup>†</sup>). Increasing glycerol concentration as to 60:40 reduced the nucleation temperature to  $-38$  °C, which agreed with the rheology data confirming the depression of the freezing point is due to colligative effects.

Next, we wanted to look whether other dipeptide gelators exhibited the same behaviour. We looked at gelators that formed different structures at high pH, had very different chemical structures, and also examples that had similar aggregation at high pH to 2NapFF (Fig. S10, ESI<sup>†</sup>). These included 2NapVG, which doesn't form aggregates at high pH,<sup>41</sup> PBI-H which forms worm-like micelles at high pH but has a very different chemical structure,<sup>42</sup> ThFF which has a similar chemical structure and forms aggregated structures at high pH<sup>43</sup> and ArFF which has a very similar chemical structure and also exhibits the same behaviour to 2NapFF after heating and cooling.<sup>17</sup>

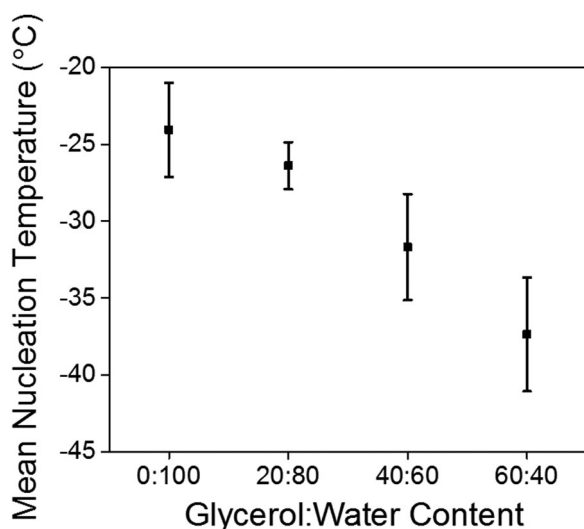


Fig. 5 Mean nucleation temperature of LMWG formed in presence of glycerol.

All these samples were prepared at  $5 \text{ mg mL}^{-1}$  of gelator with 20:80 glycerol:water, and  $8 \text{ mg mL}^{-1}$  of GdL was used to trigger gelation. For ThFF, PBI-H and 2NapVG, these all had freezing points of around  $-12$  °C, and so lower than that of 2NapFF with 20:80 glycerol:water, but still lower than expected from the glycerol content (Fig. S11 and S12, ESI<sup>†</sup>). However, ArFF had a freezing point of  $-20$  °C, similar to that of 2NapFF. This suggests that the freezing point depression is not to do with the molecular structure of the LMW gelators, but rather due to the increased viscosity. As viscosity increases the diffusion constant for the water molecules reduces, leading to a lengthening of diffusional mixing time, thus there is a larger barrier to molecular rearrangements within the sample hindering the formation of a critical nucleus causing the nucleation temperature to decrease.

## Conclusions

We have been able to show that the freezing point of hydrogels can be significantly depressed by either changing the concentration of gelator, or by gelling a glycerol:water mixture. The freezing point can also be tailored by changing the amount of glycerol present in the gel. The amount that the freezing point is depressed is more than that of glycerol:water mixtures alone can achieve and so shows that the gelator network is acting synergistically with the glycerol to prevent the formation of ice crystals. This offers the exciting possibility of using these gels not only at ambient conditions, but also at more extreme conditions. This is normally done using organogels with organic non-biocompatible solvents with low freezing points or using polymer systems which require a lot of processing to achieve this temperature stability. These results also potentially open up the opportunity of enabling easier transporting or handling as gels are less likely to dry out at the colder temperatures and/or with the addition of glycerol. In addition, these cold gels could be used to store and transport enzymes and other biological tissues as a means of cryopreservation. There is also the potential for these gels to be used to study kinetics within gels where processes are slowed down making them easier to follow, for them to be used in smart technologies where they are used outside where there is often a more demanding temperature requirement than in the laboratory, and also possibly in techniques such as DNP NMR where low temperatures are necessary.

## Experimental

### Rheological measurements

All rheological measurements were performed using an Anton Paar Physica 301 rheometer, fitted with a chiller to help with the cold temperature measurements. Temperature calibrations were performed between  $-30$  °C and  $80$  °C before starting the temperature measurements to ensure the correct temperature was being recorded. All data was collected using a vane (ST10-4V-8.8/97.5) and cup geometry (H-24-D) so samples could be prepared in aluminum cups to remove any loading issues. There was a gap distance of 1.5 mm between the bottom of the



gel and the cup. A zero force of 0 N was maintained throughout the experiments. Measurements were recorded in triplicate. All measurements were recorded in the linear viscoelastic region of the gels as determined by the strain sweeps, which are recorded first.  $G'$  and  $G''$  are determined from the frequency sweeps at 10 rad s<sup>-1</sup>. The yield point is determined at the point at where  $G'$  and  $G''$  deviate from linearity in the strain sweep, and the flow point where  $G''$  crosses over  $G'$ .

**Strain sweeps.** Strain sweeps were recorded from 0.1–1000% strain at 10 rad s<sup>-1</sup>. They were recorded at 25 °C in triplicate. They were then lowered to a temperature few degrees above the freezing point as determined by the freezing point experiments at a rate of 0.5 °C min<sup>-1</sup> and then a strain sweep was recorded.

**Frequency sweeps.** Frequency sweeps were recorded from 1–100 rad s<sup>-1</sup> at a strain of 0.5%. They were recorded at 25 °C in triplicate. They were then lowered to whatever temperature at a rate of 0.5 °C min<sup>-1</sup> and then a strain sweep was recorded.

**Freezing point determination and temperature stability measurements.**  $G'$  and  $G''$  were recorded over time at a frequency of 10 rad s<sup>-1</sup> and a strain of 0.5%. The temperature was then lowered at a rate of 0.5 °C min<sup>-1</sup> from 25 °C until there was dramatic increase in  $G'$ , this indicated that gel had frozen. The rheometer is only calibrated to -40 °C and so that was the lowest temperature the gels were taken down to, so in the case of 60:40 glycerol:water the gels did not freeze and so the freezing point could not be determined. To ensure the correct sample temperature a Eurotherm type K thermocouple was also used. This allowed us to check the temperatures past what the rheometer was calibrated to, so that the freezing point of 60:40 gels could be determined. In order to reduce the temperature of the rheometer to -40 °C, a water circulator was used at -10 °C, and cardice was used to cool the top of the cup holder.

### Ice nucleation assay

The gels were prepared as stated previously giving  $\geq 15$  0.7  $\mu$ L droplets on each slide. The slide was placed inside a Linkham Scientific cryostage. The cryostage was rapidly cooled to 0 °C at a rate of 50 °C min<sup>-1</sup> and then held at this temperature for 3 min to allow the temperature of the glass slide and droplets to equilibrate. The samples were then cooled from 0 °C to -49 °C at a rate of 2 °C min<sup>-1</sup>. Ice nucleation was observed using a Veho Discovery VMS-004 Deluxe USB microscope and Veho Microcapture software V 1.3. The experiment was repeated until at least 30 droplet freezing temperatures were recorded. The nucleation of the gels was compared to that of Milli-Q water, the nucleation of which was recorded in the same manner.

### Conflicts of interest

There are no conflicts to declare.

### Acknowledgements

ERD thanks the Leverhulme Trust for an Early Career Fellowship (ECF-2017-223) and the University of Glasgow for a Lord

Kelvin Adam Smith Leadership Award. MIG thanks the ERC for funding (638661 and 789182). We thank Bart Dietrich (University of Glasgow) for the synthesis of the 2NapFF used in this study.

### Notes and references

- X. R. Huang, P. Zhuang, L. Z. Zhang, J. Y. Liu, T. Zhang, G. P. Feng and F. Zhao, *J. Appl. Ichthyol.*, 2014, **30**, 1585–1589.
- W. F. Rall and G. M. Fahy, *Nature*, 1985, **313**, 573.
- A. Bonavia, M. Thompson, B. Schryver and R. Ehrhardt, *Protocol Exchange*, 2012, DOI: 10.1038/protex.2012.006.
- D. E. Pegg, in *Cyropreservation and Freeze-Drying Protocols*, ed. J. G. Day and G. N. Stacey, Humana Press, Totowa NJ, 2007, ch. 3, vol. 1, pp. 39–57.
- Y. Ke, C. Zhou, Y. Zhou, S. Wang, S. H. Chan and Y. Long, *Adv. Funct. Mater.*, 2018, 1800113.
- M. M. Harding, P. I. Anderberg and A. D. J. Haymet, *Eur. J. Biochem.*, 2003, **270**, 1381–1392.
- H. Park and K. Park, *Pharm. Res.*, 1996, **13**, 1770–1776.
- J. Raeburn, C. Mendoza-Cuenca, B. N. Cattoz, M. A. Little, A. E. Terry, A. Zamith Cardoso, P. C. Griffiths and D. J. Adams, *Soft Matter*, 2015, **11**, 927–935.
- S. K. Tam, J. Dusseault, S. Bilodeau, G. Langlois, J. P. Hallé and L. H. Yahia, *J. Biomed. Mater. Res., Part A*, 2011, **98**, 40–52.
- E. R. Draper and D. J. Adams, *Chem*, 2017, **3**, 390–410.
- K. J. Skilling, F. Citossi, T. D. Bradshaw, M. Ashford, B. Kellam and M. Marlow, *Soft Matter*, 2014, **10**, 237–256.
- X. Du, J. Zhou, J. Shi and B. Xu, *Chem. Rev.*, 2015, **115**, 13165–13307.
- F. Zhao, M. L. Ma and B. Xu, *Chem. Soc. Rev.*, 2009, **38**, 883–891.
- J. H. Collier, J. S. Rudra, J. Z. Gasiorowski and J. P. Jung, *Chem. Soc. Rev.*, 2010, **39**, 3413–3424.
- S. S. Panda, H. E. Katz and J. D. Tovar, *Chem. Soc. Rev.*, 2018, **47**, 3640–3658.
- B. O. Okesola and D. K. Smith, *Chem. Soc. Rev.*, 2016, **45**, 4226–4251.
- E. R. Draper, H. Su, C. Brasnett, R. J. Poole, S. Rogers, H. Cui, A. Seddon and D. J. Adams, *Angew. Chem.*, 2017, **129**, 10603–10606.
- L. Dongxia, S. Yang and W. Ling, *Chin. J. Chem.*, 2014, **32**, 123–127.
- D. J. Abdallah and R. G. Weiss, *Adv. Mater.*, 2000, **12**, 1237–1247.
- Z. Dzolic, K. Wolsperger and M. Zinic, *New J. Chem.*, 2006, **30**, 1411–1419.
- M. M. Smith and D. K. Smith, *Soft Matter*, 2011, **7**, 4856–4860.
- J. R. Moffat and D. K. Smith, *Chem. Commun.*, 2009, 316–318.
- A. Z. Cardoso, A. E. Alvarez Alvarez, B. N. Cattoz, P. C. Griffiths, S. M. King, W. J. Frith and D. J. Adams, *Faraday Discuss.*, 2013, **166**, 101–116.
- D. Berillo, B. Mattiasson, I. Y. Galaev and H. Kirsebom, *J. Colloid Interface Sci.*, 2012, **368**, 226–230.



- 25 A. Can, Q. Zhang, T. Rudolph, F. H. Schacher, J.-F. Gohy, U. S. Schubert and R. Hoogenboom, *Eur. Polym. J.*, 2015, **69**, 460–471.
- 26 S.-J. Jeon, A. W. Hauser and R. C. Hayward, *Acc. Chem. Res.*, 2017, **50**, 161–169.
- 27 X. Zhu, Y. Zhang, J. Deng and X. Luo, *ChemistrySelect*, 2018, **3**, 467–470.
- 28 Y. Zhang, B. Hui and L. Ye, *RSC Adv.*, 2015, **5**, 91414–91422.
- 29 S. Shi, X. Peng, T. Liu, Y.-N. Chen, C. He and H. Wang, *Polymer*, 2017, **111**, 168–176.
- 30 Q. Rong, W. Lei, L. Chen, Y. Yin, J. Zhou and M. Liu, *Angew. Chem.*, 2017, **129**, 14347–14351.
- 31 F. Chen, D. Zhou, J. Wang, T. Li, X. Zhou, T. Gan, S. Handschuh-Wang and X. Zhou, *Angew. Chem., Int. Ed.*, 2018, **57**, 6568–6571.
- 32 A. K. Bhowmick, J. Cho, A. MacArthur and D. McIntyre, *Polymer*, 1986, **27**, 1889–1894.
- 33 A. Z. Cardoso, L. L. E. Mears, B. N. Cattoz, P. C. Griffiths, R. Schweins and D. J. Adams, *Soft Matter*, 2016, **12**, 3612–3621.
- 34 C. Colquhoun, E. R. Draper, R. Schweins, M. Marcello, D. Vadukul, L. C. Serpell and D. J. Adams, *Soft Matter*, 2017, **13**, 1914–1919.
- 35 D. J. Adams, M. F. Butler, W. J. Frith, M. Kirkland, L. Mullen and P. Sanderson, *Soft Matter*, 2009, **5**, 1856–1862.
- 36 J. J. Towey and L. Dougan, *J. Phys. Chem. B*, 2012, **116**, 1633–1641.
- 37 T. Congdon, B. T. Dean, J. Kasperczak-Wright, C. I. Biggs, R. Notman and M. I. Gibson, *Biomacromolecules*, 2015, **16**, 2820–2826.
- 38 L. B. Lane, *Ind. Eng. Chem.*, 1925, **17**, 924.
- 39 Z. Hubálek, *Cryobiology*, 2003, **46**, 205–229.
- 40 K. E. Zachariassen and E. Kristiansen, *Cryobiology*, 2000, **41**, 257–279.
- 41 E. R. Draper, M. Wallace, R. Schweins, R. J. Poole and D. J. Adams, *Langmuir*, 2017, **33**, 2387–2395.
- 42 E. R. Draper, L. J. Archibald, M. C. Nolan, R. Schweins, M. A. Zwijnenburg, S. Sproules and D. J. Adams, *Chem. – Eur. J.*, 2018, **24**, 4006–4010.
- 43 E. R. Draper, T. O. McDonald and D. J. Adams, *Chem. Commun.*, 2015, **51**, 6595–6597.



# Curriculum Vitae

---

**Name:** Alice Fayter

**Email:** [REDACTED]

**Telephone:** [REDACTED]

**Address:** Department of Chemistry, University of Warwick, Gibbet Hill Road,  
Coventry, CV4 7AL, UK

**Website:**

[https://warwick.ac.uk/fac/sci/chemistry/research/gibson/gibsongroup/members/alice\\_faytor/](https://warwick.ac.uk/fac/sci/chemistry/research/gibson/gibsongroup/members/alice_faytor/)

## Career Summary

---

- 2016-2020** PhD in Biophysical Chemistry, Department of Chemistry, University of Warwick, Gibbet Hill Road, Coventry, CV4 7AL, UK. Supervisor: Prof. M. I. Gibson. “*Characterisation of the Effects on Ice Morphology and Growth by Ice-Active Compounds and their Cryoprotective Abilities*”.
- 2014-2015** Research Placement in Physical Chemistry, Leopold-Franzens Universität Innsbruck, Innrain 52, 6020 Innsbruck, Austria. Supervisor: Prof. T. Loerting. “*Ice XVII*”
- 2012-2016** Masters Degree in Biological and Medicinal Chemistry, University of Edinburgh, Joseph Black Building, David Brewster Rd, Edinburgh EH9 3FJ, UK. Supervisor: Dr. F. Nudelman “*1. Disassembly of Collagen by CryoTEM, 2. Biomineralisation of Collagen*”. MChem 2.1 (hons)



**2016-Present** Member of American Physical Society (APS), Society for Cryobiology, Biophysical Society (BPS), British Cryogenics Council, American Chemical Society (ACS), Biochemical Society, Institute of Physics (IOP) and Royal Society of Chemistry (RSC).

### **Awards and Honours**

---

- Conference attendance Bursary awarded by the Materials and Characterization Group of the Institute of Physics to attend the 50th British Association of Crystal Growth Annual Conference (2019)
- Travel Bursary awarded by the Knowledge Transfer Network to attend the Formulation challenges for traditional and next generation biopharmaceuticals conference (2018)
- First Prize for Poster "*New polymer formulations for cryostorage of biologics*" at BFG Formulation challenges for traditional and next generation biopharmaceuticals conference (2018)
- Second Prize for Poster "*Translationally Relevant Cryopreservatives for Biological Stabilization*" at the University of Warwick Chemistry Postgraduate Symposium 2018
- Prestigious Publication Prize awarded by the University of Edinburgh in recognition of the publication of research undertaken during undergraduate studies (2015)

### **Conference Attendance**

---

- BACG, London, July, 2019: *Oral Presentation*
- TOA, Berlin, July, 2019
- Warwick Chemistry Postgraduate Symposium, University of Warwick, Coventry, UK. May 2019: *Oral Presentation*

- CECAM workshop, Heterogeneous Ice Nucleation: The Ultimate Challenge for Molecular Modelling?, CECAM, Lausanne, Switzerland, September 2018: **Poster Presentation**
- Cryobiology 2018, CSIC, Madrid, Spain. July 2018: **Poster Presentation**
- Formulation challenges for traditional and next generation biopharmaceuticals, Manchester, UK. July 2018: **Poster and Flash Oral Presentation. “First Place Poster Prize” Awarded.**
- Warwick Chemistry Postgraduate Symposium, University of Warwick, Coventry, UK. May 2018: **Poster Presentation**
- UK Neutron and Muon Science and User Meeting, University of Warwick, Coventry, UK. April 2018.
- Astbury Conversation, Astbury Centre, Leeds, UK. April 2018.
- Neutrons and Global Challenges: Health and Healthcare, IOP, London, UK. February 2018.
- IOP Low Temperature Techniques, IOP, London, UK. November 2017.
- Society of Low Temperature Biology Science Meeting, Cambridge, UK. September 2017.
- 3rd Ice Binding Proteins Conference, Rehovot, Israel. August 2017.

## Publications

---

1. **Fayter, A. E. R.**, Stevens, R.A., Lewandowski, J. & Gibson, M.I., *in preparation*
2. **Fayter, A. E. R.**, Hasan, M., Congdon, T., Kontopoulou, I. & Gibson, M.I., *European Polymer Journal*, accepted (2020)
3. **Fayter, A. E. R.**, Huband, S. & Gibson, M.I., *The Analyst*, 145, 3666-3677 (2020)
4. Graham, B., **Fayter, A.E.R.** & Gibson, M.I., *Biomacromolecules*, 20(12), 4611-4621, (2019)
5. Biggs, C.I., Stubbs C., Graham, B., **Fayter, A.E.R.**, Hasan M. & Gibson, M.I., *Macromolecular Bioscience*, 19(7), 1900082, (2019)
6. Wilkins, L.E., Hasan, M., **Fayter, A.E.R.**, Biggs, C.I., Walker, M. & Gibson, M.I., *Polymer Chemistry*, 10, 2986-2990, (2019)
7. Mitchell, D., **Fayter, A.E.R.**, Deller, R.C., Hasan, M., Gutierrez-Marcos, J. & Gibson, M.I., *Materials Horizons*, 6, 364-368, (2019)

8. Stubbs, C., Wilkins, L.E., **Fayter, A.E.R.**, Walker, M. & Gibson, M.I., *Langmuir*, **35**(23), 7347-7353, (2019)
9. Hasan, M., **Fayter, A.E.R.** & Gibson, M.I., *Biomacromolecules*, **19**(8), 3371-3376, (2018)
10. **Fayter, A.E.R.**, Gibson, M.I., & Draper, E., *Materials Chemistry B*, **6**, 7274-7279, (2018)
11. Graham, B., **Fayter, A.E.R.**, Houston, J.E., Evans, R.C. & Gibson, M.I., *J. Am. Chem. Soc.* **140**(17), 5682-5685, (2018)
12. Biggs, C.I., Bailey, T.L., Graham, B., Stubbs, C., **Fayter, A.E.R.** & Gibson, M.I., *Nature Communications*, **8**(1), 1546, (2017)
13. Blackman, L.D., Varlas, S., Arno, M.C., **Fayter, A.E.R.**, Gibson, M.I. & O'Reilly, R.K., *ACS Macro Letters*, **6** (11), 1263-1267, (2017)
14. Seidl, M., **Fayter, A.E.R.**, Stern, J., Zifferer, G & Loerting, T., *Phys. Rev. B*, **91**, 144201, (2015)

# Contributions to published work

---

The following details personal contributions to published work that was subjected to peer review.

**Fayter, A.E.R.**, Hasan, M, Congdon T., Kontopoulou I. & Gibson, M.I., Ice Recrystallisation Inhibiting Polymers Prevent Irreversible Protein Aggregation During Solvent-Free Cryopreservation as Additives and as Covalent Polymer-Protein Conjugates, *European Polymer Journal*, accepted (2020)

*Performed all experiments on LDH, preliminary GFP experiments, data analysis of DLS experiments and LDH experiments and wrote majority of the paper.*

**Fayter, A. E. R.**, Huband, S. & Gibson, M.I., X-ray Diffraction to Probe the Kinetics of Ice Recrystallization Inhibition, *The Analyst*, 145, 3666-3677, (2020)

*Performed all X-ray diffraction experiments, undertook all data analysis and wrote the paper.*

Graham, B., **Fayter, A.E.R.** & Gibson, M.I., Synthesis of anthracene-conjugates of truncated antifreeze protein sequences. Effect of end-group and photo-controlled dimerization on ice recrystallisation inhibition activity, *Biomacromolecules*, 20(12), 4611-4621, (2019)

*Performed all X-ray diffraction experiments and assisted in the writing process.*

Biggs, C.I., Stubbs C., Graham, B., **Fayter, A. E. R.**, Hasan M. & Gibson, M.I., Mimicking the Ice Recrystallization Activity of Biological Macromolecules. When is a New Polymer 'Active'?, *Macromolecular Bioscience*, 19(7), 1900082, (2019)

*Performed all of the experimental work relating to safranin-O as well as part of experimental work for other samples, performed data analysis and assisted in the writing process.*



Wilkins, L.E., Hasan, M., **Fayter, A.E.R.**, Biggs, C.I., Walker, M. & Gibson, M.I., Site-specific Conjugation of Antifreeze Proteins onto Polymer-stabilized Nanoparticles, *Polymer Chemistry*, 10, 2986-2990, (2019)

*Performed all sucrose microscopy experiments as well as part of splat microscopy assays and assistance in protein expression. Also assisted in the writing process.*

Mitchell, D., **Fayter, A.E.R.**, Deller, R.C., Hasan, M., Gutierrez-Marcos, J. & Gibson, M.I., Ice-Recrystallization Inhibiting Polymers Stabilize Proteins Against Freeze/Thaw Stress Removing Need for Organic Solvents, *Materials Horizons*, 6, 364-368 (2019)

*Performed all assays on Green Fluorescent Protein and Insulin. Expressed the proteins used and performed all related data analysis. Also performed a significant amount of the writing process.*

Stubbs, C., Wilkins, L.E., **Fayter, A.E.R.**, Walker, M. & Gibson, M.I., Multivalent Presentation of Ice Recrystallization Inhibiting Polymers on Nanoparticles Retains Activity, *Langmuir*, 35(23), 7347-7353, (2019)

*Performed all sucrose microscopy experiments as well as part of splat microscopy assays. Also assisted in the writing process.*

Hasan, M., **Fayter, A.E.R.** & Gibson, M.I., Ice Recrystallization Inhibiting Polymers Enable Glycerol-Free Cryopreservation of Microorganisms, *Biomacromolecules*, 19(8), 3371-3376 (2018)

*Performed all experimental work bar confocal microscopy, and data analysis on all data generated. Also performed a significant amount of the writing process.*

**Fayter, A.E.R.**, Gibson, M.I., & Draper, E., Sub-Zero Temperature Mechanically Stable Low Molecular Weight Hydrogels, *Materials Chemistry B*, 6, 7274-7279, (2018)

*Performed all nucleation experiments and related data analysis. Assisted in the writing process.*

Graham, B., **Fayter, A.E.R.**, Houston, J.E., Evans, R.C. & Gibson, M.I., Facially Amphipathic Glycopolymers Inhibit Ice Recrystallization, *J. Am. Chem. Soc.* **140**(17), 5682-5685, (2018)

*Performed all sucrose microscopy experiments and related data analysis. Also assisted in the writing process.*

Biggs, C.I., Bailey, T.L, Graham, B., Stubbs, C., **Fayter, A.E.R.**, & Gibson, M.I., Polymer Mimics of Biomacromolecular Antifreezes, *Nature Communications*, **8**(1), 1546. (2017)

*Wrote section of review on macroscopic properties of antifreeze(glyco) proteins and assisted in production of various figures throughout.*

Blackman, L.D., Varlas, S., Arno, M.C., **Fayter, A.E.R.**, Gibson, M.I. & O'Reilly, R.K, Permeable protein-loaded polymersome cascade nanoreactors by polymerization-induced self-assembly, *ACS Macro Letters*, **6** (11), 1263-1267, (2017)

*Performed all protein expression experiments and related data analysis. Assisted in the writing process.*

Seidl, M., **Fayter, A.E.R.**, Stern, J., Zifferer, G & Loerting, T. Shrinking water's no man's land by lifting its low-temperature boundary, *Phys. Rev. B.*, **91**, 144201, (2015)

*Performed initial blind experiments and control experiments. Also assisted in the writing process.*